I. R. IRAN

ISSN: 1728-1431
e-ISSN: 1735-9244

International Journal of Engineering

Journal Homepage: www.ije.ir

MERC

TRANSACTIONS A: Basics

Volume 33, Number 10, October 2020

Materials and Energy Research Center

In the Name of God

INTERNATIONAL JOURNAL OF ENGINEERING
Transactions A: Basics

DISCLAIMER

The publication of papers in International Journal of Engineering does not imply that the editorial board, reviewers or publisher accept, approve or endorse the data and conclusions of authors.

International **J**ournal of **E**ngineering *Transactions A: Basics* (ISSN 1728-1431) (EISSN 1735-9244)
International **J**ournal of **E**ngineering *Transactions B: Applications* (ISSN 1728-144X) (EISSN 1735-9244)
International **J**ournal of **E**ngineering *Transactions C: Aspects* (ISSN 2423-7167) (EISSN 1735-9244)
Web Sites: www.ije.ir & www.ijeir.info E-mails: ije.editor8@gmail.com, Tel: (+9821) 88771578, Fax: (+9821) 88773352
Materials and Energy Research Center (MERC)

ISSN: 1728-1431, e-ISSN: 1735-9244

International Journal of Engineering, Volume 33, Number 10, October 2020

CONTENTS:

Civil Engineering

ISSN: 1728-1431, e-ISSN: 1735-9244

International Journal of Engineering, Volume 33, Number 10, October 2020

Electrical & Computer Engineering

Industrial Engineering

Material Engineering

ISSN: 1728-1431, e-ISSN: 1735-9244

International Journal of Engineering, Volume 33, Number 10, October 2020

Mechanical Engineering

Petroleum Engineering

International Journal of Engineering

Journal Homepage: www.ije.ir

In-depth Investigation of Project Planning and Control Software Package Application in the Construction Industry of Iran

A. Alvanchi*[a], N. Shiri[a], H. Alikhani[b]

[a] *Department of Civil Engineering, Sharif University of Technology, Tehran, Iran*
[b] *Department of Architecture, Texas A&M University, United States*

P A P E R I N F O

Paper history:
Received 06 March 2020
Received in revised form 14 August 2020
Accepted 26 August 2020

Keywords:
Planning and Control Software
Construction Industry
Project Management
Project Performance

A B S T R A C T

Inefficient project planning and control have been identified as the main contributor to the reduced performance of the construction industry in Iran. Meanwhile, improper use of planning and control software packages (PPCSPs) in these projects can be a key factor in this reduced performance. This study investigates different aspects of the PPCSP applications to draw the role of PPCSPs in the planning and control processes of construction projects in the country using a survey-based method. It is found that only 32.5% of the construction companies in Iran highly or very highly use PPCSPs. The low level of skill and the lack of management support are two main contributing factors to this reduced PPCSP application. The quality of the academic and vocational project management training programs and the lack of dependable PPCSP technical support are argued as possible sources of the issue. The identified PPCSP pattern in Iran is compared with the results reported for several developed and in-transition countries. This comparison reveals that Iran and in-transition countries fall deeply behind in employing PPCSPs in their construction projects compared to the developed countries.

***doi**: 10.5829/ije.2020.33.10a.01*

NOMENCLATURE

ANOVA	Analysis of Variance	Ph.D.	Doctor of Philosophy
CEO	Chief Executive Officer	PM	Project Management
CPI	Cost Performance Indicator	PPCSP	Project Planning and Control Software Packages
MSP	Microsoft Project		

1. INTRODUCTION

A considerable effort during project implementation is made on planning and control processes [1]. Various methods and tools are introduced to facilitate and improve these two processes during the project implementation. Project planning and control software packages (PPCSPs) are among the most frequently used tools to assist these two project management processes [2]. Positive impacts of PPCSPs on project planning and control processes in general, on the project performance have been identified in the past research efforts [3, 4]. Applications of PPCSPs cover different areas of project management (PM) body of knowledge including time, cost, resource, and communication [5, 6]. It is found that the proper use of PPCSPs increases the chance of project success [3].

Gharaibeh [6] developed a scoring model to evaluate PPCSPs capabilities. He found time management as the most important feature of the PPCSPs with a relative impact weight of 33%. Subramani et al. [7] found that use of industrialized building systems and PPCSP could save a total of 405 days or 42% of the project duration in their 18-floor building case. Pellerin et al. [4] statistically analyzed actual data of 21 large engineering projects and found that large cost-performance improvement in projects with deep engagement of PPCSPs. Riņģis and Bērziša [8] studies revealed that using Redmine, a free

*Corresponding Author Institutional Email: *alvanchi@sharif.edu* (A. Alvanchi)

Please cite this article as: A. Alvanchi, N. Shiri, H. Alikhani, In-depth Investigation of Project Planning and Control Software Package Application in the Construction Industry of Iran, International Journal of Engineering (IJE), IJE TRANSACTIONS A: Basics Vol. 33, No. 10, (October 2020)... 1817-1825

project management software, improves cost performance indicator (CPI) of projects in the State Social Insurance Agency case.

Mellentien and Trautman [9] performed a benchmark test on 1560 instances of precedence resource-constrained scheduling problems to evaluate the resource allocation capabilities of five different software packages. They concluded that although these software packages are valuable supports for the management of resource-constrained projects, they still fall short in comparison to the best practices. Reddy et al. [10] used Primavera P6 in two construction projects in Dubai, Emirate, to individually and concurrently employ the resource leveling capabilities of the software. They found that the combined resource leveling can reduce resource demand by 5.65%. Aguilera et al. [11] performed a survey on 77 different project managers and found that proper use of PPCSP enhances project managers' performance by 24.6%. Hilmi et al. [12] surveyed the use of computer software in the construction industry of Iraq. In addition to the potential project cost and time improvement, they found that the use of computer applications can improve transparency and reduce corruption. Alojairi et al. [13] identified the positive impacts of PPCSPs on project scheduling and resource allocation in the case study of Saudi Arabia Telecommunication Company. However, they found two constraints to overcome during the project implementation for every three benefits created by the use of PPCSPs. Despite various advantages reported for PPCSPs in projects, there are also disadvantages and limitations found [14]. Their high cost, the complexity of their features, and the low flexibility in meeting specified project needs were identified disadvantages. Regardless of all advantages and disadvantages found for PPCSPs in the project management processes, the important role of PPCSPs in the PM is undeniable.

Currently, many construction projects in Iran suffer from time delays and cost overruns. Researchers have identified poor project planning and control as the main causes of the reduced performance. Asnaashari et al. [15] found traditional management style and poor project scheduling among the top causes of project delays in Iranian construction projects. Khoshgoftar et al. [16] identified poor project planning skills of contractors as one of the key influential factors on construction projects. Fallahnejad [17] identified inaccurate project schedule development as one of the main root causes of the project delays in gas pipeline projects. Rafieizonooz et al. [18] identified a mistaken time and cost estimation, low level of contractors project planning skill, and poor project control as the main causes of delays in construction projects conducted by Tehran municipality. Derakhshanalavijeh and CardosoTeixeira [19] found inaccurate cost estimations and improper planning as the main causes of cost overrun in oil and gas industry in the country. Alvanchi et al. [20] identified incorrect project duration estimation among the main causes of project delays in residential building projects in Mashad, Iran.

Given the considerable impacts of PPCSPs on the planning and control of construction projects, a part of current planning and control issues in the country might return to the PPCSPs. In this perspective identifying the current condition of PPCSPs in the construction projects of the country can provide valuable information for adjusting policies and future moves. It can help construction project managers to measure their organizations' standings and to adjust their efforts in employing PPCSPs in their projects. Likewise, it would be a guide for software corporations in the country to adjust their directions for PPCSPs' development and support. However, investigations on the PPCSPs' condition in the construction projects are still missing in the county. To respond to this need, the aim of this study was set to recognize the current pattern of PPCSPs applications in the construction projects in Iran. Following, in section 2, the questionnaire-based method adopted in the research is explained. In sections 3 and 4 different parts of the designed questionnaire are described and the pilot and actual questionnaire distributions are discussed. The research findings and results are presented and analyzed in section 5, and recommendations are made to properly respond to the identified issues of the PPCSP applications in the country. Finally, in section 6, the research outcomes are summarized and concluded.

2. RESEARCH METHODOLOGY

A comprehensive picture of the PPCSPs applications in the construction projects could be drawn from the collective experience of the practitioners engaged in the construction project planning and control processes. There is no accurate estimation of the population size of these practitioners. However, it is estimated that the construction market in the country has reached $154 billion in 2016 and about 500'000 civil engineers work in this market. Consequently, it was expected that the population size of the target practitioners reaches tens of thousands. With a large number of the target statistical society, a questionnaire-based survey was adopted in the research. Construction project planning and control specialists, construction project managers, construction job site superintendents, and chief executive officers (CEOs) working in construction companies were the main groups in the target society. Practitioners in each group were involved in project planning and control activities with different perspectives. This could help reveal different aspects of PPCSPs applications and their related issues.

In the adopted research method, first, similar investigations on PM computer software packages in different regions were reviewed. A questionnaire-based method was adopted in the research. Therefore, in the second step, the questionnaire was designed based on the identified factors from the literature and the experts' input. Third, a pilot distribution of the questionnaire was performed to estimate the required number of samples and validating the designed questions before the actual questionnaire distribution. The validated designed questionnaire was distributed among different individuals in the target society in the fourth step. In the fifth step, the statistical reliability of the collected data was investigated before analyzing the collected data. In the sixth step, the statistical analysis of the collected data was performed to draw the PPCSP application pattern in the country. In this step, descriptive statistic values were calculated to represent the current standing of the corresponding items. Furthermore, the impacts of various independent variables on the dependent variables were investigated using a one-way analysis of variance (ANOVA) test. Finally, the achieved results were discussed and concluded to draw an overall picture of the current standing of PPCSPs applications. Recommendations were made to overcome the identified challenging issues.

3. SURVEY DESIGN

A total of 26 questions were designed in five different sections to extract the current condition of different aspects of PPCSPs in the country. The questionnaire was initially designed based on the identified applications and features of PPCSPs in the literature. The questions were then refined in consultation with a group of three PM experts with more than 10 years of working experience in planning and managing construction projects in the country. Later on and before the actual distribution of the questionnaire, the questions were validated by 15 respondents who participated in the pilot run of the survey. The majority of questions were based on a five-level Likert scale with 1) very low, 2) low, 3) moderate, 4) high, and 5) very high scores assigned. Following, each question section is briefly explained.

Section 1. Background information of the respondents: In this section, five different independent factors from the survey participants were collected. The job position, education level, field of study, size of the construction companies, and the type of construction projects were collected in this section.

Section 2. Diversity of PPCSPs: In this section different types of PPCSPs used and their frequencies were asked.

Section 3. PPCSPs and project specifications: Frequency of PPCSPs applications in construction projects with different sizes and complexities were asked in this section.

Section 4. PPCSP features: Three common planning and control features of PPCSPs in the construction projects, including tim [6,7,12,13], cost [4,8,12], and resource [9, 10,13], were questioned in this section.

Section 5. Management approach to PPCSPs: In this section levels of the top management's involvement and support in upgrading and purchasing PPCSPs, holding training sessions, and setting related guidelines and instructions for applying PPCSPs in the construction projects were asked.

The pilot study was conducted in the participation of 15 practitioners. They were asked to, first, answer the questions and, then, state their opinions about the validity of the questionnaire structure. Several questions were adjusted according to the feedback received from the participants in the pilot survey. The achieved results in the pilot survey were also used for estimating the minimum number of responses required. According to Cochran [21], with the maximum standard deviation of 1.44 achieved for the scores of various questions in the pilot survey, accepted confidence level of 95%, and accepted error level of 0.2, the required number of valid questionnaire responses became 200.

4. DATA COLLECTION

In the actual distribution, questionnaires were distributed among the target society and the responses were collected until 200 required responses were reached. In the end, a total number of 330 paper-questionnaires were distributed which indicated the response rate of 60%. To reach evenly distributed samples, a maximum number of three responses were collected from each contributing construction company. As a result, the collected responses were received from 74 different companies. The reliability of the collected data was confirmed by Cronbach's alpha test with a coefficient value of 0.879. About half of the respondents belonged to the construction companies with more than 50 personnel and the other half belonged to the construction companies with less than 50 personnel. Construction companies' CEOs with a frequency of 34%, job site superintendents with 27%, project managers with 15.5%, and project planners with 13%, respectively formed the highest share among the respondents. About 52.5% of respondents had an education background with Bachelor's degrees, 32.5% had Master's or Ph.D. degrees, and 15% had an Associate's degree. Figure 1 presents the frequency distribution of different groups of respondents. The majority of the respondents had experiences in the building construction projects with a frequency of 60.5% followed by the road construction projects with 49.5%, and the industrial construction projects with 32%.

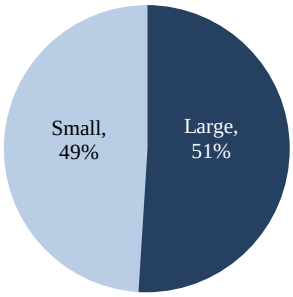

(a) Company size

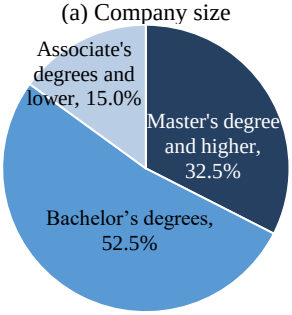

(b) Education

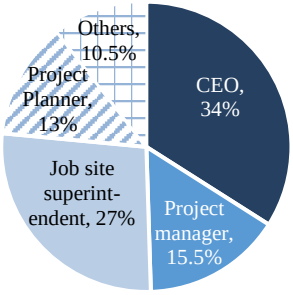

(c) Position

Figure 1. Demographic distribution of the survey participants

5. FINDINGS

Achieved results of the survey revealed different aspects of the PPCSPs applications pattern in the construction projects of Iran. Table 1 summarizes this pattern. Further explanation regarding the achieved results is provided in the rest of the section. In each sub-section, if applicable, comparisons were also made between the results achieved for the construction companies in Iran and the ones reported in the literature for other regions.

5. 1. Frequency of PPCSP Applications About 71% of respondents indicated they use some types of PPCSPs during the planning and control of construction projects. This percentage is less than the frequency of PPCSP applications reported in the past studies in 1994 in Australia with 77% [6], in the United States in 1992 and 2001 were 92 and 97%, respectively [22] and 100% portion achieved for international contracting companies [23]. However, it shows a higher percentage compared to the results achieved for Croatia with 40% [24] and Ghana with 39% [25] frequency of PPCSPs applications. The recent advances in information technology (IT) and its full-fledged penetration in different aspects of life raise the expectation that IT-based tools dominate in the construction industry. This takeover is conceivable from the trend of surveys in the western construction companies and is represented in the increased applications of PPCSPs in the construction projects. However, survey results from in-transition countries still do not represent this dominance.

TABLE 1. Summary of results achieved for application pattern of PPCSPs in the construction companies in Iran

Frequency of PPCSPs applications	71%
Frequency of high or very high level of PPCSPs applications	32.5%
Positive impacts of PPCSPs on costruction projects	70%
Most applicable PPCSPs	MSP, Primavera P6 and MS Excel
Identified contributing factors	Educational level, level of skill in using PPCSPs, top management support, company size, project size, project complexity
Identified non-contributing factors	Job position
Most employed feature	Time planning and control

Although 71% of the respondents indicated that they use PPCSPs in their construction projects, only 32.5% of them asserted that they highly or very highly use PPCSPs in the projects. Therefore, a majority of 67.5% of construction companies do not highly or very highly incorporate PPCSPs in their projects. They either depend on traditional planning and control methods or even lack implementation of proper planning and controlling processes in their projects. In the survey, about 58% of respondents from small companies, with less than 50 construction workers on the job site, indicated that they use PPCSPs in their projects. This portion was 83% for large companies, with more than 50 construction workers on the job site. A one-way ANOVA test identified the company size as a contributing factor to the frequency of PPCSP applications with a significant value of 0.02. This factor has also been identified as a contributing factor in the survey conducted by Ali et al. [3] among Project Management Institute's (PMI's) members.

5. 2. PPCSPs Impacts on PM About 70% of respondents found impacts of PPCSPs on the construction projects very highly or highly positive. Five-level Likert scores received for the positive impacts of PPCSPs were averaged based on different job positions as presented in Figure 2a. The average score of 3.73

achieved for CEOs of construction companies was the lowest among all four different job positions that participated in the survey. However, differences in different job positions were not identified as significant in the one-way ANOVA test. The relation between respondents' educational level and their perception about the positive impacts of PPCSPs was also assessed as presented in Figure 2b. The lowest average score here was achieved for practitioners with associate's degrees with an average of 3.23. In the one-way ANOVA test, the educational level of respondents was identified as a contributing factor to their perception about the advantages of PPCSPs with a significant value of 0.013.

5. 3. Type of PPCSPs Among a variety of computer software packages, Microsoft Project (MSP), Primavera P6 and Microsoft Excel were the only software packages used in the planning and control process of construction projects. No domestically developed PPCSP was reported. No practitioners indicated that they have embedded project planning and control modules into their organization's Enterprise Resource Planning or other management information systems. Among respondents with experience in using PPCSPs, MSP was the most popular PPCSP with a total frequency of 87%. It was followed by Primavera P6 with a frequency of 32% and Microsoft Excel with a frequency of 23%. Meanwhile, 50% of respondents with experience in using PPCSPs indicated they use MSP as their only PPCSP; 4% indicated that they use P6 as their only PPCSP; 23% of them indicated they use both MSP and P6 in their projects. About 9% responded that they only use Excel in project planning and control activities. Even though Excel is widely used computer software for general data management and calculations, it lacks many required capabilities from PPCSPs. Expectedly, many required planning and control features are ignored in these projects. Figure 3 presents the frequency of different combinations of PPCSPs used in the construction projects of the country.

Similar to the achieved pattern in Iran, in Malaysia, MSP was the most widely used PPCSP with 96% frequency followed by Excel (88%) and Primavera (65%). Likewise, In Australia, MSP was reported as the most widely used PPCSP with 65% frequency [6]. This order, however, was not the same in the US. According to Liberatore et al. [22], in the US Primavera with 51% and MSP with 24% were the most frequently used PPCSPs in the construction industry. Galloway [26] reported that 65% of contractors in the US use Primavera while 22% apply MSP in their projects. Primavera was also the most widely used PPCSP in Italy [27]. Nevertheless, the frequency of using PPCSP was completely different in Eastern Europe. According to Vukomanović et al. [28], the most prevalent PPCSP was Excel with 56% followed by MSP with 26.5%, GALA with 7%, and Primavera with 4.6%.

Although about 70% of respondents identified the use of PPCSPs in the construction projects very highly or highly positive, only 32.5% of them, highly or very highly, were applying PPCSPs in their projects. One reason for this gap can be linked to the low skill level of the practitioners in working with PPCSPs. For example, while 80% of practitioners with experience of using PPCSPs in the construction project were using MSP, only 46% of them were very highly or highly skilled in using this software. Here, a one-way ANOVA test was conducted by SPSS to assess whether the level of skill is a contributing factor to the level of PPCSPs applications in construction projects. The test identified the skill as a contributing factor to the level of PPCSPs applications with a significant value of 0.000. This Low level of skill in PPCSPs was despite different project planning and control courses offered in the engineering

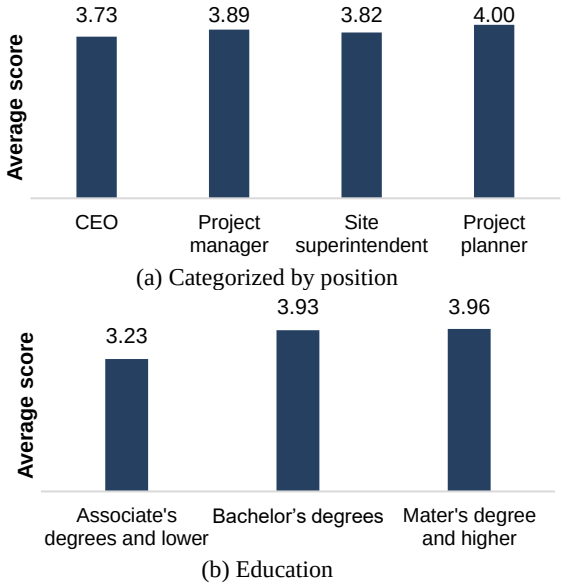

Figure 2. Respondents' perception about the positive impacts of PPCSPs on construction projects

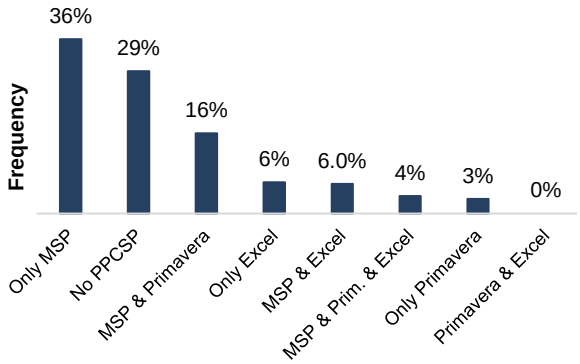

Figure 3. Frequency of different types of PPCSPs used in the construction projects

and management departments of the Universities across the country. There are also many MSP and P6 training courses held by vocational training institutions. Holding theoretical and non-practical courses in the engineering departments is an issue previously identified in Iranian Universities. This issue might have contributed to the lack of construction practitioner's knowledge about project planning and control and the way PPCSPs can be practically applied to construction projects.

5. 4. PPCSPs and Project Specification PPCSPs were more used in large and complex projects than small and simple projects. The PPCSPs applications range from 80% in the large to 11% in the small projects. The PPCSPs were used in 83% of the complex projects and were only used in 16% of the low complexity projects. The project size and complexity have also been identified as contributing factors to the level of PPCSP applications in past research efforts (e.g., [3, 5, 22, 23]). Figures 4 and 5 present results achieved for the frequency of PPCSPs applications concerning the project size and complexity.

5. 5. PPCSPs Features Time planning and control is the main feature of PPCSPs used in construction projects. About 70% of the respondents indicated PPCSPs are very highly or highly used for time planning and control. This portion was achieved 50% for the cost and 43.5% for the resource planning and control features of PPCSPs. Figure 6 presents the extent of PPCSP applications in the planning and control of the construction projects' time, cost, and resources. Project scheduling has also been previously identified as the most applicable feature of PPCSPs in construction projects in Italy [27] and the top international contractors [23]. In the construction projects in Eastern Europe, however, cost and material-resource planning have been identified as the most prevalent features used [28].

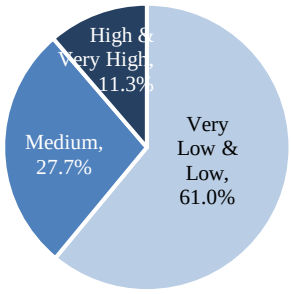

(a) Small projects

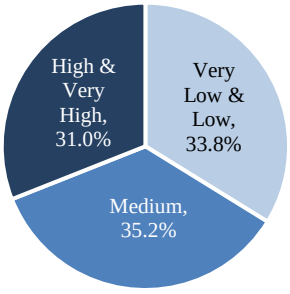

(b) Medium projects

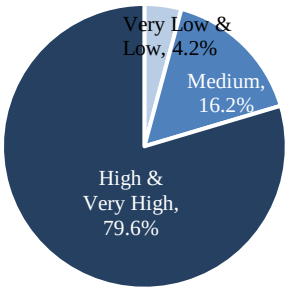

(c) Large projects

Figure 4. Frequency of PPCSPs applications in different sizes of construction projects

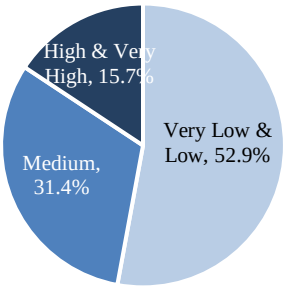

(a) Simple projects

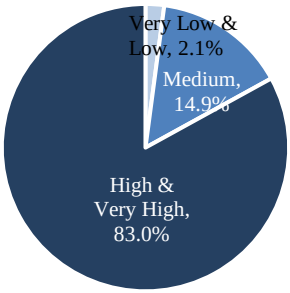

(b) Complex projects

Figure 5. Frequency of PPCSPs applications with respect to the project complexity

5. 6. Management Approach to PPCSPs Four different aspects of management support investigated in the research were 1) purchasing and upgrading PPCSPs, 2) setting training sessions, 3) urging PPCSP applications in construction projects, and 4) acknowledging PPCSPs' advantages. Among those who were using PPCSPs, at least 60% asserted that the commitment and timely action of their companies' management to all four above-mentioned aspects are in the medium or low level.

A low level of management support implies that companies' management does not see high benefits from PPCSPs applications in construction projects. Poor implementation of PPCSPs in construction projects

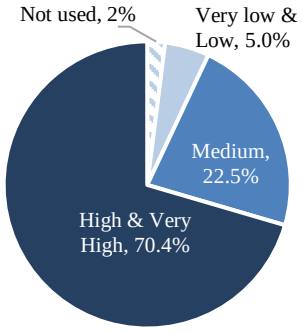

(a) Time

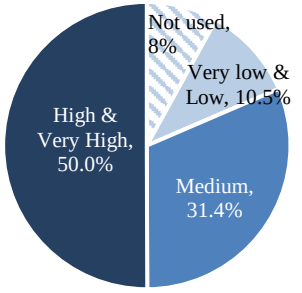

(b) Cost

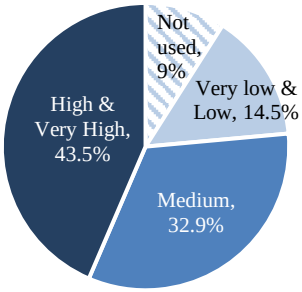

(c) Resource

Figure 6. Extent of PPCSP applications in planning and control of project time, cost and resource

resulting in minimal advantages might be a cause. Here again, the size of the construction companies was identified as a contributing factor to the level of the management support for the PPCSPs in the conducted one way ANOVA test. The test identified that management support is lower in small companies compared to large companies. Figure 7 presents the frequency of high and very high levels of different aspects of management support to PPCSPs according to the company size. It was also investigated whether the respondents' position is a contributing factor to the achieved level of management support. One way ANOVA test, however, did not identify respondents' position, e.g., CEO, PM, site superintendent, and project planner, as a contributing factor here. This means respondents with different positions have fairly similar points of view regarding different aspects of the management support to PPCSPs in construction projects.

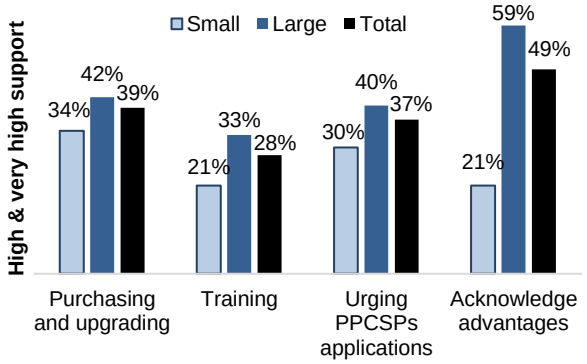

Figure 7. Frequency of high and very high level of different aspects of the management support to PPCSPs according to the company size

5. 7. Discussion The achieved results of the research indicated that despite the perceived benefits of PPCSPs in improving the construction project management, their applications are still quite low. The majority of construction companies depend on traditional project planning and control methods or even do not use them. Several contributing factors to the current conditions were identified in the research. A low level of skill was identified as a contributing factor to the low level of PPCSPs application in construction projects. Here, a reason can return to the education system which is unable to properly train and prepare prospective construction practitioners. The inability of the construction companies to hire qualified individuals can be another reason. Furthermore, the research identified the CEOs' perception of the positive impacts of PPCSPs on the project management processes the least among all other practitioners. This result conforms with the majority of responses claiming a low or medium level of their companies' management commitment and timely action to support PPCSPs implementation in construction projects. Lack of management knowledge regarding the importance of using proper project management tools can be a contributor. This means either non-qualified managers are assigned to the management positions in the construction companies or the education system lacks to properly train different aspects of construction project management.

6. CONCLUSION

Construction projects suffer from high-cost overruns, completion delays, and in general low project performance in Iran. Project planning and control software packages can make a big difference in the way that construction projects are run. Proper utilization of PPCSPs in the construction companies can improve project performance and consequently can increase the

profit margin of these companies. Given the current financial challenges imposed by foreign relations to the construction industry, internal improvement of project management methods can play an essential role. For the first time, this research investigated the pattern of project planning and control software packages and their impacts on the construction projects in Iran. The achieved results in this investigation indicated that a part of the reduced performance can be linked to the way PPCSPs are applied in the construction projects in the country. The PPCSP pattern identified in this investigation forms a basis for the construction companies to measure themselves and adjust their organizational policies regarding applications of PPCSPs. The achieved results alert the academics and contributors to the construction project management courses to update their curriculums and teaching methods. The results can also help PM software developers to extract the requirements of the construction companies and incorporate them into their prospective PPCSP development.

This investigation revealed that only one-third of the construction companies highly or very highly use PPCSPs in the planning and control processes of the construction projects. The skill level of the practitioners in working with PPCSPs and the level of management support were identified as contributing factors to this low level of PPCSPs applications. This condition is regardless of many PM-related courses and training programs offered at the country's universities and vocational institutes. This trend, however, puts the quality of the PM training programs in the country critically in doubt. Investigations regarding the adopted teaching methods and the materials taught in the project management training programs are required. The suitability of these training programs and their possible impacts on the low level of PPCSPs applications in construction projects should be assessed. Updates to the curriculum and topics taught in these courses are likely required. Especially, teaching PPCSP in parallel to the practical methods used in the construction projects can be beneficial. It should also be noted that currently there is no dependable technical support for the foreign PPCSPs applied in the country. Furthermore, there are no commonly accepted and widely known domestically developed PPCSPs in the country. New research efforts that investigate the condition of the PM software developers in the country and identifies the gaps they can fill for improving PPCSP applications are recommended.

Given the critical role of the building and construction projects in the country, any improvements in this sector can make a significant change in the country as a whole. As a result, further investigations in this area of research are strongly encouraged. One of the main sources of the identified deficiencies in this research returns to academia. Therefore, further research and investigations in this field performed by academics can directly be used in the teaching materials and reference books. Improved project management training courses and properly trained construction practitioners are the implicit results of these investigations.

7. REFERENCES

1. Guide, P., "A guide to the project management body of knowledge. Sixth edit", ***Project Management Institute, Inc***, (2017), 2-111.
2. Puška, A., Stojanović, I., Maksimović, A. and Osmanović, N., "Evaluation software of project management used measurement of alternatives and ranking according to compromise solution (MARCOS) method", ***Operational Research in Engineering Sciences: Theory and Applications***, Vol. 3, No. 1, (2020), 89-102. DOI: 10.31181/oresta2001089p
3. Bani Ali, A.S., Anbari, F.T. and Money, W.H., "Impact of organizational and project factors on acceptance and usage of project management software and perceived project success", ***Project Management Journal***, Vol. 39, No. 2, (2008), 5-33. DOI: 10.1002/pmj.20041
4. Pellerin, R., Perrier, N., Guillot, X. and Léger, P.-M., "Project management software utilization and project performance", ***Procedia Technology***, Vol. 9, (2013), 857-866. DOI: 10.1016/j.protcy.2013.12.095
5. Gamil, Y. and Rahman, I.A., "Identification of causes and effects of poor communication in construction industry: A theoretical review", ***Emerging Science Journal***, Vol. 1, No. 4, (2017), 239-247. DOI: 10.28991/ijse-01121
6. Gharaibeh, H.M., "Developing a scoring model to evaluate project management software packages based on iso/iec software evaluation criterion", ***Journal of Software Engineering and Applications***, Vol. 2014, (2013). DOI: 10.4236/jsea.2014.71004
7. Subramani, T., Sarkunam, A. and Jayalakshmi, J., "Planning and scheduling of high rise building using primavera", ***International Journal of Engineering Research and Applications***, Vol. 4, No. 6, (2014), 134-144. ISSN: 2248-9622
8. Riņģis, M. and Bērziša, S., "Efficiency measurement of project management software usage at state social insurance agency", ***Information Technology and Management Science***, Vol. 19, No. 1, (2016), 65-70. DOI: 10.1515/itms-2016-0013
9. Mellentien, C. and Trautmann, N., "Resource allocation with project management software", ***OR-Spektrum***, Vol. 23, No. 3, (2001), 383-394. DOI: 10.1007/PL00013358
10. Reddy, B., Nagaraju, S. and Salman, M., "A study on optimisation of resources for multiple projects by using primavera", ***Journal of Engineering Science and Technology***, Vol. 10, No. 2, (2015), 235-248. http://jestec.taylors.edu.my/V10Issue2.htm
11. Aguilera, C., Villalobos, M.T. and Dávila, A., "Impact of organizational and user factors on the acceptance and use of project management software in the medium-sized company in lima", in International Conference on Software Process Improvement, Springer., 274-284. DOI: 10.1007/978-3-319-69341-5_25
12. Hilmi, R.R.A.R., Breesam, H.K. and Saleh, A.H., "Readiness for e-tendering in the construction sector-designing a computer programme", ***Civil Engineering Journal***, Vol. 5, No. 8, (2019), 1764-1773. https://core.ac.uk/download/pdf/276327761.pdf
13. Alojairi, A., Bazarah, A., Basiouni, A., Tan, K.M.A. and Ali, H.M., "A socio-technical perception on the impact of project management software in logistics and distribution center: A case study in saudi arabia telecommunication company", ***Business and***

Economic Horizons, Vol. 15, No. 4, (2019), 523-541. DOI: 10.15208/pieb.2019.3

14. White, D. and Fortune, J., "Current practice in project management—an empirical study", ***International Journal of Project Management***, Vol. 20, No. 1, (2002), 1-11. DOI: 10.1016/S0263-7863(00)00029-6
15. Asnaashari, E., Knight, A., Hurst, A. and Farahani, S.S., "Causes of construction delays in iran: Project management, logistics, technology and environment", in Procs 25th Annual ARCOM Conference. 7-9. http://www.arcom.ac.uk/-docs/newsletter/2009_26-1.pdf
16. Khoshgoftar, M., Bakar, A.H.A. and Osman, O., "Causes of delays in iranian construction projects", ***International Journal of Construction Management***, Vol. 10, No. 2, (2010), 53-69. DOI: 10.1080/15623599.2010.10773144
17. Fallahnejad, M.H., "Delay causes in iran gas pipeline projects", ***International Journal of Project Management***, Vol. 31, No. 1, (2013), 136-146. DOI: 10.1016/j.ijproman.2012.06.003
18. Rafieizonooz, M., Salim, M.R., Khankhaje, E., Warid Hussin, M. and Zarebidaki, A., "Determining the causes of delay by using factor analysis in tehran's construction projects", in Applied Mechanics and Materials, Trans Tech Publ. Vol. 735, 109-116. DOI: 10.4028/www.scientific.net/AMM.735.109
19. Derakhshanalavijeh, R. and Teixeira, J.M.C., "Cost overrun in construction projects in developing countries, gas-oil industry of iran as a case study", ***Journal of Civil Engineering and Management***, Vol. 23, No. 1, (2017), 125-136. DOI: 10.3846/13923730.2014.992467
20. Alvanchi, A., "Evaluating factors causing delay in residential building projects of mashhad", (2019). DOI: 10.24200/j30.2018.2285.2163
21. Cochran, W.G., "Sampling techniques, John Wiley & Sons, (2007).
22. Liberatore, M.J., Pollack-Johnson, B. and Smith, C.A., "Project management in construction: Software use and research directions", ***Journal of Construction Engineering and Management***, Vol. 127, No. 2, (2001), 101-107. DOI: 10.1061/(ASCE)0733-9364(2001)127:2(101)
23. Demirceken, O., Keskin, B. and Sonmez, R., "Project & portfolio management software use in construction industry", ***International Organizing Committee***, No. 420. http://2016.creative-construction-conference.com/proceedings/CCC2016_65_Demirceken.pdf
24. Fabac, R., Radošević, D. and Pihir, I., "Frequency of use and importance of software tools in project management practice in croatia", in Proceedings of the ITI 2010, 32nd International Conference on Information Technology Interfaces, IEEE., 465-470. https://ieeexplore.ieee.org/abstract/document/5546330
25. Gariba, Z.P., "Application of project management software in turnkey electrification projects in ghana", in The 4th Annual IEEE International Conference on Cyber Technology in Automation, Control and Intelligent, IEEE., 638-643. DOI: 10.1109/CYBER.2014.6917539
26. Galloway, P.D., "Survey of the construction industry relative to the use of cpm scheduling for construction projects", ***Journal of Construction Engineering and Management***, Vol. 132, No. 7, (2006), 697-711. DOI: 10.1061/(ASCE)0733-9364(2006)132
27. Damiani, L., Revetria, R., Svilenova, I. And Giribone, P., "Survey and comparison of the project management softwares used by engineering, procurement and construction companies", ***Advances in Energy and Environmental Science and Engineering***, Vol. 6, (2015). http://www.wseas.us/e-library/conferences/2015/Michigan/LENFI/LENFI-11.pdf
28. Vukomanović, M., Radujković, M. and Dolaček Alduk, Z., "The use of project management software in construction industry of southeast europe", ***Tehnički Vjesnik***, Vol. 19, No. 2, (2012), 249-258. https://hrcak.srce.hr/83858

Persian Abstract

چکیده

برنامه‌ریزی و کنترل ناکارآمد پروژه به عنوان یکی از اصلی‌ترین عوامل کاهش بهره‌وری و کارایی در صنعت ساخت و ساز ایران شناخته شده است. در این میان استفاده نادرست از نرم افزارهای برنامه ریزی و کنترل پروژه در پروژه‌های عمرانی می‌تواند یکی از عوامل موثر در این کاهش بهره‌وری و کارایی باشد. این پژوهش به بررسی جنبه‌های مختلف نرم‌افزارهای برنامه ریزی و کنترل پروژه پرداخته است و نقش آن‌ها را در روند برنامه ریزی و کنترل پروژه‌های عمرانی کشور با استفاده از تحقیق میدانی شناسایی نموده است. در نتیجه انجام این پژوهش مشخص شد که تنها ۳۲/۵٪ از پیمانکاران پروژه‌های عمرانی در کشور به صورت موثر و جدی از نرم‌افزارهای برنامه‌ریزی و کنترل پروژه استفاده می‌کنند. سطح پایین مهارت مهندسین و کارشناسان فعال در پروژه‌های عمرانی در استفاده از این نرم‌افزارها و عدم حمایت مدیریت ارشد به عنوان دو عامل اصلی موثر در این امر شناخته شده اند. کیفیت پایین برنامه‌های آموزشی مدیریت پروژه که در دانشگاه‌ها و آموزشگاه‌های تخصصی کشور ارائه می‌شود و فقدان حمایت فنی و خدمات پس از فروش قابل اعتماد از نرم‌افزارهای برنامه‌ریزی و کنترل پروژه به عنوان عوامل احتمالی این مشکل در کشور شناسایی شده‌اند. در این میان الگوی شناسایی شده برای استفاده از نرم‌افزارهای برنامه‌ریزی و کنترل پروژه در ایران با نتایج ارائه شده برای چندین کشور توسعه یافته و در حال توسعه مقایسه شده است. این مقایسه نشان داد که ایران و سایر کشورهای در حال توسعه مورد مطالعه، به مراتب از سطح پایین‌تری از نرم‌افزارهای برنامه‌ریزی و کنترل پروژه در مدیریت پروژه‌های عمرانی در مقایسه با کشورهای توسعه یافته استفاده می‌نمایند.

IJE TRANSACTIONS A: Basics Vol. 33, No. 10, (October 2020) 1826-1841

International Journal of Engineering

Journal Homepage: www.ije.ir

Prediction of Mechanical Properties of Frozen Soils Using Response Surface Method: An Optimization Approach

M. Vahdani*[a], M. Ghazavi[a], M. Roustaei[b]

[a] *Faculty of Civil Engineering, K. N. Toosi University of Technology, Tehran, Iran*
[b] *Civil Engineering Department, Islamic Azad University, Qazvin Branch, Qazvin, Iran*

PAPER INFO

Paper history:
Received 24 April 2020
Received in revised form 13 May 2020
Accepted 12 June 2020

Keywords:
Frozen Soil
Mechanical Properties
Prediction Models
Response Surface Method
Statistical Optimization

ABSTRACT

The present study was based on a promoting statistical method known as response surface method (RSM). RSM has been applied as an efficient method to optimize many physical applications in industry for more than two decades. In the current study, the RSM was utilized as a platform to develop models as a function of some prescribed input factors to predict mechanical properties (responses) of frozen soils (i.e. peak tensile/compressive strength, elasticity modulus). Besides, RSM makes it possible to find significant factors and probable interactions as well. A widespread literature review was conducted and three case studies were chosen to evaluate the performance of the RSM in developing precise models and finally an optimum experiment. For each case study, less than half of the available data (an average of 40.8%) was employed to develop models and the remaining part was employed to evaluate the validity of derived models. A comparison between predicted and measured data showed a good agreement with a significant level of 0.05. This indicates that upon using the model a hundred times to predict an specific property for different input factors, the maximum five predictions may diverge from the measured values with ± confidence interval. In addition, some contours were plotted to give a comprehensive presentation of any probable correlations between investigated properties and input factors. Based on the developed models with an average correlation coefficients (R^2) of 93.69, temperature was found to be the most significant factor affecting the mechanical properties of frozen fine soil, while the dry density was not as effective as the temperature.

***doi**: 10.5829/ije.2020.33.10a.02*

1. INTRODUCTION

The frost susceptibility of soils has been of great concern to civil engineers. In spite of advances gained on the knowledge of soil freezing, there is still much evidence of annual frost damage to road surfaces. Other manifestations of the frost damage are tilting of culvert walls, shallow bridge piers, and the jacking out of utility poles. Numerous contributing factors including temperature, duration of freezing period, number of freeze and thaw (F-T) cycles, texture of soil, water content, etc. can be considered in frozen soils. It seems almost infeasible, highly time-consuming and labor intensive to prepare a multidirectional research [1, 2]. Therefore, novel methods should be employed to enhance our understanding of the frost damages. On the other hand, when the problem involves data subjected to experimental errors, statistical methods are the only objective approach for analysis. The statistical approach in experimental studies can play a significant role to obtain meaningful conclusions [3]. Thus, statistical analysis may be considered as an available optimization tool for the experimental problems comprising of different interacting input factors.

In adopting a statistical approach, design of experiment (DOE) is a powerful tool for quantitative assessment in experimental efforts which is employed through Central Composite Design (CCD), response surface method (RSM), full factorial analysis, Taguchi design, and so on. The present study focuses on RSM as

*Corresponding Author Email: *m_vahdani@sina.kntu.ac.ir* (M. Vahdani)

Please cite this article as: M. Vahdani, M. Ghazavi, M. Roustaei, Prediction of Mechanical Properties of Frozen Soils Using Response Surface Method: An Optimization Approach,International Journal of Engineering (IJE), IJE TRANSACTIONS A: Basics Vol. 33, No. 10, (October 2020) 1826-1841

a promoting statistical approach. DOE can be successfully applied to computer simulation models of physical systems. In such applications, DOE is used to build a model -a metamodel-, and optimization is carried out on the metamodel. The assumption is that if the metamodel is an acceptable representation of the real system, then optimization of the model will result in adequate determination of the optimum conditions for the real system [4].

The models are frequently used by engineers and scientists as computer-based design tools. Typical examples are finite element analysis models for mechanical and structural design and computational models for physical phenomena such as mechanical properties of soil and concrete [72–77]. As an example, consider the case of designing an earth dam to present an optimum configuration including stable slopes under seismic loading and F-T cycles, etc. Many factors may influence the design, such as the minimum freezing temperature, water content, dry density, as well as the percentage of fine particles. Many levels for each factor are potentially important. The maximum shear stress and many other mechanical properties can be considered as engineering responses. As a practical conclusion, only a small number of these potentially important factors have significant effects on the responses. Detailed analysis or testing of the continuum is required to understand which factors are important and to quantify their effect on the design. According to above mentioned issues, performing a complete mix design aiming at effects of various F-T characteristics on engineering properties takes more than dozens of individual runs, each comprises of over 60,00 elements and takes hours of computer time. Obviously, the need to optimize simulation is great. Therefore the typical approach of factor screening followed by optimizing algorithm (i.e. RSM) might well be attractive in this scenario. It is worthy to note that DOE is commonly applied to design of concrete mixture [78–80].

The RSM was firstly developed by Box et al. [81], and then within the next 30 years it was employed vastly at manufacturing process in industry. The RSM is a collection of mathematical and statistical techniques beneficial for the modeling and analysis of the problems in which a response of interest is influenced by several variables and the objective is to optimize this response [4]. The RSM is performed through some iterative analysis to find equations (models) as a function of prescribed factors, which is capable of predicting considered properties (responses). The available and reasonable range of input factors should be firstly chosen and then equations are provided using standard multiple regression methods to be fitted to some intelligently chosen data points.

Derived equations related to response surfaces are polynomials capable of linking input factors and even their interactions to responses. It is noted that an efficient experiment is obtained by identifing important factors and their valid range, the appropriate number of levels for each factor, and the proper methods and units of measurement for each factor and response. These features are sometimes conflicting, thus judgment must often be applied in abovementioned parameters. Efficiency and simplicity of the RSM make it a novel approach in recent studies with respect to other optimization methods such as neural network

In this research, the RSM is particularly employed as a platform to achieve some advantages including:

- Proposing some practical models for the investigated mechanical properties in previous studies
- Proving the ability of RSM to effectively reduce number of tests (treatments)
- Providing a comprehensive discussion on studied factors and their interactions affecting the key engineering properties

To reach these advantages, an attempt was made to review majority of recent studies. Table 1 categorizes studies related to frozen soils. Statistical approach has

TABLE 1. Summary of studies carried out on frozen/thawed soil

Type of Analysis	Soil	Main investigated parameters			
		Mechanical properties	**Hydraulic properties**	**Thermal/ice properties**	**Physical properties/durability**
Experimental	Untreated soil	[2], [1], [3], [5], [6], [7], [8], [9], [10], [11], [12], [13], [14], [15], [16], [17], [18], [19], [20], [21], [22], [23], [24], [25], [26]	[27]	[28], [17]	[2], [26]
	Stabilized soil	[29], [30], [31], [32], [33], [34], [35], [36]*, [37], [38], [39]	[33]	-	[29], [34], [35], [38], [39]
	Reinforced soil	[40], [41], [42], [31], [32], [43], [44]	-	-	[41], [42], [44]
Numerical/plasticity	Untreated soil	[45], [7], [11], [18], [46], [47], [48], [49],[50], [51], [52], [53], [54], [55], [56], [57], [20],[21], [24], [25]	[58], [59], [60], [61], [62], [63], [64], [65]	[66], [67], [59], [68], [47], [48], [69], [70], [53], [71], [63], [64], [57], [65],	-

* Conducted based on statistical approach

scarcely been employed within recent decades in geotechnical applications [9]. The performance of geogrid and geotextile in asphalt overlay to delay the rate of reflective crack propagation based on the RSM was investigated. However, the present study tries to examine potential capabilities of RSM in other geotechnical applications. In addition, it is worthy to note that the derived equations can be efficiently employed in some other areas in geotechnics such as calibration of numerical models, finding the governing equations on peak strength and ultimate stress. The latter can result in developing yield functions or bounding surface.

Three case studies were chosen to examine the RSM efficiency in reducing required tests for a comprehensive outlook to mechanical properties of some types of frozen soils. For each case study, less than half of available data (approximately 40%) was employed to develop prediction models and the remaining part was used to evaluate the validity of derived models. The derived statistical models enable us to quantify the level of significance of influencing factors including freezing temperature, water content, strain rate, etc. on responses such as peak strength, elastic modulus, etc. It was also proved that optimum values of some mechanical properties had been missed in original studies due to range of input factors. However, the optimum response could be considered as a secondary goal. Temperature was also found the most effective factor on mechanical properties among other factors such as induced strain rate, dry density, etc. This is in accordance with those reported by original studies. It should be mentioned that the conclusions are valid within the conditions expressed for each case study, and can be unreliable for different types of frozen soil and/or loading paths.

2. ANALYSIS METHOD

When number of input factor exceeds a specified number, traditional outlook of experimental design results in a high order test matrix (n factors in m levels requires m^n tests). While the RSM as an applicable method provides a much smaller test matrix, so that the test matrix consists of three portion; factorial portion (2^n), axial portion ($2n$), and central portion, where n refers to the number of input factors.

Originally, the RSM is employed to search for an optimum design that optimizes some design criterion, i.e. optimality, orthogonality and rotatability. The optimization process is basically done by means of nonlinear polynomial equations to find response surface optima. However, the process may be halted for some scientific applications as no specific optimum is required. A well discussed descriptions can be found in the literature [4, 81–84].

The RSM is performed in a staged manner to reach the highest order of precision. Thus, levels of input factors are determined at center, ends and/or other required levels of the studied range (known as *design points*) and then polynomial equations are regressed on the design points as a function of the input factors and even their interactions. The process is continued with enhancing equations by omission of non-significant factors and regeneration of the equations. Finally derived equations are verified by means of some other points (known as *verification points*) within the considered domain of factors. It is worthy to note that the process is enriched with complementary information such as correlation coefficient (R^2), confidence interval, lack of fitness, etc. The equations are developed in terms of normalized values, as shown in Equation (1). The absolute and normalized values of the parameters are presented in Table 3.

$$Coded\ values = \frac{(absolute\ \ value - center\ value)}{(Max.value - center\ value)} \quad (1)$$

where center value represents the center of studied range of the input factors corresponding to normalized value of zero. There are some other essential points to develop a more reliable equation, i.e. factorial points corresponding to normalized values of -1 and +1 and star points corresponding to normalized values higher than +1 and lower than -1. It should be mentioned that the abovementioned points are essential in response surface methodology if CCD is employed to derive quadratic equations while these points were not necessarily available in three chosen case studies.

Statistical models presented in this study are established by multi-regression analysis employing the least-square method as:

$$Y = \beta_0 + \sum_{i=1}^{n} \beta_i X_i + \sum_{i<j}^{n} \sum_{j}^{n} \beta_{ij} X_i X_j \quad (2)$$

where Y is the predicted response, X_i and X_j are the normalized values of the modeled variables, β_0 is a constant coefficient, β_i is linear coefficient, β_{ij} is coefficient of the interaction, and n is the number of the modeled variables.

The model described in Equation (2) is known as the Scheffé polynomials which is able to find the interaction between investigated factors. The significance of variables and their interactions are determined by the analysis of variance (ANOVA) using the least-square approach.

3. DISCUSSION

Three case studies in companion with input factors (independent parameters), their domains and response factors (dependent parameters) are shown in Table 2. As mentioned before, nearly half of the existing data of each case study was excluded and the remaining part was employed for derivation of statistical models. The remained and excluded parts are known as *design portion*

and *validation portion*, respectively. The size of design portion was intentionally kept smaller than the validation portion, as reduction of required mixtures for an optimum design of experiment is one of the most popular advantages of the RSM. The ratio of the numbers of treatments engaged in the model derivation to the total number of tests is called "*efficiency factor*", which represents efficiency of the RSM to reduce the number of required tests for a comprehensive perspective about studied properties.

Design points are selected to cover the considered domain of variables. However, some design points which are partly important in a perfect design of experiments could not be easily found in existing data bank, i.e. center point (design points with normalized value of zero), star points (design points beyond the design space). Contrary to inevitable limitations, well fitted models can mostly be reached utilizing the available design points, as will be illustrated in validation section. It could be partly attributed to the second order interactions included in the derived models.

Again, it should be noted that equations are developed in an evolutionary process. Thus, insignificant factors or interactions are sequentially emitted and remaining terms are again recalculated to find more reliable models. The presented coefficients are successive estimated values for each three case studies.

3. 1. Case Study 1 Li et al. [1] performed laboratory tests on a remolded clayey soil classified CL according to the Unified Soil Classification System (USCS). The clay liquid limit and plastic limit were 28.8 and 17.7%, respectively. The case study aimed to measured uniaxial compressive strength (UCS) by a screw-driven universal material testing machine. Tests were performed on frozen specimens with length of 150 mm and diameter of 61.8 mm. The obtained results are presented in Table 3 for 96 treatments, as reported by Li et al. [1]. In the current research, the model was prepared using 39 treatments which, in turn, validated using 57 remaining treatments. It is interesting to note that the efficiency factor was found 40.6%.

Table 4 shows the coefficients obtained from the statistical analysis to predict the experimental program. Statistical models were performed by full regression analyses. All factors are expressed in terms of normalized values. The coefficients are expressed by significant factors which have a p-value less than presumed significant level ($\alpha = 0.05$). The correlation coefficients (R^2) and adjusted correlation coefficient (R^2_{adj}) of the proposed models are 98.52 and 98.18%, respectively, indicating reliable models. Therefore, quadratic equation to predict peak strength of frozen-thawed clay regressed as follows, which is valid within the accepted conditions. As mentioned before, the validation of derived equations will be demonstrated subsequently.

$$q_u = -0.551T - 0.454S \times S + 0.225D + 0.188S - 0.140T \times D - 0.138T \times S + 0.106D \times D + 0.038 \quad (3)$$

where T, S, and D denote temperature, strain rate and dry density, respectively.

The coefficients of the equations are presented in the order of magnitude. The estimated coefficients for each factor refer to its contribution to the modeled response. Thus, the higher value represents more effective contribution. A negative coefficient in Equation (3) indicates that an increase in the input factor results in the reduction in predicted response. For instance, compressive strength was primarily affected by temperature (-0.551) and lightly influenced by dry density (0.225). The compressive strength was found to increase under higher dry density and strain rate. This is in agreement with those shown by Li et al. [1]. In addition, they demonstrated that strain rate and dry density also had significant effects on the compressive strength compared with temperature. It is noted that logarithmic functions had been derived by Li et al. [1].

To achieve a better understanding of existing interactions between factors, some trade-offs were drawn based on the derived equation in uncoded (absolute) format (Figure 1). It should be mentioned that allocated value for the third input factor is shown on corresponding figures.

TABLE 2. Studied factors for chosen case studies

Case study	Design factors	Applied range	Response factors
Case study 1 [1]	Dry density (gr/cm^3)	1.28 – 1.88	Peak compressive strength
	Temp (^{o}C)	-15 – -2	
	Strain rate (1/sec)	1.00E-6 – 7.03E-4	
Case study 2 [13]	Water content (%)	30.3 – 50.0	Initial yield strength , peak strength, $E_{50\%}$†
	Dry density (gr/cm^3)	1.08 – 1.43	
	Temp (^{o}C)	-10 – -0.5	
	Strain rate (1/sec)	6.14E-3 – 8.10E-7	
Case study 3 [19]	Water content (%)	15 – 30	Compressive peak strength, deformation modulus, compressive failure strain, tensile peak strength
	Temp (^{o}C)	-20 – -2	

†: $E_{50\%}$ is tangent modulus on stress-strain curve, corresponding to half of peak strength

TABLE 3. Experimental design matrix for case study 1

Design points						Validation points					
Absolute values			Normalized values			Absolute values			Normalized values		
temp. (ºC)	strain rate (1/sec)	Density (gr/cm^3)	temp.	strain rate	density	temp. (ºC)	strain rate (1/sec)	Density (gr/cm^3)	temp.	strain rate	density
-2	6.67E-04	1.38	1.00	0.90	-1.00	-2	1.04E-04	1.38	1.00	-0.71	-1.00
-2	1.10E-06	1.38	1.00	-1.00	-1.00	-2	1.04E-04	1.38	1.00	-0.71	-1.00
-10	6.05E-04	1.38	-0.23	0.72	-1.00	-2	9.10E-06	1.38	1.00	-0.98	-1.00
-10	9.27E-05	1.38	-0.23	-0.74	-1.00	-2	9.10E-06	1.38	1.00	-0.98	-1.00
-10	1.00E-06	1.38	-0.23	-1.00	-1.00	-10	6.10E-04	1.38	-0.23	0.74	-1.00
-5	6.67E-04	1.38	0.54	0.90	-1.00	-10	9.37E-05	1.38	-0.23	-0.74	-1.00
-5	9.10E-06	1.38	0.54	-0.98	-1.00	-10	8.40E-06	1.38	-0.23	-0.98	-1.00
-15	5.58E-04	1.38	-1.00	0.59	-1.00	-10	8.00E-06	1.38	-0.23	-0.98	-1.00
-2	6.67E-04	1.58	1.00	0.90	-0.20	-10	1.00E-06	1.38	-0.23	-1.00	-1.00
-2	9.10E-06	1.58	1.00	-0.98	-0.20	-5	6.67E-04	1.38	0.54	0.90	-1.00
-10	6.67E-04	1.58	-0.23	0.90	-0.20	-5	1.04E-04	1.38	0.54	-0.71	-1.00
-10	1.40E-04	1.58	-0.23	-0.60	-0.20	-5	9.10E-06	1.38	0.54	-0.98	-1.00
-10	8.91E-06	1.58	-0.23	-0.98	-0.20	-5	1.10E-06	1.38	0.54	-1.00	-1.00
-5	1.04E-04	1.58	0.54	-0.71	-0.20	-5	1.10E-06	1.38	0.54	-1.00	-1.00
-15	6.73E-04	1.58	-1.00	0.91	-0.20	-15	5.58E-04	1.38	-1.00	0.59	-1.00
-15	8.61E-06	1.58	-1.00	-0.98	-0.20	-15	1.26E-04	1.38	-1.00	-0.64	-1.00
-2	7.03E-04	1.88	1.00	1.00	1.00	-15	8.30E-06	1.38	-1.00	-0.98	-1.00
-2	1.09E-06	1.88	1.00	-1.00	1.00	-15	8.33E-06	1.38	-1.00	-0.98	-1.00
-10	6.43E-04	1.88	-0.23	0.83	1.00	-15	1.01E-06	1.38	-1.00	-1.00	-1.00
-10	8.88E-06	1.88	-0.23	-0.98	1.00	-2	1.04E-04	1.58	1.00	-0.71	-0.20
-5	6.74E-04	1.88	0.54	0.92	1.00	-2	1.04E-04	1.58	1.00	-0.71	-0.20
-5	9.05E-06	1.88	0.54	-0.98	1.00	-2	9.10E-06	1.58	1.00	-0.98	-0.20
-15	6.57E-04	1.88	-1.00	0.87	1.00	-2	1.10E-06	1.58	1.00	-1.00	-0.20
-15	1.10E-06	1.88	-1.00	-1.00	1.00	-10	6.60E-04	1.58	-0.23	0.88	-0.20
-2	6.67E-04	1.38	1.00	0.90	-1.00	-10	1.38E-04	1.58	-0.23	-0.61	-0.20
-2	1.10E-06	1.38	1.00	-1.00	-1.00	-10	9.11E-06	1.58	-0.23	-0.98	-0.20
-5	1.04E-04	1.38	0.54	-0.71	-1.00	-10	1.10E-06	1.58	-0.23	-1.00	-0.20
-15	8.94E-05	1.38	-1.00	-0.75	-1.00	-10	1.10E-06	1.58	-0.23	-1.00	-0.20
-15	1.02E-06	1.38	-1.00	-1.00	-1.00	-5	6.67E-04	1.58	0.54	0.90	-0.20
-2	6.67E-04	1.58	1.00	0.90	-0.20	-5	6.67E-04	1.58	0.54	0.90	-0.20
-2	1.10E-06	1.58	1.00	-1.00	-0.20	-5	9.10E-06	1.58	0.54	-0.98	-0.20
-5	1.04E-04	1.58	0.54	-0.71	-0.20	-5	9.10E-06	1.58	0.54	-0.98	-0.20
-15	9.94E-05	1.58	-1.00	-0.72	-0.20	-5	1.10E-06	1.58	0.54	-1.00	-0.20
-15	1.10E-06	1.58	-1.00	-1.00	-0.20	-5	1.10E-06	1.58	0.54	-1.00	-0.20
-2	6.94E-04	1.88	1.00	0.97	1.00	-15	6.62E-04	1.58	-1.00	0.88	-0.20
-2	1.08E-06	1.88	1.00	-1.00	1.00	-15	1.01E-04	1.58	-1.00	-0.72	-0.20
-5	1.07E-04	1.88	0.54	-0.70	1.00	-15	8.74E-06	1.58	-1.00	-0.98	-0.20
-15	1.05E-04	1.88	-1.00	-0.70	1.00	-15	1.07E-06	1.58	-1.00	-1.00	-0.20
-15	1.13E-06	1.88	-1.00	-1.00	1.00	-2	1.04E-04	1.88	1.00	-0.71	1.00
						-2	1.09E-04	1.88	1.00	-0.69	1.00

-2	9.05E-06	1.88	1.00	-0.98	1.00
-2	9.17E-06	1.88	1.00	-0.98	1.00
-10	6.72E-04	1.88	-0.23	0.91	1.00
-10	1.03E-04	1.88	-0.23	-0.71	1.00
-10	1.02E-04	1.88	-0.23	-0.71	1.00
-10	8.94E-06	1.88	-0.23	-0.98	1.00
-10	1.10E-06	1.88	-0.23	-1.00	1.00
-10	1.10E-06	1.88	-0.23	-1.00	1.00
-5	6.76E-04	1.88	0.54	0.92	1.00
-5	1.20E-04	1.88	0.54	-0.66	1.00
-5	9.04E-06	1.88	0.54	-0.98	1.00
-5	1.09E-06	1.88	0.54	-1.00	1.00
-5	1.08E-06	1.88	0.54	-1.00	1.00
-15	6.33E-04	1.88	-1.00	0.80	1.00
-15	1.07E-04	1.88	-1.00	-0.70	1.00
-15	9.20E-06	1.88	-1.00	-0.98	1.00
-15	8.87E-06	1.88	-1.00	-0.98	1.00

TABLE 4. Parameter estimates of derived models for peak compressive strength in normalized format

Term	Coef.	p value
Constant	0.038	0.429
T	-0.551	0.000
S	0.188	0.000
D	0.225	0.000
S*S	-0.454	0.000
D*D	0.106	0.000
T*S	-0.138	0.000
T*D	-0.140	0.000

T: Temperature , S: Strain rate , D: Dry density

Figure 1(a) illustrates the effects of temperature and dry density on the compressive strength. As expected, the lower temperature resulted in the higher compressive strength for a given density. A further increase was found for dry mass density higher than 1.65 g/cm^3. Although, there is a threshold for dry mass density beyond that soil experiences more expansion as there is no space to dissipate ice pressure. The contour diagram of compressive strength in Figure 1(b) illustrates the same trade-offs between temperature and strain rate for soil with dry mass density of 1.63 g/cm^3. Peak strength tends to increase as freezing temperature decreases regardless of strain rate. Moreover, compressive strength exhibited a maximum value at temperatures lower than -15^{o}C and strain rate of approximately 0.0005 (1/s). It should be noted that investigated range of factors can be redefined to reach an optimum response, if required.

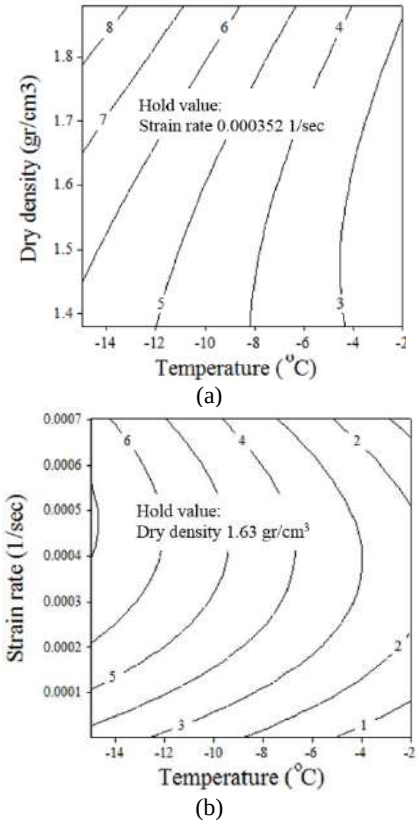

Figure 1. Absolute peak compressive strength (MPa) as a function of (a) dry density and temperature, (b) strain rate and temperature

3. 2. Case Study 2 Yuanlin and Carbee [13] have chosen a silt soil from the USA CRREL experimental permafrost tunnel at Fox, near Fairbanks, Alaska. They

conducted uniaxial compressive strength tests on remolded, saturated Fairbanks frozen silt under various constant machine speeds, temperatures and dry densities. The soil was classified as ML in the USCS. Prepared specimens had 70 mm diameter and 152 mm height. Table 5 presents absolute and normalized

TABLE 5. Experimental design matrix for case study 2

Design points								Validation points							
Absolute values				Normalized values				Absolute values				Normalized values			
water content (%)	dry density (gr/cm^3)	Temp (ºC)	strain rate (1/sec)	water content	dry density	temp	strain rate	water content (%)	dry density (gr/cm^3)	Temp (ºC)	strain rate (1/sec)	water content	dry density	temp	strain rate
43.0	1.177	-0.5	5.85E-03	0.29	-0.46	1.00	0.91	43.6	1.184	-0.5	1.06E-03	0.35	-0.42	1.00	-0.65
42.9	1.205	-1.0	5.73E-03	0.28	-0.30	0.89	0.87	45.2	1.155	-0.5	1.00E-04	0.51	-0.59	1.00	-0.97
42.7	1.187	-1.0	1.00E-05	0.26	-0.41	0.89	-1.00	43.9	1.177	-0.5	9.23E-06	0.38	-0.46	1.00	-1.00
45.4	1.155	-2.0	1.07E-03	0.53	-0.59	0.68	-0.65	41.6	1.206	-1.0	1.10E-03	0.15	-0.29	0.89	-0.64
42.8	1.206	-2.0	1.11E-04	0.27	-0.29	0.68	-0.96	42.6	1.198	-1.0	1.10E-03	0.25	-0.34	0.89	-0.64
40.8	1.227	-2.0	1.14E-04	0.07	-0.17	0.68	-0.96	42.8	1.195	-1.0	1.12E-04	0.27	-0.36	0.89	-0.96
42.9	1.187	-3.0	5.63E-03	0.28	-0.41	0.47	0.83	42.2	1.203	-1.0	1.11E-04	0.21	-0.31	0.89	-0.96
42.8	1.195	-3.0	1.08E-06	0.27	-0.36	0.47	-1.00	41.7	1.211	-1.0	1.06E-05	0.16	-0.26	0.89	-1.00
43.1	1.184	-5.0	1.11E-03	0.30	-0.42	0.05	-0.64	41.9	1.202	-1.0	1.01E-05	0.18	-0.32	0.89	-1.00
42.5	1.195	-5.0	1.12E-03	0.24	-0.36	0.05	-0.64	42.4	1.200	-1.0	1.06E-06	0.23	-0.33	0.89	-1.00
40.6	1.229	-5.0	1.15E-04	0.05	-0.16	0.05	-0.96	41.3	1.219	-2.0	1.15E-03	0.12	-0.22	0.68	-0.63
42.0	1.203	-5.0	1.06E-05	0.19	-0.31	0.05	-1.00	42.3	1.200	-2.0	1.13E-04	0.22	-0.33	0.68	-0.96
41.4	1.221	-5.0	1.13E-05	0.13	-0.21	0.05	-1.00	43.2	1.189	-2.0	1.12E-05	0.31	-0.39	0.68	-1.00
44.6	1.165	-7.0	5.57E-03	0.45	-0.54	-0.37	0.81	41.7	1.213	-2.0	1.11E-05	0.16	-0.25	0.68	-1.00
42.4	1.202	-7.0	1.11E-03	0.23	-0.32	-0.37	-0.64	42.2	1.206	-2.0	1.11E-06	0.21	-0.29	0.68	-1.00
40.7	1.222	-7.0	1.14E-06	0.06	-0.20	-0.37	-1.00	41.8	1.208	-2.0	1.03E-06	0.17	-0.28	0.68	-1.00
41.8	1.210	-10.0	1.11E-03	0.17	-0.27	-1.00	-0.64	42.0	1.190	-3.0	1.12E-03	0.19	-0.39	0.47	-0.64
42.6	1.198	-10.0	1.23E-03	0.25	-0.34	-1.00	-0.60	41.2	1.221	-3.0	1.12E-03	0.11	-0.21	0.47	-0.64
50.0	1.086	-2.0	1.00E-04	1.00	-1.00	0.68	-0.97	41.3	1.219	-3.0	1.13E-04	0.12	-0.22	0.47	-0.96
48.3	1.104	-2.0	1.01E-05	0.83	-0.89	0.68	-1.00	41.5	1.216	-3.0	1.12E-04	0.14	-0.24	0.47	-0.96
30.3	1.426	-2.0	6.14E-03	-1.00	1.00	0.68	1.00	41.5	1.216	-3.0	1.10E-05	0.14	-0.24	0.47	-1.00
31.7	1.394	-2.0	1.24E-03	-0.86	0.81	0.68	-0.60	41.9	1.208	-3.0	1.11E-05	0.18	-0.28	0.47	-1.00
31.6	1.389	-2.0	1.22E-05	-0.87	0.78	0.68	-1.00	42.4	1.198	-3.0	1.03E-06	0.23	-0.34	0.47	-1.00
31.3	1.389	-2.0	1.19E-06	-0.90	0.78	0.68	-1.00	42.0	1.211	-5.0	1.07E-06	0.19	-0.26	0.05	-1.00
30.4	1.422	-2.0	1.18E-06	-0.99	0.98	0.68	-1.00	42.3	1.203	-7.0	1.11E-03	0.22	-0.31	-0.37	-0.64
								43.3	1.174	-7.0	1.05E-04	0.32	-0.48	-0.37	-0.97
								41.4	1.211	-7.0	1.15E-05	0.13	-0.26	-0.37	-1.00
								43.1	1.187	-7.0	1.04E-05	0.30	-0.41	-0.37	-1.00
								41.7	1.210	-10.0	1.15E-04	0.16	-0.27	-1.00	-0.96
								45.9	1.168	-10.0	1.13E-05	0.58	-0.52	-1.00	-1.00
								43.7	1.179	-10.0	1.12E-05	0.36	-0.45	-1.00	-1.00
								42.3	1.202	-10.0	1.09E-06	0.22	-0.32	-1.00	-1.00
								49.3	1.099	-2.0	8.10E-07	0.93	-0.92	0.68	-1.00
								31.5	1.395	-2.0	1.24E-04	-0.88	0.82	0.68	-0.96
								31.2	1.408	-2.0	1.23E-05	-0.91	0.89	0.68	-1.00

specifications of treatments employed in the current statistical analysis. The model was derived using 25 treatments which, in turn, validated using other 35 treatments (*efficiency factor* of 41.7%). Tables 6 summarizes coefficients and their p-values. Again, probability values less than 0.05 are considered to realize significant influences on the modeled responses. Quadratic equations are derived in a sequential manner such that non-significant factors should be eliminated to attain a more precise equation.

For instance, water content exhibited no significant effect on $E_{50\%}$ while minimum temperature, strain rate and related second-order interactions had significant effects. Table 6 shows final successive estimations for remaining terms. Some logarithmic correlations were introduced by Yuanlin and Carbee [13]. Estimated coefficients are presented in descending order in Table 7. As mentioned before, the higher value represents more effective contribution. A negative coefficient indicates that an increase in the input factor results in a reduction of the predicted response. To elaborate the descriptions, corresponding coefficients are given in parenthesis.

The initial yield strength decreases with increasing the temperature, while an increasing trend is observed with increasing the strain value. Although, strain rate seems to be a neutral factor for freezing temperatures greater than -5°C (Figure 2(c)). As seen, the temperature (-0.876) is more effective on the initial yield strength compared with the strain rate (0.535) and other interactions including S*S (-0.598) and S*T (-0.352). It is clear from the corresponding equation that the peak strength of frozen silt significantly increases as temperature falls down (-0.8546) and strain rate increases (0.5510). However, dry mass density (0.7206) is more effective than induced strain rate (0.5510). Similarly, Yuanlin and Carbee [13] stated similar results with those obtained for peak strength. Regarding $E_{50\%}$, the contribution of strain rate (0.5090) is nearly similar to its contribution in other two responses (0.5510 and 0.5350). The R^2 values of the proposed models vary in the range of 96.49-98.85, indicating models can properly predict validation points. It should be mentioned that deformation modulus is not precisely estimated from the RSM analysis. Undoubtedly, this is partly due to lack of key data in existing database to perform a perfect statistical analysis, i.e. center of studied ranges (equivalent to normalized value of zero). However, the RSM takes into account the interactions which have been neglected in previous studies.

Based on equations given in Table 7, following trade-offs are shown to attain a better understanding of variations. It should be mentioned that responses were drawn as a function of strain rate and temperature while other significant factors were remained constant amidst corresponding range. As shown in Figures 2(a) and 2(b), the variation of initial yield strength and peak strength

TABLE 6. Parameter estimates of derived models in normalized format

Initial yield strength			Peak strength			$E_{50\%}$		
Term	**Coef.**	**p value**	**Term**	**Coef.**	**p value**	**Term**	**Coef.**	**p value**
Constant	0.6220	0.000	**Constant**	0.6058	0.000	**Constant**	0.0390	0.579
T	-0.8760	0.000	**W**	0.6947	0.047	**D**	-0.2398	0.000
S	0.5350	0.000	**D**	0.7206	0.037	**T**	-0.8078	0.000
S*S	-0.5980	0.000	**T**	-0.8546	0.000	**S**	0.5091	0.000
S*T	-0.3520	0.000	**S**	0.5510	0.000	**S*S**	-0.1991	0.041
			T*T	0.1040	0.041	**T*S**	-0.5473	0.000
			S*S	-0.5388	0.000			
			T*S	-0.3605	0.000			

T: Temperature, S: Strain rate, W: Water content, D:dry density

TABLE 7. Derived estimation model for experimental program

Dependent variable	Derived equation (normalized units)	R^2	R^2_{adj}
Initial yield strength	$-0.8760T + 0.6220 - 0.5980S \times S + 0.5350S - 0.3520S \times T$	97.99	97.59
Peak strength	$-0.8546T + 0.7206D + 0.6947W + 0.6058+\ldots$ $\ldots+0.5510S - 0.5388S \times S - 0.3605T \times S + 0.1040T \times T$	98.85	98.38
$E_{50\%}$	$-0.8078T - 0.5473T \times S + 0.5090S - 0.2398D - 0.1991S \times S + 0.0390$	96.49	95.57

is more affected by the temperature compared with the strain rate at high level of induced strain (shaded area). Figure 2(c) demonstrates that $E_{50\%}$ increased as the temperature drops and the strain rate increases, as contours are getting closer at top-left corner of the plot. It should be mentioned that those significant factors which were not employed as input factors in plotting trade-offs, were hold on amidst of their corresponding domains. As a practical conclusion, each three responses experience optimum values for input variables beyond the chosen domains in original studies. However, values of input factors beyond the investigated range may be practically unfeasible. It is worth noting that a more efficient design of experiment would not necessarily require more treatments.

3. 3. Case Study 3 The objective of case study 3 reported by Christ and Kim [19] was to evaluate the mechanical properties of frozen Siberian silt. They determined unfrozen water content, uniaxial compressive strength and direct-tensile strength of frozen silt samples at different water contents and temperatures. Absolute and normalized values of modeled parameters are presented in Table 8. It is interesting to note that the *efficiency factor* was kept 40.0% (8 from 20 treatments).

The derived coefficients and corresponding p-values are summarized in Table 9. The equations are stated as a function of factors with significant influences on modeled responses listing in descending order. The R^2 value of the proposed models ranges 84.85-98.62. As seen in Tables 9 and 10, probability values are relatively low which can be attributed to fewer available design points. However, the modeled responses are still reliable and reasonably validated (Figures 3-5).

Based on the equations presented in Table 10, trade-offs between temperature and water content on values of the modeled properties are plotted in Figure 6. Based on the equations presented in Table 10, trade-offs between temperature and water content are plotted in Figure 6. As seen, temperature has the most significant effect on the compressive strength and deformation modulus. However, tensile strength is significantly affected by water content. As seen in Table 10, the temperature and water content exhibit conflicting influences on all responses. Contours demonstrate a maximum value as temperature and water content decreases and increases, respectively. This is in accordance with those reported by Christ and Kim [19]. In addition, Christ and Kim [19] found an exponential and linear increase in tensile and compressive strength, respectively, as temperature dropped especially at high water content. Moreover, a linear correlation between deformation modulus and input factors was found which is also in accordance with those presented by Christ and Kim [19].

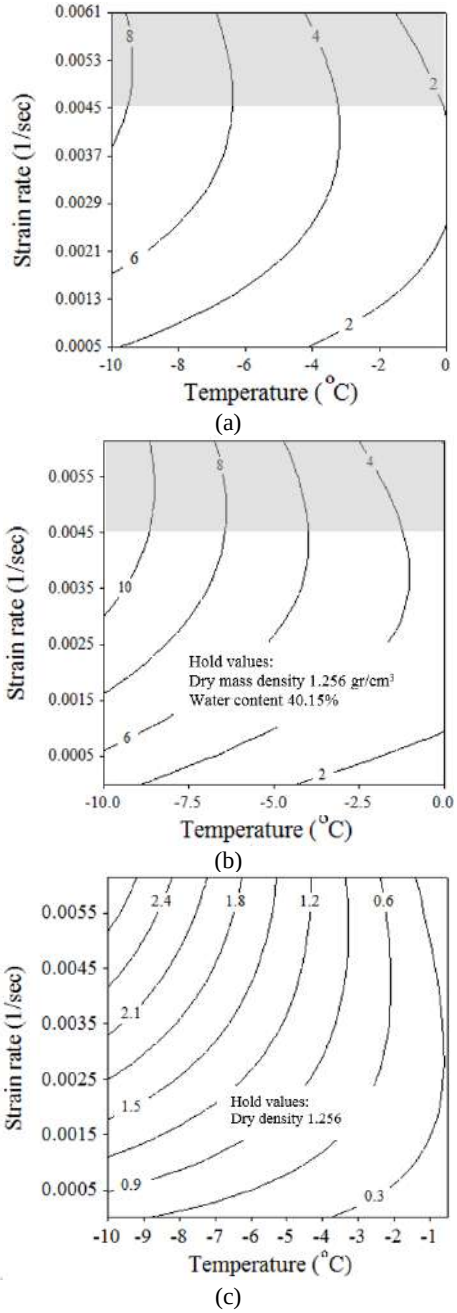

(a)

(b)

(c)

Figure 2. Trade-offs plotted for absolute values: (a) Initial yield strength (MPa), (b) Peak strength (MPa) and (c) $E_{50\%}$ (GPa)

4. REPEATABILITY AND VALIDATION OF DERIVED STATISTICAL MODELS

As mentioned above, large part of available data was intentionally excluded for validation points as listed in Tables 3, 5 and 8. The estimated relative errors corresponding to 95% confidence limit are shown in Table 11. Based on the calculated errors, Figures 3-5

TABLE 8. Details of experimental program

Design points				Validation points			
absolute values		normalized values		absolute values		normalized values	
water content (%)	temp. (ºC)	water content	temp.	water content (%)	temp. (ºC)	water content	temp.
15.0	-2	-1.00	1.00	15.0	-5	-1.00	0.67
15.0	-20	-1.00	-1.00	15.0	-10	-1.00	0.11
19.8	-5	-0.36	0.67	15.0	-15	-1.00	-0.44
19.8	-15	-0.36	-0.44	19.8	-2	-0.36	1.00
25.0	-5	0.33	0.67	19.8	-10	-0.36	0.11
25.0	-15	0.33	-0.44	19.8	-20	-0.36	-1.00
30.0	-2	1.00	1.00	25.0	-2	0.33	1.00
30.0	-20	1.00	-1.00	25.0	-10	0.33	0.11
				25.0	-20	0.33	-1.00
				30.0	-5	1.00	0.67
				30.0	-10	1.00	0.11
				30.0	-15	1.00	-0.44

TABLE 9. Parameter estimates of derived equations for modelled responses

Compressive strength			Deformation modulus			Failure strain			Tensile strength		
Term	**Coef.**	**p value**	**Term**	**Coef.**	**p value**	**Term**	**Coef.**	**p value**	**Term**	**Coef.**	**p value**
Constant	-0.200	0.094	**Constant**	-0.332	0.030	**Constant**	0.383	0.012	**Constant**	-0.918	0.002
W	0.450	0.018	**W**	0.465	0.025	**W**	0.893	0.000	**W**	0.495	0.003
T	-0.586	0.004	**T**	-0.580	0.008				**T**	-0.444	0.004
									T*T	0.457	0.034
									W*T	-0.477	0.004

W: Water content, T: Temperature

TABLE 10. Derived estimate model for experimental program

Dependent variable	Derived equation (normalized units)	R^2	R^2_{adj}
Compressive strength	$-0.586T + 0.450W - 0.200$	87.88	83.04
Deformation modulus	$-0.580T + 0.465W - 0.332$	84.85	78.79
Failure strain	$0.893W + 0.383$	86.33	84.05
Tensile strength	$-0.918 + 0.495W - 0.477W \times T + 0.457T \times T - 0.444T$	98.62	96.79

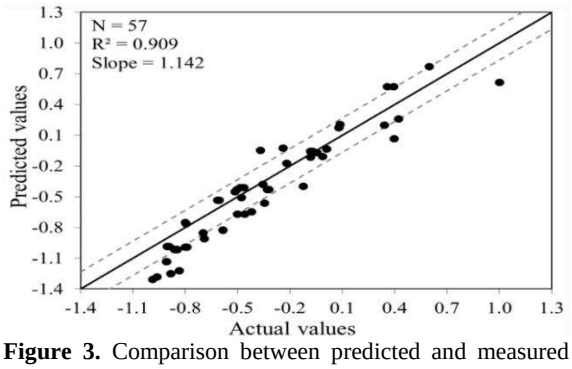

Figure 3. Comparison between predicted and measured normalized compressive strength values for case study 1

present a comparison between predicted and measured values for all three case studies to prove that the RSM can reliably be employed in experimental studies. The number of validation points is given on each plot.

In Figure 5, data points below the continuous line indicate that derived equations underestimate and those above the line overestimate the measured values. Two parallel dotted lines were drawn to present the 95% confidence interval. The majority of the predicted responses were within the 95% confidence limits which can be found in Table 11. These limits constitute experimental errors for the measurements. In case study

1, despite a small confidence limit, the predicted and measured values relatively lied within the confidence interval. The predicted-to-measured ratio and R^2 values are 1.142 and 0.909, respectively. The majority of responses for case study 2 are in close proximity with 1:1 diagonal line. This indicates good accuracy of the models for prediction of peak strength, initial yield strength and $E_{50\%}$. Although, $E_{50\%}$ was not predicted as accurate as was expected. This can be rooted in lack of key data. In the case study 3, except peak tensile strength, other modeled responses including peak compressive strength, compressive failure strain and

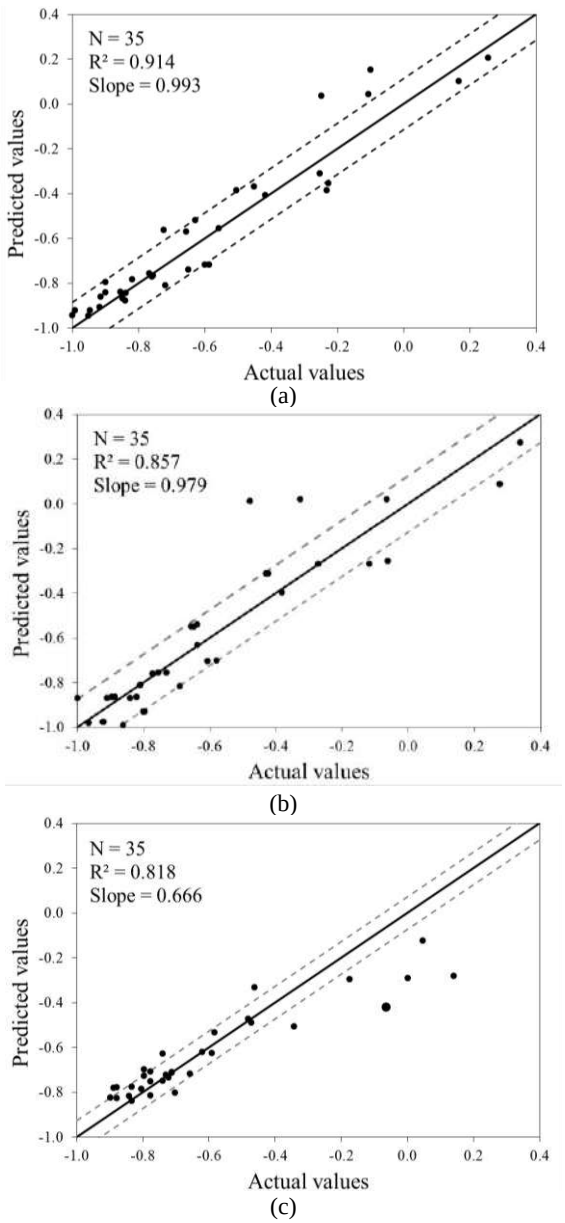

Figure 4. Comparison between predicted and measured normalized responses for in case study 2: (a) Peak strength, (b) Initial yield strength, (c) $E_{50\%}$

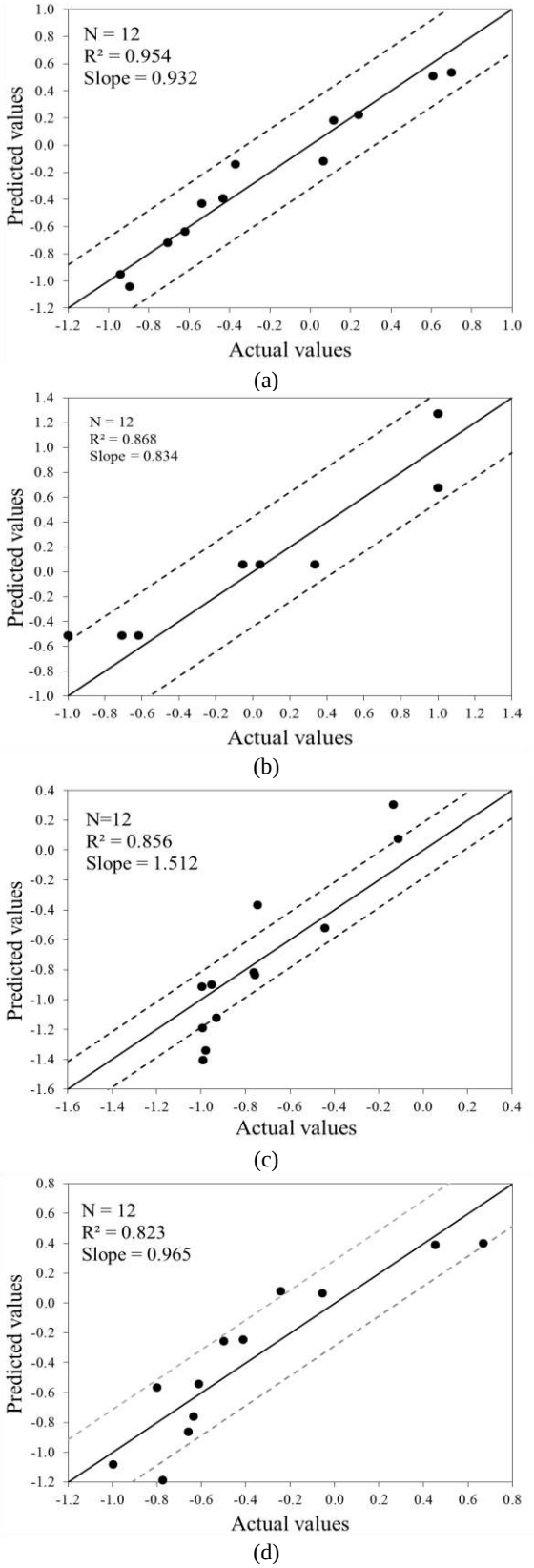

Figure 5. Comparison between predicted and measured normalized responses for case study 3: (a) Peak compressive strength, (b) Compressive failure strain, (c) Peak tensile strength (d) Deformation modulus

deformation modulus were within their corresponding confidence intervals. The ratio of predicted-to-measured values ranged between 0.834 and 0.965 for abovementioned properties. In summary, all derived equations prepared acceptable predictions within the investigated range of input factors. It is noted that the modeled responses remain valid as far as characteristics of raw material and test procedures tolerate small variations.

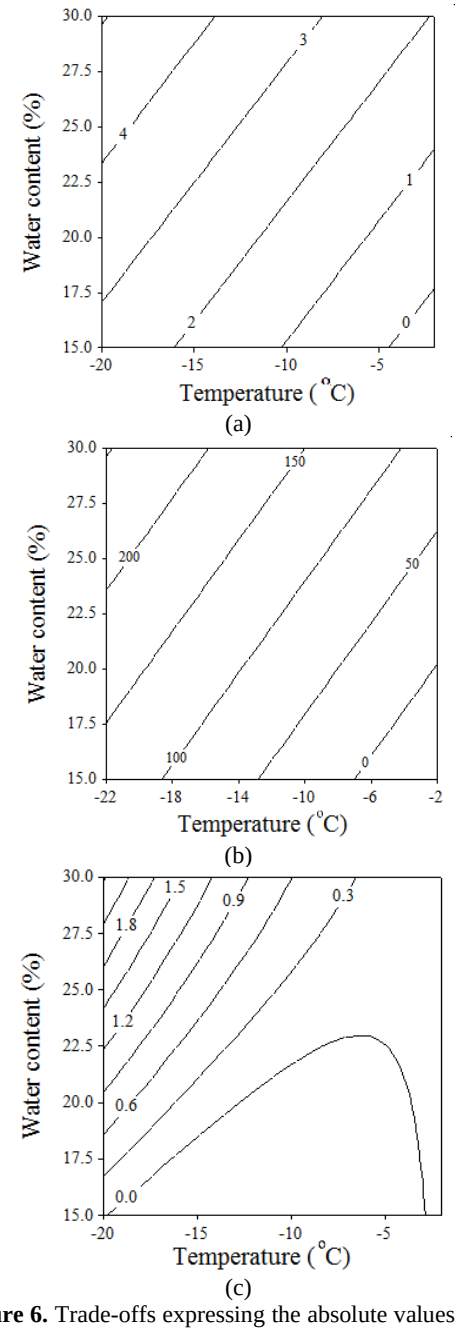

Figure 6. Trade-offs expressing the absolute values of: (a) Compressive peak strength (MPa); (b) Deformation modulus (MPa); (c) Peak tensile strength (MPa), as functions of temperature and water content

TABLE 11. Standard deviation and confidence interval for validation points based on measured normalized values (95% confidence level)

Case study	Response	Standard deviation	Confidence interval
1st	Peak compressive strength	0.566	0.167
2nd	Peak compressive strength	0.331	0.114
	Initial yield strength	0.345	0.119
	$E_{50\%}$	0.323	0.111
3nd	Peak compressive strength	0.563	0.318
	Compressive failure strain	0.779	0.441
	Peak tensile strength	0.509	0.288
	Deformation modulus	0.328	0.186

5. CONCLUSIONS

The main aim of this paper was to minimize the number of tests required to predict mechanical characteristics of frozen soil as well as to present a more comprehensive perspective about the influencing factors and their interactions on the mechanical properties of frozen soil.

RSM was employed as a promoting statistical method to evaluate three case studies. Based on the obtained results, the following conclusions can be extracted. It should be mentioned that the conclusions are valid within the conditions expressed for each case study and may be unreliable for different types of frozen soil and/or loading paths.

- Temperature showed the most effective factor on mechanical properties among other factors.
- In spite of existing limitations, less than half of available data in the investigated case studies (average *efficiency factor* of 40.8%) was enough to provide reliable models, indicating efficiency of RSM in optimization.
- The key data such as response at the centre point was not readily available and it caused more efforts to develop reliable models.
- Optimum values of mechanical properties occur beyond of investigated domain of input factors in case study. However, values of input factors beyond the investigated range may be practically unfeasible.
- As a practical conclusion, three investigated experimental programs were not efficiently cover all probable correlations. While, the RSM can provide an optimum experimental design which can cover nearly all probable interactions. It should be noted that a RSM-

designed experiment necessarily requires less treatments (tests) with respect to traditionally designed experiments.

- Under the adopted conditions for the case studies, the RSM can potentially be considered to design optimum experiments and find significant factors affecting prescribed responses.
- It should be mentioned that size of original database plays an important role in precision of the models, so that a minimum threshold should be considered to minimize any probable errors.

6. REFERENCES

1. Li, H., Zhu, Y., Zhang, J., and Lin, C. "Effects of temperature , strain rate and dry density on compressive strength of saturated frozen clay." ***Cold Regions Science and Technology***, Vol. 39, (2004), 39–45. https://doi.org/10.1016/j.coldregions.2004.01.001
2. Cui, Z., He, P., and Yang, W. "Mechanical properties of a silty clay subjected to freezing – thawing." ***Cold Regions Science and Technology***, Vol. 98, (2014), 26–34. https://doi.org/10.1016/j.coldregions.2013.10.009
3. Qi, J., Ma, W., and Song, C. "Influence of freeze – thaw on engineering properties of a silty soil." ***Cold Regions Science and Technology***, Vol. 53, No. 3, (2008), 397–404. https://doi.org/10.1016/j.coldregions.2007.05.010
4. Montgomery, D. C. Design and Analysis of Experiments (Eighth Edi.). New Jersey: John Wiley & Sons, Inc.
5. Jessbergger, H. L. "A state-of.the-art report. ground freezing: mechanical properties, processes and design." ***Engineering Geology***, Vol. 18, No. 1-4, (1981), 5–30. https://doi.org/10.1016/0013-7952(81)90042-9
6. Wang, D., Ma, W., Niu, Y., Chang, X., and Wen, Z. "Effects of cyclic freezing and thawing on mechanical properties of Qinghai – Tibet clay." ***Cold Regions Science and Technology***, Vol. 48, (2007), 34–43. https://doi.org/10.1016/j.coldregions.2006.09.008
7. Yang, Y., Lai, Y., and Chang, X. "Laboratory and theoretical investigations on the deformation and strength behaviors of artificial frozen soil." ***Cold Regions Science and Technology***, Vol. 64, No. 1, (2010), 39–45. https://doi.org/10.1016/j.coldregions.2010.07.003
8. Wang, S., Qi, J., and Yao, X. "Stress relaxation characteristics of warm frozen clay under triaxial conditions." ***Cold Regions Science and Technology***, Vol. 69, No. 1, (2011), 112–117. https://doi.org/10.1016/j.coldregions.2011.06.015
9. Yu, F., Qi, J., Yao, X., and Liu, Y. "In-situ monitoring of settlement at different layers under embankments in permafrost regions on the Qinghai – Tibet Plateau." ***Engineering Geology***, Vol. 160, (2013), 44–53. https://doi.org/10.1016/j.enggeo.2013.04.002
10. Zhang, S., Lai, Y., Sun, Z., and Gao, Z. "Volumetric strain and strength behavior of frozen soils under confinement." ***Cold Regions Science and Technology***, Vol. 47, (2007), 263–270. https://doi.org/10.1016/j.coldregions.2006.10.001
11. Xu, X., Lai, Y., Dong, Y., and Qi, J. "Laboratory investigation on strength and deformation characteristics of ice-saturated frozen sandy soil." ***Cold Regions Science and Technology***, Vol. 69, No. 1, (2011), 98–104. https://doi.org/10.1016/j.coldregions.2011.07.005
12. Dieter Eigenbrod, Sven Knutsson, D. S. "Pore-water pressure in freezing and thawing fine-graded soils." ***Journal of Cold Regions Engineering***, Vol. 10, No. 2, (1996), 77–92.
13. Z. Yuanlin and D. L. Carbee. "Uniaxial compressive strength of frozen silt under constant deformation rates." ***Cold Regions Science and Technology***, Vol. 9, (1984), 3–15.
14. Yao, X., Qi, J., Yu, F., and Ma, L. "A versatile triaxial apparatus for frozen soils." ***Cold Regions Science and Technology***, Vol. 92, (2013), 48–54. https://doi.org/10.1016/j.coldregions.2013.04.001
15. Wang, D., Zhu, Y., Ma, W., and Niu, Y. "Application of ultrasonic technology for physical – mechanical properties of frozen soils." ***Cold Regions Science and Technology***, Vol. 44, (2006), 12–19. https://doi.org/10.1016/j.coldregions.2005.06.003
16. Park, J., and Lee, J. "Characteristics of elastic waves in sand – silt mixtures due to freezing." ***Cold Regions Science and Technology***, Vol. 99, , (2014), 1–11. https://doi.org/10.1016/j.coldregions.2013.11.002
17. Akagawa, S., and Nishisato, K. "Tensile strength of frozen soil in the temperature range of the frozen fringe." ***Cold Regions Science and Technology***, Vol. 57, No. 1, (2009), 13–22. https://doi.org/10.1016/j.coldregions.2009.01.002
18. Yang, Y., Lai, Y., and Li, J. "Laboratory investigation on the strength characteristic of frozen sand considering effect of confining pressure." ***Cold Regions Science and Technology***, Vol. 60, No. 3, (2010), 245–250. https://doi.org/10.1016/j.coldregions.2009.11.003
19. Christ, M., and Kim, Y. "Experimental Study on the Physical-Mechanical Properties of Frozen Silt," Vol. 13, (2009), 317–324. https://doi.org/10.1007/s12205-009-0317-z
20. Xu, X., Wang, Y., Yin, Z., and Zhang, H. "Effect of temperature and strain rate on mechanical characteristics and constitutive model of frozen Helin loess." ***Cold Regions Science and Technology***, Vol. 136, (2017), 44–51. https://doi.org/10.1016/j.coldregions.2017.01.010
21. Liu, X., Liu, E., Zhang, D., Zhang, G., Yin, X., and Song, B. "Study on effect of coarse-grained content on the mechanical properties of frozen mixed soils." ***Cold Regions Science and Technology***, Vol. 158, (2019), 237-251. https://doi.org/10.1016/j.coldregions.2018.09.001
22. Liu, Z., Liu, J., Li, X., and Fang, J. "Experimental study on the volume and strength change of an unsaturated silty clay upon freezing." ***Cold Regions Science and Technology***, Vol. 157, (2019), 1-12. https://doi.org/10.1016/j.coldregions.2018.09.008
23. Fei, W., and Yang, Z. J. "Modeling unconfined compression behavior of frozen Fairbanks silt considering effects of temperature, strain rate and dry density." ***Cold Regions Science and Technology***, Vol. 158, (2019), 252-263. https://doi.org/10.1016/j.coldregions.2018.09.002
24. Zhang, D., Liu, E., Liu, X., Zhang, G., and Song, B. "A new strength criterion for frozen soils considering the influence of temperature and coarse-grained contents." ***Cold Regions Science and Technology***, Vol. 143, (2017), 1–12. https://doi.org/10.1016/j.coldregions.2017.08.006
25. Zhou, Z., Ma, W., Zhang, S., Mu, Y., and Li, G. "Effect of freeze-thaw cycles in mechanical behaviors of frozen loess." ***Cold Regions Science and Technology***, Vol. 146, (2018), 9–18. https://doi.org/10.1016/j.coldregions.2017.11.011
26. Vahdani, M., Ghazavi, M., and Roustaei, M. "Measured and Predicted Durability and Mechanical Properties of Frozen-Thawed Fine Soils." ***KSCE Journal of Civil Engineering***, Vol. 24, (2020), 740–751. https://doi.org/10.1007/s12205-020-2178-4
27. Wang, T., and Su, L. "Experimental Study on Moisture Migration in Unsaturated Loess under Effect of Temperature." ***Journal of Cold Regions Engineering***, Vol. 24, No. 3, (2010), 77–86. https://doi.org/10.1061/(ASCE)CR.1943-5495.0000015

28. Konrad, J. "Influence of Cooling rate on the temperature of ice lens formation in clayey silts." ***Cold Regions Science and Technology***, Vol. 16, No. 1, (1989), 25–36. https://doi.org/10.1016/0165-232X(89)90004-9
29. Ahmed, A., and Ugai, K. "Environmental effects on durability of soil stabilized with recycled gypsum." ***Cold Regions Science and Technology***, Vol. 66, No. 2–3, (2011), 84–92. https://doi.org/10.1016/j.coldregions.2010.12.004
30. Altun, S., Sezer, A., and Erol, A. "The effects of additives and curing conditions on the mechanical behavior of a silty soil." ***Cold Regions Science and Technology***, Vol. 56, No. 2–3, (2009), 135–140. https://doi.org/10.1016/j.coldregions.2008.11.007
31. Gullu, H., and Hazirbaba, K. "Unconfined compressive strength and post-freeze – thaw behavior of fine-grained soils treated with geo fi ber and synthetic fluid." ***Cold Regions Science and Technology***, Vol. 62, (2010), 142–150. https://doi.org/10.1016/j.coldregions.2010.04.001
32. Hazirbaba, K., and Gullu, H. "California Bearing Ratio improvement and freeze – thaw performance of fi ne-grained soils treated with geo fiber and synthetic fluid." ***Cold Regions Science and Technology***, Vol. 63, No. 1–2, (2010), 50–60. https://doi.org/10.1016/j.coldregions.2010.05.006
33. Kalkan, E. "Effects of silica fume on the geotechnical properties of fine-grained soils exposed to freeze and thaw." ***Cold Regions Science and Technology***, Vol. 58, No. 3, (2009), 130–135. https://doi.org/10.1016/j.coldregions.2009.03.011
34. Kamei, T., Ahmed, A., and Shibi, T. "Effect of freeze – thaw cycles on durability and strength of very soft clay soil stabilised with recycled Bassanite." ***Cold Regions Science and Technology***, Vol. 82, (2012), 124–129. https://doi.org/10.1016/j.coldregions.2012.05.016
35. Liu, J., Wang, T., and Tian, Y. "Experimental study of the dynamic properties of cement- and lime-modi fi ed clay soils subjected to freeze – thaw cycles." ***Cold Regions Science and Technology***, Vol. 61, No. 1, (2010), 29–33. https://doi.org/10.1016/j.coldregions.2010.01.002
36. Olgun, M. "The effects and optimization of additives for expansive clays under freeze – thaw conditions." ***Cold Regions Science and Technology***, Vol. 93, (2013), 36–46. https://doi.org/10.1016/j.coldregions.2013.06.001
37. Yarbasi, N., Kalkan, E., and Akbulut, S. "Modification of the geotechnical properties , as influenced by freeze – thaw , of granular soils with waste additives." ***Cold regions science and technology***, Vol. 48, (2007), 44–54. https://doi.org/10.1016/j.coldregions.2006.09.009
38. Aldaood, A., Bouasker, M., and Al-mukhtar, M. "Impact of freeze – thaw cycles on mechanical behaviour of lime stabilized gypseous soils." ***Cold Regions Science and Technology***, Vol. 99, (2014), 38–45. https://doi.org/10.1016/j.coldregions.2013.12.003
39. Sadr Karimi, J. "Compressive strength freeze and thaw durabiliy correlation in soil cement design." ***International Journal of Engineering***, Vol. 13, No. 4, (2000), 65–71. Retrieved from: file:///C:/Users/Empire/Downloads/85620000407.pdf
40. Christ, M., and Park, J. "Laboratory determination of strength properties of frozen rubber – sand mixtures." ***Cold Regions Science and Technology***, Vol. 60, No. 2, (2010), 169–175. https://doi.org/10.1016/j.coldregions.2009.08.013
41. Ghazavi, M., and Roustaei, M. "Thaw performance of clayey soil reinforced with geotextile layer." ***Cold Regions Science and Technology***, Vol. 89, (2013), 22–29. https://doi.org/10.1016/j.coldregions.2013.01.002
42. Ghazavi, M., and Roustaie, M. "The influence of freeze – thaw cycles on the unconfined compressive strength of fiber-reinforced clay," ***Cold Regions Science and Technology,*** Vol. 61, (2010), 125–131. https://doi.org/10.1016/j.coldregions.2009.12.005
43. Jafari, M., and Esna-ashari, M. "Effect of waste tire cord reinforcement on uncon fi ned compressive strength of lime stabilized clayey soil under freeze – thaw condition." ***Cold Regions Science and Technology***, Vol. 82, (2012), 21–29. https://doi.org/10.1016/j.coldregions.2012.05.012
44. Zaimoglu, A. S. "Freezing – thawing behavior of fi ne-grained soils reinforced with polypropylene fi bers." ***Cold Regions Science and Technology***, Vol. 60, No. 1, (2010), 63–65. https://doi.org/10.1016/j.coldregions.2009.07.001
45. Shoop, S., Affleck, R., Haehnel, R., and Janoo, V. "Mechanical behavior modeling of thaw-weakened soil." ***Cold Regions Science and Technology***, Vol. 52, (2008), 191–206. https://doi.org/10.1016/j.coldregions.2007.04.023
46. Li, N., Chen, F., Su, B., and Cheng, G. "Theoretical frame of the saturated freezing soil," ***Cold Regions Science and Technology***, Vol. 35, (2002), 73–80. https://doi.org/10.1016/S0165-232X(02)00029-0
47. Li, N., Chen, F., Xu, B., and Swoboda, G. "Theoretical modeling framework for an unsaturated freezing soil," ***Cold Regions Science and Technology***, Vol. 54, No. 1, (2008), 19–35. https://doi.org/10.1016/j.coldregions.2007.12.001
48. Li, N., Chen, B., Chen, F., and Xu, X. "The coupled heat-moisture-mechanic model of the frozen soil," ***Cold Regions Science and Technology***, Vol. 31, No. 3, (2000), 199–205. https://doi.org/10.1016/S0165-232X(00)00013-6
49. Qi, J., Yao, X., Yu, F., and Liu, Y. "Study on thaw consolidation of permafrost under roadway embankment." ***Cold Regions Science and Technology***, Vol. 81, (2012), 48–54. https://doi.org/10.1016/j.coldregions.2012.04.007
50. Wang, S., Qi, J., Yu, F., and Yao, X. "A novel method for estimating settlement of embankments in cold regions." ***Cold Regions Science and Technology***, Vol. 88, (2013), 50–58. https://doi.org/10.1016/j.coldregions.2012.12.009
51. Zhiwu, Z., Jianguo, N., and Shuncheng, S. "Finite-element simulations of a road embankment based on a constitutive model for frozen soil with the incorporation of damage." ***Cold Regions Science and Technology***, Vol. 62, No. 2–3, (2010), 151–159. https://doi.org/10.1016/j.coldregions.2010.03.010
52. Lai, Y., Jin, L., and Chang, X. "Yield criterion and elasto-plastic damage constitutive model for frozen sandy soil." ***International Journal of Plasticity***, Vol. 25, No. 6, (2009), 1177–1205. https://doi.org/10.1016/j.ijplas.2008.06.010
53. Liu, Z., and Yu, X. "Coupled thermo-hydro-mechanical model for porous materials under frost action : theory and implementation," ***Acta Geotech***, Vol. 6, (2011), 51–65. https://doi.org/10.1007/s11440-011-0135-6
54. Lackner, R., Pichler, C., and Kloiber, A. "Artificial Ground Freezing of Fully Saturated Soil: Viscoelastic Behavior." ***Journal of Engineering Mechanics***, Vol. 134, No. January, (2008), 1–11. https://doi.org/10.1061/(ASCE)0733-9399(2008)134:1(1)
55. Yang, Y., Lai, Y., Dong, Y., and Li, S. "The strength criterion and elastoplastic constitutive model of frozen soil under high confining pressures." ***Cold Regions Science and Technology***, Vol. 60, No. 2, (2010), 154–160. https://doi.org/10.1016/j.coldregions.2009.09.001
56. Yuanming, L., Yugui, Y., Xiaoxiao, C., and Shuangyang, L. "Strength criterion and elastoplastic constitutive model of frozen silt in generalized plastic mechanics." ***International Journal of Plasticity***, Vol. 26, No. 10, (2010), 1461–1484. https://doi.org/10.1016/j.ijplas.2010.01.007
57. Lai, Y., Pei, W., Zhang, M., and Zhou, J. "Study on theory model of hydro-thermal–mechanical interaction process in saturated freezing silty soil." ***International Journal of Heat and Mass***

Transfer, Vol. 78, (2014), 805–819. https://doi.org/10.1016/j.ijheatmasstransfer.2014.07.035

58. Shoop, S. A., and Bigl, S. R. "Moisture migration during freeze and thaw of unsaturated soils : modeling and large scale experiments." ***Cold Regions Science and Technology***, Vol. 25, (1997), 33–45.
59. Tsypkin, G. G. "Effect of the Capillary Forces on the Moisture Saturation Distribution during the Thawing of a Frozen Soil," ***Fluid Dynamics***, Vol. 45, No. 6, (2010), 942–951. https://doi.org/10.1134/S0015462810060128
60. Horiguchi, K. "An osmotic model for soil freezing." ***Cold Regions Science and Technology***, Vol. 14, No. 1, (1987), 13–22. https://doi.org/10.1016/0165-232X(87)90040-1
61. Nakano, Y. "Water expulsion during soil freezing described by a mathematical model called M 1." ***Cold Regions Science and Technology***, Vol. 29, No. 1, (1999), 9–30. https://doi.org/10.1016/S0165-232X(98)00021-4
62. Biermans, M. B. G. M., Dijkema, K. M., and De Vries, D. A. "Water movement in porous media towards an ice front." ***Journal of Hydrology***, Vol. 37, No. 1-2, (1978), 137–148. https://doi.org/10.1016/0022-1694(78)90102-6
63. Zhao, Y., Yu, B., Yu, G., and Li, W. "Study on the water-heat coupled phenomena in thawing frozen soil around a buried oil pipeline." ***Applied Thermal Engineering***, Vol. 73, No. 2, (2014), 1477–1488. https://doi.org/10.1016/j.applthermaleng.2014.06.017
64. Song, W., Zhang, Y., Li, B., and Fan, X. "A lattice Boltzmann model for heat and mass transfer phenomena with phase transformations in unsaturated soil during freezing process." ***International Journal of Heat and Mass Transfer***, Vol. 94, (2016), 29–38. https://doi.org/10.1016/j.ijheatmasstransfer.2015.11.008
65. Wu, D., Lai, Y., and Zhang, M. "Heat and mass transfer effects of ice growth mechanisms in a fully saturated soil." ***International Journal of Heat and Mass Transfer***, Vol. 86, (2015), 699–709. https://doi.org/10.1016/j.ijheatmasstransfer.2015.03.044
66. Nakano, Y., and Tice, A. R. "Transport of water due to a temperature gradient in unsaturated frozen clay." ***Cold Regions Science and Technology***, Vol. 18, No. 1, (1990), 57–75. https://doi.org/10.1016/0165-232X(90)90038-X
67. Menot, L. M. "Equations of frost propagation in unsaturated porous media." ***Engineering Geology***, Vol. 13, No. 1, (1979), 101–109. https://doi.org/10.1016/0013-7952(79)90024-3
68. Zhou, Y., and Zhou, G. "Numerical simulation of coupled heat-fluid transport in freezing soils using finite volume method," ***Heat and Mass Transfer***, Vol. 46, (2010), 989–998. https://doi.org/10.1007/s00231-010-0642-2
69. Zhihua, G., Yuanming, L., Mingyi, Z., Jilin, Q., and Shujuan, Z. "An element free Galerkin method for nonlinear heat transfer with phase change in Qinghai – Tibet railway embankment," ***Cold Regions Science and Technology,*** Vol. 48, No. 1, (2007), 15–23. https://doi.org/10.1016/j.coldregions.2006.10.004
70. Exadaktylos, G. E. "Freezing–Thawing Model for Soils and Rocks." ***Journal of Materials in Civil Engineering***, Vol. 18, No. 2, (2006), 241–249. https://doi.org/10.1061/(ASCE)0899-1561(2006)18:2(241)
71. Yang, W., Kong, L., and Chen, Y. "Numerical evaluation on the effects of soil freezing on underground temperature variations of soil around ground heat exchangers." ***Applied Thermal Engineering***, Vol. 75, (2015), 259–269. https://doi.org/10.1016/j.applthermaleng.2014.09.049
72. Saeedmonir, H., Gheyretmand, C., and Sarlak, A. "Numerical and experimental study of soil structure interaction in structures resting on loose soil using laminar shear box." ***International Journal of Engineering - Transactions B: Applications***, Vol. 30, No. 11, (2017), 1654–1663. https://doi.org/10.5829/ije.2017.30.11b.05
73. Akbari Garakani, A., Sadeghi, H., Saheb, S., and Lamei, A. "Bearing capacity of shallow foundations on unsaturated soils: analytical approach with 3D numerical simulations and experimental validations." ***International Journal of Geomechanics***, Vol. 20, No. 3, (2020). https://doi.org/10.1061/(ASCE)GM.1943-5622.0001589
74. Khanmohammadi, M., and Fakharian, K. "Evaluation of performance of pile raft foundations on soft clay: a case study." ***Geomechanics and Engineering***, Vol. 14, No. 1, (2018), 43–50. https://doi.org/10.12989/gae.2018.14.1.043
75. Safarzadeh, Z., and Aminfar, M. H. "Experimental and numerical modeling of the effect of groundwater table lowering on bearing capacity of shallow square footings." ***International Journal of Engineering - Transactions A: Basics***, Vol. 32, No. 10, (2019), 1429–1436. https://doi.org/10.5829/IJE.2019.32.10A.12
76. Iraji, A. "Reinforced soil wall analysis under working stress conditions using a two phase model with the introduction of a new design parameter." ***International Journal of Engineering Transactions C: Aspects***, Vol. 32, No. 12, (2019), 1162-1172. https://doi.org/10.5829/IJE.2019.32.12C.09
77. Poorebrahim, G. R., and Malekpoor, M. R. "Behavior of compacted lime-soil columns." ***International Journal of Engineering Transactions B: Applications***, Vol. 27, No. 2, (2014), 315-324. https://doi.org/10.5829/idosi.ije.2014.27.02b.15
78. Mehdipour, I., Vahdani, M., Amini, K., and Shekarchi, M. "Linkin stability characteristics to material performance of self-consolidating concrete equivalent mortar incorporating fly ash and metakaolin." ***Construction and Building Materials***, Vol. 105, (2016), 206-217. https://doi.org/10.1016/j.conbuildmat.2015.12.090
79. Figueiras, H., Nunes, S., Sousa, J., and Andrade, C. "Linking fresh and durability properties of paste to SCC mortar." ***Cement and Concrete Composites***, Vol. 45, (2014), 209–226. https://doi.org/10.1016/j.cemconcomp.2013.09.020
80. Hwang, S.-D., and Khayat, K. H. "Durability characteristics of self-consolidating concrete designated for repair applications." ***Materials and Structures***, Vol. 42, No. 1, (2009), 1–14. https://doi.org/10.1617/s11527-008-9362-1
81. Anderson, C., Borror, C. M., and Montgomery, D. C. "Response Surface Design Evaluation and Comparison." ***Journal of Statistical Planning and Inference***, Vol. 139, No. 2, (2009), 629–674. https://doi.org/10.1016/j.jspi.2008.04.004
82. Box, G. E. P., and Draper, N. R. Response Surfaces, Mixtures, and Ridge Analysis. John Wiley & Sons. New York.
83. Montgomery, D. C., Vining, G. G., and Borror, C. M. "Response Surface Methodology: A Retrospective and Literature Survey." Journal of Quality Technology, Vol. 36, No. 1, (2004), 53–77. https://doi.org/10.1080/00224065.2004.11980252
84. Khuri, A. I., and Cornell, J. A. Response Surfaces: Designs and Analyses (2nd edition). Routledge, New york.

Persian Abstract

چکیده

بررسی آزمایشگاهی دقیق در خصوص خواص مهندسی خاک عموما بسیار زمان بر و احتمالا پر هزینه است. این روش به عنوان یک روش کارآمد برای بهینه سازی بسیاری از مسائل فیزیکی همچون کنترل میزان تولید و ساخت در صنعت بیش از دو دهه مورد استفاده بوده است. در تحقیق حاضر روش سطح پاسخ به عنوان یک ابزار برای توسعه مدل هایی جهت پیش بینی برخی خواص مکانیکی برای خاک های منجمد (مانند مقاومت پیک کششی و یا فشاری، مدول ارتجاعی، کرنش گسیختگی و غیره) مورد استفاده قرار گرفت. همچنین روش سطح پاسخ یافتن فاکتورهای معنی دار و اندرکنش های محتمل را میسر می‌سازد. پس از انجام یک بازبینی گسترده ادبیات فنی، سه مطالعه موردی به منظور ارزیابی عملکرد روش سطح پاسخ در تولید مدل‌های دقیق آماری انتخاب گردید. برای هر مطالعه موردی کمتر از نیمی از داده‌های قابل دسترس (تقریباً ٤٠/٨ درصد) به منظور توسعه مدل‌های آماری به کار گرفته شدند و باقی مانده داده‌ها به جهت صحت‌سنجی مدل‌های استخراج شده مورد استفاده قرار گرفتند. یک مقایسه میان مقادیر پیش بینی شده و اندازه‌گیری شده تطابق مناسبی با سطح معنی داری ۰/۰۵ مشاهد شد، که این امر نشان دهنده عملکرد قابل اعتماد مدل‌ها در محدوده فرضیات در نظر گرفته شده برای هر یک از نمونه‌های موردی است. به علاوه کانتورهایی به منظور ارائه یک توصیف جامع از همبستگی‌های محتمل میان خواص و فاکتورهای بررسی شده ارائه گردیده است. بر اساس مدل‌های استخراج شده که به طور متوسط دارای ضریب همبستگی (R^2) ۹۳/٦۹ می‌باشند، دما معنی‌دارترین فاکتور اثرگذار بر خواص مکانیکی خاک‌های ریزدانه منجمد به شمار می‌رود؛ در حالی که دانسیته خشک خاک به اندازه دما اثرگذار نمی‌باشد.

International Journal of Engineering

Journal Homepage: www.ije.ir

Improving Thermal and Mechanical Property of Lightweight Concrete Using N-Butyl Stearate/Expanded Clay Aggregate with Alccofine1203

P. Kulkarni*, A. Muthadhi

Department of Civil Engineering, Pondicherry Engineering College, Pondicherry, India

P A P E R I N F O

Paper history:
Received 12 June 2020
Received in revised form 07 July 2020
Accepted 04 August 2020

Keywords:
Phase Change Material
Expanded Clay Aggregate
Immersion
Oozing Circle
Alccofine1203
Thermal Conductivity

A B S T R A C T

Phase change material (PCM) as n-butyl stearate (n-BS) was immersed in expanded clay aggregate (ECA) by two methods, direct immersion at room temperature and immersion at elevated temperature (30ºC, 40ºC and 50ºC). ECA after 90min of immersion with n-BS at 40ºC came to standby in its weight proportion (increased by 24%). After immersion, these aggregates (40ºC) were mixed in cement slurry for preventing leakage and homogenous mixture with concrete. Oozing circle a leakage test was conducted on all the ECA with and without cement slury coating (room and elevated temperatures). ECA with cement slurry coating gave a reduction in leakage of ECA-PCM by 45%. Alccofine1203 was partially replaced (10% and 20%) by cement to improve mechanical properties in lightweight aggregate concrete. Compressive, flexural, thermal conductivity, DSC analysis and leakage test on aggregate and concrete specimens were conducted on all the mixes. Compressive strength for 10% replacement gave 31.7 kN/m^2 and 32.8 kN/m^2 for 7th day and 28th day, respectively. Similarly, flexural strength gave 6.12 kN/m^2 for 28 days. DSC analysis of pure PCM (n-BS) gave 30.42ºC and 23.25 ºC for its melting and freezing temperature with 134.2 J/g and 129.3J/g as enthalpy for its melting and freezing points, respectively. Thermal conductivity for mix-3 (10%PCM-ECA +10% alccofine1203) gave the lowest value of all the mixes i.e, 13% less than the reference mix. There was no leakage or any stain marks were observed on the filter paper till 10% incorporation.

***doi**: 10.5829/ije.2020.33.10a.03*

NOMENCLATURE

R	Radius	K	Thermal Conductivity
I	Latent heat	W_t	The dry weight of ECA before submersion
W_i	Weight of ECA after submersion at any time	Q	The heat flow rate in the specimen, Watts
A	Specimen area, m^2	T_h	Hot plate temperature, °C
T_c	Temperature of Cold plate, °C	L	The thickness of the specimen, m

1. INTRODUCTION

Energy consumption has increased rapidly to provide a comfortable environment for humans worldwide. Buildings play a crucial part in the usage of a significant part of energy resources. Consumption in India is almost doubled since 2000 and energy demand per capita is 40% out of which 33% contribute to the global emission of greenhouse gases. On an average India's consumption in energy is increased by 2.4 to 3.2% per year from 2015 to 2040 [1].

Energy savings in the residential or commercial sector using different materials for thermal energy-efficient buildings has given a new scope for research. A general idea amidst the energy-efficient building design strategies is to increase the thermal mass of the building materials which can store the thermal energy during day time and release the energy at night. This can ultimately save energy consumption in building sectors and reduce

*Corresponding Author Institutional Email: *prathik.kulkarni89@pec.edu* (P. Kulkarni)

Please cite this article as P. Kulkarni, A. Muthadhi, Improving Thermal And Mechanical Property Of Lightweight Concrete Using N-Butyle Stearate/Expanded Clay Aggregate With Alccofine1203, International Journal of Engineering (IJE), IJE TRANSACTIONS A: Basics Vol. 33, No. 10, (October 2020) 1842-1851

the peak temperature and temperature fluctuations indoor [2-3]. In the last few years, many construction solutions have been proposed to improve the thermal performance of building envelope by either increasing the material mass and/or increasing the heat capacity of the construction material [2-4]. Phase changing materials (PCMs) are the materials with good heat-storage capabilities, good energy conservation performance and promising building materials [5]. There have been numerous research attempts to use PCMs through direct mixing, immersion and impregnation in building envelopes [6, 7]. There are also functional challenges when combined with elements of the structure, for example mortar, concrete gypsum sheets, wall-covering fabrics, etc.

Some of the safest PCMs are organic paraffin wax for use in concrete as it has excellent thermal consistency, not quite alkaline [8]. Other good aspects of paraffin wax, including the melting point suitable for human comfort zone, have high capacity heat, congruent melting without segregation, low or no supercooling during phase transition, lower vapor pressure, non-toxicity, non-corrosive metal containers, good chemical and thermal stability, and low cost [9-11]. Paraffin 's main limitations include its low thermal conductivity, flammability, plastics incompatibility and high volume changes

Some of the recent researches on form stable natural composite PCM impregnated with paraffin [12] based natural form stable natural PCMs into permeable materials have stood out [13, 14]. Lightweight aggregates such as expanded graphite [13, 14], expanded perlite [13-15], vermiculite [16], and expanded clay/shale aggregate [17] have been used for producing stable composite PCMs. Due, to low thermal conductivity, paraffin-based PCMs were limited, which decreases the rate of heat stored and released during melting and crystallization processes. On the other hand, paraffin was used as core material for encapsulation to form shape-stabilized composite PCM [18-21].

Incorporation of microencapsulated PCM in gypsum boards [22] resulted in a 4K reduction in the indoor room temperature [23]. Micro-encapsulation of PCM as metallic/polymeric containers in building materials is costly and may influence the mechanical quality of the structure material when get harmed during blending [24, 25]. Butyl stearate as PCM and stabilized silica sol as an economically friendly silica source (ss). Our ss-PCM boards are the first reported monoliths with high compressive strengths of 1.2 MPa at 10^{o}C and 0.7 MPa at 30^{o}C despite high PCM mass percentages up to 86 wt%. Moreover, our ss-PCMs are form-stable up to 94 wt% PCM, thermally stable up to 320^{o}C and hydrophobic, suggesting a strong weather capacity. Its latent heats vary from 85 J / g at 20°C and 100 J / g at 22°C, which are steady for at least 6000-state transformations from liquid to solid which vice versa. DSC results from the hexahydrate mixture of the encapsulated butyl stearate / calcium chloride. The temperature at which this occurs phase change occurs is 32.59^{o}C. The latent heat of fusion is 145.39 J/g. The measured thermal conductivity of regular LWA-PCM and LWA-PCM coated with carbon fiber and graphene spray was 0.1382W/mK, 0.1382W/mK, and 0.1337W/mK, respectively [26, 27].

PCMs may be blended directly into concrete matrix by means of either wet mixing or immersion / impregnation techniques [28]. During casting period in wet mixing liquid PCM is blended into the concrete mixture [28]. It means that there is no carrier / barrier between PCM and concrete mix that may increase its leakage risk and adversely affect the concrete properties. Similarly, immersion process is the procedure under which PCM is used to hold a carrier (Clay, shale, perlite .. etc) and this carrier is submerged in a liquid PCM jar from which PCM is gradually dissolved in the carrier's pores through capillary action [29].

Active inclusion of PCMs in traditional building materials [30] allows PCMs uniformly distributed and often contributes to leakage and other problems [31]. Other studies have shown that direct mixing phase change material can greatly improve the hydration cycle, but affects the mechanical properties of cement paste / concrete [32]. Alccofine1203 has improved mechanical quality properties in high intensity concrete and green concrete [32-34] with a 10% integration. Direct incorporation of PCM in concrete had been studied primarily earlier. Schossig et al. [35] commented, however, that unencapsulated PCMs are PCMs that are prone to interfere with the surrounding matrix and attempt to alter their properties, or that may have lifetime leakage issues. Therefore the immediate integration of PCM into concrete is no longer known as a functional strategy in concrete. This is probably the reason why research studies in the last decade have been scarce, in which a direct method is used to incorporate PCM into the concrete.

In the present work, to improve the thermal property of concrete, expanded clay aggregate (ECA) was used as a carrier with PCM (n-BS). The PCM (n-BS) was first kept at 50^{o}C to completely melt and then ECA was immersed at room temperature and elevated temperature (30^{o}C, 40^{o}C, 50^{o}C). Now, these aggregates were incorporated in concrete by volume-based method, 10 and 20% partial replacement of coarse aggregate in concrete. The specimens were subjected to various tests includes leakage test on ECA, compression, flexural, thermal conductivity, DSC analysis and leakage test on the concrete specimen. Alccofine1203 was partially replaced (10 and 20%) by cement to improve the mechanical properties of concrete.

2. EXPERIMENTAL PROCEDURE

2. 1. Materials

- Ordinary Portland cement of 43 grade confirming to IS: 8112 – 1989
- Locally available river sand with passing sieve no. 4.75mm to 150 microns with specific gravity 2.50 and FM = 2.36.
- Commercially available expanded clay aggregate and its properties with sieve analysis given in Table 1 and Figure 1.
- Commercially available Alccofine1203 confirming to ASTM C89-1999, physical properties and chemical composition is given in Table 2.
- Phase change material: n-BS and its properties given in Table 3.

TABLE 1. Physical properties of ECA

Properties	ECA
Specific gravity	0.54
Water absorption (%)	15
Bulk density(kg/m3)	337
Fineness modulus	7.26

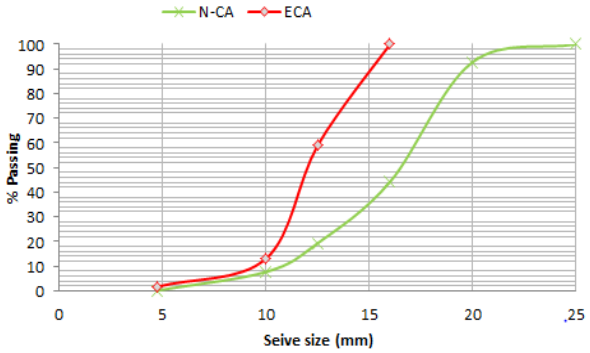

Figure 1. Sieve analysis of natural coarse aggregate (N-CA) and ECA

TABLE 2. Physical & Chemical properties of alccofine1203

Properties			Alccofine1203		
Specific gravity			2.9		
Bulk density (kg/m^3)			680		
Specific surface area (m^2/kg)			1200		
Size of the particles in the micron					
D10			1.5		
D15			5		
D90			9		
CaO	SiO_2	Al_2O_3	Fe_2O_3	SO_3	MgO
61-64	21-23	5-5.6	3.8-4.4	2-2.4	0.8-1.4

TABLE 3. Properties of PCM (n-BS)

Property	Value
Melting Temperature (°C)	27
Boiling Point (°C)	343.0
Density (25°C/4(°C)	0.854
Molecular weight (g/mol)	340.6
Molecular formula	$C_{22}H_{44}O_2$
Solubility	Insoluble in water
Color	Colorless
Physical Form	Liquid

2. 2. Preparation of PCM Aggregates The n-BS was impregnated into a lightweight aggregate (ECA) at 3 different temperatures (30°C, 40°C and 50°C). The process began with drying ECA at 105°C in the oven for 24h. After that ECA was placed in a container with liquid PCM and placed one of the containers at room temperature and other 3 containers at 30°C, 40°C and 50°C for the next 2 hours. Every 10min, the samples were taken out and weighted for its measure weight change and the degree of impregnation was calculated by the Equation (1).

$$\% \text{ Impregnation} = [(W_t - W_i) / W_i] \times 100 \quad (1)$$

where
W_t = dry weight of ECA before submersion
W_i = weight of ECA after submersion at any time.
The process continued until the highest weight impregnation was achieved with constant weight change over time. Now, these aggregates were used in preparing PCM lightweight aggregate.

2. 3 Preparing Concrete Samples The ECA-PCM aggregates were prepared using the findings obtained in section 2.2 for the shortest time period for the largest impregnation at ECA. Several trial blends for achieving the best in terms of workability (slump) and power were performed. A comprehensive proportion of the trial mix with the total number of specimens is shown in Table 4.

2. 4. Experimental Series After preparing the PCM-ECA aggregates are partially replaced by coarse aggregate with 10 and 20% with coarse aggregate. Alccofine1203 was also partially replaced with cement by 10 and 20% in concrete. All the specimens are prepared and cured for 7 and 28 days and are subjected to the series of tests. Mix proportion of M30 grade concrete with number of Specimens are given in Table 5.

1. Leakage test on ECA material
2. Compressive strength (100x100x100mm)

TABLE 4. n-BS absorption capacity in ECA at different temperature and time

Temperature / Time (min)	RT	30^{0}C	40^{0}C	50^{0}C
10	100	101	101	102
20	105	103	103	104
30	107	105	107	107
40	110	106	109	108
50	112	109	115	115
60	113	103	118	119
70	113	115	121	122
80	114	118	123	123
90	114	120	124	123
100	118	121	124	124
110	118	121	124	124
120	118	121	124	124

3. Flexural strength (100x100x500mm)
4. Thermal Conductivity (10mmx180mm dia)
5. DSC analysis
6. Leakage test on specimens (100x100x100mm)

2. 5. Thermal Properties

2. 5. 1. Thermal Conductivity (K) Thermal conductivity (K) test conducted on all the specimens using a two-slab guarded hot plate method according to IS3346 (1980). The following equation used to find the value of K

$$K = Q/2A(L/(Th - Tc)) \quad (2)$$

where;
K = Thermal Conductivity of a sample, W / m^2.k
Q = Heat flow rate in the specimen, Watts
A = Metering area of the specimen, m^2
T_h = Hot plate temperature, °C
T_c = Cold plate temperature, °C
L = Thickness of specimen, m

2. 5. 2. DSC Analysis DSC research on Pure PCM content (n-BS) was conducted. DSC analysis is a method used to measure the latent heat that is contained in the material. It is the methodology in which as a function of temperature the difference of the volume of heat needed to increase the sample pan temperature with reference pan is determined. In the DSC the temperature is regulated in such a manner that the temperature of the sample holder decreases linearly as a function of time. The experiment was conducted for both heating and cooling from -10 ^{o}C to 60^{o}C with a temperature period of as 2^{o}C. To determine the melting/freezing point and latent heat stored in material, TA Instrument with Model: DSC Q2000.

2. 6. Leakage Test on Concrete Specimens After 28 days of curing time, concrete specimens of all the mix are tested for its leakage test according to literature [26]. The specimens are completely wrapped with filter paper and weight before wrapping and after wrapping is noted. The specimens are kept in an oven at 60^{o}C for 1hour. After 1h the filter paper is weighed and the percentage of PCM leakage is determined, the filter paper is carefully examined for any stain marks on it.

3. RESULTS AND DISCUSSION

3. 1. Sieve Analysis and Chemical Composition Of Alccofine1203 Sieve analysis was conducted on natural fine, coarse aggregate and ECA using standard 4.75mm to 150-micron sieve for fine aggregate with the properties according to IS: 2386-2016, IS 383-2016. Coarse aggregate (CA) and ECA were sieved using 20mm to 4.75mm sieve and its properties are evaluated according to IS: 2386-196. Figure 1 shows the same pattern of the curve for CA and ECA. The physical and

TABLE 5. Mix proportions of M30 grade concrete

Mix designation	Cement (kg/m^3)	Fine aggregate (kg/m^3)	Coarse aggregate (kg/m^3)	Superplasticizer (lit/m^3)	ECA (kg/m^3)	Alccofine1203 (kg/m^3)	Total No of Specimens
1 Reference	410		1148		-	-	
2 (0%Alc -10% ECA)	410		1033.2		35		
3 (0%Alc -20% ECA)	410		918.4		70		
4 (10%Alc -10% ECA)	369	664	1033.2	1.75	35	41	91
5 (10%Alc -20% ECA)	369		918.4		70	41	
6 (20%Alc -10% ECA)	328		1033.2		35	82	
7 (20%Alc -20% ECA)	328		918.4		70	82	

chemical properties of ECA and alccofine1203 are given in Tables 1 and 2. The specific gravity of alccofine1203 is nearly equal to cement with a specific surface area 4 times more than cement. Chemical composition of alccofine1203, when compared with cement, is nearly the same with more percentage of Cao (61-64%), followed by SiO_2, Al_2O_3, and Fe_2O_3 by 21, 5 and 3.8%, respectively.

3. 2. Composite Absorption Characteristics

The maximum absorption capacity at room temperature and elevated temperature is found and described in section 2.2 and Table 4. Using diffusion oozing circle test leakage of these composite aggregates is found. PCM-ECA aggregates are placed on a filter paper and kept in an oven at 50°C which is above the melting point of PCM (n-BS) for one hour. Figure 2 shows that PCM-ECA without coating (WC) of cement slurry had much leakage but it was improved when cement slurry coating was applied on PCM-ECA. Up to 45% leakage was reduced with (W) Coating of the cement slurry at 40°C with 90min of immersion time.

3. 3. Mechanical Properties

3. 3. 1. Compressive Strength From Figure 2 it is clear as the percentage of ECA increased, strength decreased, and vice versa. The strength of the concrete has improved as alccofine1203 was added to concrete with partially replaced (10 and 20%) of cement. When PCM (n-BS) was incorporated into the pores of ECA from section 2.2, the strength of concrete has reduced but not less than the required strength. Most of the studies showed that LWA has an adverse effect on the mechanical properties of concrete [36-39].

When ECA-PCM composite is partially replaced with CA by 10 and 20% for 7th day compressive strength an decrease in its pattern was observed in mix-2 and mix-3 from Figure 3. Without PCM in ECA gave an increase in strength by 4.4% for mix-2 and a drastic reduction was observed in mix-3 (20% ECA only) with 46%. When alccofine1203 was added with ECA-PCM in mix-4, there was an increase in strength by 4.4% but for the same percentage (10%) of alccofine1203 and increase in ECA-PCM by 20% (mix-5) there was a reduction in strength by 7.9 and 14.9% when compared with mix-2 and reference mix., respectively. Now when alccofine1203 was increased to 20% in mix-6 with ECA-PCM (10%), strength was the same as that of reference mix. Similarly, when ECA-PCM was increased by 20% in mix-7, strength was reduced by 20.4% when compared with the reference mix. There was a drastic reduction observed in mix-4.

Different scholars hypothesized that the loss in compressive strength is largely attributable to breakage of the microcapsules (shells) and consequent leakage of PCM during the mixing or filling process [40-43], or due to chemical reactions [44] which can cause conflict with the hydration reaction of cement [45]. For 28th day compressive strength, the same pattern of the 7th-day graph was observed in Figure 4. With ECA-PCM strength was increased for all the mix except for mix-5 and mix-7. This is because of an increase in ECA

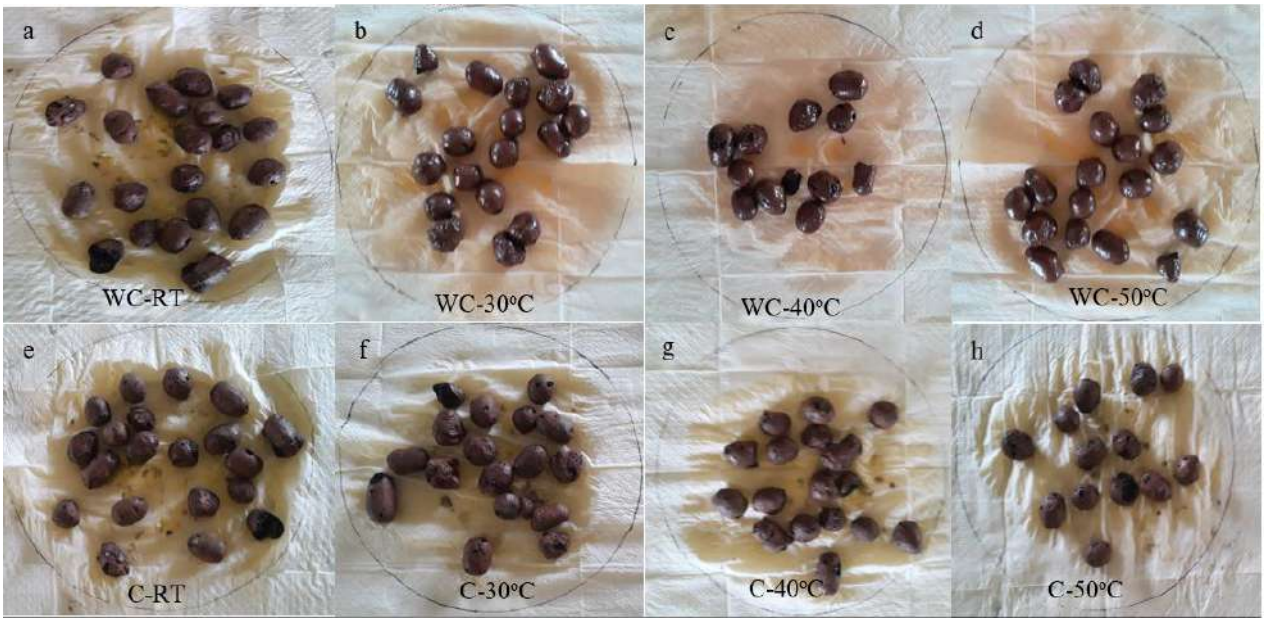

Figure 2. Diffusion oozing circle test for ECA without coating (WC) and with coating (C) a & e) Room temperature (RT), b & f) at 30°C, c & g) at 40°C, d & h) at 50°C

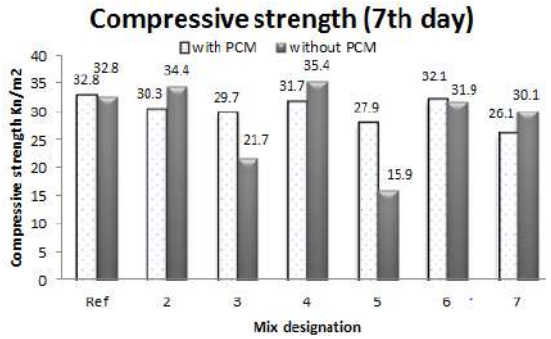

Figure 3. Compressive strength of PCM- ECA & Alccofine1203 composite (7 days)

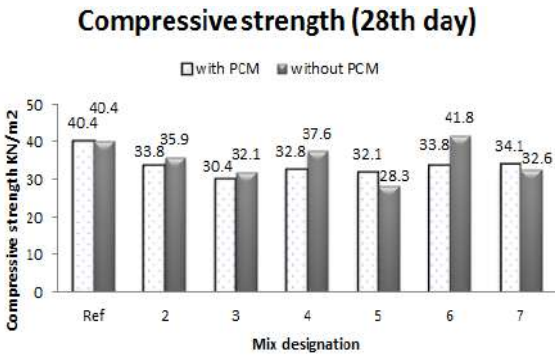

Figure 4. Compressive strength of PCM- ECA & Alccofine1203 composite 28 days

material from 10 to 20% in concrete. When ECA-PCM only was incorporated in concrete, its strength was reduced by 11.11 and 20.5% for mix-2 and mix-3, respectively when compared with reference mix. The strength improved when alccofine1203 was mixed in concrete with ECA-PCM (Mix-4) by 4.5% when compared with mix-2.

When the same amount of alccofine1203 (10%) was added with 20% of ECA-PCM (mix-5) a drastic reduction was observed in strength by 11.83% when compared with mix-3. The highest gain in strength was observed in mix-6 with 3.3% when compared with the reference mix. For ECA-PCM in mix-7, a reduction in strength by 19.3% was observed when compared with the reference mix. When alccofine1203 with ECA-PCM showed improvement in strength for mix-5 and mix-7. It is observed that mix-4 is the best combination to be incorporated in concrete.

Flexural strength of with and without PCM-ECA was evaluated after 28 days of curing in Figure 5. Without PCM the strength was increased for mix-2, mix-4 and mix-5 but similarly strength was reduced for mix-3, mix-5 and mix-6. It is observed from Figure 5 that, when ECA-PCM alone was incorporated in concrete its flexural strength was improved by 2.7% and reduced by 9.1% for mix-2 and mix-3, respectively. When only ECA material was incorporated in concrete without PCM immersion its flexural strength was reduced by 5.3 and 10.6% for mix-2 and mix-3, respectively. This is due to the density of ECA is 4 to 5 times less than natural CA. When alccofine1203 was incorporated with ECA-PCM, strength was gradually increased for mix-4 and mix-5. Strength was reduced when alccofine1203 was increased to 20% in mix-6 and mix-7 for both with and without ECA-PCM. Mix-2 with ECA-PCM gave the best result of all the mixes.

3. 4. Thermal Properties

3. 4. 1. DSC Analysis In the research conducted by Kastiukas et al. [39], a DSC experiment was used to measure the temperature difference in process and the conservation of LWA-PCM thermal energy. Pure PCM (n-BS) material was analyzed for DSC. The melting point and freezing point of pure n-BS are 30.45ºC and 23.75ºC, respectively, is evident from Figure 6. Stored enthalpy at heating and cooling, 134.2J/g and 129.3J/g were nearly similar to the data reported in literature [25]. When n-BS was impregnated with silica source, DSC analysis after 6000 heating and cooling cycles showed 85 J/g at 20ºC and 100 J/g at 2-22ºC, pure n-BS also reported 103.0 J/g and 101.8 J/g. To carry out the LWA-PCM DSC examination, the aggregates have to be compressed to a fine powder first. The latent heat stored in its purest state (RT25) is 130.5 J/g according to data reported in literature [46], while DSC analysis was conducted on LWA with RT25 being 57.93 J/g. Different test carried out by Min et al. [38], an experiment of DSC on LWA concrete was conducted to evaluate precise heat. The findings revealed that its basic heat often decreased as the PCM content rises in LWA. Despite the improvements, the ratio of LWA-PCM to cement is not significant. The specific heat measured for the temperature range from 10 to 24 ° C was 0.46 J/gK, 0.62 J/gK, 0.80 J/gK and 0.93 J/gK for 0%, 10%, 20% and 30% LWA-PCM, respectively [38].

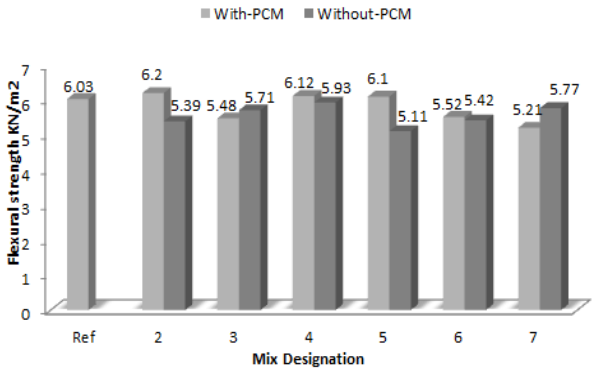

Figure 5. Flexural strength of PCM- ECA & Alccofine1203 composite (28th day)

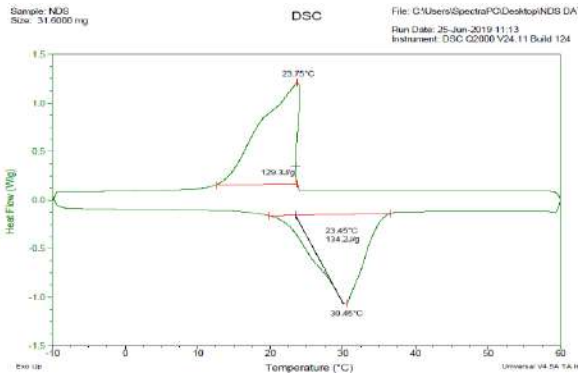

Figure 6. DSC analysis of n-Butyle Stearate

Similar to previous studies carried out by Ma et al. [37], a DSC analysis was used to find different proportions of the energy storage of concrete specimens containing LWA-PCM. Reports found that 86.40 and 82.73%, respectively in the heating cycle demonstrated the same real heat efficiency and the equivalent energy recovery of concrete with 20% LWA-PCM. Similarly in the cooling process, 60.10 and 56.94%, respectively increased the equivalent specific heat capacity and the equivalent energy storage of concrete with 20% LWA-PCM. The melting and freezing point with n-BS enthalpy is suitable for building envelopes to improve indoor temperature, because the temperature is in the comfort of humans.

3. 4. 2. Thermal Conductivity (K) In concrete materials, thermal conductivity (K) is used to determine the flow of power. From Figure 7 it is clear that its K value decreased as the percentage of PCM in ECA increased. In mix-2 the same amount of with and without PCM was found in concrete. While the amount of ECA-PCM Increased in mix-3 to 20%, its K value was significantly decreased by 13% relative to the reference combination. Adding with ECA-PCM in mix-4 and mix-5, Alccofine1203 raised the K value linearly by 20 and 40% relative to mix-3 but was lower by 13 and 8.6%,

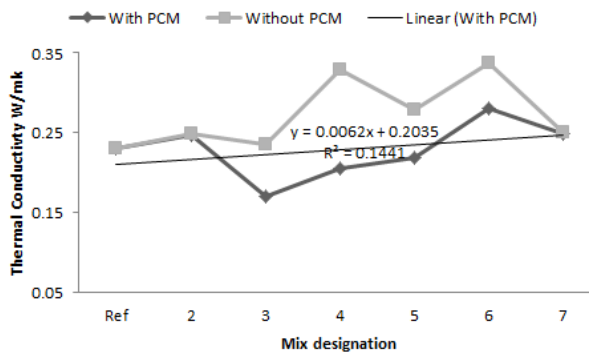

Figure 7. Thermal conductivity of ECA-PCM composite material

respectively than the reference combination. When alccofine1203 in mix-6 and mix-7 was increased to 20%, the K value increased by 14.8 and 4.1%, respectively. When only ECA was incorporated in concrete without PCM, its k value increased in all the mixes except in mix-3 which gave equal value to that of reference mix. The highest increase in k value was observed in mix-5 with 30.3% followed by mix-4, mix-5, mix-7, mix-3, and mix-2.

Data from other experiments found that the thermal conductivity of concrete mixtures treated with epoxy and adjusted cement paste LWA-PCM was approximately 0.615 W/mK and 0.738 W/mK, with an overall thermal conductivity loss of approximately 24.7 and 9.7%, respectively, for control concrete (0.817 W/mK) [47]. Heat conductivity of hardened concrete comprising LWA-PCM has also been assessed [48]. As in the analysis carried out by Memon et al. [27]. An alternative was found to increase the K value of LWA-PCM concrete composites, and Memon et al. [27] studied the addition of a conductive material as a coating for LWA-PCM. To enhance the thermal conductivity of LWA-PCM a mixture of epoxy and graphite powder was used as a coating material. Test findings found that thermal conductivity improved by 69.4, 126.9, 162.3 and 176.4% respectively for 5, 10, 15 and 20% graphite powder mass fractions. The thermal properties of the final concrete that comprises LWA-PCM coated with graphite powder have not been published.

The thermal conductivity of a hard concrete comprising LWA-PCM was also calculated by Wang et al. [26]. Similar to the analysis conducted by Memon et al. [27], the investigators observed that the addition of 1, 3, 5, 7 and 9% graphite powder improved LWA-PCM thermal conductivity by 17, 34, 55, 119 and 193%, respectively. Nonetheless, owing to the poor thermal conductivity of PCM packed in LWA pores, the thermal conductivity of concrete comprising LWA-PCM decreases with an rise in LWA-PCM content. Kastiukas et al. [39] also assessed the use of various coating materials such as carbon fibers (CF) [49] and graphite spray (GS) to improve LWA-PCM or macro-encapsulated LWA thermal conductivity. In comparison to previous studies [26, 27], the application of carbon fibers or graphite spray did not improve the LWA-PCM thermal conductivity. The standard LWA-PCM and LWA-PCM coated with CF and GS calculated thermal conductivity were 0.1382 W/mK, 0.1382 W/mK, and 0.1337 W/mK, respectively.

In the research performed by Niall et al. [36], the writers used an modified hot plate apparatus to assess the conductivity of composite LWA-PCM panels with 100% PCC and 50% GGBS. In addition, the recorded temperature data were used to determine the thermal storage behavior of the panels together with the measured densities and thermal conductivities. Research results

showed that both panels had a 47.4 and 42.8%, respectively reduction in thermal conductivity. This is induced by the low conductivity of the PCM material, according to the scientists. The authors have suggested that lower conductivity and higher heat storage potential of the PCM panels result in lower thermal diffusivity, which in effect decreases the PCM 's performance when depth rises as the heat takes longer to enter the PCM [36, 38]. By using n-BS as a PCM with ECA in concrete, the temperature inside the house can be controlled and can be maintained suitable according to the human comfort zone.

3. 5. Leakage Test on the Concrete Specimen After 28 days of curing for all the concrete specimens are taken out from the curing tank and placed in an open atmosphere for removal of moisture content. Now, the specimens are thoroughly cleaned on the surface and wrapped with filter paper on all sides. All the wrapped specimens are placed in the oven with 60^{o}C for the next 1h. All the mixes before and after oven treatment were carefully examined for its weight. It was observed that till 10% incorporation of ECA-PCM in mix-2 did not find any change in the weight of filter paper but some stain marks in mix-3 were observed. Similarly, for mix-4 and mix-5 there were no stain marks visible on filter paper. For mix-6 and mix-7 there was very little change in the weight of filter paper by 0.8 and 1.0%, respectively was observed which is considerable.

4. CONCLUSION

A novel form of the stable composite material was developed using immersing n-BS in ECA for normal room temperature and elevated temperature. Then these aggregates were immersed in cement slurry to reduce leakage of PCM in concrete. This aggregate ECA-PCM was partially replaced in concrete by 10 and 20% of natural coarse aggregate. The diffusion oozing circle test showed a decrease in leakage test of ECA-PCM aggregate by 45% for with and without coating at 40^{o}C with 90 min of immersion time. When ECA-PCM aggregate was mixed in concrete, there was a reduction in strength for both the mixes (mix-2 and mix-3). When alccofine1203 was added with ECA-PCM in mix-4, there was an increase in strength by 4.4% but for the same percentage (10%) of alccofine1203 and increase in ECA-PCM by 20% (mix-5) there was a reduction in strength by 7.9 and 14.9% when compared with mix-2 and ref mix for 7th day. The same pattern of the 7th-day graph was observed for the 28th-day compression test. It is observed that mix-4 is the best combination to be incorporated in concrete to improve the mechanical properties of concrete.

Flexural strength of concrete of ECA-PCM with alccofine1203 composite concrete was developed. When alccofine1203 was incorporated with ECA-PCM, strength was gradually increased for mix-4 and mix-5 when compared with mix-3 but was less than the reference mix. Alccofine1203 with a 10% incorporation was recommended in concrete.

DSC analysis was conducted on pure PCM (n-BS) material. Heating and cooling point was in the human comfort zone with 30.45 and 23.75^{o}C. Enthalpy stored in the PCM was 134.2 and 129.3 J/g for heating and freezing points, respectively. The thermal conductivity of ECA-PCM concrete gave much reduction in thermal conductivity value for all the types of mixes. Mix-3 had a great reduction in its thermal conductivity by 13%. When alccofine1203 was incorporated with ECA-PCM, thermal conductivity was linearly increased when compared with mix-3 but was less than the reference mix. Leakage test conducted on all the mixes showed that till 10% incorporation of ECA-PCM did not show any change in the weight of filter paper.

5. ACKNOWLEDGMENT

There was financial support from UGC Minor Project [MRP-6460/16(SERO/UGC)] in 2017 and Research work carried out at Pondicherry Engineering College was highly appreciated.

6. REFERENCES

1. Association, I.E., "India energy outlook: World energy outlook special report", (2015), https://www.gita.org.in/Attachments/Reports/indiaenergyoutlook_WEO2015.pdf.
2. Pérez-Lombard, L., Ortiz, J. and Pout, C., "A review on buildings energy consumption information", ***Energy and Buildings***, Vol. 40, No. 3, (2008), 394-398. Doi.10.1016/j.enbuild.2007.03.007
3. Soares, N., Costa, J.J., Gaspar, A.R. and Santos, P., "Review of passive pcm latent heat thermal energy storage systems towards buildings' energy efficiency", ***Energy and Buildings***, Vol. 59, (2013), 82-103. Doi.org/10.1016/j.enbuild.2012.12.042
4. Baetens, R., Jelle, B.P. and Gustavsen, A., "Phase change materials for building applications: A state-of-the-art review", ***Energy and Buildings***, Vol. 42, No. 9, (2010), 1361-1368. Doi:https://doi.org/10.1016/j.enbuild.2010.03.026
5. Sakulich, A.R. and Bentz, D.P., "Increasing the service life of bridge decks by incorporating phase-change materials to reduce freeze-thaw cycles", ***Journal of Materials in Civil Engineering***, Vol. 24, No. 8, (2012), 1034-1042. Doi.10.1061/(ASCE)MT.1943-5533.0000381
6. Hawes, D., Banu, D. and Feldman, D., "The stability of phase change materials in concrete", ***Solar Energy Materials and Solar Cells***, Vol. 27, No. 2, (1992), 103-118. Https://doi.org/10.1016/0927-0248(92)90113-4
7. Bentz, D.P. and Turpin, R., "Potential applications of phase change materials in concrete technology", ***Cement and Concrete Composites***, Vol. 29, No. 7, (2007), 527-532. Doi. 10.1016/j.cemconcomp.2007.04.007

8. Ling, T.-C. and Poon, C.-S., "Use of phase change materials for thermal energy storage in concrete: An overview", ***Construction and Building Materials***, Vol. 46, (2013), 55-62. DOI: 10.1016/j.conbuildmat.2013.04.031
9. Cedeño, F.O., Prieto, M.a.M., Espina, A. and García, J.R., "Measurements of temperature and melting heat of some pure fatty acids and their binary and ternary mixtures by differential scanning calorimetry", ***Thermochimica Acta***, Vol. 369, No. 1-2, (2001), 39-50. https://doi.org/10.1021/je990164z
10. Inoue, T., Hisatsugu, Y., Ishikawa, R. and Suzuki, M., "Solid–liquid phase behavior of binary fatty acid mixtures: 2. Mixtures of oleic acid with lauric acid, myristic acid, and palmitic acid", ***Chemistry and Physics of Lipids***, Vol. 127, No. 2, (2004), 161-173. DOI: 10.1016/j.chemphyslip.2003.10.013
11. Rozanna, D., Chuah, T., Salmiah, A., Choong, T.S. and Sa'ari, M., "Fatty acids as phase change materials (PCMS) for thermal energy storage: A review", ***International Journal of Green Energy***, Vol. 1, No. 4, (2005), 495-513. https://doi.org/10.1081/GE-200038722
12. Ramakrishnan, S., Wang, X., Sanjayan, J. and Wilson, J., "Thermal energy storage enhancement of lightweight cement mortars with the application of phase change materials", ***Procedia Engineering***, Vol. 180, (2017), 1170-1177. Doi.org/10.1016/j.proeng.2017.04.277
13. Li, M., Wu, Z. and Tan, J., "Heat storage properties of the cement mortar incorporated with composite phase change material", ***Applied Energy***, Vol. 103, (2013), 393-399. Doi. 10.1016/j.apenergy.2012.09.057
14. Yu, Y., Liu, J., Xing, S., Zuo, J. and He, X., "Experimental research of cement mortar with incorporated lauric acid/expanded perlite phase-change materials", ***Journal of Testing and Evaluation***, Vol. 45, No. 4, (2017), 1338-1343. DOI: 10.1520/JTE20160021.ISSN 0090-3973
15. Xu, B., Ma, H., Lu, Z. and Li, Z., "Paraffin/expanded vermiculite composite phase change material as aggregate for developing lightweight thermal energy storage cement-based composites", ***Applied Energy***, Vol. 160, (2015), 358-367. Doi. 10.1016/j.apenergy.2015.09.069
16. Nepomuceno, M.C. and Silva, P.D., "Experimental evaluation of cement mortars with phase change material incorporated via lightweight expanded clay aggregate", ***Construction and Building Materials***, Vol. 63, (2014), 89-96. Doi.10.1016/j.conbuildmat.2014.04.027
17. Ma, B., Adhikari, S., Chang, Y., Ren, J., Liu, J. and You, Z., "Preparation of composite shape-stabilized phase change materials for highway pavements", ***Construction and Building Materials***, Vol. 42, (2013), 114-121. Doi. 10.1016/j.conbuildmat.2012.12.027
18. Sarı, A., "Form-stable paraffin/high density polyethylene composites as solid–liquid phase change material for thermal energy storage: Preparation and thermal properties", ***Energy Conversion and Management***, Vol. 45, No. 13-14, (2004), 2033-2042. Doi.10.1016/j.enconman.2003.10.022
19. Xiao, M., Feng, B. and Gong, K., "Preparation and performance of shape stabilized phase change thermal storage materials with high thermal conductivity", ***Energy Conversion and Management***, Vol. 43, No. 1, (2002), 103-108. Doi.10.1016/S0196-8904(01)00010-3
20. Inaba, H. and Tu, P., "Evaluation of thermophysical characteristics on shape-stabilized paraffin as a solid-liquid phase change material", ***Heat and Mass Transfer***, Vol. 32, No. 4, (1997), 307-312. Doi.10.1007/s002310050126
21. Shukla, N., Fallahi, A. and Kosny, J., "Performance characterization of pcm impregnated gypsum board for building applications", ***Energy Procedia***, Vol. 30, (2012), 370-379. Doi.10.1016/j.egypro.2012.11.044
22. Voelker, C., Kornadt, O. and Ostry, M., "Temperature reduction due to the application of phase change materials", ***Energy and Buildings***, Vol. 40, No. 5, (2008), 937-944. Doi.10.1016/j.enbuild.2007.07.008
23. Dong, Z., Cui, H., Tang, W., Chen, D. and Wen, H., "Development of hollow steel ball macro-encapsulated pcm for thermal energy storage concrete", ***Materials***, Vol. 9, No. 1, (2016), 59. DOI: 10.3390/ma9010059
24. Drissi, S., Eddhahak, A., Caré, S. and Neji, J., "Thermal analysis by dsc of phase change materials, study of the damage effect", ***Journal of Building Engineering***, Vol. 1, (2015), 13-19. Doi. 10.1016/j.jobe.2015.01.001.hal-01174646
25. Cellat, K., Beyhan, B., Kazanci, B., Konuklu, Y. and Paksoy, H., "Direct incorporation of butyl stearate as phase change material into concrete for energy saving in buildings", ***Journal of Clean Energy Technol***, Vol. 5, No. 1, (2017), 64-68. Doi: 10.18178/jocet.2017.5.1.345
26. Wang, R., Ren, M., Gao, X. and Qin, L., "Preparation and properties of fatty acids based thermal energy storage aggregate concrete", ***Construction and Building Materials***, Vol. 165, (2018), 1-10. DOI: 10.1016/j.conbuildmat.2018.01.034
27. Memon, S.A., Cui, H., Zhang, H. and Xing, F., "Utilization of macro encapsulated phase change materials for the development of thermal energy storage and structural lightweight aggregate concrete", ***Applied Energy***, Vol. 139, (2015), 43-55. DOI: 10.1016/j.apenergy.2014.11.022
28. Rao, V.V., Parameshwaran, R. and Ram, V.V., "Pcm-mortar based construction materials for energy efficient buildings: A review on research trends", ***Energy and Buildings***, Vol. 158, No., (2018), 95-122. https://doi.org/10.1016/j.enbuild.2017.09.098
29. Navarro, L., De Gracia, A., Colclough, S., Browne, M., McCormack, S.J., Griffiths, P. and Cabeza, L.F., "Thermal energy storage in building integrated thermal systems: A review. Part 1. Active storage systems", ***Renewable Energy***, Vol. 88, No., (2016), 526-547. DOI: 10.1016/j.renene.2015.11.040
30. Wang, X., Yu, H., Li, L. and Zhao, M., "Research on temperature dependent effective thermal conductivity of composite-phase change materials (PCMS) wall based on steady-state method in a thermal chamber", ***Energy and buildings***, Vol. 126, No., (2016), 408-414. DOI:10.1016/J.ENBUILD.2016.05.058
31. Pasupathy, A., Velraj, R. and Seeniraj, R., "Phase change material-based building architecture for thermal management in residential and commercial establishments", ***Renewable and Sustainable Energy Reviews***, Vol. 12, No. 1, (2008), 39-64. https://doi.org/10.1016/j.rser.2006.05.010
32. Sagar, B. and Sivakumar, M., "An experimental and analytical study on alccofine based high strength concrete", ***International Journal of Engineering***, Vol. 33, No. 4, (2020), 530-538. DOI: 10.5829/IJE.2020.33.04A.03
33. Narasimha Reddy, P. and Ahmed Naqash, J., "Experimental study on tga, xrd and sem analysis of concrete with ultra-fine slag", ***International Journal of Engineering***, Vol. 32, No. 5, (2019), 679-684. DOI: 10.5829/ije.2019.32.05b.09
34. Narasimha Reddy, P. and Ahmed Naqash, J., "Effect of alccofine on mechanical and durability index properties of green concrete", ***International Journal of Engineering***, Vol. 32, No. 6, (2019), 813-819. DOI: 10.5829/ije.2019.32.06c.03
35. Schossig, P., Henning, H.-M., Gschwander, S. and Haussmann, T., "Micro-encapsulated phase-change materials integrated into construction materials", ***Solar Energy Materials and Solar Cells***, Vol. 89, No. 2-3, (2005), 297-306. DOI: 10.1016/j.solmat.2005.01.017
36. Niall, D., Kinnane, O., West, R.P. and McCormack, S., "Mechanical and thermal evaluation of different types of pcm–concrete composite panels", ***Journal of Structural Integrity and***

Maintenance, Vol. 2, No. 2, (2017), 100-108. https://doi.org/10.1080/24705314.2017.1318039

37. Ma, Q. and Bai, M., "Mechanical behavior, energy-storing properties and thermal reliability of phase-changing energy-storing concrete", ***Construction and Building Materials***, Vol. 176, (2018), 43-49. DOI: 10.1016/j.conbuildmat.2018.04.226
38. Min, H.-W., Kim, S. and Kim, H.S., "Investigation on thermal and mechanical characteristics of concrete mixed with shape stabilized phase change material for mix design", ***Construction and Building Materials***, Vol. 149, (2017), 749-762. DOI: 10.1016/j.conbuildmat.2017.05.176
39. Kastiukas, G., Zhou, X. and Castro-Gomes, J., "Development and optimisation of phase change material-impregnated lightweight aggregates for geopolymer composites made from aluminosilicate rich mud and milled glass powder", ***Construction and Building Materials***, Vol. 110, (2016), 201-210. https://doi.org/10.1016/j.conbuildmat.2016.02.029
40. Dehdezi, P.K., Hall, M.R., Dawson, A.R. and Casey, S.P., "Thermal, mechanical and microstructural analysis of concrete containing microencapsulated phase change materials", ***International Journal of Pavement Engineering***, Vol. 14, No. 5, (2013), 449-462. https://doi.org/10.1080/10298436.2012.716837
41. Lecompte, T., Le Bideau, P., Glouannec, P., Nortershauser, D. and Le Masson, S., "Mechanical and thermo-physical behaviour of concretes and mortars containing phase change material", ***Energy and Buildings***, Vol. 94, (2015), 52-60. https://doi.org/10.1016/j.enbuild.2015.02.044
42. Jayalath, A., San Nicolas, R., Sofi, M., Shanks, R., Ngo, T., Aye, L. and Mendis, P., "Properties of cementitious mortar and concrete containing micro-encapsulated phase change materials", ***Construction and Building Materials***, Vol. 120, (2016), 408-417. DOI: 10.1016/j.conbuildmat.2016.05.116
43. Meshgin, P. and Xi, Y., "Effect of phase-change materials on properties of concrete", ***ACI Materials Journal***, Vol. 109, No. 1, (2012).
44. Wei, Z., Falzone, G., Wang, B., Thiele, A., Puerta-Falla, G., Pilon, L., Neithalath, N. and Sant, G., "The durability of cementitious composites containing microencapsulated phase change materials", ***Cement and Concrete Composites***, Vol. 81, (2017), 66-76. DOI: 10.1016/j.cemconcomp.2017.04.010
45. Eddhahak-Ouni, A., Drissi, S., Colin, J., Neji, J. and Care, S., "Experimental and multi-scale analysis of the thermal properties of portland cement concretes embedded with microencapsulated phase change materials (PCMS)", ***Applied Thermal Engineering***, Vol. 64, No. 1-2, (2014), 32-39. DOI: 10.1016/j.applthermaleng.2013.11.050
46. Pilehvar, S., Cao, V.D., Szczotok, A.M., Valentini, L., Salvioni, D., Magistri, M., Pamies, R. and Kjøniksen, A.-L., "Mechanical properties and microscale changes of geopolymer concrete and portland cement concrete containing micro-encapsulated phase change materials", ***Cement and Concrete Research***, Vol. 100, (2017), 341-349. DOI: 10.1016/j.cemconres.2017.07.012
47. Berardi, U. and Gallardo, A.A., "Properties of concretes enhanced with phase change materials for building applications", ***Energy and Buildings***, Vol. 199, (2019), 402-414. https://doi.org/10.1016/j.enbuild.2019.07.014
48. Paksoy, H., Kardas, G., Konuklu, Y., Cellat, K. and Tezcan, F., "Characterization of concrete mixes containing phase change materials", in IOP Conference Series: Materials Science and Engineering, Vol. 251, p. 012118 (12 pp.), IOP Publishing. (2017). DOI:10.1088/1757-899X/251/1/012118
49. Cholker, A.K. and Tantray, M.A., "Strain-sensing characteristics of self-consolidating concrete with micro-carbon fibre", ***Australian Journal of Civil Engineering***, Vol. 18, No. 1, (2020), 46-55. DOI: 10.1080/14488353.2019.1704206

Persian Abstract

چکیده

مواد تغییر فاز (PCM) به عنوان استارات n-butyl (n-BS) در مصالح رس (ECA) با دو روش ، غوطه وری مستقیم در دمای اتاق و در دمای بالا (۳۰ درجه سانتیگراد ، ۴۰ درجه سانتیگراد و ۵۰ درجه سانتیگراد) غوطه ور شد. ECA پس از ۹۰ دقیقه غوطه وری با n-BS در دمای ۴۰ درجه سانتیگراد به نسبت وزن خود آماده به کار شد (۲۴٪ افزایش یافته است). پس از غوطه وری ، این مصالح (۴۰ درجه سانتیگراد) برای جلوگیری از نشت و مخلوط همگن با بتن در دوغاب سیمانی مخلوط شدند. آزمایش نشت آزمایش نشتی بر روی کلیه ECA با و بدون روکش کاری سیمان (دمای اتاق و درجه حرارت بالا) انجام شد. ECA با پوشش دوغاب سیمانی باعث کاهش نشتی ECA-PCM به میزان ۴۵٪ شد. Alccofine1203 به طور جزئی با سیمان (۱۰٪ و ۲۰٪) با سیمان جایگزین شد تا خصوصیات مکانیکی در بتن دانه سبک را بهبود بخشد. فشار، خمش ، هدایت حرارتی ، تجزیه و تحلیل DSC و آزمایش نشت در نمونه های بتن و در تمام مخلوط ها انجام شد. مقاومت فشاری برای جایگزینی ۱۰٪ به ترتیب ۳۱/۷ کیلو لیتر در مترمربع و ۳۲/۸ کیلو نیوتن در متر مربع به مدت ۷ روز و ۲۸روز به دست آمد. به طور مشابه ، مقاومت خمشی به مدت ۲۸ روز به ۱۲/۶ کیلو لیتر در مترمربع رسید. تجزیه و تحلیل DSC از PCM خالص (n-BS) برای دمای ذوب و انجماد آن با دمای ۱۳۴.۲ J / g و ۱۲۹/۳ JJ / g به عنوان آنتالپی برای نقاط ذوب و انجماد آن به ترتیب ، ۳۰/۳۴ درجه سانتیگراد و ۲۳.۲۵ درجه سانتیگراد به دست آورد. هدایت حرارتی برای مخلوط ۳ ۱۰درصد PC PCM-ECA + 10 al (alccofine1203)کمترین مقدار از تمام مخلوط ها ، یعنی ۱۳ درصد کمتر از مخلوط مرجع است. تا ۱۰٪ اختلاط ، هیچ گونه نشتی مشاهده نشد و هیچگونه لکه بر روی کاغذ فیلتر مشاهده نشد.

International Journal of Engineering

Journal Homepage: www.ije.ir

Hybrid Artificial Intelligence Model Development for Roller-compacted Concrete Compressive Strength Estimation

A. Ranjbar, N. Barahmand*, A. Ghanbari

Department of Civil Engineering, Larestan Branch, Islamic Azad University, Larestan, Iran

P A P E R I N F O

Paper history:
Received 06 March 2020
Received in revised form 20 April 2020
Accepted 12 June 2020

Keywords:
Artificial Neural Network
Artificial Bee Colony Algorithm
Roller-compacted Concrete
Compressive Strength

A B S T R A C T

This study implemented the artificial bee colony (ABC) metaheuristic algorithm to optimize the Artificial Neural Network (ANN) values for improving the accuracy of model and evaluate the developed model. Compressive strength of RCC was investigated using mix design materials in three forms, namely volumetric weight input (cement, water, coarse aggregate, fine aggregate, and binder), value ratio (water to cement ratio, water to binder ratio, and coarse aggregate to fine aggregate ratio), as well as the percentage of mix design values of different ages. A comprehensive, proper-range dataset containing 333 mix designs was collected from various papers. The accuracy of the research models was investigated using error indices, namely correlation coefficient, root-mean-square-error (RMSE), mean absolute error (MAE), and developed hybrid models were compared. External validation and Monte Carlo simulation (MCS)-based uncertainty analysis was also used to validate the models and their results were reported. The experimental stage of the prediction of compressive strength values showed significant accuracy of the ANN-ABC model with (MAE=11.49, RMSE=0.920, RME=5.21) compared to other models in this study. Besides, the sensitivity analysis of predictor variables in this study revealed that the variables "specimen age," "binder," and "fine aggregate" were more effective and important in this research. Comparison of the results showed that the improved proposed model using the ABC algorithm was more capable and more accurate in reducing the error rate in providing computational relations compared to the default models examined in the prediction of the compressive strength of RCC and also tried in simplifying computational relations.

***doi**: 10.5829/ije.2020.33.10a.04*

1. INTRODUCTION

Over the past few years, our country has been moving rapidly towards the construction of roads and streets using concrete to achieve economic growth benefits and consider environmental problems. Concrete road construction has become even more prominent, especially over the last decade, during which sustainable development and environmental problems have been much discussed. The cost of concrete pavement construction is lower than that of asphalt pavements and has a much longer shelf life. In addition, other advantages such as high compressive strength, desirable tensile and shear strength at low thickness, high corrosion and water penetration resistance, high abrasion resistance, and ease of maintenance have made it possible to justify the use of relevant devices to implement it. However, the relatively short life span of this type of pavement and the complex design of this type of concrete necessitates the need for strong scientific support in the design and optimization of mix design. The problem of concrete mix design and achieving optimum strength to perform various engineering issues including dam construction, pavement, high-rise buildings, and large foundations (including hospitals, stadiums, etc.) has a long history. Nevertheless, this is achieved by spending a lot of money and time due to the specific complexities involved in selecting the type of constituents and their ratio to prepare the concrete with a certain strength. The importance and necessity of this issue become apparent when a

*Corresponding Author Email: *naderbarahmand2010@gmail.com* (N. Barahmand)

Please cite this article as: A. Ranjbar, N. Barahmand, A. Ghanbari, Hybrid Artificial Intelligence Model Development for Roller-compacted Concrete Compressive Strength Estimation, International Journal of Engineering (IJE), IJE TRANSACTIONS A: Basics Vol. 33, No. 10, (October 2020) 1852-1863

substantial amount of time and money is allocated to the concrete mix design in a project similar to RCC.

Roller-compacted concrete (RCC) is a zero-slump concrete that becomes stiff due to roller vibration. Two types of RCC are used in construction work: low-cement mass RCC (mass RCC with low cement content) for the construction of dams and mass structures such as retaining walls, heavy foundations, and embankments where high strength is not required. For the relatively high-cement RCC (RCC with relatively high cement content) is used for rapid application of highway pavement layers and similar coatings; where high mechanical and wear strength is required. The main advantage of this type of concrete is its low cost [1].

Numerous methods have been proposed to determine the RCC mix ratios by concrete associations and committees, which are generally experimental, quasi-experimental, and based on theoretical methods. Nonetheless, soil compaction and liquidity (performance) approaches are generally used in different mix ratio design methods. These two approaches are defined based on optimizing the dry density of the sample by optimum moisture content and mix design by absolute volume, respectively.

Therefore, artificial intelligence methods are nowadays widely used to model and predict problems in civil engineering due to its significant benefits. On the other hand, among the things that have made it necessary to present a model for the RCC mix design are the range of materials used in this type of concrete, the complexity of the mix design, the effect of different parameters on the mix design, as well as finding the relationships between the various parameters of its mix design. Predicting and modeling the mix design or the resistance of these types of concrete is particularly complex in accordance with effective parameters similar to other types of concrete. On the other side, concrete mix design has become more complex as a result of the introduction of a variety of pozzolans, new materials added to the mix design of this type of concrete, as well as the impact of various concrete methods on this concrete, mix, and compaction. Moreover, the models that are trained can be used to predict the compressive strength of this type of concrete for engineering predictions and to obtain the most economical or optimal mix design using optimization techniques.

Here, we refer to a number of studies that have been conducted on modeling the mechanical properties of RCC using artificial intelligence methods. In a study, Ni and Wang [1] showed that it is possible to predict resistance at different ages and RCC vibration time in a very short time with acceptable accuracy using neural networks obtained. In a study, Ashrafian et al. [2] demonstrated that the ANN model is more capable than the adaptive neural fuzzy inference system (ANFIS) models and SVM in predicting the compressive strength of RCC. Furthermore, the resistances estimated by ANN and the SVM have the highest and lowest compliance with the actual compressive strength, respectively.

In their study, Amlashi et al. [3] observed that compressive strength will increase with an increase in the cement content as the rate of increase in strength decreases with an increase in the amount of fine RAP according to the results of the model sensitivity analysis. In addition, the compressive strength will increase with a decrease in the amount of fine RAP or an increase in curing time at a fixed amount of coarse aggregate. It was also observed that the effect of curing time on compressive strength decreases with an increase in the percentage of fine RAP.

Ayaz et al. [4] studied the indices of compressive strength and ultrasonic pulse velocity (UPV) as a criterion to detect the quality of concrete containing natural additives using artificial intelligence methods. This study used tree modeling algorithms to predict these two components using 40 data collected from 10 mix designs. The results of the samples were examined at the ages of 3, 7, 28, and 120 days.

Ashrafian et al. [5] used intelligent data-driven methods to estimate the compressive strength and UPV in nano-silica concrete. Five data-driven methods including linear regression, SVM, ANN, tree model, and multivariate adaptive regression splines (MARS) were investigated to provide computational relations of compressive strength and pulse velocity and prediction models were presented with high accuracy. Additionally, a number of computational relations have been introduced to estimate this type of concrete or nano property using the MARS method and the tree model.

Al-Sudani et al. [6] investigated the prediction of water flow using the MARS method coupled with differential evolution (DE) algorithm (hybrid DE-MARS). The results of this hybrid model were compared with those of classical data-driven modeling (DDM) models such as SVMs and simple MARS. The results presented in the form of error indices showed that the model quality was improved as a result of using a metaheuristic algorithm.

Mansouri et al. [7] evaluated the behavior of Fiber Reinforced Polymer (FRP) (also called fiber-reinforced plastic) using a variety of artificial intelligence methods. 3042 laboratory data from 253 different studies were selected to develop models, 60% of which were used for training, 20% for testing, and 20% for validating the presented models. The results of this study, presented in the form of RMSE statistics, showed that the tree model and MARS method performed better than the neural network and fuzzy neural network.

Kaveh et al. [8] estimated the properties of self-compacting concrete (SCC) containing fly ash (also known as pulverised fuel ash in the United Kingdom) using the MARS method and the tree model. This study presented 114 data collected from various literature review articles and computational relations to predict

SCC properties including compressive strength, tensile strength, flexural strength, and modulus of elasticity (MOE). The results indicate that artificial intelligence methods are considered reliable to predict the mechanical properties of this type of concrete.

Asteris et al. [9] conducted a study to provide computational relations to predict the compressive strength of SCC containing metakaolin (MK). In this study, they considered and analyzed the size of the largest aggregate as an input for the first time. In this regard, they used the nonlinear and non-parametric MARS method as well as the M5p tree model to develop estimated relationships and presented the relationship-based models.

In a study, Ashrafian et al. [10] investigated their newly developed model to estimate the compressive strength of lightweight concrete and compared its results with those of classical data-driven modeling techniques including ANN, SVMs, and MLR. In this study, the appropriate combination of inputs was used in the dataset using Mallow's Cp evaluation and a suitable structure was chosen for the inputs. The results of this study reported a more accurate and appropriate performance of the developed model compared to other methods.

Regarding the background to the prediction and modeling of the compressive strength of RCC, it can be stated that only few studies have attempted to model the compressive strength of this type of concrete and find a solution to estimate this mechanical component. Thus, it is necessary to propose a modeling approach for predicting and modeling the compressive strength of RCC. Furthermore, previous studies have shown that using the neural network method alone yields poor performance (esp. determination of optimal model parameters). Hence, it is necessary to develop new models to solve the problem. In this regard, the central question (major problem) of the present study is whether the metaheuristic algorithms are considered as a suitable solution to increase the accuracy of artificial intelligent models for estimating the compressive strength of RCC. Research sub-questions include:

How much increase in accuracy and decrease in error is observed in the proposed ANN-ABC method compared to the ANN method and other regression methods? Which component in the RCC mix design has the largest impact on compressive strength?

In addition, the assumptions of the present study for modeling a 28-day RCC resistance are as follows:

- For modeling, the laboratory moisture and temperature of the concrete samples are not found in the model.
- Influential factors such as concrete construction, curing, transfer, and placing are not found in the model.
- The grading of each fine and coarse aggregate constituting RCC is assumed to be uniform.

2. MATERIALS AND METHODS

This study evaluates the ANN and ANN-ABC models in terms of performance accuracy, and compares and contrasts the model with the best results as the preferred model for each method to determine the best method for predicting the compressive strength of pavement RCC. It should be noted that modeling aims to evaluate the capability of these methods in predicting the compressive strength of pavement RCC. The results were then compared with those of the MLR model.

2. 1. Development of Hybrid ANN-ABC Model

The ABC algorithm is used in a wide variety of fields, including in the training of feedforward ANNs, which is considered one of the most interesting applications. Applying the ABC algorithm to train ANNs is a simple and convenient method. The multidimensional search space employed by the ABC algorithm is the space associated with the weights of network connections and neurons. Food resource competency is measured by the standard measure of network output performance, including SSE of the "network training set" data. The most important advantage of this algorithm is the simultaneous search of the entire solution space.

The present study has used the ABC algorithm as a method for learning ANN to overcome the disadvantages created by the recursive extension algorithm in ANN training. The ABC algorithm is selected as an optimization tool because it can find optimal solutions along with relatively moderate computations. In addition, the ABC algorithm is used in the process of training ANNs to achieve the desired parameters such as network weight and bias to minimize the error function. These parameters are updated gradually to achieve the desired convergence criterion. Figure 1 shows the process of optimizing the values of ANN parameters by the ABC algorithm.

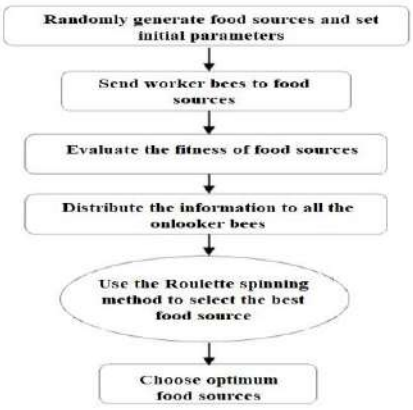

Figure 1. Artificial Bee Colony Algorithm Used in ANN Training

It seems that using swarm intelligence (SI)-based algorithms such as ABC algorithm is an appropriate solution to optimize the performance of ANNs, given the limitations of the backpropagation training algorithm.

2. 2. The Dataset Used in the Present Study A comprehensive laboratory database is needed to estimate the compressive strength of pavement RCC using the above models. Thus, 333 laboratory datasets were collected from published and validated laboratory studies for modeling the compressive strength of the pavement RCC [11–21]. Of the total data, 75% (i.e., 250 data) were considered to perform the training phases and 25% (i.e., 83 data) to perform the test phases, respectively. Figure 2 shows the flowchart of the implementation steps of this research during the modeling, analysis, and validation processes.

3. RESULTS AND DISCUSSION

3. 1. Selection of Input Parameters to Develop the Proposed Models According to Table 1, three scenarios with different input combination arrangements under different conditions are considered to select the optimal input state to develop the proposed model. In this evaluation, three different input types of values were evaluated as volumetric weight (dimensional), the ratio of values to each other (dimensionless), and percentage of values.

According to Table 2, Scenario 1 presented the most optimal results based on statistical analysis with respect to the results of statistical indices. In this analysis, the Mallows index is a function of the predictor variables in Scenario 1 considering the compressive strength (CS) in this study, as shown in Equation (1). Accordingly, according to Equation (1), predictor inputs for model development are compressive strength (CS) of pavement RCC including cement (C), coarse aggregate (CA), fine aggregate (FA), water (W), binder (cement + pozzolan) (B), and specimen age (AS). In this selected combination, the specimen age unit is presented on a daily basis and the rest of the input variables are in kg/m^3.

$$\mathrm{CS} = f\ (CA, FA, C, W, B, AS) \quad (1)$$

3. 2. Statistical Analysis of Input and Output Parameters in the Present Study A large standard deviation (SD) indicates a significant data sparsity (dispersion). According to Table 3, the data collected in this study have a significant sparsity over the study area and have facilitated the modeling process.

3. 3. Development of Multivariate Linear Regression Model In this section, the modeling process is performed using the MLR method to compare the values with the results of other developed methods. Hence, the configuration structure derived from the six predictor inputs is used. The MLR method structure used the "minimum mean square error (MMSE)" algorithm to optimize the weights and parameters of the model values to establish a linear relationship between the input variables and the output variables. Model learning process performed in MATLAB using training data and

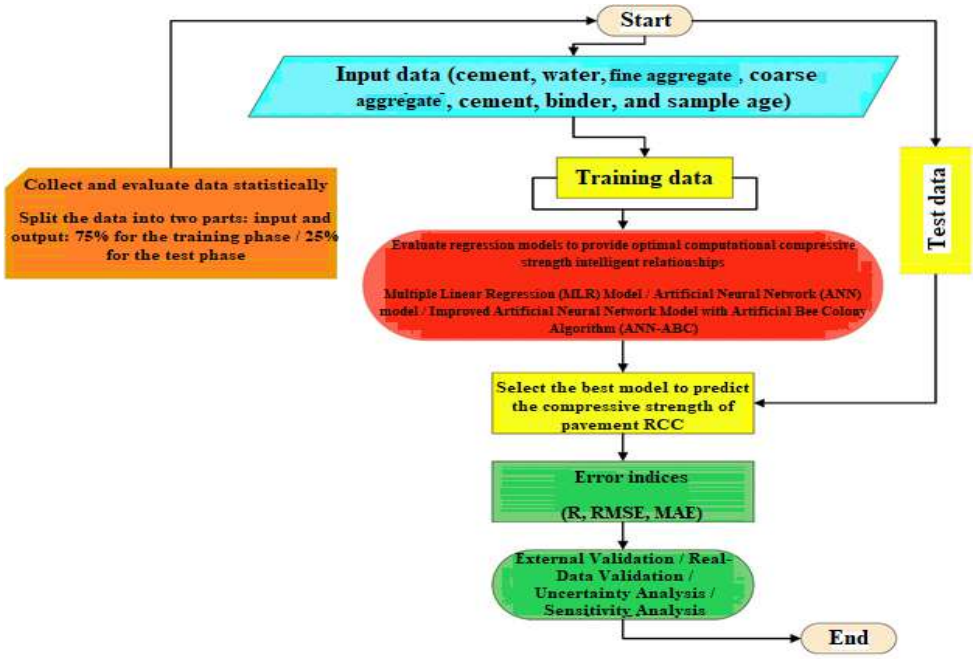

Figure 2. Flowchart of the implementation steps of the modeling process in this study

TABLE 1. Predicted scenarios for selecting the best input state for model development

Scenario	Input Values	Description
1	6	$CS = f\ (CA, FA, C, W, B, AS)$
2	4	$CS = (\frac{W}{B}, \frac{W}{C}, \frac{CA}{FA}, AS\ )$
3	6	$CS = (\%CA, \%FA, \%C, \%W, \%B, AS\ )$

TABLE 2. Results of investigation of scenarios to select the best input state in Minitab

Scenario	1	2	3
C_p	7.86	9	**9.11**
R^2	76.18	69.55	**67.60**

TABLE 3. Statistical analysis of predictor variables

Variables	Mode	SD	Mean	Min Value	Max Value
Coarse Aggregate	1095	178.09	1058.01	585	1316
Fine Aggregate	807	197.67	801.56	272.50	1263
Binder	295	67.98	310.71	200	672.50
Water	114	41.22	128.77	78	336.25
Cement	400	91.02	211.12	49	400
Specimen Age	28	44.58	47.549	7	180
Compressive Strength	24	15.23	37.78	6.80	75.50

a developed linear relationship has been reported below as Equation (2) to predict compressive strength with a correlation coefficient of 0.59:

$$CS = 0.14\ AS + 0.0002FA + 0.0644C - 0.1531W + 0.0555B + 19.894 + 0.0001CA \quad (2)$$

3. 4. Development of the Artificial Neural Network Model This study used a multilayer perceptron (MLP) neural network, which has a hidden layer. Fifty neural network models were constructed and evaluated to determine the optimal number of nerves in hidden layers. To do this, the number of nerves is added up one by one in the first hidden layer (n = 1-50) and the performance of each model was examined. The Levenberg-Marquardt (LM) algorithm was used to train the neural network. This algorithm is often considered as the fastest backpropagation algorithm and is strongly recommended as the first choice in supervised learning algorithms. Tangent sigmoid, logarithmic sigmoid, and logarithmic linear functions were used to determine the appropriate excitation function in the hidden and output layers. The best result was related to the tangent sigmoid function in the hidden layer and the linear function in the output layer.

75% (n = 250) and 25% (n = 83) of the information were used to train and test networks, respectively. Table 4 presents the results of the performance evaluation of each step. The final model is determined based on its performance in the test phase. It should be noted that different weights are assigned to the network with each analysis of the ANN model in MATLAB; thus, a different solution is obtained with each analysis. To overcome this problem, neuron analysis was performed in hidden layers for 50 times for each ANN model. Table 4 reports fifteen appropriate performance results. The Neural Network 6 (with six neurons in the hidden layer) is the best developed model selected as the final model. In this study, the optimal model has a training rate of 0.25, a momentum index of 0.3, and 2000 repeats. As can be deduced from (Table 4), the six nerves in the hidden layer (i.e., the architecture of the network 1-6-6) yielded the best results and the Neural Network 6 Model is the best ANN model.

Figure 3 shows the evaluation criteria in each ANN model in the form of a graph. High values of parameter R and low values of RMSE indicate the high performance of the model.

Moreover, Figure 4 shows the architectural structure of the developed neural network model. The computational time of the ANN model in the

TABLE 4. Neural network performance evaluation criteria in the training phase

Model	Training Stage		Test Stage	
	R	RMSE	R	RMSE
NN1	0.808	85.900	0.829	**71.452**
NN2	0.811	83.122	0.844	**62.480**
NN3	0.812	83.117	0.840	**63.623**
NN4	0.811	83.122	0.848	**63.442**
NN5	0.801	90.618	0.854	**66.263**
NN6	**0.861**	76.68	**0.857**	**65.41**
NN7	0.770	95.329	0.805	**78.946**
NN8	0.766	95.800	0.800	**80.976**
NN9	0.741	95.612	0.745	**88.845**
NN10	0.722	98.845	0.722	**91.013**
NN11	0.720	98.010	0.711	**96.852**
NN12	0.733	93.621	0.739	**89.999**
NN13	0.800	900.60	0.718	**93.569**
NN14	0.819	84.329	0.822	**73.699**
NN15	0.800	900.060	0.839	**64.020**

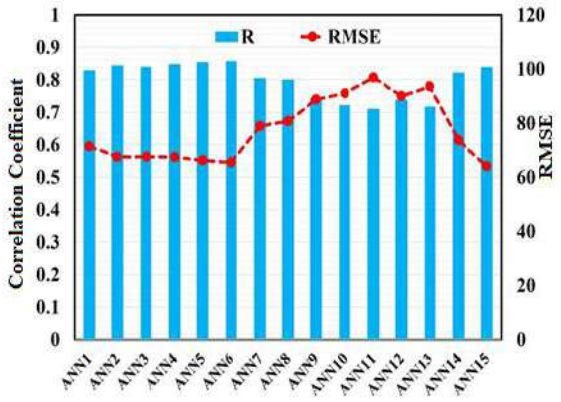

Figure 3. Evaluation criteria for ANN models

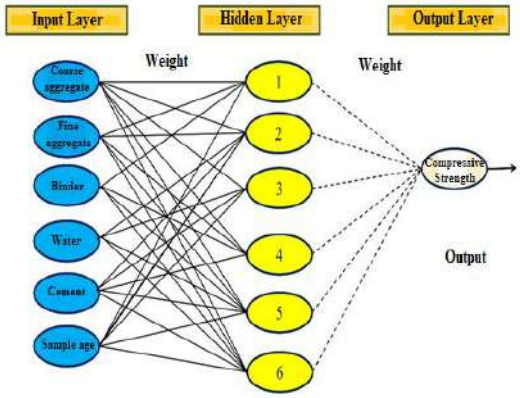

Figure 4. Architecture structure of the developed neural network model

computational analysis of this study is 9.12 seconds and the time spent for model structure formation is 0.62 seconds.

3. 5. Development of an Improved ANN Model Using ABC Algorithm Evaluations showed that the optimal network has a 6-8-6 architecture with eight neurons in the hidden layer, six neurons in the input layer, and one neuron in the output layer. Table 5 shows the parameters for the ABC algorithm to optimize the network weights and biases. The number of iterations was assumed 1000 at each time and the initial population to be 50.

TABLE 5. ABC algorithm parameters to optimize network values

Parameter	Value
Initial population size	10-100
No. of repetitions	10-1000
Maximum number of cycles	100
Local search	15

Furthermore, Figure 5 evaluates the convergence of the ABC algorithm in combination with the neural network model to achieve optimal values. Due to the convergence process, the algorithm takes a constant trend at the 140th iteration that turns into a linear process from the 480th iteration and optimal values are found from the solutions.

3. 6. Comparison of Models Developed to Predict the Compressive Strength of RCC According to Table 6, the correlation coefficients at the training phase are 0.603, 0.821, and 0.938 for the LRM, ANN, and neural network improved with the ABC algorithm, respectively. In addition, the RMSE values at this stage are 145.47, 76.68, and 39.97 MPa for the proposed MLR, ANN, and ANN-ABC models, respectively. Furthermore, the MAE for the ANN-ABC (4.71) model was better than the other three models. Thus, the statistical indices show that the proposed ANN-ABC model has a better performance and higher accuracy at the training stage than the other models. Applying a metaheuristic algorithm approach to model learning has played a fundamental role in better estimating the intelligent model. At the test stage, the newly developed ANN-ABC model with a correlation coefficient of 0.920 and RMSE and MAE values of 49.11 and 5.21 MPa, respectively, had more significant accuracy compared to the other two models. Additionally, the ANN-ABC model reduced the error generation process by 105.52 and 16.3 to reduce the error rate of the models presented in this study.

As shown in Figure 6, the neural network model, in combination with the ABC algorithm, involves less error in training compared to multiple regression and ANN in predicting the compressive strength values of pavement RCC. In a qualitative comparison, most compressive strength values are concentrated on the bisector (i.e., ideal line) and only a few of these points are outside the focus area (outliers). As shown in Figure 6c, in the model evaluation, a deviation of more than 20% was observed in the prediction of the estimated points in the range of

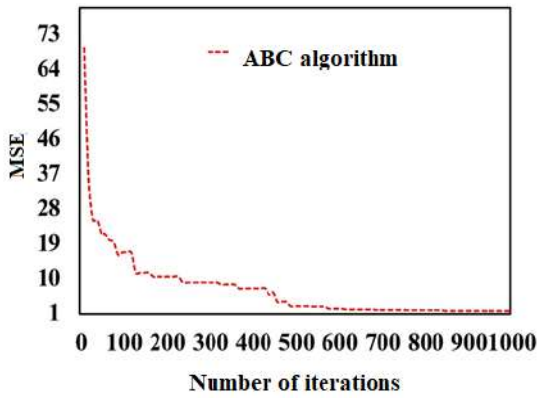

Figure 5. Evaluation of convergence in the iteration of the ABC algorithm

TABLE 6. Performance evaluation of the proposed models

Stages	Models	R	RMSE	MAE
Training	MLR	0.603	145.47	9.86
	ANN	0.821	76.68	6.47
	ANN-ABC	**0.938**	**39.97**	**4.71**
Test	MLR	0.590	154.63	10.32
	ANN	0.857	65.41	5.90
	ANN-ABC	**0.920**	**49.11**	**5.21**

20-40 MPa which was reduced severely using the ABC metaheuristic algorithm. The predicted values in this range were mostly higher than the actual values; however, the estimates were largely lower than the laboratory values with an increase of more than 50 MPa in values. Overall, the methods used in this study were well-trained for evaluation.

According to Figure 7, the compressive strength values of the models are predicted with good accuracy in the test phase. In predicting these values, the computational error was mainly less than 20% and the correlation between actual and predicted laboratory values was more than 85%. Furthermore, due to the percentage of the absolute error in the test phase, the combination of a metaheuristic algorithm with the ANN model reduced the error by 11.69%.

As shown by red dashed lines in Figure 8, the weak-prediction data (i.e., less fitness) are mainly over-estimated or under-estimated in the calculation of the reference values. This error rate has been reduced by applying refinement methods to the model, such as hybrid algorithms (i.e., hybrid models) and a more efficient and accurate model.

Based on the time series plot, the local minima and maxima predictions are better evaluated in the training and testing stages shown in Figure 9. The MLR and ANN

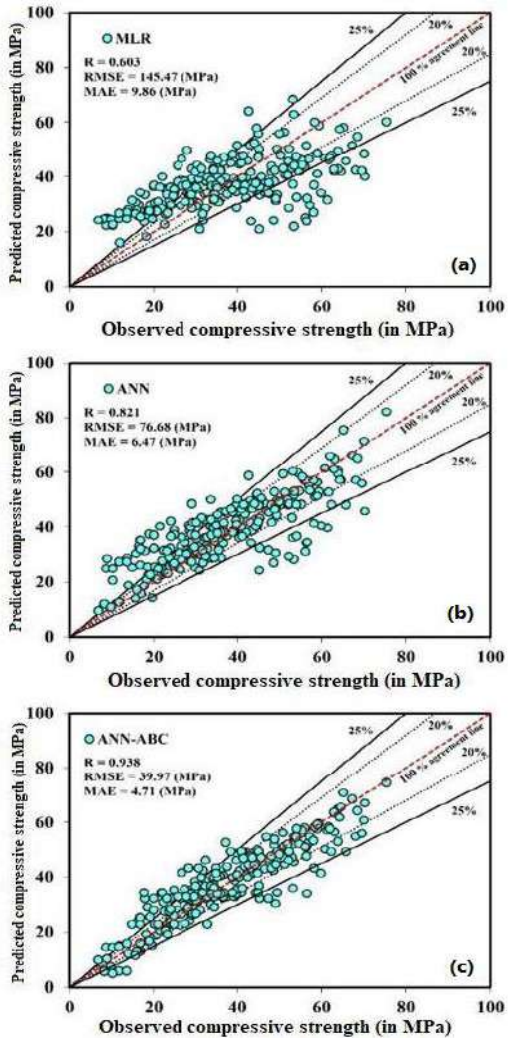

Figure 6. Scatter plot of the compressive strength values in the training phase for the proposed models

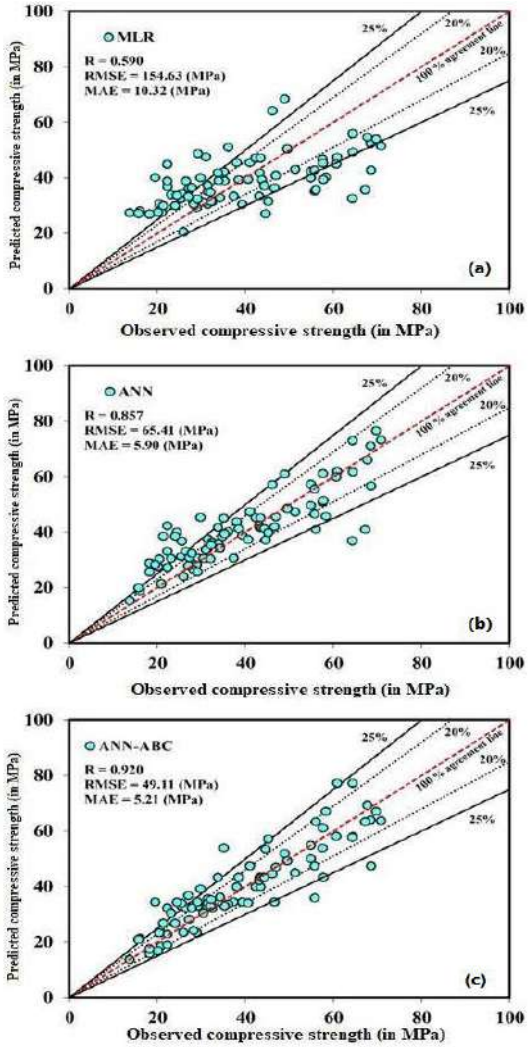

Figure 7. Scatter plot of the compressive strength values in the test phase for the proposed models

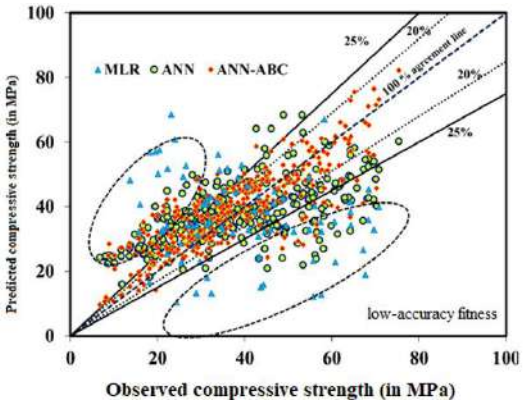

Figure 8. Compressive strength values of RCC in the test phase for all the proposed models

methods had relatively poor performance compared to the developed ANN-ABC model in this study. The hybrid ANN-ABC algorithm has been more successful in estimating local maxima and minima in the test phase. Moreover, the analysis of the presented models shows that local maxima are predicted with a greater error with an increase in the compressive strength values. This weakness is largely remedied by improving the neural network model by combining it with the ABC metaheuristic algorithm.

Figure 10 shows the error distribution values of the three methods used. The error distribution was mainly in the range of -20 to -30. Besides, the error range in the ANN-ABC model was between -10 and 10.

3. 7. Sensitivity Analysis This study has selected the ANN-ABC model (i.e., the best model in this study) to perform a sensitivity analysis to determine the effect of each input parameter on the compressive strength of pavement RCC. According to Table 7, the results of the sensitivity analysis show that the omission of the predictor variable "specimen age" with the correlation coefficient of R = 0.601 and MAE = 9.383 had the largest effect on the proposed ANN-ABC model in estimating the compressive strength of pavement RCC. Furthermore, among the mix design variables, the variables “binder” and “fine aggregate” had the greatest impact on the compressive strength, with a 22.1% and 17.7% decrease, respectively, in the result of the correlation coefficient at the experimental stage.

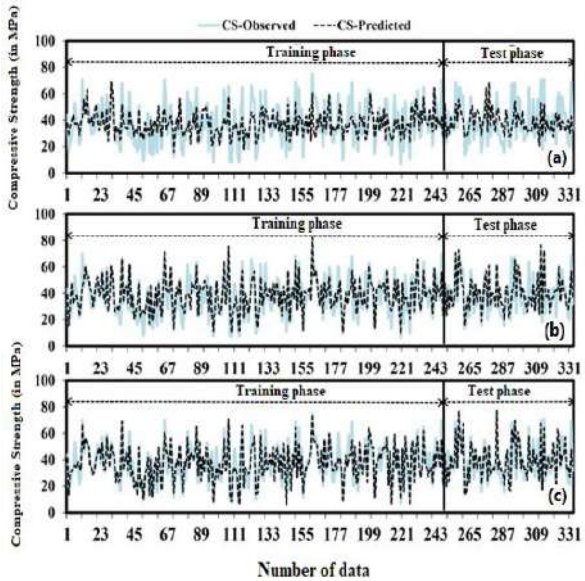

Figure 9. Time series plot of the proposed models; A: MLR, B: ANN, C: ANN-ABC

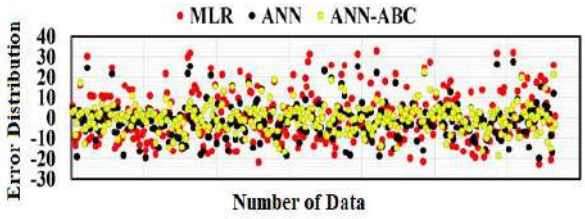

Figure 10. Error distribution values for the three methods used

3. 8. External Validation of the Proposed Models A new external validation criterion is presented to evaluate the proposed models based on their performance with the test dataset. Accordingly, at least one slope of the regression line from the origin for the predicted values to the observed values (K) or vice versa (K′) should be close to 1 as stated in Equations (3) and (4) [22].

$$K = \sum_{i=1}^{n}(O_i \times P_i)/P_i^2 \quad (3)$$

$$K' = \sum_{i=1}^{n}(O_i \times P_i) \,/\, O_i^2 \quad (4)$$

In addition, using the coefficient of determination (R^2) resulted from Equations (5) and (6), the regression line from origin should be less than 0.1.

TABLE 7. Sensitivity analysis of predictor parameters in compressive strength

Input Parameters	R	MAE
The omission of “Binder” variable	0.699	7.031
The omission of “Water” variable	0.823	5.796
The omission of “Cement” variable	0.780	6.873
The omission of “Fine aggregate” variable	0.743	7.893
The omission of “Coarse aggregate” variable	0.745	7.234
The omission of “Specimen age” variable	0.601	9.383

$$m = (R^2 - R_0^2) / R^2 \quad (5)$$

$$n = (R^2 - R_0'^2) / R^2 \quad (6)$$

where R_0^2 is the square of the correlation coefficient from origin between the predicted and observed values, and $R_0'^2$ is the square of the correlation coefficient between the observed and predicted values calculated via Equations (7) to (9) as follows [23]:

$$R_m = R^2 \times \left(1 - \sqrt{|R^2 - R_0^2|}\right) > 0.5 \quad (7)$$

$$R_0^2 = 1 - \sum_{i=1}^{n} P_i^2(1-K)^2 / \sum_{i=1}^{n}(P_i - \bar{P})^2 \quad (8)$$

$$R_0'^2 = 1 - \sum_{i=1}^{n} O_i^2(1-K')^2 / \sum_{i=1}^{n}(O_i - \bar{O})^2 \quad (9)$$

As can be seen in Table 8, the ANN-ABC model performed well within the scope of this validation based on validation criteria. Therefore, this method has high prediction accuracy and the amount of correlation between predicted and observed values in this method has not been estimated randomly.

Proposed models can be used to predict natural events if some or all of the validation conditions are valid for them. Accordingly, the R_m parameter for each of the improved models is greater than 0.5. The coefficients of determination of *n* and *m* are also less than 0.1 for all models. As can be seen from Table 8, the methods used can be introduced as predictor models by satisfying the relevant validation criteria. In addition, this correlation between the predicted and observed values of compressive strength cannot be random [24].

3. 9. Uncertainty Analysis Simply put, uncertainty refers to what happens outside human control. In this section, a quantitative evaluation is presented of uncertainties based on the Monte-Carlo simulation (MCS) approach using intelligent models to estimate the compressive strength of pavement RCC. The uncertainty analysis is implemented for 333 laboratory data used in this dissertation (thesis for MSc) with 250,000 iterations. Besides, this analysis can add to the advantages of the proposed intelligent methods over empirical relationships. The relevant analysis is performed using the following equations that consider uncertainty in the range of less than 35% as acceptable [25], as shown in Table 9. Mean absolute deviation and uncertainty can be derived using Equations (10) and (11) as follow:

- Mean Absolute Deviation (MAD):

$$MAD = \frac{1}{M}\sum_{i=1}^{M}|P_i - Median(P)| \quad (10)$$

- Uncertainty%:

$$Uncertainty\% = \frac{100 \times MAD}{Median(P)} \quad (11)$$

TABLE 8. External validation criterion for predicting compressive strength

Model	*K*	*K'*	*m*	*n*	R_m
MLR	1.04	0.914	-0.446	-0.400	0.444
ANN	1.02	0.936	-0.364	-0.334	0.533
ANN-ABC	0.973	0.999	-0.244	-0.252	0.565
Conditions	(85/0< K, K' <1.15)		(*m*, *n* <0.1)		(R_m > 0.5)

3. 10. Validation of the Proposed Models Using Real Data This study used eight unused pavement RCC data at 7, 28, 90, and 180 days of age that were not used in model development to validate models and to control their reliability conditions, whose values are described in Table 10. Input data for this evaluation are collected from Ref. [26–28].

The results of this evaluation, presented in Table 11, clearly show that the real and computational values are consistent for each of the six samples and the accuracy of the predictions is accompanied by an acceptable error. The MARS-ABC model with RMSE and MAE of 21.85 and 4.79, respectively, and a correlation coefficient above 0.8, which is an acceptable correlation condition (0.94), is validated at this stage. Based on the results, the proposed models, the accuracy of the predicted values of the developed models, and the accuracy of their estimation have been validated. [29, 30].

TABLE 9. Monte Carlo uncertainty analysis for the proposed models

Models	Median	MAD	Uncertainty %
MLR	33.62	14.23	58.47
ANN	38.90	10.26	33.40
ANN-ABC	40.96	9.11	26.63

TABLE 10. Input data for validation of the model prediction

	AS	CA	FA	C	W	B
A	7	841	1235	150	105	250
B	7	1209	801	295	114	295
C	90	1209	801	175	130	295
D	90	772	1158	330	105.6	330
E	90	1095	807	125	94	313
F	180	1209	801	295	114	295
G	28	1095	807	193	103	322
H	90	633.75	427.78	210	165	300

TABLE 11. Evaluation of the models at the validation stage

Sample (Specimen)	Actual Compressive Strength	Calculated Compressive Strength	Error Rate	R	RMSE	MAE
A	21.8	23.65	-1.857	0.94	21.85	**4.79**
B	26.5	31.29	-4.798			
C	70.25	56.33	13.917			
D	45	46.84	-1.847			
E	54.3	58.08	-3.788			
F	53.4	54.21	-0.811			
G	48.8	47.53	1.2626			
H	40.35	41.99	-1.649			

4. CONCLUSIONS

This study utilized novel data-driven modeling techniques, namely Multiple Linear Regression (MLR) and Artificial Neural Network (ANN), as well as a newly developed ANN-ABC approach to predict the comprehensive strength of pavement RCC. Initially, three different scenarios were defined to extract the parameters affecting the compressive strength of this type of concrete. The best combination of input variables, including six input parameters, namely coarse aggregate, fine aggregate, cement, water, binder, and specimen age, were used to develop the proposed models based on Cp mallow and R^2 indices in Minitab. According to the error statistical indices in the training phase, the ANN-ABC model (RMSE = 39.97, R = 0.938) performed better in estimating the compressive strength of the pavement RCC than ANN (RMSE = 76.68, RR = 0.821) and MLR (RMSE = 145.47, R = 0.603). Furthermore, the MAE statistical index for the improved ANN (4.71 MPa) reported a lower mean error. As a result, the statistical indices show that the proposed ANN-ABC model has a better performance and higher accuracy in the training phase than the other models. In other words, the application of metaheuristic algorithms to the model learning process improves the accuracy of the developed model. At the experimental stage, the compressive strength values of the models are predicted with good accuracy. The ANN-ABC model (MAE = 5.21, RMSE = 49.11, R = 0.920) reported significant accuracy compared to the other models used in this study. Sensitivity analysis results show that the omission of the predictor variable "specimen age" with the highest correlation coefficient of R = 0.601 and MAE = 9.383 had the highest effect on the proposed ANN-ABC model (i.e., the best model in this study) in estimating the compressive strength of pavement RCC. Furthermore, the mix design variables, namely the variables “binder” and “fine aggregate,” had the greatest impact on compressive strength, with a 22.1% and 17.7% decrease, respectively, in the result of the correlation coefficient at the test stage. The validity of the developed compressive strength models was evaluated using external validation, Monte Carlo uncertainty analysis, and validation of real laboratory values. The results suggested that the models presented are within the acceptable range of the indicators of this evaluation and are valid.

5. SUGGESTIONS FOR FUTURE RESEARCH

In recent years, great attention has been devoted to laboratory analyses and resulting modeling given the importance of RCC in industries and the attainment of appropriate resistance. This section offers a number of suggestions for future research and continuing the path of data-driven research:

Emerging concrete such as geopolymer concrete, heavy concrete, and SCC containing nanomaterials can be considered in the data-driven modeling process due to the multiplicity of influential materials.

Considering the structure of the MSE method in artificial neural models, it is suggested to use other metaheuristic algorithms such as ant colony optimization (ACO), particle swarm optimization (PSO) and genetic algorithm (GA) to improve performance and evaluate accuracy and speed.

Other data-driven models such as Model Tree (MT), Support Vector Machine (SVM), and Evolutionary Polynomial Regression (EPR) can be used to estimate the compressive strength of pavement RCC.

Consideration of other experiments on the properties of pavement RCC may also be of interest to continue this study.

6. REFERENCES

1. Ni, H. G., and Wang, J. Z. “Prediction of compressive strength of concrete by neural networks.” ***Cement and Concrete Research***, Vol. 30, No. 8, (2000), 1245–1250. https://doi.org/10.1016/S0008-8846(00)00345-8

2. Ashrafian, A., Gandomi, A. H., Rezaie-Balf, M., and Emadi, M. "An evolutionary approach to formulate the compressive strength of roller compacted concrete pavement." ***Measurement: Journal of the International Measurement Confederation***, Vol. 152, (2020), 107309. https://doi.org/10.1016/j.measurement.2019.107309
3. Amlashi, A. T., Alidoust, P., Ghanizadeh, A. R., Khabiri, S., Pazhouhi, M., and Monabati, M. S. "Application of computational intelligence and statistical approaches for auto-estimating the compressive strength of plastic concrete." ***European Journal of Environmental and Civil Engineering***, (2020). https://doi.org/10.1080/19648189.2020.1803144
4. Ayaz, Y., Kocamaz, A. F., and Karakoç, M. B. "Modeling of compressive strength and UPV of high-volume mineral-admixtured concrete using rule-based M5 rule and tree model M5P classifiers." ***Construction and Building Materials***, Vol. 94, (2015), 235–240. https://doi.org/10.1016/j.conbuildmat.2015.06.029
5. Ashrafian, A., Taheri Amiri, M. J., Rezaie-Balf, M., Ozbakkaloglu, T., and Lotfi-Omran, O. "Prediction of compressive strength and ultrasonic pulse velocity of fiber reinforced concrete incorporating nano silica using heuristic regression methods." ***Construction and Building Materials***, Vol. 190, (2018), 479–494. https://doi.org/10.1016/j.conbuildmat.2018.09.047
6. Abdulelah Al-Sudani, Z., Salih, S. Q., sharafati, A., and Yaseen, Z. M. "Development of multivariate adaptive regression spline integrated with differential evolution model for streamflow simulation." ***Journal of Hydrology***, Vol. 573, (2019), 1–12. https://doi.org/10.1016/j.jhydrol.2019.03.004
7. Mansouri, I., Kisi, O., Sadeghian, P., Lee, C.-H., and Hu, J. "Prediction of Ultimate Strain and Strength of FRP-Confined Concrete Cylinders Using Soft Computing Methods." ***Applied Sciences***, Vol. 7, No. 751, (2017), 1–14. https://doi.org/10.3390/app7080751
8. Kaveh, A., Bakhshpoori, T., and Hamze-Ziabari, S. M. "M5' and mars based prediction models for properties of selfcompacting concrete containing fly ash." ***Periodica Polytechnica Civil Engineering***, Vol. 62, No. 2, (2018), 281–294. https://doi.org/10.3311/PPci.10799
9. Asteris, P. G., Ashrafian, A., and Rezaie-Balf, M. "Prediction of the compressive strength of self-compacting concrete using surrogate models." ***Computers and Concrete***, Vol. 24, No. 2, (2019), 137–150. https://doi.org/10.12989/cac.2019.24.2.137
10. Ashrafian, A., Shokri, F., Taheri Amiri, M. J., Yaseen, Z. M., and Rezaie-Balf, M. "Compressive strength of Foamed Cellular Lightweight Concrete simulation: New development of hybrid artificial intelligence model." ***Construction and Building Materials***, Vol. 230, (2020), 117048. https://doi.org/10.1016/j.conbuildmat.2019.117048
11. Rao, S. K., and Sravana, P. "Experimental Investigation On Pozzolanic Effect Of Fly Ash In Roller Compacted Concrete Pavement Using Manufactured Sand As Fine Aggregate." ***International Journal of Applied Engineering Research***, Vol. 10, No. 8, (2015), 20669–20682. Retrieved from http://www.ripublication.com
12. Rao, S. K., Sravana, P., and Rao, T. C. "Experimental studies in Ultrasonic Pulse Velocity of roller compacted concrete pavement containing fly ash and M-sand Studies in Ultrasonic Pulse Velocity of Roller compacted concrete pavement." ***International Journal of Pavement Research and Technology***, Vol. 9, No. 4, (2016), 289–301. https://doi.org/10.1016/j.ijprt.2016.08.003
13. Tangtermsirikul, S., Kaewkhluab, T., and Jitvutikrai, P. "A compressive strength model for roller-compacted concrete with fly ash." ***Magazine of Concrete Research***, Vol. 56, No. 1, (2004), 35–44. https://doi.org/10.1680/macr.2004.56.1.35
14. Rao, S. K., Sravana, P., and Rao, T. C. "Experimental studies in ultrasonic pulse velocity of roller compacted concrete containing GGBS and M-sand." ***ARPN Journal of Engineering and Applied Sciences***, Vol. 11, No. 3, (2016), 2016–1819. Retrieved from www.arpnjournals.com
15. Ghahari, S. A., Mohammadi, A., and Ramezanianpour, A. A. "Performance assessment of natural pozzolan roller compacted concrete pavements." ***Case Studies in Construction Materials***, Vol. 7, (2017), 82–90. https://doi.org/10.1016/j.cscm.2017.03.004
16. Hesami, S., Modarres, A., Soltaninejad, M., and Madani, H. "Mechanical properties of roller compacted concrete pavement containing coal waste and limestone powder as partial replacements of cement." ***Construction and Building Materials***, Vol. 111, (2016), 625–636. https://doi.org/10.1016/j.conbuildmat.2016.02.116
17. Atiş, C. D., Sevim, U. K., Özcan, F., Bilim, C., Karahan, O., Tanrikulu, A. H., and Ekşi, A. "Strength properties of roller compacted concrete containing a non-standard high calcium fly ash." ***Materials Letters***, Vol. 58, No. 9, (2004), 1446–1450. https://doi.org/10.1016/j.matlet.2003.10.007
18. Mardani-Aghabaglou, A., and Ramyar, K. "Mechanical properties of high-volume fly ash roller compacted concrete designed by maximum density method." ***Construction and Building Materials***, Vol. 38, (2013), 356–364. https://doi.org/10.1016/j.conbuildmat.2012.07.109
19. Modarres, A., and Hosseini, Z. "Mechanical properties of roller compacted concrete containing rice husk ash with original and recycled asphalt pavement material." ***Materials and Design***, Vol. 64, (2014), 227–236. https://doi.org/10.1016/j.matdes.2014.07.072
20. Pavan, S., and Rao, S. K. "Effect of Fly ash on Strength Characteristics of Roller Compacted Concrete Pavement." ***IOSR Journal of Mechanical and Civil Engineering***, Vol. 11, No. 6, (2014), 8. Retrieved from www.iosrjournals.org
21. Rashad, A. M. "A preliminary study on the effect of fine aggregate replacement with metakaolin on strength and abrasion resistance of concrete." ***Construction and Building Materials***, Vol. 44, (2013), 487–495. https://doi.org/10.1016/j.conbuildmat.2013.03.038
22. Tropsha, A., Gramatica, P., and Gombar, V. K. "The importance of being earnest: Validation is the absolute essential for successful application and interpretation of QSPR models." In QSAR and Combinatorial Science (Vol. 22, pp. 69–77). Wiley-VCH Verlag. https://doi.org/10.1002/qsar.200390007
23. Binder, K., and Heermann, D. W. Monte Carlo Simulation in Statistical Physics. Cham: Springer International Publishing. https://doi.org/10.1007/978-3-030-10758-1
24. Tung, Y., and Yen, B. Hydrosystems engineering uncertainty analysis. American Society of Civil Engineers, and McGraw-Hill Book Company. Retrieved from https://cedb.asce.org/CEDBsearch/record.jsp?dockey=0150035
25. Verbeeck, H., Samson, R., Verdonck, F., and Lemeur, R. "Parameter sensitivity and uncertainty of the forest carbon flux model FORUG: A Monte Carlo analysis." In ***Tree Physiology*** (Vol. 26, pp. 807–817). Oxford University Press. https://doi.org/10.1093/treephys/26.6.807
26. Chi, M., and Huang, R. "Effect of circulating fluidized bed combustion ash on the properties of roller compacted concrete." ***Cement and Concrete Composites***, Vol. 45, (2014), 148–156. https://doi.org/10.1016/j.cemconcomp.2013.10.001
27. Kuddus, M. A., and Dey, P. P. "Cost Analysis of RCC, Steel and Composite Multi-Storied Car Parking Subjected to High Wind Exposure in Bangladesh." ***Civil Engineering Journal***, Vol. 3, No. 2, (2017), 95–104. https://doi.org/10.28991/cej-2017-00000076
28. Rastegarian, S., and Sharifi, A. "An Investigation on the Correlation of Inter-story Drift and Performance Objectives in

Conventional RC Frames." ***Emerging Science Journal***, Vol. 2, No. 3, (2018), 140–147. https://doi.org/10.28991/esj-2018-01137

29. Karimnader-Shalkouhi, S., Karimpour Fard, M., and Machado, S. "An ANN Based Sensitivity Analysis of Factors Affecting Stability of Gravity Hunched Back Quay Walls." ***Civil Engineering Journal***, Vol. 3, No. 5, (2017), 301–318. https://doi.org/10.28991/cej-2017-00000092
30. Jalali, M., Pasbani Khiavi, M., and Ghorbani, M. A. "Investigation of to the Effect of Bedrock Stiffness on Seismic Behaviour of Roller Compacted Concrete Dam." ***Civil Engineering Journal***, Vol. 3, No. 8, (2017), 626–639. https://doi.org/10.28991/cej-2017-00000117

Persian Abstract

چکیده

در این پژوهش، به منظور بهبود بخشیدن دقت مدل ارائه شده، الگوریتم فراابتکاری کلونی زنبور عسل مصنوعی (ABC) برای بهینه کردن مقادیر روش شبکه‌ی عصبی مصنوعی (ANN) پیاده‌سازی شده و مدل توسعه‌داده‌شده ارزیابی شد. مقاومت فشاری بتن غلتکی با استفاده از مصالح طرح اختلاط در سه فرم ورودی وزنی حجمی (سیمان،آب، درشت دانه، ریزدانه و چسباننده)، نسبت مقادیر (نسبت آب به سیمان، نسبت آب به چسباننده، نسبت درشت‌دانه به ریزدانه) و همچنین درصد مقادیر طرح اختلاط در سنین مختلف بررسی گردید. مجموعه‌ی جامع و دارای محدوده‌ی مناسب داده‌ها شامل ۳۳۳ طرح اختلاط از مقالات مختلف جمع‌آوری شد. دقت مدل‌های این پژوهش با استفاده از شاخص‌های خطا شامل ضریب همبستگی، ریشه‌ی میانگین مربعات خطا، میانگین خطای مطلق بررسی و مدل‌های ترکیبی توسعه داده شده، مقایسه گردید. همچنین، برای اعتبار سنجی مدل‌ها، اعتبارسنجی خارجی و تحلیل عدم قطعیت مونت کارلو انجام و نتیجه گزارش گردید. در مرحله‌ی آزمایش پیش‌بینی مقادیر مقاومت فشاری، معلوم شد که مدل شبکه‌ی عصبی مصنوعیِ بهبودیافته با الگوریتم کلونی زنبور عسل (ANN-ABC) با (R=۰/۹۲۰, RMSE=۱۱/٤۹, MAE=۵/۲۱) در مقایسه با دیگر مدل‌های این مطالعه دقت قابل توجهی داشته است. همچنین، تحلیل حساسیت متغیرهای پیش‌بین در این مطالعه مشخص کرد که سن نمونه، چسباننده و ریزدانه متغیرهایی با اثرگذاری و اهمیت بیشتر در این تحقیق بوده است. مقایسه‌ی نتایج نشان‌گر این است که مدل بهبودیافته‌ی پیشنهادی با الگوریتم کلونی زنبور عسل مصنوعی در ارائه‌ی روابط محاسباتی توانایی بیشتری در کاهش خطا و دقت بالاتری نسبت به مدل‌های پیش‌فرض بررسی شده در پیش‌بینی مقاومت فشاری بتن غلتکی نشان داده و همچنین سعی در ساده سازی روابط محاسباتی داشته است.

IJE TRANSACTIONS A: Basics Vol. 33, No. 10, (October 2020) 1864-1871

International Journal of Engineering

Journal Homepage: www.ije.ir

Vertical and Lateral Displacement Response of Foundation to Earthquake Loading

A. F. I. Al-Ameri*[a], F. W. Jawad[b], M. Y. Fattah[c]

[a] *Civil Engineering Department, College of Engineering, University of Baghdad, Iraq*
[b] *Ministry of Higher Education and Scientific Research, Department of Reconstruction and Projects, Baghdad, Iraq*
[c] *Building and Construction Engineering Department, University of Technology, Baghdad, Iraq*

PAPER INFO

Paper history:
Received 03 April 2020
Received in revised form 15 June 2020
Accepted 04 August 2020

Keywords:
Earthquake Loading
Vertical and Lateral Displacements
Stiffness Ratio
Abaqus Program

ABSTRACT

Risks are confronting the foundations of buildings and structures when exposed to earthquakes which leads to high displacements that may cause the failure of the structures. This research elaborates numerically the effect of the earthquake on the vertical and lateral displacement of footing resting on the soil. The thickness of the footing and depth of soil layer below the footing was taken as (0.5, 1.0, and 2.0 m) and (10, 20 and 40m), respectively. The stiffness ratio of soil to footing was also elaborated at 0.68, 0.8, 1.0, and 1.7. The results showed an increase in the verticle displacement of footing as the duration of the earthquake increases. The increase of soil layer thickness below the footing leads to a reduction in the vertical and lateral displacement. While an increase in the thickness of the footing leads to a decrease in the lateral displacement of the footing meanwhile no effect was noticed in the vertical displacement. It was noticed that the time lag between the maximum vertical displacement and the highest value of the earthquake loading is about 0.27 s. It was found that as the distance between the footing and the source of earthquake load increases, the effect of damping on the earthquake load increases while the lateral displacement decreases. The results revealed that an increase in the stiffness ratio leads to a decrease in the vertical displacement and a reduction in the response of the lateral displacement till reaching the value of stiffness ration of unity.

***doi**: 10.5829/ije.2020.33.10a.05*

NOMENCLATURE

b	Width of the footing	S	Soil factor
d	Thickness or depth of the soil layer under the footing	av	vertical ground acceleration
$\bar{F}$	dimensionless soil inertia force	g	acceleration of gravity
Ec	Modulus of elasticity for concrete	**Greek Symbols**	
Es	Modulus of elasticity for soil	$\phi'd$	Design angle of the shearing resistance of soil
Nc, $N\gamma$ and Nγq	Bearing capacity factors	γ_d	Dry unit weight of soil
RSM	Rubber-soil mixture	ψ	Dilation angle
t	Thichness of the footing	γ_c	Unit weight of concretet
$Nmax$	seismic vertical centred load		

1. INTRODUCTION

Building under seismic waves depends mainly on deformation of members and bonded of the lateral load resisting system; while importance of deformation demand/capacity in performance-based frameworks has been defined for decades. There is still a major unbonded to this philosophy when it comes to soil foundation systems. Because current seismic design/assessment codes only go as far as recognizing the finite stiffness and the finite bearing capacity of foundation with no consideration to their deformation

*Corresponding Author Email: *alameri.abbas@gmail.com* (A. F. I. Al-Ameri)

Please cite this article as: A. F. I. Al-Ameri, F. W. Jawad, M. Y. Fattah, Vertical and Lateral Displacement Response of Foundation to Earthquake Loading, International Journal of Engineering (IJE), IJE TRANSACTIONS A: Basics Vol. 33, No. 10, (October 2020) 1864-1871

ability. The failures which have been illustrated from the past earthquakes are two types (bearing capacity failure and settlement of foundation). The building may fail upon subjected to earthquake and the building tilted up to 60º and sunk up to 3.8 m in Nigata [1]. The loading is defined as dynamic load when it changes over time in value and or direction [2].

The type of dynamic load applied to soil or foundation relies on the nature of its creator source [3]. As well as, the soil deformation may change from small amplitude (elastic) to large (plastic) during earthquake [4]. It is well known that the behaviour of soil under dynamic is different from that under static loads through the stress-strain relationship of soil and is always nonlinear behaviour.

It always needs to state earthquake loading as plastic behaviour since high deformation occurs and it is mainly depending on the power and severity of the earthquake [5].

From a structural point of view, the footing should satisfy two requirements. The first one is the factor of safety against shear failure would be more than or equal to 2 under seismic loads and the second one is the permanent soil deformation is adjusted by the footing and superstructure. Some of the empirical steps available to calculate these issues for footing types have been discussed. Common strategies adopted by geotechnical engineers in the footing design have also been briefly discussed [6].

The problem of the earthquake bearing capacity of shallow footing has been solved indirectly, either by an increase of the static allowable ground, pressures connected to the probability of occurrence of the design seismic or by adopting an equivalent pseudo-static procedure [7].

A solution was presented by Maeda et al. [8] that can be applied widely to compute bearing capacity of shallow footings subjected to both inclined loads applied of the superstructure and inclined bearing soil during seismic loading. The solution is based on the seismic coefficient method and velocity field method from the upper bound theorem. The solution was verified by a series of experiments. It was found that the results in the case of severe seismic loading, most of the available solutions are over-estimating the bearing capacity.

A large-scale model was performed with five series of tests consisting of (40 models) of shear wall foundations to study the nonlinear load-deformation behaviour during cyclic and seismic loading [9]. The parameters that were systematically studied were footing dimensions, depth of embedment of footing, wall weight, and initial static vertical factor of safety, unit weight of soil, and soil type (dry sand and saturated clay). It was found that there is a reduction in stiffness of which may be due to the deformed shape of the foundation–soil interface and uplift associated with large rotations. Moreover, it was concluded that the permanent settlement beneath the foundation continue to accumulate with the number of cycles of loads, though the rate of accumulation of settlement decreases as the foundation embeds.

The effect of ground inclination and embedment depth for footing subjected to earthquake excitation was studied [10]. It was found that the bearing capacity factors (Nc and Nγq) decreased with an increase in kh (values of seismic acceleration coefficient). Unlike most of the results reported in the literature for the seismic case, the computational results take into account the shear resistance of soil mass above the footing level. An increase in the depth of the embedment leads to an increase in the magnitudes of both Nc and Nγq.

The inertia loads in the ground and beneath the footings reducing the bearing capacity of the footing when subjected vertical loading. These results cannot be applied for seismic bearing capacity of shallow footing due to the transient nature of the seismic loading as compared to the sustained nature of static loads. This technical note appears in the bearing capacity calculation given in Part 5 of Euro code 8, which declares that shallow footing bearing strength for cohesive soils is not sensitive to the seismic horizontal acceleration, but dry cohesionless soil may be more sensitive [11].

Experimental and numerical studies for the effect of harmonic dynamic loading on a shallow foundation of different sizes and depth of embedment in dry and saturated sand with different relative density was performed [12]. It was found that displacement amplitude for dry dense sand is less than of dry loose sand. They showed that for foundation rested at the surface, the ratio of displacement amplitude between dense sand to lose sand varying from (0.27 to 1.00) and (0.03 to 0.94) for footing dimensions (100×200 mm) and (200×400 mm), respectively. At the same time, the ratio for the embedded footing becomes (0.24 to 0.99) and (0.10 to 0.97) for the footing dimensions (100×200 mm) and (200×400 mm), respectively. These results are attributed to the increase of soil stiffness in the dense state that makes the soil stiffer and resist vibrations as well as it can be due to trench and sidewall effects when embedded.

The mechanical property of soil and reaction of forced vibration is responsible to the behaviour of frequency and propagation of the dynamic waves. They convert the periodic motion of input to the nonlinear loading. The liquefaction with high magnitude occurs in the deep of soil foundation, as well as the pore water pressure magnitude reduces near the surface, this fluctuation of pore water pressure causes differential settlement. There is no direct effect of frequency on the differential settlement, during which soil is under the

liquefied state [13]. Same observations were noticed by Fattah et al. [14] for machine foundations.

Moghaddas Tafreshi et al. [15] stated that the results of plate load tests that imposed incremental cyclic loading to a sandy soil bed containing multiple layers of granulated rubber-soil mixture (RSM) at large model scale when the thickness of the RSM layer is smaller, or larger, settlements increase and, at large thicknesses may even exceed those of untreated soil. Layers of the RSM reduced the vertical stress transferred through the foundation depth by distributing the load over a wider area. With the inclusion of RSM layers, the coefficient of elastic uniform compression decreases by a factor of around 3-4. A softer response was obtained when more RSM layers were included beneath the footing damping capacity improves appreciably when the sand bed incorporates RSM layers. Numerical modelling using "FLAC-3D" confirms that multiple RSM layers will improve the performance of a foundation under heavy loading.

The effect of near-fault ground motion on a timber beam was investigated with reference to small displacement theory [16]. The simulated near-fault ground motion is applied to the fixed base of a timber frame model. The beam is placed in a single span of a timber frame. The beam has two different length sizes of 1.8 and 3.3 meters. The seismic load-displacement, seismic load-strain, and strain-displacement was calculated for all models. The beam was modelled as a nonlinear analysis. The numerical analysis results indicate that the inertial interaction, energy dissipation, and nonlinear deformation of beams in timber frames have directly related with frame span. In beams with a smaller length, higher seismic loading caused lower displacement. Also, the displacement was reduced by reducing the length of the beam. The inertial interaction, energy dissipation, and nonlinear deformation were changed with respect to the length of the beam.

The purpose of this research is to determine the vertical and lateral displacement under the influence of the earthquake. In addition, it is required to know the influence of the soil layer on the impact of the earthquake on the displacement and the effect of changing the stiffness ratio of soil to the footing on the value of lateral and vertical displacement. The adopted technique of numerical analysis by using Abaqus is of great interest to improve the seismic behaviour of soil foundation system under the earthquake excitation.

2. EARTHQUAKE LOADING

Figure 1 shows the time history for the El Centro earthquake which is applied to the model of the foundation-soil system that would built in the Abaqus program.

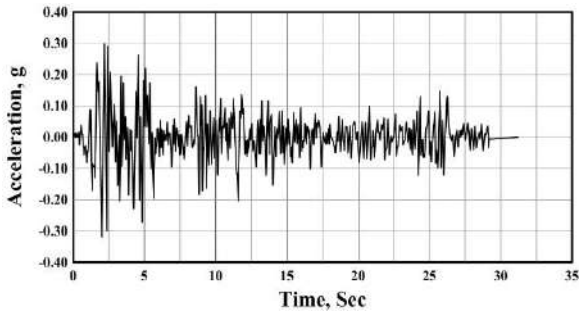

Figure 1. Time–history of acceleration of the El Centro earthquake

In order to obtain the accuracy of the program, the model was built by using the Abaqus program in this research and then the model was verified with the results of the ultimate bearing capacity of the foundation under seismic vertical centred load $Nmax$ as given in Equation (1). The results of the verification are shown in Table 1.

$$N_{max} = \frac{1}{2}\rho g\ (1 \pm \frac{av}{g})B\ 2N\gamma \quad (1)$$

where:
g: acceleration of gravity;
av: vertical ground acceleration, that may be taken as being equal to 0.5 $ag.S$;
$N\gamma$: Bearing capacity factor.
S: Soil factor defined in EN 1998 – 1:2004

The dimensionless soil inertia force F is obtained by Equation (2):

$$F = \frac{ag}{g\ tan(\phi' d)} \quad (2)$$

where: $\phi' d$: Design angle of the shearing resistance of soil.

For cohesionless soils, inertia forces may be neglected if $ag.S < 0.1g$.

3. FAILURE CRITERIA

Strain levels are produced in the ground with different magnitudes. If strains below the order of 10^{-5}, the deflection of soils is elastic and recoverable, the small strains would be small amplitude vibration or wave propagation through the ground. The strain between (10^{-4} and 10^{-2}), the behaviour of soils is elastic-plastic and produces irrecoverable permanent deflections [17]. This criterion will be followed in this research.

4. MODEL CONFIGURATION

The models of soil-foundation system were implemented in the Abaqus program as two parts, one

TABLE 1. Results of Verification of model

Method	Parameters						
	B	ρ	g	av	S	$N\gamma$	Nmax
Ultimate bearing capacity of the foundation under seismic vertical load	14	1.55	9.81	1.99	1.35	9.7	17343.5
Finite element using Abaqus	14	1.55	9.81	----	----	----	16212.3

of them is the shallow foundation with dimensions of (14 m × 14 m) and the thickness taken as (0.5, 1.0 and 2.0 m) while the other part is the soil media with dimensions of (60 m × 60 m) and the depth of soil was 10, 20 and 40 m. Figure 2 shows the two parts of the footing and the soil domain after the assembly. The interaction of the base footing and the top surface of the soil is activated to be of type normal behaviour hard contact. Parameters that would be addressed in this research is summarized in Table 2.

5. MATERIAL PROPERTIES OF THE MODEL

As previously explained, the model consists of two parts, one of them is the footing and the other is soil. For the purpose of distinguishing each part from the other, the properties of the materials were defined

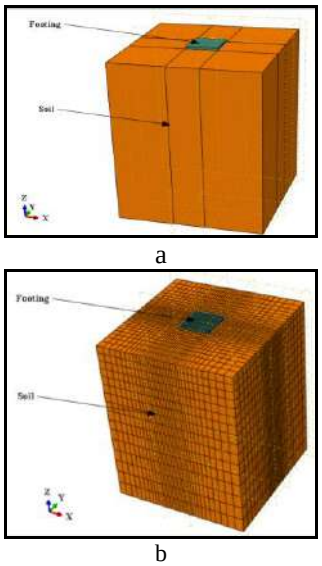

a

b

Figure 2. The assembly and mesh of footing and soil

TABLE 2. The parametric study

Model	Parameter			
	Width of footing, b (m)	Thickness of footing, t (m)	Thickness (depth) of soil layer, d (m)	Stiffness ratio (Es/Ec)
Model 1	14	0.5	10	0.68
Model 2	14	0.5	20	0.68
Model 3	14	0.5	40	0.68
Model 4	14	1	10	0.68
Model 5	14	1	20	0.68
Model 6	14	1	40	0.68
Model 7	14	2	10	0.68
Model 8	14	2	20	0.68
Model 9	14	2	40	0.68
Model 10	14	2	10	0.85
Model 11	14	2	10	1.0
Model 12	14	2	10	1.7

including the footing concrete materials which follows linear elastic behaviour. For soil, Jefferies and Been [6] stated that the soil is the best modelled as plastic materials when subjected to earthquake loading of high level of strain resulting from the high magnitude of energy of such loading. Hence, the soil is represented by extended Drucker-Prager family of plasticity model which is the best suited for the behaviour of granular soils in which the yield behaviour related to the equivalent pressure stress. The inelastic behaviour may be associated with frictional mechanisms such as sliding of particles across each other. Tables 3 and 4 show the properties of the materials for both footing and sand.

TABLE 3. Properties of concrete footing

Property	Value
Unit weight, γ_c (kN/m^3)	24
Elastic modulus, Ec (kN/m^2)	23500
Poisson's ratio, v	0.15

TABLE 4. Properties of sand soil

Property	Value
Angle of friction, ^{o}	32
Flow stress ratio	1
Dilation angle, ψ^o	3
Poisson's ratio, v	0.25
Modulus of deformation, Es (kN/m^2)	16000
Dry unit weight of soil, γ_d (kN/m^3)	15.5

6. DEFINITION OF LOADING AND BOUNDARY CONDITIONS

In this section, the earthquake loading explained in section 2, is applied at the base of the soil model towards the base of the footing. The application of loading and the boundary conditions are defined as shown in Figure 3, whereas displacements are allowed in horizontal and vertical directions for lateral boundaries.

6. RESULTS AND DISCUSSION

Figures 4 to 6 show the vertical displacement-time history response generated due to earthquake loading of the model. It can be noticed in general that, as the duration of earthquake increases, the vertical displacement of the footing increases. This behaviour can be attributed to the loose state of soil prior to the application of the earthquake loading and when the earthquake loading is applied, the state of the soil changes from loose to dense. As a result of continuous earthquakes, the soil state changes from dense to loose by dilation which results in high displacement in the footing. Clearly, it can be illustrated from the figures

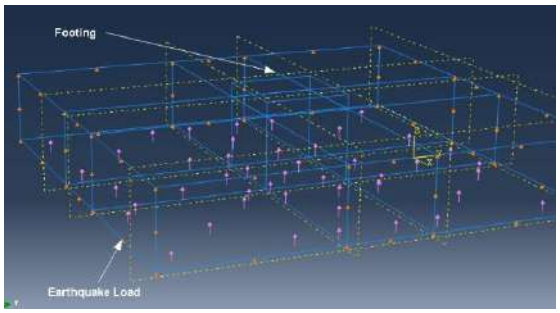

Figure 3. The applied earthquake load in the model

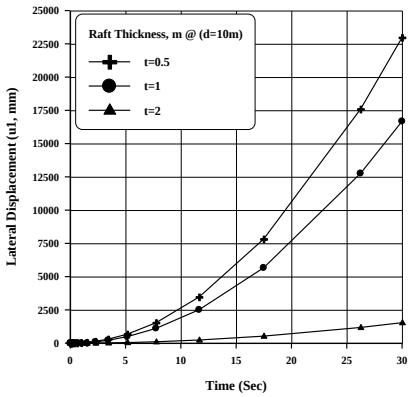

Figure 4. Lateral displacement with time for footings with different thicknesses placed on soil layer of depth (d=10 m) below the footing

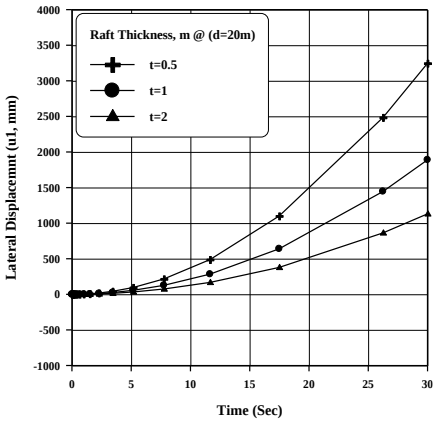

Figure 5. Lateral displacement with time for footings with different thicknesses placed on soil layer of depth (d=20 m) below the footing

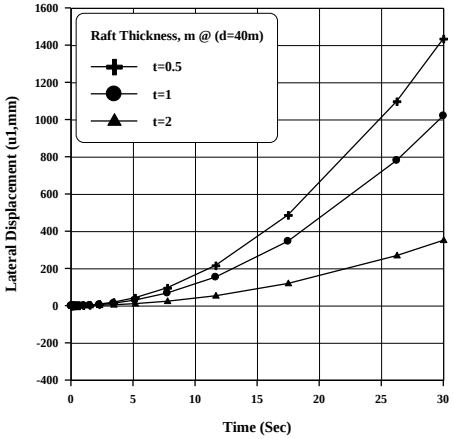

Figure 6. Lateral displacement with time for footings with different thicknesses placed on soil layer of depth (d=40 m) below the footing

that with an increase of the soil layer thickness below the footing, the vertical displacement decreases. In addition, the vertical displacement decreases from (80, 12, and 2 mm) when the distance between the footing and the point of influence of the earthquake loading varies from (10, 20, and 40 m), respectively. It was expected that the highest value of vertical displacement incidence with the highest value of the earthquake loading but the results revealed that there is a time lag of about 0.27 s.

Figure 7 shows the calculated vertical displacement versus the distance between the footing and the point of influence of the earthquake, it can be noticed that there is no apparent effect of the footing thickness on the vertical displacement because the direction of the earthquake load is perpendicular to the base of the foundation and an increase in the distance between the footing and the point of influence of the earthquake loading leads to decrease in the vertical displacement.

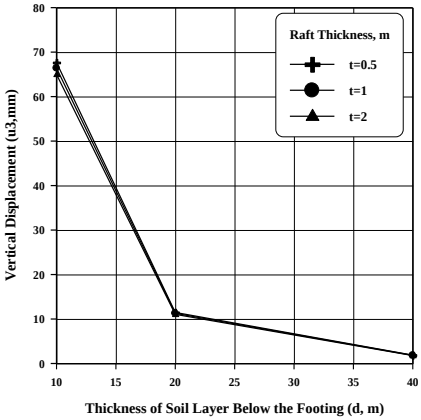

Figure 7. Vertical displacement versus soil layer thickness below the footing

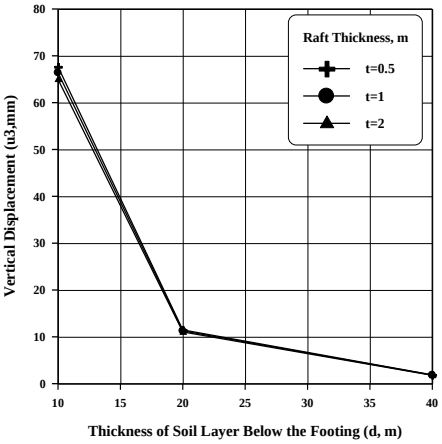

Figure 8. Lateral displacement versus soil layer thickness below the footing

Figure 8 illustrates variations of the calculated lateral displacement with the distance between the footing and the point of influence of the earthquake. It can be noticed that the greater the distance between the footing and the point of influence of earthquake load, the greater the effect of damping to the earthquake load and consequently decrease in lateral displacement as well as the depth of soil layer is great, the length of the wave increase that cause more attenuation during earthquake. The effect of damping appears clearly when the depth of soil is 40 m.

The effect of soil stiffness on the vertical and lateral displacement of the footing was elaborated by changing soil stiffness several times with keeping footing stiffness constant. Figures 9 and 10 show the vertical and lateral displacement response with respect to time at different values of stiffness ratio (Es/Ec), where Ec is the modulus of elasticity of concrete and Es is the modulus of elasticity of soil. In general, an increase of the stiffness ratio value (Es/Ec) leads to a decrease in the vertical displacement of the footing. The vertical displacement decreases from (65, 52, 44, and 26 mm) when the stiffness ratio increases from (0.68, 0.85, 1, and 1.7), respectively. On the other hand, the response of the lateral displacement decreases with an increase in the value of stiffness ratio until reach the value of (Es/Ec =1).

It can be noticed that the lateral displacement starts to increase with an increase in the value of stiffness ratio, this is attributed to the state of the soil which has changed from loose to dense that leads to and facilitate the rapid transmission of the shockwave. The lateral displacement decreases from (1538, 1303, and 744 mm) when the value of stiffness ratio increases from (0.68, 0.85, and 1.00), respectively.

The shape of the model after completing the analysis and the deformation that occurred for the models due to the shockwave loading can be seen in Figure 11.

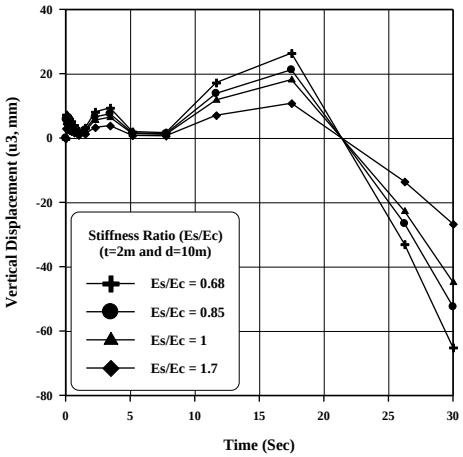

Figure 9. Vertical displacement with time for footings of different stiffness ratios (t= 2.0 m and d=10 m)

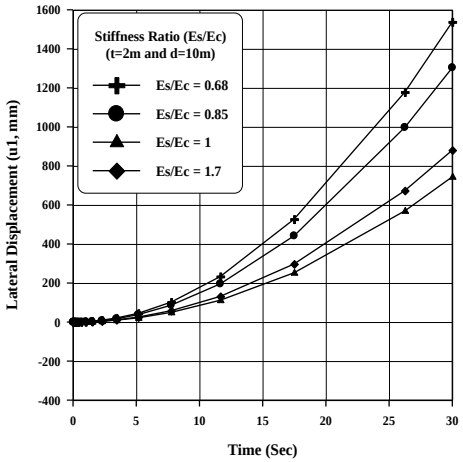

Figure 10. Lateral displacement with time for footings of different stiffness ratios (t= 2.0 m and d=10 m)

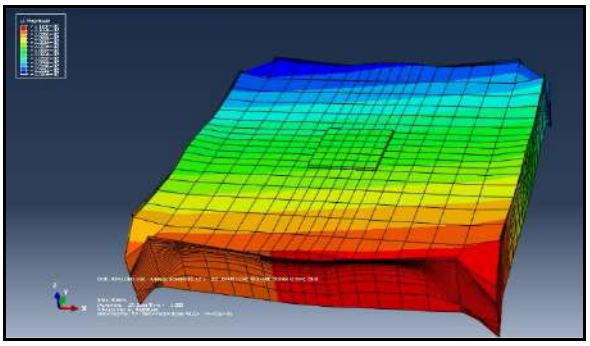

Figure 11. The deformed shape of deflection when (t= 0.5 m and the soil layer thickness below the footing, d=10 m)

7. CONCLUSIONS

From the discussions carried out in this work and other observations made during the numerical analyses, the following conclusions are made.

- As the time of applied earthquake increases, the vertical displacement of the footing increases.
- The vertical and lateral displacement increase with an increase in the depth of soil layer below the footing.
- The time lag between the maximum vertical displacement and the highest value of the earthquake loading is about (0.27 s).
- An increase in the thickness of the footing lead to a decrease in lateral displacement of the footing, while there is no obvious effect of the footing thickness on the vertical displacement since the direction of the earthquake load is perpendicular to the base of the footing.
- An increases in the depth of the soil layer below the footing lead to an increase in the attenuation of the earthquake load and consequently to decrease in lateral displacement.
- An increase in the stiffness ratio value (Es/Ec) leads to a decrease in the vertical displacement. The response of the lateral displacement decreases with an increase in the value of stiffness ratio until the value of (Es/Ec =1). The lateral displacement starts to increase with an increase in the value of stiffness ratio.

8. REFERENCES

1. Ishihara, K. and Koga, Y., "Case studies of liquefaction in the 1964 niigata earthquake", ***Soils and Foundations***, Vol. 21, No. 3, (1981), 35-52. doi:10.3208/sandf1972.21.3_35
2. Moura, A., Neto, S. and de Aguiar, M., "A comparative study of vibration frequency estimates of the surface foundations of wind turbines built on the sand dunes of the ceará coast", (2008).
3. Das, B.M. and Luo, Z., "Principles of soil dynamics, Cengage Learning, (2016).
4. Richart, F.E., "Foundation vibrations", ***Transactions of the American Society of Civil Engineers***, Vol. 127, No. 1, (1962), 863-897.
5. Jefferies, M. and Been, K., "Soil liquefaction: A critical state approach, CRC press, (2015).
6. Roy, D., "Design of shallow and deep foundations for earthquakes", ***J. Geotech. Earthq. Eng***, (2013), 1-8.
7. Tiznado, J.C. and Paillao, D., "Analysis of the seismic bearing capacity of shallow foundations", (2014). doi.org/10.4067/S0718-915X2014000200005
8. Maeda, Y., Irie, T. and Yokota, Y., "Bearing capacity formula for shallow foundations during earthquake", in 13th world conference on earthquake engineering. Vancouver, BC. 1-6.
9. Gajan, S., Kutter, B.L., Phalen, J.D., Hutchinson, T.C. and Martin, G.R., "Centrifuge modeling of load-deformation behavior of rocking shallow foundations", ***Soil Dynamics and Earthquake Engineering***, Vol. 25, No. 7-10, (2005), 773-783. doi:10.1016/j.soildyn.2004.11.019
10. Chakraborty, D. and Kumar, J., "Seismic bearing capacity of shallow embedded foundations on a sloping ground surface", ***International Journal of Geomechanics***, Vol. 15, No. 1, (2015), 04014035. doi:10.1061/(ASCE)GM.1943-5622.0000403
11. Pender, M., "Earthquake inertia effects on shallow foundation bearing strength", ***Géotechnique***, Vol. 68, No. 7, (2018), 640-645. doi:10.1680/jgeot.17.T.006
12. Fattah, M.Y., Al-Mosawi, M.J. and Al-Ameri, A.F., "Dynamic response of saturated soil-foundation system acted upon by vibration", ***Journal of Earthquake Engineering***, Vol. 21, No. 7, (2017), 1158-1188. doi:10.1080/13632469.2016.1210060
13. Namdar, A., "Liquefaction zone and differential settlement of cohesionless soil subjected to dynamic loading", ***Electronic Journal of Geotechnical Engineering***, Vol. 21, (2016), 593-605.
14. Fattah, M.Y., Al-Mosawi, M.J. and Al-Americ, A.F., "Stresses and pore water pressure induced by machine foundation on saturated sand", ***Ocean Engineering***, Vol. 146, (2017), 268-281. doi:10.1016/j.oceaneng.2017.09.055
15. Moghaddas Tafreshi, S., Darabi, J. and Dawson, A., "Cyclic loading response of footing on multi-layered rubber-soil mixtures", ***Geomechanics and Engineering***, Vol. 14, No. 2, (2020). doi:10.12989/gae.2018.14.2.115
16. Namdar, A., Dong, Y. and Liu, Y., "Timber beam seismic design–a numerical simulation", ***Frattura ed Integrità Strutturale***, Vol. 13, No. 47, (2019), 451-458. doi:10.3221/IGF-ESIS.47.35
17. Daghigh, Y., "Numerical simulation of dynamic behaviour of an earthdam during seismic loading", (1993).

Persian Abstract

چکیده

هنگام زلزله بنیاد ساختمانها و سازه ها با خطراتی مواجه هستند و منجر به جابجایی های زیاد می شوند که می تواند باعث خرابی سازه ها شود. این تحقیق به صورت عددی اثر زلزله را بر جابجایی عمودی و جانبی پی های در حال سکون در خاک توضیح می دهد. ضخامت پی و عمق لایه خاک زیر پی به ترتیب (۰.۵ ، ۱.۰ و ۲.۰ متر) و (۱۰ ، ۲۰ و ۴۰m) در نظر گرفته شد. همچنین نسبت سختی خاک به پایه نیز در ۰/۶۸ ، ۰.۸ ، ۱.۰ و ۱.۷ بیان شده است. نتایج نشان می دهد با افزایش مدت زمان وقوع زلزله ، افزایش جابجایی عمودی در پی را نشان می دهد. افزایش ضخامت لایه خاک زیر پی منجر به کاهش جابجایی عمودی و جانبی می شود. در حالی که افزایش ضخامت پی منجر به کاهش جابجایی جانبی پی می شود ، در عین حال هیچ تأثیری در جابجایی عمودی مشاهده نشده است. مشاهده شد که فاصله زمانی بین حداکثر جابجایی عمودی و بیشترین مقدار بارگذاری زلزله حدود ۰.۲۷ ثانیه است. مشخص شد که با افزایش فاصله بین پی و منبع بار زلزله ، در حالی که جابجایی جانبی کاهش می یابد ، تأثیر میرایی بر بار زلزله افزایش می یابد. نتایج نشان داد که افزایش نسبت سفتی منجر به کاهش جابجایی عمودی و کاهش پاسخ جابجایی جانبی تا رسیدن به ارزش سختی قریب به یک می شود.

International Journal of Engineering

Journal Homepage: www.ije.ir

The Comparison of Punching Shear Capacity in Solid and Void Two-Way Slabs on Soil Substrate in Relation to Spring Stiffness Changes

H. Azizian[a], M. A. Lotfollahi-Yaghin*[b], A. Behravesh[a]

[a] *Department of Civil Engineering, Mahabad Branch, Islamic Azad University, Mahabad, Iran*
[b] *Civil Engineering Faculty, University of Tabriz, Tabriz, Iran*

PAPER INFO

Paper history:
Received 02 May 2020
Received in revised form 05 July 2020
Accepted 04 August 2020

Keywords:
Laboratory Model
Numerical Model
Punching Shear Capacity
Soil and Spring Model
Spherical Plastic Hollow Formers
Two-Way Solid and Hollow Slabs

ABSTRACT

This study aims to investigate punching shear in solid and void slabs as well as simulated soil and spring models as distributed loads on the mentioned slabs. To this end, the slabs were tested using the nonlinear finite element analysis under static loading to assess their failure in terms of the final load and cracking patterns on the soil substrate and spring. For this purpose, a 3D finite element analysis was performed based on the element size, mesh, and concrete characteristic modeling. In Finite Element Software ABAQUS 6.19, the nonlinear behavior of brittle materials was defined based on the concrete damaged plasticity (CDP) model. Next, the results of the numerical analysis of the slabs were calibrated and validated based on a comparison with experimental specimens on a soil substrate. At the end, by optimizing the spring constant and obtaining the soil spring constant, the results of the numerical analysis of the slabs on the spring support were compared to the experimental results, which showed the calibrated models correctly predicted the punching cutting response of the slabs.

***doi**: 10.5829/ije.2020.33.10a.06*

NOMENCLATURE

f_c	Concrete Strength (MPa)	φ	Angle of Internal Friction of the Soil (degrees)
Ecm	Concrete Young's Modulus (GPa)	ψ	Effective angle of internal friction (degree)
f_t	Concrete Tensile Strength (MPa)	*R*	Solid slab
υ	Poisson's Ratio	S_1	Void slab
γ_c	Density of concrete (kg/m3)	h	The depth of slab (mm)
Es	Steel Young's Modulus (MPa)	d	The effective depth of slab = 100 mm
f_r	Reinforcement Tensile Strength (MPa)	P_1R_1	Point one slab R
γ	unit weight (mm)	P_1S_1	Point one slab one the depth of slab (mm)
E	Young's soil modulus (MPa)	Cc	Coefficient of curvature
σ	Pressure or stress (MPa)	Cu	Coeffi cient of uniformity
ε	Strain	D10	Grain sizes for which 10% of the soil grains are smaller
C	Cohesion of a soil	D30	Grain sizes for which 30% of the soil grains are smaller

1. INTRODUCTION

The first study on punching shear was conducted by a series of experiments on reinforced concrete foundations and also the interaction between the foundations and soil through steel springs was simulated. Later on, many researchers evaluated different methods of simulating soil-structure interactions. Employing a system driven by hydraulic cylinders to simulate a uniform load distributed over a foundation, their study was used as a reference work for future studies [1, 2], for instance testing slab-column fixtures by examining foundations with

*Corresponding Author, E-mails: *lotfollahi@tabrizu.ac.ir* (M. A. Lotfollahi-Yaghin)

Please cite this article as: H. Azizian, M. A. Lotfollahi-Yaghin, A. Behravesh, The Comparison of Punching Shear Capacity in Solid and Void Two-Way Slabs on Soil Substrate in Relation to Spring Stiffness Changes, International Journal of Engineering (IJE), IJE TRANSACTIONS A: Basics Vol. 33, No. 10, (October 2020) 1872-1885

uniformly distributed loading systems [3]. Punching investigation of the footing rested on real soil was done in practice only by using a sandbox test system to simulate soil effects and sand density, with the latter factor being a variable ranging from loose to dense [4–6]. Later on, similar experiments were conducted using a mixture of river sands [7]. Other studies were also carried out to investigate the punching shear of slabs [8]. Some experiments were conducted at the University of Pretoria in 2014, in which they used concrete slabs on 9 springs as supports and compared spring stiffness with soil stiffness [9, 10].

Analyses free vibration of a beam on elastic foundation by applying the variational iteration method (VIM) for three different axially loaded cases were adopted including one end clamped and the other end simply supported, both ends clamped, and both ends simply supported cases. In this paper, for different ratios of axial load acting on the beam to Euler buckling load, analytical solutions and frequency factors are evaluated. It is shown that the results obtained by VIM method in this paper are in compliance with the differential transform method (DTM) results for fixed-pinned case [10–14]. Also, homotopy perturbation method (HPM) was applied for free vibration of a beam on elastic foundation by Ozturk and Coskun [15]. In another research, analytical solutions for free vibration of a beam on elastic foundation were analyzed by Ozturk and Coskun [16] for the three cases considered above. Also, frequency factors were calculated for different ratios of axial load acting on the beam to Euler buckling load. The results obtained by the analytical solution are in good agreement with the_variational iteration method (VIM) results achieved in the previous research and homotopy perturbation method (HPM) results for three different axially loaded cases.

In reinforced concrete (RC) column footings, the soil stiffness can significantly affect the punching shear strength of the foundation slab. The present study conducted eccentric compression tests on three RC column footings considering the complex interaction between the soil and structure, and investigated the load-carrying capacity, displacement distribution, reaction distribution, failure mode, crack development, and strain distribution. However, column footings are generally subjected to eccentric compression. Thus, it is necessary to investigate the punching failure mechanism of column footings under eccentric compression. As the flexural reinforcement ratio increased, the observed critical angle of failure cone was increased from 44° to 54°. Such failure angle was steeper than that of flat slabs (30° to 45° when a/d = 3.22 to 8.80). The flexural reinforcement ratio affected the crack distribution area and the spalling of concrete cover [17].

By evaluating previous studies on punching shear, majority of the studies used simply support and concentrate load to the center of top face of slab, thus obtaining a punch shear. In this study, soil and spring have been used to simulate distributed load to obtain the punching shear capacity with low bending effect in two way bubble voided slabs. For a more accurate comparison, it was not possible to perform the spring test. In future research, it is possible to test such springs with the stiffness obtained from Abaqus software and to compare the soil and spring results.

However, in cases where the slab is placed on the soil support when applying the load to the column, if the soil is under the slab, the underside of the column itself will be completely rigid due to slight deformation occurring to the slab, which exhibits a high capacity that functions almost like a rigid wedge. In other words, the bottom of the column in the soil, with its relatively rigid performance, carries the main load of the column; thus, it could not be clear for which load the punching shear occurs. In addition, when one part of the column load is supported by the soil beneath the column and another part is loaded on other parts of the soil, it will not be practically detectable at the time of shear failure which simply occurs due to the area outside the cutting line. However, when the part under the foundation is emptied or replaced with low strength materials, most of the column load will be carried through the punching shear. In addition, when the slab undergoes failure, it will be determinable at which load the slab undergoes failure in the form of punching shear [10].

Furthermore, in cases where the slab is placed on the spring support when applying the load to the column, the area under the column will be displaced more than the areas around it. If the springs are placed beneath the column, they will impose heavier loads on the slab than farther springs, thereby preventing the slab from being displaced and thus preventing the area under the column from falling. This will, in turn, prevent slab failure, and the column springs will carry the main load of the column; hence, it could not be determined under which load the slab will undergo shear failure.

This paper is organized in three sections; in the first part, the punching shear capacity and the failure mechanism of the solid slabs were tested against two-way void slabs under the influence of a centralized load at the slab center, on the soil substrate, by the elimination of errors. Given that the application of the distributed load to the slab and the maintenance of column equilibrium in the laboratory analysis of slab punching require advanced devices and equipment, another method was adopted in this study for performing this experiment. For this purpose, the space under the slab column was emptied because slab thickness is relatively low in the laboratory, and the slab does not function totally as a rigid object. Thus, the space beneath the foundation is left empty by inserting a sponge until the error is reduced, and the net load leading to the punching shear failure of the slab is

calculated. In this manner, the slab and the column are inverted on a uniform granular soil substrate in the form of a surface foundation, and axial loading is applied to the column. In the second part, the laboratory specimens are simulated using Finite Element Software ABAQUS, and then the punching shear of the hollow and solid slabs on the soil substrate is examined. In the third part, the laboratory specimens are simulated using Finite Element Software ABAQUS, and the punching shear of the hollow and solid slabs on springs with different constants are investigated, i.e. the springs are modeled instead of uniformly distributed loads. To eliminate the errors and problems mentioned above, no spring should be placed under the area exposed to the punching shear. However, the best area that should be left empty (for both the soil substrate and the spring) is the region encompassing the column area in addition to d, i.e. effective slab thickness, provided that the location of the failure is exactly on a plate. However, this happens neither in practice nor in ABAQUS because the failure area has a significant width across which several elements reach the failure area simultaneously; thus, this area could be of variable widths. In the end, the experimental results are compared with those of the numerical analysis for the springs and the soil substrate.

2. EXPERIMENTAL STUDY

2. 1. Specimens and Materials In this study, a two-way solid slab (R) and a void slab (S_1) were used as reference specimens as shown in Figures 1 and 2. In the specimen, spherical hollow formers are arranged 100 mm away from the edge of the column. The dimensions of all slabs were 1300×1300 mm. Slab thickness and effective thickness were 120 mm and 100 mm, respectively. Slab slots were filled using traditional spherical plastic hollow formers. The diameter of the spherical plastic hollow formers was 70 mm in the designed layout, and the balls were arranged at 20 mm and 90 mm center-to-center distances, with these distances and scales set by a string as Figures 3a and 3b display. The slabs were made of plain concrete with the same mixing scheme as shown in Table 1. Given that in numerical modeling, the elastic and plastic behavior of concrete (CDP) as well as the rebar must be correctly inserted in ABAQUS software, it was required to test the mechanical properties of the concrete. To this end, 5 cylindrical specimens were produced and tested after 28 days (Figure 4a). The stress-strain curve of the concrete produced in the material tests showed that the average strength of the cylindrical specimen was 31.77 N/mm^2. Figure 4b shows the stress-strain curve of the concrete specimens where the average tensile strength of the concrete was 3.57 MPa for the 5 specimens. Table 2 summarizes the mechanical properties of the concrete.

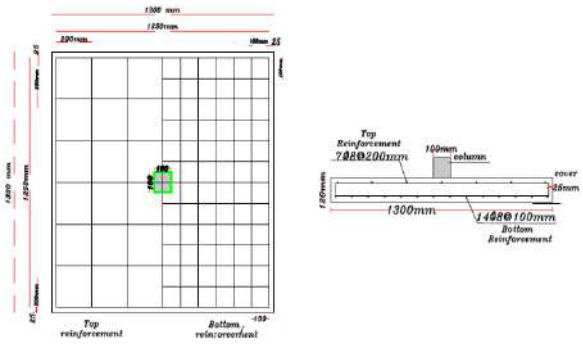

Figure 1. Double-sided solid slab R and the layout of bending bars in the specimens

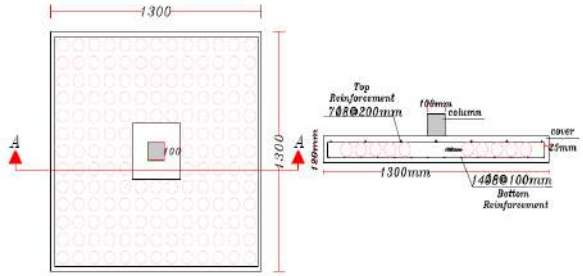

Figure 2. Implementation details of the balls in the S1 void slab specimen (dimensions in mm)

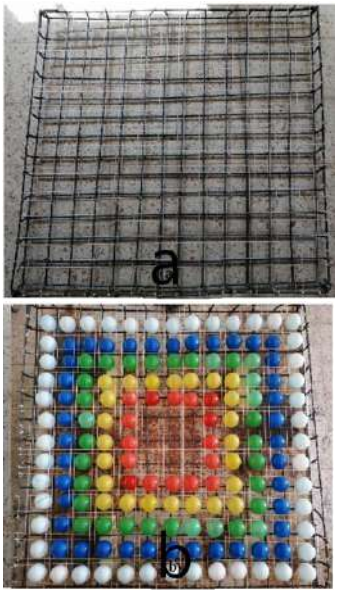

Figure 3. (a) The layout of bending bars in the specimens for determining spacing and scaling with the string, as well as (b) the S1 void slab specimen

TABLE 1. The concrete mixing design used for slabs Strouhal number for different geometric cases [12]

Water (kg/m^3)	Cement (kg/m^3)	Gravel (m^3)	Sand (m^3)	Slump (mm)
175.49	443	902	910	65

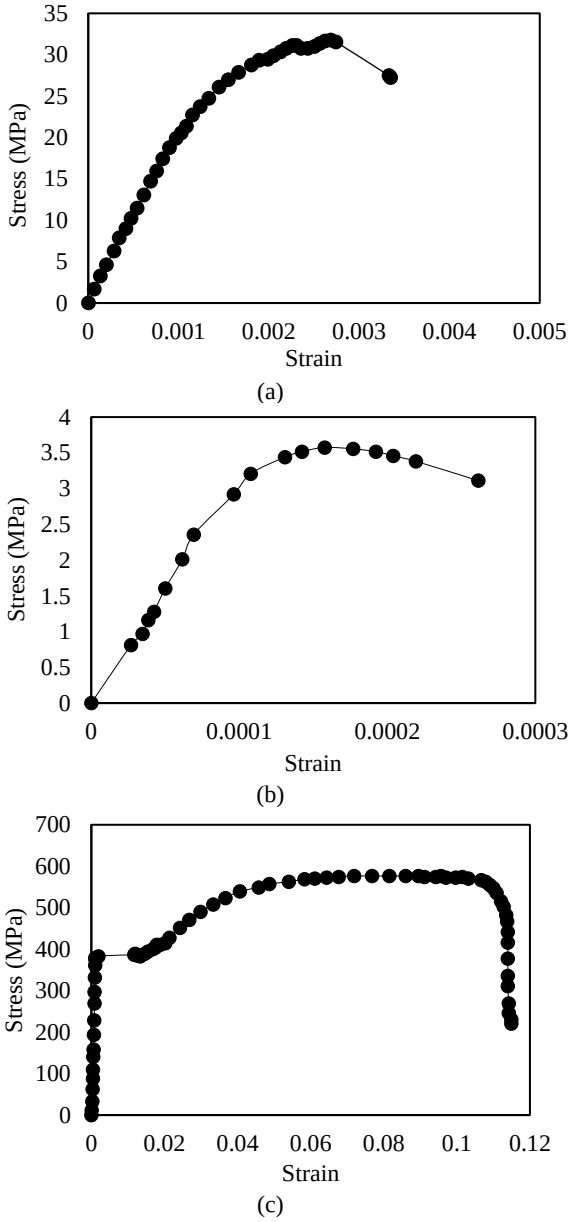

Figure 4. Material test results; (a) Concrete compressive strength; (b) Concrete tensile strength; (c) Rebar tensile strength

Figure 4c demonstrates the stress-strain curve of the rebar with D8 diameter, with the yield strength and tensile strength of 383.062 MPa and 576.547 MPa, respectively. The slabs were fitted with longitudinal and transverse steel bars. Table 3 lists the mechanical features of the test slab bars. The bars located at the bottom and top substrates were 8 mm in width [12].

The results of soil aggregation, classification properties, as well as plastic, elastic, and weight-volumetric parameters are presented as well. Mechanical soil aggregation was tested using the dry method, with the aggregation curve shown in Figure 5. Since

TABLE 2. Specifications of the concrete used in slab construction [12]

fc, MPa	Ecm, GPa	fr, MPa	υ	Density
31.77	25.47	3.57	0.15	2400

TABLE 3. Specifications of the rebar used in slab construction [12]

Diameter (mm)	Es, GPa	fr, MPa	υ	Density (kg/m^3)	Elo, (%)
8	201.45	576.54	0.3	7850	**17**

uniformity and curvature coefficients are Cu <6 and Cc <1 or Cc> 3, respectively, the soil is classified as SP, i.e. poorly graded. Direct shear tests were done to determine the plastic parameters (C and φ) of the soil specimen, with the results of which presented in Figure 6. Given that another parameter required in numerical modeling is the elastic modulus (E) of the soil, the loaded soil was used in a uniaxial test device to simulate soil natural conditions so as to determine the E value. Figure 7 demonstrates the stress-strain curve of the soil specimen, which is extracted based on the initial fitness slope of the stress-strain curve of the elastic modulus for the soil specimen.

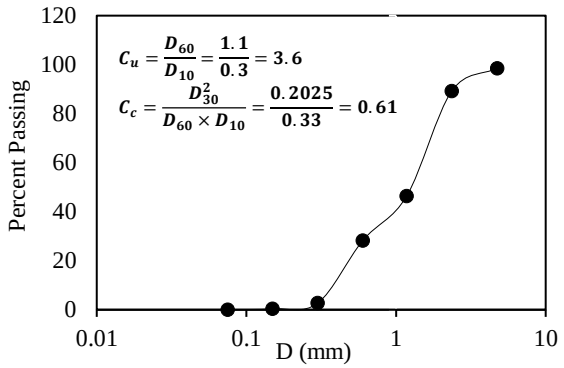

Figure 5. The grading curve

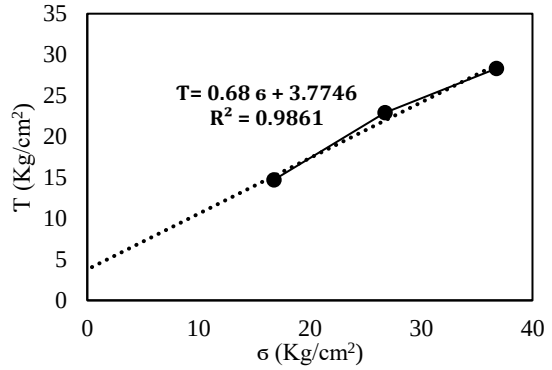

Figure 6. Fracture coverage obtained from direct shear test results

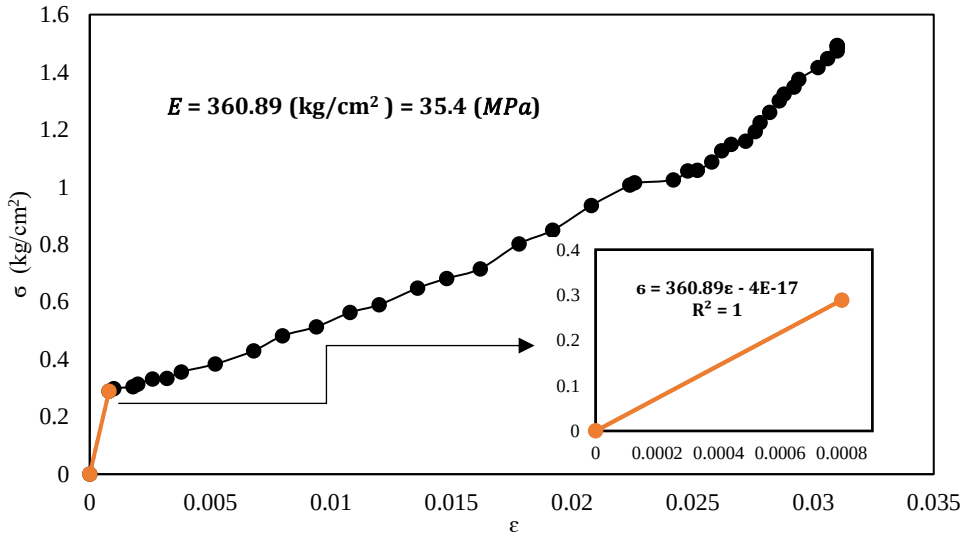

Figure 7. The stress-strain curve for the soil specimen

The value of the Poisson coefficient (ν) for the soil specimen (SP) ranged from 0.15 to 0.4 with an average of ν = 0.3. Tables 4 and 5 show the calculated values ofthe specific weight (γ) and the saturation specific weight (γ_sat) of the soil. Table 6 demonstrates the results of all soil engineering tests.

2. 2. The Laboratory Program First of all, a 370×340×340 mm sponge or a low resistance material was installed under the column in the middle of a 1300×1300×500 mm cubic steel box to minimize box deformation. Accordingly, the space under the slab column was left empty. Next, the box was filled with uniform granular soil up to 37 cm high, which reached the upper level of the sponge. As Figures 8 and 9 show, solid slab R and void slab S1 were placed on the soil substrate as the support. When applying the load, a 150×100×100 mm metal piece was used at the slab center to replace the column, as Figure 10 shows. As the column was rigid and did not undergo any deformations, it applied the jack load exactly to the slab. Accordingly, if the reference point was placed either on the slab, at the center of the column, on the top, or in the middle of the column, it would make no change to the results. Therefore, the column midpoint was considered the load-displacement reference point. A 200-ton hydraulic system, based at the Civil Engineering Laboratory and controlled by a computer system, was used for loading purposes. A linear variable differential transformer (LVDT) with a 100 mm course and 0.01mm accuracy was attached to the loading jaw, with the vertical

TABLE 4. Soil specific weight

W_1 (g)	W_2 (g)	V_i (cm^3)	W_i (g_r)	$\gamma_i = \frac{W_i}{V_i}$ ($\frac{KN}{m^3}$)
306	420	76.9	114	14.82

TABLE 5. Soil engineering specifications

E (Mpa)	υ	C (kN/m^2)	φ°	ψ°	ɣ	$ɣ_{sat}$
35. 4	0.3	3.77	34	4	14.82	18.72

TABLE 6. A comparison of experimental and numerical final loads for solid and void slab models

Slab Model Symbol	Ultimate Load Pu (kN)	Deflection (mm)	1st Crack Load P_{cr} (kN)	Difference Ratio %	Failure Mode
R	7.60	96.04	-	-	Punching shear
S_1	7.26	85.26	14.48	14.48	Punching shear

Figure 8. Test Setup [13]

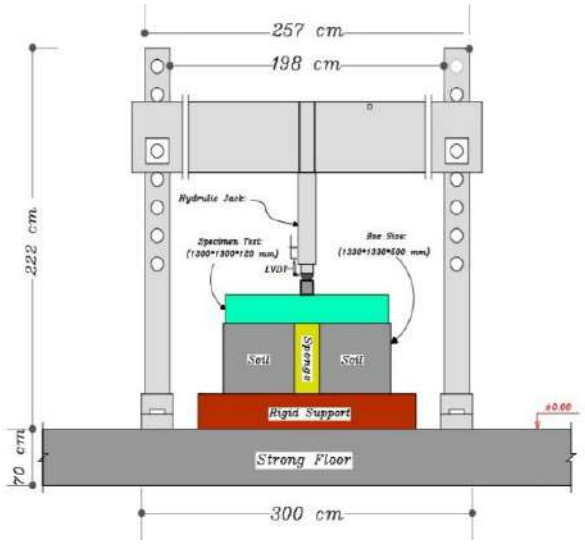

Figure 9. Schematic testing equipment

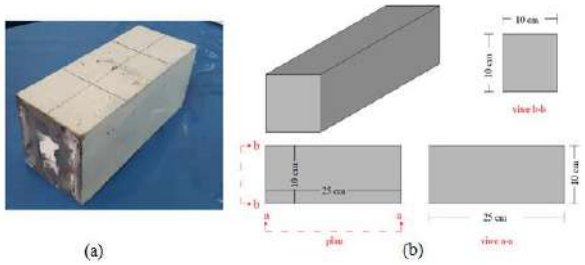

Figure 10. Steel column specification

displacement of the slab surface midpoint measured during the experiment. The load applied to the column increased gradually by 1kN/s until the specimens were broken, and the load-displacement diagram failed abruptly. The load-displacement rate was automatically saved to the software installed on the computer [12].

2. 3. Experimental Results

2. 3. 1. Load-Deflection Results Upon applying the load to the center of the slab, the first cracks appeared in both specimens in the tensile area, near one or more corners of the column. Upon more loading, the number of cracks in the central area of the slab increased, and the slab stretched to its four edges. In fact, the first shear cracking of the solid and void slabs started upon applying the final loads (45.79% and 47.54%) (See Table 6). According to Figure 11, the load-deflection response curves of both laboratory specimens show elastoplastic behavior. Besides, the slope of the curves is approximately the same for both slabs because it depends on slab stiffness and the type of loads. The effect of spherical balls, in the void concrete slabs, on the final punching shear capacity was determined as well. As Table 6 presents, due to the presence of the void formers, the final loads applied to the void slabs were smaller than those applied to the solid slabs. In the meantime, the ductility of the void slabs was higher than that of the solid ones. The slabs underwent punching shear after reaching the final load. The shear failure of the specimens was measured abruptly for R and S1 slabs at the final loads of 209.72 and 179.34 kN, respectively, with the force decreased immediately after the specimen failed. The values of the punching shear capacity were different in these two slabs by about 14.48%. In addition, vertical deflection in the middle of the slabs, measured by the linear variable differential transformer (LVDT), was almost similar in both slabs. However, the deflection was not affected by the spherical void formers until the initial cracking.

2. 3. 2. The Slab Fracture Mechanism As it was mentioned earlier, after the final loading, the slabs were fractured through punching shear and carefully examined for the type and location of the developed cracks. Accordingly, it is noteworthy that the shape of the failure region was asymmetric even if the shape of the slab, rebar, and load was symmetric. Several cracks were developed in the lower surface of the slabs, as Figures (12a) to (13a) show, which demonstrate the final crack patterns of the slabs. The failure pattern occurred at the initial loading in the form of a partially oblique and pyramidal shape on the slab surface. Besides, the presence of the bending bars that increased the tensile capacity of the slab affected the failure angle, thereby extending the crack length from the slab middle point to the edge. Bending failure modes were observed in the two-way solid and void slabs with irregular elliptical shapes below the slabs. The irregular shape could be the result of the heterogeneity of the materials, including the concrete, the soil beneath it, and the existence of steel bars. However, there were no cracks on the slab surface visible to the naked eye.

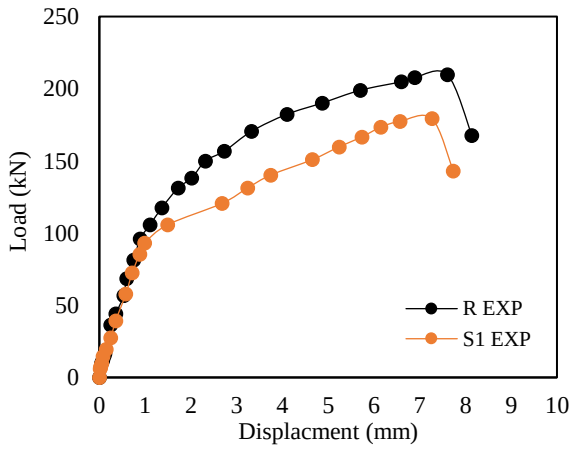

Figure 11. The load-displacement curve obtained from the loading test

To measure the slab angle after punching shear, the slabs were incised, and the reference points were used for measuring the punching shear angle on AA or BB sections (Figures 12b to 13b) by taking into account the punching shear failure intersection on the bottom surface of the slab and the outer edge of the column on the upper surface.

Next, the ideal model of the latest punching shear condition was plotted and fitted to the actual image of the laboratory concrete slab specimens. Figures 12b to 13b show the loading area with a yellow square, the critical results obtained from the experiment at the reinforcement level of the loaded slab model with a green curve (C), and the expansion of cracks with a red curve (D). The cracks are spread in the slabs through the cross-section of the steel rebar and the lower surface of the slab.

The slope of the developing critical shear cracks between the column edge and the reinforced bending surface was measured according to Figures 12b to 13b. Four points were selected at the reinforced bending surface for each slab with an effective depth (d) of 100 mm. Table 8 summarizes the related values. As it can be seen, the mean value of the points specified on the shapes is 21.6 cm, and the mean punching shear angle is 24.9 degrees. As Table 7 and Figures 12b to 13b demonstrate, it is concluded that the diameter of the punching cone in solid slab R is greater than that of void slab S_1; in addition, the location of the critical shear crack at the stress surface is on average 2.16d away from the edge of the column. The punching shear angle of the solid slab R cones is slightly smaller than that of the void slab S_1 cone.

3. NONLINEAR SLAB ANALYSIS

3. 1. Slab Modeling in Finite Element Software for both Soil and Spring Models ABAQUS was used to model the specimens assessed in the present study. In addition, the concrete damaged plasticity (CDP) model was used to model the slabs, which is a robust

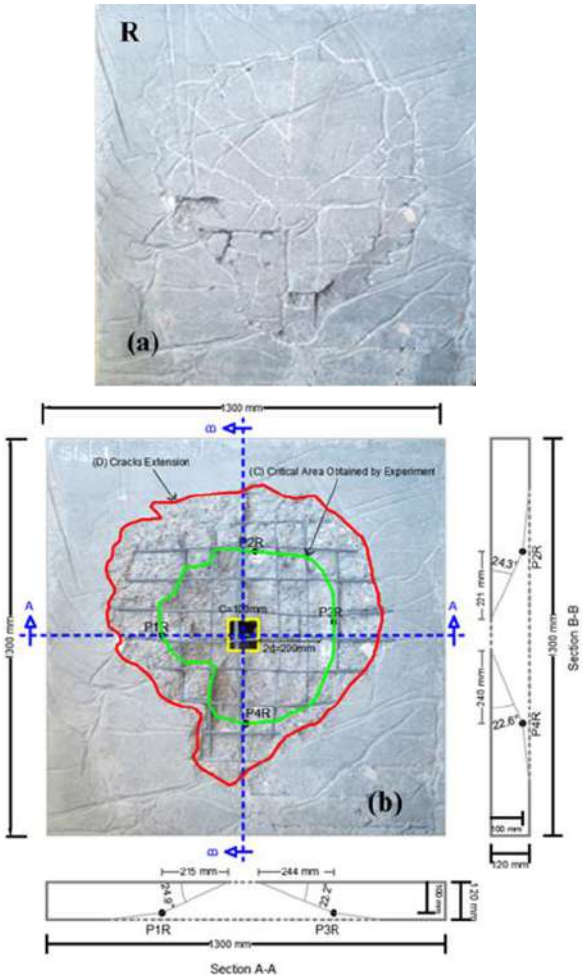

Figure 12. Slabs after punching shear: (a) specimen R before the autopsy; (b) specimen R after the autopsy and the measured punching shear angle

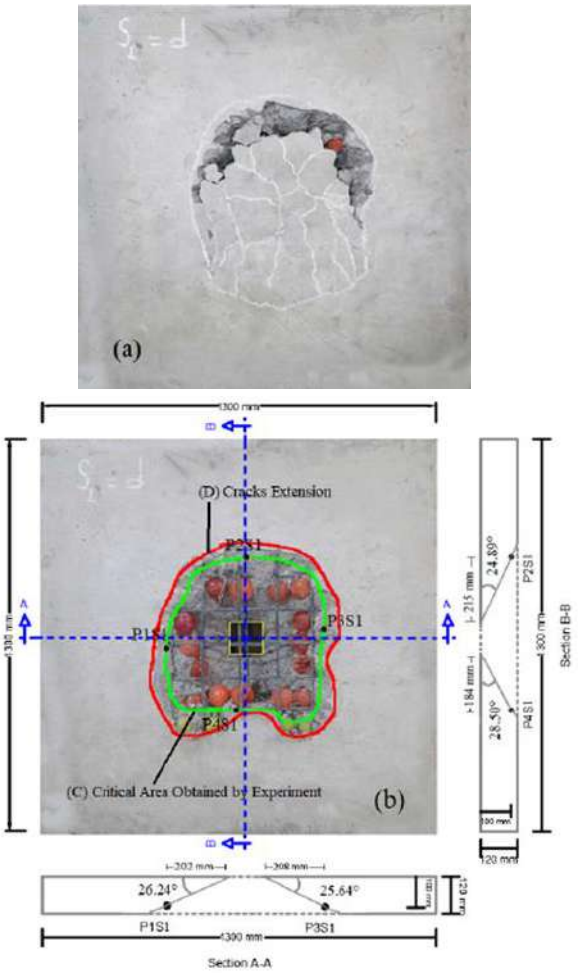

Figure 13. Slabs after punching shear: (a) specimen S_1 before the autopsy; (b) specimen S_1 after the autopsy and the measured punching shear angle

TABLE 7. The distance of shear cracks from the column edge and the mean crack distance from the column edge and punching inclination

Specimen	Values relative to the level of reinforcement				Average value for the distance of the crack from the column edge (mm)
	Marked points	Distance of the crack from the column edge (mm)	*In tension face	Angle of inclination (°)	
R	P1R	215	2.15d*	24.9	230
	P2R	221	2.21d	24.3	
	P3R	244	2.44d	22.2	
	P4R	240	2.40d	22.6	
S_1	P1S1	202	2.02d	26.2	202
	P2S1	215	2.15d	24.9	
	P3S1	208	2.08d	25.6	
	P4S1	184	1.84d	28.5	
Ave distance= 216 (mm)			Ave=2.16d	Ave failure angle=24.9	

*d = the effective depth of slab = 100 mm

*One could conclude that the critical shear crack site at the tension area is on average 2.16d away from the column edge, which is in general very close to EC2 [14]

model used for different loads to measure concrete behavior more accurately by expressing its distinct behavior under pressure and tension. In this model, the nonlinear behavior of concrete is expressed using the concepts of damaged isotropic elasticity as well as tensile and compressive plastics. To follow the simulation procedure more accurately, the mechanical properties of concrete, steel, and soil were entered into the software as shown inTables 2, 3, 5, and 8. According to Skorpen and Dekker [10], all constraints involved in these elements were entered into the software. The program used an average mesh size of 25 mm utilized an 8-node linear hexahedral solid element with a reduced integration (C3D8R) element for the solid slab concrete (R), soil, and the column. In addition, a 4-node tetrahedral (C3D4) element was used for the void slab (S1), and a 2-node linear truss (T3D2) was used to model the steel bars. Specimen R had 13520 mesh elements and 16854 nodes, specimen S1 contained 92110 mesh elements and 19230 nodes, the column had 160 mesh elements and 275 nodes, the soil had 40800 mesh elements and 45696 nodes, and the bars contained 52 mesh elements and 53 nodes. To model the springs, the linear model of Point to Ground was used, with a spring underneath each node.

Figure 14 shows the details of the geometry and boundary conditions of the specimens used for the simulations. Both slabs R and S1 were analyzed using the static method in the ABAQUS/Standard analyzer. In the static analysis, the load was applied perpendicular to the entire column surface, using the displacement control.

TABLE 8. CDP input data for concrete with $\acute{f}_c$=31.77 Mpa-Plasticity [9]

Dilatation Angle (◦)	Eccentricity	$F = \sigma_{b_0}/\sigma_{b_c}$	$K_c = \bar{q}_{TM}/\bar{q}_{cm}$	Viscosity Parameter
35	0.1	1.16	0.667	0.001

3. 2. Description of the Analyzed Specimens on the Soil and Springs To validate numerical models for measuring the punching shear capacity, finite element models (S1 and R) were simulated exactly similar to the corresponding laboratory specimens on the soil substrate and spring. However, to measure the soil spring constant for the spring support, various spring constants were investigated in Finite Element Software ABAQUS. For this purpose, 6 specimens of two-sided solid slabs were modeled and analyzed with springs placed 120 mm away from the column with different constants. After optimizing the spring constant and determining the soil-spring constant, a void slab with spherical void formers, placed 100 mm from the column, was modeled similar to the laboratory specimen, and then the punching shear capacity was evaluated numerically. In addition, the results of the punching shear capacity of the slabs on the soil substrate and springs were compared with those of the laboratory work. At the end, the failure mechanism of the modeled slabs in both supports (soil and springs) was compared with that of the laboratory specimens so that in case they matched each other, the results of finite element modeling would be considered reliable.

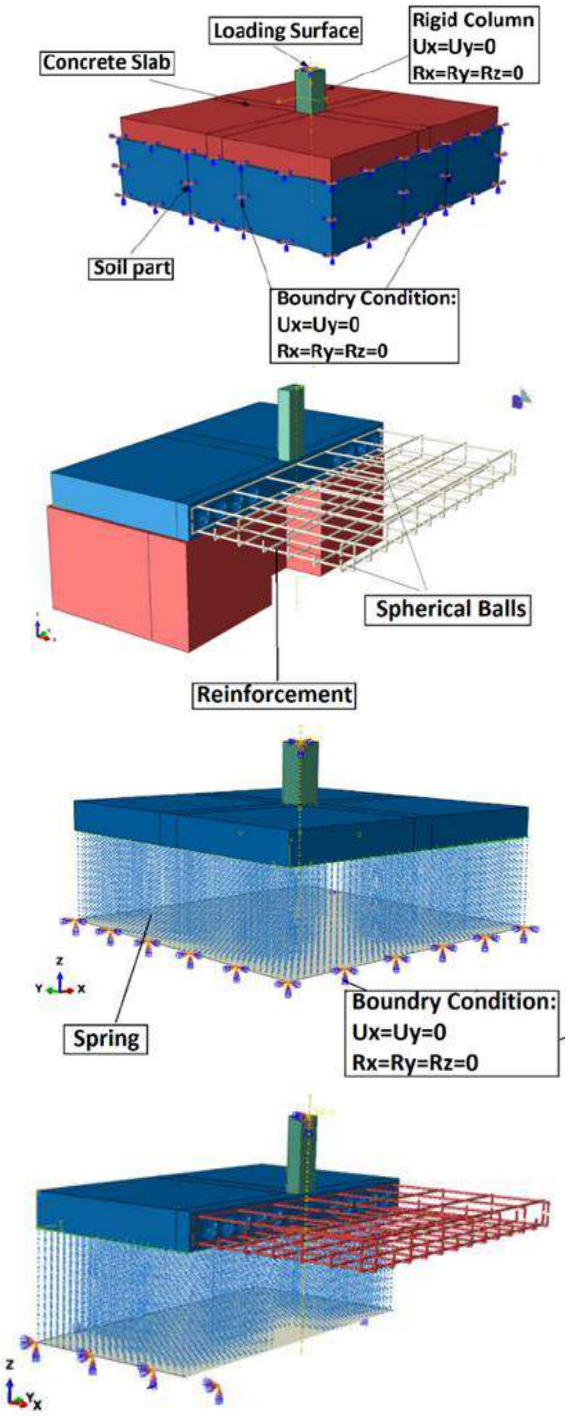

Figure 14. Introducing slab parts (geometry and boundary conditions) on the spring as the support and meshing of the finite element model for the concrete slab

4. NUMERICAL RESULTS

4. 1. Load-displacement Results of the Specimens Analyzed on Soil The numerical results of the final loads, load-displacement curves, and initial crack loads were compared with those of the experimental section. The comparison was performed for the purpose of numerical model validation. Table 9 demonstrates the results from the comparison of the experimental and numerical final loads for the models of the study. In addition, Table 10 depicts the comparison of the numerical and experimental results of the first cracking load for the solid and void slab models.

In general, the final loads predicted by the numerical analysis were heavier than the ones determined by the experiments. The differences in the final loads varied from 5.25 to 7.52% for both solid and void models, as Table 9 shows. The numerical data for all cases showed that the numerical values recorded for the soil and void models were higher than the experimental values with the difference of 10.48% and 8.17%, respectively.

According to the comparison results, the numerical models are stiffer; in addition, the numerical analysis demonstrates a lower value for deflection and a higher value for the final load with a slight difference in the final load values (see Figure 15). This could be due to four reasons; firstly, the concrete used in the experimental models was not fully homogeneous as assumed in the numerical models; secondly, the finite element model was inherently stiffer than the experimental specimen because of the reduced degrees of freedom in the elements; thirdly, the connection between the steel bars and the concrete slab was assumed to be completely continuous, with no slippage; and fourthly, since the elements representing the steel bars were modeled in longitudinal and transverse directions at the same height, there was a great deal of stiffness in the nodes where these elements intersected. However, there was no connection between the steel bars in the two directions in the laboratory specimen. Therefore, this method did not fully model the intersection points of the steel bars. As a result, the load-deflection response of the model had a steeper slope than the laboratory specimen.

TABLE 9. A comparison between experimental and numerical final loads

Slab Model Symbol	Ultimate Load Pu kN		Difference Ratio %
	Experimental	FEM	
R	209.72	220.73	5.25
S_1	179.34	192.83	7.52

TABLE 10. A comparison between the numerical and experimental results of the first cracking load

Slab Model symbol	1st Cracking Load kN		$\frac{Pcr)Num}{Pcr)Exp}$
	Experimental Pcr Exp.	Numerical Pcr *Num*	
R	96.04	106.11	1.10
S_1	85.26	92.23	1.08

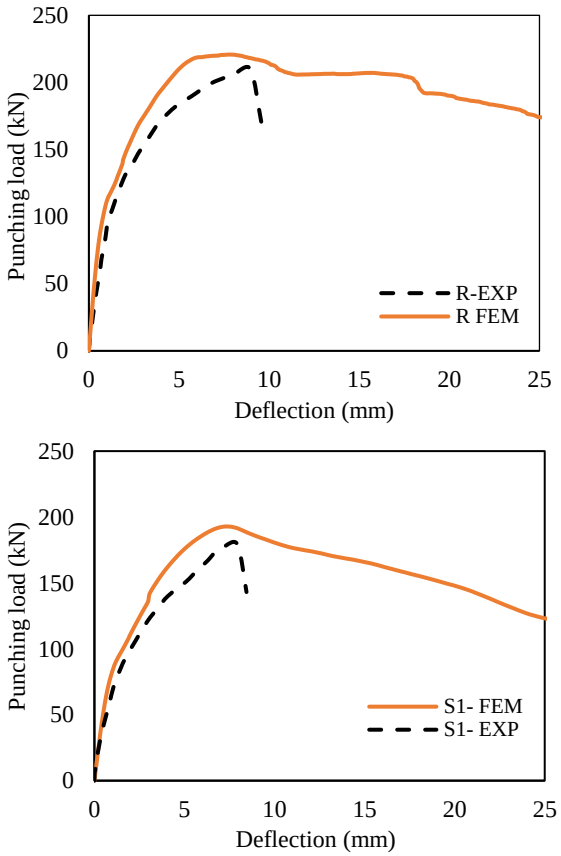

Figure 15. Loads versus central displacement curves

4. 2. Spring Stiffness Optimization and Slab Load-Deflection Evaluation To determine the soil-spring constant, 6 solid slab specimens were modeled and analyzed on the spring support, with the springs positioned 120 mm away from the column side. The analysis results are presented in the form of final load deflection in Table 11 as well as load deflection in Figure 16. As displayed in the final load-spring constant curve in Figure 17 as well as in the final deflection-spring constant curve in Figure 18, with an increase in the spring constant from 1000 to 6000 kN/m, the final load values increased and their corresponding deflection values decreased. Within the constant range of 4000-6000 kN/m, the displacement values and the final punching load were minimized and became fixed. As Figure 16 shows, the solid slabs generally exhibit the same behavior in the elastic zone so that they overlay roughly in the elastic zone of the solid slab on the soil substrate. Therefore, it could be concluded that the optimal spring constant is 5000 kN/m when the spring is placed at a distance of 120 mm from the column side.

Similar to the laboratory specimen, a numerical model was modeled and analyzed for the S1 void slab (Slab 7) under optimum constant conditions of the springs, Kopt = 5000 kN/m, where the springs were positioned at a distance of 120 mm from the column edge. The numerical values obtained for the final loads, displacement-load curves, and initial crack loads were compared with those of the experimental results. This comparison was performed to validate the numerical

TABLE 11. Different spring constants at three different distances from the edge of the column for optimizing the spring constant

Slab Model Symbol	Constant Springs (kN/m)	Punching Load (kN)	Deflection (mm)
Slab1	1000	182.18	9.00
Slab 2	2000	216.14	8.49
Slab 3	3000	220.10	8.14
Slab 4	4000	227.19	7.56
R-(Slab 5)	5000	235.10	7.55
Slab 6	6000	235.40	7.55

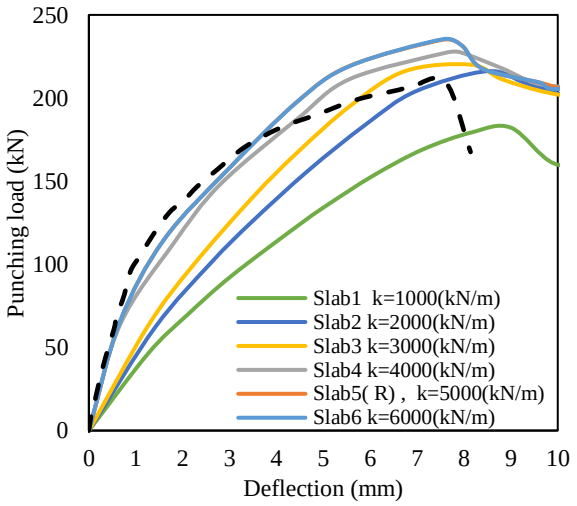

Figure 16. The comparison of load- deflection curves in two-way solid slabs with varying constant values at d=120 mm from the edge of the column

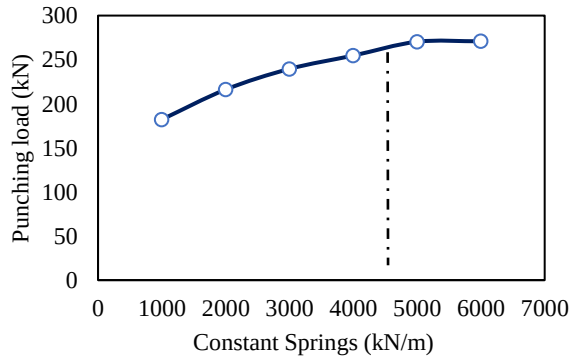

Figure 17. The ultimate deflection-spring constant diagram of the column edge for a two-way solid slab

model. Table 12 shows the comparison results of the experimental and numerical values of the final loads in the models of the study. Likewise, Table 13 demonstrates the comparison of the numerical and experimental results for the first load cracks in the slab and void models. The difference ratio of the final loads is 12.10% and 15.65% for the solid and void slabs, respectively, as Table 12 shows. The numerical data for all cases implied that the numerical values recorded for the soil and void models were higher than the experimental values, with the difference of 10.20% and 12.64%, respectively.

Figure 19 shows the results of the comparison made between the experimental and numerical values for the load versus the central displacement curves in the solid and hollow models on the spring support. The comparison results indicate that the use of numerical models is more difficult; in addition, the numerical analysis shows a lower value for deflection and a higher value for the final load, with a slight difference in the final load values.

4. 3. The fracture Mechanism of the Soil and Spring Specimens Figures 20 to 23 show the cracking patterns obtained from the finite element (FE) analysis. In numerical models, crack patterns are visualized using maximum plastic strains. According to the plastic strain counters, for the maximum main stress in the light blue areas where the strain is greater than 0.0015, the slab has reached its maximum puncture resistance. In infinite element models, the fracture mechanism is shown as a single slope, with the effective depth under the slab being 100 mm. Accordingly, the crack width, path, and shear fracture mode are plotted.

The crack width for the punching shear zone ranges from 198 to 231 mm for the hollow and solid slabs on the

TABLE 12. Experimental and numerical values of the final loads for solid and void slab models on the spring support

Slab Models Symbol	Ultimate Load Pu kN		Difference Ratio %
	Experimental	FEM	
R	209.72	235.10	12.10
S1	179.34	207.42	15.65

TABLE 13. Experimental and numerical values of the initial cracking loads for solid and void slab models on the spring support

Slab Model Symbol	1st Cracking Load kN		$\frac{Pcr)num}{Pcr)exp}$
	Experimental Pcr) exp.	Numerical Pcr) *num.*	
R	96.04	105.84	1.10
S1	85.26	96.04	1.12

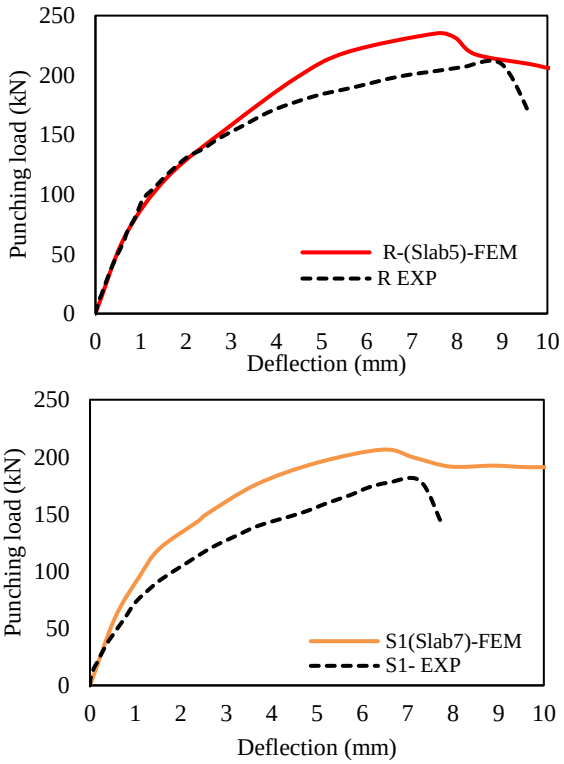

Figure 19. Deflection-load curves for solid and hallow models

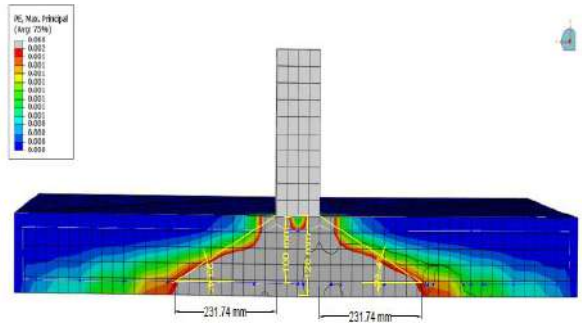

Figure 20. The fracture pattern for slab R (on the soil) at the final load under maximum plastic strains

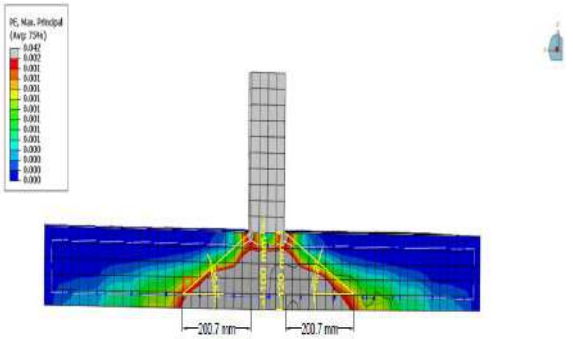

Figure 21. The fracture pattern for slab S1 (on the soil) at the final load under maximum plastic strains

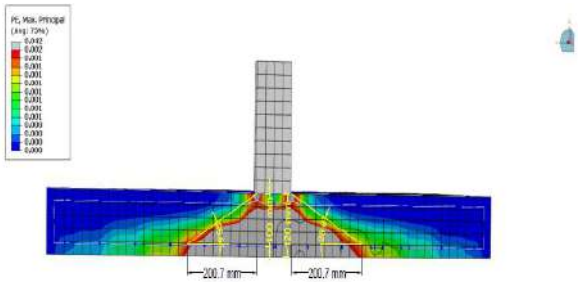

Figure 22. The fracture pattern for slab R (on the spring) at the final load under maximum plastic strains

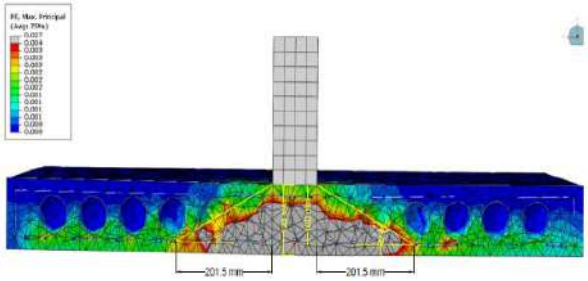

Figure 23. The fracture pattern for slab S1 (on the spring) at the final load under maximum plastic strains

soil, and from 200 to 201 mm for the hollow and solid slabs on springs. Besides, the angles of the diagonal fracture surface range from 26.2 to 23.4° for the slabs on the soil and 26.3 to 25.6° for the hollow and solid slabs on the spring as Table 14 shows.

Compared to the crack patterns in the experimental study, the proposed nonlinear model made an accurate prediction of crack propagation locations and directions. Figures 24 and 25 show the schemes of the final crack patterns for the slabs. The crack patterns in the laboratory experiments and those in the nonlinear models fit well. In general, the initial cracks appearing at the end of the elastic phase moved obliquely from the slab center to the slab edges.

TABLE 14. The crack width of the punching shear zone and the crack skew angle in the punching shear

Support Type	Specimen	Average Crack Angle	Distance of the Crack from the Column Edge (mm)
Soil-EXP	R	Ave (for 4 points) =23.5	230
Soil-FEM	R	23.4	23.1
Spring-FEM	R-(Slab5)	25.6	200
Soil-EXP	S1	Ave (for 4 points) =26.3	202
Soil-FEM	S1	26.2	198
Spring-FEM	S1-(Slab7)	26.3	201

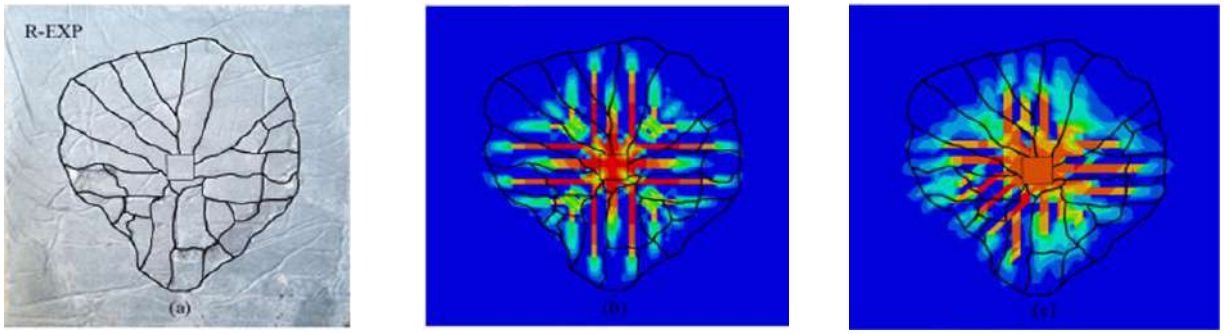

Figure 24. Crack patterns in (a) the laboratory experiment on specimen R, (b) nonlinear model R on soil, and (c) nonlinear mod springs

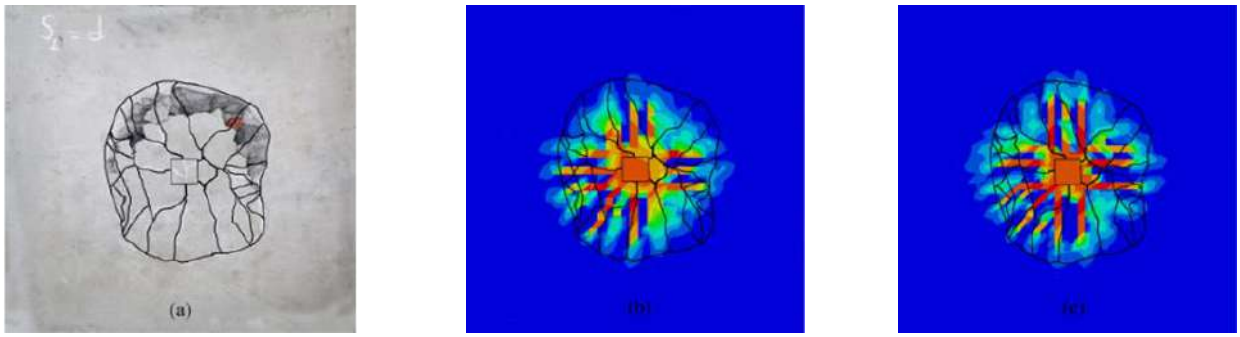

Figure 25. Crack patterns in (a) the laboratory experiment on specimen S_1, (b) nonlinear model S_1 on soil, and (c) nonlinear model S_1 on springs

5. CONCLUSION

Considering the results from the experimental data as well as the finite element analysis for the solid and hollow models of the study, the following conclusions were drawn:

- The solid and void slabs under analysis underwent a fracture due to the punching shear at 209.72 and 179.34 kN, respectively, at an average distance of 2.16d from the column circumference. The cracks in both slabs had irregular oval shapes that could be resulted from different performances of the materials, such as soil, concrete, and bars.
- In general, the first shear cracking for solid and void slabs started with 45.79 and 47.54% of the final load. Due to the presence of the balls, the final loads of the void slabs were smaller than those of the solid ones. The value of the punching shear resistance of the void slab was by 14.48% different from that of the solid slab.
- Vertical deflection (displacement or deformation) in the midpoint of the slabs, measured by the LVDT, was almost similar in both laboratory slabs, and deflection was not affected by the spherical balls until initial cracking.
- The cracking patterns in the experimental experiments and in nonlinear models were highly consistent. In general, the initial cracks appearing at the end of the elastic phase moved obliquely from the slab center to the slab edges.
- In general, the final loads predicted by the numerical analysis were heavier than those calculated in the laboratory experiments on the soil substrate and springs. Percentage differences in the final loads were 5.25% and 7.52% for the solid and hollow models, respectively, on the soil substrate. In addition, percentage differences for the final loads varied from 12.10 to 15.65% for both solid and hollow models on the springs.
- According to the experimental and numerical results, the punching shear strength of the slab model was higher than that of the void slab, and crack propagation in the former slab was higher than in the void slab.
- At the spring constant of 5000 kN/m, the solid slabs behaved similarly in the elastic zone until they roughly matched the elastic zone of the solid slab on the soil substrate and reached the soil spring constant.
- The 3D numerical analysis by ABAQUS showed that the actual behavior of the solid and void slab models on the soil and springs could be effectively simulated with a certain degree of accuracy. One of the main points in this analysis is the right choice of the modeling technique for the materials used.
- In the end, based on the findings explained above, it could be concluded that the uniformly-grained soil and springs could be reliable materials for the simulation of a uniformly distributed load, i.e. the dead load of the ceiling, applied to the column. Thus, the critical area of the punching shear is about 2d, which matches the Eurocode 2 (EC2).

6. REFERENCES

1. Dieterle, H., and Steinle, A. "Blockfundamente für Stahlbetonfertigstützen." Deutscher Ausschuss für Stahlbeton, Heft 387, Berlin, Germany, (1981). Retrieved from https://trid.trb.org/view/1032408 [German]
2. Dieterle, H., and Rostásy, F. "Tragverhalten quadratischer Einzelfundamente aus Stahlbeton." Deutscher Ausschuss für Stahlbeton, Heft 387, Berlin, Germany, (1987).
3. Hallgren, M., Kinnunen, S., and Nylander, B. "Punching Shear Tests of Column Footings." ***Nordic Concrete Research***, Vol. 21, (1998), 1–22. Retrieved from https://www.diva-portal.org/smash/record.jsf?pid=diva2:474585
4. Hegger, J., Sherif, A. G., and Ricker, M. "Experimental Investigations on Punching Behavior of Reinforced Concrete Footings - ProQuest." ***ACI Structural Journal***, Vol. 103, No. 4, (2006), 604–613. Retrieved from https://search.proquest.com/docview/198357965?pq-origsite=gscholar&fromopenview=true
5. Hegger, J., Ricker, M., Ulke, B., and Ziegler, M. "Investigations on the punching behaviour of reinforced concrete footings." ***Engineering Structures***, Vol. 29, No. 9, (2007), 2233–2241. https://doi.org/10.1016/j.engstruct.2006.11.012
6. Hegger, J., Ricker, M., and Sherif, A. "Punching strength of reinforced concrete footings." ***ACI Structural Journal***, Vol. 107, No. 4, (2010), 494–496.
7. Bonić, Z., and Folić, R. "Punching of column footings - Comparison of experimental and calculation results." ***Gradjevinar***, Vol. 65, No. 10, (2013), 887–899. https://doi.org/10.14256/jce.916.2013
8. Falkner, H., and Teutsch, M. "Comperative investigations of plain and steel fibre reinforced industrial ground slabs." Institut Fur Baustoffe, Massivbau und Brandschutz, (1993).
9. Jankowiak, T., and Łodygowski, T. "Identification of parameters of concrete damage plasticity constitutive model." ***Foundations of Civil and Environmental Engineering***, Vol. 6, (2005), 53–69. Retrieved from https://www.infona.pl/resource/bwmeta1.element.baztech-article-BPP1-0059-0053
10. S A Skorpen, and N W Dekker. "The application and interpretation of linear finite element analysis results in the design and detailing of hogging moment regions in reinforced concrete flat plates." ***Journal of the South African Institution of Civil Engineering***, Vol. 56, No. 1, (2014), 77–92. Retrieved from http://www.scielo.org.za/scielo.php?script=sci_arttext&pid=S1021-20192014000100009
11. Abaqus Theory Manual (6.14). Dassault Systemes, Providence, RI, USA, 2014.
12. Valivonis, J., Skuturna, T., Daugevičius, M., and Šneideris, A. "Punching shear strength of reinforced concrete slabs with plastic void formers." ***Construction and Building Materials***, Vol. 145, (2017), 518–527. https://doi.org/10.1016/j.conbuildmat.2017.04.057
13. Eurocode 2: Design of Concrete Structures-Part 1-1. General rules and rules for buildings. BS EN 1992-1-1, 2004: 97–105.
14. Ozturk, B. "Free vibration analysis of beam on elastic foundation by the variational iteration method." ***International Journal of Nonlinear Sciences and Numerical Simulation***, Vol. 10, No. 10,

(2009), 1255–1262. https://doi.org/10.1515/IJNSNS.2009.10.10.1255

15. Ozturk, B., and Coskun, S. B. "The Homotopy Perturbation Method for free vibration analysis of beam on elastic foundation." ***Structural Engineering and Mechanics***, Vol. 37, No. 4, (2011), 415–425. https://doi.org/10.12989/sem.2011.37.4.415
16. Ozturk, B., and Coskun, S. B. "Analytical solution for free vibration analysis of beam on elastic foundation with different support conditions." ***Mathematical Problems in Engineering***, Vol. 2013, , (2013). https://doi.org/10.1155/2013/470927
17. Zhang, W. X., Li, B., Hwang, H. J., Zhang, J. Y., Xiao, L. J., Yi, W. jian, and Park, H. G. "Punching shear strength of reinforced concrete column footings under eccentric compression: Experiment and analysis." ***Engineering Structures***, Vol. 198, (2019), 109509. https://doi.org/10.1016/j.engstruct.2019.109509

Persian Abstract

چکیده

در این تحقیق به منظور بررسی برش منگنه‌ای در دال‌های مجوف و توپر و شبیه‌سازی مدل خاک و فنر به عنوان بار گسترده بر روی این دالها، با آنالیز المان محدود غیرخطی این دال‌ها تحت بارگذاری استاتیک برای بررسی حالت خرابی آن‌ها از نظر بار نهایی و الگوهای ترک خوردگی روی بستر خاک و فنر انجام شد. آنالیز المان محدود سه بعدی با مدل‌سازی مناسب از لحاظ سایز المان، مش و مدل‌سازی مشخصه بتن انجام شد. در نرم‌افزار المان محدود ABAQUS 6.19، رفتار غیرخطی مصالح ترد براساس مدل آسیب‌دیدگی بتن (CDP) تعریف شد. نتایج آنالیز عددی دالها بر اساس مقایسه با نمونه‌های تجربی روی بستر خاک در همین تحقیق کالیبره و صحت‌سنجی شدند. در نهایت با بهینه نمودن ثابت فنر و رسیدن به ثابت فنر خاک، جهت صحت سنجی نتایج آنالیز عددی دالها روی تکیه‌گاه فنر با نتایج تجربی مقایسه گردید. مقایسه بین نتایج تجربی و عددی نشان می‌دهد که مدل‌های کالیبره شده به درستی پاسخ برش منگنه‌ای دالها را پیش‌بینی می‌کند و می‌توان فنر را به عنوان بار گسترده یکنواخت (بار مرده) در مدل‌سازی بکار برد.

International Journal of Engineering

Journal Homepage: www.ije.ir

New Steel Divergent Braced Frame Systems for Strengthening of Reinforced Concrete Frames

M. A. Kafi*, A. Kheyroddin, R. Omrani

Civil Engineering Faculty, Semnan University, Semnan, Iran

P A P E R I N F O

Paper history:
Received 12 June 2020
Received in revised form 20 July 2020
Accepted 04 August 2020

Keywords:
Eccentric Braced Frame Bracing
Steel Braced Frame
Strengthening
Concrete Moment Frame
Ductility

A B S T R A C T

The seismic strengthening methods are very important in earthquake-prone countries. Steel divergent bracing with replaceable link beam tied in steel frame and embedded in a concrete frame is a new method for a concrete frame strengthening. That is low cost and easy repairable after an earthquake. In this article six concrete frame strengthening methods have been investigated, including X-bracing, reverse chevron bracing, divergent bracing with concrete link beam, divergent bracing with steel link beam connected to steel columns in the steel frame, divergent bracing with steel link beam connected to the steel frame and with steel columns between those two, divergent bracing with steel link beam connected to the steel frame. All strengthening models are attached to concrete frames by a steel frame surrounding them . These models are investigated by ETABS and PERFORM-3D softwares. In concrete frame strengthed by steel divergent bracing with steel link beam, the base shear is decreased about 20%, steel consumption decreased to 40% in 6-story, and 15% in 14- and 20-story compared to X-bracing, and the existing to allowable stress ratio decreased to 50% in 6-story, to 40% in14-story and 35% in 20-story. As the structure's height is increased, the interaction between the frame and the brace, and the lateral force in the frames increased. Nonlinear static and dynamic analysis have shown more elastic hardness, ductility, behavior coefficient, and base shear in strengthed concrete frame with divergent bracing with steel link beam connected to the steel frame model than others.

***doi**: 10.5829/ije.2020.33.10a.07*

1. INTRODUCTION

Some existing buildings need to be strengthed because of extra story construction, poor performance, design deficiencies, usage and regulation changes [1-3]. In comparison of strengthening methods by the shear wall and steel braces, steel bracing method was more preferred for its easy implementation, low weight, stiffness increase and lateral displacement decrease [4]. Bracing systems include convergent, divergent and unbuckling bracings, and different bracing dampers. Proper hysteretic plasticity will be achieved by design to prevent early buckling of braces [5]. Reinforced concrete buildings needed appropriate strength, stiffness, and ductility to resist properly high intensity earthquakes. The ductility of reinforced concrete structures depended on the details of its components and the location of the plastic hinges. Coaxial bracing was a very custom lateral resistant system, but its hysteresis behavior showed rapid collapse under cyclic loads due to local buckling. Buckling-resistant braces show appropriate hysteresis energy dissipation even under large axial deformation [6]. Studies indicated that conventional seismic design codes were more conservative than Code No. 360. In other words, design of steel moment frames with conventional design codes leads to stronger beams and columns. This phenomenon could be due to controlling lateral interstory drift and weak beam-strong column criterion in moment frames that control final design results of these structures [7]. The effect of three indirect strengthening models of concrete frames by steel braces, was tested cyclically (Figure 1). The experimental results

*Corresponding Author Institutional Email: *mkafi@semnan.ac.ir* (M. A. Kafi)

Please cite this article as: M. A. Kafi, A. Kheyroddin, R. Omrani, New Steel Divergent Braced Frame Systems for Strengthening of Reinforced Concrete Frames, International Journal of Engineering (IJE), IJE TRANSACTIONS A: Basics Vol. 33, No. 10, (October 2020) 1886-1896

revealed the buildings strength improvement compared to numerical values [8]. The reliability of reinforced concrete frames with steel braces was investigated by Liu et al. [9]. The modeling and the steel brace failure mode are shown in Figure 2. Experimental results showed the effect of strengthening by steel bracing models on the resistance, ductility, and energy dissipation capacity of the strengthened concrete structures [9]. In addition, investigations showed that the braced structures had more stable hysteresis behavior, more energy dissipation capacity, and significantly, lesser damage than the case strengthened with shear panels [10].

The seismic performance of the unbuckling braced frame with a direct connection to the reinforced concrete frame showed that it increased stiffness and ductility to the level of proper seismic performance. The energy dissipation was about 5 times, and the lateral load capacity was about 4 times larger than the concrete frame [11]. Performance evaluation of the existent reinforced concrete frame and strengthened reinforced concrete frame showed that the strengthened system worked suitably [12]. Based on seismic damage analysis, the concrete frames strengthed by steel x-bracing reduced the possibility of damage more than chevron braces [13]. Investigation on concrete frames structural performance with 16 different bracing models showed better performance, and the different bracing showed a significant seismic performance effect on the buildings [14]. Past studies showed strengthened concrete buildings by external braces had more ductility than the strengthened concrete buildings with internal bracings [15]. The results of the seismic performance analysis of steel building revealed that seismic design codes generally had more limited criteria than the improvement codes [16]. Investigation and comparison of seismic behavior of divergent braced frames with vertical and knee joint beams in strengthened concrete frame, showed that knee bracing systems were more effective than vertical bracing, in increasing stiffness, reducing lateral displacement and stress ratio in concrete frame members; but, drastically reduced ductility [17]. Also, the short link beams in experiments showed more resistance than the code specific design. Seismic damage assessment of reinforced concrete frames conducted by convergent steel brace, it showed strengthened concrete frames with steel braces could reduce the possibility of damage [18]. Nateghi and Vatandoost [19] experimentally investigated steel braces for strengthening concrete frames with three indirect bracing models and observed that the the structural resistance was increased in comparison to the results obtained by numerical analysis. In this paper, a new method of braced steel frame with divergent bracing is introduced to strengthen the existing reinforced concrete frame, with the aim of rapid return of the building to service with minimal changes in the existing concrete frame. This method of seismic strengthening, with the ductile behavior of the beam as a shear fuse, will reduce or not damage other members of the structure at different levels of risk. Limiting damage to replaceable shear fuses reduces the time and cost of repairing the structure and returning the building to service quickly. Due to the extensive studies of recent years on different methods of concrete frame strengthening with convergent and divergent braces, in this article it is necessary to evaluate and compare the performance of these methods and the new method of concrete frame strengthening with steel braced frame with divergent bracing.

Figure 1. Strengthening of a concrete frame by indirect bracing [8]

Figure 2. Concrete frame strengthed by steel brace and its fracture mode [9]

2. MODELING AND STUDY METHODOLOGY

In this article, six models of strengthened reinforced concrete frames with four bays in X-direction, five bays in Y-direction, span length of 5 meters and story height of 3.5 meters in 6-story , 14-story and 20-story were considered as a short, middle, and high-rise structures, respectively. Figure 3 presents the 3-D view of reinforced concrete frames strengthened by steel braces. The cross-sections of beams and columns were considered by Iran profiles sections (IPE). The number and location of bracing in the structures showed that the structures did not need local strengthening, and the performance of frames was similar to each other. In all strengthened models, the steel frame was made by studs that were attached to the existing concrete frame. The studs dimensions for connecting the bracing system to the existent concrete frame were considered based on braces cross-section. In this study, seven models including reinforced concrete frame (M0), concrete frame with X-

convergent bracing (M1), concrete frame with reverse chevron bracing (M2), concrete frame with divergent bracing with concrete link beam (M3), concrete frame with divergent bracing with steel link beam connected to steel columns in the steel frame (M4), concrete frame with divergent bracing with steel link beam connected to the steel frame and with steel columns between those two (M5) and concrete frame with divergent bracing with steel link beam connected to the steel frame (M6) were considered. All strengthening models were attached to concrete frames by a steel frame surrounding them. The strengthened models are shown in Figure 4. The dead load of the floor, the partition load and the live load of floors were considered to be 4000 N/m^2, 1000 N/m^2, and 2000 N/m^2, respectively [20]. Also, the compressive strength of concrete and yield strength of steel were considered as 24 MPa and 400 MPa, respectively. Linear dynamic analysis and design of models were performed by ETABS software. The Iranian seismic code(4th edition) was applied for seismic loading [21]. In this article, it was assumed that unstrengthened concrete frames could sustain only 40% of seismic load. The ACI 318-14 and AISC 360-10 have been used for the reinforced concrete and steel members design, respectively [22, 23]. The nonlinear static and dynamic analysis were done by PERFORM-3D software. The link beam length and geometric properties were considered to shear behaviour of link beam that increase the energy dissipation and ductility. All braces and columns of steel frames were designed basis on their capacity.

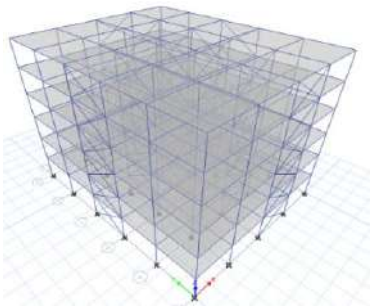

Figure 3. 3D-view of models

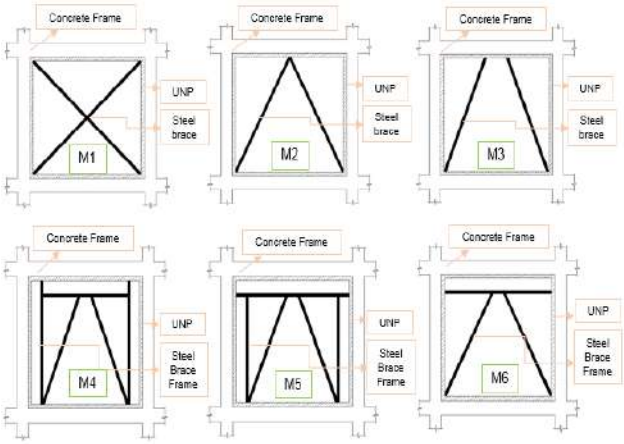

Figure 4. Strengthed concrete frame models

3. VALIDATION OF STRUCTURAL MODELS

As a steel bracing is commonly used to enhance the seismic shear strength of existent reinforced concrete frames, numerous experimental studies have been conducted on strengthened concrete frame systems with steel braces. In order to control the accuracy of the results and make sure the modeling and analysis process of frames; in this study, an experimental strengthened model of a single-span and single-story concrete frame of 1:3 in scale was used to validate the structural models. Then the lateral load capacity curves of the models were investigated. In experimental setup, a link beam in a divergent bracing system was attached directly to the concrete frame and were subjected to a lateral reciprocal resistance capacity. Figure 5 presented the details of the reinforced concrete frame and its experimental setup. The length of the link beam was assumed to be 50mm in the reinforced concrete frame system, and the steel bracing system was considered by normal strength steel. Reinforced concrete frame with compressive strength of 28 MPa of class C20/25 was considered in the experimental model. In this experimental specimen, the link beam and steel sections were considered to be IPE100 and M16 bolts and ST37 steel connectors. Experimental models of the strengthened concrete frame were modeled in PERFORM-3D software. The FEMA element was used for modeling of the concrete beams and columns [24]. Nonlinear static analysis was done on analytical model. In the nonlinear static analysis method, the lateral load was increased, such that the displacement at a given point exceeds from the code specified limit. Thus, the deformation and forces were constantly monitored by load increment. The control point in analytical model was considered to be the mass center of the beam. Also based on FEMA356, lateral load distribution at height was considered based on the static linear method.

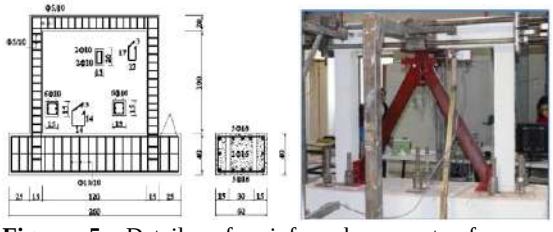

Figure 5. Details of reinforced concrete frame and experimental setup [24]

In Figure 6 the base shear-displacement curves of experimental and analytical models by the PERFORM-3D software was presented. The curves of this figure were shown insignificant difference between the analytical model results and experimental model results. So the PERFORM-3D software could be used for investigating the behavior of models.

4. LINEAR DYNAMIC ANALYSIS RESULTS

The most important reason of structural weakness was gravity and lateral load, or lateral displacement. So by determining the structural weakness reason, a suitable strengthening system could be suggested. If the structural weakness was due to lateral load and displacement, it could be strengthened by different bracing systems. But if it was due to the gravity loads, the bracing systems could not simply eliminate the structural weakness and unsuitable members should be retrofitted. Figure 7 showed the baseshear comparison of M1-M6 models in 6-, 14- and 20-story. The base shear coefficient was the sum of the lateral seismic force divided by the weight of the structure.

As shown in Figure 7, M1 model showed the maximum base shear coefficient compared to other models, Investigation of the new proposed models including M4, M5 and M6 revealed the reduction of the base shear coefficient in this models compared to the M1 model. The base shear of the M4, M5 and M6 models were reduced to 18, 15 and 10%, respectively in 6-story; and to 15, 16 and 17%, respectively in 14-story and finally in the 20-story the base shear of M4, M5 and M6 were reduced to 17%. Thus, by reducing the base shear coefficient in the this models, the lateral force on the structure in the floors was also reduced and the stress of the structural members were reduced. Tables 1-3 summarized the average of the computational stress to allowable stress ratio of the concrete columns in 6-,14- and 20-story models compared with M0 model. In this tables, a negative sign indicate a decrement and a positive sign indicate an increment of computational stress to allowable stress ratio compared with M0 model.

Generally, except in the columns of the braced spans, the computational stress-to-allowable stress ratio of the concrete frame members in strengthened models members was reduced about to 50%. The maximum computational-to-allowable stress ratio, in the M1 to M6 models, were observed on the upper floors. That was found to decrease to 50, 40 and 30% in the 6-, 14- and 20-story, respectively. It could be observed by results that the computational stress to allowable stress ratio in concrete columns in 6-story has decreased to 30% in

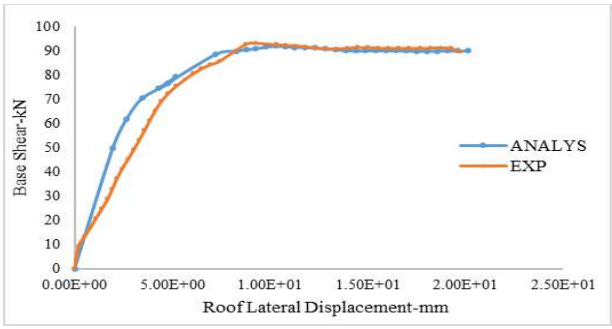

Figure 6. Base shear-displacement curves of experimental and analytical models

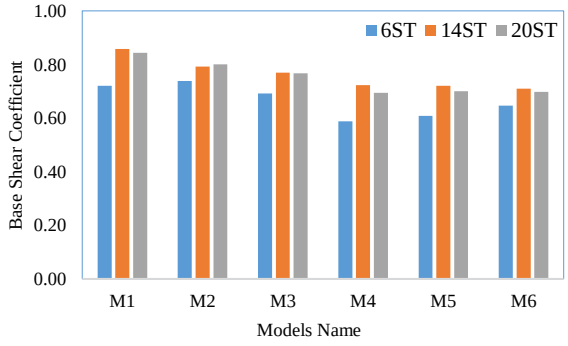

Figure 7. Base shear coefficient. 6-, 14- and 20-st.

TABLE 1. computational-to-allow stress ratios of concrete columns in 6-story models compared to M0 model

Story	M1	M2	M3	M4	M5	M6
1-2	-28	-26	-26	-26	-17	-26
3-4	-3	19	-42	-43	-37	-38
5-6	-50	-3	-51	-45	-47	-46

TABLE 2. computational-to-allow stress ratios of concrete columns in 14-story models compared to M0 model

Story	M1	M2	M3	M4	M5	M6
1-4	-8	-9	-9	-13	-7	-10
5-8	-25	-25	-26	-29	-24	-25
9-11	-33	-33	-34	-35	-31	-27
12-14	-38	-39	-39	-42	-41	-40

TABLE 3. computational-to-allow stress ratios of concrete columns in 20-story models compared to M0 model

Story	M1	M2	M3	M4	M5	M6
1-4	8	7	7	2	6	6
5-8	4	-1	2	-3	1	2
9-12	-2	-2	-3	-7	-3	-3
13-16	-26	-25	-27	-30	-26	-26
17-20	-32	-33	-34	-36	-34	-34

lower floors and to 50% in the upper floors, and in 14-story, it decreased to 10% in lower floors, 30% in the middle floors and 40% in the upper floors. Similarly, in 20-story models, this stress ratio has decreased to 20% in the lower floors and up to 30% in the middle and upper floors. Generally, braced systems for reducing the stress ratio is more effective in 6-story. By increasing the height of the structure, it will be less effective in the stress ratio reduction. Figures 8-10 show the models' relative lateral displacement-relative height by linear dynamic analysis.

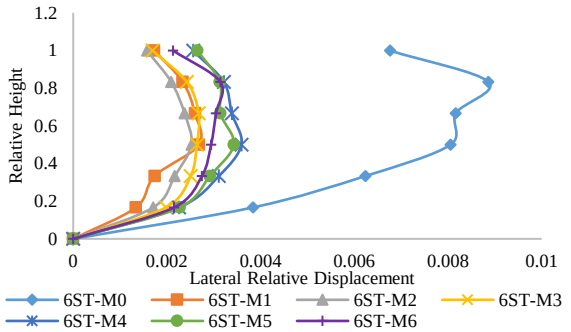

Figure 8. Lateral relative displacement, 6-st models

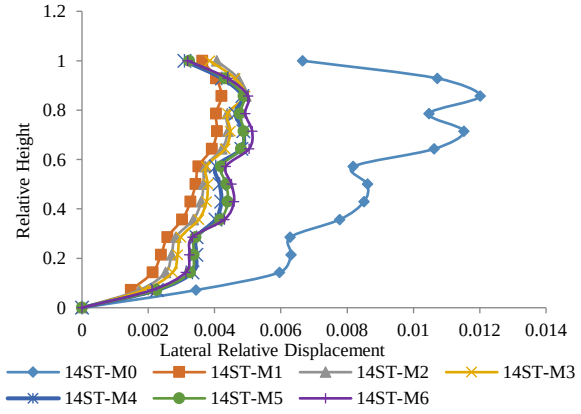

Figure 9. Lateral relative displacement, 14-st.

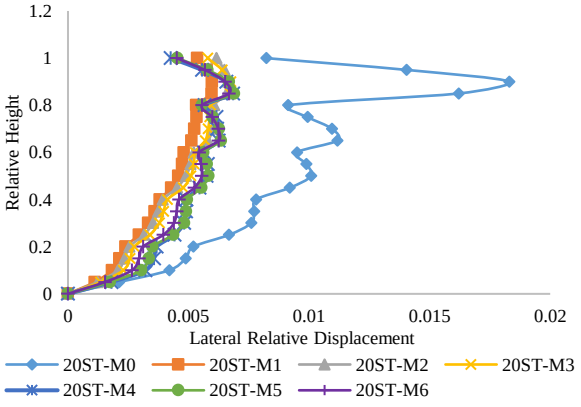

Figure 10. Lateral relative displacement, 20-st.

The results of this tables showed a significant decrease in the relative lateral displacement of the M1 to M6 models in compared with the M0 model. The relative lateral displacement of the structures was reduced to the regulation limits. The interaction of the existent concrete frame and the bracing systems of the M1-M6 models were investigated. Figures 11-13 showed the interconnection curves of the existent concrete frame and the strengthening systems added to the concrete frame in the 6-,14-, and 20-story. In these Figures, the letter F

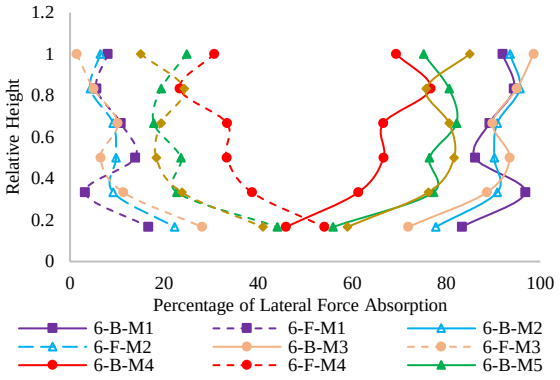

Figure 11. Concrete frame and brace Interaction,6-st.

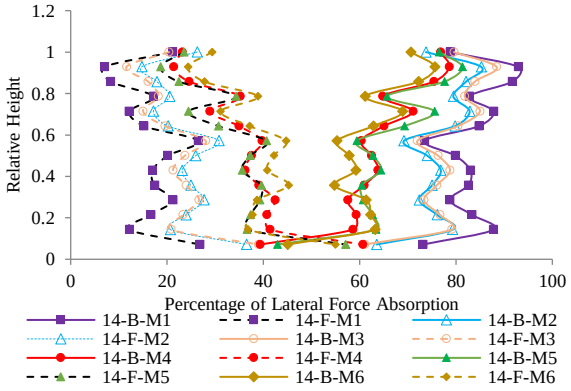

Figure 12. Concrete frame and brace Interaction14-st.

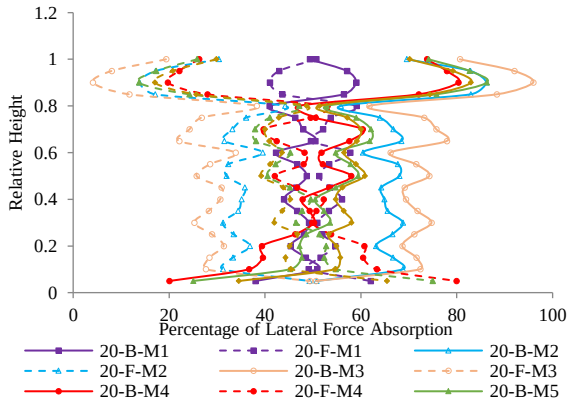

Figure 13. Concrete frame and brace Interaction20-st.

means the absorption of the lateral load by the concrete frame and letter B means the absorption of the lateral load by the braces. The concrete frame in strengthed models, showed more lateral resistance capacity than unstrengthed models. The concrete frame participation in the lateral resistance system in M1, M2 and M3 models was less than M4, M5 and M6 models.

Therefore, the concrete frame of M4, M5 and M6 models showed better ductility and performance than other models. The results in M1 to M3 models of 6-story models showed more than 85% of the lateral load is supported by the braces and on average 15% of the lateral load is supported by the concrete frame. Also in 14-story, results revealed that 80% of the lateral load is supported by the braces and on average 20% of the lateral load is supported by the concrete frame, while in M6 model of 6- and 14-story these percentages were obtained 60% and 40%, respectively. In 20-story 65% of the lateral load is supported by the braces and on average 35% of the lateral load is supported by the concrete frame while in M6 model of 6- and 14-story were obtained 50% and 50%, respectively. Undoubtedly, the columns and foundations of the braced spans need to be strengthed. However, the 85% participation of the braces in the lateral load has made their strengthening costly, This is despite the fact that the capacity of other members of the concrete frame and columns has not been well used.

5. NONLINEAR STATIC ANALYSIS RESULTS (PUSHOVER)

The static nonlinear behavior was evaluated based on FEMA356 by PERFORM-3D software. The structural members were defined by its geometrical, material, and plastic hinge properties and were modeled by FEMA356 elements in PERFORM-3D software [25-27]. Figures 14-16 illustrated the base shear-roof lateral displacemen results concluded by nonlinear static analysis of the M0-M6 models in the 6-, 14-, and 20-story, respectively. The M1, M2 and M6 models in the 6-story and 14-story increased the unstrengthed concrete frame stiffness almost 2 times and in the 20-story models all strengthened models increased the stiffness of the unstrengthed concrete frame by about 1.5 times. Based on the pushover curves results, all the models improved the nonlinear performance and ductility of the existent concrete frame. Comparison of the pushover curves obtained by nonlinear static analysis of the studied models showed the M6 model concluded more ductility than other models.

6. NONLINEAR DYNAMIC ANALYSIS RESULTS

The models' seismic performance was evaluated by nonlinear dynamic analysis with a strong far-fault record set. These records were obtained from FEMA P695 and listed in Table 4. PERFORM-3D software was used for performing the nonlinear dynamic analysis of the models [28].

Relative lateral displacement results were concluded by nonlinear dynamic analysis in relative height of the 6-, 14- and 20-story models, are shown in Figures 17-19.

It was revealed by Figure 17 that the maximum relative lateral displacement was equal to 0.035 and in the M0 model in the 6-story, and the minimum relative

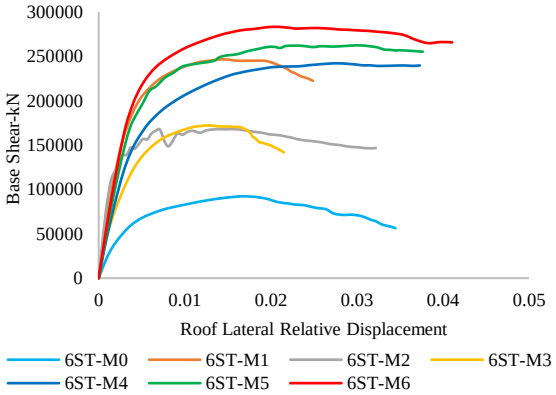

Figure 14. Pushover curves of 6-story models

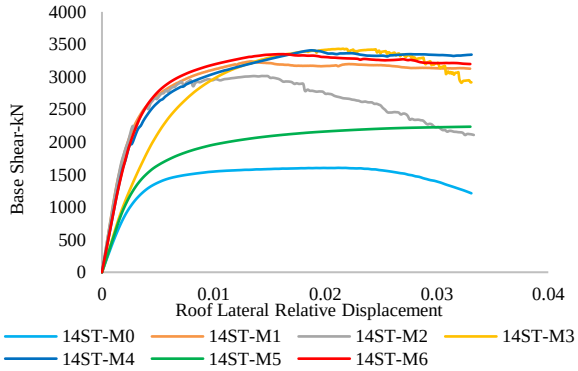

Figure 15. Pushover curves of 14-story models

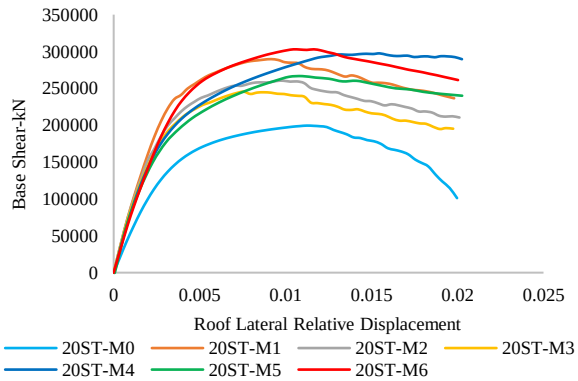

Figure 16. Pushover curves of 20-story models

TABLE 4. Records for nonlinear dynamic analysis

Record number	Record Name	Record year
1	CHI-CHI, Taiwan	1999
2	Imperial Valley	1979
3	Manjil, IRAN	1990
4	Tabas, IRAN	1978
5	Kobe, JAPAN	1995

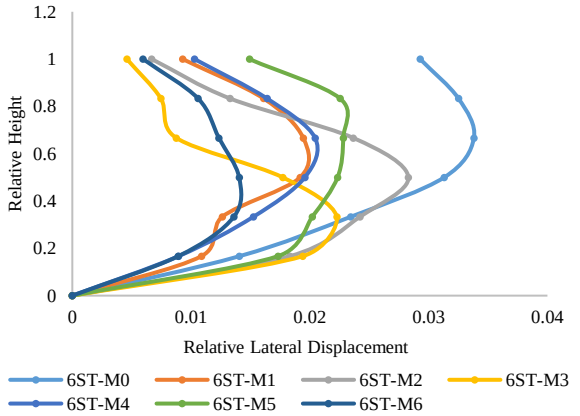

Figure 17. Relative lateral displacement by nonlinear dynamic analysis in 6-story

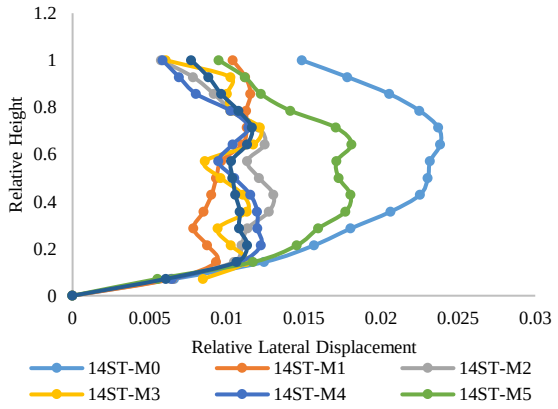

Figure 18. Relative lateral displacement by nonlinear dynamic analysis in 14-story

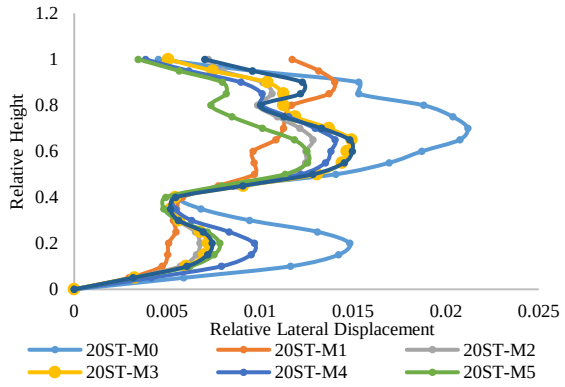

Figure 19. Relative lateral displacement by nonlinear dynamic analysis in 20-story

lateral displacement have seen in M6 model in the 6-story and was equal to 0.015. The relative lateral displacement in the M6 model was decreased 25% compared to M1 model and was decreased 60% compared to M0 model. In 14-story models, the results of the relative lateral displacement in the M1 to M4 and M6 models were close to each other. The relative lateral displacement in the M6 model was reduced about 60% compared to the M0 model. Also, in 20-story models, lateral displacement reduction was significant in all M1 to M6 models compared to M0 model. However, in the M1-M6 models, the lateral displacement reduction in the middle storys , to 40% compared to the M0 model, was significant.

In Figures 20-22 was presented the maximum lateral force to weight ratio of the 6-, 14 and 20-story models by nonlinear dynamic analysis. In 6-story models, the M0 and M5 models showed the maximum lateral force to weight ratio on all floors.

However, the lateral force to weight ratio of the M6 model was about 50% less than other models. Also, in the 14-story models, M3 and M6 models showed the maximum and minimum lateral force to weight ratio respectively, and their difference was about 40% on all floors. As shown in Figure 22, all the 20-story models revealed close results together, but in the M6 model, that is almost 15% less than other models.

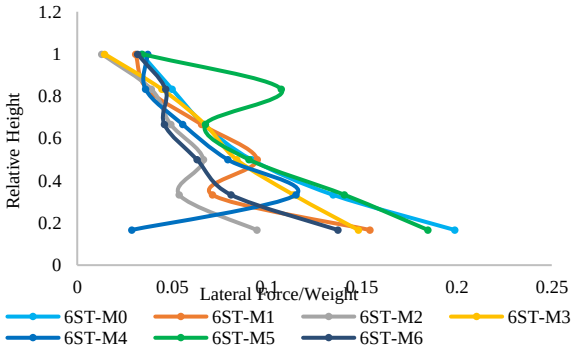

Figure 20. Lateral force/ weight by nonlinear dynamic analysis in 6-story

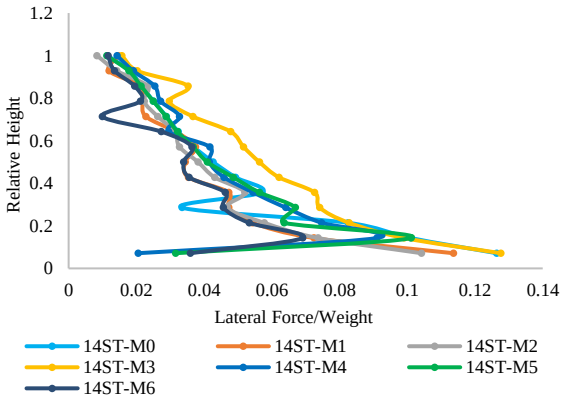

Figure 21. Lateral force/ weight by nonlinear dynamic analysis in 14-story

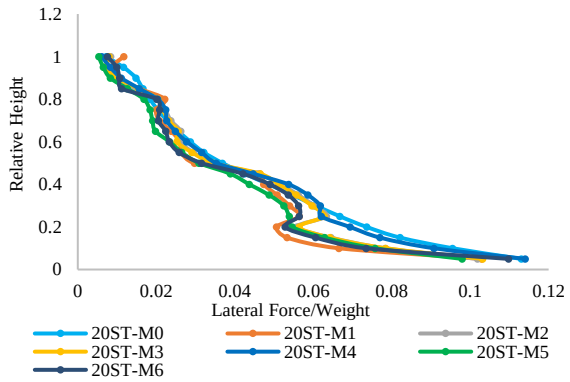

Figure 22. Lateral force/ weight by nonlinear dynamic analysis in 20-story

7. INVESTIGATIONS OF BEHAVIOR COEFFICIENT

New proposed strengthening models were not specifically mentioned in the design codes. Therefore, determining the structural design parameters was very important. The most important method for calculating the behavior coefficient was ductility theory method, energy method, capacity spectrum method, and Uang ductility method. In this article, the Uang plasticity method was used to determine the multiplication of behavior. In 1994, a new formulation was presented for the behavior coefficient known as the Uang method [29,30]. The behavior coefficient was defined as:

$$R=R_R.R_\mu.\Omega_0 \quad (1)$$

where R_R was the indefinite coefficient. In the structural models were presented for strengthening due to the high indefinite degrees, this value was considered to be maximum, i.e. 1. Due to the structural ductility, a significant amount of earthquake energy was depreciated by hysteresis behavior, which depends on the total ductility value of the structure. The energy dissipation capacity could be reduced by the elastic design force to the yield resistance (R_μ). When the plastic hinge was formed in one of the structural members from a design standpoint, the operation of the structural resistance was finished; but this phenomenon was not the end of the ultimate structural resistance, Because the deformed plastic member could still absorb the input energy to the point of destruction. The process of forming plastic hinges continued with increasing external force, and more hinges were created in the structure. Therefore, the resistance of that structure after the first plastic hinge deformation (V_s) to the mechanism step (V_y) was called as incremental resistance and could be expressed as:

$$\Omega_0 = V_y/V_s \quad (2)$$

It has been observed that as the structural height was increased, the behavioral coefficients (R) and elastic stiffness (K_y) of the models were decrease. The elastic stiffness of 6-, 14- and 20-story models are shown in Figure 23. In 6-story models, dual resistant concrete frame systems in M1, M5 and M6 models revealed the maximum elastic stiffness. In the 14-story the M3, M4 and M6 models and in 20-story the M1, M2, M3, and M6 models showed the maximum elastic stiffness. Figure 24 showed the behavior coefficient of 6-, 14- and 20-story models. The M2, M3 and M6 models in 6-story models, the M1, M2 and M6 models in 14-story and the M2 and M6 models in 20-story revealed the maximum behavior coefficient values. Figures 25-27 concluded base design shear (V_{design}) and structural yield shear (V_y) in 6-, 14- and 20-story models. In dual structural strengthened concrete frame models, the results showed that in the M6 model yielding base shear (V_y) was more about 1.25

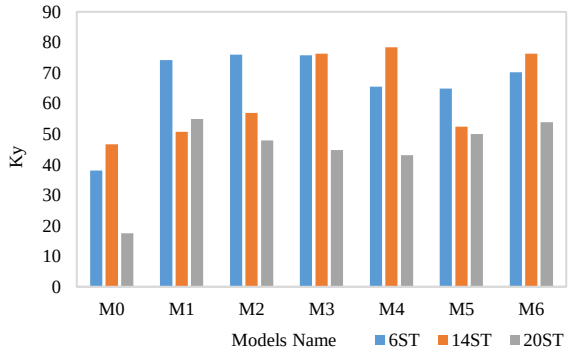

Figure 23. Elastic stiffness 6-,14-, 20-st.

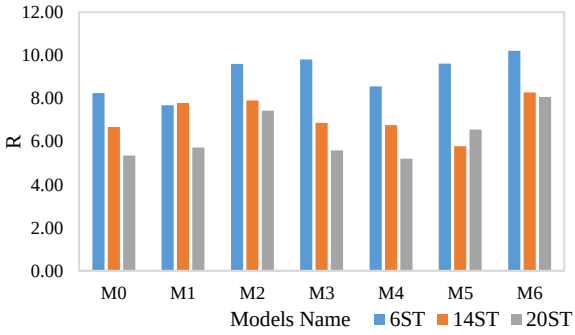

Figure 24. Behavior coefficient.6-,14-,20-st.

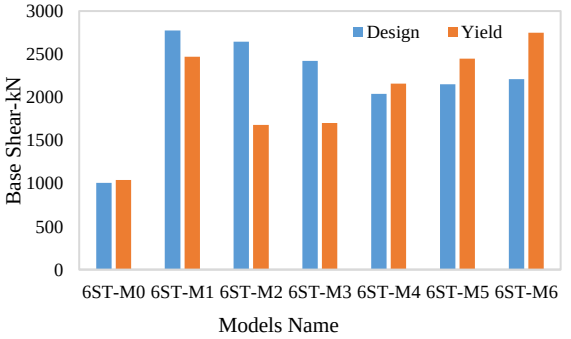

Figure 25. Design baseshear and yield base shear in 6st.

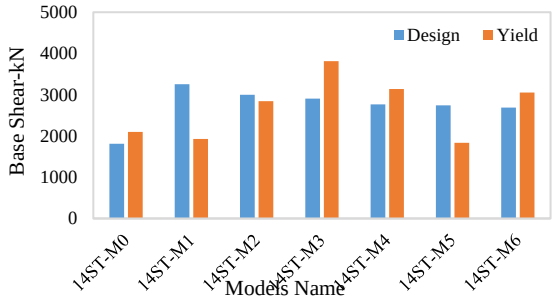

Figure 26. Design baseshear and yield base shear in 14st.

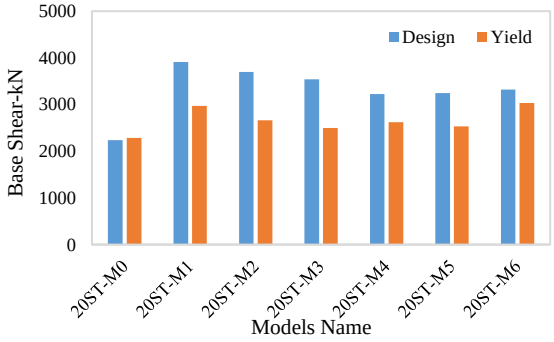

Figure 27. Design baseshear and yield base shear in 20st.

times (Figure 25), 1.10 times (Figure 26), and 1 time (Figure 27) than design base shear (V_{Design}) respectively in 6-story, 14-story and 20-story.

8. CONCLUSION

The steel braced frame systems as a new strengthening system of the concrete frame were introduced and compared with other strengthening systems. These systems were remarkable for their structural fuse, economical cost, and good structural behavior. The performance of concrete frame with six indirect strengthed models were investigated, including steel X-reverse chevron and eccentric braced frame (EBF) with cocrete link beam, and steel EBF braced frame by steel column connection to concrete beam, steel EBF braced frame by steel beam connection to the concrete column and concrete frame with EBF bracing by steel beam connection to a concrete column in 6-, 14-, and 20-story. At first, a linear dynamic analysis was conducted on the structures. Based on linear dynamic analysis results, the determination of the type of structural weakness to provide a suitable strengthening solution was necessary. If the structural weakness was due to lateral force and displacement, it could be strengthened by using different bracing models. Then, using the nonlinear static and dynamic analysis, the seismic performance of the structures were investigated. According to these analysis, the conclusions could be summarized as follows:

In strengthened concrete frame models in 6-, 14- and 20-story there was significant increase in the stiffness and base shear of models compared to that of the M0 concrete frame. But the results of strengthened concrete frame models with steel braced frame in 6-, 14- and 20-story structures showed about a 20% reduction in base shear compared to the strengthened concrete frame with X-bracing by linear dynamic analysis.

The new strengthening method of a concrete frame with a steel braced frame reduced steel consumption compared to reinforced concrete frame strengthened with X-bracing. The reduction in steel consumption was 30, 10, and 15%, in 6-, 14- and 20-story models, respectively. Also, these models reduced significantly the computational stress-to-allowable stress ratio of concrete frame members. As such the maximum stress ratio reduction was observed in the upper stories of models which is 50, 40, and 35% in 6-, 14- and 20-story models, respectively and this value is more than the concrete frame with X-bracing.

Linear dynamic analysis results showed that the relative lateral displacement of the existent concrete frame decreased by using strengthening models. The relative lateral displacement of the concrete frame strengthed by a steel braced frame was more than the concrete frame strengthed by X-bracing. Generally, by increasing the models height, relative lateral displacement results of strengthened models are approximately similar .

Interaction of concrete frame and strengthening system shows that the lateral load absorbed by the strengthening system and the existent concrete frame was on average 80 and 20%, respectively in 6-story models; 40 and 60%, respectively in 14-story models; and 50 and 50%, respectively in 20-story.

Nonlinear static analysis curves showed that all strengthened models had better performance and energy absorption than the concrete frame. However concrete frame strengthened with the steel EBF braced frame model had more energy absorption and hardness than the other models which was about 3 and 2 times of concrete frame, respectively.

By increasing the height of models, the behavior coefficient of a dual concrete frame with bracing strengthening systems decreased. Concrete frame with EBF bracing and with steel beam connection to the concrete column model showed more behavioral coefficient than other models. This model increases the ductility of the concrete frame by about 2 times and elastic hardness of concrete frame by 3 times in 6-story models and by 2 times in 14-story and 20-story models. Also, this model showed that the yielding base shear was 1.25, 1.10 and1 times of design base shear. So in high-rise structures the proposed models nonlinear behavior were not appropiate.

9. REFERENCES

1. Siddika, A., Al Mamun, M.A., Alyousef, R. and Amran, Y. M., ″Strengthening of Reinforced Concrete Beams by Using Fiber-Reinforced Polymer Composites: A Review″, ***Journal of Building Engineering***, Vol. 25, (2019). 100798, https://doi.org/10.1016/j.jobe.2019.100798
2. Mohammadi, H., Esfahani, M. and Riyazi, M., ″Behavior of Coupling Beams Strengthened with Carbon Fiber Reinforced Polymer Sheets″. ***International Journal of Engineering, Transactions B: Applications***, Vol. 20, No.1, (2007), 49-58.
3. Pohoryles, D.A. and Bournas, D. A., ″Seismic Retrofit of Infilled RC Frames with Textile Reinforced Mortars: State-of-the-art Review and Analytical Modelling″ ***Composites Part B: Engineering***, Vol. 183, (2020)., 107702, https://doi.org/10.1016/j.compositesb.2019.107702
4. Tsionis,G., Apostolska, R. and Taucer, F., ″Seismic Strengthening of RC Buildings″, ***JRC Science and Policy Reports***, (2014).
5. Kumar, R.Y. and Deoliya, S.R., ″Review of Retrofitting Techniques for Masonry Infilled RC Frame Buildings″. ***Trends and Challenges in Structural and Construction Technologies***, Roorkee, India, (2009).
6. Maheri, M.R. and Ghaffarzade, H., ″Seismic Design Basis For Internally-Braced RC Frames″, The 14th World Conference on Earthquake Engineering, October 12-17 Beijing, China, (2008).
7. Najafgholipour, M.A., Hadianfard, M.A., Malekjamshidi, SH. and Dehghan, M., ″Match Compliance of Conventional Design Codes with Instructions for Seismic Rehabilitation of Buildings in Performance Evaluation of Steel Moment Frames″, ***Journal of Structural and Construction Engineering***, (2017), DOI: 10.22065/jsce.2018.96056.1300.
8. Ishimura, M. K., Sadasue, Y., Miyauchi, T., Yokoyama, T.F. and K. Minami., ″Seismic Performance Evaluation for Retrofitting Steel Brace of Existing RC Buildings with Low-Strength Concrete″, 15th World Conference of Earthquake Engineering, Lisbon, Portugal, (2012).
9. Liu, F. L., Wang and X, Lu., ″Experimental Investigations of Seismic Performance of Unretrofitted and Retrofitted RC Frames″, 15th World Conference of Earthquake Engineering, Lisbon, Portugal, (2012).
10. Durucan, C. and M, Dicleli., ″Analytical Study on Seismic Retrofitting of Reinforced Concrete Buildings Using Steel Braces with Shear-Link″, ***Engineering Structures,*** Vol. 32, No. 10, (2010). 2995–3010.
11. Mahrenholtz, C., Lin, P.C., Wu. A.C., Tsai K.C., Hwang, S.J., Lin R.Y. and Bhayusukma Y.M., ″Retrofit of Reinforced Concrete Frames with Buckling-Restrained Braces″. ***Earthquake Engineering & Structural Dynamics,*** (2014). DOI: 10.1002/eqe 2458.
12. Qu, Z., Xie, J.Z. and Wang, T., ″Experimental Tests of Reinforced Concrete Frame Subassemblies with Buckling Restrained Braces in Double-K Configuration″, 6th International Conference on Advances in Experimental Structural Engineering, 11th International Workshop on Advanced Smart Materials and Smart Structures Technology, University of Illinois, Urbana-Champaign, United States, August 1-2, (2015).
13. Akbari, R., Aboutalebi, M.H. and Maheri, M.R., ″Seismic Fragility Assessment Of Seel X-Braced And Chevron-Braced RC Frames″, ***Asian Journal of Civil Engineering (BHRC)*** Vol. 16, No. 1, (2015).
14. Harshitha, M.K. and Vasudev, M.V., ″Analysis Of RC Framed Structure With Structural Steel Braced Using Etabs″. ***International Research Journal of Engineering and Technology***, Vol. 5, No. 1, (2018).
15. Kheirodin, A. and Hamidi, J., ″Investigation the Behavior of Reinforced Concrete Structures Strengthed with External Steel Bracing″. Seventh National civil engineering congress, nikbakht engineering faculty. Zah`edan, (2013).
16. Mirtaheri, M., Farhoudi, N. and Nazeryan, M., ″Case Study and Evaluation of Two Steel Bracing Systems in the Bam Earthquake and Methods of Retrofitting″. ***Journal of Structural and Construction Engineering,*** (2018), 120-138. DOI: 10.22065/jsce.2017.88069.1220
17. Saghafi, F., Seyedkazemi, A., Mehrabian H. and Hosseinali Beygi, M., ″Comparison of Seismic Behavior of Eccentrically Braced Frames with Vertical and Knee Links in Retrofitting the Reinforced-Concrete Buildings with Intermediate Moment-Resisting Frame Systems″. ***Bulletin de la Société Royale des Sciences de Liège,*** Vol. 85, (2016), 540-552.
18. Akbari, R., Aboutalebi, M.H., Maheri, M.R., ″Seismic Fragility Assessment of Steel X-Braced and Chevron-Braced RC Frames***″. Asian Journal of Civil Engineering (BHRC),*** (2015). 16. 13-27.
19. Nateghi, A.F., Vatandoost, M., ″Seismic Retrofitting RC Structures with Precast Prestressed Concrete Braces- ABAQUS FEA Modeling″, ***International Journal of Engineering, Transactions C: Aspects,*** Vol. 31, No. 3, (2018), 394-404.
20. National Building Regulation Office Secretary of Housing and Urban Planning Ministry of Roads and Urban Development. Loads on the Building***.*** (2013).
21. Building and Housing Research Center, Regulations of Design of Building Against Earthquake, (2014).
22. ACI Committee 318. ″Building Code Requirements for Structural Concrete (ACI 318-14)″: An ACI Standard: Commentary on Building Code Requirements for Structural Concrete(ACI 318R-14), an ACI Report. American Concrete Institute, (2015).
23. AISC, A.A., 360-10, ″Seismic Provisions for Structural Steel Buildings″, Chicago (IL): American Institute of Steel Construction., (2010).

International Journal of Engineering

Journal Homepage: www.ije.ir

Influence of Fiber on Shear Behavior of Concrete Exposed to Elevated Temperature

A. Varghese, N. Anand*, P. G. Arulraj

Department of Civil Engineering, Karunya Institute of Technology and Sciences (KITS), Coimbatore, India

P A P E R I N F O

Paper history:
Received 07 April 2020
Received in revised form 03 July 2020
Accepted 04 August 2020

Keywords:
Elevated Temperature
Fiber Reinforced Concrete
Shear Strength
Spalling

A B S T R A C T

Fire accidents are inevitable and it is one of the significant hazards, which causes loss of life and valuables. The present investigation focused to study the influence of fibers on shear strength of concrete exposed to elevated temperature as per ISO 834. The fibers used in the study were Basalt, Carbon, Glass, Polypropylene and Poly vinyl alcohol. M20, M30, M40 and M50 grades of concrete were used for the investigation. The results revealed that the shear strength is declined with increase in temperature. The shear strength is enhanced by the addition of fiber in the reinforced concrete beams exposed to elevated temperature. Carbon fiber reinforced concrete specimens exhibited better residual shear strength than the other specimens. Addition of carbon fiber and basalt fiber in concrete reduced the micro cracks in the specimens exposed to elevated temperature. Addition of polypropylene fiber and poly vinyl alcohol fiber reduced the spalling but the crack propagation was not prevented in the specimens exposed to high temperatures.

***doi**: 10.5829/ije.2020.33.10a.08*

NOMENCLATURE

T	Furnace temperature at time t	PVAFRC	Poly vinyl alcohol FRC
T_0	Initial furnace temperature	t	Duration heat exposure (min)
°C/t	Rate of heating	°C/min.	Degree celcius per minute
°C/hr	Degree celcius per hour	RC	Reinforced Concrete
CC	Control Concrete (without fiber)	E	Young's modulus (GPa)
FRC	Fiber Reinforced Concrete	L	Length (mm)
CFRC	Carbon FRC	T_m	Melting point (°C)
BFRC	Basalt FRC	Vol/%	Dosage of fiber (%)
GFRC	Glass FRC	P	Load
PPFRC	Polypropelne FRC	ϕ	Diameter (mm)

1. INTRODUCTION

Fiber Reinforced Concrete (FRC) is known for many property enhancements in conventional concrete. There are numerous studies carried out during last three decades to overcome the weak tensile behavior of concrete. The performance of concrete is always associated with its compressive strength and tensile strength. These two properties are much important that decides the characteristics of concrete. The fibers added in concrete helps to reduce the brittleness of the concrete by bridging the micro cracks and thus prevented the macro crack development [1]. Only limited studies have been carried out on the effects of elevated temperature on the shear strength of FRC. Majority of the investigations focused on the effect of steel fibers and PolyPropylene Fiber (PPF) on the shear strength of the concrete. Considering FRC in terms of fire resistance, some tests have been conducted to identify the effect of fibers in resisting the fire related damages that occurs in concrete structures [1, 2]. Mainly, these are emphasized on the effect of fibers on the basis of its shape, type and the percentage of addition (quantity) on the strength parameters of concrete. Commonly the experiments are carried out in

*Corresponding Author E-mail: *davids1612@gmail.com* (N. Anand)

Please cite this article as: A. Varghese, N. Anand, P. G. Arulraj, Influence of Fiber on Shear Behavior of Concrete Exposed to Elevated Temperature, International Journal of Engineering (IJE), IJE TRANSACTIONS A: Basics Vol. 33, No. 10, (October 2020) 1897-1903

terms of compressive strength, tensile strength and modulus of elasticity [1–5]. Widely used fibers in the concrete industry are synthetic fibers such as PPF and Poly Vinyl Alcohol Fiber (PVAF), Steel Fibers (SF), and hybrid of SF and PPF. There are also a few examinations, which tested concrete with Carbon Fibers (CF), and Glass Fibers (GF) [4, 5].

Kurup and Senthil-Kumar [6] found that addition of PVC fibers improved the ductility behavior of concrete and reduced the brittle failure of concrete. Shear strength values were reduced in the case of fiber reinforced concrete with respect to the addition of PVC fibers and silica fibers (0.6 to 1%) [6]. Bae et al. [7] concluded that, an increase in shear strength according to inclusion of steel fiber was more effective than the four times volume fraction of shear reinforcement. Based on experimental results of the study conducted by Abdi Moghadam and Izadifard [8] it is found that although the inclusion of steel fibers decreased the compressive strength, it has improved the shear strength of plain concrete at 28 days of curing. Smith et al. [9] experimentally investigated the shear strength of fire affected (622℃) beam specimens. The rate of heating was 10℃/min. It was found that 30% reduction in shear strength occurred. Cai et al. [10] studied the residual shear strength of concrete beam specimens after exposure to ISO 834 time temperature curve and the reduction in shear strength was found. For the exposure time of 30 min., 60 min. and 90 min the shear strength reductions were 15, 23 and 26%, respectively. Yusuf [11] examined the residual shear strength of concrete push off specimens after exposure to 200℃, 350℃ and 500℃ with a rate of 17℃/h. heating. The residual strengths after the specimens exposure to 200℃, 350℃ and 500℃, were 26%, 41% and 66%, respectively. Concrete with PP fibers showed the negative performance on improving the mechanical properties beyond the critical temperature (more than 500°C). It was due to the loss of bond between the fiber and cement matrix. It may be due to the development extra pores during melting of PPF [12–14]. Information are limited on the effect of fibers on shear strength of concrete exposed to elevated temperature.

The shear strength is a significant property, which enables concrete to withstand against the fatigue forces. It is considerably less than the compressive strength, because the micro cracks developed in concrete can spread and widen under bending loads. When exposed to fire, bending strength of concrete is reduced due to the spalling that occurs within concrete elements [15–17].

Information on the residual shear strength of FRC with CF, Basalt Fiber (BF), GF, PPF and PVAF exposed to standard fire curve (ISO 834) was found to be missing in the literature. Effect of elevated temperature on FRC with different strength grades are to be evaluated. Hence, it is necessary to understand the influence of different types of fibers on the strength and surface defects of concrete when exposed to elevated temperature. An attempt has been made to study the key factors such as type of fibers, grade of concrete and intensity of temperature, which affect the residual shear properties of concrete.

This paper investigates the shear response of FRC exposed to elevated temperature. The fibers used in the study are BF, CF, GF, PPF and PVAF. The study was conducted in M20, M30, M40 and M50 grades of concrete. Residual shear capacity of different grades of concrete with different fibers are presented in this work.

The main objective of the investigation is to examine the influence of fibers on the shear strength of concrete after exposure to elevated temperature.

2. EXPERIMENTAL INVESTIGATION

2. 1. Materials The ordinary Portland cement of grade 53 conforming to IS: 12269–2013 and Manufactured sand (M-sand) as fine aggregate (Zone II) as per IS: 383:2016 were used. Crushed granite stones of size 20mm confirming to IS 383:2016 were used as coarse aggregate. The quality of water was found to satisfy the requirements of IS 456:2000. Considering the properties of materials, the mix proportion of concrete was designed as per IS 10262:2019. A water reducing agent Master Glenium SKY 8233 was used to control the workability (slump cone test) of all concrete mixtures. The water reducing agent maintained the workability of the mix in between 75 and 100mm even after the addition of fibers into the mix without affecting the water cement ratio. Fe 500 steel bars were used as reinforcement. Table 1 shows the details of fibers.

2. 2. Preparation of Specimens and Test Procedure Singly reinforced FRC beams were cast and used for testing the shear behavior after exposure to elevated temperature. 700 x 150 x 150mm size beams were used for the investigation considering the limitation of the furnace size. Two numbers of 6mm diameter bars were used at top and bottom of the specimens. In order to ensure shear failure, two legged 6mm diameter stirrups are provided at supports and loading points only to hold the main bars (Figure 1). With respect to the proposed

TABLE 1. Details of fibers

Fibers	L (mm)	E (GPa)	σt (MPa)	T_m (℃)	Vol/%
PPF	12	165	317	165	0.25
PVA	12	220	396	220	0.25
GF	12	77	2050	1500	0.25
BF	12	100	3100	1400	0.25
CF	12	240	3500	1200	0.25

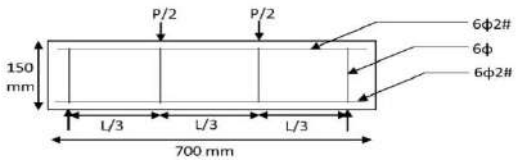

Figure 1. Details of RC beam

beam size molds were made with cast iron. The two-point loading arrangement was adopted from IS 516:1959.

After 24 hours of casting, the sides of the formwork were removed and the specimens were cured in water for 28 days. After curing, specimens were dried and heated following stranded fire curve.

A computer controlled electrical furnace with inner dimensions of 700 × 400 × 400 mm having the capacity power of 100kW was used to heat the specimens (Figure 2). The maximum operating temperature of the furnace is 1200°C, with a capability to set the standard fire temperature curve (Equation (1)). Type K thermocouples connected to a microprocessor based data acquisition unit were used to monitor the temperature inside the furnace.

$$T - T_0 = 345 \log_{10}(8t + 1) \quad (1)$$

Concrete specimens were exposed to heating durations of 30 min (821°C), 60 min (925°C) and 90 min (986°C) as per standard fire curve (Figure 3) following ISO 834. Heated specimens were cooled in ambient condition before the test. The furnace temperature of the heated specimens and its surface cooling rate are shown in Figure 3. The investigation was carried out for different grades of concrete such as M20, M30, M40 and M50. After cooling in air, the shear resistance of Reinforced Concrete (RC) beams were tested using a computerized Universal Testing Machine (UTM) of capacity 1000 kN. Two-point load was applied with appropriate test setup to ensure constant shear in the specimens. The loading gauge was connected with the digital testing machine that records the failure load of the specimens. After curing, cube specimens were exposed to 90 minutes of elevated temperature (986°C) to observe the surface defects. Figure 4 shows the methodology adopted.

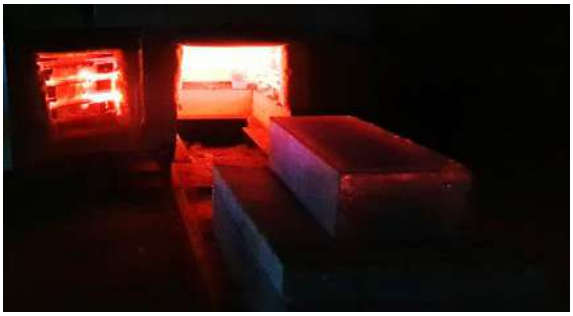

Figure 2. View of furnace and heated specimens

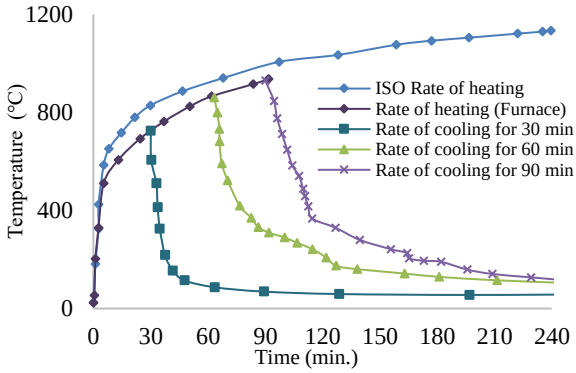

Figure 3. Heating and cooling regime of specimen

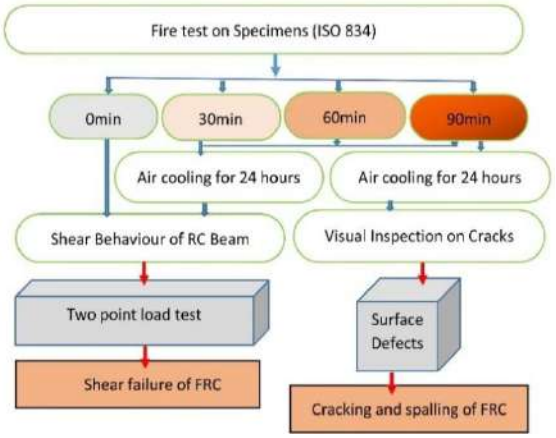

Figure 4. Methodology

3. RESULTS AND DISCUSSION

3. 1. Shear Strength During loading, shear failure was observed in the beam specimens and it is confirmed by the diagonal cracks developed near the support (Figure 5). The ultimate load was delayed according to the type of fibers added in the concrete specimens. For the RC specimens exposed to elevated temperature, the shear resistance decreased with the increase in the duration of elevated temperature.

Figure 5. Shear failure of specimen and inset view of crack

3. 1. 1. Effect of Fiber Type on Unheated FRC Tables 2 to 5 summarized data for the shear failure load of different FRC specimens. It is evident from the results, that all the FRC specimens exhibited more shear capacity than the control concrete (CC). The increment of shear resistance of FRC with respect to CC were found to vary according to the fibers added in the concrete. In the case M20 grade unheated CC specimens (Table 2), carbon FRC (CFRC) exhibited 1.7 times the shear resistance of CC. This was followed by Basalt FRC (BFRC) (1.6 times) and Glass Fiber Reinforced Concrete (GFRC) (1.5 times). The significant increase in the shear strength may be due to the high tensile load carrying capacity (Table 1) of CF, BF and GF [18]. Poly Vinyl Alcohol FRC (PVAFRC) and Polypropylene FRC (PPFRC) specimens exhibited a marginal increase (1.2 times) in shear strength with respect to CC. All FRC specimens exhibited more shear resistance than the CC specimens for M20, M30, M40 and M50 grades after exposure to elevated temperature for 30, 60 and 90 minutes of exposure duration.

Figure 6 depicts the increment in shear resistance of unheated M20, M30, M40 and M50 grade specimens with respect to unheated CC. It is evident that the increment of shear resistance is depended on the elastic modulus and tensile strength of fibers added in the concrete. The results proved that fibers with high tensile strength (CF) has the highest ratio of shear resistance in an unheated condition (1.7 for M20 grade CFRC, 1.5 for M30 grade CFRC, 1.7 for M40 grade CFRC and 1.6 for M50 grade CFRC). This was followed by BFRC, GFRC, PVAFRC and PPFRC specimens that have a lower shear strength (Tables 2-5).

3. 1. 2. Contribution of Fibers in Concrete Exposure to High Temperatures Figures 7 - 10 show the comparison of the shear resistance of M20 (Figure 7), M30 (Figure 8), M40 (Figure 9) and M50 (Figure 10) grade heated FRC specimens with respect to the heated M20 grade CC, M30 grade CC, M40 grade CC and M50 grade CC specimens. This was calculated by taking the ratio of shear resistance of any specimen with the shear resistance of control concrete (CC) of a same grade exposed to same elevated temperature. It can be seen from the figures that, M20 grade CFRC, M30 grade CFRC, M40 grade CFRC and M50 grade CFRC exhibited the maximum shear resistance when exposed to elevated temperature for durations of 30, 60 and 90 minutes. These figures clearly indicate the contribution of fibers in improving the shear resistance of FRC exposed to higher temperature. The fibers in the heated M20 grade CFRC specimens exhibited almost similar contribution in the shear resistance (1.8 times) even after exposed to 30, 60 and 90 minutes. Similar phenomenon was visible on shear resistance of M30 grade CFRC, M40 grade CFRC and M50 grade CFRC specimens.

TABLE 2. Shear resistance (kN) of M20 RCC specimens

t	CC	CFRC	BFRC	GFRC	PPFRC	PVAFRC
00	70.09	116.11	110.82	105.08	84.60	85.08
30	62.57	112.60	97.67	89.92	80.87	81.53
60	51.33	92.69	78.84	71.78	62.52	62.98
90	46.04	81.52	69.91	56.06	48.88	49.10

TABLE 3. Shear resistance (kN) of M30 RCC specimens

t	CC	CFRC	BFRC	GFRC	PPFRC	PVAFRC
00	84.58	125.45	120.33	108.82	92.35	94.69
30	72.54	120.12	110.65	95.45	82.95	82.10
60	60.29	98.85	88.24	76.54	63.00	64.10
90	51.50	83.71	73.69	59.21	52.45	52.12

TABLE 4. Shear resistance (kN) of M40 RCC specimens

t	CC	CFRC	BFRC	GFRC	PPFRC	PVAFRC
0	101.5	170.52	161.60	155.68	146.25	147.55
30	86.54	152.37	138.21	120.43	109.54	109.99
60	70.54	122.16	111.05	83.58	82.37	83.02
90	55.00	94.35	85.75	61.58	57.15	57.90

TABLE 5. Shear resistance (kN) of M50 RCC specimens

t	CC	CFRC	BFRC	GFRC	PPFRC	PVAFRC
0	119.6	192.54	175.55	167.55	155.57	156.83
30	94.57	163.55	150.54	136.13	129.54	130.02
60	81.07	135.25	128.46	101.25	90.68	92.51
90	66.00	108.55	102.55	72.46	68.25	69.55

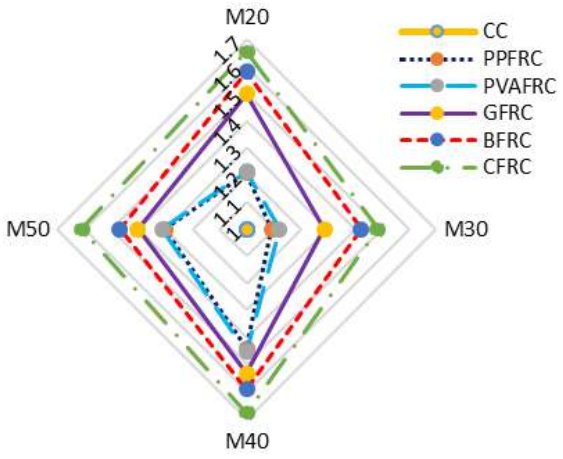

Figure 6. Ratio of shear resistance for unheated specimens

The shear resistance of M20 grade BFRC specimens were found to be 1.5 times that of the M20 grade CC specimens at elevated temperature conditions (30, 60 and 90 minutes). In addition, M30 grade BFRC (1.5 times), M40 grade BFRC (1.6 times) and M50 grade BFRC (1.6 times) exhibited similar behavior in the case of temperature exposed conditions. There was a sudden drop in the shear resistance of M20 grade GFRC specimens (1.4 times to 1.2 times) when exposed to 90 minutes of elevated temperature. M30 grade GFRC, M40 grade GFRC and M50 grade GFRC also exhibited a similar pattern. It may be due to the loss in tensile strength of glass fiber when exposed to elevated temperature [19]. With prolonged heat exposure, the shear resistance of the specimens declined but it can be strengthened by increasing the tensile strength of concrete [10].

In the case of M20 grade PPFRC and M20 grade PVAFRC specimens, a sudden drop (1.2 times to 1.06 times) was observed on the shear resistance of concrete, when exposed to 60 and 90 minutes. In the case of PPFRC and PVAFRC, the similar pattern is observed for other grades (M30, M40 and M50) of concrete. It may be because of the low melting point of these fibers which causes melting of fibers inside the specimens when exposed to elevated temperatures. This reduced the tensile strength of fibers in heated specimen compared to CC. The melting of fibers leads to the creation of pore holes in concrete specimens, which helps to reduce the crack propagation [20, 21]. Hence it shows better shear resistance capacity (1.1-1.2 times) than CC.

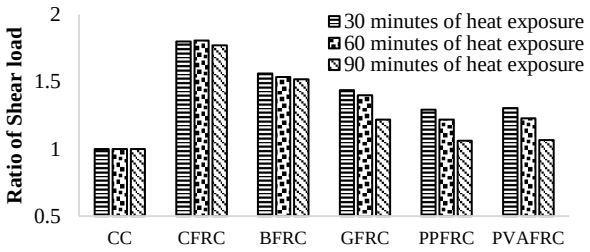

Figure 7. Shear resistance of M20 heated FRC specimens

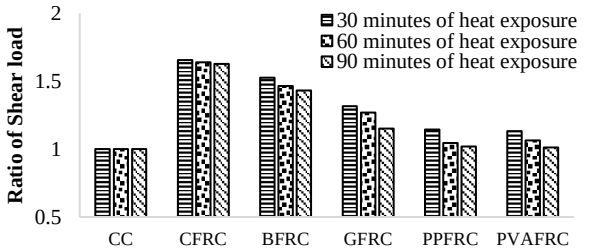

Figure 8. Shear resistance of M30 heated FRC specimens

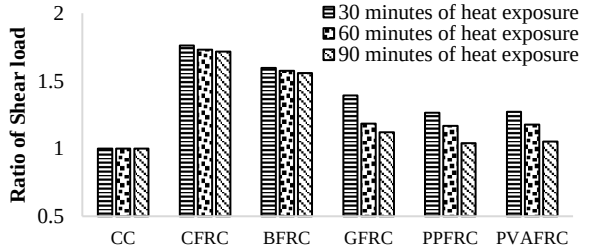

Figure 9. Shear resistance of M40 heated FRC specimens

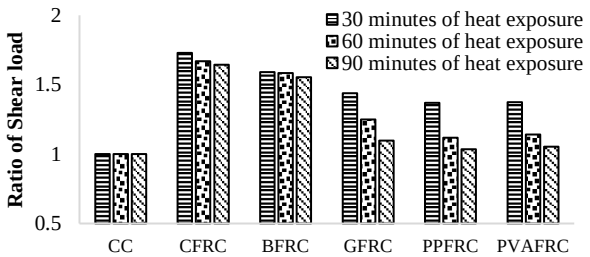

Figure 10. Shear resistance of M50 heated FRC Specimens

3. 2. Thermal Crack Formation

Figure 11 (11A, 11B, 11C, 11D, 11E, 11F) shows the surface view of M20 grade specimens heated up to 90 minutes. It is evident from the figures that the M20 grade CC had more surface pitting than the BFRC, CFRC, GFRC, PPFRC and PVAFRC specimens. For PPFRC and PVAFRC specimens, only surface pitting was observed. This is because of reduction in pore pressure through pore channel created when these specimens exposed to elevated temperature [20] GFRC, BFRC and CFRC specimens had less thermal cracks than CC. It may be due to the bridging effect of high melting point fibers (GF, BF and CF) [22]. The GFRC have small amount of progressive cracks. This is because of the reduction in the tensile capacity of GF, when it is exposed to elevated temperature [19]. Hence reduction in bridging effect between cement matrixes occurs.

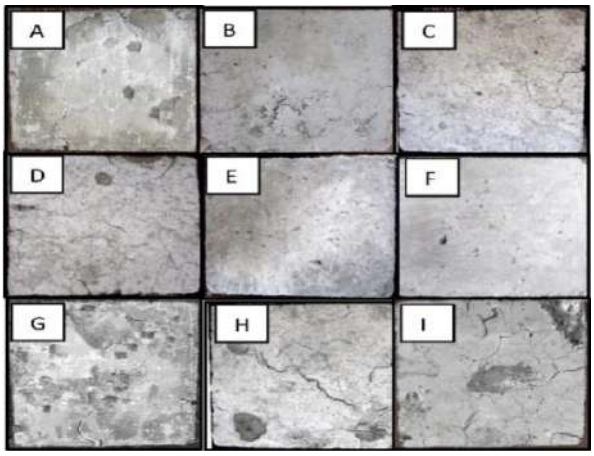

Figure 11. Surface view of specimens: A. M20 CC, B. M20 PPFRC, C. M20 PVAFRC, D. M20 GFRC, E. M20 BFRC, F. M20 CFRC, G. M30 CC, H. M40 CC and I. M50 CC

Also Figure 11 (11A, 11G, 11H, 11I) shows the surface view of the M20 grade CC, M30 grade CC, M40 grade CC and M50 grade CC specimens after being exposed to 90 minutes of heat exposure. From the visual inspection, it is identified that M50 grade CC has the maximum surface damage when compared to M20 grade CC specimens. This may be due to the high density of concrete (M50 grade CC) with less porosity [2]. When the specimens were exposed to elevated temperature, the pore pressure developed within the concrete is high in higher-grade concrete and this induced more surface cracks.

4. CONCLUSIONS

FRC specimens were exposed to elevated temperature up to 90 minutes' duration of heating following the standard fire curve. Shear resistance of FRCs were analyzed before and after heating. The higher grade concrete (M50) is found to retain high shear strength. Addition of fibers improved the shear strength of concrete. The effect of fibers on concrete in terms of shear strength and crack control after being exposed to elevated temperature are concluded below:

- The concrete specimens with CF show better residual shear strength in all grades and at different temperature levels. For 90 minutes of heat exposure, CFRC retained 116 and 91% shear strength of the unheated CC specimen for M20 grade and M50 grade, respectively.
- Concrete specimen with BF (99 - 86%) and GF (80 - 61%) also exhibited high shear strength after exposure to 90 minutes of elevated temperature but the shear strength was found to be lower than that of concrete specimens with CF.
- The residual shear strength of the PPFRC and PVAFRC specimens after exposure to 30 minutes, were found to be 115% (M20) - 108% (M50) and 116% (M20) - 109% (M50), respectively. From 60 minutes of heat exposure onwards, residual shear strength was found to be decreasing. In addition, at 90 minutes of heat exposure, PPFRC and PVAFRC specimens exhibited marginal increment in shear strength than control concrete specimen. It is proved that fibers improve the shear resistance of concrete exposed to elevated temperature. Also addition of fibers prevented the spalling of concrete specimens.
- The concrete specimens with CF and BF were found to have minimum micro cracks even after exposure to elevated temperature. Addition of PPF and PVAF reduced the spalling but the crack propagation could not be prevented at high temperatures. The specimens with GF had more cracks and more surface damage after the exposure. Concrete with higher strength grade (M50) had high rate of crack propagation.

The results of the research are applicable for RC beams exposed to standard fire following ISO 834 fire curve. In case of external fire curve, the behavior of fiber reinforced concrete may change. In addition, there is a scope to compare the performance of different FRC with the corresponding optimum volume fraction of fibers.

5. ACKNOWLEDGEMENT

The authors wish to acknowledge the Science and Engineering Research Board, Department of Science and Technology of the Indian Government for the financial support (YSS/2015/001196) provided for carrying out this research.

6. REFERENCES

1. Varghese, A., N, A., Arulraj G, P., and Johnson Alengaram, U. "Influence of fibers on bond strength of concrete exposed to elevated temperature." ***Journal of Adhesion Science and Technology***, Vol. 33, No. 14, (2019), 1521–1543. https://doi.org/10.1080/01694243.2019.1602889
2. Alwyn Varghese, M Agrima, M Balakrishnan, C Greeshma, and P S Krishnapriya. "Pure Shear Strength of PVA Fiber Reinforced Concrete." ***International Journal of Recent Technology and Engineering***, Vol. 8, No. 2, (2019), 217–221. https://doi.org/10.35940/ijrte.A2218.078219
3. Lura, P., and Terrasi, G. Pietro. "Reduction of fire spalling in high-performance concrete by means of superabsorbent polymers and polypropylene fibers: Small scale fire tests of carbon fiber reinforced plastic-prestressed self-compacting concrete." ***Cement and Concrete Composites***, Vol. 49, (2014), 36–42. https://doi.org/10.1016/j.cemconcomp.2014.02.001
4. Tanyildizi, H. "Effect of temperature, carbon fibers, and silica fume on the mechanical properties of lightweight concretes." ***Xinxing Tan Cailiao/ New Carbon Materials***, Vol. 23, No. 4, (2008), 339–344. https://doi.org/10.1016/s1872-5805(09)60005-6
5. Cheng, F.-P., Kodur, V. K. R., and Wang, T.-C. "Stress-Strain Curves for High Strength Concrete at Elevated Temperatures." ***Journal of Materials in Civil Engineering***, Vol. 16, No. 1, (2004), 84–90. https://doi.org/10.1061/(ASCE)0899-1561(2004)16:1(84)
6. Kurup, A. R., and Senthil Kumar, K. "Effect of Recycled PVC Fibers from Electronic Waste and Silica Powder on Shear Strength of Concrete." ***Journal of Hazardous, Toxic, and Radioactive Waste***, Vol. 21, No. 3, (2017), 06017001. https://doi.org/10.1061/(ASCE)HZ.2153-5515.0000354
7. Bae, B. Il, Chung, J. H., Choi, H. K., Jung, H. S., and Choi, C. S. "Experimental study on the cyclic behavior of steel fiber reinforced high strength concrete columns and evaluation of shear strength." ***Engineering Structures***, Vol. 157, (2018), 250–267. https://doi.org/10.1016/j.engstruct.2017.11.072
8. Abdi Moghadam, M., and Izadifard, R. "Evaluation of shear strength of plain and steel fibrous concrete at high temperatures." ***Construction and Building Materials***, Vol. 215, (2019), 207–216. https://doi.org/10.1016/j.conbuildmat.2019.04.136
9. Smith, H. K. M., Reid, E. R. E., Beatty, A. A., Stratford, T. J., and Bisby, L. A. "Shear strength of concrete at elevated temperature." ***Applications of Structural Fire Engineering***, (2011), 133–138. Retrieved from http://fire.fsv.cvut.cz/ASFE11/

10. Cai, B., Xu, L. F., and Fu, F. "Shear Resistance Prediction of Post-fire Reinforced Concrete Beams Using Artificial Neural Network." ***International Journal of Concrete Structures and Materials***, Vol. 13, No. 1, (2019), 1–13. https://doi.org/10.1186/s40069-019-0358-8
11. Yusuf, M. A. Shear Transfer Strength of Concrete After Exposure to Elevated Temperature, Master's Thesis, Queen's University, Canada. Retrieved from https://www.researchgate.net/publication/335795861
12. Li, H., and Liu, G. "Tensile Properties of Hybrid Fiber-Reinforced Reactive Powder Concrete After Exposure to Elevated Temperatures." ***International Journal of Concrete Structures and Materials***, Vol. 10, No. 1, (2016), 29–37. https://doi.org/10.1007/s40069-016-0125-z
13. Kalifa, P., Chéné, G., and Gallé, C. "High-temperature behaviour of HPC with polypropylene fibres - From spalling to microstructure." ***Cement and Concrete Research***, Vol. 31, No. 10, (2001), 1487–1499. https://doi.org/10.1016/S0008-8846(01)00596-8
14. Irshidat, M. R., Al-Nuaimi, N., and Rabie, M. "The Role of Polypropylene Microfibers in Thermal Properties and Post-Heating Behavior of Cementitious Composites." ***Materials***, Vol. 13, No. 2676, (2020), 1–18. https://doi.org/10.3390/ma13122676
15. Ding, Y., Zhang, Y., and Thomas, A. "The investigation on strength and flexural toughness of fibre cocktail reinforced self-compacting high performance concrete." ***Construction and Building Materials***, Vol. 23, No. 1, (2009), 448–452. https://doi.org/10.1016/j.conbuildmat.2007.11.006
16. Ding, Y., Azevedo, C., Aguiar, J. B., and Jalali, S. "Study on residual behaviour and flexural toughness of fibre cocktail reinforced self compacting high performance concrete after exposure to high temperature." ***Construction and Building Materials***, Vol. 26, No. 1, (2012), 21–31. https://doi.org/10.1016/j.conbuildmat.2011.04.058
17. Li, M., Qian, C. X., and Sun, W. "Mechanical properties of high-strength concrete after fire." ***Cement and Concrete Research***, Vol. 34, No. 6, (2004), 1001–1005. https://doi.org/10.1016/j.cemconres.2003.11.007
18. Mészöly, T., and Randl, N. "Shear behavior of fiber-reinforced ultra-high performance concrete beams." ***Engineering Structures***, Vol. 168, (2018), 119–127. https://doi.org/10.1016/j.engstruct.2018.04.075
19. Terro, M. J. "Properties of concrete made with recycled crushed glass at elevated temperatures." ***Building and Environment***, Vol. 41, No. 5, (2006), 633–639. https://doi.org/10.1016/j.buildenv.2005.02.018
20. Soleimanzadeh, S., and Mydin, M. A. O. "Influence of High Temperatures on Flexural Strength of Foamed Concrete Containing Fly Ash and Polypropylene Fiber." ***International Journal of Engineering - Transactions B: Applications***, Vol. 26, No. 2, (2013), 117–126. https://doi.org/10.5829/idosi.ije.2013.26.02b.02
21. Hafiz, T. A. "Life prediction of carbon fiber reinforced polymers using time temperature shift factor." ***International Journal of Engineering - Transactions A: Basics***, Vol. 33, No. 7, (2020), 1340–1346. https://doi.org/10.5829/ije.2020.33.07a.21
22. Li, W., and Xu, J. "Mechanical properties of basalt fiber reinforced geopolymeric concrete under impact loading." ***Materials Science and Engineering A***, Vol. 505, No. 1–2, (2009), 178–186. https://doi.org/10.1016/j.msea.2008.11.063

Persian Abstract

چکیده

سوانح آتش سوزی اجتناب ناپذیر است و یکی از مهمترین خطراتی است که باعث از بین رفتن جان و اشیاء با ارزش می شود. تحقیق حاضر به بررسی تأثیر الیاف بر استحکام برشی بتن در معرض دمای بالا طبق استاندارد ISO 834 پرداخته است. الیاف مورد استفاده در این تحقیق شامل بازالت ، کربن ، شیشه ، پلی پروپیلن و پلی وینیل الکل بودند. بتن از M20، M30، M40 و M50 استفاده شد. نتایج نشان داد که با افزایش دما مقاومت برشی کاهش یافته است. استحکام برشی با افزودن الیاف در تیرهای بتن مسلح که در معرض دمای بالا است افزایش می یابد. نمونه های بتن مسلح با فیبر کربن نسبت به سایر نمونه ها مقاومت برشی باقیمانده بهتری نشان دادند. افزودن الیاف کربن و بازالت در بتن باعث کاهش ریزگردها در نمونه های در معرض دمای بالا می شود. افزودن الیاف پلی پروپیلن و پلی وینیل الکل باعث کاهش فاصله می شود اما از انتشار ترک در نمونه هایی که در معرض دمای بالا قرار دارند ممانعت نخواهد کرد.

IJE TRANSACTIONS A: Basics Vol. 33, No. 10, (October 2020) 1904-1916

International Journal of Engineering

Journal Homepage: www.ije.ir

Experimental Modeling and Evaluation Sediment Scouring in Riverbeds around Downstream in Flip Buckets

K. Khalifehei*[a], G. Azizyan[a], M. Shafai-Bajestan[b], K. W. Chau[c]

[a] *Department of Civil Engineering, University of Sistan and Baluchestan, Zahedan, Iran*
[b] *Department of Hydraulic Structures, Faculty of Water Science Engineering, Shahid Chamran University of Ahvaz, Ahwaz, Iran*
[c] *Department of Civil and Structural Engineering, Hong Kong Polytechnic University, Yuk Choi Road, Hung Hom, Kowloon, Hong Kong*

PAPER INFO

Paper history:
Received 14 May 2020
Received in revised form 8 July 2020
Accepted 04 August 2020

Keywords:
Sediment Scour
Sediment Transport
Hydraulic Structures
Stilling Basin
Large Dam

ABSTRACT

Flip buckets are a common configuration for side channel spillways. Similar to other spillways, the flip bucket or ski jump has its disadvantages, among which the scour hole downstream due to the flip bucket jet is the most important. The structure safety and stability may be influenced by the scour holes generated at the downstream side of bucket type energy dissipators. This study has employed an experimental model in order to examine the sediment scour created at the end of flip bucket energy dissipators at various flow rates and tail water depths. A total of 45 experiments were performed under different conditions. The experimental invistigation was conducted at the hydraulic laboratory of Shahid Chamran University in Iran. The main objective of this research was to identify the maximum depth of sediment scour (d_{sm}) and the maximum distance of sediment scour hole (L_{sm}) from the structures. The results showed that the maximum depth of scour and its distance from the structure increased by increasing discharge. The results of experimental models show that, at the downstream depths (Y_t) of 0.2 and 0.3 m, the stack was formed by the scouring at the upstream side of the hole, and at a depth of 0.1 m, this stack was transferred to the area after the scour hole. This could be explained by the fact that at downstream depths of 0.2 and 0.3 m, the rolling flow moved from the bottom upwards in the opposite direction of the water flow and sequestrated the sediments upstream. According to Equation Mean Absolute Relative Error (*MARE*) proposed relation based on laboratory studies has MARE of about 34.2%.

***doi**: 10.5829/ije.2020.33.10a.09*

1. INTRODUCTION

The erosion and morphological changes of the rivers naturally arise from the erosive effects of the water flow as well as the construction of various hydraulic structures in the waterway. Excessive erosion can gradually weaken the foundation of hydraulic structures and ultimately lead to their failure. The sediment scour at the downstream area of hydraulic structures represents a highly important zone for research because it is frequently occurring in engineering installations. In different countries around the world, various methods have been proposed for protection against scouring. These methods include rip-rap, concrete block unit armor, articulated block mattress, gabions mattress, green coatings, stabilizers, etc. [1, 2].

Dams reservoirs not only suppress floods but also provide water for activities such as aquaculture human consumption, irrigation, industrial use and navigability. The release of stored water behind these structures produces a lot of energy at the downstream side and the bases of hydraulic structures. The kinetic energy that turbulent jets produce may lead to erosion at downstream channels and failure at hydrological constructions. It, therefore, entails local scour at the downstream regions of such hydraulic structures as vertical barrages, flip bucket jets, spillways and culverts. In general, the

*Corresponding Author: *kamran.khalifehei@pgs.usb.ac.ir* (K. Khalifehei)

Please cite this article as: K. Khalifehei, G. Azizyan, M. Shafai-Bajestan, K. W. Chau, Experimental Modeling and Evaluation Sediment Scouring in Riverbeds around Downstream in Flip Buckets, International Journal of Engineering (IJE), IJE TRANSACTIONS A: Basics Vol. 33, No. 10, (October 2020) 1904-1916

structures which dissipate energy are commonly utilized in order to prevent such issues. These protective structures dissipate the excessive energy that turbulent jets carry [3]. One of these dissipating structures is known as the flip bucket jet, which is designed as an attachment to the spillway that mixes the air and jet by conducting high velocity flows upwards and reduces the impact of the jet core and the flow of jets from the structure. The flip bucket jet is designed with various jet angles, radii and structures. This structure is an economical alternative to other conventional dissipators such as stilling basins, etc. [4, 5]. So far several studies have been carried out to address scouring downstream of flip bucket jets by Bormann and Julien [6]; Jafari and Khiavi [7], Mason and Arumugan [8], Amanian and Urroz [9], Stein et al. [10], Afify and Urroz [11] and Cordier et al. [12]. Furthermore, scholars such as Hoffmans and Verheij [13], Khalifehei et al. [14], Ghodsian et al. [15], Juon and Hager [16], Pagliara et al. [17], Yamini [18], and Movahedi et al. [19] used experimental data to provide empirical predictive relationships for the maximum depth of scour caused by the jet. The results of their studies were presented as non-dimensional diagrams and relations. Few quantitative studies were undertaken regarding the erosion pattern as well as the maximum distance of the scour hole from the structures [20]. More recently, Zhang et al. [21], and Movahedi et al. [22] established an expression to predict the sediment scour depth using Flow3D or Fluent, a computational fluid dynamics (CFD) software [23-27].

A variety of hydraulic parameters (such as flow depth, flow velocity, jet impact angle, and turbulence intensity on the basin), hydrological factors (such as flood frequency, discharge flood, and flood duration) and geological parameters (shuch as the type of bed materials, grain size distribution, and cohesive or non-cohesive sediment) make the mechanism of scouring extremely complicated. The evolution of scouring characteristics is one of the significant issues in hydraulic and hydrology engineering. Over the past five decades, numerous empirical formulations, based on the regression of the scouring data observed from laboratory experiments in the field, have been developed to predict scouring characteristics (typically the equilibrium scour depth); nevertheless, these empirical formulations are sensitive to the uncertainty of effective parameters and in some cases could not comprehend the actual internal mechanism between variables. The motivation of the current research is to exhibit all the established research works on the implementation of empirical formulations models for multiple scouring depths modeling such as ski jump, flip bucket, and spillway structures. A comprehensive review of the up-to-date research works on the scouring depth phenomena is presented, placing special emphasis on the recent and basic applications of empirical formulations models and also recalling all the performed experimental laboratory studies. The review includes an informative evaluation and assessment of the surveyed research efforts. The improvement in prediction performance provided by the empirical formulations models when compared to empirical formulations is discussed. It should be noted that the process of scour at the downstream side of a ski jump is experimentally investigated using three different non-cohesive bed materials with the densimetric Froude number, the Reynolds Number of the jet, the angle of the ski jump lip, and the sediment non-uniformity constant taken into consideration. In the final section of this paper, the results and achievements of the experimental studies are briefly presented.

2. MATERIALS AND METHODS

2. 1. Empirical Formula for Calculating the Maximum Depth of Scour The formulas developed for estimating sediment scour under a jet flow are collected in Table 1. The authors list them and, where the author has developed more than one expression, they are also referenced by a letter. These Equations can be generally written as:

$$d_s = \frac{cq^x H^y \alpha^w}{d^z} \quad (1)$$

In which d_s scour depth, in terms of the head drop from upstream to downstream water level H, the unit discharge of the jet at the point of impact q, angle of impact jet α, and, in some cases, the characteristic particle size of the bed material d. Also, other terms c, x, y, z and w are all constant for any given formula.

It may be noted, based on Table 1, that first the maximum sediment scour depth is considered a function of q (the discharge per width), H (at bucket lip level), or H_1 (at tailwater level) is the second to play a role [32]. The bed sediment materials diameter and the angle of impact of the jet flow (α) play no significant parts. Schoklitsch **[**25**]**, Chee and Kung [28] noted that the particles diameter have a significant impact. Chee and Kung [28] used α angle in their formulas. Schoklitsch [25] used d_{90} (a sediment diameter bigger than 90% of materials) in his computations, whereas they took d_{50} into consideration [28].

2. 2. Dimensional Analysis To determine the scouring pattern of the bed in a laboratory model under the changes in the size of bed sediments and to make a comparison with other existing relations, it is necessary first to carry out a precise dimensional analysis using the parameters affecting this phenomenon. The most important parameters affecting the scouring phenomenon, according to Figure 1, are stated as Equation (2):

TABLE 1. Literature empirical formula proposed for estimation of the maximum scour depth

Method	Equation	c	x	y	z	w
Schoklitsch [25]	$d_s = \frac{0.521q^{0.57}H^{0.2}}{d^{0.32}}$	0.521	0.57	0.2	0.32	0
Veronese I [26]	$d_s = \frac{0.202q^{0.54}H^{0.225}}{d^{0.42}}$	0.202	0.54	0.225	0.42	0
Veronese II [26]	$d_s = 1.9q^{0.54}H^{0.225}$	1.9	0.54	0.225	0	0
Damle I [27]	$d_s = 0.652q^{0.5}H^{0.5}$	0.652	0.5	0.5	0	0
Damle II [27]	$d_s = 0.543q^{0.5}H^{0.5}$	0.543	0.5	0.5	0	0
Damle III [27]	$d_s = 0.362q^{0.5}H^{0.5}$	0.362	0.5	0.5	0	0
Chee and Kung [28]	$d_s = \frac{1.663q^{0.6}H^{0.2}\alpha^{0.1}}{d^{0.1}}$	1.663	0.6	0.2	0.1	0.1
Chee and Padiyar [29]	$d_s = \frac{2.126q^{0.51}H^{0.18}}{d^{0.061}}$	2.126	0.67	0.18	0.063	0
Wu [30]	$d_s = \frac{1.18q^{0.51}H^{0.6}}{d^{0.1}}$	1.18	0.51	0.6	0.1	0
Martins [31]	$d_s = 1.5q^{0.6}H^{0.6}$	1.5	0.6	0.1	0	0
Incyth [32] ()	$d_s = 1.413q^{0.5}H^{0.25}$	1.413	0.5	0.25	0	0
Khatsuria [20]*	$d_s = 0.9q^{0.5}H^{0.5}$	0.9	0.5	0.5	0	0
Azmathullah et al. [33]**	$d_s = 1.42q^{0.44}H_1^{0.3}$	1.42	0.44	0.3	0	0

Damle's equation modified for the ultimate scour according to further data obtained from the laboratory and the field, proposed by Khatsuria [20]; ** H_1: The head amid the upper water level and the tail water level (m).

$$d_s = f(V_t, Y_j, \theta, g, \vartheta, Y_{tsm}, d_{50}, D', \rho_w, \rho_s, \mu, T, t, \delta) \quad (2)$$

Some of the parameters of Equation (2) are presented in the previous sections, but the other parameters include d_s: the depth of the scour hole, Y_j: the mean flow depth at the lip of the ski jump, θ: the lip angle of the ski jump, ϑ: the jet impact angle on the basin, d_{50}: 50% finer particle sizes of sediment, D': representative particle size, ρ_s: the sediment density, ρ_w: the water density, μ: the water dynamics viscosity, T: the turbulence intensity on the basin, t: time, δ: the geometric standard deviation of the sediment bed material size, and g: acceleration due to gravity. Taking into consideration that jet velocity at the lip of the ski jump (V_t), mean flow depth at the lip of the ski jump (Y_j) and density (ρ_w) are the repeating variables, the dimensionless grouping of Equation (3) is obtained:

$$\frac{d_s}{d_{50}} = f\left(Re, We, Fr, \frac{d_s}{d}, \left(\frac{\rho_s-\rho_w}{\rho_w}\right), D', T, \theta, \vartheta, \tau\right) \quad (3)$$

In this equation; $Fr = \frac{V_t}{\sqrt{gd}}$: the Froude number, $\left(\frac{\rho_s-\rho_w}{\rho_w}\right)$: the relative specific density, $Re = \frac{\rho V_t Y_j}{\mu}$: the Reynolds number, $We = \frac{V_t}{\sqrt{\delta/\rho_w Y_j}}$: the Weber number, and $\tau = \frac{V_t t}{Y_j}$: the dimensionless time factor. The mean velocity of the flow may be written in a non-dimensional form, as is usual in the research on the sediment scour produced under the action of free jets, as $F_g = \frac{V_t}{\sqrt{(\frac{\rho_s-\rho_w}{\rho_w})gd_{50}}}$; where V_t denotes the velocity of the jet at the ski jump jet, $\left(\frac{\rho_s-\rho_w}{\rho_w}\right)$ is the relative sediment density, ρ_s represents the sediment particle density, ρ_w is the water density, g is acceleration of gravity, and d_{50} denotes the sediment material particle size.

2. 3. Equipment and Testing Methods The experiments were carried out in a flume with a length, width and depth of 7.3, 0.65 and 0.6 m, respectively, and a longitudinal slope of 0.0028 at the hydraulic experimental laboratory of Shahid Chamran University in Iran. At upstream of the flume, an ogee spillway connects the reservoir to a galvanized flip bucket with a radius of 0.16 m through a chute. This work incorporated bed materials whose δ (geometric standard deviation) values refer to their non-uniform nature. The investigated bed material was a uniformly sanded gravel with a grain size distribution of $D_{50} = 2.31\ mm$. Bed materials were selected in a way to keep the value of about $D_{85} = 3.25 \times 10^{-3}\ m$, $D_{90} = 3.64 \times 10^{-3}\ m$, $\rho_s = 2.70\ kg/m^3$ and $D' = 1.78$. The walls and the bottom of the flume were made of transparent Plexiglas. The required flow entered the stilling tank from the water supply tank via a centrifuge pump at the beginning of the flume. With the

aim of eliminating the input turbulence, a distilling lattice plate was used at a distance of 1 meter from the flume inlet. The flow entered a pond after leaving the flume and then re-entered the water supply tank. The flow discharge was measured using an ultrasonic flow meter mounted on the inlet pipe of the pump. Due to the sub-criticality of the flow, the flow depth control was carried out using a sliding gate located at the end of the flume.

Point gauges with a precision of 0.2 millimeters were installed on a rail and helped measure levels of free surface, depths of flow, and depths of scouring. The flow rate has been measured with a 2.5% uncertainty. Measurements of the flow depth in the ski-jump helped calculations of the flow velocity of the jet.

The experiments were carried out at different discharges (q) between 0.005 and 0.03 (m^3/s) at different depths (Y_t) of 0.1, 0.2, and 0.3 m. It is worth noting that at high flows, the depth of the cavity reached the bottom of the flume due to the increase in scouring; therefore, this issue was not considered in the analysis of the experiments.

In the experiments, the distance between the sediment level and the edge of the jet was selected as $Y_{level} = 0.2\ m$. In this way, the depth of 0.1 m did not submerge the edge of the bucket. In the second case (0.2 m), the tail water depth was at the edge of the jet, and in the third case ($Y_t = 0.3\ cm$), the bucket was submerged (Table 2).

The scouring downstream of the flip bucket jet is a time function and increases over time until an equilibrium condition is reached. Hence, it is important for designers to identify the time needed for the hole to reach equilibrium. With the purpose of determining the equilibrium time of the tests, a 5-hour test was performed at a rate of 0.025 (m^3/s) and the equilibrium time, approximately 3 hours in this test, was obtained based on the slight changes in the scour hole versus time.

TABLE 2. Laboratory experimental conditions.

	Run 1	Run 2	Run 3	Run 4	Run 5
q (m^3/s)	0.005	0.01	0.015	0.02	0.025
Y_t (m)	0.1	0.1	0.1	0.1	0.1
	0.2	0.2	0.2	0.2	0.2
	0.3	0.3	0.3	0.3	0.3
Y_{level} (m)	0.2	0.2	0.2	0.2	0.2
Re	1.02×10^5	1.14×10^5	1.22×10^5	1.25×10^5	1.27×10^5
We^*	39	42	48	62	77

* Chanson et al. [34] suggested that in order to minimize the scale effects in a two-phased air water flow in a turbulent flow such as a jet, it is required that the Weber number and the Reynolds number be greater than Re = 10^5 and We = 32, respectively, which has been controlled and verified in these experiments.

At the beginning of each test, the slider was completely closed, and the water entered the flume slowly so that the water gradually entered the flume through a 0.102 m tube to allow the water to reach the desired level. The inlet gate was then opened to the flume tank, and the discharge into the reservoir was adjusted by reading the flow meter. As soon as the concurrent flow spilled, the end gate was opened to the point that the downstream water level remained constant. After the flow was completed for 3 hours, the end gate was closed, and the pump was switched off to allow the water in the channel to slowly drain from the bottom of the flume with no effects on the topography of the bed. After a few hours and full discharge of water from the channel, the topography of the bed was taken around the base in a 1 × 1 grid by the laser depth meter. The most important components of the laboratory model are the reservoir, the centrifuge pump, the input flow, the bottom transform, the flip bucket jet, the sedimentary bed and the sliding gate. Figure 1(a) shows the experimental system, and Figure 1(b) shows a schematic view of the section of the laboratory model and its important hydraulic and geometric parameters.

To guarantee replication of the prototype tests by these experiments, geometric and Froudian protocols of scaling were run in the models. The Froude law was incorporated in the present study because gravitational and inertial forces fundamentally affect the mobility of water in any ski-jump no matter in a spill way or in a bottom outlet design. Viscosity and surface tension must be modeled to allow accurate simulation of the two-phased flow (water and air). This refers to the Froude, Reynolds and Weber laws fulfillment at the same time. Theingi et al. [35] concluded that employing very small scale models might influence the scour dimensions despite the limited advice given to modellers. The scour profile data must be normalized to provide for a comparison between varied experimental scales, and after a dimensional analysis of the governing quantities, it has been customary to non-dimensionalize the scour depth and the scour length by respectively employing the maximum scour depth, d_{sm}, and the maximum scour length, L_{sm} [36]. This results in demonstration of an appropriate match between the classical profiles including those of Lim and Chin [37], Aminoroaya et al. [1, 23] and others. Nonetheless, incorporating d_{sm} and L_{sm} entails restriction of data to intersect the origin, which is the point of the maximum scour and the maximum scour length, potentially hiding any differences between the tests and the role that small scale models could play. In another dimensionless group with the scour depth and length normalized utilizing the tail water depth Y_t could be taken into consideration, and this may potentially prove more useful if the results are scaled to prototype dimensions. This analysis will employ the latter.

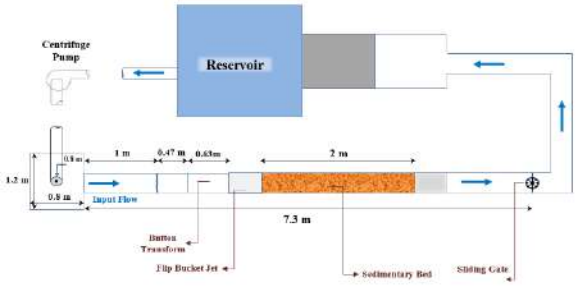

(a)

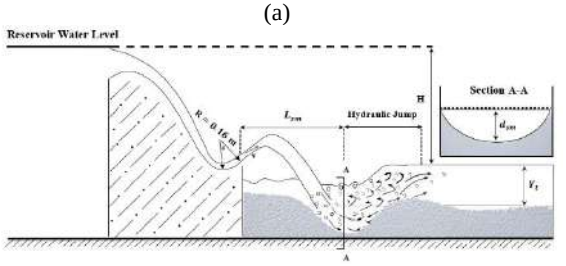

(b)

Figure 1. (a): Plan view of the experimental setup, and (b): Sketch of the experimental setup. Bucket radius (R), distance of the maximum scour from bucket lip (L_{sm}), total head (H), the maximum depth of scour (d_{sm}), tail water depth (Y_t), discharge intensity (q), bucket lip angle (θ). Section A-A configuration of geometric parameters of d_{sm} and Cross section of scour

3. RESULTS AND DISCUSSION

3. 1. Analysis of the Scouring Pattern In Figure 2, the longitudinal profile of the bed is shown at the downstream side of the flip bucket under different flows conditions. According to Figure 2, the water pad prevents erosion and reduces scouring by increasing depth. The overall profile of different flows shows that when the flow increases, especially at lower depths, a larger length is affected by erosion and sedimentation. It also decreases as the depth increases.

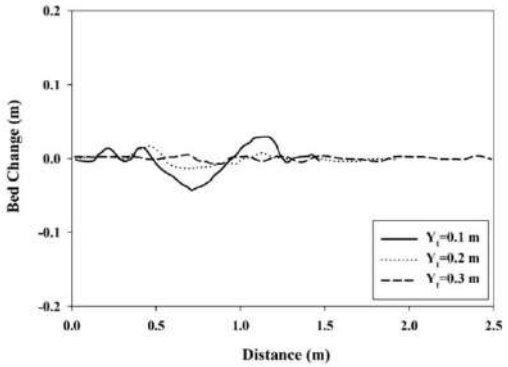

(a)

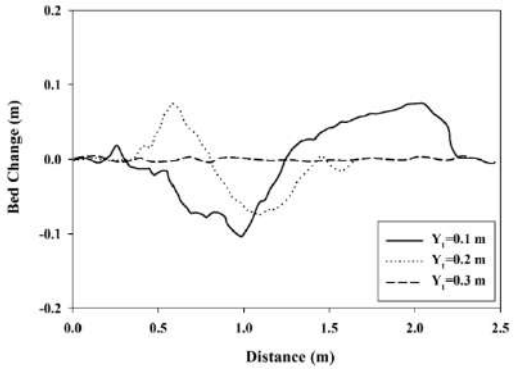

(b)

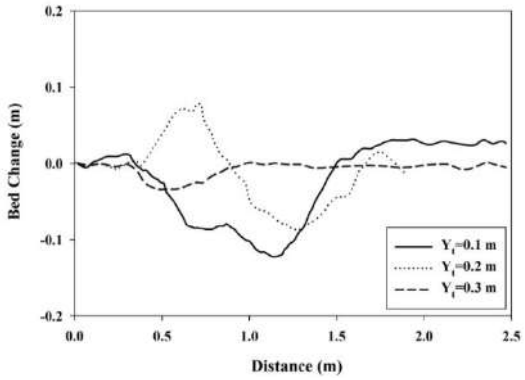

(c)

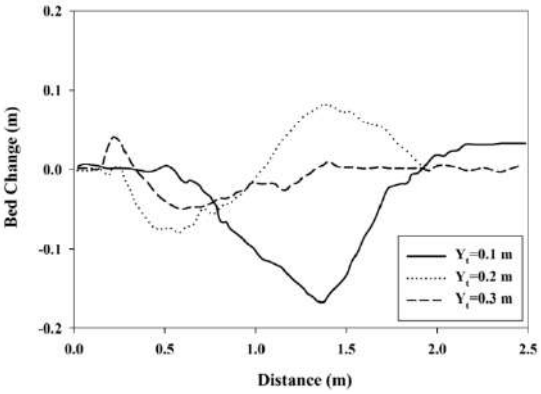

(d)

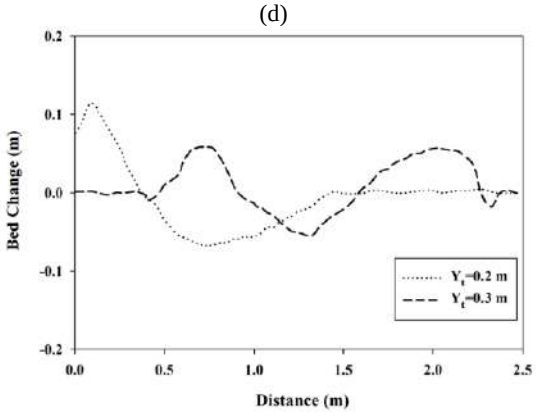

(e)

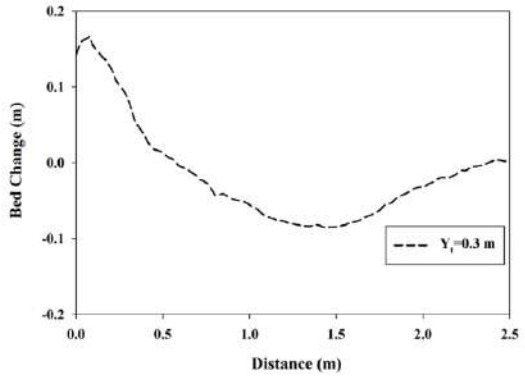

(f)

Figure 2. Variations in the longitudinal profile of the bed at different downstream depths of (a) 5 lit/s, (b) 10 lit/s, (c) 15 lit/s, (d) 20 lit/s, (e) 25 lit/s, and (f) 30 lit/s

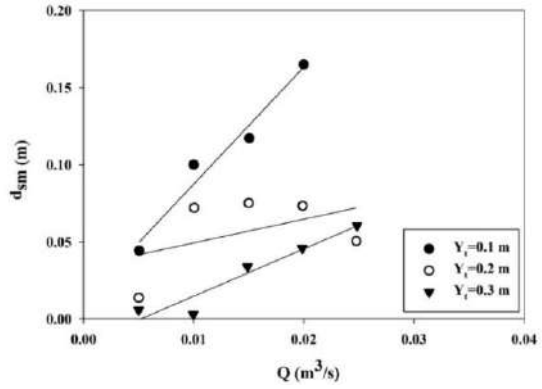

(a)

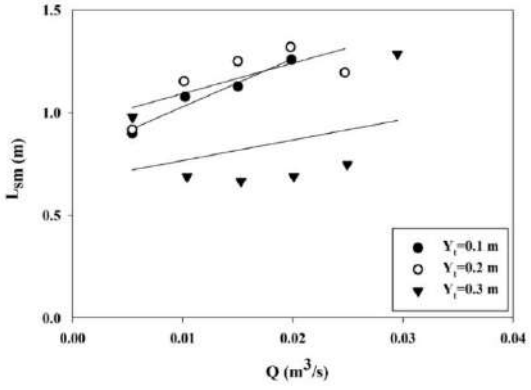

(b)

Figure 3. Variations in: (a) the maximum depth of the scour hole; and (b) the distance of the maximum scour from bucket lip (L_{sm}) at different flow rates

Figures 3(a) and 3(b) present the longitudinal profile of the bed for different discharges and tail water depths. As shown in Figure 3(a), increasing the depth of tail water (Y_t) will reduce the depth of scour (d_{sm}). Also, Figure 3(b) shows that increasing the flow discharge (Q) will increase the distance of the maximum scour from bucket lip (L_{sm}). Increasing the flow discharge (Q) will increase the jet velocity and cause the jet to hit the bed farther away.

Moreover, at the downstream depths (Y_t) of 0.2 and 0.3 m, the stack was formed by the scouring upstream of the hole, and at a depth of 0.1 m, this stack was transferred to the area after the scour hole. This could be explained by the fact that at downstream depths of 0.2 and 0.3 m, the rolling flow moved from the bottomupwards in the opposite direction of the water flow and sequestrated the sediments upstream. By reducing the depth to 0.1 m, the rolling flow containing suspended sediments was transmitted downstream by the inlet jet due to the high flow rate, and the sequestration occurred at the bottom of the hole by reducing the speed of the inlet jet.

Variations in the normalized scour depth d_{sm}/Y_t with the densimetric particle Froude number (F_g) are shown in Figure 4(a). The results showed that as the densimetric particle Froude number increased and the depth declined, the water pad had a low ability under the jet's dynamic force, and the amount of erosion rose. Besides, L_{sm}/Y_t variations versus the Froude number of the particle (F_g) are shown in Figure 4(b). According to the figure, the distance of the maximum scour from bucket lip expands with the increase in the Froude number.

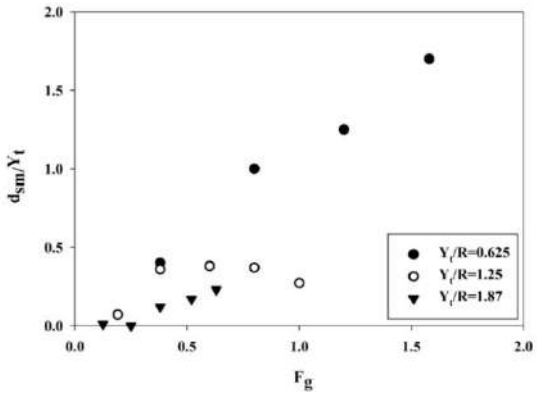

(a)

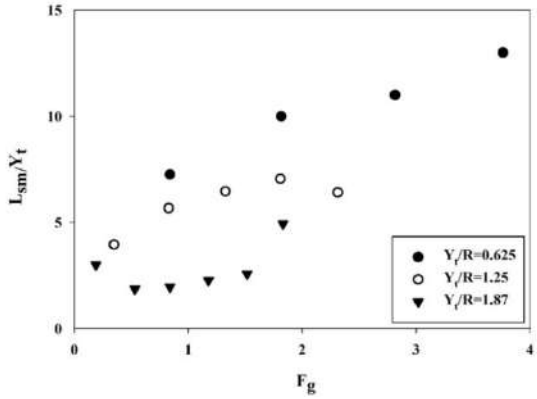

(b)

Figure 4. Variations in (a) d_{sm}/Y_t; and (b) relative to the particle's Froude number

In this study, the above-mentioned dimensionless groups of parameters were related to each other based on non-linear regression (SPSS 22 software). This yielded the following equations for estimating the maximum depth of scour, the maximum scour width, and the distance of the maximum scour location, respectively.
This relation is derived to predict the maximum scour depth and the distance of the maximum scour from bucket lip (L_{sm}), and to compare the results with previous investigations (Equations (4) and (5)):

$$\frac{d_{sm}}{Y_t} = 0.12(F_g)^{0.8}(\frac{H}{Y_t})^{1.12} \quad (4)$$

$$\frac{L_{sm}}{Y_t} = 2.7(F_g)^{0.37}(\frac{H}{Y_t})^{0.69} \quad (5)$$

Figures 5(a) and 5(b) present the experimental and calculated normalized scour depths d_{sm}/Y_t derived using Equations (4) and (5) relative to the 45° line. A comparison of the results showed that despite the complexity of the scouring phenomenon, the relations had good accuracy for predicting these parameters in the flip bucket jet structure. The coefficient of determination R^2 and the minimum root-mean-square error (RMSE) were 0.97 and 0.8, respectively, for Equation (4), while these values were 0.94 and 0.8 for Equation (5), respectively.

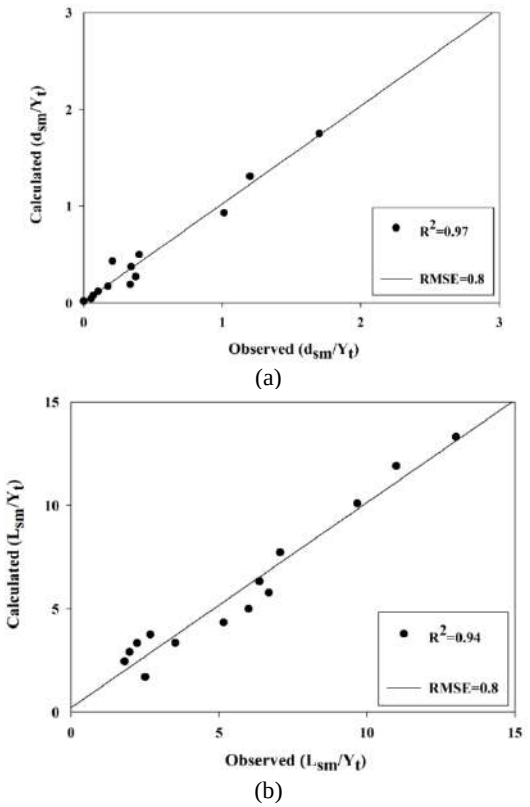

Figure 5. A comparison of experimental and regression model results (a) Equation (4), and (b) Equation (5)

In Figure 6(a), the linear regression fit was made between the experimental values and the calculated values presented for the dimensionless parameter $\frac{d_{sm}}{Y_t}$ (Equation (4)), so that the correlation coefficient R^2 and the regression line slope α equaled 0.97 and 1.01, respectively, which suggested a very good performance of the relationship. Moreover, in Figure 6(b), the same comparison was made for Equation (5), so that the correlation coefficient R^2 and regression line slope α equaled 0.93 and 0.98, respectively, which also showed that the relationship had a good performance.

To evaluate the presented relations (Table 2), the results of this study were compared with the relationships provided by other studies in Figure 7. Azmathullah et al. [33] proposed the equations below for the evaluation of the maximum depth of scour and the distance between the hole and the structure (Equations (6) and (7)):

$$\frac{d_s}{Y_t} = 6.914\left(\frac{q}{\sqrt{gY_t^3}}\right)^{0.694}\left(\frac{H}{Y_t}\right)^{0.0815}\left(\frac{R}{Y_t}\right)^{-0.233}\left(\frac{d_{50}}{Y_t}\right)^{0.196}\theta^{0.196} \quad (6)$$

$$\frac{d_s}{Y_t} = 9.85\left(\frac{q}{\sqrt{gY_t^3}}\right)^{0.42}\left(\frac{H}{Y_t}\right)^{0.28}\left(\frac{R}{Y_t}\right)^{0.043}\left(\frac{d_{50}}{Y_t}\right)^{0.037}\theta^{0.346} \quad (7)$$

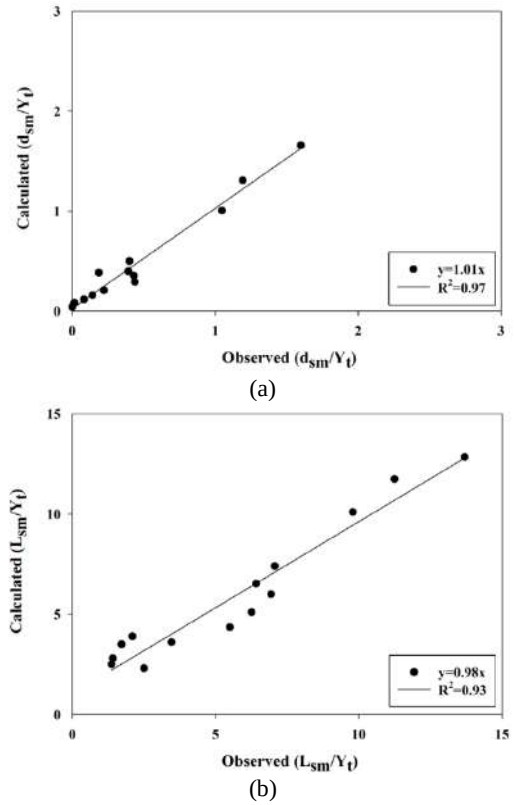

Figure 6. Regression fit of experimental and calculated results (a): Relative scour depth (d_{sm}/Y_t), and (b): Relative distance of the maximum scour from bucket lip (L_{sm}/Y_t)

where H represents the head between the upper (reservoir) water level and the tailwater level, and R is the radius of the bucket. Besides, Naghikhani et al. [38] suggested similar relationships for estimating the scour hole depth and its distance from the structure using the granular computing method as Equations (8) and (9):

$$\frac{d_s}{Y_t}=1.94+0.389\left(\frac{q}{\sqrt{gY_t^3}}\right)-19.414\left(\frac{d_{50}}{Y_t}\right)-0.504\left(\frac{R}{Y_t}\right) \quad (8)$$

$$\frac{d_s}{Y_t}=3.117+0.21\left(\frac{q}{\sqrt{gY_t^3}}\right)+0.904\left(\frac{H}{Y_t}\right) \quad (9)$$

Figure 8 shows the comparison of the experimental results with previous studies, including those of Mason [39], Sofrelec [40], Jaeger [41], and Yen [42]. As shown in Figure 8, the proposed relationship of the present study is in very good agreement with previous relationships. Also, the regression coefficient (R^2) of the proposed relationship is higher than previous relationships and increases the accuracy of predicting the depth of scour.

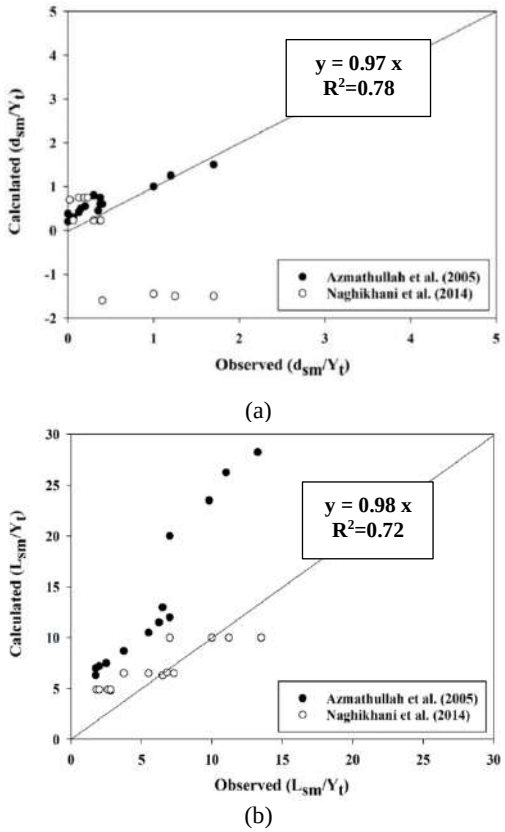

Figure 7. A comparison of experimental results with equations provided by previous researchers (**a**): scour depth, and (**b**): distance of the maximum scour from bucket lip (the reason for the significant differences is the different experiment conditions of Azmathullah et al. [33] and Naghikhani et al. [38]

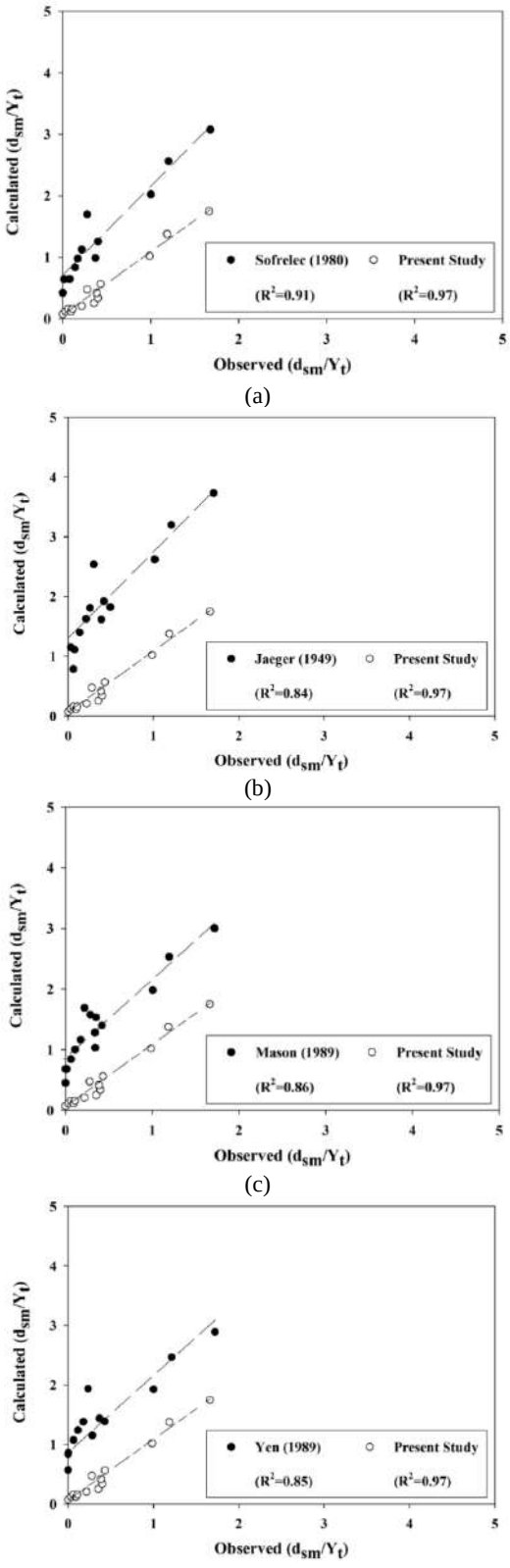

Figure 8. A comparison of experimental and calculated values of the dimensionless parameter d_{sm}/Y_t in previous studies; (**a**) Sofrelec [40], (**b**) Jaeger [41], (**c**) Mason [39], and (**d**) Yen [42]

3. 2. Comparison and Analysis of Empirical Formulas for Scour Depth Because the most important parameters of scouring are q, H, Y_t and the bed materials size (d_{50}) for d_{sm} estimation, the generalized form can be shown as Equation (10):

$$d_{sm}/Y_t = k\frac{q^{\alpha}H^{\beta}}{Y_t d_{50}^{\gamma}} \quad (10)$$

where k (an experimental value) is a multiplication constant, while α, β, and γ are exponential constants. Table 3 provides a list of these constants matching various scour depth estimation formulas. It is noteworthy that the values of k fall into a wide range between 0.36 and 3.27, while α values vary over a much shorter range of 0.45 and 0.7; β between 0.05 and 0.5; and γ between 0.062 and 0.32, which means k variation can result in a wide range of values for ds with different formulas applied (Table 3) [38-44].

Table 3 presents the formula which were employed to predict d_{sm} matching different experimental data including q, H, d_{50}, and Y_2 as reported in previous studies. Then, as also illustrated in Figures 9 and 10, the d_{sm} calculated through this list was compared to the empirical ds. There is a linear relationship between the estimated depth obtained from experimental formulas and the scour depth collected in the laboratory, as shown in Equation (11).

$$\text{Estimated depth with empirical formulae } (d_{sm}) = (\Gamma) \times \text{observed depth in the experiment } (d_{sm}) \quad (11)$$

As shown by the constant Γ values provided in Table 4, the experimental formulas accurately predict the scour depth. Table 4 presents a summary of such values with the aim of estimating the scour depth according to experimental data.

TABLE 3. Coefficients for sediment scour prediction formulas

No. of Eq.	Author (Year)	k	α	β	γ
1	Schoklitsch [25]	0.52	0.57	0.20	0.32
2	Hartung [43]	1.4	0.64	0.36	0
3	Martins [31]	1.5	0.6	0.42	0.1
4	Mason [39]	3.27	0.6	0.05	0.3
5	Ervine et al. [44]	0.36	0.55	0.5	0
6	Castillo [45]	2.2	0.65	0.2	0.06
7	Melo et al. [46]	1.67	0.7	0.2	0.1
8	Federspiel [47]	1.5	0.6	0.1	0
9	Castillo and Carrillo [48]	0.63	0.45	0.25	0.12
10	Fiorotto et al.[49]	2.3	0.6	0.1	0.24

When Γ approaches unity, the estimation is considered accurate. If such a value is smaller or greater than 1, underestimation and overestimation occur respectively. These figures along with Table 4 refer to the fact that none of the equations produced a perfect prediction for d_{sm} with the exception of Federspiel [47]. Equations such as Schoklitsch [25], and Hartung [43] exhibited over prediction of d_{sm}; whereas, equations such as Martins [31], Mason [39], Ervine et al. [44] and Castillo [45] underpredicted d_{sm}. With a more careful investigation into the results, it is concluded that most overestimated equations produce great values ($k > 1.5$). For $k < 1$, the values are mostly underpredicted. For Federspiel [47] and Fiorotto et al. [49] formulas, $1 < k < 1.5$, d_{sm} prediction is better than other relations. It can be further noted that there is not much influence of exponential parameters of Equation (9) [38-44].

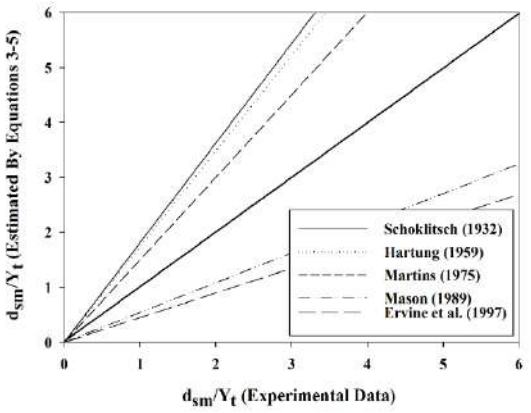

Figure 9. Estimates with empirical formula and the observed sediment scour depth according to laboratory data using Equations (1) to (5) listed in Table 3

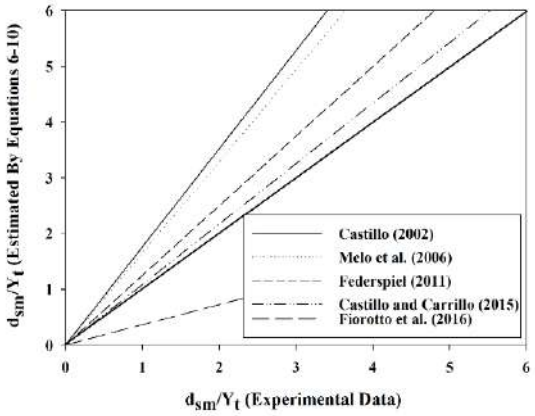

Figure 10. Estimates with empirical formula and the observed sediment scour depth according to laboratory data using Equations (5) to (10) in Table 3.

TABLE 4. Summary of Γ values for sediment scour depth prediction according to experimental data

No. of Eq.	Author (Year)	Γ	*Remark*
1	Schoklitsch [25]	1.78	overprediction
2	Hartung [43]	1.43	overprediction
3	Martins [31]	0.56	underprediction
4	Mason [39]	0.48	underprediction
5	Ervine et al. [44]	0.32	underprediction
6	Castillo [45]	1.75	overprediction
7	Melo [46]	1.82	overprediction
8	Federspiel et al. [47]	1.10	Best prediction
9	Castillo and Carrillo [48]	0.38	underprediction
10	Fiorotto et al. [49]	1.3	overprediction

3. 3. Evaluation of the Effect of Particle Size on Ski Jump Scour To be more comprehensibly stated, it is anticipated that an increase in the velocity of the jet flow and the density of fluid increases the depth of the sediment scour hole. To the contrary, it is expected that addition of density and size of the particle distribution materials decreases the scour depth. Experiments carried out on prototypes demonstrated that air entrainment into the fluid reduces the scour depth under the same flow conditions [45]. There is a simple physical interpretation of these phenomena. The specific weight of the aerated flow is less than that of the non-aerated flow. Mason and Arumugam [8] showed that the angle of jet impinging on the stilling basin is a function of the bucket lip angle (θ) and jet velocity (V_t) and thus, the parameter (ϑ) can be removed from the dimensional analysis list (Equation (3)). Due to the fact that the analysis on the results of scour depth values was performed under the scour hole equilibrium, the time parameter (t') is also removed from the dimensional analysis. According to Chanson [34] and Pagliara et al. [17] studies, the jet flow leaving the ski jump will be a fully developed flow (Tu: Turbulence intensity) controlled by the Reynolds and Froude numbers, and this parameter can be removed from the dimensional analysis. Yamini et al. [50, 51] and Chanson et al. [34] suggested that in order to minimize the scale effects in a two-phased air water flow in a turbulent flow such as a jet, it is required that the Weber number and Reynolds number be greater than Re = 10^5 and We = 32, respectively, which has been controlled and verified in these experiments (Table 2). Accordingly, Equation (12) can be summarized as follows:

$$\frac{d_s}{d_{50}} = f(Re, F_g, \theta, D') \quad (12)$$

By using the experimental model, attempts have been made to confirm Equation (12) using the changes in bed material. Thus, according to Table 5, the specifications of bed materials are evaluated in the laboratory model in the following three cases. With the aim of confirming the assumptions given in Equation (12), the relative depth of scouring versus the variation of the squared densimetric particle Froude number (F_g^2) are plotted based on the experimental model results. The dependence between the parameters of relative depth variations and the densimetric particle Froude number is evident in Figure 11.

By performing multivariate regression on different experimental conditions using the Sigmaplot software, the following equation is obtained with the regression coefficient R^2 = 0.89, which is presented in Equation (13):

$$\frac{d_s}{d_{50}} = \frac{0.08 \cdot (Re)^{0.227} \cdot (F_g^2) \cdot \sin\theta}{D'} \quad (13)$$

For comparison of the present relation with other relations in this context, it should be noted that in most relations, not all parameters of dimensional analysis are involved in the relations. Accordingly, the multivariate regression was repeated using the experimental model data, and due to the smaller effect, the parameters of bucket lip angle and sediment density are not involved in this relation. Figure 12 is presented to compare the experimental data with other previous studies. This diagram is based on the data from individuals such as

TABLE 5. Type of the sand materials employed in the experimental investigation

Type of Sand (1)	Type of Sand (2)	Type of Sand (3)
$D_{50} = 2.31 \times 10^{-3}\ m$	$D_{50} = 5.42 \times 10^{-3}\ m$	$D_{50} = 7.57 \times 10^{-3}\ m$
$D_{85} = 3.25 \times 10^{-3}\ m$	$D_{85} = 6.83 \times 10^{-3}\ m$	$D_{85} = 8.87 \times 10^{-3}\ m$
$D_{90} = 3.64 \times 10^{-3}\ m$	$D_{90} = 7.23 \times 10^{-3}\ m$	$D_{90} = 9.24 \times 10^{-3}\ m$
$\rho_s = 2.70\ kg/m^3$	$\rho_s = 2.70\ kg/m^3$	$\rho_s = 2.70\ kg/m^3$
$D' = 1.78$	$D' = 1.32$	$D' = 1.19$

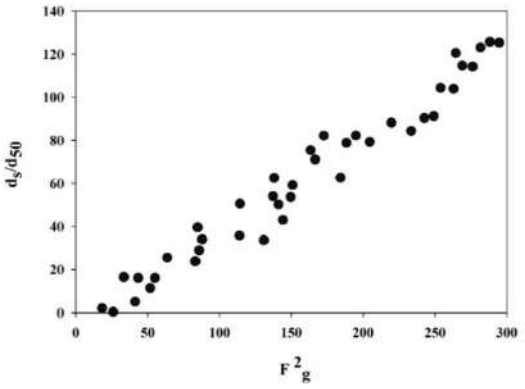

Figure 11. Normalized scour depths vs. F_g^2

Azmathullah et al. [33], Movahedi et al. [22], Amanian and Urroz [9], and Castillo and Carrillo [48]. Accordingly, the simpler regression relation is presented as Equation (14):

$$\frac{d_s}{d_{50}} = 0.23 \cdot (Re)^{0.048} \cdot (F_g^2) \quad (14)$$

In this case, the regression coefficient is $R^2 = 0.92$, which is a relatively high coefficient. In order to compare the relation presented in this study with relations provided by other researchers for estimating the scour values due to the jet impingement on the bed of the stilling basin, the mean relative absolute error is considered based on Equation (15):

$$MARE = \frac{1}{n}\sum_{i=1}^{n}\left(\frac{\left|(d_s)_{calculated} - (d_s)_{empirical}\right|}{(d_s)_{calculated}}\right) \quad (15)$$

According to Equation (15), parameters (n) are the numbers of laboratory observations and the parameters $(ds)calculated$, and $(ds)empirical$ are the computational and measurement values of the scour depth, respectively. The proposed relation based on laboratory studies has MARE of about 34.2%, while the studies by Azmathullah et al. [33] and Amanian and Urroz [9] have an error of 38.2% and 72.9%, respectively. It should be noted that the present relations have two input variables, while their relations have four input variables. Other relations presented in the table have a relative absolute error of more than 100%. Using the relation presented in the range of Reynolds and Weber numbers, acceptable results can be predicted for the bed sediments over a relatively large range (see Figure 13).

The proposed relation based on laboratory studies has MARE of about 34.2%, while the studies by Azmathullah et al. [33] and Amanian and Urroz [9] have an error of 38.2% and 72.9%, respectively.

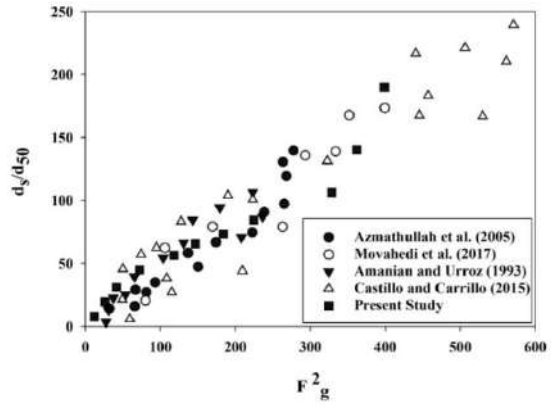

Figure 12. The depth of scour ($\frac{d_s}{d_{50}}$) normalized as a function of (F_g^2) with different Reynolds numbers (Re). Source: Azmathullah et al. [33], Movahedi et al. [22], Amanian and Urroz [9], Castillo and Carrillo [48], and the present work

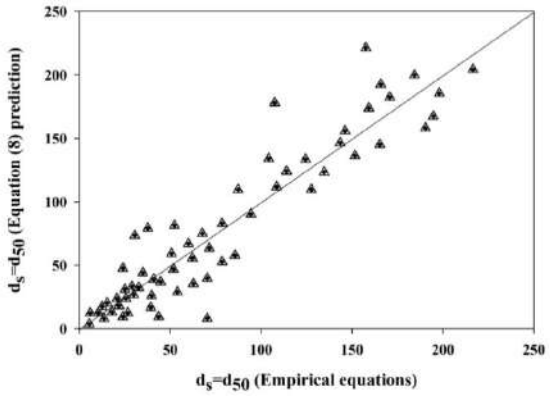

Figure 13. Equation (14) estimation of capacity by applying the data measurements obtained from the present work, Azmathullah et al. [33], Movahedi et al. [22], Amanian and Urroz [9], and Castillo and Carrillo [48], and comparing it with the line of 100% agreement

4. CONCLUSION

The main purpose of this study is to exhibit all the established research works on the implementation of empirical formulations models for multiple scouring depths modeling such as ski jump, flip bucket, and spillway structures. It presents an extensive review on the state of the art research studies on the scour depth phenomena with a specific focus on the most recent and basic implementation of models of experimental formulas as well as references to every experimental laboratory study carried out.

The results of experimental models show that, at the downstream depths (Y_t) of 0.2 and 0.3 m, the stack was formed by the scouring upstream of the hole, and at a depth of 0.1 m, this stack was transferred to the area after the scour hole. This could be explained by the fact that at downstream depths of 0.2 and 0.3 m, the rolling flow moved from the bottom upwards in the opposite direction of the water flow and sequestrated the sediments upstream. By reducing the depth to 0.1 m, the rolling flow containing suspended sediments was transmitted downstream by the inlet jet due to the high flow rate, and the sequestration occurred at the bottom of the hole by reducing the speed of the inlet jet.

According to Equation $MARE = \frac{1}{n}\sum_{i=1}^{n}\left(\frac{\left|(d_s)_{calculated} - (d_s)_{empirical}\right|}{(d_s)_{calculated}}\right)$, parameters n are the numbers of laboratory observations and the parameters $(ds)_{Calculated}$, and $(ds)_{empirical}$ are the computational and measurement values of the scour depth, respectively.

Most of the energy distributed by the flip buckets system is found at the impact point of the jet and the tail water and riverbed. Such an impact means enough force, which changes the riverbed topography even in spite of hard rock materials included in the bed. Hence, implementation of flip buckets must only be advised in

case the bed scour, because of the impacting jet, does not have an adverse influence on the dam and other structures such as the flip bucket, or has no harms to the environment. The equation presented in the study is different from the existing empirical equations since it also involves (Fr^2), which physically means that Fr_d^2 has a direct relationship with hydrodynamic forces leading to scour; whereas, it has an indirect relationship with scour-resistant forces. Therefore, the conclusion is that the scour process is under the influence of the force on the bed materials entrained in the jet flow. This force is related to the velocity squared but is reversely related to the density on a linear basis. Thus, this approach physically justifies the sediment scour process in 3 phases of "water, air, and soil".

5. REFERENCES

1. Aminoroayaie Yamini, O., S. Hooman Mousavi, M. R. Kavianpour, and Azin Movahedi. "Numerical Modeling of Sediment Scouring Phenomenon around the Offshore Wind Turbine Pile in Marine Environment." ***Environmental Earth Sciences*** Vol. 77, No. 23, (2018), 776-787, Doi: 10.1007/s12665-018-7967-4.
2. Ekeleme, Anthony Chibuzo, and Jonah C. Agunwamba. "Experimental Determination of Dispersion Coefficient in Soil." ***Emerging Science Journal***, Vol.2, No. 4, (2018), 213-218.
3. Ghorbani, Mortaza Ali, Majid Pasbani Khiavi, and Parya Ahmadi. "Investigation of Nonlinear Behavior of Concrete on Seismic Performance of an Arch Dam Using Finite Element Method." ***Civil Engineering Journal***, Vol 2, No. 6, (2016), 295-305. doi:10.28991/cej-2016-00000034.
4. Emeka, Arinze Emmanuel, Agunwamba Jonah Chukwuemeka, and Mama Benjamin.Okwudili. "Deformation Behaviour of Erodible Soil Stabilized with Cement and Quarry Dust." ***Emerging Science Journal,*** Vol 2, No. 6, (2018), 383. Doi: 10.28991/esj-2018-01157
5. Ghodsi, Habibeh, and Ali Asghar Beheshti. "Evaluation of Harmony Search Optimization to Predict Local Scour Depth around Complex Bridge Piers." ***Civil Engineering Journal***, Vol 4, No. 2, (2018), 402-412. Doi: 10.28991/cej-0309100.
6. Bormann, N. E. and Julien, P. Y. Scour Downstream of Grade-Control Structures. ***Journal of Hydraulic Engineering***, ASCE, Vol 131, No. 10, (1991), 898-908.
7. Jafari, Seyed Reza, and Majid Pasbani Khiavi. "Parametric Study of the Modal Behavior of Concrete Gravity Dam by Using Finite Element Method." ***Civil Engineering Journal,*** Vol 5, No. 12 (2019), 2614-2625. doi:10.28991/cej-2019-03091437.
8. Mason, P.J. and Arumugan, K., Free jet scour below dams and flip bucket, ***Journal of Hydraulic Engineering***, ASCE, Vol. 111, (1985). 220-235. Doi: 10.1061/(asce)0733-9429(1985)111:2(220)
9. Amanian, N. and Urroz, G. E.. Design of Pre-excavated Scour Hole Below Flip-bucket Spillways. Proceedings of the 1993 ASCE National Conference on Hydraulic Engineering, San Francisco, (1993), 856-860.
10. Stein, O. R., P. Y. Julien, and C. V. Alonso. "Mechanics of jet scour downstream of a headcut." ***Journal of Hydraulic Research,*** Vol 31, No. 6, (1993), 723-738. Doi: 10.1080/00221689309498814
11. Al-Ani, Rami Raad Ahmed, and Basim Hussein Khudair Al-Obaidi. "Prediction of Sediment Accumulation Model for Trunk Sewer Using Multiple Linear Regression and Neural Network Techniques." ***Civil Engineering Journal***, Vol 5, No. 1, (2019), 82. Doi: 10.28991/cej-2019-03091227
12. Cordier, Clémence, Killian Guyomard, Christophe Stavrakakis, Patrick Sauvade, Franz Coelho, and Philippe Moulin. "Culture of Microalgae with Ultrafiltered Seawater: A Feasibility Study." ***SciMedicine Journal,*** Vol 2, No. 2, (2020), 56-62. doi: 10.28991/scimedj-2020-0202-2..
13. Hoffmans, G. J., and H. J. Verheij. "Scour Manual Vol. 96, (1997).
14. Khalifehei, Kamran, Gholamreza Azizyan, Mahmood Shafai-Bajestan, and Kwok-wing Chau. "Stability of A-Jack concrete block armors protecting the riverbeds." ***Ain Shams Engineering Journal,*** (2020). Doi: 10.1016/j.asej.2020.04.018.
15. Ghodsian, M., Melville, B., Coleman, S., "Scour caused by rectangular impinging jet in cohesiveless beds", Proc. Third International Conference on scour and erosion, ICSE, Nov. (2006). 1-3, Amsterdam, The Netherlands.
16. Juon, R., and W. H. Hager. Flip bucket without and with deflectors. ***Journal of Hydraulic Engineering,*** Vol 126, No. 11, (2000), 837-845. Doi: 10.1061/(asce)0733-9429(2000)126:11(837).
17. Pagliara, Stefano, Willi H. Hager, and Hans-Erwin Minor. "Plunge pool scour in prototype and laboratory." In Proc., Int. Conf. Hydraulics of Dams and River Structures, 165-172. Lisse, the Netherlands: Balkema, 2004. Doi: 10.1201/b16994-24.
18. O. A. Yamini, M. R. Kavianpour, and S. Hooman Mousavi. "Wave Run-up and Rundown on ACB Mats Under Granular and Geotextile Filters' Condition." ***Marine Georesources & Geotechnology*** Vol 36, No. 8, (2017), 895-906. doi:10.1080/1064119x.2017.1397068.
19. Movahedi, Azin, M. R. Kavianpour, and O. Aminoroayaie Yamini. "Evaluation and modeling scouring and sedimentation around downstream of large dams." ***Environmental Earth Sciences,*** Vol 77, (2018), 1-17. Doi: 10.1007/s12665-018-7487-2.
20. Khatsuria, Rajnikant M. Hydraulics of spillways and energy dissipators. CRC Press, (2004). Doi: 10.1201/9780203996980-24.
21. Zhang, S., Pang, B., & Wang, G. A new formula based on computational fluid dynamics for estimating maximum depth of scour by jets from overflow dams. ***Journal of Hydroinformatics***, (2014), Vol 16, No. 5, 1210-1226.
22. Movahedi, Azin, Mohammadreza Kavianpour, and O. A. Yamini. "Experimental and numerical analysis of the scour profile downstream of flip bucket with change in bed material size." ***ISH Journal of Hydraulic Engineering,*** (2017), 1-15. Doi: 10.1080/09715010.2017.1398111.
23. Aminoroayaie Yamini, O., S. H. Mousavi, and M. R. Kavianpour. "Experimental Investigation of Using Geo-Textile Filter Layer in Articulated Concrete Block Mattress Revetment on Coastal Embankment." ***Journal of Ocean Engineering and Marine Energy***, Vol 5, No. 2, (2019), 119-133. Doi: 10.1007/s40722-019-00133-y
24. Gamil, Yaser, Ismail Bakar, and Kemas Ahmed. "Simulation and Development of Instrumental Setup to Be Used for Cement Grouting of Sand Soil." ***Emerging Science Journal,*** Vol. 1, No. 1, (2017), Doi: 10.28991/esj-2017-01112.
25. Schoklitsch, A. "Scour downstream of falling jet." **Water**, Vol 25, No 24, 341-343, (1932).
26. Veronese, A. "Erosion de fond en aval d'une decharge." In IAHR, meeting for hydraulic works, Berlin. 1937.

27. Damle, P.M., Venkatraman, C.P., and Desai, S. C., Evaluation of scour below ski-jump buckets of spillways, CWPRS Golden Jubilee Symposia, London (1966).
28. Chee, S. P., and T. Kung. "Piletas de derrubio autoformadas." In 6th Latin American Congress of the International Association for Hydraulic Research, Bogota, Columbia, Paper D, Vol. 7. 1974.
29. Chee, S. P., and P. V. Padiyar. "The stability of blocks subjected to plunging water jets." JAWRA Journal of the American Water Resources Association 5, No. 3, (1969), 57-63.
30. Wu, C.M. (1973). Scour at Downstream End of Dams in Taiwan‖. In: International Symposium on River Mechanics, Bangkok, Thailand, Vol. I(A 13), 1-6.
31. Martins, R., 1975. Scouring of rocky riverbeds by free-jet spillways. ***Water Power Dam Const***. April (1975).
32. Incyth, L. (1982). ―Estudio sobre modelo del aliviadero de la Presa Casa de Piedra, Informe Final‖. DOH-044–03-82, Ezeiza, Argentina.
33. Azmathullah, H. M. Deo, M. C. Deolalikar, P. B. Neural Networks for Estimation of Scour Downstream of a Ski-Jump Bucket. ***Journal of Hydraulic Engineering***, ASCE, Vol 117, No. 5, (2005), 579-594. Doi: 10.1061/(asce)0733-9429(2005)131:10(898)
34. Chanson, H.and Yit-Haw T. "Physical modelling of breaking tidal bores: comparison with prototype data." ***Journal of Hydraulic Research,*** Vol 53, No. 2, (2015), 264-273. Doi: 10.1080/00221686.2014.989458
35. Theingi, Mya, Kay Thi Tun, and Nwe Nwe Aung. "Preparation, Characterization and Optical Property of $LaFeO_3$ Nanoparticles via Sol-Gel Combustion Method." ***SciMedicine Journal*** Vol 1, No. 3, (2019), 151–157, doi: 10.28991/scimedj-2019-0103-5.
36. Jalili, Mehdi, Mohmad Reza Ghasemi, and Ali Reza Pifloush. "Stiffness and Strength of Granular Soils Improved by Biological Treatment Bacteria Microbial Cements." ***Emerging Science Journal***, Vol 2, No. 4, (2018), Doi: 10.28991/esj-2018-01146.
37. Lim, S. Y., & Chin, C. O. Scour by circular wall jets with non-uniform sediments. ***Advances in hydro-science and engineering***, Vol 1 (Part B), (1993), 1989-1994.
38. Naghikhani, A., Noori, R., Sheikhian, H., Ghiasi, B., Estimation of the dimensions of the scour hole in downstream scour of flip bucket jet with granular computing model, Scientific and Research ***Journal of Hydraulic***, Vol. 9, No. 3, (2014), 45-60. Doi: 10.1007/s11269-016-1526-0.
39. Mason, P.J., Effects of air entrainment on plunge pool scour. ***Journal of Hydraulic Engineering,*** Vol 115, No. 3, (1989) 385-399. Doi: 10.1061/(asce)0733-9429(1989)115:3(385).
40. Sofrelec (1980) "Kandadji Dam, Niger, 3rd Phase Design Report," Society Frangaise d'Etudes et de Realisation d'Equipement Electriques, Paris, France, Feb., 1980.
41. Jaeger,C.(1949). Technische Hydraulik (Technical Hydraulics). Birkhiiu-ser, Basel, Switzerland (in German).
42. Yen, Ben Chie, ed. Channel flow resistance: centennial of Manning's formula. Water Resources Publication, 1989.
43. Hartung, W. Die Kolkbildung hinter Uberstromen wehren im Hinblick auf eine beweglich Sturzbettgestaltung. Die Wasser Wirtschaft, Vol. 49, No. 1, (1959) 309-313 (in German).
44. Ervine, D.A., Falvey, H.R., Whiters, W., Pressure fluctuations on Fplunge pool floors. ***Journal Hydraulic Research***. Vol 35, No. 2, (1997). Doi: 10.1080/00221689709498430
45. Castillo, L., Parametrical analysis of the ultimate scour and mean dynamic pressures at plunge pools. Workshop on Rock Scour due to High Velocity Jets (2002). École Polytechnique Fédérale de Lausanne.
46. Melo, J. F., A. N. Pinheiro, and C. M. Ramos. "Forces on plunge pool slabs: Influence of joints location and width." Journal of Hydraulic Engineering 132.1 (2006): 49-60.
47. Federspiel, Matteo Paolo Elia Antonio, E. F. R. Bollaert, and A. J. Schleiss. "Dynamic response of a rock block in a plunge pool due to asymmetrical impact of a high-velocity jet." In Proceedings of the 34th World Congress of the International Association for Hydro-Environment Research and Engineering: 33rd Hydrology and Water Resources Symposium and 10th Conference on Hydraulics in Water Engineering, p. 2404. Engineers Australia, 2011.
48. Castillo, L.G., Carrillo, J.M., Characterization of the dynamic actions and scour estimation downstream of a dam. In: Dam Protections against Overtopping and Accidental Leakage. ***CRC Press***, (2015), 231–243. Doi: 10.1201/b18292-26.
49. Fiorotto, V., Barjastehmaleki, S., Caroni, E., Stability analysis of plunge pool linings. ***Journal Hydraulic Engineering*** Vol. 10 No. 3 (2016) Doi: 10.1061/(ASCE)HY.1943-7900.0001175.
50. Yamini, O. Aminoroayaie, M. R. Kavianpour, and Azin Movahedi. "Pressure distribution on the bed of the compound flip buckets." ***The Journal of Computational Multiphase Flows,*** Vol 7, No. 3, (2015), 181-194. Doi: 10.1260/1757-482x.7.3.181
51. Yamini, O. A., Kavianpour, M. R., & Mousavi, S. H. Experimental investigation of parameters affecting the stability of articulated concrete block mattress under wave attack. ***Applied Ocean Research,*** Vol. 64, (2017), 184-202, Doi: 10.1016/j.apor.2017.03.003

Persian Abstract

چکیده

پرتابه های جامی شکل به عنوان سازه مستهلک کننده انرژی در انتهای سرریز سدهای بلند به منظور کاهش هزینه ها در مقایسه با دیگر مستهلک کننده های انرژی به کار می رود. در این مطالعه با استفاده از یک مدل آزمایشگاهی به منظور بررسی حفره آبشستگی در ناحیه پایین دست سرریزهای پرتاب کننده های جامی در آزمایشگاه هیدرولیک دانشگاه شهید چمران انجام شده است. هدف اصلی از این تحقیق شناسایی حداکثر عمق آبشستگی (d_{sm}) و فاصله حداکثر آن از لیفت سطل (L_{sm}) است که برای نیل به این هدف آزمایش های مختلف در شرایط متفاوت برنامه ریزی شده است. نتایج نشان مطالعه حاضر داد که با افزایش دبی ، حداکثر عمق آبشستگی و فاصله حفره آبشستگی از محل پرتابه دورتر خواهد شد. همچنین، با افزایش عدد فرود ذرات Fg و یا کاهش عمق ، میزان آبشستگی و حفره ایجاد شده گسترش می یابد. در این مطالعه دو رابطه تجربی برای پیش بینی حداکثر عمق آبشستگی و فاصله آن از محل سرریز با استفاده از رگرسیون چند متغیره غیرخطی ایجاد شد و صحت سنجی این رابطه با مطالعه گذشته مورد ارزیابی قرار گرفته است. بر اساس رابطه MARE ارائه شده برای نتایج مطالعه حاضر برابر با ۳٤/۲ درصد است که نشان دهنده دقیق تر بودن رابطه ارائه شده است. نتایج این مطالعه می تواند با دقت بسیار زیادی مشخصات حفره آبشستگی در پایین دست سرریزهای سدها بزرگ را برای طراحان پیش بینی نماید.

International Journal of Engineering

Journal Homepage: www.ije.ir

Investigation of Vibration Modes of Double-lap Adhesive Joints: Effect of Slot

F. Marchione*

Dipartimento di Ingegneria Civile, Edile e Architettura (DICEA), Università Politecnica delle Marche, via B. Bianche, Ancona, Italy

P A P E R I N F O

Paper history:
Received 10 May 2020
Received in revised form 11 August 2020
Accepted 26 August 2020

Keywords:
Modal Analysis Distribution
Adhesively Bonded Joints
Double-lap Joints
Adhesives
Effect of Slot

A B S T R A C T

Adhesive joints represent a viable alternative to traditional joining methods. The analysis of frequencies and modal shapes is fundamental to predict the vibrational behaviour of a structural component subjected to dynamic stress. There are numerous studies in the literature to determine the trend of stresses in the bonded region. It has been proved that the introduction of a slot in the inner adherend allows to reduce the stress concentration at the edges of the adhesive region. In this paper, the influence of imperfections in the central adherend is investigated by FEM analysis. The FE software ANSYS©19 is used for the modal analysis of the double lap adhesive joints and the first five modes are considered. The results show the influence of Young's modulus and density ratio on the natural frequencies, varying with the material. Moreover, the introduction of the imperfection is found to influence the vibrational behavior as the frequency increases. It is also observed that the mass reduction due to the introduction of the crack does not change the shape and modal frequency for the most significant modes, while it causes more important changes for the last vibrational mode. Therefore the introduction of the crack does not significantly change the dynamic behaviour of the joint and allows to realize a more even distribution of stresses, reducing the stress peaks values.

***doi**: 10.5829/ije.2020.33.10a.10*

NOMENCLATURE

EPX	Epoxy Adhesive	T0	Perfect inner adherend configuration
Tslot	Slot thickness	T1	1 mm thick slot configuration
Et	Young Modulus in tension	T2	2 mm thick slot configuration
ρ	Density	T3	3 mm thick slot configuration
$\boldsymbol{\nu}$	Poisson ratio	DLJ	Double-Lap joint
EPX	Epoxy Adhesive	T0	Perfect inner adherend configuration

1. INTRODUCTION

The use of structural adhesives has increased considerably in the field of civil engineering. Adhesive joining offers numerous advantages, including the possibility of joining different materials, reducing overall weight, uniform stress distribution, sealing capacity, and vibration dampening [1-7]. Adhesive joints find widespread applications in various industrial fields. The reliability of adhesive type joints depends on an accurate analysis of the mechanical properties as well as on the design, materials, and production methods [8-10]. Some of the best-known types of adhesive type joints are represented by the following: Single-Lap Joints (SLJ), Double-Lap Joints (DLJ), Strap Joints (SJ), Double-Strap Joints (DSJ), Scarf Joints (ScJ), single-L joints, T-joints and T-peel joints [11]. Among these types, the most used to experimentally evaluate mechanical performance are Lap Joints [12, 13]. For a correct design of adhesive joints, a thorough knowledge of both static and and dynamic characteristics is necessary to determine the correct distribution of stresses, as is the case in recent research developments [14]. Numerous studies have been carried out by performing dynamic analyses on both theoretical and FEM joints.

*Corresponding Author Institutional Email: *f.marchione@pm.univpm.it* (F. Marchione)

Please cite this article as: F. Marchione, Investigation of Vibration Modes of Double-lap Adhesive Joints: Effect of Slot, International Journal of Engineering (IJE), IJE TRANSACTIONS A: Basics Vol. 33, No. 10, (October 2020) 1917-1923

To determine the free vibrations in adhesive joints, double lap joints are the most widely used due to their simple geometry. Miles and Reinhall [15] studied a model for the vibration behavior of a layered beam considering both the effects of shear and thinning of the adhesive layer. Ko et al. [16], Lin et al. [17] used FEM analysis to determine the free vibration behavior of adhesive joints. Saito and Tani [18] studied the natural frequencies and loss factors of adhesive joints subjected to both longitudinal and transverse coupled vibrations. Praveen and Reddy [19] studied the dynamic response of functionally classified ceramic-metal plates taking into account transverse shear deformations, rotational inertia, and moderately large rotations in the direction of von Karman. Loy et al. [20] studied the free vibration of functionally classified (St-Ni) cylindrical shells and the influence of constituent volume fractions on natural frequencies. Hamdan [21] investigated the effects of non-dimensional geometric parameters on stress concentration factors (SCFs) of circular hollow section CHS brace-to-H-shaped section T-connections under axial compression. The results showed that SCFs in the brace and chord increases. Ettefagh et al. [22] tested a flexible joint via explicit model predictive control method. First, the equations are derived and linearized, then the algorithm is applied. The results confirmed that the method was able to control the vibrations of the flexible joint. Balamuralikrishnan et al. [23] assessed the behaviour of beam-column joint reinforced with GFRP reinforcements using the FEA analysis. The experimental results obtained are compared with the analytical ones for both the beam-column joints reinforced with steel and GFRP reinforcements. Döner [24] studied the corrosion behavior of bare titanium and titanium dioxide. The main result showed that higher polarization resistance was obtained on porous TiO_2 than that of bare titanium.

The aim of this research is to optimize the use of materials in the field of civil engineering, in particular in the field of structural adhesives. As mentioned above, the introduction of imperfections in the joint is able to even out the stresses distribution in the bonding region.

For a proper design it is also necessary to consider the vibrational behaviour of a structure. Therefore, the effect of imperfections on the oscillations of the structure is analysed in detail. In this paper, a numerical investigation of the influence of geometrical adherends' imperfections on the free torsional vibration of double lap adhesive joints is presented and discussed. Different materials–among the most representative in structural adhesive applications–are considered. In particular, the effect of a slot introduction, as shown in Figure 1, in the middle adherend is analysed. In the following, the results obtained and the comparison with perfect middle adherend are shown and discussed. The numerical analysis are carried out with FE method using the ANSYS©19 commercial software. The flowchart shown in Figure 2 summarizes the research program which is discussed in the following.

2. PROBLEM STATEMENT

The free oscillation of a structural system is evidence of its mechanical oscillatory behavior. The harmonic motion of a system is the result of the cyclic interchange of kinetic and potential energies between the components of the system itself. To guarantee a high level of structural performance compared to the demand for external actions, an accurate design phase of the

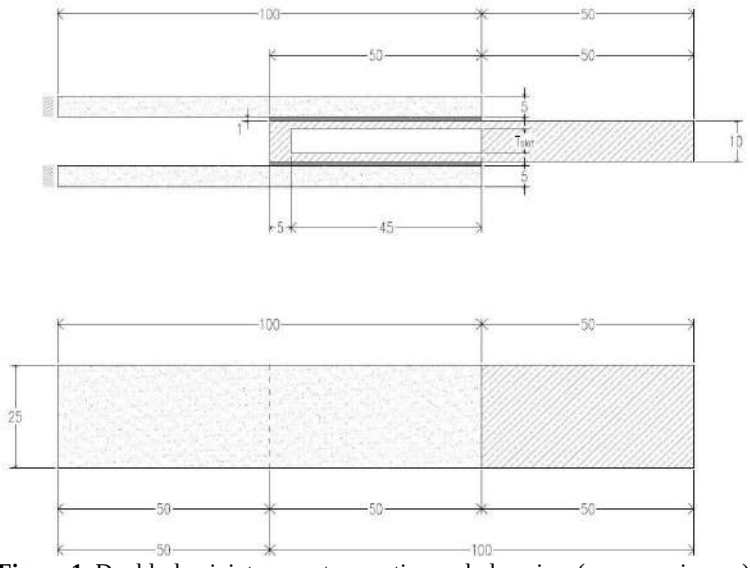

Figure 1. Double-lap joint geometry: section and plan view (measures in mm)

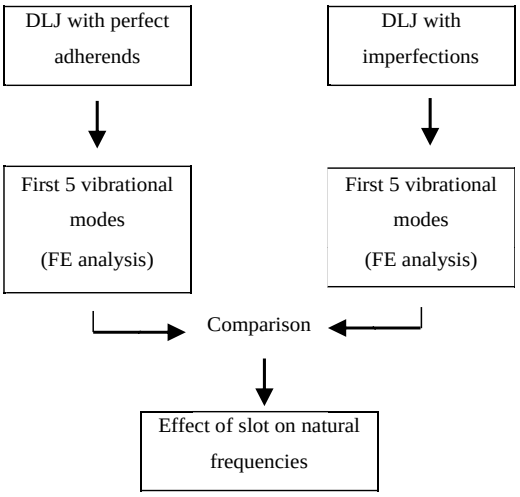

Figure 2. Research methodology

structural elements is necessary. For this purpose it is necessary to consider and predict the oscillatory behavior of a structural element. A generic structural element if not subject to external damping, when subjected to an initial disturbance, will tend to perpetuate its oscillation according to its own frequency while maintaining a particular geometric shape. This is the "natural frequency" of the system, and its shape is called a "modal shape". The object of modal analysis mainly concerns the determination of the natural frequencies and modal forms of a dynamic system. Once the modes are determined, they could be used in understanding the dynamic nature of systems, and in design and control.

In the case of adhesive joints, due to the involvement of geometrical, mechanical characteristics, it is difficult to determine the correct mechanical behavior of the joint. Several studies have been carried out regarding the stress distribution. Chen and Cheng [25] analyzed the stress distribution in a ScJ junction. The butt joint analysed is treated as a special case. Cheng et al. [26] analyzed the case of joints with different adhesive layers. In Lin and Lin's paper [17] a finite element model for stress analysis in the adhesive of a single lap joint is presented. Many studies in literature have proposed different methods in order to increase the joint structural efficiency. This is obtained by reducing the normal and shear stresses concentration by changing the geometry of the adhesives and of the aderends. The effects of tapering adherends were investigated by Sancaktar and Nirantar [27]. Hou et al. [28] have shown that the insertion of a defect in the internal adhesion of a double lap type joint led to a reduction of the stress peaks recorded at the edges of the adhesive region while reducing the overall weight of the joint.

In this paper the dynamic behavior of a DLJ is investigated, using an epoxy adhesive with both normal and cracked adherends, considering the geometries considered in literature [28]. The geometry is shown in Figure 1. The models analyzed are labelled as follows: T0-T1-T2-T3, where 0, 1, 2, 3 indicate the dimension in height (in mm) of the slot in the middle adherend, respectively. The joints are made of outer glass adherends and inner ones made of aluminum, GFRP, or S235JR steel.

Tables 1 and 2 summarize the mechanical parameters of the materials considered.

3. MODAL ANALYSIS

Adhesive joints find many applications. In some of these (e.g. naval or aeronautical applications) the vibrating component is fundamental in evaluating their mechanical performance. Modal analysis makes it possible to determine the vibration characteristics of structural components.

4. RESULTS AND DISCUSSION

This section reports on the modal dynamic analysis of the double-lap epoxy adhesive joints illustrated in

TABLE 1. Materials' characteristics for the FEA model

Glass		
E_t [GPa]	ρ [N/m^3]	$\boldsymbol{\nu}$ [-]
75	27000	0.30
Aluminium[1]		
E_t [GPa]	ρ [N/m^3]	$\boldsymbol{\nu}$ [-]
69	27100	0.30
GFRP[2]		
E_t [GPa]	ρ [N/m^3]	$\boldsymbol{\nu}$ [-]
26	26300	0.30
Steel S235JR		
E_t [GPa]	ρ [N/m^3]	$\boldsymbol{\nu}$ [-]
69	78000	0.30

[1] According to EN 755-2

[2] According to ASTM D904-99.

TABLE 2. Adhesive's characteristics for the FEA model

Epoxy Adhesive		
E_t [GPa]	ρ [N/m^3]	$\boldsymbol{\nu}$ [-]
3.25	12500	0.40

section 2. Different combinations of inner and outer adherends (i.e. Aluminium-Glass, GFRP-Glass, Steel-Glass) and of slots of different sizes inside the inner adherend are considered. The modal analysis is carried out using the commercial software ANSYS©19, with the "Modal" analysis. The geometry is meshed with PLANE 182 elements, a 4-node structural solid and a maximum element size of 0.10 mm.

Figures 3 to 6 show the first five modal shapes for each combination. Table 3 summarizes the frequency value for each modal form of the T0 configuration for the number of modes considered for the different combinations. Tables 4 to 6 show the frequency value for each modal form of the T1-T3 configurations concerning the number of modes considered.

The Steel-Glass combination shows the lowest natural frequencies of any other configuration; the Aluminium-Glass combination shows the highest ones. The difference is due to the different density of the materials. In fact, the ratio between the density of Steel and Aluminum is 2.87. The ratio between the frequencies of the first mode is about 1.5, remaining almost the same for the following modes. The natural frequencies of the Aluminum-Glass and GFRP-Glass joints are almost the same for the first two modes of vibration, while there is a deviation for the remaining modes, especially modes 3 and 5. In particular, the T1 configuration sees the greatest amount in terms of frequency in 4th mode for the GFRP-Glass combination.

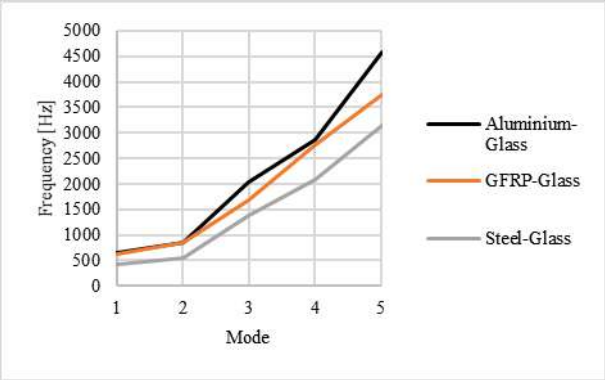

Figure 3. T0 DLJ modal analysis

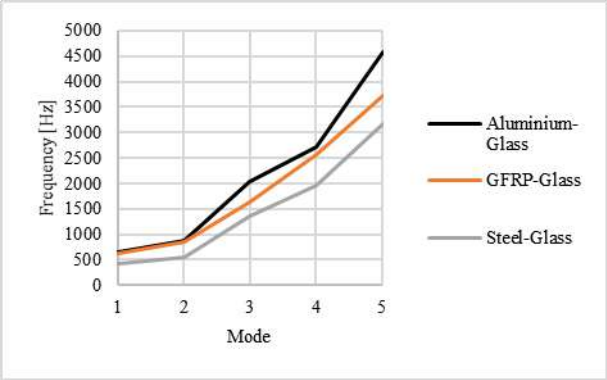

Figure 4. T1 DLJ modal analysis

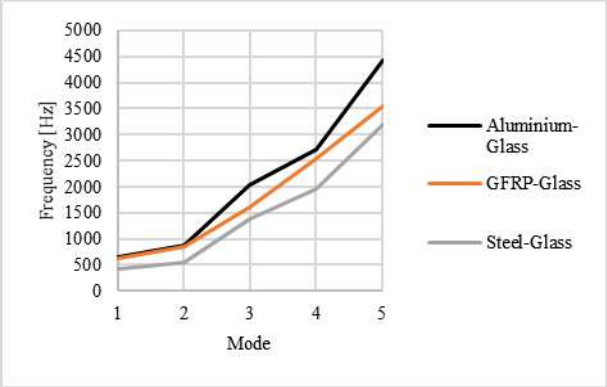

Figure 5. T2 DLJ modal analysis

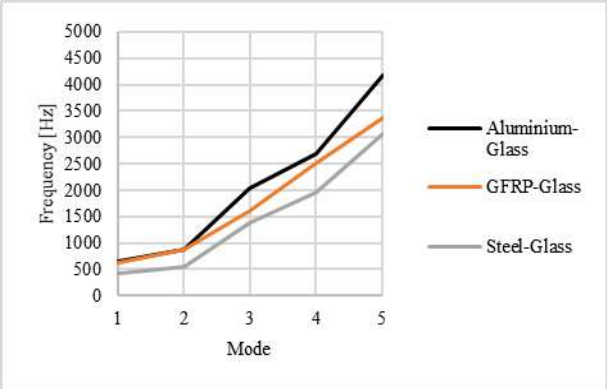

Figure 6. T3 DLJ modal analysis

TABLE 3. Modal frequencies for T0 configuration

Materials	f_1 **[Hz]**	f_2 **[Hz]**	f_3 **[Hz]**	f_4 **[Hz]**	f_5 **[Hz]**
Aluminium – Glass	641.81	861.51	2046.50	2863.30	4589.50
GFRP – Glass	633.02	855.43	1681.00	2759.10	3739.80
Steel - Glass	421.53	540.62	1373.90	2086.60	3151.20

TABLE 4. Modal frequencies for T1 configuration

Materials	f_1 [Hz]	$\Delta f_1/f^{T0}{}_1$ [%]	f_2 [Hz]	$\Delta f_2/f^{T0}{}_2$ [%]	f_3 [Hz]	$\Delta f_3/f^{T0}{}_3$ [%]	f_4 [Hz]	$\Delta f_4/f^{T0}{}_4$ [%]	f_5 [Hz]	$\Delta f_5/f^{T0}{}_5$ [%]
Aluminium Glass	641.55	0.04	866.93	-0.63	2034.00	0.61	2721.30	4.96	4574.70	0.32
GFRP Glass	622.81	1.61	859.44	-0.47	1633.60	2.82	2566.80	6.97	3723.70	0.43
Steel Glass	422.51	-0.23	544.30	-0.68	1364.30	0.70	1973.50	5.42	3165.70	-0.46

TABLE 5. Modal frequencies for T2 configuration

Materials	f_1 [Hz]	$\Delta f_1/f^{T0}{}_1$ [%]	f_2 [Hz]	$\Delta f_2/f^{T0}{}_2$ [%]	f_3 [Hz]	$\Delta f_3/f^{T0}{}_3$ [%]	f_4 [Hz]	$\Delta f_4/f^{T0}{}_4$ [%]	f_5 [Hz]	$\Delta f_5/f^{T0}{}_5$ [%]
Aluminium Glass	645.69	-0.60	872.45	-1.27	2036.00	0.51	2707.40	5.44	4425.60	3.57
GFRP Glass	623.51	1.53	863.97	-1.00	1620.60	3.59	2547.10	7.68	3557.20	4.88
Steel Glass	425.36	-0.91	548.09	-1.38	1371.30	0.19	1967.30	5.72	3183.90	-1.04

TABLE 6. Modal frequencies for T3 configuration

Materials	f_1 [Hz]	$\Delta f_1/f^{T0}{}_1$ [%]	f_2 [Hz]	$\Delta f_2/f^{T0}{}_2$ [%]	f_3 [Hz]	$\Delta f_3/f^{T0}{}_3$ [%]	f_4 [Hz]	$\Delta f_4/f^{T0}{}_4$ [%]	f_5 [Hz]	$\Delta f_5/f^{T0}{}_5$ [%]
Aluminium Glass	649.05	-1.13	877.77	-1.89	2035.30	0.55	2691.30	6.01	4180.10	8.92
GFRP Glass	623.12	1.56	868.17	-1.49	1603.50	4.61	2526.30	8.44	3383.60	9.52
Steel Glass	429.76	-1.95	551.70	-2.05	1376.00	-0.15	1959.50	6.09	3063.60	2.78

The variation in T1-T3 configurations compared to T0 configurations is always within 10%. In particular, for the first three modes the variation is always whithin -1.0 and 2.05 %. Greatest variations could be observed in T3 configurations for the GFRP-Glass and Aluminum-Glass combinations (8.92 and 9.52, respectively). An increase in terms of natural frequencies with regard to T0 configuration is similar due to comparable values of density and Young's modulus. Steel-Glass combination does not show a significant increment (2.78%).

The results obtained show that the introduction of an imperfection, which could reduce the stress distributions in the bonded area, does not affect the modal behavior significantlly, especially for the first three modes.

5. CONCLUSIONS

The adhesive joints represent a viable alternative to the classic joining methods. In the design and control of a structural element, the modal analysis (frequency and modal shape) of the adhesive joint is of great importance. The study of the modal analysis of the adhesive joint is necessary in the design and monitoring process of the joint. The study of natural frequencies provides the designer with an indication of how the joint will respond to different dynamic loads. This aspect finds several applications (e.g. naval, areonautical), where dynamic behaviour plays a fundamental role in the design and service life phase. The modal analysis makes it possible to avoid resonance phenomena at a specific frequency. Previous studies, concerning static load conditions, aimed to determine how to reduce the stress peaks commonly present in the edges of bonded regions. It has been demonstrated that the introduction of a slot in the middle adherend enables these stress peaks to be reduced. The novel concept introduced in this study is to consider not only the static response of the joint, but the dynamic behavior as well. The main aim of this study is to consider the modal analysis of a double-lap joint both in the perfect adherends configuration and in the one with imperfections (i.e. slot) in the inner adherend. The results illustrated in this paper show the correlation between natural frequencies and mechanical (i.e. elastic modulus) and material (i.e. material density) parameters.

The similarity between elastic modulus and density characteristics is reflected in the frequencies and modes of vibration. It has also been observed that the introduction of imperfections makes it possible to reduce the stress peaks at the edges of the bonded region without modifying either the shapes or the natural frequencies for the most significant modes of vibration (i.e. the first modes of vibration).

6. REFERENCES

1. Jairaja, R. and Naik, G.N., "Numerical studies on weak bond effects in single and dual adhesive bonded single lap joint between cfrp and aluminium", ***Materials Today: Proceedings***, Vol. 21, (2020), 1064-1068. doi: 10.1016/j.matpr.2020.01.006
2. Adamos, L., Tsokanas, P. and Loutas, T., "An experimental study of the interfacial fracture behavior of titanium/cfrp adhesive joints under mode i and mode ii fatigue", ***International Journal of Fatigue***, Vol. 136, (2020), 105586. doi: 10.1016/j.ijfatigue.2020.105586
3. Min, J., Wan, H., Carlson, B.E., Lin, J. and Sun, C., "Application of laser ablation in adhesive bonding of metallic materials: A review", ***Optics & Laser Technology***, Vol. 128, (2020), 106188. doi: 10.1016/j.optlastec.2020.106188
4. Banea, M., Rosioara, M., Carbas, R. and Da Silva, L., "Multi-material adhesive joints for automotive industry", ***Composites Part B: Engineering***, Vol. 151, (2018), 71-77. doi: 10.1016/j.compositesb.2018.06.009
5. Loureiro, A., Da Silva, L.F., Sato, C. and Figueiredo, M., "Comparison of the mechanical behaviour between stiff and flexible adhesive joints for the automotive industry", ***The Journal of Adhesion***, Vol. 86, No. 7, (2010), 765-787. doi: 10.1080/00218464.2010.482440
6. Kinloch, A.J., "Adhesion and adhesives: Science and technology, Springer Science & Business Media, (2012). doi: 10.1007/978-94-015-7764-9
7. Arenas, J.M., Alía, C., Narbón, J.J., Ocaña, R. and González, C., "Considerations for the industrial application of structural adhesive joints in the aluminium–composite material bonding", ***Composites Part B: Engineering***, Vol. 44, No. 1, (2013), 417-423. doi: 10.1016/j.compositesb.2012.04.026
8. He, X., "A review of finite element analysis of adhesively bonded joints", ***International Journal of Adhesion and Adhesives***, Vol. 31, No. 4, (2011), 248-264. doi: 10.1016/j.ijadhadh.2011.01.006
9. Liao, L., Huang, C. and Sawa, T., "Effect of adhesive thickness, adhesive type and scarf angle on the mechanical properties of scarf adhesive joints", ***International Journal of Solids and Structures***, Vol. 50, No. 25-26, (2013), 4333-4340. doi: 10.1016/j.ijsolstr.2013.09.005
10. Silva, L.F., Öchsner, A. and Adams, R.D., Introduction to adhesive bonding technology, in Handbook of adhesion technology. 2011. doi: 10.1007/978-3-319-55411-2_1
11. Ramalho, L., Campilho, R., Belinha, J. and da Silva, L., "Static strength prediction of adhesive joints: A review", ***International Journal of Adhesion and Adhesives***, Vol. 96, (2020), 102451. doi: 10.1016/j.ijadhadh.2019.102451
12. Kanani, A.Y., Hou, X. and Ye, J., "The influence of notching and mixed-adhesives at the bonding area on the strength and stress distribution of dissimilar single-lap joints", ***Composite Structures***, Vol. 241, (2020), 112136. doi: 10.1016/j.compstruct.2020.112136
13. Hiremath, M.M., Sen, B., Prusty, R.K. and Ray, B.C., "Influence of loading rate on adhesively bonded tin-glass/epoxy single lap joint", ***Materials Today: Proceedings***, (2020). doi: 10.1016/j.matpr.2020.02.406
14. Yousefsani, S.A., Tahani, M. and Selahi, E., "Analytical solution of stress field in adhesively bonded composite single-lap joints under mechanical loadings", ***International Journal of Engineering***, ***Transactions C: Aspects,*** Vol. 27, No. 3, (2014), 475-486. doi: 10.5829/idosi.ije.2014.27.03c.16
15. Miles, R.N. and Reinhall, P., "An analytical model for the vibration of laminated beams including the effects of both shear and thickness deformation in the adhesive layer", Vol. 108, No. 1, (1986). doi: 10.1115/1.3269304
16. Ko, T.-C., Lin, C.-C. and Chu, R.-C., "Vibration of bonded laminated lap-joint plates using adhesive interface elements", ***Journal of Sound and Vibration***, Vol. 184, No. 4, (1995), 567-583. doi:10.1006/jsvi.1995.0334
17. Chien-Chang, L. and Yee-Shown, L., "A finite element model of single-lap adhesive joints", ***International Journal of Solids and Structures***, Vol. 30, No. 12, (1993), 1679-1692. https://doi.org/10.1016/0020-7683(93)90197-F
18. Saito, H. and Tani, H., "Vibrations of bonded beams with a single lap adhesive joint", ***Journal of Sound and Vibration***, Vol. 92, No. 2, (1984), 299-309. doi:10.1016/0022-460X(84)90563-7
19. Praveen, G. and Reddy, J., "Nonlinear transient thermoelastic analysis of functionally graded ceramic-metal plates", ***International Journal of Solids and Structures***, Vol. 35, No. 33, (1998), 4457-4476. doi:10.1016/S0020-7683(97)00253-9
20. Loy, C., Lam, K. and Reddy, J., "Vibration of functionally graded cylindrical shells", ***International Journal of Mechanical Sciences***, Vol. 41, No. 3, (1999), 309-324. doi:10.1016/S0020-7403(98)00054-X
21. Hamdan, A.I., "Stress concentration factors (SCFS) in circular hollow section chs-to-h-shaped section welded t-joints under axial compression", ***Civil Engineering Journal***, Vol. 5, No. 1, (2019), 33-47. doi: 10.28991/cej-2019-03091223
22. Ettefagh, M.H., Naraghi, M. and Towhidkhah, F., "Position control of a flexible joint via explicit model predictive control: An experimental implementation", ***Emerging Science Journal***, Vol. 3, No. 3, (2019), 146-156. doi: 10.28991/esj-2019-01177
23. Balamuralikrishnan, R. and Saravanan, J., "Finite element analysis of beam–column joints reinforced with gfrp reinforcements", ***Civil Engineering Journal***, Vol. 5, No. 12, (2019), 2708-2726. doi: 10.28991/cej-2019-03091443
24. Döner, A., "Comparison of corrosion behaviors of bare ti and TiO_2", ***Emerg Sci J***, Vol. 3, No. 4, (2019), 235-240. doi: 10.28991/esj-2019-01185
25. Cheng, S., Chen, D. and Shi, Y., "Analysis of adhesive-bonded joints with nonidentical adherends", ***Journal of Engineering Mechanics***, Vol. 117, No. 3, (1991), 605-623. doi: 10.1061/(ASCE)0733-9399(1991)117:3(605)
26. Chen, D. and Cheng, S., "Stress distribution in plane scarf and butt joints", Vol. 57, No. 1, (1990), 78-83. doi:10.1115/1.2888327
27. Sancaktar, E. and Nirantar, P., "Increasing strength of single lap joints of metal adherends by taper minimization", ***Journal of Adhesion Science and Technology***, Vol. 17, No. 5, (2003), 655-675. doi:10.1163/156856103321340796
28. Hou, X., Kanani, A.Y. and Ye, J., "Double lap adhesive joint with reduced stress concentration: Effect of slot", ***Composite Structures***, Vol. 202, No., (2018), 635-642. doi: 10.1016/j.compstruct.2018.03.026

Persian Abstract

چکیده

اتصالات چسب جایگزین مناسبی برای روشهای اتصال سنتی است. تجزیه و تحلیل فرکانس ها و اشکال معین برای پیش بینی رفتار ارتعاش یک جزء ساختاری در معرض استرس پویا اساسی است. مطالعات بسیاری در ادبیات برای تعیین روند استرس در منطقه پیوندی وجود دارد. ثابت شده است که ورود یک شکاف در چسبندگی داخلی باعث کاهش مقدار استرس در لبه های منطقه چسب می شود. در این مقاله ، تأثیر نواقص موجود در پیوند مرکزی با تجزیه و تحلیل FEM بررسی شده است. از نرم افزار FE ANSYS © 19 برای آنالیز مفاصل اتصالات چسب دو دامان استفاده می شود و پنج حالت اول در نظر گرفته می شود. نتایج نشان می دهد که تأثیر مدول و نسبت چگالی یانگ در فرکانسهای طبیعی متفاوت است. علاوه بر این ، معرفی نقص با افزایش فرکانس ، بر رفتار ارتعاشی تأثیر می گذارد. همچنین مشاهده می شود که کاهش جرم به دلیل معرفی ترک باعث تغییر شکل و فرکانس مودال برای مهمترین حالت ها نمی شود ، در حالی که باعث تغییرات مهم تر برای آخرین حالت ارتعاشی می شود. بنابراین معرفی ترک باعث تغییر چشمگیر رفتار پویا در مفصل نمی شود و امکان تحقق توزیع گسترده تر تنش ها را کاهش می دهد و باعث کاهش مقادیر قله های استرس می شود.

IJE TRANSACTIONS A: Basics Vol. 33, No. 10, (October 2020) 1924-1938

International Journal of Engineering

Journal Homepage: www.ije.ir

Projectiles Optimization: A Novel Metaheuristic Algorithm for Global Optimization

M. R. Kahrizi*, S. J. Kabudian

Department of Computer Engineering and Information Technology, Razi University, Kermanshah, Iran

PAPER INFO

Paper history:
Received 27 November 2019
Received in revised form 13 March 2020
Accepted 11 June 2020

Keywords:
Global Optimization
Metaheuristic Optimization Algorithm
Population-based Algorithm
Stochastic Optimization

ABSTRACT

Metaheuristic optimization algorithms are a relatively new class of optimization algorithms that are widely used for difficult optimization problems in which classic methods cannot be applied and are considered as known and very broad methods for crucial optimization problems. In this study, a new metaheuristic optimization algorithm is presented, the main idea of which is inspired by models in kinematics. This algorithm obtains better results compared to other optimization algorithms in this field and is able to explore new paths in its search for desirable points. Hence, after introducing the projectiles optimization (PRO) algorithm, in the first experiment, it is evaluated by the determined test functions of the IEEE congress on evolutionary computation (CEC) and compared with the known and powerful algorithms of this field. In the second try out, the performance of the PRO algorithm is measured in two practical applications, one for the training of the multi-layer perceptron (MLP) neural networks and the other for pattern recognition by Gaussian mixture modeling (GMM). The results of these comparisons are presented in various tables and figures. Based on the presented results, the accuracy and performance of the PRO algorithm are much higher than other existing methods.

***doi**: 10.5829/ije.2020.33.10a.11*

1. INTRODUCTION

Optimization is a procedure for reaching a state in which the problem has a certain advantage and improvement over other states. In other words, the purpose of optimization is to find a point in the problem space where the measure of fitness is maximized. The problem space is the range of values that exist for each dimension of the problem, and points can be selected from these intervals. The criterion for the fitness of points in the problem space varies according to the nature of the problem. If the type of our problem is of the cost or error, the point where the cost (or error) function has the least value is more fit than other points. This type of optimization is also called minimization. On the other hand, there are some problems in which the optimization is to find a point in the problem space where the value of its objective function is maximum. These problems in the field of optimization are called maximization.

Metaheuristic optimization algorithms are a new class of optimization algorithms that are applied to optimization problems in which classic methods cannot be used and are considered as well-known methods for difficult optimization problems. Metaheuristic algorithms are often inspired by nature. Also, in metaheuristic algorithms, many steps are taken at random. For example, several points in the problem space are randomly selected, and they undergo a series of changes during the execution of the algorithm based on the random mechanism of each algorithm, which ultimately leads to access to the optimal global point.

The rest of this paper is organized as follows. The effective methods and existing studies in the field of metaheuristic optimization are reviewed in Section 2. The proposed algorithm is described in Section 3. The comparison of the proposed method with other algorithms and results are discussed in Section 4. Finally, in Section 5, the conclusions are presented.

*Corresponding Author Email: *kahrizi.mr@gmail.com* (M. R. Kahrizi)

Please cite this article as: M. R. Kahrizi, S. J. Kabudian, Projectiles Optimization: A Novel Metaheuristic Algorithm for Global Optimization, International Journal of Engineering (IJE), IJE TRANSACTIONS A: Basics Vol. 33, No. 10, (October 2020) 1924-1938

2. LITERATURE REVIEW

Metaheuristic optimization algorithms are classified into different groups. References [1, 2] can be referred to for more information about optimization algorithm classification. Here, the purpose is to review some of the known and effective algorithms in the development of the projectiles optimization (PRO) algorithm, and in this section, a specified classification is not followed. Also, the available surveys, such as [3-5] can be referred to for more comprehensive information.

One of the oldest and most known optimization algorithms are genetic algorithms (GA). These algorithms are classified as evolutionary algorithms because they use evolutionary computation. The genetic algorithm is a general application algorithm and can be applied in various forms due to its properties. These properties refer to the difference in the chromosome representation, various procedures of parent selection, and different methods in crossover and mutation. The methods of parent selection in the genetic algorithm have been compared in [6, 7]. Different genetic methods with a focus on new subjects were studied in [8]. However, different types of genetic algorithms have been presented over time, and in [9-12] the hybrid type, multi-objective, parallel, and the new version of this algorithm were presented, respectively. Furthermore, reference [13] can be referred to for more information.

Another old algorithm in the optimization field is the simulated annealing (SA) algorithm [14, 15], in which the Metropolis algorithm [16] has been used. Similar to other algorithms, the various versions of the SA algorithm have been proposed, such as the microcanonical annealing (MA) algorithm [17] in which the Creutz algorithm has been utilized instead of the Metropolis algorithm. In [18], another kind of SA algorithm has been proposed that was called threshold accepting (TA). The comparison between this algorithm and the SA algorithm can be observed in [19]. Noised method (NM) is another version of the SA algorithm. This algorithm and its various versions along with their survey have been studied in [20-23]. Another version of the SA algorithm for continuous spaces can be observed in [24]. In [25], the hybrid version of the SA algorithm has been presented for performance improvement in which the SA algorithm has been combined with the GA. Furthermore, the papers [26-29] can be referred to as a comprehensive history.

Ant colony optimization (ACO) is another optimization algorithm, which has been inspired by the ant colony's motion and is classified under swarm intelligence (SI) based algorithms. Reference [30] can be referred to for more information. ACO algorithms have different classes. For example, in [31], the hybrid type of the ACO algorithm has been presented. References [32-35] can be referred to as examples, the development in the ACO algorithm, and the applicability of the ACO algorithm.

Particle swarm optimization (PSO) algorithm is one of the well-known and powerful optimization algorithms that is inspired by a type of motion based on swarm intelligence. This algorithm is attractive due to its desirable performance, and a great amount of research has been performed on it. Various kinds of PSO algorithms have been presented over time. In [36-38], the topology, structure, and the ideas available in PSO have been discussed. Early convergence and hence getting stuck in local optimum points are drawbacks of the PSO algorithm. In [39-44], an attempt was made to resolve these weaknesses. In [45], a kind of PSO algorithm has been presented for discrete spaces. In [46], another version of the PSO algorithm has been presented for dynamic spaces. In [47], the parallel mode of PSO has been examined. In [48], a multi-objective type of algorithm has been discussed. Other various kinds of PSO algorithms can be followed in [49-51], which have been discussed in conjunction with algorithms and other methods for productivity improvement. The particle swarm algorithm has been used in wide fields due to its generality. The details and statistics of these fields have been given in [52]. Also, papers [53-57] can be referred to for more information about some applications and other hybrid versions of the PSO algorithm and their surveys.

The differential evolution (DE) algorithm [58] is another powerful optimization algorithm classified as an evolutionary algorithm. The DE algorithm is a simple algorithm in the optimization field. As with other algorithms, different types of DE algorithms have been proposed. In [59, 60], the multi-objective models of the DE algorithm have been discussed and used. In [61], the differences between PSO and DE algorithms have been studied. Another version of the DE algorithm has been introduced in [62]. The hybrid versions of the DE algorithm have been given in [63, 64]. Moreover, in [65-68], some methods and applications have been presented in which the DE algorithm determines its parameters in a self-adaptive manner.

3. PROJECTILES OPTIMIZATION ALGORITHM

In the PRO algorithm [69], we have attempted to double the accuracy and power. At PRO, we took advantage form the innovations and pros of other algorithms to avoid reinventing the wheel. This algorithm is inspired by the projectile motion in physics and is governed by its laws.

The basic idea behind the PRO algorithm is derived from missiles launches. Since missiles must have the highest accuracy and least error in targeting, the process of moving

these projectiles can be considered as a model for optimization.

As with the laws of physics related to this type of motion, we are faced with a set of parameters that control the motion of the projectiles. Such as acceleration of gravity in the launch environment, initial projectile velocity, launch angle, and intrusive forces such as friction. In the following the method of quantifying and calculating these parameters is described in the projectile algorithm step by step.

Based on the pseudo-code presented in Figure 1, in the PRO algorithm similar to the other metaheuristic optimization algorithms, the first part is the initialization, in which all of the variables involved in the algorithm are introduced and initialized. After initializing the variables, to create each member of the population, which is called "projectile" here, random numbers with the uniform probability distribution are used in a determined range for each problem. Then, the cost of each member is calculated according to the considered cost function. Then, their maximum and minimum value are obtained.

In the following, the main body of the algorithm is studied, which is inside the main loop. In this part of the algorithm, we use some of the principles, properties, and quantities of physics, such as the projectile motion rules, velocity, and gravitational acceleration. In the main loop of the algorithm, the members are sorted based on their costs in such a way that a member with the minimum cost is ranked as "first," and a member with the maximum cost is ranked as the "last." Then, the fitness of each member of the population is calculated by Equation (1), which results in a number in the range of (0, 1].

$$F(x_i) = \frac{N-(Rank(x_i)-1)}{N} \quad (1)$$

In Equation (1), N denotes the total number of members (projectiles) and $Rank(x)$ having a value in the range of $\{1,2,\ldots, N\}$, determines the rank of each member i among all the members that is calculated based on $C(x_i)$ sorting, and $C(x_i)$ is the cost of member i that can be obtained through using the considered function (cost function) for optimization.

After calculating the fitness $F(x)$ for each member of the population, this fitness is used to determine the projectile launch angle according to Equation (2). It should be noted that as can be observed in Table 1, we have empirically considered the minimum and maximum angles tantamount to $45°$ and $84°$, respectively.

$$\theta(x_i) = \theta_{\min} + F(x_i)(\theta_{\max} - \theta_{\min}) \quad (2)$$

In addition, to determine the gravitational acceleration for each projectile, fitness $F(x)$ is used according to Equation (3). Here, we have experimentally considered the maximum and minimum values of the gravitational acceleration equal to 10 m/s^2 and 1 m/s^2, respectively.

$$G(x_i) = G_{\min} + F(x_i)(G_{\max} - G_{\min}) \quad (3)$$

In Equations (2) and (3) all parameters are determined at the beginning of the algorithm, at the initialization section, except $F(x)$ that is in the main loop of the algorithm and it is calculated separately for each member i, and in each iteration, it has a different value. The values given to the used parameters in the PRO algorithm are presented in Table 1.

PRO Algorithm

Initializing the projectile population (N) with random position, and velocity, gravitation, theta and change probability (CP) of each dimension (D) of the projectiles for moving in the search space;
Evaluating the cost $C(x_i)$ for each projectile i;
Evaluating the rank $Rank(x_i)$ for each projectile i by sorting the costs $C(x)$;

For $n = 1,\ldots, N_{iter}$ *(number of iterations)* **do**

For $i = 1,\ldots,N$*(number of projectiles)* **do**

Evaluate the fitness $F(x_i)$ using

$F(x_i) = (N - (Rank(x_i) - 1))/N$;

Update the theta $\theta(x_i)$ using

$\theta(x_i) = \theta_{\min} + F(x_i)(\theta_{\max} - \theta_{\min})$;

Update the gravitation $G(x_i)$ using

$G(x_i) = G_{\min} + F(x_i)(G_{\max} - G_{\min})$;

Update the velocity $V(n)$ using

$V(n) = V_{\max} - ((n-1)/(N_{iter} - 1))(V_{\max} - V_{\min})$;

For $d = 1,\ldots,D$*(number of dimensions)* **do**

Create random numbers $r_{i,d}, r2_{i,d}$ by a uniform distribution $U(0,1)$;

Evaluate the horizontal range $R(x_{i,d})$ using $R(x_i) = V^2(n)\sin(2\theta(x_i))/G(x_i)$ and multiplied by $r_{i,d}$;

Create the new projectile $x2_{i,d}$ randomly using a normal distribution $N(x_{i,d}, R^2(x_{i,d}))$ with CP probability for each dimension,

$$x2_{i,d} = \begin{cases} N(x_{i,d}, R^2(x_{i,d})) & if \quad r2_{i,d} \le CP \\ x_{i,d} & otherwise \end{cases};$$

End

Evaluate the cost $C2(x2_i)$ for each new projectile i;

End

Sort the x and $x2$ by costs of them (C, $C2$) and remove the worse half of them;

Evaluate the rank $Rank(x_i)$ for each projectile i that remain from competitive exclusion by sorting costs;

End

Figure 1. PRO algorithm pseudo code

TABLE 1. The parameters and their determined values in the PRO algorithm which are the same and constant for all test functions

Symbol	Quantity	Value
N	Number of projectiles	D
N_{iter}	Number of iterations in each run	10E+4
D	Number of problem's dimensions	10, 50
$MaxFE$	Maximum function evaluation	10E+4 × D
$LimUp$	The upper limit of the search space	100
$LimLo$	The lower limit of the search space	-100
G_{max}	Maximum value of gravitational acceleration	10 m/s^2
G_{min}	Minimum value of gravitational acceleration	1 m/s^2
θ_{max}	Maximum initial launch angle in degree	84°
θ_{min}	Minimum initial launch angle in degree	45°
CP	The Change Probability of each dimension in each projectile	0.1
V_{max}	Maximum value of initial velocity	$\sqrt{Limup - LimLo}$ m/s
V_{min}	Minimum value of initial velocity	V_{max} × 0.1 m/s

Parameters are initialized in such a way to provide similar and impartial conditions for the comparison of this algorithm with other algorithms. These conditions have been presented in [70] and are not the best condition for the PRO algorithm.

After determining the parameters of the launch angle and the gravitational acceleration, the initial velocity of the projectiles should be calculated. This value is constant here and similar for all the projectiles in each iteration. And in the first iteration, the initial velocity is equal to the predetermined value V_{max}. In each iteration of the algorithm, an amount of the projectiles' initial speed is reduced based on Equation (4) so that in the last iteration, the initial speed is reached the predetermined value V_{min}.

However, to determine the initial values of the variables and update their values in this algorithm, other methods appropriate to the problem conditions may be applied. For example, the Euclidean distance of each projectile to the best projectile (member with the lowest cost) can be used to determine the fitness level, launch angle, gravitational acceleration, and initial velocity.

$$V(n) = V_{\max} - \frac{n-1}{N_{\text{iter}} - 1}\left(V_{\max} - V_{\min}\right) \quad (4)$$

where n denotes the current iteration of the algorithm, and the minimum and maximum of its values are 1 and N_{iter}, respectively.

After determining the required parameters, the horizontal range of each projectile should be calculated that is calculated from Equation (5) based on the physics laws governing the projectiles' motion.

$$R(x_i) = \frac{V^2(n)\, sin(2\theta(x_i))}{G(x_i)} \quad (5)$$

As can be seen in Figure 2, this figure shows the variations of the range (it is considered here as a movement in the problem space) with the variations in the launch angle. In this figure, the initial velocity and the gravitational acceleration in the launch site are considered to be equal to 20 m/s and 10 m/s^2, respectively. In addition, in Figures 3 and 4, the projectiles range amount with respect to the variations in the gravitational acceleration in the launch site, and the projectiles range amount with respect to the variations in the launch initial velocity are depicted respectively in which the launch angle is considered equal to 45°.

After determining the horizontal range value $R(x_i)$ for all members of the algorithm population, these values are multiplied by a random array in the range (0, 1) with a uniform distribution. These random numbers are different for each member and each dimension. This can be assumed as the effect of the disruptive forces on the projectiles' motion. However, we decide to apply the effect of the disruptive forces in two stages, and the first phase is applied in this section.

Then, we determine in which dimension the member (projectile) can be altered, in other words, in which dimension of the problem space the projectile can be moved. This action is performed randomly and with CP probability for each dimension of the members. CP determines the change probability of each member in every dimension that is initialized at the beginning of the algorithm.

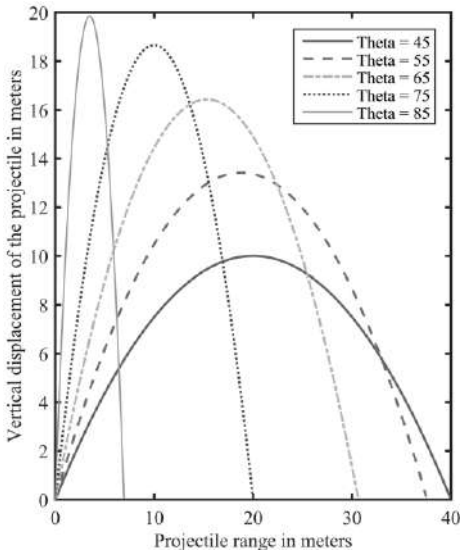

Figure 2. The projectile range with respect to the variation of the launch angle, with the initial velocity of 20 m/s and the gravitational acceleration of 10 m/s^2

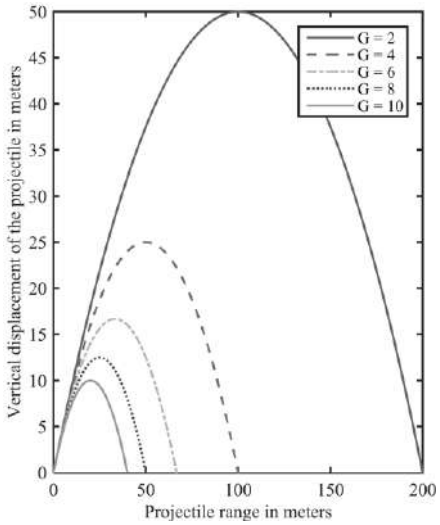

Figure 3. The projectile range with respect to the variation of the gravitational acceleration in the launch point, with the initial velocity of 20 m/s and the launch angle of 45°

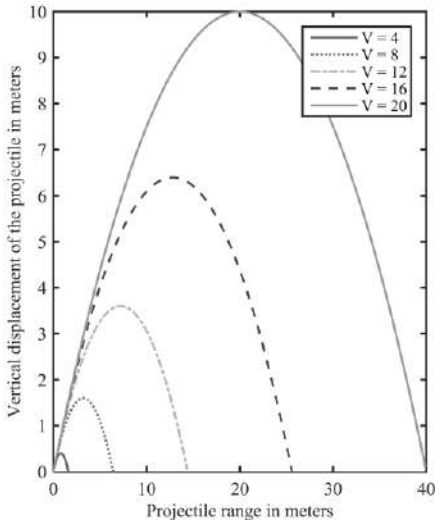

Figure 4. The projectile range with respect to the variation of the projectile initial velocity with an angle equal to 45°and the gravitational acceleration of 10 m/s^2

Now, after performing the previous steps, we can create new members in the algorithm; in other words, the projectiles can be launched. Obviously, each member is recognized by its coordinates in problem space, which are the dimensions' values of each member here. In order to specify the new members, we use the projectiles coordinates and their range amount ($R(x)$) and the dimensions that should be changed in each member. In this way, the coordinates of the new members are determined randomly by the normal probability distribution with the mean value $x_{i,d,}$ and the standard deviation $R(x_{i,d})$, where $x_{i,d}$ represents the mean value of dimension d for member i. Also, the number of new members of the algorithm is the same as the number of initial population members here and in each iteration of the algorithm. As mentioned earlier, the effect of the disruptive forces are applied in two stages due to the experimental observations on the PRO algorithm, the first stage was at the projectiles range $R(x)$ determination time that was in the form of multiplying by random numbers with uniform distribution, and the second stage is implicitly in the new members' creation. As mentioned, in the section of creating new members, we used random numbers with normal distribution for creating new members. These random numbers are implicitly the second phase of applying the disruptive and friction forces. Otherwise, the randomly creation new members is not necessary, and the coordinates of the new member can be obtained by having the current coordinates and range of each member.

Now, in this step of the algorithm, the number of population members in the algorithm has doubled since the beginning of the algorithm main loop reached $2N$; now, it is the time to apply the specified cost function to the new members of the population. This is necessary to perform the next stage, which is sorting all members according to their costs. After applying the cost function on the new members and sorting all the new and old members with respect to their costs, half of the population members with inappropriate (higher) costs are removed from the population. This action is called competitive exclusion.

At the end of the algorithm main loop, the cost of the best member in each iteration can be stored in a variable such as C_{best}. Then the counter of the algorithm loop is increased by one, and we return to the beginning of the loop that is the investigation of the loop end condition.

All of the stages that have mentioned from the beginning of this section are repeated until the end condition of the loop will be satisfied; for example, until the value of the loop repetition counter reaches the predetermined amount. At this point, the repetition ends, and the algorithm is completed. At the end, the algorithm converges to the object point with the maximum fitness and minimum cost.

4. ALGORITHM COMPARISON AND RESULTS

In the PRO algorithm, we aimed for a better performance than other known algorithms in the optimization field. Thus, we compared it with the powerful and well-known particle swarm and differential evolution algorithms. In Tables 2 and 3, the values corresponding to the parameters of these algorithms can be seen. These values are experimental and represent the algorithm's best performance.

In this comparison, we used the test functions that have been introduced in [70] for measuring the algorithms' performance in the IEEE CEC 2017 conference. In addition, we compared the PRO algorithm with the particle swarm and differential evolution algorithms in two applied cases of multi-layer perceptron (MLP) neural networks training and pattern recognition by the GMM method. The obtained results from different cases are presented in Tables 4 to 7. Also, the obtained results for the practical cases have been presented in a graph form in Figures 5 and 6. As can be seen, the results show that the proposed algorithm performs better than the other algorithms.

4. 1. Comparison Using the Test Functions As mentioned earlier, the PRO algorithm was compared with the particle swarm and differential evolution algorithm on some test functions that have been used in the IEEE CEC 2017 conference for algorithm comparison. In [70], the test functions have been introduced comprehensively.

TABLE 2. The parameters and their determined values in the PSO algorithm which are the same and constant for all comparisons

Symbol	Quantity	Value
Iteration	Number of iterations	10E+4
Dimension (D)	Number of problem dimensions	10, 50
MaxFE	Maximum function evaluation	10E+4×D
Particle	Number of particles	D
$\varphi 1$	Value of $\varphi 1$	0.3
$\varphi 2$	Value of $\varphi 2$	0.7
W_{max}	Initial value of inertia weight	0.9
W_{min}	final value of inertia weight	0.4

TABLE 3. The parameters and their determined values in the DE algorithm which are the same and constant for all comparisons

Symbol	Quantity	Value
Iteration	Number of iterations	10E+4
Dimension (D)	Number of problem dimensions	10, 50
MaxFE	Maximum function evaluation	10E+4 × D
PopSize	Number of populations	D
F	Impact factor of difference	1
CR	Probability of crossover	0.5

The results of this comparison are presented in Tables 2, 3, and 4. These comparisons were made similar to the presented method in [70], and based on the error between the difference of the optimization algorithms' output and the ideal output as Equation (6). It should be noted that the purpose of optimization in these comparisons was to find the minimum value of the functions in the given range [-100,100] for each function (minimization).

$$E = C(x_i) - C^*(x_i) \quad (6)$$

where $C(x_i)$ is the output of the optimization algorithm or the minimum acquired cost, and $C^*(x_i)$ is the ideal output or the minimum accessible cost for each function by the optimization algorithms.

Here, the comparisons were performed in such a way that appropriate initial conditions were considered for each of the three algorithms, and these conditions were constant for all comparisons. The initial conditions for the PRO algorithm are presented in Table 1.

The comparison between the optimization algorithms was performed with an equal population size for algorithms. The number of members was equal to the number of problem dimensions (10 and 50). Moreover, each comparison was repeated 50 times, and each time the seed of random number generator was identical for all algorithms. So, the generation of random values would be the same for all algorithms, and the randomly generated numbers for the algorithms would be the same if possible. Also, the seed of the random number generators was different for each order of the comparison repetition. Furthermore, the maximum amount of the function evaluation for all algorithms was assumed to be equal to 10E+4 × D, which was the end condition for the main loop of the algorithms.

As can be seen in the comparison tables of the algorithms (Tables 4, 5, and 6), the results show that the performance of the PRO algorithm generally is much better than other algorithms for all the cases and on all the test functions.

The tables give the best, worst, mean, median, and standard deviation (SD) of the results in 50 complete and separate runs of each algorithm for each test, respectively, in 10 and 50-dimensional states in the corresponding columns. In these tables, the best results in each experiment are written in bold. As can be seen, in most cases the best results are for the PRO algorithm, especially when the dimensions are large.

4. 2. Comparison Using Case Studies In this section, we attempted to evaluate the PRO algorithm in real and practical applications. For this purpose, we compared it

TABLE 4. Comparison results of algorithms using the test functions 1 to 10

Test	Method	Dimensions	Result				
			Best	Worst	Mean	Median	SD
F1	PSO	10	1.24E+06	6.65E+09	1.29E+09	1.14E+09	1.56E+09
		50	1.24E+10	5.83E+10	3.20E+10	3.21E+10	1.06E+10
	PRO	10	1.74E+00	**1.11E+04**	**2.61E+03**	1.56E+03	**2.80E+03**
		50	**2.20E+03**	**3.49E+04**	**1.10E+04**	**8.62E+03**	**7.81E+03**
	DE	10	**7.82E-11**	7.01E+07	2.83E+06	**8.19E-09**	1.39E+07
		50	2.12E+10	3.17E+10	2.75E+10	2.76E+10	2.33E+09
F2	PSO	10	4.03E+04	1.80E+13	1.01E+12	5.77E+08	3.27E+12
		50	1.49E+50	1.16E+74	2.78E+72	3.05E+62	1.65E+73
	PRO	10	6.30E-06	**9.19E-03**	**1.44E-03**	**3.92E-04**	**2.26E-03**
		50	**9.82E-06**	**6.34E+04**	**1.43E+03**	**8.05E+01**	**8.96E+03**
	DE	10	**1.24E-07**	3.03E+08	1.26E+07	2.46E+01	5.99E+07
		50	6.48E+57	2.18E+64	5.27E+62	4.29E+60	3.08E+63
F3	PSO	10	4.35E+03	1.47E+05	3.33E+04	2.06E+04	3.13E+04
		50	1.85E+05	7.84E+05	3.93E+05	3.79E+05	1.26E+05
	PRO	10	6.05E-05	**5.90E-03**	**1.28E-03**	9.70E-04	**1.12E-03**
		50	**1.01E+00**	**1.65E+01**	**4.09E+00**	**3.36E+00**	**2.94E+00**
	DE	10	**1.95E-09**	9.55E+03	4.17E+02	**1.83E-05**	1.52E+03
		50	2.51E+05	3.78E+05	3.15E+05	3.14E+05	2.66E+04
F4	PSO	10	9.29E+00	1.34E+03	1.37E+02	9.57E+01	1.91E+02
		50	1.41E+03	9.93E+03	4.66E+03	3.92E+03	2.32E+03
	PRO	10	**2.09E-03**	7.18E+01	3.60E+00	**9.31E-01**	1.36E+01
		50	**2.10E+01**	**2.18E+02**	**1.14E+02**	**1.08E+02**	**5.64E+01**
	DE	10	1.13E-02	**8.30E+00**	**1.61E+00**	1.20E+00	**1.85E+00**
		50	1.95E+03	3.32E+03	2.55E+03	2.53E+03	3.18E+02
F5	PSO	10	2.46E+01	1.35E+02	7.14E+01	6.89E+01	2.50E+01
		50	3.53E+02	6.75E+02	4.95E+02	4.95E+02	7.58E+01
	PRO	10	6.96E+00	3.38E+01	2.02E+01	1.99E+01	7.22E+00
		50	**1.99E+02**	**5.07E+02**	**3.29E+02**	**3.31E+02**	5.77E+01
	DE	10	**6.14E+00**	**2.05E+01**	**1.41E+01**	**1.46E+01**	**3.00E+00**
		50	5.50E+02	6.39E+02	5.98E+02	5.96E+02	**1.87E+01**
F6	PSO	10	6.45E+00	7.70E+01	4.13E+01	3.96E+01	1.61E+01
		50	5.25E+01	1.06E+02	7.33E+01	7.29E+01	1.03E+01
	PRO	10	**9.71E-05**	**2.54E-03**	**4.23E-04**	**3.00E-04**	**3.97E-04**
		50	**1.04E-02**	**6.53E-01**	**9.77E-02**	**1.64E-02**	**1.74E-01**
	DE	10	1.95E-02	3.91E+00	5.36E-01	3.86E-01	6.58E-01
		50	5.49E+01	6.79E+01	6.15E+01	6.16E+01	2.83E+00
F7	PSO	10	3.54E+01	2.52E+02	9.16E+01	8.44E+01	3.98E+01
		50	7.23E+02	1.78E+03	1.23E+03	1.22E+03	2.40E+02
	PRO	10	**1.09E+01**	4.43E+01	**2.53E+01**	**2.47E+01**	7.20E+00
		50	**2.10E+02**	**3.92E+02**	**2.97E+02**	**2.94E+02**	**4.32E+01**
	DE	10	1.84E+01	**4.24E+01**	3.09E+01	3.10E+01	**4.67E+00**
		50	1.34E+03	1.86E+03	1.67E+03	1.69E+03	1.08E+02

F8	PSO	10	1.76E+01	1.33E+02	4.69E+01	4.46E+01	2.18E+01
		50	3.85E+02	6.77E+02	5.08E+02	5.00E+02	6.67E+01
	PRO	10	**5.97E+00**	5.17E+01	2.27E+01	2.09E+01	**1.05E+01**
		50	**2.28E+02**	**4.80E+02**	**3.39E+02**	3.31E+02	5.61E+01
	DE	10	9.98E+00	**2.40E+01**	**1.68E+01**	**1.70E+01**	3.22E+00
		50	5.63E+02	6.34E+02	5.99E+02	6.01E+02	**1.74E+01**
F9	PSO	10	6.59E+01	4.44E+03	1.02E+03	8.61E+02	7.72E+02
		50	1.17E+04	3.46E+04	2.11E+04	2.09E+04	4.98E+03
	PRO	10	**8.81E-08**	1.11E+03	4.36E+01	**5.08E-06**	1.84E+02
		50	**6.27E+03**	**2.24E+04**	**1.24E+04**	**1.31E+04**	3.42E+03
	DE	10	1.32E-05	**7.70E-01**	**7.76E-02**	2.68E-02	**1.37E-01**
		50	2.10E+04	3.60E+04	2.88E+04	2.84E+04	**3.20E+03**
F10	PSO	10	6.49E+02	2.54E+03	1.47E+03	1.46E+03	4.33E+02
		50	6.34E+03	1.11E+04	9.37E+03	9.40E+03	1.01E+03
	PRO	10	**1.25E+02**	1.07E+03	6.08E+02	6.03E+02	2.22E+02
		50	**3.39E+03**	**6.96E+03**	**5.38E+03**	**5.45E+03**	8.44E+02
	DE	10	2.01E+02	**8.53E+02**	**5.43E+02**	**5.37E+02**	**1.42E+02**
		50	1.15E+04	1.30E+04	1.25E+04	1.25E+04	**3.45E+02**

TABLE 5. Comparison results of algorithms using the test functions 11 to 20

Test	**Method**	**Dimensions**	**Result**				
			Best	**Worst**	**Mean**	**Median**	**SD**
F11	PSO	10	1.44E+01	7.26E+03	9.47E+02	3.38E+02	1.53E+03
		50	1.83E+03	3.14E+04	9.15E+03	7.56E+03	6.81E+03
	PRO	10	1.02E+00	**2.41E+01**	**1.09E+01**	1.10E+01	**5.75E+00**
		50	**1.05E+02**	**3.52E+02**	**2.23E+02**	**2.27E+02**	**5.23E+01**
	DE	10	**4.10E-01**	3.11E+02	2.21E+01	**7.75E+00**	4.86E+01
		50	2.03E+03	3.88E+03	2.59E+03	2.58E+03	3.38E+02
F12	PSO	10	2.41E+04	5.55E+08	4.29E+07	3.36E+06	1.21E+08
		50	1.76E+09	3.94E+10	8.98E+09	7.07E+09	6.80E+09
	PRO	10	**4.77E+02**	**4.18E+04**	**1.39E+04**	1.04E+04	**1.28E+04**
		50	**2.29E+05**	**4.76E+06**	**2.04E+06**	**1.77E+06**	**1.16E+06**
	DE	10	8.48E+02	4.94E+06	1.99E+05	**1.61E+03**	9.78E+05
		50	1.01E+09	1.96E+09	1.42E+09	1.42E+09	1.97E+08
F13	PSO	10	1.03E+03	8.64E+04	1.84E+04	1.33E+04	1.86E+04
		50	1.80E+05	1.27E+10	2.09E+09	1.41E+09	2.61E+09
	PRO	10	2.25E+01	3.13E+04	1.22E+04	9.60E+03	1.11E+04
		50	**2.18E+02**	**3.66E+04**	**9.42E+03**	**4.09E+03**	**1.06E+04**
	DE	10	**6.40E+00**	**1.34E+03**	**1.36E+02**	**6.89E+01**	**2.47E+02**
		50	1.83E+05	1.77E+06	6.69E+05	5.92E+05	3.50E+05
F14	PSO	10	1.57E+02	2.74E+04	8.31E+03	3.19E+03	8.51E+03
		50	1.24E+05	3.19E+07	3.44E+06	1.39E+06	5.44E+06
	PRO	10	6.28E+00	2.26E+04	5.96E+03	2.77E+03	6.85E+03
		50	**1.68E+04**	**3.79E+05**	**9.05E+04**	**7.84E+04**	**6.88E+04**
	DE	10	**2.93E-01**	**3.24E+01**	**2.00E+01**	**2.13E+01**	**7.38E+00**
		50	2.36E+05	1.18E+06	5.49E+05	5.29E+05	1.97E+05

F15	PSO	10	2.17E+02	1.09E+05	2.81E+04	2.01E+04	2.65E+04
		50	3.27E+04	4.19E+08	1.14E+07	1.16E+05	6.05E+07
	PRO	10	2.21E+00	2.57E+04	6.74E+03	4.55E+03	6.68E+03
		50	**2.30E+02**	**3.08E+04**	**8.91E+03**	**8.30E+03**	**7.50E+03**
	DE	10	**1.09E-01**	**1.26E+02**	**3.20E+01**	**2.06E+01**	**3.29E+01**
		50	1.42E+04	5.94E+04	3.45E+04	3.26E+04	1.27E+04
F16	PSO	10	1.87E+02	8.83E+02	4.90E+02	4.96E+02	1.54E+02
		50	1.30E+03	4.34E+03	2.76E+03	2.72E+03	6.92E+02
	PRO	10	**5.56E-01**	4.99E+02	2.21E+02	2.19E+02	1.39E+02
		50	**9.10E+02**	**2.93E+03**	**1.92E+03**	**1.90E+03**	3.86E+02
	DE	10	2.78E+00	**3.10E+02**	**8.65E+01**	**4.39E+01**	**7.64E+01**
		50	2.70E+03	3.76E+03	3.29E+03	3.30E+03	**2.47E+02**
F17	PSO	10	4.19E+01	6.11E+02	1.85E+02	1.26E+02	1.23E+02
		50	1.50E+03	1.15E+04	2.48E+03	2.12E+03	1.40E+03
	PRO	10	**1.31E+00**	1.78E+02	5.17E+01	3.17E+01	4.88E+01
		50	**7.07E+02**	2.30E+03	**1.44E+03**	**1.38E+03**	3.27E+02
	DE	10	8.55E+00	**1.20E+02**	**3.29E+01**	**2.45E+01**	**2.02E+01**
		50	1.51E+03	**2.20E+03**	1.88E+03	1.89E+03	**1.67E+02**
F18	PSO	10	7.79E+02	5.39E+04	1.80E+04	1.13E+04	1.68E+04
		50	8.83E+05	1.51E+08	1.44E+07	7.00E+06	2.50E+07
	PRO	10	1.99E+02	3.69E+04	1.09E+04	7.17E+03	9.88E+03
		50	**5.13E+04**	**1.19E+06**	**5.37E+05**	**5.48E+05**	**2.75E+05**
	DE	10	**2.01E+01**	**2.71E+03**	**1.51E+02**	**3.84E+01**	**5.20E+02**
		50	2.11E+06	1.23E+07	6.30E+06	6.27E+06	2.18E+06
F19	PSO	10	1.54E+02	1.99E+07	4.31E+05	1.33E+04	2.80E+06
		50	3.57E+05	1.38E+09	3.69E+07	4.60E+06	1.95E+08
	PRO	10	3.58E+00	2.81E+04	8.08E+03	5.46E+03	8.47E+03
		50	**1.59E+02**	**4.25E+04**	**1.65E+04**	**1.55E+04**	**1.21E+04**
	DE	10	**3.43E-01**	**2.19E+02**	**1.28E+01**	**2.92E+00**	**3.49E+01**
		50	6.15E+02	1.71E+05	4.75E+04	3.77E+04	3.95E+04
F20	PSO	10	9.11E+01	5.14E+02	2.48E+02	2.44E+02	1.01E+02
		50	9.31E+02	2.54E+03	1.66E+03	1.65E+03	3.66E+02
	PRO	10	**2.74E-03**	**3.42E+01**	**1.17E+01**	**6.78E+00**	**1.09E+01**
		50	**5.07E+02**	1.85E+03	**1.15E+03**	**1.14E+03**	2.92E+02
	DE	10	4.17E-02	2.07E+02	2.92E+01	2.12E+01	3.44E+01
		50	9.69E+02	**1.68E+03**	1.37E+03	1.43E+03	**1.79E+02**

TABLE 6. Comparison results of algorithms using the test functions 21 to 30

Test	Method	Dimensions	Result				
			Best	Worst	Mean	Median	SD
F21	PSO	10	1.15E+02	3.30E+02	2.46E+02	2.60E+02	5.60E+01
		50	5.66E+02	9.96E+02	7.45E+02	7.51E+02	9.93E+01
	PRO	10	**1.00E+02**	2.69E+02	2.22E+02	2.35E+02	**5.14E+01**
		50	**4.07E+02**	**6.96E+02**	**5.48E+02**	**5.37E+02**	5.65E+01
	DE	10	1.02E+02	**2.34E+02**	**1.74E+02**	**2.20E+02**	6.06E+01
		50	7.08E+02	8.14E+02	7.82E+02	7.88E+02	**2.12E+01**

F22	PSO	10	1.05E+02	2.73E+03	5.22E+02	1.79E+02	6.38E+02
		50	3.53E+03	1.12E+04	9.43E+03	9.81E+03	1.34E+03
	PRO	10	1.00E+02	1.60E+03	3.58E+02	**1.04E+02**	4.73E+02
		50	**1.00E+02**	**8.26E+03**	**6.09E+03**	**6.26E+03**	1.49E+03
	DE	10	**1.43E+01**	**1.53E+02**	**9.64E+01**	1.06E+02	**3.35E+01**
		50	1.14E+04	1.36E+04	1.28E+04	1.29E+04	**3.91E+02**
F23	PSO	10	3.39E+02	6.49E+02	4.13E+02	3.91E+02	7.37E+01
		50	9.69E+02	1.80E+03	1.43E+03	1.41E+03	1.98E+02
	PRO	10	3.13E+02	3.71E+02	3.36E+02	3.34E+02	1.51E+01
		50	**7.02E+02**	**9.98E+02**	**8.33E+02**	**8.35E+02**	7.72E+01
	DE	10	**3.11E+02**	**3.30E+02**	**3.18E+02**	**3.18E+02**	**4.50E+00**
		50	9.09E+02	1.03E+03	9.96E+02	9.97E+02	**2.30E+01**
F24	PSO	10	1.17E+02	5.96E+02	3.97E+02	4.15E+02	1.16E+02
		50	1.07E+03	1.81E+03	1.35E+03	1.34E+03	1.60E+02
	PRO	10	**1.00E+02**	4.64E+02	3.67E+02	3.89E+02	9.37E+01
		50	**8.86E+02**	1.39E+03	1.07E+03	1.04E+03	1.18E+02
	DE	10	1.17E+02	**3.71E+02**	**3.18E+02**	**3.54E+02**	**7.49E+01**
		50	9.47E+02	**1.05E+03**	**1.01E+03**	**1.02E+03**	**2.12E+01**
F25	PSO	10	4.10E+02	1.21E+03	5.17E+02	4.74E+02	1.42E+02
		50	1.21E+03	6.76E+03	3.13E+03	2.70E+03	1.45E+03
	PRO	10	2.00E+02	5.24E+02	4.30E+02	4.45E+02	**4.20E+01**
		50	**4.61E+02**	**5.81E+02**	**5.35E+02**	**5.40E+02**	**3.64E+01**
	DE	10	**1.16E+02**	**4.33E+02**	**3.90E+02**	**3.99E+02**	5.34E+01
		50	2.00E+03	3.45E+03	2.78E+03	2.81E+03	3.48E+02
F26	PSO	10	3.19E+02	2.09E+03	1.27E+03	1.40E+03	5.39E+02
		50	5.81E+03	1.41E+04	9.71E+03	9.67E+03	1.63E+03
	PRO	10	**2.00E+02**	1.76E+03	8.87E+02	7.08E+02	5.52E+02
		50	**3.45E+03**	**6.45E+03**	**4.93E+03**	**4.90E+03**	6.84E+02
	DE	10	3.00E+02	**4.30E+02**	**3.77E+02**	**3.87E+02**	**3.92E+01**
		50	5.55E+03	7.35E+03	6.93E+03	6.98E+03	**3.05E+02**
F27	PSO	10	4.08E+02	5.84E+02	4.77E+02	4.80E+02	4.48E+01
		50	9.92E+02	2.09E+03	1.34E+03	1.29E+03	2.35E+02
	PRO	10	**3.89E+02**	5.01E+02	4.25E+02	4.09E+02	3.38E+01
		50	6.48E+02	1.13E+03	8.59E+02	8.65E+02	1.23E+02
	DE	10	3.90E+02	**4.10E+02**	**3.95E+02**	**3.95E+02**	**3.85E+00**
		50	**6.13E+02**	**7.49E+02**	**6.82E+02**	**6.80E+02**	**2.91E+01**
F28	PSO	10	3.16E+02	1.11E+03	6.53E+02	6.19E+02	1.79E+02
		50	1.44E+03	7.81E+03	3.96E+03	3.69E+03	1.61E+03
	PRO	10	**3.00E+02**	6.46E+02	5.01E+02	5.84E+02	1.39E+02
		50	**4.59E+02**	**6.10E+02**	**4.98E+02**	**5.04E+02**	**2.62E+01**
	DE	10	3.70E+02	**6.12E+02**	**4.46E+02**	**4.29E+02**	**6.42E+01**
		50	1.16E+03	4.30E+03	2.57E+03	2.43E+03	8.09E+02
F29	PSO	10	3.13E+02	9.18E+02	5.46E+02	5.21E+02	1.54E+02
		50	2.54E+03	7.62E+03	3.73E+03	3.63E+03	9.54E+02
	PRO	10	2.52E+02	5.00E+02	3.30E+02	3.23E+02	5.98E+01
		50	**5.31E+02**	**2.23E+03**	**1.32E+03**	**1.31E+03**	3.59E+02
	DE	10	**2.38E+02**	**2.86E+02**	**2.54E+02**	**2.53E+02**	**1.13E+01**
		50	2.09E+03	3.24E+03	2.78E+03	2.80E+03	**2.76E+02**

F30	PSO	10	1.00E+04	1.56E+07	2.84E+06	1.87E+06	3.23E+06
		50	4.72E+07	2.75E+09	3.76E+08	1.44E+08	5.52E+08
	PRO	10	1.43E+03	1.28E+06	**2.67E+05**	**1.63E+04**	4.39E+05
		50	**6.55E+05**	**2.25E+06**	**1.11E+06**	**1.02E+06**	**3.63E+05**
	DE	10	**1.34E+03**	**8.83E+05**	3.67E+05	1.71E+05	**3.70E+05**
		50	1.74E+07	4.98E+07	3.10E+07	2.98E+07	8.71E+06

with the PSO and DE algorithms in two practical cases, one is relevant to minimizing the mean squared error (MSE) in training level of the MLP neural networks, and the other is to obtain the most suitable pattern for a predetermined Gaussian mixture by the Gaussian mixture model (GMM) method. Both cases can be considered as a type of minimization. As can be seen in Table 7 and Figures 5 and 6, the performance of the PRO algorithm in these cases is better than other algorithms.

In the case that was relevant to the MLP neural network training [71], the MLP method was used for the classification of the Iris flower dataset. In this case, the purpose was to minimize the cost function, mean squared error, in the MLP neural network training. This error shows the difference between the actual and ideal output of the neural network. The number of hidden neurons was considered equal to 10, in which case the dimensions of the vector of neural network parameters (weights and biases) had 83 dimensions for optimization. Moreover, 50% of the whole dataset was used for training the neural network, in other words, we set the value of the variable, fraction of data for training, equal to 0.5.

In the application about the GMM, it should be noted that this model has several applications in different problems such as data processing, for example, speech and image processing, as in [72, 73]. The application of GMM is usually in the pattern recognition and modeling stage. In a standard approach for the training of the Gaussian mixture model parameters, the EM algorithm [74] has been used; however, we used the PSO, DE, and PRO algorithms for comparison instead of EM algorithm. In this case, we used a Gaussian test model with four Gaussian components by ten dimensions. Then by using GMM that was based on the intended optimization algorithms, the best pattern for this model was adapted. In this experiment, based on the determined properties for the test model, the number of the dimensions of the GMM vector parameters for the optimization was equal to 84, and these parameters included mean vectors, covariance matrix, and Gaussian weights.

Figures 5 and 6 show that the PSO and DE algorithms have the drawback of early convergence to the local optimum points and stick in these local optimum points. According to these graphs, PSO and DE algorithms have been converged approximately in iteration 200 and even earlier. However, the PRO algorithm performed much better than these two algorithms from this point of view. As can be seen from these figures, the PRO algorithm has not been fully converged even until the last iteration of the algorithm. It can be drawn from results that the PRO did not stick in local optimum points and tended to more optimization. In addition, the speed of convergence to the global optimum point was much higher in the PRO algorithm than the other two algorithms in comparison. this notable difference in the convergence speed of algorithms can be clearly seen in Figures 5 and 6. Also in Table 7, the best results in each test are written in bold. As can be seen, in both cases the best results are for the PRO algorithm.

TABLE 7. algorithms comparison results in GMM and MLP experiment in 50 separate runs and population members quantity equal to 10 members and the maximum function evaluation of 10E+4

Test	Method	Result				
		Best	**Worst**	**Mean**	**Median**	**SD**
MLP	PSO	1.13E-01	1.02E+00	2.93E-01	2.59E-01	1.52E-01
	PRO	**5.12E-03**	**1.86E-01**	**5.75E-02**	**5.06E-02**	**3.74E-02**
	DE	6.62E-01	2.01E+00	1.29E+00	1.33E+00	2.81E-01
GMM	PSO	5.16E+01	5.61E+01	5.37E+01	5.38E+01	1.17E+00
	PRO	**3.74E+01**	**5.29E+01**	**4.25E+01**	**4.13E+01**	3.56E+00
	DE	5.41E+01	5.58E+01	5.49E+01	5.49E+01	**3.64E-01**

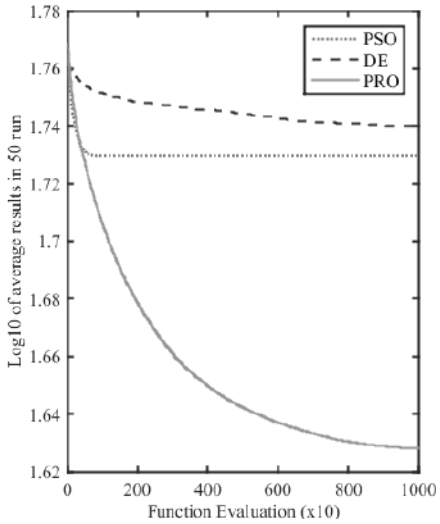

Figure 5. Comparison of the convergence rate of the algorithms in the GMM test

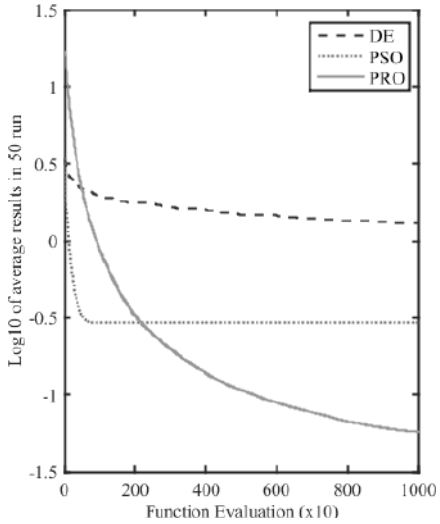

Figure 6. Comparison of the convergence rate of the algorithms in the MLP test

5. CONCLUSION

In this paper, we introduced a new optimization algorithm. The projectiles optimization (PRO) algorithm is a new metaheuristic optimization algorithm that its method is based on the projectiles' motion, and its main idea is based on the properties of this type of motion in physics. In addition, the PRO algorithm is a population-based algorithm.

In this essay, we attempted to introduce the PRO algorithm and analyze its performance and compare it with the two most powerful algorithms in the optimization field, in which they were selected among the metaheuristic optimization algorithms and were most similar to the PRO algorithm. These comparisons were performed to evaluate the accuracy and performance level of the PRO algorithm with respect to other algorithms.

The obtained results from the comparison of PRO algorithm with PSO and DE algorithms generally showed the preference of this algorithm in all the cases and even despite the limitations applied on the comparison to get more fair conditions. The preference of the performance and accuracy of the PRO algorithm was much more notable than the PSO and DE algorithms, especially in high dimensional tests.

In the experiments, we observed that the PRO algorithm had a higher degree of desire for optimization than other algorithms. This means that the PRO algorithm performs much better than the other algorithms and has not the early convergence and sticking in local optimum points, which are considered as drawbacks and weak points. Furthermore, the speed of convergence to the global optimum point in the PRO algorithm is much higher than other algorithms. In other words, the PRO algorithm is able to provide a better balance between the exploration and exploitation compared to the other algorithms. Because a metaheuristic algorithm performs more efficiently if it can provide an appropriate balance between diversification and intensification.

In the next work, we intend to improve the power and accuracy of the PRO algorithm to the best possible level by using the dynamic and optimum updating and self-adaptive initialization of variables associated with the algorithm.

6. REFERENCES

1. Talbi, E.G., "Metaheuristics: From design to implementation",Vol. 74, John Wiley & Sons. (2009). https://doi.org/10.1002/9780470496916
2. Birattari, M., Paquete, L., Strutzle, T. and Varrentrapp, K., Classification of metaheuristics and design of experiments for the analysis of components. Technical Report No. AIDA-01-05, (2001). Retrieved from http://citeseerx.ist.psu.edu/viewdoc/download?doi=10.1.1.12.4407&rep=rep1&type=pdf
3. Boussaïd, I., Lepagnot, J. and Siarry, P., "A survey on optimization metaheuristics," ***Information Sciences***, Vol. 237, (2013), 82-117. https://doi.org/10.1016/j.ins.2013.02.041
4. Blum, C. and Roli, A., "Metaheuristics in combinatorial optimization: Overview and conceptual comparison," ***ACM Computing Surveys (CSUR)***, Vol. 35, No. 3, (2003), 268-308. https://doi.org/10.1145/937503.937505
5. Bianchi, L., Dorigo, M., Gambardella, L.M. and Gutjahr, W.J., "A survey on metaheuristics for stochastic combinatorial optimization," ***Natural Computing: an International Journal***, Vol. 8, No. 2, (2009), 239-287. https://doi.org/10.1007/s11047-008-9098-4
6. Goldberg, D.E. and Deb, K., "A comparative analysis of selection schemes used in genetic algorithms," ***Foundations of genetic***

algorithms, Vol. 1, (1991), 69-93. https://doi.org/10.1016/b978-0-08-050684-5.50008-2

7. Blickle, T. and Thiele, L., A comparison of selection schemes used in genetic algorithms. (1995), TIK-Report. https://doi.org/10.1162/evco.1996.4.4.361
8. Beasley, D., Bull, D.R. and Martin, R.R., "An overview of genetic algorithms: Part 2, research topics," ***University computing***, Vol. 15, No. 4, (1993), 170-181. Retrieved from http://citeseer.ist.psu.edu/16527.html
9. Becerra, R.L. and Coello, C.A.C., A cultural algorithm with differential evolution to solve constrained optimization problems, in Advances in Artificial Intelligence–IBERAMIA 2004. Springer, (20040, 881-890. https://doi.org/10.1007/978-3-540-30498-2_88
10. Konak, A., Coit, D.W. and Smith, A.E., "Multi-objective optimization using genetic algorithms: A tutorial," ***Reliability Engineering & System Safety***, Vol. 91, No. 9, (2006), 992-1007. https://doi.org/10.1016/j.ress.2005.11.018
11. Alba, E. and Troya, J.M., "A survey of parallel distributed genetic algorithms," ***Complexity***, Vol. 4, No. 4, (1999), 31-52. https://doi.org/10.1002/(SICI)1099-0526(199903/04)4:4<31::AID-CPLX5>3.0.CO;2-4
12. Elsayed, S.M., Sarker, R.A. and Essam, D.L., "A new genetic algorithm for solving optimization problems," ***Engineering Applications of Artificial Intelligence***, Vol. 27, (2014), 57-69. https://doi.org/10.1016/j.engappai.2013.09.013
13. Goldberg, D.E., "Genetic algorithms in search optimization and machine learning," Addison-Wesley Reading Menlo Park, Vol. 412, (1989). https://doi.org/10.5860/choice.27-0936
14. Kirkpatrick, S. and Vecchi, M.P., "Optimization by simulated annealing," ***Science***, Vol. 220, No. 4598, (1983), 671-680. https://doi.org/10.1126/science.220.4598.671
15. Černý, V., "Thermodynamical approach to the traveling salesman problem: An efficient simulation algorithm," ***Journal of Optimization Theory and Applications***, Vol. 45, No. 1, (1985), 41-51. https://doi.org/10.1007/BF00940812
16. Metropolis, N., Rosenbluth, A.W., Rosenbluth, M.N., Teller, A.H. and Teller, E., "Equation of state calculations by fast computing machines," ***The Journal of Chemical Physics***, Vol. 21, No. 6, (1953), 1087-1092. https://doi.org/10.1063/1.1699114
17. Creutz, M., "Microcanonical Monte Carlo simulation," ***Physical Review Letters***, Vol. 50, No. 19, (1983), 1411-1414. https://doi.org/10.1103/PhysRevLett.50.1411
18. Dueck, G. and Scheuer, T., "Threshold accepting: A general-purpose optimization algorithm appearing superior to simulated annealing," ***Journal of Computational Physics***, Vol. 90, No. 1, (1990), 161-175. https://doi.org/10.1016/0021-9991(90)90201-B
19. Dréo, J., Petrowski, A., Siarry, P. and Taillard, E., "Metaheuristics for hard optimization: Methods and case studies, Springer Science & Business Media, (2006).
20. Charon, I. and Hudry, O., "The noising method: A new method for combinatorial optimization," ***Operations Research Letters***, Vol. 14, No. 3, (1993), 133-137. https://doi.org/10.1016/0167-6377(93)90023-A
21. Charon, I. and Hudry, O., "The noising methods: A generalization of some metaheuristics," ***European Journal of Operational Research***, Vol. 135, No. 1, (2001), 86-101. https://doi.org/10.1016/S0377-2217(00)00305-2
22. Charon, I. and Hudry, O., The noising methods: A survey, in Essays and surveys in metaheuristics. 2002, Springer.245-261. https://doi.org/10.1007/978-1-4615-1507-4
23. Charon, I. and Hudry, O., "Self-tuning of the noising methods," ***Optimization***, Vol. 58, No. 7, (2009), 823-843. https://doi.org/10.1080/02331930902944911
24. Courat, J.-P., Raynaud, G., Mrad, I. and Siarry, P., "Electronic component model minimization based on log simulated annealing," ***IEEE Transactions on Circuits and Systems I: Fundamental Theory and Applications***, Vol. 41, No. 12, (1994), 790-795. https://doi.org/10.1109/81.340841
25. Jeong, I.-K. and Lee, J.-J., "Adaptive simulated annealing genetic algorithm for system identification," ***Engineering Applications of Artificial Intelligence***, Vol. 9, No. 5, (1996), 523-532. https://doi.org/10.1016/0952-1976(96)00049-8
26. Suman, B. and Kumar, P., "A survey of simulated annealing as a tool for single and multiobjective optimization," ***Journal of the Operational Research Society***, Vol. 57, No. 10, (2006), 1143-1160. https://doi.org/10.1057/palgrave.jors.2602068
27. Chopard, B., and Tomassini, M., "Simulated annealing, Natural Computing Series (First Edition). IN-TECH Education and Publishing, (2018). https://doi.org/10.1007/978-3-319-93073-2_4
28. Hasani, A. and Soltani, R., "A hybrid meta-heuristic for the dynamic layout problem with transportation system design," ***International Journal of Engineering - Transactions B: Applications,*** Vol. 28, No. 8, (2015), 1175-1185. https://doi.org/10.5829/idosi.ije.2015.28.08b.10
29. Fallah, M., Mohajeri, A. and Barzegar-Mohammadi, M., "A new mathematical model to optimize a green gas network: A case study," In CIE 2016: 46th International Conferences on Computers and Industrial Engineering, 1142–1149. Retrieved from https://www.researchgate.net/publication/320920905
30. Chan, F.T. and Tiwari, M.K., "Swarm Intelligence: Focus on Ant and Particle Swarm Optimization, IntechOpen, (2007). https://doi.org/10.5772/5121
31. Saenphon, T., Phimoltares, S. and Lursinsap, C., "Combining new fast opposite gradient search with ant colony optimization for solving travelling salesman problem," ***Engineering Applications of Artificial Intelligence***, Vol. 35, (2014), 324-334. https://doi.org/10.1016/j.engappai.2014.06.026
32. Dorigo, M. and Stutzle, T., The ant colony optimization metaheuristic: Algorithms, applications, and advances, In Handbook of metaheuristics. Springer, (2003), 250-285. https://doi.org/10.7551/mitpress/1290.003.0004
33. Dorigo, M., Birattari, M. and Stutzle, T., "Ant colony optimization," ***IEEE Computational Intelligence Magazine***, Vol. 1, No. 4, (2006), 28-39. https://doi.org/10.1109/MCI.2006.329691
34. Dorigo, M. and Stützle, T., Ant colony optimization: Overview and recent advances, In International Series in Operations Research and Management Science (Vol. 272), Handbook of metaheuristics, Springer, 311–351. https://doi.org/10.1007/978-3-319-91086-4_10
35. Mohajeri, A., Mahdavi, I., Mahdavi-Amiri, N. and Tafazzoli, R., "Optimization of tree-structured gas distribution network using ant colony optimization: A case study," ***International Journal of Engineering - Transactions A: Basics***, Vol. 25, No. 2, (2012), 141-158. https://doi.org/10.5829/idosi.ije.2012.25.02a.04
36. Eberhart, R.C. and Kennedy, J., "A new optimizer using particle swarm theory," In Proceedings of the International Symposium on Micro Machine and Human Science, Vol. 1, IEEE, (1995), 39-43. https://doi.org/10.1109/mhs.1995.494215
37. Kennedy, J., Eberhart, R.C. and Shi, Y., "Swarm Intelligence", IEEE Technology and Society Magazine (Vol. 21). Morgan Kaufmann. IEEE, (2002). https://doi.org/10.1109/MTAS.2002.993595
38. Kennedy, J. and Mendes, R., "Population structure and particle swarm performance," In The 2002 IEEE Congress on Evolutionary

Computation, CEC'02, (2002), 1671-1676. https://doi.org/10.1109/CEC.2002.1004493

39. Gulcu, S. and Kodaz, H., "A novel parallel multi-swarm algorithm based on comprehensive learning particle swarm optimization," ***Engineering Applications of Artificial Intelligence***, Vol. 45, (2015), 33-45. https://doi.org/10.1016/j.engappai.2015.06.013
40. Shi, Y. and Eberhart, R., "A modified particle swarm optimizer," In The 1998 IEEE International Conference on Evolutionary Computation, CEC'98, (1998), 69-73. https://doi.org/10.1109/ICEC.1998.699146
41. Shi, Y. and Eberhart, R.C., "Empirical study of particle swarm optimization," In The 1999 IEEE Congress on Evolutionary Computation , CEC'99, (1999), 1945-1950. https://doi.org/10.1109/CEC.1999.785511
42. Clerc, M. and Kennedy, J., "The particle swarm-explosion, stability, and convergence in a multidimensional complex space," ***IEEE Transactions on Evolutionary Computation,*** Vol. 6, No. 1, (2002), 58-73. https://doi.org/10.1109/4235.985692
43. Ozcan, E. and Mohan, C.K., "Particle swarm optimization: Surfing the waves," in The 1999 IEEE Congress on Evolutionary Computation, CEC'99, (1999), 1939-1944. https://doi.org/10.1109/CEC.1999.785510
44. Van den Bergh, F. and Engelbrecht, A.P., "A study of particle swarm optimization particle trajectories," ***Information Sciences***, Vol. 176, No. 8, (2006), 937-971. https://doi.org/10.1016/j.ins.2005.02.003
45. Kennedy, J. and Eberhart, R.C., "A discrete binary version of the particle swarm algorithm," In The 1997 IEEE International Conference on Systems, Man, and Cybernetics, (1997), 4104-4108. https://doi.org/10.1109/icsmc.1997.637339
46. Blackwell, T., Particle swarm optimization in dynamic environments, In Evolutionary computation in dynamic and uncertain environments. 2007, Springer. 29-49. https://doi.org/10.1007/978-3-540-49774-5_2
47. Jam, S., Shahbahrami, A. and Sojoudi Ziyabari, S., "Parallel implementation of particle swarm optimization variants using graphics processing unit platform," ***International Journal of Engineering - Transactions A: Basics***, Vol. 30, No. 1, (2017), 48-56. https://doi.org/10.5829/idosi.ije.2017.30.01a.07
48. Reyes-Sierra, M. and Coello, C.C., "Multi-objective particle swarm optimizers: A survey of the state-of-the-art," ***International Journal of Computational Intelligence Research***, Vol. 2, No. 3, (2006), 287-308. https://doi.org/10.5019/j.ijcir.2006.68
49. Ling, S.H., Chan, K.Y., Leung, F.H.F., Jiang, F. and Nguyen, H., "Quality and robustness improvement for real-world industrial systems using a fuzzy particle swarm optimization," ***Engineering Applications of Artificial Intelligence***, Vol. 47, (2016), 68-80. https://doi.org/10.1016/j.engappai.2015.03.003
50. Mahmoodabadi, M., Taherkhorsandi, M. and Safikhani, H., "Modeling and hybrid pareto optimization of cyclone separators using group method of data handling (gmdh) and particle swarm optimization (pso)," ***International Journal of Engineering - Transactions C: Aspects***, Vol. 26, No. 9, (2012), 1089-1102. https://doi.org/10.5829/idosi.ije.2013.26.09c.15
51. Valdez, F., Melin, P. and Castillo, O., "An improved evolutionary method with fuzzy logic for combining particle swarm optimization and genetic algorithms," ***Applied Soft Computing***, Vol. 11, No. 2, (2011), 2625-2632. https://doi.org/10.1016/j.asoc.2010.10.010
52. Poli, R., "Analysis of the publications on the applications of particle swarm optimisation," ***Journal of Artificial Evolution and Applications***, Vol. 2008, (2008), 1-10. https://doi.org/10.1155/2008/685175
53. Poli, R., Kennedy, J. and Blackwell, T., "Particle swarm optimization," ***Swarm Intelligence***, Vol. 1, No. 1, (2007), 33-57. https://doi.org/10.1007/s11721-007-0002-0
54. Pant, M., Thangaraj, R. and Abraham, A., Particle swarm optimization: Performance tuning and empirical analysis, In Foundations of computational intelligence. 2009, Springer. 101-128. https://doi.org/10.1007/978-3-642-01085-9_5
55. Thangaraj, R., Pant, M., Abraham, A. and Bouvry, P., "Particle swarm optimization: Hybridization perspectives and experimental illustrations," ***Applied Mathematics and Computation***, Vol. 217, No. 12, (2011), 5208-5226. https://doi.org/10.1016/j.amc.2010.12.053
56. Deepa, S., Babu, S.R. and Ranjani, M., "A robust statcom controller using particle swarm optimization," ***International Journal of Engineering - Transactions B: Applications***, Vol. 27, No. 5, (2013), 731-738. https://doi.org/10.5829/idosi.ije.2014.27.05b.08
57. Daliri, H., Mokhtari, H. and Nakhai, I., "A particle swarm optimization approach to joint location and scheduling decisions in a flexible job shop environment," ***International Journal of Engineering-Transaction C: Aspects***, Vol. 28, No. 12, (2015), 1756-1764. https://doi.org/10.5829/idosi.ije.2015.28.12c.08
58. Storn, R. and Price, K., "Differential evolution–a simple and efficient heuristic for global optimization over continuous spaces," ***Journal of Global Optimization***, Vol. 11, No. 4, (1997), 341-359. https://doi.org/10.1023/A:1008202821328
59. Mezura-Montes, E., Reyes-Sierra, M. and Coello, C.A.C., Multi-objective optimization using differential evolution: A survey of the state of the art, In Advances in differential evolution. Vol. 143, (2008), Springer. 173-196. https://doi.org/10.1007/978-3-540-68830-3_7
60. Amirian, H. and Sahraeian, R., "Multi-objective differential evolution for the flow shop scheduling problem with a modified learning effect," ***International Journal of Engineering - Transactions C: Aspects***, Vol. 27, No. 9, (2014), 1395-1404. https://doi.org/10.5829/idosi.ije.2014.27.09c.09
61. Angeline, P.J., "Evolutionary optimization versus particle swarm optimization: Philosophy and performance differences," In Evolutionary Programming VII, Springer. (1998), 601-610. https://doi.org/10.1007/bfb0040811
62. Price, K., Storn, R.M. and Lampinen, J.A., "Differential evolution: A practical approach to global optimization, Springer Science & Business Media, (2006).
63. Das, S. and Suganthan, P.N., "Differential evolution: A survey of the state of the art," ***IEEE Transactions on Evolutionary Computation,*** Vol. 15, No. 1, (2011), 4-31. https://doi.org/10.1109/TEVC.2010.2059031
64. Karci, A., Imitation of bee reproduction as a crossover operator in genetic algorithms, in PRICAI 2004: Trends in artificial intelligence. (Vol. 3157), Springer, (2004). 1015-1016. https://doi.org/10.1007/978-3-540-28633-2_141
65. Brest, J. and Maučec, M.S., "Self-adaptive differential evolution algorithm using population size reduction and three strategies," ***Soft Computing***, Vol. 15, No. 11, (2011), 2157-2174. https://doi.org/10.1007/s00500-010-0644-5
66. Teng, N.S., Teo, J. and Hijazi, M.H.A., "Self-adaptive population sizing for a tune-free differential evolution," ***Soft Computing***, Vol. 13, No. 7, (2009), 709-724. https://doi.org/10.1007/s00500-008-0344-6
67. Liu, J. and Lampinen, J., "A fuzzy adaptive differential evolution algorithm," ***Soft Computing***, Vol. 9, No. 6, (2005), 448-462. https://doi.org/10.1007/s00500-004-0363-x
68. Tummala, A.S., Chintala, M.R. and Pilla, R., "Tuning of extended kalman filter using self-adaptive differential evolution algorithm for

sensorless permanent magnet synchronous motor drive," ***International Journal of Engineering - Transactions A: Basics***, Vol. 29, No. 11, (2016), 1565-1573. https://doi.org/10.5829/idosi.ije.2016.29.11b.00

69. Kahrizi, M.R. Projectiles optimization (pro) algorithm. 2017 [cited 2020 Jun. 22]; IEEE Dataport. Available from: https://doi.org/10.21227/H2TK92
70. Awad, N.H., Ali, M.Z., Liang, J.J., Qu, B.Y. and Suganthan, P.N., Problem definitions and evaluation criteria for the CEC 2017 special session and competition on single objective bound constrained real-parameter numerical optimization. 2016. Available: https://www.ntu.edu.sg/home/EPNSugan/index_files/CEC2017/CEC 2017.htm. Accessed: 21/06/2020.
71. Haykin, S., "Neural networks: A comprehensive foundation, Prentice Hall PTR, (1994).
72. Reynolds, D.A. and Rose, R.C., "Robust text-independent speaker identification using Gaussian mixture speaker models," ***IEEE Transactions on Speech and Audio Processing***, Vol. 3, No. 1, (1995), 72-83. https://doi.org/10.1016/0167-6393(95)00009-D
73. Kahrizi, M.R. and Kabudian, S.J., "Long-term spectral pseudo-entropy (ltspe): A new robust feature for speech activity detection," ***Journal of Information Systems & Telecommunication (JIST)***, Vol. 6, No. 4, (2018), 204-208. https://doi.org/10.7508/jist.2018.04.003
74. Dempster, A.P., Laird, N.M. and Rubin, D.B., "Maximum likelihood from incomplete data via the em algorithm," ***Journal of the Royal Statistical Society: Series B (Methodological)***, Vol. 39, No. 1, (1977), 1-22. https://doi.org/10.1111/j.2517-6161.1977.tb01600.x

Persian Abstract

چکیده

الگوریتم‌های بهینه‌سازی فراابتکاری گونه‌های نسبتا جدیدی از الگوریتم‌های بهینه‌سازی هستند که برای مسائل بهینه‌سازی دشوار که نمی‌توان از روش‌های کلاسیک برای آنها استفاده کرد کاربرد فراوانی دارند و روشی شناخته‌شده و بسیار گسترده برای مسائل دشوار بهینه‌سازی به حساب می‌آیند. در این مقاله یک الگوریتم بهینه‌سازی فراابتکاری جدید که ایده‌ی اصلی آن از یک نوع حرکت در فیزیک ایده‌برداری شده‌است ارائه می‌شود تا به وسیله‌ی آن بتوان به نتایج بهتری نسبت به سایر الگوریتم‌های بهینه‌سازی در این حوزه دست یافت و برای رسیدن به نقطه‌ی مطلوب‌تر مسیر جدیدی را تجربه کرد. از این رو در این مقاله بعد از معرفی الگوریتم بهینه‌سازی پرتابه‌ها، ابتدا این الگوریتم بهینه‌سازی را با الگوریتم‌های شناخته شده و قدرتمند این حوزه و بر روی توابع سنجش معروف، مقایسه کردیم و در ادامه، عملکرد الگوریتم بهینه‌سازی پرتابه‌ها را در دو مورد از کاربردهای عملی با الگوریتم‌های دیگر مورد سنجش قرار دادیم و نتایج این مقایسه‌ها را در جدول‌ها و شکل‌های گوناگون و برای حالت‌های مختلف آورده‌ایم که نشان‌دهنده‌ی دقت به مراتب بیشتر الگوریتم بهینه‌سازی پرتابه‌ها نسبت به الگوریتم‌های دیگر می‌باشد.

IJE TRANSACTIONS A: Basics Vol. 33, No. 10, (October 2020) 1939-1950

International Journal of Engineering

Journal Homepage: www.ije.ir

A Multilayer Motion Direction Based Model for Tracking Vehicles at Intersections

M. Delavarian*[a], O. Marouzi[b], H. Hassanpour[a]

[a] *Faculty of Computer Engineering, Shahrood University of Technology, Shahrood, Iran*
[b] *Faculty of Electrical & Robotic Engineering, Shahrood University of Technology, Shahrood, Iran*

PAPER INFO

Paper history:
Received 18 March 2020
Received in revised form 20 May 2020
Accepted 26 May 2020

Keywords:
Machine Vision
Motion Flows
Multilayer Model
Multi-object Tracking
Tracking at Intersection
Vehicle Tracking

ABSTRACT

Visual vehicle tracking is an important topic in intelligent transportation systems. Intersections are challenging locations for visual systems to track vehicles which are simultaneously moving in different directions. In addition, normal traffic flow may change at intersections due to accidents. Congestion, occlusion and undetermined motion flows are the nominated challenging issues of vehicle tracking at intersections. In this paper, a method for tracking multiple vehicles is proposed considering the vehicle motion directions to overcome undetermined motion flows. For this purpose, a multilayer model is presented, which assigns each motion flows to distinct layers. Moreover, we introduce different neighborhoods for various layers considering the regular motion flows in a layer. Hence, vehicles entering from the same side of intersection with the same motion direction are assigned to the same layer. Then the tracking is performed on different layers separately. In special cases such as vehicles crossing each other, misdetections or occlusion, the proposed tracking method can predict the vehicles tracks by using the stored tracking history and considering neighborhoods in that layer. Experimental results show consistency between proposed tracking method results and ground truth, also outperformance of other tracking methods in tracking vehicles crossing the intersection.

***doi**: 10.5829/ije.2020.33.10a.12*

1. INTRODUCTION

Visual tracking methods are generally used in various applications to increase the quality of factors such as safety managements and accident avoidance. The demand for fast and efficient tracking system algorithms is increasing for traffic management and roads safety. In recent years, monitoring at intersections has gained attention due to a growth in the accident rate. Several challenging issues were conveyed regarding to Vehicle Tracking at Intersection (VTI) such as different and undetermined motion flows (Figure 1), occlusion and congestion [1, 2]. Driving at intersections is significantly more dangerous in comparison to other locations due to a higher possible rate of conflict between vehicles motion flows (see Figure 1). Therefore, it is of the concern by many researches in the literature. As a result, tracking vehicles is the main phase of vehicle monitoring at intersections.

Vehicle monitoring process consists of two stages: vehicle tracking and vehicle behavior analysis. Active and passive sensors can be used for vehicle sensing at intersection [3]. Cameras are used as one of the passive sensors, and are often used in intersections due to their lower cost and wider field of view. The studying on vehicle tracking is an ongoing research as the systems are not yet reliable and robust for tracking vehicles under highly non-similar circumstances.

Researches have recently paying special attention to vision-based detection and tracking systems [4–8]. Lots of researches have been conducted on vehicle tracking and traffic monitoring in general [9–11]. Tracking at intersection has gained more attention over the past decade. Lately, special reviews are focused on intersection monitoring [1, 2]. In the research done by Datondji et al. [1], they reviewed vision based systems about intersection monitoring including sensing technologies, datasets, vehicles detection, tracking and

*Corresponding Author Email: *delavarian.mohadeseh@shahroodut.ac.ir* (M. Delavarian)

Please cite this article as: M. Delavarian, O. Marouzi, H. Hassanpour, A Multilayer Motion Direction Based Model for Tracking Vehicles at Intersections, International Journal of Engineering (IJE), IJE TRANSACTIONS A: Basics Vol. 33, No. 10, (October 2020) 1939-1950

monitoring methods and their challenges. In another study reported in literature [2], they focused on behavior and safety analysis of vehicles, drivers and pedestrians at intersections besides techniques for automating visual sensing.

Tracking at intersection is usually discussed in a Bayesian framework [12, 13]. Among the Bayesian tracking methods, Kalman filter is one of the most popular algorithms. The Kalman filter tries to estimate the probability of the next state using previous information and measurements. Song and Nevatia [13] proposed a Markov Chain Monte Carlo (MCMC) in order to segment multiple overlapped vehicles into separate ones with respective orientation. In another research, a two level tracker, low-level and high-level, was introduced for VTI [14]. The first part tracks binary blobs. The high-level tracker models the target and estimates the route via the frame information. They used Kalman filter for predicting movements. Their proposed method could not track motionless vehicles and in crowded scenes.

Nateghinia et al. [15] introduced a video-based system for vehicle detection and tracking via dynamic texture modeling for background estimation. They used a point tracking method with weighted recursive least square. Liu et al. [16] proposed a three-dimensional particle filter tracking method. By collaborative tracking via visual information complementation, the robustness of tracking is improved.

For vehicle sensing at intersections, most systems require one or more cameras installed at certain positions which could cover most of the intersection area [17]. In some researches one camera above the ground or fisheye camera is used [18–20]. Wang et al. [19] proposed a real time system for tracking and counting multiple vehicles. They used fisheye camera based on simple feature points. In another research, drone floating camera is used [20]. In their proposed method, in the first phase they used background subtraction. Then, Kalman filter is applied to footage from a drone-floating camera. Another real time vision system at urban crossroad is reported in literature [12]. They used monocular images from pole-mounted video cameras. Their proposed system consists of segmentation with robust background updating and feature based motion tracking method.

A video-based system for obtaining traffic-flow statistics is presented for road intersections by training a deep learning architecture from a pre-trained model [21]. Some studies used more than one camera. Subedi et al. [22] proposed 3D vehicle tracking for a multiple-camera system. A calibration method is introduced, then vehicle silhouettes are detected, and tracking is performed by Kalman filtering.

In the research done by Li et al. [23], they developed an unsupervised vehicle tracking system for urban environments. This method is based on tracklets. Raw tracklets are considered as sample points and are grouped to build different vehicle candidates. Min et al. [24] introduced an approach for tracking multiple vehicles. In this method, they used an improved ViBe algorithm and the gray-scale spatial information for accurate vehicle detection. They used SVM (Support Vector Machine) and CNN (Convolutional Neural Network) classifiers to address occlusions in their tracking. Bedruz et al. [25] proposed an algorithm for detecting and tracking vehicles at intersections in real time. The algorithm is based on blob analysis for main tracking and mean shift kernel tracking when a blob merging occurred.

Some researches track all road users at intersection. Tracking all road users at intersection can be very useful for transportation systems, as all trajectories can be used for monitoring and safety analysis. Jodoin et al. [26] developed a method to track all road users at intersection. At first their method starts from background subtraction to extract the potential a priori unknown road users. Afterwards, each user is tracked by key points inside the detected region. In the Ko-PER project, a dataset for intersection monitoring has been released [27]. This dataset contains laser-scanners and video cameras information. Also, they developed a system for tracking all road users by using all measurements of this dataset including laser-scanners and video frames information. They presented a general-purpose multi-sensor tracking algorithm. Therefore, a multiple-model method is needed in their approach. So, an extension of PHD (Probability Hypothesis Density) filter is proposed [28].

The method proposed by Yang and Bilodeau [29] tracks road users at intersection. Their method combines background subtraction and KFC (Kernelized Correlation Filter) tracker for data association and when an occlusion happens. In another research, a deep learning detection approach is used for object classification and labeling, then labels were employed in tracking users at intersection [30]. After that, they expanded the method to use background subtraction and detection labels by color and class to predict tracks in MOT [31]. Chan et al. [32] proposed city tracker that is a tracking framework in urban traffic scenes that applies a predetermined deep learning based detector and predicts tracks based on DeepSORT.

In this paper, a vehicle tracking method is proposed to overcome undetermined motion flows and the occlusion caused in VTI systems. Our focus is on tracking multiple vehicles at intersection from a camera view. The camera may be installed somewhere around the intersection and has almost a full view. A multilayer model is proposed to distinguish motion flows in distinct layers. The movements are based on the layers acceptable motion flows and the side through which vehicles enter the intersection. Different neighborhoods are introduced for each and distinct layers. Neighborhoods are constructed based on regular and acceptable motion

flows associated with the entering side of an intersection. Acceptable motion flows for an intersection are depicted in Figure 1. After constructing the multilayer and neighborhoods for an intersection, in tracking phase, vehicles entering to each side of intersection are assigned to its associated layer. Tracking is performed in each layer separately based on vehicles movements and the neighborhoods. In case of occlusions or misdetections during tracking, the proposed method considers history of tracks and routes the vehicles based on neighborhoods of layers. The proposed tracking method is based on initial model introduced in literature [33].

The rest of the paper is organized as follows: In section 2 the proposed tracking method is described. Experimental results are presented in section 3. In section 4 experimental scenarios are discussed. Section 5 concludes the paper.

2. THE PROPOSED METHOD

VTI is a challenging task due to the involvement of various parameters, including the simultaneous movement of multiple vehicles and pedestrians. Once vehicles cross the intersection, different directions are possible to be taken. Figure 1 depicts different motion flows at an intersection from each entry-exit side. It can be seen that motion flows may collide with each other, consequently accidents may happen.

One standard approach in multi-object tracking algorithms is tracking-by-detection [34]. Detecting is performed separately. Therefore, detection performance does not affect tracking performance. The proposed method initially detects vehicles only, (excluding pedestrians or bicycles), using an existing detection method. It is assumed that vehicles crossing intersection only follow predefined directions (see Figure 1).

2. 1. Multilayer Model Construction A multilayer model is employed for tracking, in which different motion flows are distributed in distinct layers.

The proposed model assigns one layer for each entry-exit side, so based on the number of entry-exit sides, we have layers, $1 \le l \le L$, L is the total number of layers. In this study, we assume that each intersection has four entry-exit sides, so $L=4$. However, there is no limitation in the total number of layers (entry-exit sides).

The area of tracking, i.e. the field of view (FOV) is indicated manually. The sides of FOV, that are associated with each entry side and layer, are labeled clockwise, say from 1 to 4 starting from top side as it can be seen in Figure 2. After that a grid is constructed over the ground of intersection as it is shown in Figure 2. The size of grid cells is determined by the distance between grid lines. This distance is a user determined, variable in pixels, which shall be called the *step* parameter. The y-intercept of the grid lines that is called *y Intercept Change* should be modified as shown in Equation (1), where a is the line slope.

$$y\ Intercept\ Change = step \Big/ \sqrt{1/(1+a^2)} \quad (1)$$

Afterwards all crossing points of grid lines are stored in matrix p. Then, a grid cell matrix C is created where each $C(i,j)$ is associated with four points of the matrix p like $[\ p(i,j),\ p(i,j+1),\ p(i+1,j+1),\ p(i+1,j)\ ]$. So, each cell of grid matrix C represents a part of the intersection. The sample grids for the values 20 and 40 of *step* parameter for Ko-PER dataset intersection [27] are shown in Figure 3. As can be seen with a smaller *step* parameter, the grid matrix has more cells with a smaller size. The size and number of cells, as results of the value of *step* parameter, have direct effect in tracking results and run time that will be discussed in section 3.

Vehicles in each layer can only move in permissible directions. Also, layers are independent of each other, which means vehicles cannot move between layers. We introduced neighborhoods to model allowed acceptable motion directions for each layer separately. Hence, the difference between the layers is equivalent to the cell's neighborhoods in each layer. If a vehicle is at cell $C(i,j)$ of layer k at time t, it can be at cell $C(i,j)$ or cell $C(i',j')$

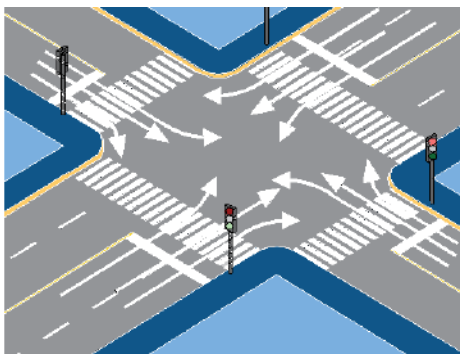

Figure 1. Motion directions of each side for a sample intersection

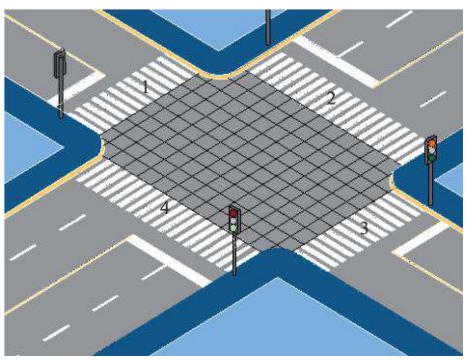

Figure 2. Labeled sides, layers and grid cells of FOV for a sample intersection

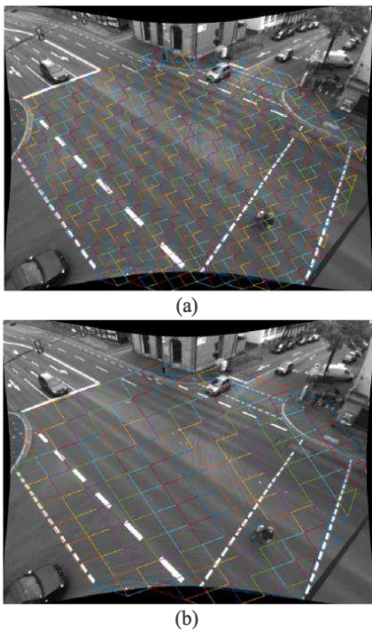

Figure 3. Grid cells of FOV in Ko-PER dataset for *step* parameter equals to (a) 20, (b) 40

where *(i',j')* is neighbors of cell (i,j) at time *(t+1)* and layer *k*. Neighbors are based on the layer's motion directions. For example, neighbors of *(i,j)* in layer 1 can be *(i, j-1)* (for turning left), *(i,j+1)* (for turning right), *(i+1,j)* (for going straight) and finally *(i+1,j-1)* and *(i+1,j+1)* (for turning left and right, respectively). So, two of the neighbors are adjacent and the other three are in front of those two and itself (the front direction is determined relative to the movement direction of the layer). The set of these five neighborhood cells are called *Near* neighborhood. This neighborhood is more useful when the *step* parameter is big or the recording frame rate is high.

When the frame rate is low or the value of *step* parameter is small, a vehicle can move more than one neighboring cell. Another case is that due to variations of camera view angle for different grid cells, there is some confusion in positioning far and near cells to the camera. Therefore, in addition to the *Near* neighborhood, a bigger neighborhood is needed. Hence, *Far* neighborhood is introduced. In the *Far* neighborhood, each cell of the *Near* neighborhood has another neighboring cell in the motion directions of that layer. For instance, in layer 4 (left side) cell *C(i,j)* has *(i,j+1)* as its neighbors in *Near* neighborhood. Cell *C(i,j+2)* is added for *Far* neighborhood and this goes on for other neighbors. The *Near* and *Far* neighborhoods of layer 2 are defined in Table 1. The index *(i,j)* is the cell where the vehicle is currently located. The cells in the gray background are *Near* neighbors and the cells with white background are *Far* neighbors. Each layer has different *Near* and *Far* neighborhood cells based on its motion direction flows. The neighborhoods of other layers are computed the same way as it shows for layer 2 in Table 1 and layer 1 in previous paragraph.

2. 2. The Tracking Algorithm Multilayer model including layers and neighborhoods is constructed for an intersection before tracking is performed. During tracking, when a vehicle enters the intersection, a new tag number, *(tag>0)*, is assigned to it. Also, the vehicle is assigned to the associated layer. Afterwards, tracking is performed for each layer separately. During the tracking phase, track records are stored. Track records for vehicles consist of main information and are saved in the format of Equation (2):

$$TrackRecord=[time, layer, tag, i, j, middlePoint] \quad (2)$$

where *time* is the frame number or tracking time, *layer* and *tag* are the layer number and vehicle identification number, respectively; *i* and *j* are cell index of the grid matrix *C* which is the vehicle position on FOV and *middlePoint* for middle point of their bounding boxes.

For the next frames, the detected vehicles may remain motionless or move to one of their neighboring cells. Each grid cell can only contain one vehicle at a time. For the following frames, we looked for previously recognized vehicles' trajectories in neighborhoods of detected vehicles cells. This repeats for every detected vehicle on next frames. When a vehicle enters the intersection, after incrementing the previous tag number, it is assigned to the vehicle. However, if it had been entered previously, it already has a trajectory, layer and tag number. So, it gets the tag and layer number from the trajectory that this vehicle belongs to based on the above procedure.

We introduced two neighborhoods including *Near* and *Far*. Therefore, for checking neighborhoods, three cases can be considered. In the first case, only the *Near* neighborhood is checked. This neighborhood can be used when the *step* parameter is big or scenes are crowded. In the second one, the *Far* neighborhood is checked which is used when *step* parameter is small. In the third case, both neighborhoods are considered. At first, the temporary destination is checked based on *Near* neighborhood and if there is no track in *Near* neighborhood's previous frame then the *Far* neighborhood is checked.

TABLE 1. *Near* and *Far* neighborhoods for right side layer (Layer 2)

i-2 , j-2	*i-2 , j-1*	*i-2 , j*
i-1 , j-2	*i-1 , j-1*	*i-1 , j*
i , j-2	*i , j-1*	*i , j*
i+1 , j-2	*i+1 , j-1*	*i+1 , j*
i+2 , j-2	*i+2 , j-1*	*i+2 , j*

The previous steps are performed for vehicles contained in each frame. Each track ends when the vehicle crosses other side lines or the detections are out of FOV.

One of the advantages of the proposed tracking algorithm is that no collision occurs. Because during the tracking phase vehicles that come from different sides are assigned to different layers. The other advantage is that if an occlusion or misdetection occurs according to the history of tracks and checking the neighborhoods based on *Far* neighborhood of *Near* neighborhood cells, the tracking algorithm can predict tracks. Finally, at the end or any time in the middle of tracking, all tracks can be computed by using the tag number and saved history of the tracks. The final proposed tracking method based on the multilayer model, *Near* and *Far* neighborhoods is summarized in Algorithm 1. The preprocessing is done once for each intersection and tracking is performed for each frame and detection.

For a better demonstration of the proposed tracking method, two sample consecutive frames during tracking are shown in Figure 4. At time *t* and *t+1*, middle point of detected and tracked vehicles are shown. Different colors show vehicles in different layers. *Near* neighborhood cells of some vehicles are drawn with red dots. The correspondent arrows with the same layer color show the correspondent tracked vehicle in frame *t+1*. As the figure illustrates, the vehicles appear in their neighborhoods based on the layers' motion flows.

3. EXPERIMENTAL RESULTS

The proposed tracking method contains a number of parameters including values of *step* and different neighborhoods. By the *step* value, resolution of tracking is controlled. Before the tracking phase, the multilayer model is constructed as a preprocessing phase and is computed just once for each intersection.

ALGORITHM 1. Proposed tracking method based on multilayer model

```
Preprocessing:
    // Multilayer model construction
    Indicating FOV
    Labeling entry-exit sides clockwise starting from top side
    Determining step parameter value
    Constructing grid cells over the ground of intersection
    Assigning a layer to each entry-exit side
    Determining Near and Far neighborhoods for all layers and cells
Tracking:
for each frame t do
    Extract detections from a detector for frame t
    for each detection det in t do
        if det entering the intersection then
            l ← layer number
            tag ← tag number
            middlePoint ← the centroid of det
            [i,j] ← the cell that middlePoint is located at
            Create TrackRecord = [t, layer, tag, i, j, middlePoint]
        else
            middlePoint ←the centroid of det
            [i',j'] ← the cell that middlePoint is located at
            if (check Near neighborhood based on layer and tag number) then
                Add TrackRecord = [t, layer, tag, i', j', middlePoint]
            else
                if (check Far neighborhood based on layer and tag number) then
                    Add TrackRecord = [t, layer, tag, i', j', middlePoint]
                else
                    //occlusion and misdetection handling
                    if (history checking and predicting this detection belongs to which track) then
                        Add TrackRecord = [t, layer, tag, i', j', middlePoint]
                    end if
                end if
            end if
        end if
    end for
end for
Tracks ← Compute tracks based on track records, tags, and multilayer model
```

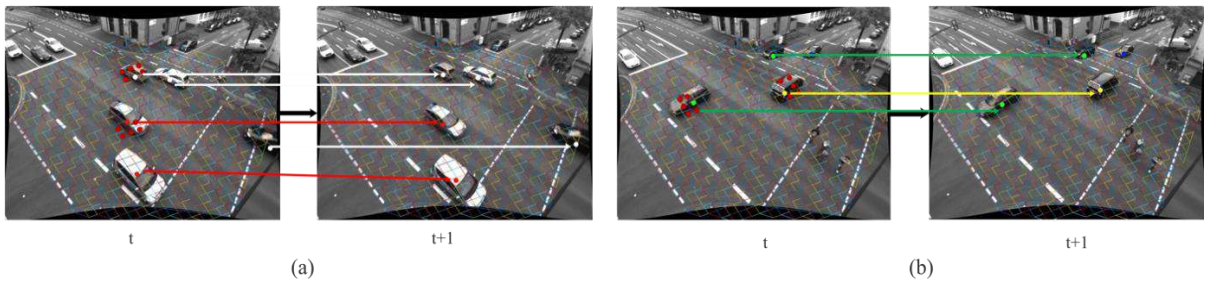

Figure 4. Two sample consecutive frames showing tracked vehicles and their correspondence at time *t* and *t+1*

3. 1. The Datasets The Ko-PER dataset is used in our experiments [27] as the main dataset. In Germany, the intersection is an actual four way crossing and cameras are monochrome. The first camera has a complete FOV such that the whole intersection information can be acquired. In our experiments, sequence 1 is used that it is divided into four parts named 1a, 1b, 1c and 1d that have the same duration and are considered separately. The detection results that have been released with the Ko-PER dataset is used and extracted from the dataset viewer. In research done by Meissner et al. [28], information from all views and laser-scanners are used, so the detection results are accurate enough. The sequences are considered crowded since there are several vehicles that are crossing the street at the same time. The sample frame and view of the Ko-PER dataset is shown in Figure 3.

Another dataset that is used for comparison is Urban Tracker dataset [26, 35]. It includes vehicles and pedestrians for tracking. Here from the dataset, three sequences are selected as Sherbrooke, Rouen, St-Marc. The sample frames of Urban Tracker dataset are presented in Figure 5. As can be seen the cameras placement and views are different in each sequence. However, they are less crowded in comparison with Ko-PER dataset.

3. 2. Evaluation Metrics For evaluating multi-object trackers CLEAR MOT metrics are known as a standard metric [36]. In CLEAR MOT metrics, the accuracy of trackers is defined by Multi-Object Tracking Accuracy (MOTA) that is defined as Equation (3):

$$MOTA = 1 - \frac{\sum_t (m_t + fp_t + mme_t)}{\sum_t g_t} \quad (3)$$

where g_t is the number of ground truth detections, fp_t is the number of false positives, m_t is the number of misdetections, and mme_t is the number of identity switches. The MOTA is computed by comparing tracking results with Ground Truth (GT).

There exists quality metrics that were presented in [37] to compare trackers all by comparison with GT and are defined as follows:

- Mostly Tracked (MT) - the percentage of tracks that are successfully tracked for more than 80%.
- Mostly Lost (ML) - the percentage of tracks that are tracked for less than 20%.
- Partially Tracked (PT) - the percentage of tracks that are tracked between 20 and 80% *(1-MT-ML)*.
- Identity Switch (IDS) - the number of times two tracks switch their IDs.

For these metrics, higher MT and lower ML, PT, IDS is preferred.

3. 3. Evaluation of the Proposed Tracking Method For validation of the proposed tracker and parameters' effect, Ko-PER dataset is selected since it is the longest and crowded one. During our experiments to assess the proposed tracking algorithm, we noted that for the Ko-PER dataset, due to camera placement, vehicles that enter from the right side and make a sharp turn to the bottom side can easily be lost. To solve this, we modified neighborhoods of the right-side layer (layer 2). We added some neighbors to the right side of both *Near* and *Far* neighborhoods.

To assess the neighborhood effect, experiments are done on three cases considering neighborhoods: *Near*, *Far* or both neighborhoods. Besides to neighborhoods, another important parameter is the value of *step*. To evaluate its effect, the tracking procedure is performed

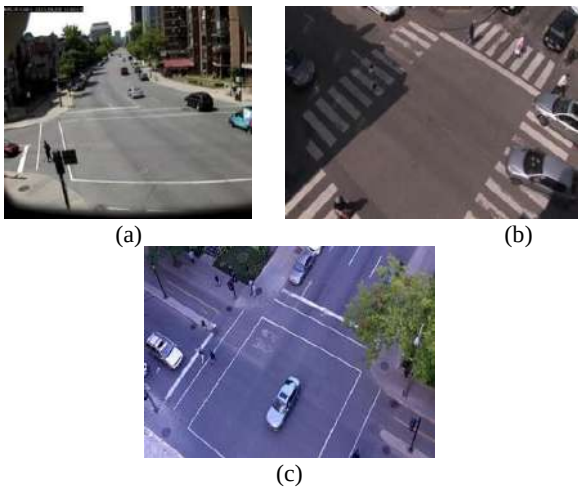

Figure 5. Urban Tracker dataset (a) Sherbrooke, (b) Rouen, (c) St-Marc

for *step* values from 10 to 40 in steps of 5 to demonstrate its effect. In Figure 3, FOV cells of Ko-PER dataset for *step* values 20 and 40 are depicted. Here, the effect of *step* value in the number and size of grid cells can be seen visually. As mentioned for predicting the tracks when collision, occlusion or misdetections occur, the history of tracks is checked. The parameter for checking the history is α which means checking $(t\text{-}\alpha)$ tracks history. For all experiments, α is equal to 2.

Three cases of neighborhoods and different *step* values are considered to investigate the effect of them in tracking results. Each case is reviewed separately.

Case 1. Tracking based on *Near* neighborhood: The results based on MT, ML, PT and IDS for all four sequences of Ko-PER dataset are revealed in Figure 6 for comparison. As the figure shows in all four sequences for small values of *step*, the value of ML and PT is bigger. The reason is that when only checking *Near* neighborhood with a small value of *step* that results in small cells, a vehicle could cross more than just one cell of its neighborhood. So, it does not exist in the cell that is predicted based on *Near* neighborhood. However, as *step* value increases, this does not happen. As a result, using *Near* neighborhood for bigger values of *step* can lead to better results.

Case 2. Tracking based on *Far* neighborhood: The tracking results are shown in Figure 7. More identity switches happen when *step* value is bigger in comparison with when using just *Near* neighborhood (see the difference between Figures 6 and 7, IDS column especially for bigger value of *step*). A lot of identity switches mean tracks appear in each other's neighborhood and this is the result of checking bigger neighborhood when it is not necessary. Also, we have fewer ML and PL tracks when *step* is small in comparison with using just near neighborhood. Therefore, this neighborhood works better with smaller values of *step*.

Case 3. Tracking using both neighborhoods: The tracking is performed based on both neighborhoods respectively. First, *Near* neighborhood is checked and if a trajectory cannot be found, then the *Far* neighborhood is checked. The results are presented in Figure 8. This case has the benefit of the two previous cases. When the *step* value is small, ML and PT are less. Also, when *step* has bigger values identity switches occur less. However, still ML and PT tracks and IDS exist especially when *step* value is very small or very big. The reason is for parts of the intersection that are far from the camera, from camera viewpoint the movement seems bigger as the size of the

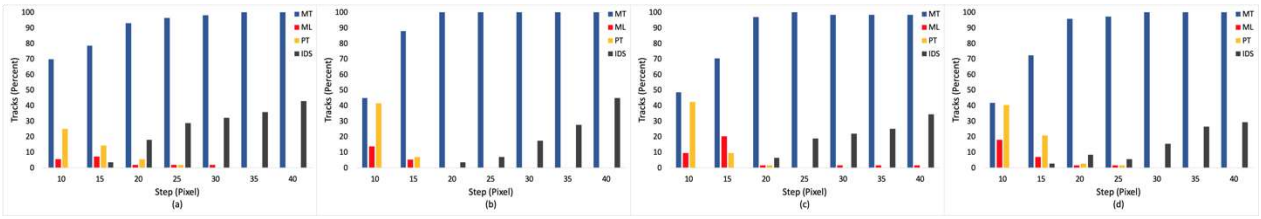

Figure 6. Tracking results based on *Near* neighborhood and different values of *step* (a) sequence 1a, (b) sequence 1b, (c) sequence 1c, (d) sequence 1d

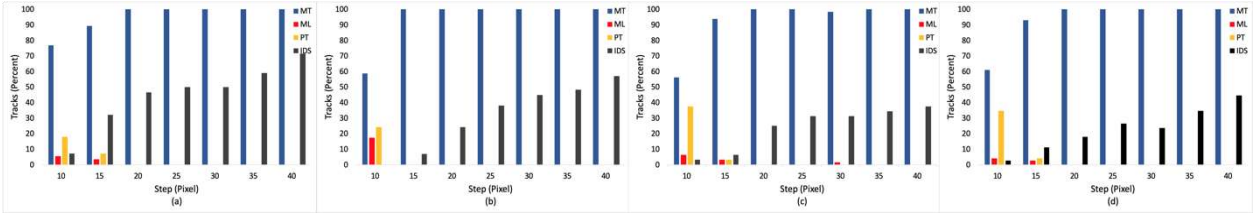

Figure 7. Tracking results based on *Far* neighborhood and different values of *step* (a) sequence 1a, (b) sequence 1b, (c) sequence 1c, (d) sequence 1d

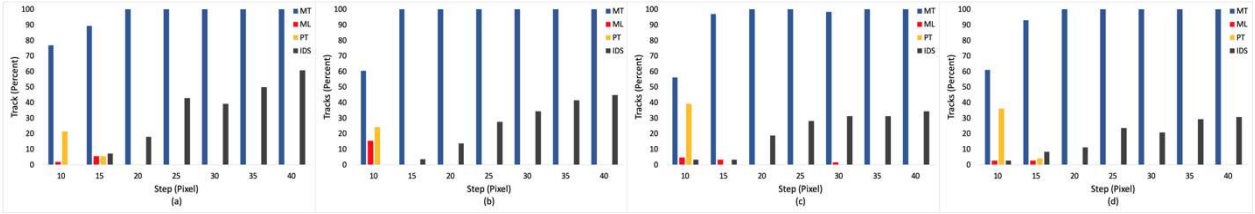

Figure 8. Tracking results based on both neighborhoods and different values of *step* (a) sequence 1a, (b) sequence 1b, (c) sequence 1c, (d) sequence 1d

cells are the same. For identity switches that happen in bigger values of *step* the same reason applies.

After studying the results of the three cases, the best strategy is case 3 using both *Near* and *Far* neighborhoods, respectively. As discussed before, *step* is an important parameter, smaller values of *step* result in more cells with smaller size. The importance can be demonstrated by the results obtained so far. Smaller or bigger values of *step* are not suitable choices and affect the results negatively (more ML and PT or more IDS respectively). The best *step* value for the Ko-PER dataset intersection is 20 or 25. It provides the highest number of MT tracks and fewer ML, PT or IDS in comparison with other values.

After determining the best neighborhood strategy and value of *step* parameter, all evaluation metric for all four sequences of Ko-PER dataset are presented in Table 2. In all sequences above 96% of trajectories are tracked completely and the accuracy is above 0.9; however, still identity switches happen.

To evaluate the tracker runtime, we run the tracking algorithm for all four sequences for *step* values from 10 to 40. Out of the three possible cases for checking the neighborhood, the third case is selected as previous results show its better performance. Each runtime is the average of running the algorithm for 10 times. Also, we divided the whole sequence to batches of 60 frames. The last frame of each batch and first frame of the next batch overlap so that the tracks from the previous batch can continue correctly. Using batches has the advantage that small tracks can be acquired quickly, since vehicles cross the intersection in frames that are a lot fewer than the whole sequence. Our proposed multilayer tracker was implemented in MATLAB on a system with 2.2GHz Intel Corei7 and 16GB of RAM. Since the camera records 25 Frames Per Second (25FPS) [27], and we considered 60 frames in each batch, the algorithm running time up to 2.4 seconds per batch is considered real time.

Runtimes for all sequences are presented in Figure 9. As the figure illustrates for *step* value equals to 10, as a result of too many small cells, the running time has a high value. However, for *step* parameter equals to 40, the number of cells is less so the algorithm running time decreases too. For *step* value equals to 20 and more, the tracks can be acquired in real time in this dataset.

Based on the results of neighborhoods and execution time, setting the *step* parameter equal to 20 is the best choice for this intersection. Also, the results show that our proposed tracking algorithm can be applied in real time applications.

Sample tracking results are shown in Figure 10. Tracks in different color belong to different layers, red for layer 1 (top side layer), green for layer 2 (right side layer), black for layer 3 (bottom side layer), yellow for layer 4 (left side layer). The blue color shows that vehicles are out of FOV. The first row in Figure 10 shows tracks while tracking is performed, and the second row shows final tracks after tracking is done. The tracks are from Ko-PER dataset for *step* value equals to 20 and using both neighborhoods.

3.4 Comparison with Other Methods In this part, to validate our proposed tracker, it is compared with other trackers. The results are reported on Urban Tracker dataset for Sherbrooke, Rouen, St-Marc videos in Table 3. The cars part of the Urban Tracker dataset is selected as here tracking vehicles at intersection is considered. One of the trackers is Traffic Intelligence that is a feature-

TABLE 2. All evaluation metrics for sequences of Ko-PER dataset for proposed tracking method (parameters: *step* equals to 20 and using both neighborhoods)

	MT	ML	PT	IDS	MOTA
Sequence 1a	98.25	1.75	0.00	17.54	0.9411
Sequence 1b	100.00	0.00	0.00	13.79	0.9452
Sequence 1c	96.92	1.54	1.54	18.46	0.9080
Sequence 1d	100.00	0.00	0.00	11.11	0.9497

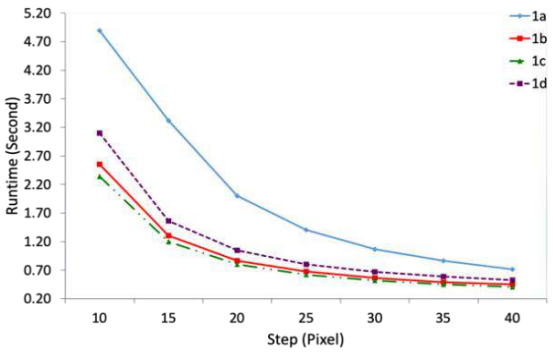

Figure 9. Runtime for all sequences of Ko-PER dataset with different *step* values using both neighborhoods

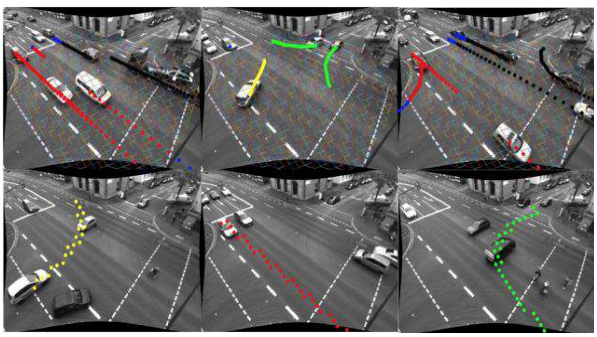

Figure 10. Sample tracking results, first row: tracks while tracking is performed, second row: sample final tracks

based tracking algorithm [38]. The other, which is Urban Tracker, is introduced with the dataset and tracks all road users, detection are done by performing background subtraction and tracking is performed by Kalman filter [26, 35]. Mendes et al. [39] combined background subtraction with blob detection and optical flow. MKCF (Multiple Kernelized Correlation Filter) tracker is introduced in literature [29], that applies background subtraction and multiple KCF trackers. As can be seen, our proposed multilayer tracker outperforms the accuracy of the other trackers in all three videos of the dataset.

The MT, ML and PT of Urban Tracker dataset for proposed tracker and two other trackers are reported in Table 4 for better comparison.

4. DISCUSSION

Vehicles are detected before tracking, and detections are not always accurate. For demonstrating the effect of misdetections (vehicles are not detected) and false positives (other objects being identified as vehicles) that are caused by reasons such as occlusion, shadow and collision, some experiments are performed and the results are invstigated here. To study how these, affect the tracking results and how the proposed tracking method deals with them, tracking sequences are recreated from the original ones. The reported results are the average of 10 runs with different missed and false detections on each run. The other tracking parameters are as follows: third case (using both neighborhoods respectively), *step* value equals to 20 and checking the history of two previous frames. Checking more frames for history leads to better results but because real time execution is pursued, it is not used.

Different scenarios are created. The first one is applying misdetections. So, detections are deleted randomly. We considered 2, 5 and 10% of misdetections. As a result, sequences detections are recreated based on these values randomly. The results are presented in Table 5. As it shows for 2% misdetections, tracking results do not show much difference from the original one (see Table 2). But, as the number of misdetections increases so does the number of ML and PT tracks, and MOTA decreases. However, even in 10% misdetections most of the tracks are found and the accuracy is around 0.8.

The other scenario is applying false detections. False detections are created randomly with two strategies called addition and replacement. In the addition strategy, detections that are not vehicles are added randomly. In the replacement strategy, a number of detections are deleted from their original frames and are added randomly to other frames detections, so misdetections are created simultaneously. The results are presented in Table 6 for 2, 5 and 10% of false detections with addition strategy and in Table 7 for replacement strategy.

The results of the addition strategy demonstrate that it does not affect the evaluation metrics. Even with 10% false detections with addition strategy, the results are unaffected. Therefore, the proposed tracker is robust to this strategy. However, because false positives are added, MOTA decreases. Table 7 shows the results of false detections created with the replacement strategy, since misdetections are added at the same time, there are more ML tracks, and the results are similar to just adding misdetections. But here, since there are miss and false detections at the same time, MOTA decreases more.

The proposed tracking method based on multilayer model thoroughly tracks vehicles by considering their motion flows without any visual features, although in

TABLE 3. Trackers comparison for Urban Tracker dataset

	MOTA				
	Proposed Multilayer Tracker	**MKCF [29]**	**Urban Tracker[26]**	**Mendes et al. [39]**	**Traffic Intelligence [38]**
Sherbrooke (Cars)	0.962	0.789	0.887	0.707	0.825
Rouen (Cars)	0.980	0.813	0.897	0.918	0.185
St-Marc (Cars)	0.939	0.590	0.889	0.713	-0.178

TABLE 4. Trackers MT, ML and PT comparison for Urban Tracker dataset

	Proposed Multilayer Tracker			**Urban Tracker[26]**			**Traffic Intelligence [38]**		
	MT (%)	**ML (%)**	**PT (%)**	**MT (%)**	**ML (%)**	**PT (%)**	**MT (%)**	**ML (%)**	**PT (%)**
Sherbrooke (Cars)	96.2	1.8	2.0	85.0	5.0	10.0	60.0	25.0	15.0
Rouen (Cars)	98.0	0.0	2.0	75.0	0.0	25.0	37.5	37.5	25.0
St-Marc (Cars)	92.9	1.5	5.5	64.3	7.1	28.6	60.7	17.9	21.4

specific situations losing tracks and identity switch could happen. Since detections and tracks are distributed among different layers, as the results show, tracking time becomes real time.

TABLE 5. Tracking results for all sequences with misdetections of Ko-PER dataset

	MT	ML	PT	IDS	MOTA
Misdetection 2%					
Sequence 1a	100.00	0.00	0.00	21.05	0.9177
Sequence 1b	100.00	0.00	0.00	17.24	0.9324
Sequence 1c	93.85	3.08	3.08	13.85	0.9107
Sequence 1d	98.61	0.00	1.39	11.11	0.9382
Misdetection 5%					
Sequence 1a	89.47	1.75	8.77	17.54	0.9140
Sequence 1b	93.10	5.17	1.72	17.24	0.8702
Sequence 1c	95.38	4.62	0.00	18.46	0.8948
Sequence 1d	98.61	0.00	1.39	11.11	0.9364
Misdetection 10%					
Sequence 1a	89.47	5.26	5.26	24.56	0.8512
Sequence 1b	84.48	12.07	3.45	17.24	0.8518
Sequence 1c	76.92	10.77	12.31	24.62	0.7729
Sequence 1d	86.11	8.33	5.56	11.11	0.8658

TABLE 6. Tracking results for all sequences of Ko-PER dataset with false detections with addition strategy

	MT	ML	PT	IDS	MOTA
False detection 2%					
Sequence 1a	98.25	1.75	0.00	17.54	0.865
Sequence 1b	100.00	0.00	0.00	13.79	0.9317
Sequence 1c	98.46	0.00	1.54	18.46	0.8948
Sequence 1d	100.00	0.00	0.00	11.11	0.9355
False detection 5%					
Sequence 1a	98.25	1.75	0.00	17.54	0.9348
Sequence 1b	100.00	0.00	0.00	13.79	0.9135
Sequence 1c	98.46	1.54	0.00	18.46	0.8737
Sequence 1d	100.00	0.00	0.00	11.11	0.9213
False detection 10%					
Sequence 1a	98.25	1.75	0.00	17.54	0.8023
Sequence 1b	100.00	0.00	0.00	13.79	0.8846
Sequence 1c	98.46	1.54	0.00	18.46	0.8519
Sequence 1d	100.00	0.00	0.00	11.11	0.8902

TABLE 7. Tracking results for all sequences of Ko-PER dataset with false detections with replacement strategy

	MT	ML	PT	IDS	MOTA
False detection 2%					
Sequence 1a	98.25	1.75	0.00	17.54	0.9252
Sequence 1b	98.28	0.00	1.72	13.79	0.9151
Sequence 1c	100.00	0.00	0.00	21.54	0.8800
Sequence 1d	98.61	0.00	1.39	11.11	0.9308
False detection 5%					
Sequence 1a	94.74	0.00	5.26	21.05	0.8843
Sequence 1b	89.66	6.90	3.45	24.14	0.8567
Sequence 1c	92.31	3.08	4.62	24.62	0.8365
Sequence 1d	97.22	0.00	2.78	5.56	0.9097
False detection 10%					
Sequence 1a	87.72	3.51	8.77	24.56	0.8144
Sequence 1b	86.21	5.17	8.62	17.24	0.7807
Sequence 1c	86.15	4.62	9.23	21.54	0.7774
Sequence 1d	86.11	8.33	5.56	15.28	0.8118

5. CONCLUSON

In this paper, we proposed a new method for tracking vehicles at intersection. It uses a multilayer model for tracking, a distinct layer for each entering side of the intersection. The layers are constructed considering the permissible motion flows and neighborhoods for the associated entering side. Then in tracking procedure each entering vehicle is detected and assigned to its associated layer and the movements are tracked. Indeed, tracks can be predicted as each vehicle has permissible directions to follow depending to its entering side. To evaluate performance of the proposed method, we tested the method with various scenarios, each of which imposed up to 10% false and misdetections on the Ko-PER dataset. The results showed that the proposed method can thoroughly track vehicles at intersection in many scenarios. Also, it outperforms other trackers. Therefore, we can claim that the proposed multilayer tracking method is computationally effective and can be used in real time tracking applications.

6. REFRENCES

1. Datondji, S. R. E., Dupuis, Y., Subirats, P., and Vasseur, P. "A Survey of Vision-Based Traffic Monitoring of Road Intersections." ***IEEE Transactions on Intelligent Transportation Systems***, Vol. 17, No. 10, (2016), 2681–2698. https://doi.org/10.1109/TITS.2016.2530146

2. Shirazi, M. S., and Morris, B. T. "Looking at Intersections: A Survey of Intersection Monitoring, Behavior and Safety Analysis of Recent Studies." ***IEEE Transactions on Intelligent Transportation Systems***. Vol. 18, No. 1, (2017), 4-24. https://doi.org/10.1109/TITS.2016.2568920
3. Gandhi, T., and Trivedi, M. M. "Pedestrian protection systems: Issues, survey, and challenges." ***IEEE Transactions on Intelligent Transportation Systems***, Vol. 8, No. 3, (2007), 413–430. https://doi.org/10.1109/TITS.2007.903444
4. Buch, N., Velastin, S. A., and Orwell, J. "A review of computer vision techniques for the analysis of urban traffic." ***IEEE Transactions on Intelligent Transportation Systems***. Vol. 12, No. 3, (2011), 920-939 https://doi.org/10.1109/TITS.2011.2119372
5. Sivaraman, S., and Trivedi, M. M. "Looking at vehicles on the road: A survey of vision-based vehicle detection, tracking, and behavior analysis." ***IEEE Transactions on Intelligent Transportation Systems***, Vol. 14, No. 4, (2013), 1773–1795. https://doi.org/10.1109/TITS.2013.2266661
6. Hasanzadeh, R. P. R., Shahrouzi, S. N., and Mahdavi, M. "A Novel Method for Tracking Moving Objects using Block-Based Similarity." ***International Journal of Engineering - Transactions B: Applications***, Vol. 22, No. 1, (2009), 35–42. Retrieved from http://www.ije.ir/article_71756.html
7. Sadegh Moghadasi, S., and Faraji, N. "An efficient target tracking algorithm based on particle filter and genetic algorithm." ***International Journal of Engineering - Transactions A: Basics***, Vol. 32, No. 7, (2019), 915–923. https://doi.org/10.5829/ije.2019.32.07a.03
8. Jain, N. K., Saini, R. K., and Mittal, P. A review on traffic monitoring system techniques. ***Advances in Intelligent Systems and Computing***, Vol. 742, (2019), 569-577. https://doi.org/10.1007/978-981-13-0589-4_53
9. Kastrinaki, V., Zervakis, M., and Kalaitzakis, K. "A survey of video processing techniques for traffic applications." ***Image and Vision Computing***, Vol. 21, No. 4, (2003), 359–381. https://doi.org/10.1016/S0262-8856(03)00004-0
10. Yilmaz, A., Javed, O., and Shah, M. "Object tracking: A survey." ***ACM Computing Surveys***. Vol. 38, No. 4, (2006). https://doi.org/10.1145/1177352.1177355
11. Sun, Z., Bebis, G., and Miller, R. "On-road vehicle detection: A review." ***IEEE Transactions on Pattern Analysis and Machine Intelligence***. Vol. 28, No. 5, (2006), 694-711. https://doi.org/10.1109/TPAMI.2006.104
12. Messelodi, S., Modena, C. M., and Zanin, M. "A computer vision system for the detection and classification of vehicles at urban road intersections." ***Pattern Analysis and Applications***, Vol. 8, No. 1–2, (2005), 17–31. https://doi.org/10.1007/s10044-004-0239-9
13. Song, X., and Nevatia, R. "Detection and tracking of moving vehicles in crowded scenes." In 2007 IEEE Workshop on Motion and Video Computing, WMVC, (2007). https://doi.org/10.1109/WMVC.2007.13
14. Veeraraghavan, H., Masoud, O., and Papanikolopoulos, N. P. "Computer vision algorithms for intersection monitoring." ***IEEE Transactions on Intelligent Transportation Systems***, Vol. 4, No. 2, (2003), 78–89. https://doi.org/10.1109/TITS.2003.821212
15. Nateghinia, E., and Moradi, H. "Video-based multiple vehicle tracking at intersections." In 2014 2nd RSI/ISM International Conference on Robotics and Mechatronics, ICRoM 2014, (2014), 215–220. Institute of Electrical and Electronics Engineers Inc. https://doi.org/10.1109/ICRoM.2014.6990903
16. Liu, L., Xi, Z., and Sun, Q. "Multi-vision tracking and collaboration based on spatial particle filter." ***Journal of Visual Communication and Image Representation***, Vol. 59, (2019), 316–326. https://doi.org/10.1016/j.jvcir.2018.12.050
17. Shi, Y., and Real, F. D. "Smart cameras: Fundamentals and classification." In Smart Cameras (pp. 19–34). Springer. https://doi.org/10.1007/978-1-4419-0953-4_2
18. Liu, L., Xing, J., and Ai, H. "Multi-view vehicle detection and tracking in crossroads." In 1st Asian Conference on Pattern Recognition, ACPR, (2011), 608–612. https://doi.org/10.1109/ACPR.2011.6166688
19. Wang, W., Gee, T., Price, J., and Qi, H. "Real time multi-vehicle tracking and counting at intersections from a fisheye camera." In Proceedings - 2015 IEEE Winter Conference on Applications of Computer Vision, WACV, (2015), 17–24. https://doi.org/10.1109/WACV.2015.10
20. Lira, G., Kokkinogenis, Z., Rossetti, R. J. F., Moura, D. C., and Rúbio, T. "A computer-vision approach to traffic analysis over intersections." In IEEE Conference on Intelligent Transportation Systems, Proceedings, ITSC, (2016), 47–53. https://doi.org/10.1109/ITSC.2016.7795530
21. Dey, B., and Kundu, M. K. "Turning video into traffic data - An application to urban intersection analysis using transfer learning." ***IET Image Processing***, Vol. 13, No. 4, (2019), 673–679. https://doi.org/10.1049/iet-ipr.2018.5985
22. Subedi, S., and Tang, H. "Development of a multiple-camera 3D vehicle tracking system for traffic data collection at intersections." ***IET Intelligent Transport Systems***, Vol. 13, No. 4, (2019), 614–621. https://doi.org/10.1049/iet-its.2018.5163
23. Li, C., Chiang, A., Dobler, G., Wang, Y., Xie, K., Ozbay, K., Ghandehari, M., Zhou, J., and Wang, D. "Robust vehicle tracking for urban traffic videos at intersections." In 2016 13th IEEE International Conference on Advanced Video and Signal Based Surveillance, AVSS, (2016), 207–213. https://doi.org/10.1109/AVSS.2016.7738075
24. Min, W., Fan, M., Guo, X., and Han, Q. "A New Approach to Track Multiple Vehicles with the Combination of Robust Detection and Two Classifiers." ***IEEE Transactions on Intelligent Transportation Systems***, Vol. 19, No. 1, (2018), 174–186. https://doi.org/10.1109/TITS.2017.2756989
25. Bedruz, R. A., Sybingco, E., Bandala, A., Quiros, A. R., Uy, A. C., and Dadios, E. "Real-time vehicle detection and tracking using a mean-shift based blob analysis and tracking approach." In HNICEM 2017 - 9th International Conference on Humanoid, Nanotechnology, Information Technology, Communication and Control, Environment and Management (Vol. 2018), (2018), 1–5. https://doi.org/10.1109/HNICEM.2017.8269528
26. Jodoin, J. P., Bilodeau, G. A., and Saunier, N. "Tracking All Road Users at Multimodal Urban Traffic Intersections." ***IEEE Transactions on Intelligent Transportation Systems***, Vol. 17, No. 11, (2016), 3241–3251. https://doi.org/10.1109/TITS.2016.2545245
27. Strigel, E., Meissner, D., Seeliger, F., Wilking, B., and Dietmayer, K. "The Ko-PER intersection laserscanner and video dataset." In 2014 17th IEEE International Conference on Intelligent Transportation Systems, ITSC, (2014), 1900–1901. https://doi.org/10.1109/ITSC.2014.6957976
28. Meissner, D., Reuter, S., Strigel, E., and Dietmayer, K. "Intersection-based road user tracking using a classifying multiple-model PHD filter." ***IEEE Intelligent Transportation Systems Magazine***, Vol. 6, No. 2, (2014), 21–33. https://doi.org/10.1109/MITS.2014.2304754
29. Yang, Y., and Bilodeau, G. "Multiple Object Tracking with Kernelized Correlation Filters in Urban Mixed Traffic." In 2017 14th Conference on Computer and Robot Vision (CRV), (2017), 209–216. https://doi.org/10.1109/CRV.2017.18
30. Ooi, H.-L., Bilodeau, G.-A., Saunier, N., and Beaupré, D.-A. "Multiple Object Tracking in Urban Traffic Scenes with a Multiclass Object Detector." In Advances in Visual Computing (pp. 727–736). Cham: Springer International Publishing.

31. Ooi, H.-L., Bilodeau, G.-A., and Saunier, N. "Tracking in Urban Traffic Scenes from Background Subtraction and Object Detection." In Image Analysis and Recognition (pp. 195–206). Springer International Publishing.
32. Chan, Z. Y., and Suandi, S. A. "City Tracker: Multiple Object Tracking in Urban Mixed Traffic Scenes." In Proceedings of the 2019 IEEE International Conference on Signal and Image Processing Applications, ICSIPA, (2019), 335–339. https://doi.org/10.1109/ICSIPA45851.2019.8977783
33. Delavarian, M., and Maarouzi, O. "Vehicle tracking at intersection in image sequences with multilayer concept." In 2017 3rd Iranian Conference on Intelligent Systems and Signal Processing (ICSPIS), (2017), 131–135. https://doi.org/10.1109/ICSPIS.2017.8311603
34. Ciaparrone, G., Luque Sánchez, F., Tabik, S., Troiano, L., Tagliaferri, R., and Herrera, F. "Deep learning in video multi-object tracking: A survey." ***Neurocomputing***, Vol. 381, (2020), 61–88. https://doi.org/10.1016/j.neucom.2019.11.023
35. Jodoin, J. P., Bilodeau, G. A., and Saunier, N. "Urban Tracker: Multiple object tracking in urban mixed traffic." In 2014 IEEE Winter Conference on Applications of Computer Vision, WACV, (2014) 885–892. https://doi.org/10.1109/WACV.2014.6836010
36. Bernardin, K., and Stiefelhagen, R. "Evaluating multiple object tracking performance: The CLEAR MOT metrics." ***Eurasip Journal on Image and Video Processing***, Vol. 2008, No. 1, (2008), 1–10. https://doi.org/10.1155/2008/246309
37. Li, Y., Huang, C., and Nevatia, R. "Learning to associate: HybridBoosted multi-target tracker for crowded scene." In 2009 IEEE Conference on Computer Vision and Pattern Recognition, (2009), 2953–2960. https://doi.org/10.1109/CVPR.2009.5206735
38. Saunier, N., and Sayed, T. "A feature-based tracking algorithm for vehicles in intersections." In Third Canadian Conference on Computer and Robot Vision, CRV (Vol. 2006), (2006), 59-65. https://doi.org/10.1109/CRV.2006.3
39. Mendes, J. C., Gomes Campos Bianchi, A., and Júnior, Á. R. P. "Vehicle Tracking and Origin-destination Counting System for Urban Environment." In Proceedings of the 10th International Conference on Computer Vision Theory and Applications - Volume 3: VISAPP, (2015), 600–607. https://doi.org/10.5220/0005317106000607

Persian Abstract

چکیده

رهگیری تصویری یک موضوع مهم در سیستم‌های حمل و نقل هوشمند است. تقاطع‌ها مکان چالش برانگیزی برای رهگیری در سیستم‌های تصویری هستند، زیرا وسایل نقلیه در جهت‌های متفاوتی همزمان در حرکت هستند. علاوه بر این، در صورت رخداد تصادف جهت‌های ترافیکی نرمال ممکن است با تغییر مواجه شوند. ازدحام، انسداد و جهت حرکت نامعین از جمله چالش‌های مهم رهگیری وسایل نقلیه در تقاطع است. در این مقاله، یک روش برای رهگیری وسایل نقلیه در تقاطع با در نظر گرفتن جریان‌های حرکتی برای غلبه بر جهت‌های حرکت نامعین پیشنهاد شده است. برای این منظور، مدلی چند لایه پیشنهاد شده است که جهت‌های حرکتی را به لایه‌های جداگانه انتساب می‌دهد. علاوه بر این، همسایگی‌های متفاوتی برای هر لایه بر اساس جهت حرکت پیشنهاد شده است. بنابراین وسایل نقلیه‌ای که از یک سمت تقاطع وارد می‌شوند و جهت حرکتی مشابه دارند به لایه یکسان انتساب داده می‌شوند. سپس رهگیری در لایه‌های متفاوت به صورت جداگانه انجام می‌شود. در حالت‌های خاص انسداد، آشکارسازی از دست رفته و عبور وسایل نقلیه از کنار یکدیگر روش رهگیری پیشنهادی بر اساس تاریخچه رهگیری و همسایگی‌ها در هر لایه ادامه ره‌های وسایل نقلیه را پیش‌بینی می‌کند. نتایج نشان می‌دهد که سازگاری مناسبی بین نتایج روش پیشنهادی و حقیقت اصلی وجود دارد و در رهگیری وسایل نقلیه عبوری از تقاطع نسبت به سایر روش‌ها بهتر عمل می‌کند.

International Journal of Engineering

Journal Homepage: www.ije.ir

Seamless Transition in Grid-connected Microgrid System using Proportional Resonant Controller

V. Lavanya*, N. Senthil Kumar

School of Electrical Engineering, Vellore Institute of Technology, Chennai, Tamilnadu, India

PAPER INFO

Paper history:
Received 28 December 2019
Received in revised form 14 July 2020
Accepted 07 August 2020

Keywords:
Grid-connected
Microgrid
Seamless Transition
Distributed Generation
Indirect Current Control
Proportional Resonant

ABSTRACT

In this paper, the design of an inverter control structure based on the Proportional Resonant (PR) controller is dealt with in detail for attaining smooth transitions between the operating modes of a grid-connected microgrid system. The control strategy applied for the inverter is cascaded three-loop control viz., the grid current, voltage across the load, and the inverter output current loops. The inverter control is mainly focused to retain the voltage magnitude within the prescribed set limits and to have a good quality of the voltage across the load under all the modes of operation. A proportional resonant controller is designed by considering the transients and stability criteria into account under varying modes of operation. The design procedure of the Proportional resonant controller is given in detail. The three-phase grid-connected microgrid system considered under study is simulated in MATLAB/Simulink environment to operate under islanding condition as well as grid-connected condition and also changing modes from islanding to grid connected and vice versa. The simulation results are presented under various modes of operation to validate the controller design for a smooth transition between the modes of operation.

***doi**: 10.5829/ije.2020.33.10a.13*

1. INTRODUCTION

Renewable energy sources (RES) based power generation becomes a more and more viable solution for meeting the increase in the energy demand of today's electricity market. The power electronic interfaces such as boost converters, inverters are used as intermediate structures to connect the Distributed Energy Resources (DER) like Solar PV, Wind, fuel cells, etc., to the grid. A microgrid (MG) is one that comprises a low voltage (LV) or medium voltage (MV) group of DERs which are controlled locally. A MG may look like a single power producer or a load [1-4] when considered from the grid's perspective. A MG can operate in conjunction with the utility to feed in a fraction of the total load while operating in grid connected condition and feeds critical loads in islanded mode i.e. when the utility grid is lost during any abnormal conditions [5]. The islanding state can be detected by islanding detection methods [6]. Under islanded mode, the microgrid feeds the critical loads while preserving the load voltage as well as the frequency within the limits, hence improving the reliability of the system [7]. The inverter which is between the sources and the loads and its control plays a vital role in the environment of a distributed generation when dealing with voltage quality and hence power quality.

The three-phase inverter of the DG system should be controlled to be operated under both grid-connected and islanded mode. The design of the inverter control is to be focused on the operating modes of the MG system and also it needs to take care of the smooth transition among the different states of microgrid operation like grid on and grid off, to reduce the voltage fluctuations across the critical loads when islanded and any sort of sudden changes in the current that is fed to the grid in grid-connected mode [8].

There are different control structures proposed in the literature for achieving fluctuations free transfer between the operating modes [9-21] to retain the power quality

*Corresponding Author Institutional Email: *lavanya.v@vit.ac.in* (V. Lavanya)

Please cite this article as: V. Lavanya and N. Senthil Kumar, Seamless Transition in Grid connected Microgrid System using Proportional Resonant Controller, International Journal of Engineering (IJE), IJE TRANSACTIONS A: Basics Vol. 33, No. 10, (October 2020) 1951-1958

during the transfers. Conventionally, an inverter that is connected to the grid is controlled as PQ control to feed/take power to/from the utility, and when the inverter gets disconnected from the grid V/f control is used for the maintenance of voltage across the load. When there is a need for switching between the modes, then switching between the controllers has to take place, which may lead to large transients and further may lead to system collapse. The inverter, when being operated as utility connected, is to be treated as a current source and when it gets disconnected from the utility, it is operated as a voltage source [9-11]. A droop characteristic adjustment based control scheme has been proposed in [12]. An inverter control technique with an inner voltage control loop and outer current control loop has been discussed in [13] for seamless transfer in microgrids. In [14], the output current of the inverter is controlled to regulate the current fed to the grid, at the same time the load voltage is maintained without any variation.

Indirect current control with Proportional Integral (PI) controller, which is based on synchronous reference (d–q) frame, has been used for seamless transfer [15-23], in which case the grid current is indirectly controlled with the help of capacitor voltage control. To improve the dynamics, the damping is introduced with the inverter side inductor current control loop or the filter capacitor voltage control loop. Under islanded mode, limiters are placed to limit the set value of the voltage for the inner voltage loop. Although seamless transitions between the modes have been achieved, the quality of the voltage waveform is a little bit affected as the voltage set value is limited with the threshold value. Proportional resonant (PR) control in a stationary reference frame has been proposed for transient free mode transitions [24-26].

In this paper, indirect current control based seamless transition is discussed in detail. Also, the design procedure of the Proportional resonant controller for the cascaded three-loop inverter control structure is presented in detail for achieving the smooth transition between the operating modes of a microgrid system.

2. MODELING AND DESIGN OF GRID CONNECTED INVERTER SYSTEM

2. 1. Modeling of the Power Stage The power stage of a three-phase inverter system is modeled based on a stationary reference frame and is shown in Figure 1.

The input voltage of the inverter is considered as a constant voltage and therefore, the control structure of the source side converter like a DC-DC boost converter [27, 28] that may be required to increase and regulate the dc-link voltage in a PV based system is not discussed in this paper.

After the inverter, the output voltage is filtered with the help of a passive filter of type, inductor-capacitor-inductor (LCL) filter and is then connected to the utility grid. The critical/local loads are connected across the filter capacitor. The switches on both, grid side and the inverter side are turned on while operating in grid-connected condition and the grid side switch is turned off under faulty conditions leading the system to operate under islanded mode.

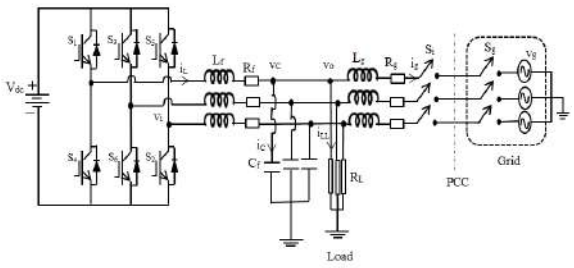

Figure 1. Power stage of a grid-connected inverter system

The basic mathematical equations governing the grid-connected inverter system with an LCL filter are given by Equations (1) and (2).

$$\frac{V_{dc}}{2}.\begin{pmatrix} d_a \\ d_b \\ d_c \end{pmatrix} = L_f.\frac{d}{dt}\begin{pmatrix} i_{La} \\ i_{Lb} \\ i_{Lc} \end{pmatrix} + R_f.\begin{pmatrix} i_{La} \\ i_{Lb} \\ i_{Lc} \end{pmatrix} + \begin{pmatrix} v_{ca} \\ v_{cb} \\ v_{cc} \end{pmatrix} \quad (1)$$

$$\begin{pmatrix} i_{La} \\ i_{Lb} \\ i_{Lc} \end{pmatrix} = C_f.\frac{d}{dt}\begin{pmatrix} v_{ca} \\ v_{cb} \\ v_{cc} \end{pmatrix} + \begin{pmatrix} i_{LLa} \\ i_{LLb} \\ i_{LLc} \end{pmatrix} + \begin{pmatrix} i_{ga} \\ i_{gb} \\ i_{gc} \end{pmatrix} \quad (2)$$

These a-b-c reference frame quantities are transformed into stationary reference frame parameters with the help of Clarke's transformation and the controllers are designed in the α-β reference frame.

2. 2. Design of LCL Filter The specification of the parameters used in the DG system considered is given in Table 1.

TABLE 1. Simulation Parameters of the MG System

Parameters	Symbol	Value
DC link voltage	V_{dc}	700 V
Filter inductor	L_f	3.11 mH
Filter capacitor	C_f	10 µF
Switching frequency	f_s	20 kHz
Grid side inductor	L_g	3.11 mH
Grid frequency	f_g	50 Hz
Grid voltage	V_g	220 V(rms)
Rated power of DG	P_{DG}	10 kW
Power rating of Load	P_L	5 kW

The filter and the control loop parameters are designed based on the DG specifications. As the output from the DG system is to be connected to the load/grid via a power electronics interface, harmonics gets into the system parameters. Hence, the inverter output is to be filtered to remove the harmonics present in it. The passive filter of type LCL is being used to filter out the harmonics and is designed to have the harmonics within the limits for the current as per standard IEEE Standard 519 -2014 [29].

The base impedance and the base capacitance values are calculated based on the Equations (3) and (4).

$$Z_{base} = \frac{V_{L-L}^2}{P_{nominal}} \quad (3)$$

$$C_{base} = \frac{1}{\omega_g Z_{base}} \quad (4)$$

The filter capacitance is found out from (5) by considering the variation seen by the grid as 5%.

$$C_f = 0.05 * C_{base} \quad (5)$$

The current ripple is calculated based on (6) by considering the ripple present as 10% of the rated current.

$$\Delta I_{max} = 10\% * I_{max} \quad (6)$$

where I_{max} is given by (7).

$$I_{max} = \frac{\sqrt{2} P_{nominal}}{3 V_{ph}} \quad (7)$$

The filter inductors, L_f in the inverter side and L_g in the grid side are calculated based on the Equations (8) and (9),

$$L_f = \frac{V_{dc}}{16 f_s \Delta I_{max}} \quad (8)$$

$$L_g = r L_f \quad (9)$$

where V_{dc} is the dc link voltage, f_s is the switching frequency of the inverter switches and r is the ratio between inverter side inductor and grid side inductor and the value of r is be considered based on the nominal grid impedance and the resonant frequency from the transfer function of the filter. The resonant frequency is specified by (10) and the constraint is given by (11).

$$\omega_{res} = \sqrt{\frac{L_f + L_g}{L_f L_g C_f}} \quad (10)$$

$$10 f_g < f_{res} < 0.5 f_s \quad (11)$$

2. 3. Controller Design The basic control diagram representation of the indirect current control scheme based on the PR controller is shown in Figure 2. The cascaded three-loop control structure consists of an outer grid current control loop, inner capacitor voltage control loop, and an innermost inductor current control loop. The cascaded loops are designed with proper bandwidth

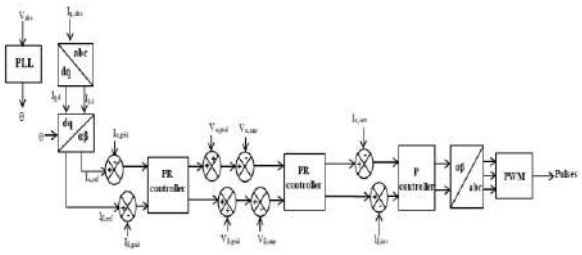

Figure 2. Indirect current control structure based on the PR controller

selection. The design of the inner voltage control loop is done to get the voltage across the load to be maintained as per the requirement in all the operating modes.

2. 3. 1. Design of Innermost Inductor Current Control Loop The innermost inductor current controller structure is shown in Figure 3.

From Figure 3, the plant transfer function is given by (12) and the open-loop transfer function of the current control loop is given by (13).

$$G(s) = \frac{I_L(s)}{V_i(s)} = \frac{s C_f}{s^2 L_f C_f + 1} \quad (12)$$

$$G_{OL,IC}(s) = \frac{K_{PWM} * k_{p1} * s C_f}{s^2 L_f C_f + 1} \quad (13)$$

where k_{p1} is the proportional controller gain and K_{PWM} is the gain of the converter and is considered as 1 for simplicity.

The closed-loop transfer function of the inner current controller is given by (14).

$$\frac{I_L(s)}{I_{L,ref}(s)} = \frac{s k_{p1} k_{PWM} C_f}{s^2 L_f C_f + s k_{p1} k_{PWM} C_f + 1} \quad (14)$$

The root locus plot is used to design the controller gains and is shown in Figure 4. From Figure 4, the proportional gain of the current controller is chosen to be 35.3 as the oscillations get damped out when the gain k_{p1} is ≥ 35.3.

2. 3. 2. Design of the Capacitor Voltage Control Loop The capacitor voltage control loop structure is shown in Figure 5. The root locus plot is used to find the values of k_p and k_i of the PR controller. Figure 6 shows the root locus plot of the system which is used for finding the value of k_p with k_i=0. The value of k_p is found to be 0.0285 for a damping ratio of 0.707.

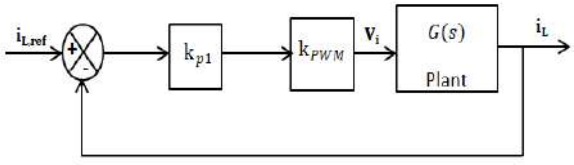

Figure 3. Innermost inductor current controller

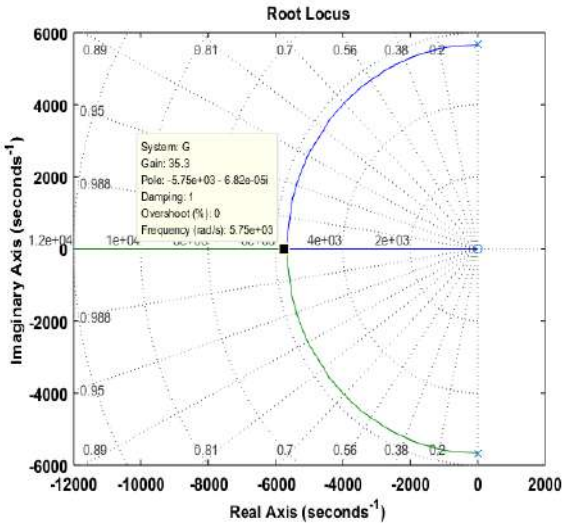

Figure 4. Root locus plot of the innermost current control loop

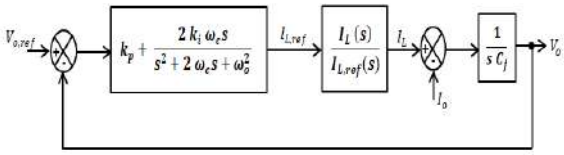

Figure 5. Capacitor voltage control loop structure

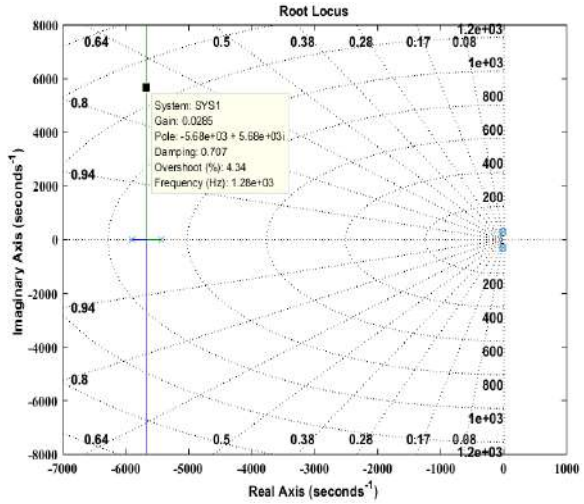

Figure 6. Root locus plot of voltage controller considering k_i=0

The closed-loop transfer function of the voltage control loop is given by (15).

$$\frac{V_o(s)}{V_{o,ref}(s)} = \frac{\left(k_p + \frac{2 k_i \omega_c s}{s^2 + 2 \omega_c s + \omega_o^2}\right) * \frac{I_L(s)}{I_{L,ref}(s)} * \frac{1}{sC}}{1 + \left(k_p + \frac{2 k_i \omega_c s}{s^2 + 2 \omega_c s + \omega_o^2}\right) * \frac{I_L(s)}{I_{L,ref}(s)} * \frac{1}{sC}} \quad (15)$$

Figure 7 shows the root locus plot of the voltage control loop with k_p= 0. The value of k_i is found to be 4.86 for a damping ratio of 0.707. The bode diagram of the open-loop transfer function (OLTF) of PR based voltage control loop with k_p=0.0285 and k_i =2.43 is shown in Figure 8. The gain at the fundamental frequency is 38.7 dB and the phase margin of the controller is 118.3°.

2. 3. 3. Design of the outer Grid Current Control Loop The outer grid current control loop structure is shown in Figure 9. The parameters of PR based current controller are found out to be $k_{p,1}$=6, and $k_{i,1}$=25 by using the same procedure as described above. Figure 10 shows the bode diagram of the OLTF of the grid current control, which gives the large gain at the fundamental frequency of 50 Hz and the phase margin of 61°.

The root locus plot and the bode diagram of the closed-loop transfer function (CLTF) of the overall system are shown in Figures 11 and 12.

3. SIMULATION RESULTS AND DISCUSSION

The system described in Figure 1 is simulated in MATLAB / Simulink environment. The parameters used for simulation studies are specified in Table 1. The

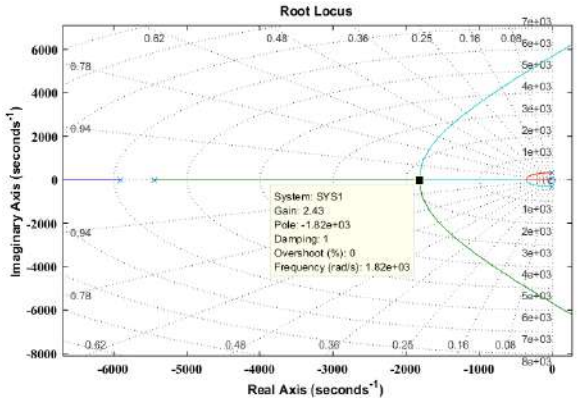

Figure 7. Root locus plot of voltage controller considering k_p=0

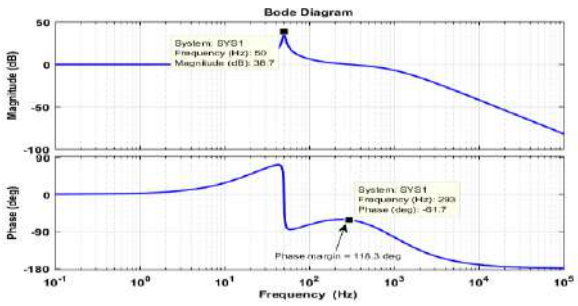

Figure 8. Bode diagram of OLTF of the Voltage controller

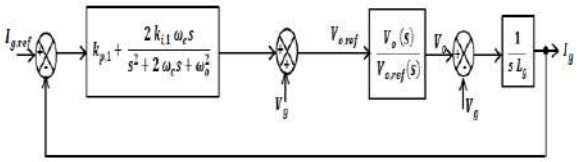

Figure 9. Outer grid current control loop structure

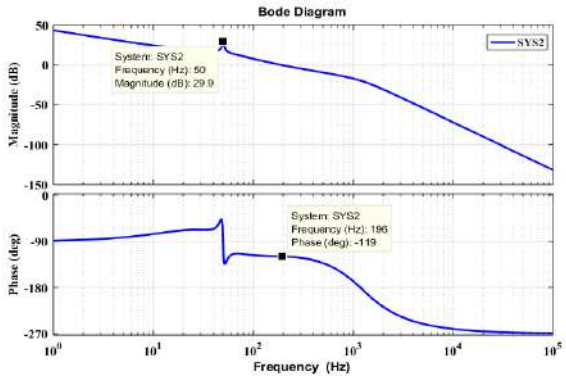

Figure 10. Bode diagram of OLTF of the grid current controller

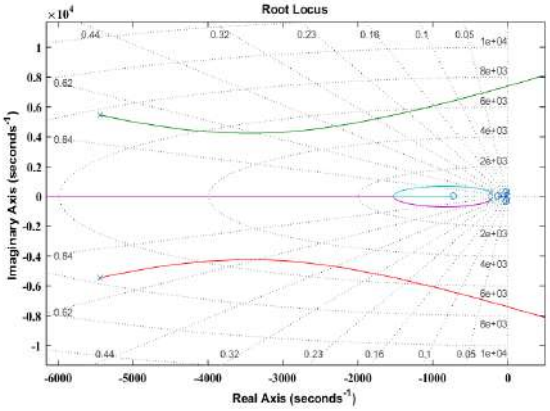

Figure 11. Root locus plot of the overall system

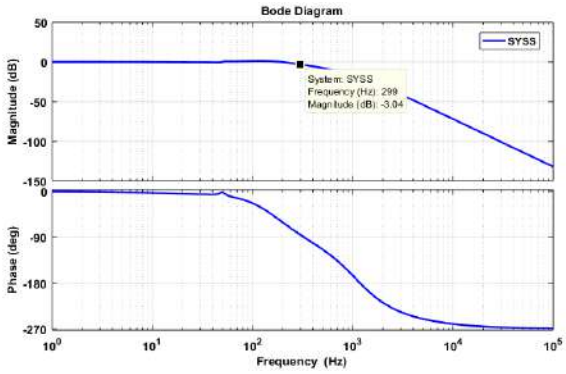

Figure 12. Bode diagram of the CLTF of grid current controller

system is first considered to be connected with the utility, feeding the local load as well as the grid. Simulation studies considering intentional and unintentional islanding have been carried out and the results are presented in this section.

3. 1. Intentional Islanding and Seamless Transfer to Grid Connected Mode Initially, the system is considered to be of grid-connected mode and is moved to islanded mode intentionally and then brought back to the grid-connected mode again. The DG system is in grid-connected mode from 0 – 0.32s and at 0.32s, both the switches 'S_g' and 'S_i' are opened and the system is moving to islanded mode. The system is feeding the load with the demanded power without any interruption. Both the switches are closed at 0.5s after the confirmation of synchronization of MG voltage with that of the utility and hence the DG system is reconnected to the utility at 0.5s. The waveforms of the voltage at the grid side and current fed to the grid under different operating conditions are shown in Figures 13-15.

The grid current falls to zero when moving to islanded mode, which is presented in Figure 14 and the grid current increases to the specified value (10A peak) within 2 cycles i.e., 40ms, immediately after the synchronization process is done, which is shown in Figure 15. The load parameters under different operating conditions are shown in Figures 16 and 17. At the time of moving to

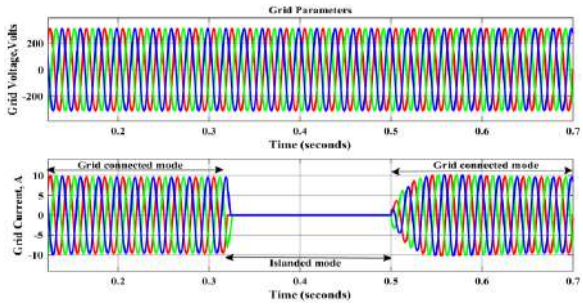

Figure 13. Voltage and Current waveforms at the grid side

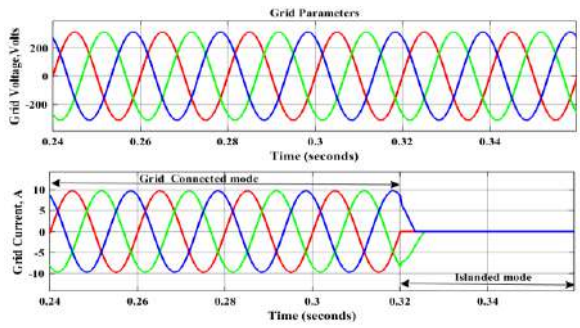

Figure 14. Grid voltage and grid current waveforms when mode changes from grid-connected to islanded mode

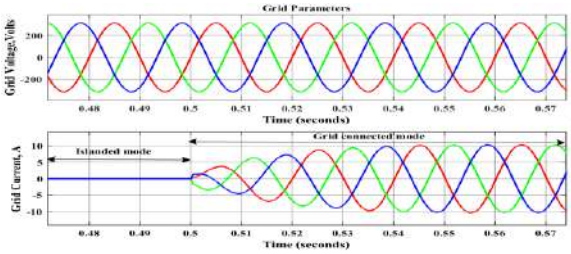

Figure 15. Grid voltage and grid current waveforms when mode changes from islanded to grid-connected mode

islanded mode i.e., at 0.32s, when the switch at the grid side opens, transient which occurs in the load parameters are damped and steady-state is reached within 20ms and the voltage across the load remains almost at the required steady value of about 220 V (rms) and the current is of 7.57 A (rms). The d-q components of the voltage across the load are shown in Figure 18 to show the voltage almost remains the same throughout the operating time. The power consumed by the load is shown in Figure 19.

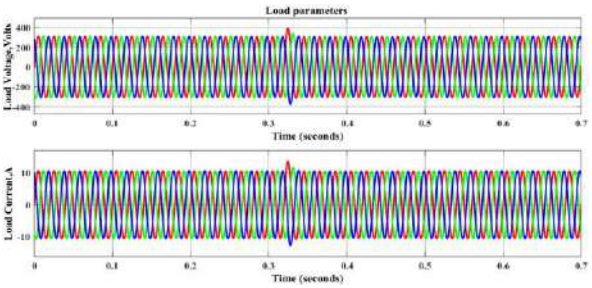

Figure 16. Load voltage and load current under different operating conditions

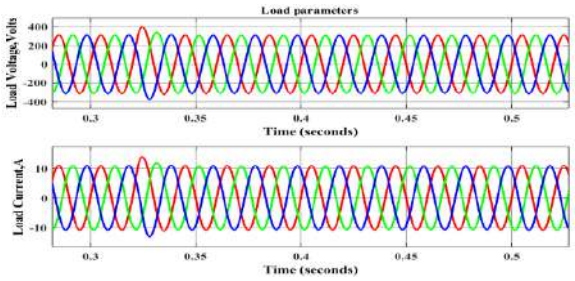

Figure 17. Load voltage and load current while moving to islanding mode and the grid-connected mode

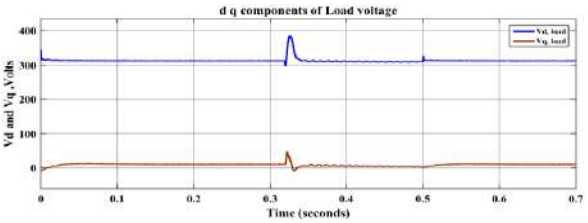

Figure 18. d q components of the load voltage

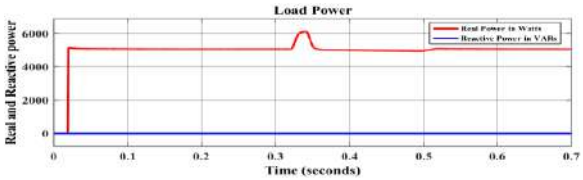

Figure 19. Real and reactive power consumed by the load

3. 2. Unintentional islanding and Seamless Transfer to Grid-connected Mode The system is initially considered to be operating in the grid-connected mode. A three-phase fault is simulated at 0.32s and the switch 'S_g' at the grid side is opened at 0.32s immediately after the occurrence of the fault. The switch 'S_i' in the inverter side is opened at 0.35 s after detecting the islanding condition. The duration between 0.32 s and 0.35s is called a Pre-islanded condition where the terminal voltage is slightly higher than the prescribed limit which is due to the occurrence of the disturbance. Then as the switch 'S_i' gets opened, the system enters into the islanded mode and the load is fed with the desired voltage and frequency without any distortion. After the clearance of the fault, the switch 'S_g' is closed at 0.55 s and the grid is restored. The DG can be connected to the grid only after the synchronization of the voltage at the DG with that of the grid. Hence after the synchronization process, the switch 'S_i' is closed at 0.7 s. The grid current reference is changed to the set value at 0.75 s and till then it remains zero. The current fed into the grid gradually increases and reaches the set value at 0.78s without any transients in the voltage as well in the current waveform.

The voltage and the current waveform at the grid side during the changeover of modes are shown in Figure 20 and Figure 21. The load voltage and load current waveforms are shown in Figure 22. Thus seamless transition between the modes of operation is achieved successfully with the help of an Indirect current control strategy using Proportional resonant controllers.

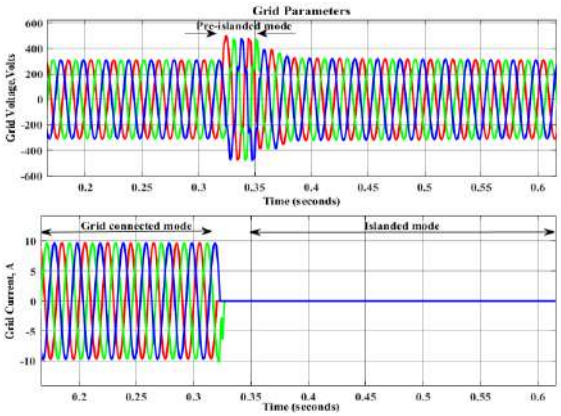

Figure 20. Grid voltage and grid current waveforms–grid-connected mode to islanded mode under unintentional islanding

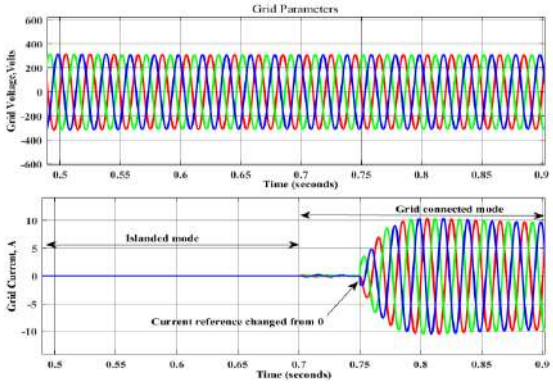

Figure 21. Grid voltage and grid current waveforms – islanded mode to grid-connected mode under unintentional islanding

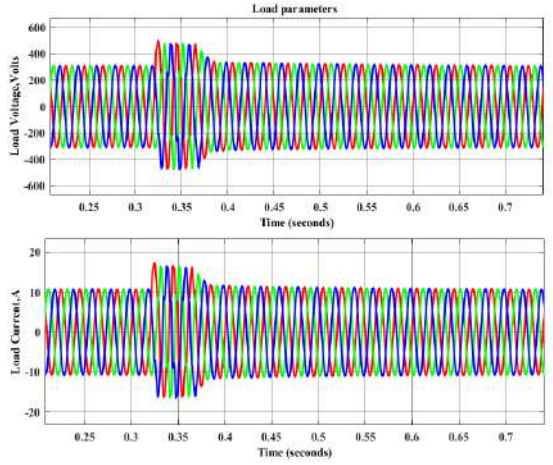

Figure 22. Load voltage and load current waveforms from the islanding mode to grid-connected mode

4. CONCLUSION

A three-phase grid-connected microgrid system has been designed and simulation studies have been carried out in MATLAB / Simulink environment. The proportional resonant controller-based indirect current control strategy has been designed for achieving the seamless transfer between the operating modes of a microgrid. The system considered is simulated in MATLAB/Simulink environment, under islanded and grid-connected modes of operation and the results are presented. Simulation studies have been carried out under intentional islanding and unintentional islanding conditions. The results validate the controller design. The PR based controller for the voltage source inverter works efficiently and effectively. Thus, the seamless transfer between the modes of operation with a very minimal transient period has been attained and the steady-state is reached within 0.04s after the closure or opening of the switches for changing of modes of operation based on the utility conditions.

5. REFERENCES

1. Chowdhury, S., Chowdhury, S. and Crossley, P., "Microgrids and active distribution networks (energy engineering)", Published by The Institution of Engineering and Technology, (2009),
2. Driesen, J. and Katiraei, F., "Design for distributed energy resources", ***IEEE Power and Energy Magazine***, Vol. 6, No. 3, (2008), 30-40. DOI:10.1109/MPE.2008.918703
3. Hatziargyriou, N., Asano, H., Iravani, R. and Marnay, C., "Microgrids", ***IEEE Power and Energy Magazine***, Vol. 5, No. 4, (2007), 78-94. DOI: 10.1109/MPAE.2007.376583
4. Lasseter, R.H., "Microgrids", in 2002 IEEE Power Engineering Society Winter Meeting. Conference Proceedings (Cat. No. 02CH37309), IEEE. Vol. 1, 305-308. DOI.10.1109/PESW.2002.985003
5. Olivares, D.E., Mehrizi-Sani, A., Etemadi, A.H., Cañizares, C.A., Iravani, R., Kazerani, M., Hajimiragha, A.H., Gomis-Bellmunt, O., Saeedifard, M. and Palma-Behnke, R., "Trends in microgrid control", ***IEEE Transactions on Smart Grid***, Vol. 5, No. 4, (2014), 1905-1919. DOI:10.1109/TSG.2013.2295514
6. Gholami, M., "Islanding detection method of distributed generation based on wavenet", ***International Journal of Engineering***, Vol. 32, No. 2, (2019), 242-248. DOI: 10.5829/ije.2019.32.02b.09
7. "IEEE Standard for Interconnection and Interoperability of Distributed Energy Resources with Associated Electric Power Systems Interfaces," in IEEE Std 1547-2018 (Revision of IEEE Std 1547-2003) ,1-138, 2018, doi: 10.1109/IEEESTD.2018.8332112.
8. Carrasco, J.M., Franquelo, L.G., Bialasiewicz, J.T., Galván, E., PortilloGuisado, R.C., Prats, M.M., León, J.I. and Moreno-Alfonso, N., "Power-electronic systems for the grid integration of renewable energy sources: A survey", ***IEEE Transactions on Industrial Electronics***, Vol. 53, No. 4, (2006), 1002-1016. DOI: 10.1109/TIE.2006.878356
9. Balaguer, I.J., Lei, Q., Yang, S., Supatti, U. and Peng, F.Z., "Control for grid-connected and intentional islanding operations of distributed power generation", ***IEEE Transactions on Industrial Electronics***, Vol. 58, No. 1, (2010), 147-157. DOI: 10.1109/TIE.2010.2049709
10. Gaonkar, D., Pillai, G. and Patel, R., "Seamless transfer of microturbine generation system operation between grid-connected and islanding modes", ***Electric Power Components and Systems***, Vol. 37, No. 2, (2009), 174-188. DOI:10.1080/15325000802388815
11. Ahmed, I., Longting, S. and Xin, C., "A novel control scheme for microgrid inverters seamless transferring between grid-connected and islanding mode", in 2017 China International Electrical and Energy Conference (CIEEC), IEEE. 75-80. DOI: 10.1109/CIEEC.2017.8388423
12. Jia, Y., Liu, D. and Liu, J., "A novel seamless transfer method for a microgrid based on droop characteristic adjustment", in Proceedings of The 7th International Power Electronics and Motion Control Conference, IEEE. Vol. 1, 362-367. DOI: 10.1109/IPEMC.2012.6258878
13. Shen, G., Xu, D. and Yuan, X., "A novel seamless transfer control strategy based on voltage amplitude regulation for utility-interconnected fuel cell inverters with an lcl-filter", in 2006 37th IEEE Power Electronics Specialists Conference, IEEE. 1-6. DOI: 10.1109/pesc.2006.1712073
14. Yanjie, W. and Guopeng, Z., "An output current based seamless transfer control strategy for three-phase converter with energy storage in micro-grid", International Conference on Renewable Power Generation (RPG 2015), Beijing, China**,** (2015) 1-6. DOI: 10.1049/cp.2015.0310.

15. Gao, F. and Iravani, M.R., "A control strategy for a distributed generation unit in grid-connected and autonomous modes of operation", ***IEEE Transactions on Power Delivery***, Vol. 23, No. 2, (2008), 850-859. DOI:10.1109/TPWRD.2007.915950
16. Hu, S.-H., Kuo, C.-Y., Lee, T.-L. and Guerrero, J.M., "Droop-controlled inverters with seamless transition between islanding and grid-connected operations", in 2011 IEEE Energy Conversion Congress and Exposition, IEEE. 2196-2201. DOI: 10.1109/ECCE.2011.6064059
17. Yu, T., Choi, S. and Kim, H., "Indirect current control algorithm for utility interactive inverters for seamless transfer", in 2006 37th IEEE Power Electronics Specialists Conference, IEEE. 1-6. DOI**:** 10.1109/pesc.2006.1712024
18. Kim, H., Yu, T. and Choi, S., "Indirect current control algorithm for utility interactive inverters in distributed generation systems", ***IEEE Transactions on Power Electronics***, Vol. 23, No. 3, (2008), 1342-1347. DOI: 10.1109/TPEL.2008.920879
19. Kwon, J., Yoon, S. and Choi, S., "Indirect current control for seamless transfer of three-phase utility interactive inverters", ***IEEE Transactions on Power Electronics***, Vol. 27, No. 2, (2011), 773-781. DOI: 10.1109/APEC.2011.5744661
20. Liu, Z., Liu, J. and Zhao, Y., "A unified control strategy for three-phase inverter in distributed generation", ***IEEE Transactions on Power Electronics***, Vol. 29, No. 3, (2013), 1176-1191. DOI: 10.1109/TPEL.2013.2262078
21. Liu, Z. and Liu, J., "Indirect current control based seamless transfer of three-phase inverter in distributed generation", ***IEEE Transactions on Power Electronics***, Vol. 29, No. 7, (2013), 3368-3383. DOI**:** 10.1109/TPEL.2013.2282319
22. Mohamed, Y.A.-R.I. and Radwan, A.A., "Hierarchical control system for robust microgrid operation and seamless mode transfer in active distribution systems", ***IEEE Transactions on Smart Grid***, Vol. 2, No. 2, (2011), 352-362. DOI: 10.1109/TSG.2011.2136362
23. Lavanya, V. and Kumar, N.S., "Control strategies for seamless transfer between the grid-connected and islanded modes of a microgrid system", ***International Journal of Electrical & Computer Engineering***, Vol. 10, No. 5, (2020), 4490-4506 DOI:10.11591/ijece.v10i5.pp4490-4506
24. Lim, K. and Choi, J., "Pr based indirect current control for seamless transfer of grid-connected inverter", in 2016 IEEE 8th International Power Electronics and Motion Control Conference (IPEMC-ECCE Asia), IEEE. 3749-3755. DOI: 10.1109/IPEMC.2016.7512895
25. Lim, K. and Choi, J., "Seamless grid synchronization of a proportional+ resonant control-based voltage controller considering non-linear loads under islanded mode", ***Energies***, Vol. 10, No. 10, (2017), 1514. DOI: 10.3390/en10101514
26. Lim, K., Song, I., Choi, J., Yoo, H.-J. and Kim, H.-M., "Seamless mode transfer of utility interactive inverters based on indirect current control", ***Journal of Power Electronics***, Vol. 19, No. 1, (2019), 254-264. DOI:10.6113/JPE.2019.19.1.254
27. Sagar, G. and Debela, T., "Implementation of optimal load balancing strategy for hybrid energy management system in dc/ac microgrid with pv and battery storage", ***International Journal of Engineering***, Vol. 32, No. 10, (2019), 1437-1445. DOI : 10.5829/ije.2019.32.10a.13
28. Gholizade-Narm, H., "A novel control strategy for a single-phase grid-connected power injection system", ***International Journal of Engineering***, Vol. 27, No. 12, (2014), 1841-1849. DOI:10.5829/idosi.ije.2014.27.12c.06
29. "IEEE Recommended Practice and Requirements for Harmonic Control in Electric Power Systems," in IEEE Std 519-2014 (Revision of IEEE Std 519-1992) , pp.1-29, 11 June 2014, doi: 10.1109/IEEESTD.2014.6826459.

Persian Abstract

چکیده

این مقاله به طراحی ساختار کنترل اینورتر مبتنی بر کنترلر متناسب با رزونانس (PR) برای دستیابی به انتقالهای صاف بین حالتهای عملیاتی یک سیستم میکروگرید متصل به شبکه پرداخته است. استراتژی کنترلی که برای اینورتر استفاده می شود عبارتست از کنترل سه حلقه آبشار ، جریان شبکه ، ولتاژ در طول بار و حلقه های جریان خروجی اینورتر. کنترل اینورتر عمدتاً برای حفظ مقدار ولتاژ در محدوده تعیین شده تعیین شده و داشتن کیفیت مناسب ولتاژ در طول بار تحت همه حالت های کار متمرکز است. یک کنترل کننده رزونانس متناسب با در نظر گرفتن معیارهای گذرا و پایداری در نظر گرفته شده در حالت های مختلف عملکرد طراحی شده است. روش طراحی کنترلر رزونانس متناسب با جزئیات ارائه شده است. سیستم میکروگرید متصل به شبکه سه فاز که مورد بررسی قرار گرفته است در محیط MATLAB / Simulink شبیه سازی شده است تا در شرایط جزیره ای و همچنین در شرایط اتصال به شبکه و همچنین تغییر حالت از جزیره به شبکه به شبکه متصل شده و برعکس. نتایج شبیه سازی تحت حالت های مختلف عملیاتی برای تأیید اعتبار طرح کنترل برای انتقال صاف بین حالت های عملکرد ارائه شده است.

International Journal of Engineering

Journal Homepage: www.ije.ir

A Fast Processing Discontinuous Control Strategy for Vienna Rectifier

T. Fadaeian, S. A. Gholamian*, H. Ghoreishy

Department of Electrical and Computer Engineering, Babol Noshirvani University of Technology, Babol, Iran

P A P E R I N F O

Paper history:
Received 22 October 2019
Received in revised form 04 August 2020
Accepted 13 August 2020

Keywords:
Vienna Rectifier
Discontinuous Pulse-width Modulation
Fast Prosecing
Circuit-Level Decoupling
Current Total Harmonic Distortion
Neutral Point Balancing

A B S T R A C T

In this paper, Vienna rectifier has been inspected as one of the prominent topologies among three-level switched-mode rectifiers. A fast processing discontinuous modulation strategy has been proposed with the aim of improving the rectifier's performance. The proposed method not only takes advantage of special properties available in three-phase three-level rectifiers, but also reduces the control design complexity and the switching loss. Moreover, neutral point voltage balancing is inherently realized. To achieve these goals, the rectifier is decoupled into two 2-level boost converters in every defined region, leading to simple modulation algorithm and fast processing control strategy. The validity of the proposed technique has been verified via simulation and experimental results conducted on a laboratory prototype.

***doi**: 10.5829/ije.2020.33.10a.14*

1. INTRODUCTION

Nowadays, power electronics is widely used in power conversion and power generation applications. Conventional power electronics converters have the disadvantages of low power factor and high current total harmonic distortion (THD), which are of significant concern in power quality aspect. Hence, Three-phase power factor correction active rectifiers are increasingly used in applications such as high voltage DC systems, uninterruptable power supplies, variable speed drives, etc. So far, several structures of three-phase active rectifiers have been introduced, all presenting some advantages and disadvantages in various applications [1-4]. Amongst three-phase active converters, Vienna rectifier, a non-regenerative three-level boost converter has been one of the most popular topologies due to its good performance and simple structure. The rectifier presents high power factor correction (PFC) performance, low electromagnetic interference (EMI), low voltage stress and low cost. Therefore, it can be used in medium voltage/high power applications such as telecommunication and wind energy conversion systems [3-6]. In addition, electric or hybrid vehicles, in which both power density and reduced weight are of the most importance, have been the potential applications of Vienna rectifier. The whole system configuration is shown in Figure 1.

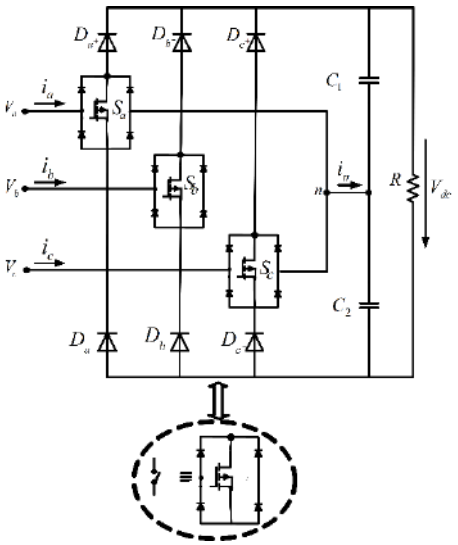

Figure 1. Vienna rectifier schematic diagram

*Corresponding Author Institutional Email: *gholamian@NIT.ac.ir* (S. A. Gholamian)

Please cite this article as: T. Fadaeian, S. A. Gholamian, H. Ghoreishy, A Fast Processing Discontinuous Control Strategy for Vienna Rectifier, International Journal of Engineering (IJE), IJE TRANSACTIONS A: Basics Vol. 33, No. 10, (October 2020) 1959-1967

Up to now, various switching methods and control techniques have been addressed in the literature for Vienna rectifier, which are completely different from the conventional strategies, used for three-level rectifier structures. Space vector modulation (SVM) control strategy for Vienna rectifier is developed [7-9]. The voltage vector selection and calculation of the duration time are much more complicated than other strategies. The complexity and the computation burden is further increased due to the dependency of phase voltage to the input current direction.

In Carrier-based pulse width modulation (CB-PWM) method reported in literature [7, 8], two carrier waves are employed to realize the pulse width modulation (PWM). Neutral point potential is also balanced by adding offset signals to the phase reference voltages, which leads to continuous switching method, known as continuous PWM. Reference voltage generation is much easier compared with SVM strategy. However, its practical implementation is complicated in terms of synchronization of two carrier waves with same frequencies. Single-carrier wave PWM is realized to overcome the problem existing in CB-PWM, but still balancing DC-link voltage remains a challenge [10]. Hysteresis current controller introduced by Foureaux et al.[11], has the merit of fast dynamic response and simple implementation allowing the usage of minimum hardware. However, the controller presents inherent disadvantage of variable switching frequency, which is an issue in converter protection.

Most of the continuous PWM strategies can considerably satisfy the control objectives of Vienna rectifier. However, in case of Vienna rectifier, with satisfactory operational characteristics in high power applications, applying discontinuous approaches can significantly decrease the switching loss [12-14]. Discontinuous PWM (DPWM) methods are advantageous with respect to efficiency. When high efficiency is of the most importance, employing methods with lower switching loss seems practical [13]. SVM-based DPWM method is introduced within a limited range of modulation index [12]. Implementation of DPWM method based on SVM seems complicated using low performance microcontroller units, while high performance is achieved in the expense of more cost. Lee and Lee [14] developed a carrier-based DPWM strategy for Vienna rectifier. In this method, DC-link voltage balancing is realized through injection an offset to the phase reference voltages. This strategy offers simpler implementation than SVDPWM techniques. Yet, to satisfy the important requirement (IR) existing in Vienna rectifier, that is; the sign of the current should be the same as that of the input voltage, an additional offset calculation has to be performed to modify the reference voltage. A discontinuous space vector modulation (DSVM) method is proposed by Zhu et al. [15] for Vienna rectifier, in which the clamping area to the neutral point is varied by adding a clamping factor. In this condition, the optimum clamping area is defined and low-order harmonic contents in input currents will be reduced effectively.

In Vienna rectifier, the neutral point (NP) is connected to the input inductors via semiconductor switches. Though, DC-link voltage unbalance is the most challenging problem in converter control, since it results in high voltage stress on semiconductor devices and input current distortion. Hence, some considerations should be introduced to overcome the unbalance problem in the rectifier structure. A virtual space vector is introduced by Choudhury et al. [16] to control the fluctuations in the neutral point. The voltage of the capacitors in the DC-link is measured and an optimal switching sequence is selected and applied to three-level neutral-point clamped (NPC) inverter, based on a lookup table (LUT). Redundant switching states are used to control the NP voltage [17]. Here, voltage in the capacitors are measured and based on the current of the NP and an active or passive vector is selected; then, a switching table is proposed for the selection of the switching state to the NPCVSI for smooth switching criteria. However, an extra sensor in the experimental setup is still necessary. In most conventional control strategies for Vienna rectifier, an offset voltage injection or an extra feedback control loop including PI controller is modified to provide DC-link voltage regulation. An additional balancing leg including two extra MOSFET switches and an inductor, has been applied to the space vector modulated Vienna rectifier [18]. The relationship between the controlled duty cycle and the voltage unbalance is established through the state-space model of the system and based on this relationship, an optimal zero-sequence component for the duty cycle is found to achieve zero current injection to the DC-link neutral point [19]. Ma et al. [20] introduced a high-frequency model based on the relationship between the neutral point voltage and the AC currents. Here, the neutral point voltage balance is effectively managed by regulating the time of SVM redundant small vector pair during a duty cycle.

Another limitation existing in Vienna rectifier is the current distortion occurring at current zero-crossing points due to the dependency of the rectifier voltage to the current polarity. If one of the phase currents crosses zero during a switching period, any phase in which the corresponding switch is off, will produce an erroneous voltage of opposite polarity from what was intended by the control. Consequently, a current spike will appear at the vicinity of current zero-crossing, which results in grid current distortion and EMI Interference. The challenge will be avoided by clamping the related phase to zero. To achieve this goal, Johnson and Aliprantis [21] proposed a modified SVPWM scheme by using the certain state

combinations of short vectors in each sector. In this method, the calculation of duty ratio will not be affected by the direction of phase, current near the zero-crossing point and therefore the current distortion will be eliminated.

A control technique is proposed, based on an analysis of the switching dynamics near current zero crossing for Vienna rectifier in Wind Turbine application [22]. Here, the current ripple, induced by PWM, is calculated and the maximum angular deviations of the current space vector from the fundamental are found. Hence, the timing of the clamping signal will be determined. An improved optimal switching sequence model predictive control (OSS-MPC) strategy based on SVM is presented for Vienna rectifier, in which the control objective is shaping of the rectifier input currents [23]. Since rectifier side voltages are dependent on input currents direction, hence, applying appropriate switching sequence and voltage vectors are inevitable. Moreover, DC-link voltage regulation and the neutral-point voltage balancing are realized by a PI control and a redundant vector pre-selection technique, respectively. However due to SVM switching method, the implementation of the controller still remains as a challenge.

In this paper, a novel discontinuous PWM method, based on circuit level decoupling (CLD) concept is introduced for Vienna rectifier. In the proposed method, Vienna rectifier is decoupled into two two-level separately controlled boost converters in every 60˚ region, in which the closed loop controller design can be simplified to the control of DC-DC converters. The salient features of the proposed strategy are as follow: 1) In the proposed method, Vienna rectifier is decoupled into two two-level separately controlled boost converters in every *60˚* region, in which the closed loop controller design can be simplified to the control of DC-DC converters. 2) The proposed strategy has the merit of using just one carrier-wave for modulation action. 3) Since one of three switches are not operated at any instant, the switching loss is reduced by one-third. 4) The DC-link capacitor voltages are inherently balanced with no requirement for extra control action. Hence, a fast processing controller is achieved. In section 2, the detailed analysis of the proposed PWM modulation strategy for Vienna rectifier is given. The effect of the proposed control on the capacitor voltage balancing is discussed in section 3. Finally, simulation and experimental verification is presented in section 4.

2. PRINCIPLE OF THE PROPOSED PWM MODULATION STRATEGY

Vienna rectifier structure consists of three semiconductor switches (S_a, S_b and S_c), low loss silicon carbide diodes and DC-link capacitors (C_1 and C_2) as shown in Figure 1. The detailed operations of the Vienna rectifier is discussed in literature [24]. Sinusoidal input current, desired output voltage, and balanced capacitor voltages are achieved based on the switching pattern applied on S_a , S_b and S_c. The rectifier side voltages (V_{an} , V_{bn} and V_{cn}) depend on the switching states of switches and polarity of the input currents and are expressed as follows:

$$V_{an} = \frac{V_{dc}}{2}\text{sgn}(i_a)(1-S_a)$$
$$V_{bn} = \frac{V_{dc}}{2}\text{sgn}(i_b)(1-S_b) \quad (1)$$
$$V_{cn} = \frac{V_{dc}}{2}\text{sgn}(i_c)(1-S_c)$$

where; and V_{dc} is the rectifier's output voltage, S_a, S_b, and S_c are the switching states of the switches (S_a; S_b; S_c=*1* when switches are on and S_a; S_b; S_c=*0* when switches are off).

In this paper, a discontinuous PWM method with the circuit-level decoupling concept has been proposed for Vienna rectifier, based on the existing strategy for three-level NPC inverters [25]. The proposed control method is described through the following sections.

2. 1. Circuit-Level Decoupling Concept Three-phase input voltages (V_a, V_b and V_c) are shown in Figure 2. According to the figure, each phase voltage can be divided into 6 regions per fundamental cycle. Inspecting three-phase voltages in each 60˚ region, one common fact is that, there is a sign transition in one phase voltage while the sign of the other two voltages is remained unchanged. Considering this fact, the switch with transitional phase voltage is always kept on during the whole 60˚ region, whereas the remaining phase switches will be modulated with duty cycles (d_p and d_n). That means; just two of the three switches in the converter is pulse width modulated at any instant. Hence, compared with continuous strategies, the number of turning-on and turning-off times of each switch and its corresponding diode in bridge structure, will decrease by a factor of 1/3. Applying the above analysis, the rectifier equivalent circuit for region I, is presented in Figure 3. As seen in the figure, since the voltage of phase (*a*) has transitional sign, its corresponding switch (S_a) is kept on during the entire period. Likewise, the voltage in phase (*c*) is positive during the whole region and S_1 is switched

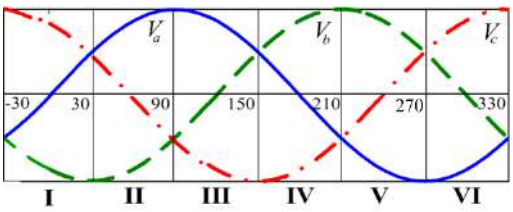

Figure 2. Three phase input voltages

between *p* and *n*. While, the voltage of phase (*b*) is always negative and S_2 will be switched between *N* and *n*.

Since the switching frequency is much higher than the fundamental frequency, Vienna rectifier circuit can be decoupled into two two-level DC-DC boost converters during each *60°* region as in Figure 4. Duty cycles for switches in phase (*c*) and (*b*) can be defined as d_p and d_n:

$$d_p = \frac{T_{0S_1}}{T_{sw}} \quad , \quad d_n = \frac{T_{0S_2}}{T_{sw}} \tag{2}$$

where; $T_{0_{Si}}\,(i=1,2)$ is the on-time of each switch and T_{sw}, is the switching period.

2. 2. Analysis of Decoupled Converters As shown in Figure 2, for the period *(-30°~0°)*, the absolute value of phase (c) voltage is higher than that of phase (b) and thus, $(d_p < d_n)$. The opposite is found during *(0°~30°)*. Regarding the above relation between d_p and d_n, two different switching sequences must be applied on decoupled converters, during each switching cycle; 1,2,4 for ($d_p < d_n$) and 1,3,4 for ($d_p > d_n$). The switching sequences and the resulting inductor voltages in region I are summarized in Table 1.

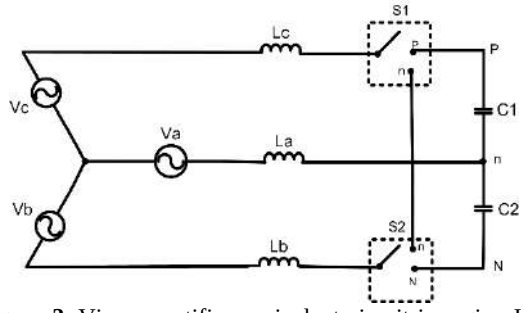

Figure 3. Vienna rectifier equivalent circuit in region I; (-30°~30°)

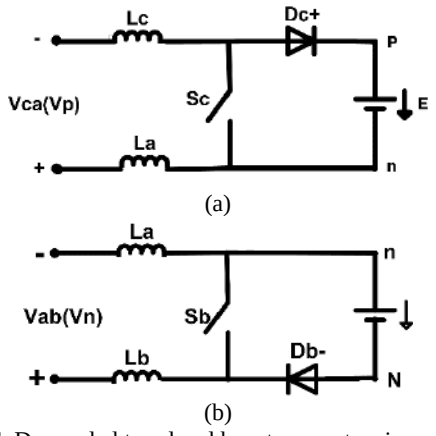

Figure 4. Decoupled two-level boost converters in region I; (-30°~30°)

TABLE 1. Switching states and inductor voltages in region I

Switching States	S_b	S_c	V_{Lb}	V_{Lc}	V_{La}
1	on	on	V_b	V_c	V_a
2	on	off	$V_b+\frac{1}{3}E$	$V_c-\frac{2}{3}E$	$V_a+\frac{1}{3}E$
3	off	on	$V_b+\frac{2}{3}E$	$V_c-\frac{1}{3}E$	$V_a-\frac{1}{3}E$
4	off	off	V_b+E	V_c-E	V_a

To give a better illustration of the analysis carried out, the extraction process of inductor voltages is presented below.

Considering the decoupled circuits in Figure 4, KVL equations for switching state (2) are written as follow:

$$-V_c + L\frac{di_c}{dt} - L\frac{di_a}{dt} + V_a + E = 0 \tag{3}$$

$$-V_a + L\frac{di_a}{dt} - L\frac{di_b}{dt} + V_b = 0 \tag{4}$$

In above equations, parameter '*E*' represents DC-link voltage and $i_i(i=a,b,c)$ are the rectifier input currents.

Assuming the three-phase input voltages and currents to be symmetrical, the inductor voltages, are extracted for region I:

$$V_{La} = V_a + \frac{1}{3}E\,,\, V_{Lb} = V_b + \frac{1}{3}E\,,\, V_{Lc} = V_c - \frac{2}{3}E \tag{5}$$

Accordingly, duty cycles of the switches will be obtained through applying volt-second balance to the inductors during a switching cycle, as:

$$\begin{cases} V_c d_n + \left(V_c - \frac{1}{3}E\right)\left(d_p - d_n\right) + \left(V_c - E\right)\left(1 - d_p\right) = 0 \\ -V_b d_n + \left(-V_b - \frac{2}{3}E\right)\left(d_p - d_n\right) + \left(-V_b - E\right)\left(1 - d_p\right) = 0 \\ V_a d_n + \left(-V_a - \frac{1}{3}E\right)\left(d_p - d_n\right) + V_a\left(1 - d_p\right) = 0 \end{cases} \tag{6}$$

$$\Rightarrow \begin{cases} d_p = \dfrac{E - (2V_c + V_b)}{E} \\ d_n = \dfrac{E - (-V_c - 2V_b)}{E} \end{cases}$$

The same analysis has been extended to other switching states and regions, which are eliminated here to avoid tedious calculations.

2. 3. Implementation of the Proposed Switching Strategy Implementation process of the proposed method is illustrated in Figure 5 and is divided into 4 major blocks: Region selector, Modulation Signal Selector (MSS), PWM unit, Duty Cycle Allocator (DCA). The active operating region is determined

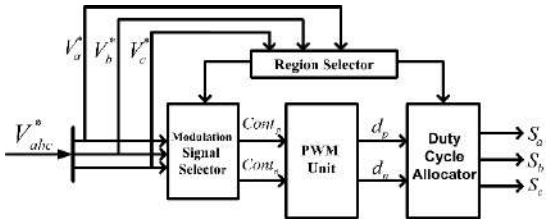

Figure 5. Schematic diagram of the proposed CLD-DPWM switching strategy

through observation of the input reference voltages (V^*_{abc}) in region selector. $Cont_p$ and $Cont_n$ signals are derived from MSS block based on the active operating region number and the information listed in Table 2. The resulting modulation signals are then compared with carrier wave in PWM unit and the duty cycle signals d_p and d_n are obtained. The duty cycles are evaluated through applying a simple PWM technique on two decoupled boost converters in each region. These signals are then allocated to the switches S_a, S_b and S_c in DCS block, according to the information acquired from region selector. Assignment of duty cycles (d_p, d_n *and* d_t) along with the derivation of the modulation signals ($Cont_p$ and $Cont_n$) are listed in Table 2 for each region. d_t=1 is allocated to the switch with on state during each region. Taking into account the analysis conducted in Table 2, algorithm of the modulator is so simple and the modulation is performed using just one carrier wave. Accordingly, the implementation can be processed very quickly in comparison to the conventional methods such as SVPWM and CB-PWM strategies. It is worth mentioning that the proposed control algorithm imposes more boosting voltage than other modulation strategies. For instance, considering region I in Figure 2, the following condition should be met:

$$\frac{V_{dc}}{2} > V_{ca_{\max}} \tag{7}$$

which occurs at $\omega t=30°$ and minimum voltage over positive boost converter (Figure 4 (a)) is obtained as:

$$\left.\frac{V_{dc}}{2}\right|_{\min} = V_m \sin(\omega t+120) - V_m \sin(\omega t) = \frac{3}{2}V_m \tag{8}$$

Thus, the minimum output DC voltage will be:

$$V_{dc_{\min}} = \sqrt{3}V_{LL_{\max}} \tag{9}$$

where, V_m is the peak phase voltage and V_{LLmax} is the peak line voltage. As in Equation (9), V_{dcmin} is 73% more than the line voltage obtained through other existing modulation strategies for Vienna rectifier presented in literature [7-11,14,15], which makes the structure compliant with high voltage industrial installations.

2. 4. Implementation of the Closed-Loop Control

The whole closed-loop control structure is presented in Figure 6, which consists of two control loops; the inner current loop providing sinusoidal input current and the outer voltage loop applied to achieve fixed voltage at the rectifier output. As observed in Figure 6, in the proposed method the feedback control loop for capacitor voltage regulation is remove due to the inherent self-balancing capability of the method. In Figure 6, the reference current amplitude is derived based on the error between the DC voltage reference (V^*_{dc}) and its measured value (V_{dc}) in voltage controller block, which then is passed through a PI controller. The angle of the three-phase grid voltage is derived through the PLL block, which is used to generate the current reference (i^*_{abc}) in phase with V_{abc}.

Input current error is then passed through a proportional controller, providing the reference signals (V^*_{abc}) for the proposed CLD-DPWM method. The controller parameters are chosen based on error and trial method as: K_{pv}=*0.016*, K_{iv}=*3*, K_{pi}=*0.2*. where, K_{pv} and K_{iv} are the voltage controller and K_{pi} is the current controller parameters. It should be mentioned that under the above controller design, the rectifier output voltage can be reached in the range of:

$$1.73V_m < V_{dc} < 6.7V_m \tag{10}$$

As for the closed-loop controller design, the design methods for DC-DC converters can be utilized easily to implement the output voltage control of the three-level Vienna rectifier, due to the circuit decoupling concept.

3. NUETRAL POINT SELF-BALANCING ABILITY

Referring to decoupled circuit for Vienna rectifier in Figure 4, it can be found that positive boost rectifier will transfer its energy to C_1, while the negative boost rectifier will transfer its energy to C_2. As a result, an equal power is transferred to C_1 and C_2 during a fundamental cycle and though, DC-link capacitors will be naturally balanced. The following mathematical analysis is carried out as a proof to the fact. When a switch is turned on and clamped to the neutral point, the corresponding phase current is conducted into or drawn out from the neutral point. In consequence, the neutral point voltage will deviate from zero. The mean value of the neutral point current during a modulation period can be obtained as follows:

$$i_n = d_{a0}i_a + d_{b0}i_b + d_{c0}i_c \tag{11}$$

here, d_{i0} *(i=a,b,c)*; is the time ratio of the associated switch. For instance, in region I, switches in phase (*b*) and (*c*) are controlled via d_p and d_n. While, the switch in phase (*a*) is always kept on and connected to the neutral point for the entire period, that is; d_{a0}=1. Taking into account Table 2 and Equation (11), the following formula will be met in region I:

TABLE 2. Derivation of switching signals

Region	V_p	V_n	Control Signal Selector		Gate Signal Distributor		
			$Cont_p$	$Cont_n$	d_p	d_n	$d_t=1$
I	V_{ca}	V_{ab}	$E-(2V_c+V_b)$	$E-(-V_c-2V_b)$	S_c	S_b	S_a
II	V_{ac}	V_{cb}	$E-(2V_a+V_b)$	$E-(-V_a-2V_b)$	S_a	S_b	S_c
III	V_{ab}	V_{bc}	$E-(2V_a+V_c)$	$E-(-V_a-2V_c)$	S_a	S_c	S_b
IV	V_{ba}	V_{ac}	$E-(2V_b+V_c)$	$E-(-V_b-2V_c)$	S_b	S_c	S_a
V	V_{bc}	V_{ca}	$E-(2V_b+V_a)$	$E-(-V_b-2V_a)$	S_b	S_a	S_c
VI	V_{cb}	V_{ba}	$E-(2V_c+V_a)$	$E-(-V_c-2V_a)$	S_c	S_a	S_b

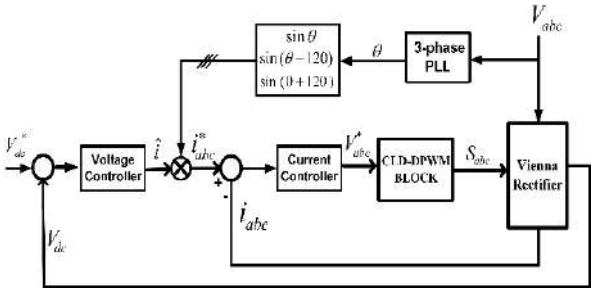

Figure 6. The whole closed-loop control system

$$\begin{aligned} i_{n_I} &= d_p \times i_c + i_a + d_n i_b \\ &= \left[1-(2V_c+V_b)\right]\times i_c + 1\times i_a + \left[1-(-V_c-2V_b)\right]\times i_b. \end{aligned} \quad (12)$$

where; i_{nI} is the average neutral point current during region I. The above equation can be generalized for regions (II-VI). The summation of average neutral point currents related to all six regions (i_n), is given below:

$$i_n = \sum_{x=I}^{VI} i_{n_x} = 0 \quad (13)$$

Equation (13) indicates that due to the proposed method, no current is injected into the neutral point during a fundamental cycle and hence, DC-link capacitors are naturally balanced with no requirement for an extra feedback loop.

5. SIMULATION AND EXPERIMENTAL VERIFICATION

In order to verify the performance of the proposed CLD-DPWM technique, a 600 W Vienna rectifier is simulated in MATLAB/Simulink and the simulation parameters are listed in Table 3. Rectifier's 3-phase input current and its harmonic spectrum are illustrated in Figures 7 and 8, respectively. It can be observed from the figure that the input current is completely spike-free specially at zero-crossing points, since the phase with near-zero current is clamped to the neutral point by keeping its switch on and hence, the impact of current direction on rectifiers voltage will be eliminated. The rectifier input current in the proposed method, like other existing discontinuous approaches, is subjected to distortion and its THD is slightly increased in comparison to the continuous strategies [14]. According to Figure 8, the input current harmonic distortion in the proposed method is 2.87%, which satisfies IEEE 519 (i.e. max. of THD for each order: 5%). Consequently, taking into account the aforementioned advantages of the proposed method, this minor increase in THD can be justified. It should be noted that in Figure 8, the fundamental component bar exceeds the limits due to the better illustration of other harmonic contents. The corresponding waveforms of single phase input voltage/current and DC output voltage are shown in Figure 9. In the presence of the proposed discontinuous switching strategy, the unity power factor is achieved and IR is satisfied with no need for additional actions. Moreover, the DC bus voltage accurately tracks the reference and the voltage ripple will be kept within less than 1%. Phase (a) voltage on both the grid side and the switch side are shown in Figure 10. As in the figure, the switch side voltage is clamped to *(-Vdc/2), 0, (+Vdc/2)*.

TABLE 3. Parameters used in simulation

Input line voltage	$V_{L\text{-}L}$=122 V
Input inductor	L=3 mH
DC-link capacitor	C_1,C_2=1300 μF
DC-link reference voltage	V_{dc}=300 V
Switching frequency	f_s=10 kHz
Line frequency	f_m=50 Hz
Load resistance	R_L=150 Ω

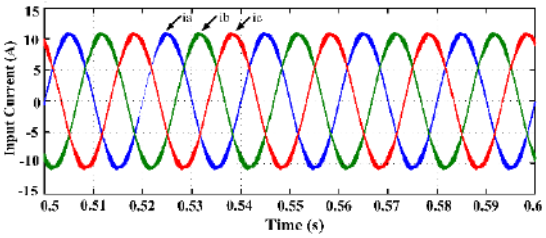

Figure 7. Three phase grid current

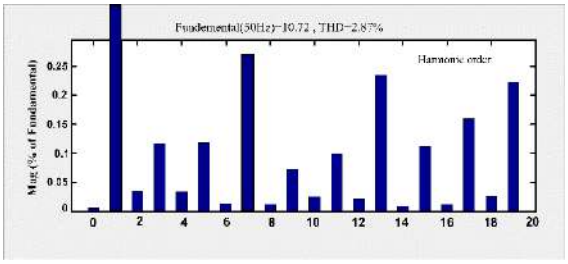

Figure 8. FFT analysis of the proposed DPWM method

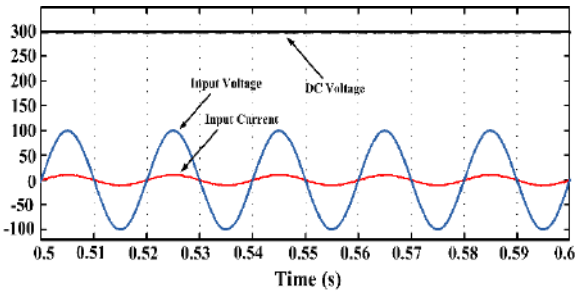

Figure 9. Simulation results for: (a) input current and voltage, (b) DC-link voltage

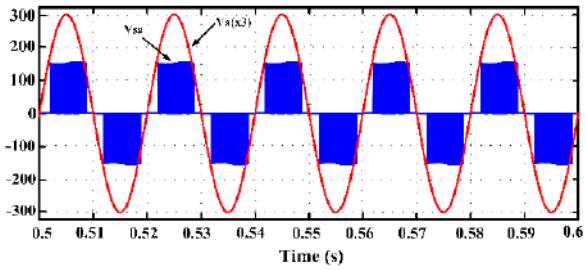

Figure 10. Waveform of (a) input phase voltage and phase voltage over switches

Furthermore, since the phase with transitional state is clamped to zero during each 60˚ region, two zero intervals occur in the switch side voltage waveform during each switching cycle. DC-link voltages V_{C1} and V_{C2} are also presented in Figure 11. As in the figure, the capacitor voltages are essentially well-balanced without any balancing feedback loop. Figure 12 shows the dynamic balancing process in which the initial voltages on DC-link capacitors are unbalanced as $V_{C1} = 200\ V$ and $V_{C2} = 100\ V$, which converge after a very short time interval. To further verify the effectiveness of the proposed control strategy, a 253 W experimental prototype is built at laboratory scale. The power stage consists of Dual Common Cathode Ultrafast Rectifiers (FEP30J) and Si MOSFETs (IRFP260N), and the control system is executed in MCU TMS320F28335 DSP with the switching and sampling frequency of 10 kHz. The input voltage is 40 Vrms/50 Hz and the input inductors are 5 mH. The two DC-link capacitors connected in series at the DC-side are 1360 µF, and the load resistance is 145 Ω. Moreover, the DC reference voltage is 190 V. Figure 13 presents grid voltage and input current in phase (*a*). The figure verifies the simulation results in terms of power factor and current distortion at zero-crossing points. The current THD of 4.46% under modulation index of 0.5968 have been achieved from experimental prototype, which also assures IEEE519 standard.

Moreover, as seen in the figure, under the proposed modulation algorithm the unity power factor is realized without applying any modifications on switching signal. Figure 14, illustrates the experimental results of phase (*a*) current, line to line voltages at the grid side (V_{ab}) and the switch side (V_{AB}). The five-level characteristic of V_{AB} is apparent from the waveform. As in the figure, the voltage levels of $\pm 95\ V$, 0, $\pm 190\ V$ are obtained under $190\ V$ reference voltage. Figure 15 shows the experimental results of DC-link voltages; V_{c1}, V_{c2} and V_{dc}. The waveforms well prove the self-balancing behavior of the proposed method, since the output voltage is controlled in $190\ V$ reference voltage and the capacitor voltages are both balanced in $95\ V$.

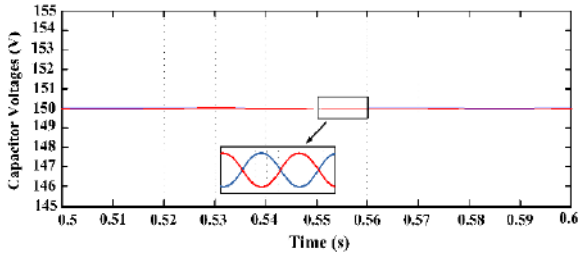

Figure 11. Averaged voltages across the capacitors C_1 and C_2 along with their ac voltage ripple

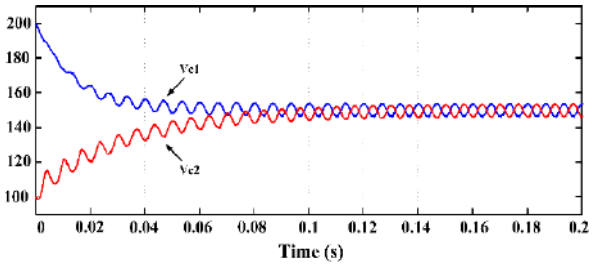

Figure 12. Dynamic balancing process of capacitors with initial voltage $V_{C1} = 200\ V$ and $V_{C2} = 100\ V$

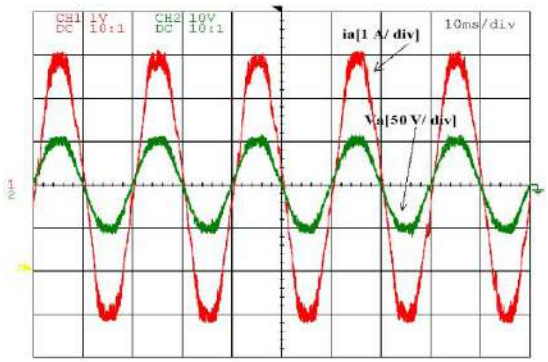

Figure 13. Experimental results of grid voltage and input current in phase (*a*)

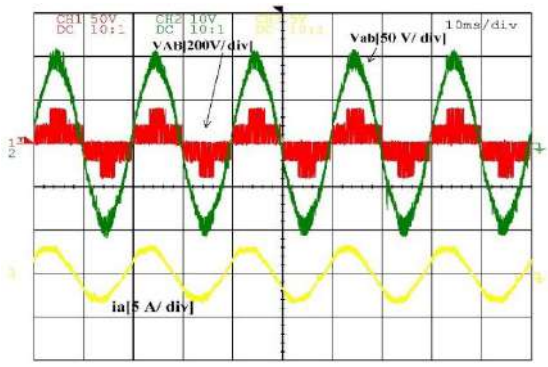

Figure 14. Experimental results of phase (*a*) current, line to line voltage at the grid side (V_{ab}) and the switch side (V_{AB})

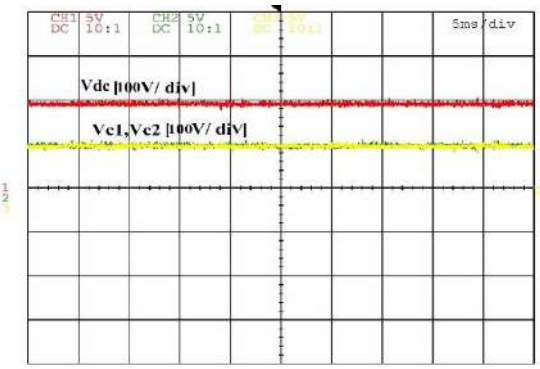

Figure 15. Experimental waveforms of DC-link voltages; V_{c1}, V_{c2} and V_{dc}

6. CONCLUSION

This paper has developed a simple and fast-processing modulation strategy for three-phase three-level Vienna rectifier. The proposed strategy employs circuit-level decoupling concept and is able to decouple the rectifier structure into two 2-level boost converters in every predefined region. This method is fully compatible for industrial applications such as, variable speed drives, high voltage DC systems and renewable energy systems where high power and low switching loss are essential. The main features of this strategy compared to other conventional three level ones are its simple and fast implementation, average NP voltage self-balancing, and low switching loss. Furthermore, current zero crossing distortion, which is problematic due to the generation of erroneous voltage vectors in Vienna rectifier, is inherently removed due to the switching scheme. The above capabilities of the proposed method is well verified through simulation and experimental tests on a 253 W and 10 kHz laboratory prototype.

7. REFERENCES

1. Nishimoto, M., Dixon, J.W., Kulkarni, A.B. and Ooi, B.-T., "An integrated controlled-current pwm rectifier chopper link for sliding mode position control", ***IEEE Transactions on Industry Applications***, Vol. 23, No. 5, (1987), 894-900. DOI: 10.1109/TIA.1987.4505000
2. Singh, B., Gairola, S., Singh, B.N., Chandra, A. and Al-Haddad, K., "Multipulse ac–dc converters for improving power quality: A review", ***IEEE Transactions on Power Electronics***, Vol. 23, No. 1, (2008), 260-281. DOI: 10.1109/TPEL.2007.911880
3. Rajaei, A., Mohamadian, M. and Varjani, A.Y., "Vienna-rectifier-based direct torque control of pmsg for wind energy application", ***IEEE Transactions on Industrial Electronics***, Vol. 60, No. 7, (2012), 2919-2929. DOI: 10.1109/TIE.2012.2227905
4. GHOLAMIAN, S.A., Ghoreishy, H. and Rasouli Khatir, M., "Virtual flux based direct power control on vienna rectifier", ***International Journal of Engineering, Transactions B: Applications***, Vol. 31, No. 2, (2018), 284-291. DOI: 10.5829/ije.2018.31.02b.12
5. Radomski, C., "Analysis of vienna rectifier", ***Electrical Power Quality and Utilisation. Journal***, Vol. 11, No. 1, (2005), 49-56.
6. Bhumika, S. and Shri Harsha, J., "Three phase vienna rectifier for wind power generation system", ***IJRET: International Journal of Research in Engineering and Technology***, Vol. 3, No. 03, (2014). DOI: 10.15623/ijret.2014.0315078
7. Hang, L., Li, B., Zhang, M., Wang, Y. and Tolbert, L.M., "Equivalence of svm and carrier-based pwm in three-phase/wire/level vienna rectifier and capability of unbalanced-load control", ***IEEE Transactions on Industrial Electronics***, Vol. 61, No. 1, (2013), 20-28. DOI: 10.1109/TIE.2013.2240637
8. Burgos, R., Lai, R., Pei, Y., Wang, F., Boroyevich, D. and Pou, J., "Space vector modulator for vienna-type rectifiersbased on the equivalence betweentwo-and three-level converters: A carrier-based implementation", ***IEEE Transactions on Power Electronics***, Vol. 23, No. 4, (2008), 1888-1898. https://doi.org/10.1109/PESC.2007.4342473
9. Viitanen, T. and Tuusa, H., "Experimental results of vector controlled and vector modulated vienna i rectifier", in 2004 IEEE 35th Annual Power Electronics Specialists Conference (IEEE Cat. No. 04CH37551), IEEE. Vol. 6, (2004), 4637-4643. https://doi.org/10.1109/PESC.2004.1354819
10. Kim, H.-W., Yoon, B.-C., Cho, K.-Y., Lim, B.-K. and Hwang, S.-S., "Single carrier wave comparison pwm for vienna rectifier and consideration for dc-link voltage unbalance of offset voltage effects", in 2011 IEEE 33rd International Telecommunications Energy Conference (INTELEC), (2011), 1-6. https://doi.org/10.1109/INTLEC.2011.6099769

11. Foureaux, N.C., Oliveira, J.H., de Oliveira, F.D., Cardoso Filho, B.d.J. and de Faria, R.S., "Command generation for wide-range operation of hysteresis-controlled vienna rectifiers", ***IEEE Transactions on Industry Applications***, Vol. 51, No. 3, (2014), 2373-2380. DOI: 10.1109/TIA.2014.2382757
12. Dalessandro, L., Round, S.D., Drofenik, U. and Kolar, J.W., "Discontinuous space-vector modulation for three-level pwm rectifiers", ***IEEE Transactions on Power Electronics***, Vol. 23, No. 2, (2008), 530-542. DOI: 10.1109/TPEL.2007.915160
13. Kolar, J.W. and Drofenik, U., "A new switching loss reduced discontinuous pwm scheme for a unidirectional three-phase/switch/level boost-type pwm (vienna) rectifier", in 21st International Telecommunications Energy Conference. INTELEC'99 (Cat. No. 99CH37007), IEEE. (1999), 572. https://doi.org/10.1109/INTLEC.1999.794128
14. Lee, J.-S. and Lee, K.-B., "Carrier-based discontinuous pwm method for vienna rectifiers", ***IEEE Transactions on Power Electronics***, Vol. 30, No. 6, (2014), 2896-2900. DOI: 10.1109/TPEL.2014.2365014
15. Zhu, W., Chen, C., Duan, S., Wang, T. and Liu, P., "A carrier-based discontinuous pwm method with varying clamped area for vienna rectifier", ***IEEE Transactions on Industrial Electronics***, Vol. 66, No. 9, (2018), 7177-7188. DOI: 10.1109/TIE.2018.2873524
16. Choudhury, A., Pillay, P. and Williamson, S.S., "Dc-bus voltage balancing algorithm for three-level neutral-point-clamped (NPC) traction inverter drive with modified virtual space vector", ***IEEE Transactions on Industry Applications***, Vol. 52, No. 5, (2016), 3958-3967. DOI: 10.1109/TIA.2016.2566600
17. Mohan, D., Zhang, X. and Foo, G.H.B., "Three-level inverter-fed direct torque control of ipmsm with torque and capacitor voltage ripple reduction", ***IEEE Transactions on Energy Conversion***, Vol. 31, No. 4, (2016), 1559-1569. DOI: 10.1109/TEC.2016.2588339
18. Alahuhtala, J. and Tuusa, H., "Space vector modulated four-wire unidirectional three-phase/level/switch (vienna) rectifier with an additional leg for dc link voltage balancing", in 2008 Twenty-Third Annual IEEE Applied Power Electronics Conference and Exposition, IEEE. (2008), 238-244. https://doi.org/10.1109/APEC.2008.4522728
19. Lai, R., Wang, F., Burgos, R., Boroyevich, D., Jiang, D. and Zhang, D., "Average modeling and control design for vienna-type rectifiers considering the dc-link voltage balance", ***IEEE Transactions on Power Electronics***, Vol. 24, No. 11, (2009), 2509-2522. DOI: 10.1109/TPEL.2009.2032262
20. Ma, H., Xie, Y., Sun, B. and Mo, L., "Modeling and direct power control method of vienna rectifiers using the sliding mode control approach", ***Journal of Power Electronics***, Vol. 15, No. 1, (2015), 190-201. DOI: 10.6113/JPE.2015.15.1.190
21. Johnson, M.H. and Aliprantis, D.C., "Analysis and control of pmsg-based wind turbine with vienna rectifier near current zero crossings", in 2014 Power and Energy Conference at Illinois (PECI), IEEE. (2014), 1-8. https://doi.org/10.1109/PECI.2014.6804551
22. Yao, W., Lv, Z., Zhang, M. and Lin, Z., "A novel svpwm scheme for vienna rectifier without current distortion at current zero-crossing point", in 2014 IEEE 23rd International Symposium on Industrial Electronics (ISIE), IEEE. (2014), 2349-2353. https://doi.org/10.1109/ISIE.2014.6864986
23. Xie, S., Sun, Y., Su, M., Lin, J. and Guang, Q., "Optimal switching sequence model predictive control for three-phase vienna rectifiers", ***IET Electric Power Applications***, Vol. 12, No. 7, (2018), 1006-1013. DOI: 10.1049/iet-epa.2018.0033
24. Minibock, J., Stogerer, F. and Kolar, J.W., "A novel concept for mains voltage proportional input current shaping of a vienna rectifier eliminating controller multipliers. I. Basic theoretical considerations and experimental verification", in APEC 2001. Sixteenth Annual IEEE Applied Power Electronics Conference and Exposition (Cat. No. 01CH37181), IEEE. Vol. 1, (2001), 582-586. https://doi.org/10.1109/APEC.2001.911705
25. Zhang, Z., Thomsen, O.C. and Andersen, M.A., "Discontinuous pwm modulation strategy with circuit-level decoupling concept of three-level neutral-point-clamped (npc) inverter", ***IEEE Transactions on Industrial Electronics***, Vol. 60, No. 5, (2012), 1897-1906. DOI: 10.1109/TIE.2012.2227901

Persian Abstract

چکیده

در این مقاله، یکسوساز وینا، به عنوان یکی از ساختارهای محبوب در میان یکسوسازهای سه‌سطحی مبتنی بر کلیدزنی، مورد بررسی قرار گرفته‌است. یک استراتژی مدولاسیون ناپیوسته با قابلیت پردازش بسیار سریع و با هدف بهبود عملکرد یکسوساز وینا ارائه گردیده‌است. روش پیشنهادی، نه‌تنها از مزایای یکسوسازهای سه‌فاز سه‌سطحی بهره برده‌است، بلکه از پیچیدگی کنترل و تلفات کلیدزنی نیز کاسته و قابلیت متعادل‌سازی ذاتی ولتاژ نقطه خنثی را نیز دارا می‌باشد. به‌منظور دستیابی به اهداف فوق‌الذکر، ساختار یکسوساز در هر ناحیه تعیین شده، به دو مبدل بوست دوسطحی تجزیه می‌گردد که در نتیجه آن، الگوریتم مدولاتور ساده شده و حلقه کنترلی با سرعت بالاتری پردازش خواهد شد. صحت روش پیشنهادی، به‌واسطه شبیه‌سازی و نتایج تست عملی برروی نمونه آزمایشگاهی مورد راستی‌آزمایی قرار گرفته‌است.

IJE TRANSACTIONS A: Basics Vol. 33, No. 10, (October 2020) 1968-1977

International Journal of Engineering

Journal Homepage: www.ije.ir

A Proposed Approach for Separation between Short Circuit Fault, Magnetic Saturation Phenomenon and Supply Unbalance in Permanent Magnet Synchronous Motor

Z. Gherabi*[a], D. Toumi[b], N. Benouzza[a], A. Bendiabdellah[a]

[a] *Electrical Engineering Faculty, Diagnosis Group, LDEE Laboratory, University of Sciences and Technology of Oran (USTO-MB), Algeria*
[b] *Electrical Engineering Department, L2GEGI Laboratory, University of Ibn-Khaldoun of Tiaret, Algeria*

PAPER INFO

Paper history:
Received 31 October 2019
Received in revised form 12 July 2020
Accepted 21 July 2020

Keywords:
Fault Indicators
Inter-Turns Short-Circuit Fault
Magnetic Saturation Phenomenon
Permanent Magnet Synchronous Motor
Supply Voltage Unbalance

ABSTRACT

This paper proposes a new approach for discrimination between short circuit fault, magnetic saturation phenomenon and supply voltage unbalance in permanent magnet synchronous motor. This proposed approach is based on tracking the simultaneous position in the polar coordinates of the amplitude and phase angle of the voltage and current indicator FFT signals of the harmonics characterizing the three phenomena. The voltage indicator set using three supply voltages to check the status of the power source. In the same way, the current indicator defined using three line currents to discriminate between the short circuit fault and the magnetic saturation phenomenon. To highlight the effectiveness and the capability of this approach, a series of simulations are performed on signals obtained from a permanent magnet synchronous motor mathematical model. This model is based on a 2D-extension of the modified winding function approach.

***doi**: 10.5829/ije.2020.33.10a.15*

NOMENCLATURE

PMSM	: Permanent Magnet Synchronous Motor	UVU	: Under-Voltage Unbalance
ITSC	: Inter-Turns Short-Circuit	OVU	: Over-Voltage Unbalance
MSP	: Magnetic Saturation Phenomenon	FFT	: Fast Fourier Transform
SVU	: Supply Voltage Unbalance	ANN	: Artificial Neural Network

1. INTRODUCTION

The main industrial application areas, related to electric traction, processing, machining, material shaping, and recently electric propulsion are increasingly implementing the PMSM. These have a more compact structure, a high mass power, a higher dynamic response compared to conventional structures [1–4].

Although these motors are reliable, under certain electrical, thermal, mechanical, or environmental constraints, they are subjected to unexpected failures. Among these failures, approximately 30 % to 40 % fall into the category of faults related to stator windings [5–7]. For this reason, early detection of this type of fault is important because a simple ITSC can produce more severe damage. This detection will preserve the safety of goods and people and avoid the unscheduled shutdown of the production line and therefore increases the life of these motors and minimize financial losses.

Several diagnostic techniques have been developed to detect this type of fault, depending on the selected physical quantities [8–16]. Among these techniques, the spectral analysis of the stator current is a promising approach. Its main advantages are the easy installation of the sensors and the information richness of the current spectrum for the detection of almost all faults that can appear in the electrical machines. Indeed, several studies [8, 9] have shown that the ITSC fault is manifested by the increase of the third harmonic amplitude of the PMSM current spectrum.

*Corresponding Author Email: *zgherabi@yahoo.com* (Z. Gherabi)

Please cite this article as: Z. Gherabi, D. Toumi, N. Benouzza, A. Bendiabdellah, A Proposed Approach for Separation between Short Circuit Fault, Magnetic Saturation Phenomenon and Supply Unbalance in Permanent Magnet Synchronous Motor, International Journal of Engineering (IJE), IJE TRANSACTIONS A: Basics Vol. 33, No. 10, (October 2020) 1968-1977

Unfortunately, these signatures may also be due to the SVU and the MSP. The appearance of these three phenomena by the creation of the same harmonics makes it difficult to discriminate between them.

Several techniques have been recently deployed to discriminate between the ITSC faults from other secondary phenomena such as MSP and SVU [17–19].

Paper [17] presents a simple method for the diagnosis and the discrimination between the ITSC fault and the SVU. The authors of this paper have used the ANN approach, where they chose the percentage of the amplitude of the third harmonic compared to the fundamental one, as input quantities in different cases of the motor operation. Unfortunately, the method used does not deal with the distinction of the third harmonic due to the MSP. In [18], a structure using a feed-forward type ANN, based on the analysis of active and reactive power to discriminate between a stator ITSC fault and an SVU in induction motors, is proposed. The simulation and experimental results obtained show the advantage of the use of the phase shift between the two powers as a simple diagnostic technique compared to the analysis of the signals of the stator current. Despite the advantages presented by these two techniques, they have significant drawbacks, such as the absence of a systematic method to define the best topology of the neural network and the number of neurons in the hidden layer.

To overcome the various drawbacks mentioned above, this paper proposes a new approach of separation between the ITSC fault, the MSP, and the SVU in PMSM. This approach is based on tracking the simultaneous position in the polar coordinates of the amplitude and phase angle of the FFT signals of the voltage and the current indicator of the harmonic characterizing of three phenomena. The voltage indicator set using the three supply voltages to check the status of the power source. In the same way, the current indicator defined using three line currents to discriminate between the ITSC fault and the MSP. To highlight the effectiveness of this approach, a series of simulations will be carried out on a known and improved PMSM model. This model is based on the modified winding function approach, of which the permanent magnet is considered as a fictitious coil traversed by an excitation current $''\, i_f\, ''$.

2. INTER-TURNS SHORT-CIRCUIT

Electrical faults such as the degradation of the insulating material are internal faults that develop in the machine during its operation. They are caused by the increased temperature of the winding and stator yoke, natural thermal aging of the material, mechanical stresses at start-up, lack of eccentricity, contamination caused by hydrocarbons and moisture, and the fast switching of power electronics components [20, 21]. In most cases, this degradation causes an ITSC fault, which can generate a very large value of the current flowing in the short-circuit branch of the phase, which results in excessive heating of the conductors. In its operating conditions, a failure can be caused after a few minutes of its start. In fact, and as a rule, an increase of 10 °C in temperature compared to its nominal value, reduces the life of drivers twice as fast [22]. On the other hand, the ITSC fault also causes a risk of the permanent magnets irreversible demagnetization and the saturation of the magnetic circuit due to the high magnetic field.

3. MAGNETIC SATURARATION PHENOMENON

The saturation of ferromagnetic materials is a complex physical phenomenon that is difficult to model. In electrical machines, the MSP first appears in areas where the cross-section of the magnetic field lines is the weakest, usually in the stator and rotor teeth, but also in polar arcs for machines with salient poles; therefore, it is a local phenomenon. One of the leading causes of magnetic saturation is the increase of the current, which consequently causes an increase in the intensity of the magnetic field. Therefore, the magnetic induction is beyond the saturation bend. This increase in current is caused either by an increase in the supply voltage or by an ITSC fault [23–25]. To detect the MSP, a problem arises because many studies have proven that the MSP indicators manifest themselves in the same signatures as those of the ITSC fault [23–25].

4. UNBALANCE OF POWER SUPPLY VOLTAGE

A three-phase system is said to be unbalanced or asymmetrical if the three-phase voltages and currents do not have the same amplitude and/or are not out of phase with each other by 120 °. This phenomenon is one of the most common interferences in electrical systems. The unbalances are generally due to single-phase loads because, in this case, the currents absorbed on the three phases are of amplitude and/or different phases, resulting in an unbalance of the three voltages. Voltage unbalance can also be due to three-phase loads, when these are not symmetrical. Indeed, several cases of SVU have the same unbalance factor but have different effects on the loads. Among these unbalances, one can quote [26–28]:

- Under-voltage: decrease of a single-phase, two phases, or all three phases at the same time.
- Over-voltage: increase of a single-phase, two phases, or all three phases at the same time.

To diagnose this type of phenomenon by the stator current spectral analysis technique. Several studies [26–28] have shown that the SVU is manifested with the same signatures as those of the ITSC fault and the MSP.

The appearance of the effect of these three phenomena on harmonics of the same frequency makes the distinction between them a difficult task.

The purpose of our work is to develop a new approach to discriminate between these three phenomena. To do this, it is crucial to establish a mathematical model of the Permanent Magnet Synchronous Motor.

5. MODELING OF THE HEALTHY PMSM

The modeling approach is based on a semi-analytical method of Permanent Magnet Synchronous Motor. This modeling method is rather generic in the sense that it relies on a description of the electromagnetic couplings within the machine based on the geometric and constitutive topology of the machine. This approach has already been proven for the modeling of squirrel cage induction machines [29, 30]. It has also been adapted to the PMSM in [31, 32]. In this section, we will present more precisely the model where the taking into account of permanent magnets is carried out, to preserve the notion of magnetic coupling with the stator, by the use of the fictitious coils.

5. 1. Modeling of Permanent Magnets The modeling method is based on the exploitation of an Ampere model which makes it possible to identify a permanent magnet whose magnetization M to the distribution of fictitious currents (ampere currents) constituted by:

- A surface current density σ defined by:

$$\vec{\sigma} = \vec{M} \wedge \vec{ds} \tag{1}$$

- A surface volume current density ρ defined by:

$$\vec{\rho} = rot(\vec{M}) \tag{2}$$

In our case, the permanent magnet is characterized by a constant magnetization. Thanks to the Equations (1) and (2) of the ampere model, we can deduce that there exists a fictitious surface current density. In contrast, the volume current density is zero because of the constant magnetization. In conclusion, we can represent the permanent magnet of the rotor by fictitious coils traversed by currents, as illustrated in Figure 1, which will allow us to implement the magnetically coupled electrical circuit approach [32].

5. 2. Modeling of the Machine The PMSM equation system can be represented as fellow [21, 32]:

$$\begin{bmatrix} V_{sa} \\ V_{sb} \\ V_{sc} \end{bmatrix} = \begin{bmatrix} R_s & 0 & 0 \\ 0 & R_s & 0 \\ 0 & 0 & R_s \end{bmatrix} \begin{bmatrix} i_{sa} \\ i_{sb} \\ i_{sc} \end{bmatrix} + \frac{d}{dt} \begin{bmatrix} \phi_{ia} \\ \phi_{ib} \\ \phi_{ic} \end{bmatrix} + \frac{d}{dt} \begin{bmatrix} \phi_{ma} \\ \phi_{mb} \\ \phi_{mc} \end{bmatrix} \tag{3}$$

Such that:

$[V_{sabc}] = [V_{sa} \quad V_{sb} \quad V_{sc}]^T$: Stator voltages vectors;

$[i_{sabc}] = [i_{sa} \quad i_{sb} \quad i_{sc}]^T$: Stator currents vectors;

$[R] = R_s[I]$: Stator résistance matric;

$[\phi_i] = [\phi_{ia} \quad \phi_{ib} \quad \phi_{ic}]^T$: Stator fluxes vectors;

$[\phi_m] = [\phi_{ma} \quad \phi_{mb} \quad \phi_{mc}]^T$: Mutual fluxes vectors between stator and rotor.

where,

$$\begin{bmatrix} \phi_{ia} \\ \phi_{ib} \\ \phi_{ic} \end{bmatrix} = \begin{bmatrix} L_{aa} & M_{ab} & M_{ac} \\ M_{ba} & L_{bb} & M_{bc} \\ M_{ca} & M_{cb} & L_{cc} \end{bmatrix} \begin{bmatrix} i_{sa} \\ i_{sb} \\ i_{sc} \end{bmatrix} \tag{4}$$

The mutual fluxes between the stator and the rotor of a machine consisting of 4 poles (corresponding to 4 fictitious coils) are given by the following matrix system [21, 32]:

$$\begin{bmatrix} \phi_{ma} \\ \phi_{mb} \\ \phi_{mc} \end{bmatrix} = \begin{bmatrix} M_{saf1} & M_{saf2} & M_{saf3} & M_{saf4} \\ M_{sbf1} & M_{sbf2} & M_{sbf3} & M_{sbf4} \\ M_{scf1} & M_{scf2} & M_{scf3} & M_{scf4} \end{bmatrix} \begin{bmatrix} i_{f1} \\ i_{f2} \\ i_{f3} \\ i_{f4} \end{bmatrix} \tag{5}$$

The modeling of the rotating part of the machine is based on the use of Newton's second law. We will have:

$$J\frac{d}{dt}\Omega + F\Omega = C_{em} - C_r \tag{6}$$

By carrying out an energy balance, it is shown that the electromagnetic torque is equal to the partial derivative of the magnetic Co-energy with respect to the position of the rotor. Consequently, the torque is expressed by the following equation [21, 32]:

$$C_{em} = \frac{\partial W_{comag}}{\partial \theta_r} = [i_{sabc}]\frac{\partial [M_{ss}]}{\partial \theta_r}[i_{sabc}] + [i_{sabc}]\frac{\partial [M_f]}{\partial \theta_r}[i_f] \tag{7}$$

6. INDUCTANCES CALCULATION

It is essential to know that the accuracy of inductance calculation is the crucial point for a successful PMSM

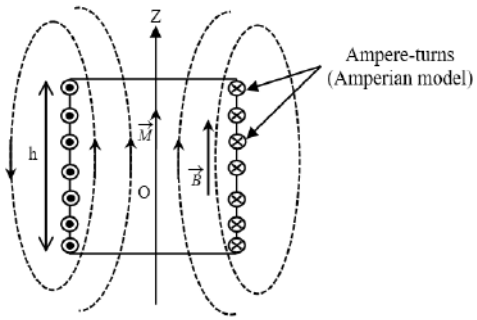

Figure 1. Illustration of the ampere model on a cylindrical permanent magnet [19]

simulation. All inductances are calculated by using the winding function approach [29–31], which is based on the following formula:

$$L_{A.B} = \mu_o rl \int_o^{2\pi} N_A(\varphi,\theta_r) n_B(\varphi,\theta_r) g^{-1}(\varphi,\theta_r) d\varphi \quad (8)$$

where, μ_o is the air permeability, r is the mean radius of the gap, l is the actual length of the machine, $N_A(\varphi,\theta_r)$ is the winding function of the winding *" a "*, $n_B(\varphi,\theta_r)$ is the distribution function of the winding *" b "* and $g^{-1}(\varphi,\theta_r)$ is the inverse of the gap function (see Figure 2).

6. 1. Inductances Calculation in the Healthy Case

To calculate the PMSM inductances in the healthy case, the air gap becomes uniform, so the inverse of the air gap $g^{-1}(\varphi, \theta_r)$ must be constant and equal to the inverse of the nominal air gap g_o, which therefore allows the Equation (8) to be rewritten as follows:

$$L_{ab} = \frac{\mu_o rl}{g_o} \int_o^{2\pi} N_a(\varphi,\theta_r) n_b(\varphi,\theta_r) d\varphi \quad (9)$$

6. 2. Inductances Calculation in the Presence of MSP

The MSP can be modeled by a variation in the function of the air gap [24, 25].

The inductances calculation is made in the same way as in the one of a uniform air gap, except the inverse of the air gap function is replaced by the following equation:

$$g(\varphi,\theta_r) = g_o\left[1 - k_{gsat}\, cos(\,2(p\varphi - \theta_f))\right] \quad (10)$$

$$g^{-1}(\varphi,\theta_r) = \frac{1}{g_o}\left[1 + k_{gsat}\, cos(\,2(p\varphi - \theta_f))\right] \quad (11)$$

where g_o is the average value of the gap length, φ is the position of the stator, θ_f is the position of the air gap flux, p is the pole pair number, *kgsat* is the saturation factor.

6. 3. Inductances Calculation in the Presence of ITSC Fault

The presence of the fault modifies the equation system of the PMSM, so when the Short circuit occurs between the turns of the phase *" a "*, the system of the Equation (3) becomes [21, 22]:

$$\begin{bmatrix} V_{sa} \\ V_{sb} \\ V_{sc} \\ V_{sd} \end{bmatrix} = \begin{bmatrix} R'_{sa} & 0 & 0 & 0 \\ 0 & R_{sb} & 0 & 0 \\ 0 & 0 & R_{sc} & 0 \\ 0 & 0 & 0 & R_{sd} \end{bmatrix} \begin{bmatrix} i_{sa} \\ i_{sb} \\ i_{sc} \\ i_{sd} \end{bmatrix} + \frac{d}{dt} \begin{bmatrix} \phi_{ia} \\ \phi_{ib} \\ \phi_{ic} \\ \phi_{id} \end{bmatrix} + \frac{d}{dt} \begin{bmatrix} \phi_{ma} \\ \phi_{mb} \\ \phi_{mc} \\ \phi_{md} \end{bmatrix} \quad (12)$$

The inductances calculation is made in the same way as in the healthy PMSM. During an ITSC, the winding function of the faulty phase *" a "* changes as well as its inductance, its resistance, and its mutual inductances with the other branches of the PMSM [21].

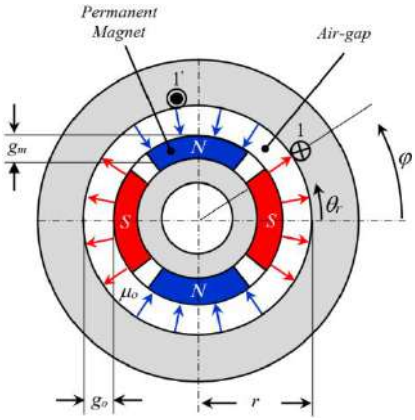

Figure 2. Cross-section of 4 poles surface-mounted PMSM with main dimensions

7. PROPOSED APPROACH

The approach proposed in this paper aims to precisely discriminate between the effects of ITSC failures to those due to secondary phenomena such as the SVU and the MSP. The flowchart (Figure 4) of the proposed method is briefly explained by the procedure steps below:

1st Step: Generation of the signature of the current and the voltage from the simulated model

2nd Step: Determination of the voltage indicator

- Extraction of the voltage indicator by the use of the following equation:

$$ind\_v(t) = |V_{sa} - V_{sb}| + |V_{sb} - V_{sc}| + |V_{sc} - V_{sa}| \quad (13)$$

- Calculation of the spectra (amplitude and phase angle) of this indicator by using the FFT.
- Determination from the spectra of the voltage indicator the magnitude and phase angle of the harmonic characteristics of the power unbalance that is (2fs).

$$\begin{cases} mag = |ind\_v(f)|_{f=2f_s} \\ \varphi = arg(ind\_v(f))_{f=2f_s} \end{cases} \quad (14)$$

With: $ind\_v(f) = FFT(ind\_v(t))$

- Plot of the position in polar coordinates as a function of the magnitude and the phase angle of the harmonic (2fs), as shown in Figure 3.

3rd Step: Determination of the current indicator

- Extraction of the current indicator by the use of the following equation:

$$ind\_i(t) = |I_{sa} - I_{sb}| + |I_{sb} - I_{sc}| + |I_{sc} - I_{sa}| \quad (15)$$

- Calculation of the spectra (amplitude and phase angle) of this indicator by using the FFT.
- Determination from the current indicator spectra of the amplitude and the phase angle of the ITSC fault and the MSP characteristic harmonic.
- Plot of the position in polar coordinates as a function of the amplitude and phase angle of the harmonic (2fs) as shown in Figure 3.

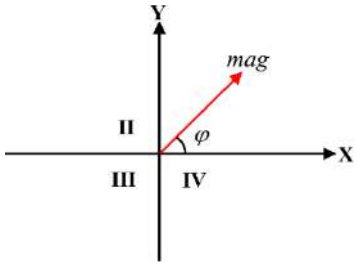

Figure 3. Representation in polar coordinates of the amplitude and phase of the second harmonic ($2f_s$)

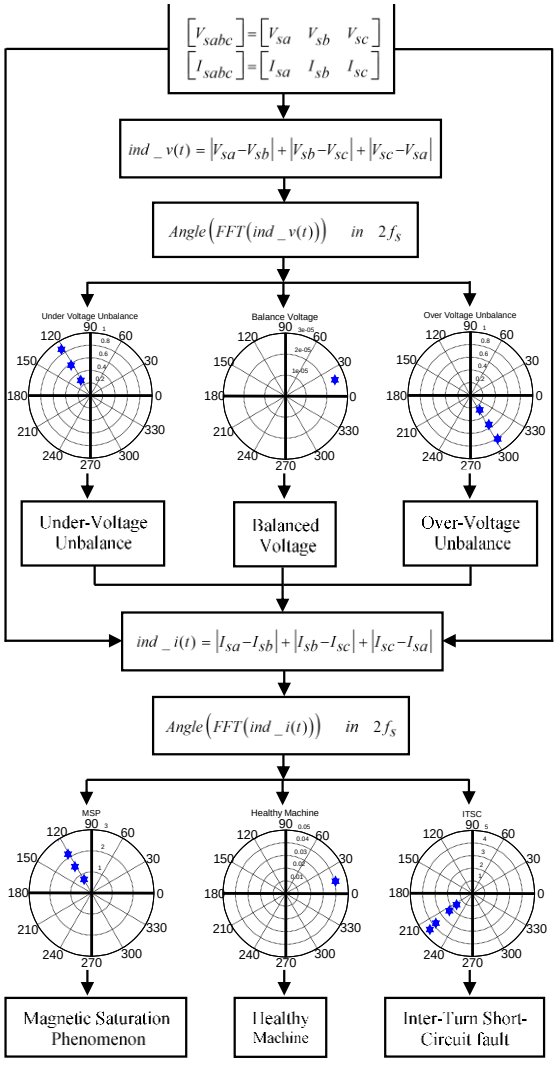

Figure 4. Flowchart of the proposed approach

4th Step: Exploitation of the voltage and current indicator in the separation between the ITSC fault and the secondary phenomena

First, the state of the power source is determined by tracking the position of the plot (in one of the four quadrants) of the voltage indicator.

- If the plot position is in the first quadrant, this implies the absence of power unbalances.
- The presence of under-voltage or over-voltage unbalances indicated by the position of the voltage indicator plot in the second and fourth quadrants, respectively.

Secondly, the ITSC fault is discriminated from the MSP fault by tracking the position of the plot (in one of the four quadrants) of the current indicator.

If the plot position is in the first quadrant, this implies the absence of the ITSC fault and the MSP.

- If the plot is positioned in the second quadrant, this implies the existence of the MSP. However, if it is placed in the third quadrant, this means the presence of the ITSC fault.

It is necessary to note that the SVU does not influence the current indicator. In the same way, the presence of the MSP or the ITSC faults does not influence the voltage indicator.

8. SIMULATION RESULTS

To demonstrate the effectiveness of the proposed approach, a mathematical model of the PMSM developed in Section 5 is used for the different modes of operation:

- Healthy PMSM powered by a balanced voltage;
- Healthy PMSM powered by unbalanced voltage;
- Motor operation in the presence of the ITSC fault;
- Motor operation in the presence of the MSP.

The simulation is performed on a PMSM with the following specifications: 3.6 kW, 4 poles, 36 stator slots, and 4 fictitious rotor coils. The arrangement of the stator and the rotor windings of this motor and its parameters are indicated in the appendix (Table A). The mathematical model obtained, and all the expressions of the inductances are implemented under the MATLAB environment. In all the simulations of this work, the machine at no-load is started, and a load torque is applied at the instant 0.5 s. The load torque corresponds to that of the nominal torque of 17.5 Nm.

8. 1. Analysis of the Current by the Classical Power Spectral Density Estimation

The spectral analysis of the obtained stator currents signature from the mathematical model of the simulated PMSM gives us the following results according to the established operating mode.

8. 1. 1. Healthy PMSM Powered by Balanced Voltage

Figure 5 illustrates the stator current spectrum in the healthy motor operation mode (without ITSC fault, without MSP, and with a balanced power source).

It can be noted that the spectrum contains in addition to the fundamental harmonic, a series of harmonics that

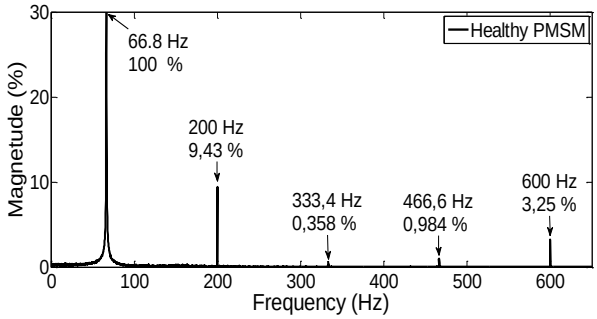

Figure 5. Healthy PMSM powered by a balanced voltage: Stator current spectrum

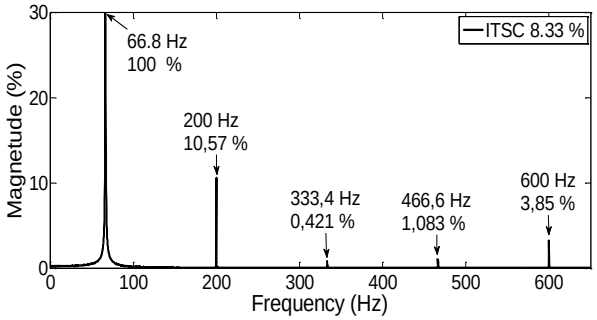

Figure 7. Motor operation in case of 8.33 % ITSC fault: Stator current spectrum

represents the space harmonics whose frequencies can easily be checked using the Equation (16). This spectrum will be considered as the reference one.

$$f_{sh} = [2.k + 1]f_s \quad (16)$$

8. 1. 2. Healthy PMSM Powered by Unbalanced Voltage Figure 6 gives the spectrum of the stator current for a healthy operation under an SVU.

From that figure, it can be noticed that there is an increase in the amplitude of the harmonic 200 Hz compared to the healthy case. This increase is due to the unbalance of the supply voltage.

8. 1. 3. Motor Operation in the Presence of the ITSC Fault Figure 7 illustrates the stator current spectrum for a balanced supply and with an ITSC fault of 8.33 % (that is six turns in short-circuit).

In reference to Figure 5, the stator current spectrum presented in Figure 7 depicts an increase in the magnitude of the characteristic harmonics of ITSC fault *($3f_s$)*, which is of the order of 200 Hz.

8. 1. 4. Motor Operation in the Presence of the MSP Figure 8 shows the stator current spectrum in the presence of the effect of the MSP (Kgsat = 0.06) with a balanced supply voltage.

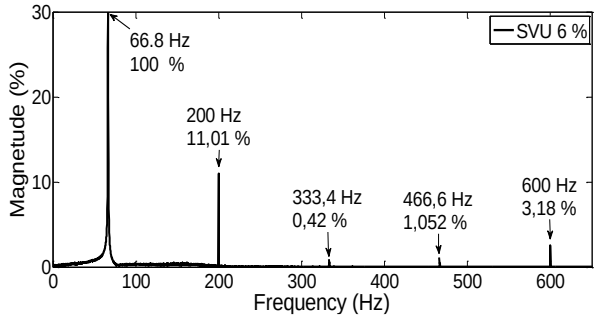

Figure 6. Healthy PMSM powered by an unbalanced voltage: Stator current spectrum

In the light of the results obtained, it is noticed that the frequencies due to the effect of the SVU are similar to the frequencies of the ITSC faults and that of the MSP.

According to these results, it is noted that the use of the technique of spectral analysis of the signature of the stator current is insufficient to discriminate between these three phenomena.

8. 2. Discrimination between ITSC Fault, MSP, and SVU Using the Proposed Approach The advantage of the proposed approach is the use not only of the amplitude but also the phase angle to discriminate between three phenomena (ITSC, MSP, and SVU).

The adaptation of the proposed algorithm is based on the amplitude and phase angle of the second harmonic obtained from the two indicators, voltage and current.

The results found are plotted in polar coordinates to simplify the interpretation and analysis of the different modes of operation.

8. 2. 1. Voltage Indicator Figure 9 shows the location of the harmonic reference *($2f_s$)* of the first indicator. This position represents the healthy operation of the motor (without faults) powered by a balanced voltage, and according to the figure, it is noted that the location of the plot is positioned in the first quadrant of the circle ($0 \leq \varphi \leq 90°$) in the polar coordinates graphical representation.

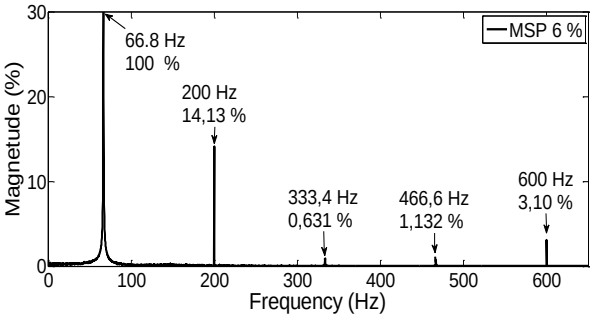

Figure 8. Motor operation in the presence of the MSP (Kgsat= 0.06): stator current spectrum

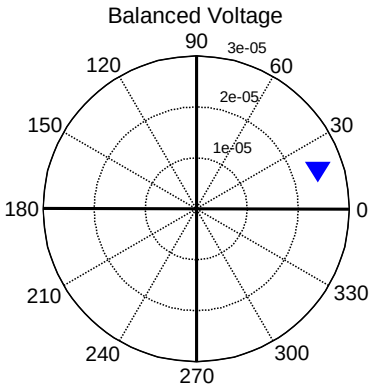

Figure 9. Position of the harmonic *(2f_s)* plot of the first indicator for the healthy operation a balanced voltage

On the one hand, if the healthy machine is powered by an unbalanced voltage source (Under-Voltage Unbalance UVU), this position occurs in the second quadrant of the circle around 120° (see Figure 10(a)). On the other hand, if the healthy machine is powered by an unbalanced voltage source (Over-Voltage Unbalance OVU), the position of the plot moves to the fourth quadrant of the circle around 300° (see Figure 10(b)). In the case of increasing the degree of the SVU (UVU), the plot position remains the same (in the same quadrant) but causes the displacement of the plot position upwards to the left from the center of the circle. In the same way, the increase of the SVU (OVU) degree does not modify the position of the plot, but only causes the displacement of the plot position down to the right.

8. 2. 2. Current indicator The location of the harmonic reference *(2f_s)* of the second indicator is illustrated in Figure 11. This position represents the healthy operation of the motor under a balanced power supply; this figure indicates that the location of the plot is at the first quadrant of the circle ($0 \leq \varphi \leq 90°$) in the graphical representation in polar coordinates.

The MSP is manifested by the plot position in the second quadrant of the circle around 120°, as shown in Figure 12. Moreover, increasing the saturation factor does not change the plot position, but causes the plot position to move upwards to the left from the center of the circle (Figure 12). In the case of an ITSC fault, the

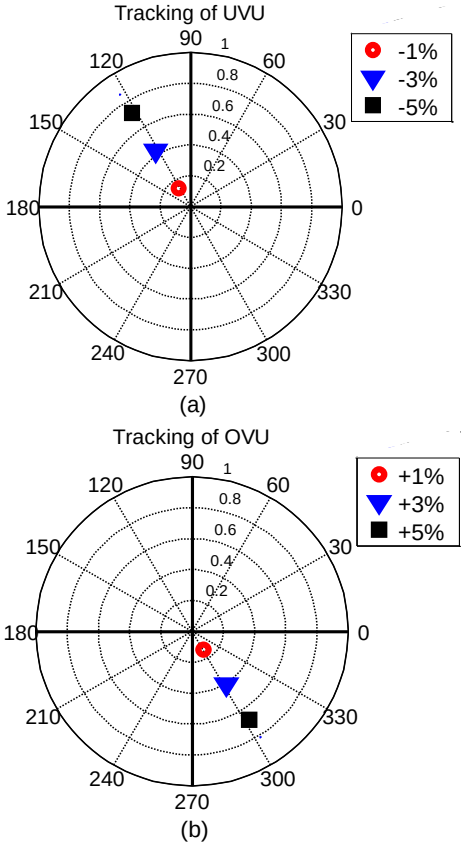

Figure 10. Position of the harmonic *(2f_s)* plot of the first indicator as a function of the severity of the SVU: (a) Under-voltage unbalance, (b) Over-voltage unbalance

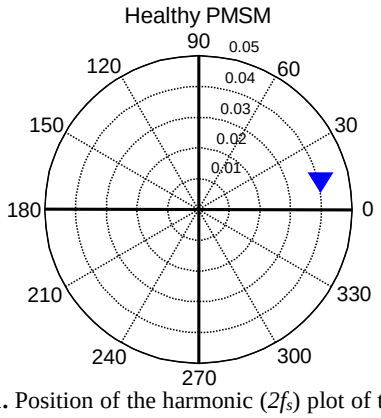

Figure 11. Position of the harmonic (*2f_s*) plot of the second indicator for the healthy PMSM under a balanced voltage

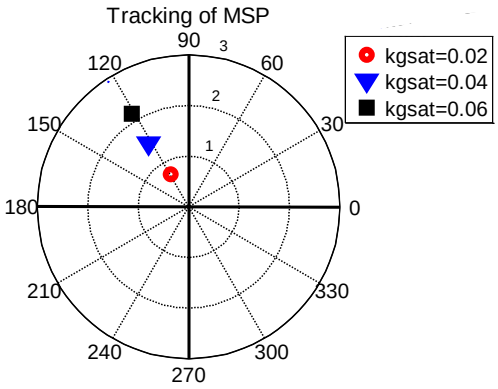

Figure 12. Position of the harmonic (*2f_s*) plot of the second indicator as a function of the severity of the MSP

plot is positioned in the third quadrant of the circle around 210° (Figure 13). Increasing the severity of the ITSC fault causes the position to move down to the left from the center of the circle in the same quadrant.

The simultaneous presence of the ITSC fault and the MSP is manifested by an intermediate position relative to the two phenomena (between the second and third quadrants), as shown in Figure 14. This position can vary between the second and third quadrant depending on the predominance of the phenomenon:

- In the second quadrant, if the MSP is predominant (see Figure 14 in blue).
- In the third quadrant, if the ITSC fault is predominant (see Figure 14 in black).

As indicated at the end of section 7, the presence of the SVU does not influence the current indicator, and the presence of the MSP or the ITSC fault does not influence the voltage indicator.

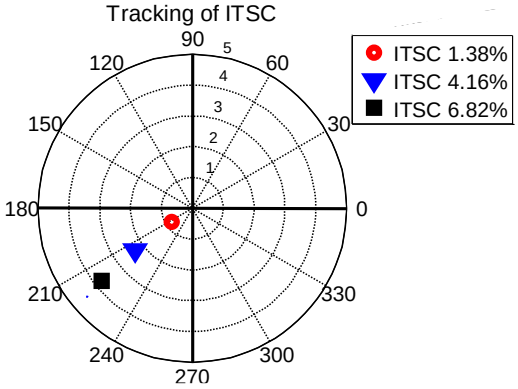

Figure 13. Position of the harmonic ($2f_s$) plot of the second indicator as a function of the severity of the ITSC Fault

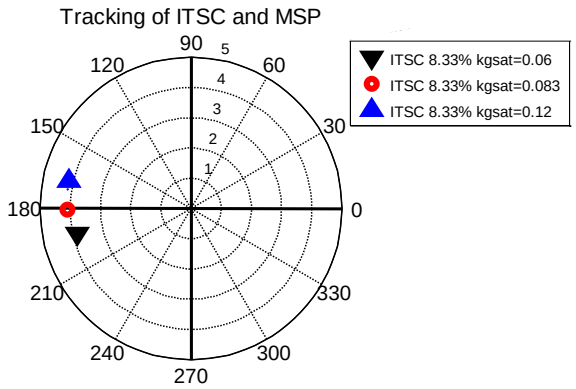

Figure 14. Position of the harmonic ($2f_s$) plot of the second indicator as a function of the severity of the ITSC Fault and the MSP

Therefore, to diagnose the ITSC fault in the presence of the SVU, it is sufficient to track the current and voltage indicator plot position simultaneously. Our study shows that if the PMSM experiences an ITSC fault and powered by an unbalanced voltage source (UVU), the voltage indicator plot position takes place in the second quadrant of the circle around 120° (see Figure 10(a)) and the current indicator plot position takes place in the third quadrant of the circle around 210° (Figure 13).

On the other hand, if the PMSM is powered by an unbalanced voltage source (OVU), the position of the voltage indicator plot moves to the fourth quadrant of the circle around 300° (see Figure 10(b)). Otherwise, the position of the current indicator plot always remains in the third quadrant (see Figure 13).

The different positions of the voltage and current indicators, depending on the state of the machine and the power source, are summarized in Table 1.

TABLE 1. Position of voltage and current indicators for different cases of operation

Plot Position	Healthy PMSM	SVU		ITSC	MSP	SVU and ITSC	
		UVU	OVU			UVU	OVU
Voltage Indicator	Q1	Q2	Q4	------	------	Q2	Q4
Current Indicator	Q1	------	------	Q3	Q2	Q3	Q3

9. CONCLUSION

In this paper, a new approach is proposed to discriminate between the inter-turns short-circuit fault, the magnetic saturation phenomenon, and the supply voltage unbalances in permanent magnets synchronous motors.

This approach is based on the tracking of the simultaneous position of the polar coordinates of the amplitude and phase angle of the signals of the voltage and current indicators of the harmonic characteristics of the three phenomena. These indicators are based on the supply voltages (Vsa, Vsb, and Vsc) and the stator currents (Isa, Isb, and Isc) that are available in any drive system and do not require additional hardware.

The simulation results prove the effectiveness and reliability of the proposed approach. For this purpose, the method using polar graphical representation shows better readability in terms of the spectrum and speed of decision making concerning the distinction between these three phenomena (ITSC, MSP, and the SVU).

10. REFERENCES

1. M'hamed, L., Zakaria, G. and Khireddine, D. "A Robust Sensorless Control of PMSM Based on Sliding Mode Observer and Model Reference Adaptive System." ***International Journal of Power Electronics and Drive System (IJPEDS)***, Vol. 8, No. 3, (2017), 1016–1025. https://doi.org/10.11591/ijpeds.v8i3.pp1016-1025
2. Faiz, J., and Hassan-Zadeh, M. R. "Impacts of eccentricity fault on permanent magnet generators for distributed generation." In Proceedings - 2017 International Conference on Optimization of Electrical and Electronic Equipment, OPTIM 2017 and 2017 Intl Aegean Conference on Electrical Machines and Power Electronics, ACEMP 2017, (2017), 434–441. https://doi.org/10.1109/OPTIM.2017.7975008
3. Arehpanahi, M., and Kheiry, E. "A New Optimization of Segmented Interior Permanent Magnet Synchronous Motor Based on Increasing Flux Weakening Range and Output Torque (Research Note)." ***International Journal of Engineering - Transactions C: Aspects***, Vol. 33, No. 6, (2020), 1122–1127. https://doi.org/10.5829/ije.2020.33.06c.09
4. Arish, N., and Teymoori, V. "Development of Linear Vernier Hybrid Permanent Magnet Machine for Wave Energy Converter." ***International Journal of Engineering - Transactions B: Applications***, Vol. 33, No. 5, (2020), 805–813. https://doi.org/10.5829/IJE. 2020.33.05B.12
5. Faiz, J., and Exiri, S. A. H. "Short-circuit fault diagnosis in permanent magnet synchronous motors- an overview." In ACEMP 2015: Aegean Conference on Electrical Machines and Power Electronics, OPTIM 2015: Optimization of Electrical and Electronic Equipment and ELECTROMOTION 2015: International Symposium on Advanced Electromechanical Motion Systems, (2015), 18–27. https://doi.org/10.1109/OPTIM.2015.7427038
6. Zafarani, M., Bostanci, E., Qi, Y., Goktas, T., and Akin, B. "Interturn short-circuit faults in permanent magnet synchronous machines: An extended review and comprehensive analysis." ***IEEE Journal of Emerging and Selected Topics in Power Electronics***. Vol. 6, No. 4, (2018), 2173-2191. https://doi.org/10.1109/JESTPE.2018.2811538
7. Qi, Y., Bostanci, E., Gurusamy, V., and Akin, B. "A Comprehensive Analysis of Short-Circuit Current Behavior in PMSM Interturn Short-Circuit Faults." ***IEEE Transactions on Power Electronics***, Vol. 33, No. 12, (2018), 10784–10793. https://doi.org/10.1109/tpel.2018.2809668
8. Haddad, R. Z., and Strangas, E. G. "On the Accuracy of Fault Detection and Separation in Permanent Magnet Synchronous Machines Using MCSA/MVSA and LDA." ***IEEE Transactions on Energy Conversion***. Vol. 31, No. 3, (2016), 924-934. https://doi.org/10.1109/TEC.2016.2558183
9. Çira, F., Arkan, M., and Gümüş, B. "A new approach to detect stator fault in permanent magnet synchronous motors." In Proceedings - SDEMPED 2015: IEEE 10th International Symposium on Diagnostics for Electrical Machines, Power Electronics and Drives, (2015), 316–321. https://doi.org/10.1109/DEMPED.2015.7303708
10. Li, H., Hang, J., Fang, J., Zhang, P., Ding, S., and Wang, Q. "Inter-turn fault diagnosis of permanent magnet synchronous machine based on variational mode decomposition." In Proceedings of the 13th IEEE Conference on Industrial Electronics and Applications, ICIEA 2018, (2018), 2422–2425. https://doi.org/10.1109/ICIEA.2018.8398115
11. Hang, J., Zhang, J., Cheng, M., and Huang, J. "Online Interturn Fault Diagnosis of Permanent Magnet Synchronous Machine Using Zero-Sequence Components." ***IEEE Transactions on Power Electronics***, Vol. 30, No. 12, (2015), 6731–6741. https://doi.org/10.1109/TPEL.2015.2388493
12. Jeong, H., Lee, H., and Kim, S. W. "Classification and Detection of Demagnetization and Inter-Turn Short Circuit Faults in IPMSMs by Using Convolutional Neural Networks." In 2018 IEEE Energy Conversion Congress and Exposition, ECCE 2018, (2018), 3249–3254. https://doi.org/10.1109/ECCE.2018.8558191
13. Li, X., Han, L., Xu, H., Yang, Y., and Xiao, H. "Rolling Bearing Fault Analysis by Interpolating Windowed DFT Algorithm." ***International Journal of Engineering - Transactions A: Basics***, Vol. 32, No. 1, (2018), 121–126. https://doi.org/10.5829/ije.2019.32.01a.16
14. Heidari, M. "Fault Detection of Bearings Using a Rule-based Classifier Ensemble and Genetic Algorithm." ***International Journal of Engineering - Transactions A: Basics***, Vol. 30, No. 4, (2017), 604–609. https://doi.org/10.5829/idosi.ije.2017.30.04a.20
15. Zaza, G., Hammou, A. D., Benchatti, A., and Saiah, H. "Fault Detection Method on a Compressor Rotor Using the Phase Variation of the Vibration Signal." ***International Journal of Engineering - Transactions B: Applications***, Vol. 30, No. 8, (2017), 1176–1181. https://doi.org/10.5829/ije.2017.30.08b.09
16. Eftekhari, M. "The Effect of Damping and Stiffness of Bearing on the Natural Frequencies of Rotor-bearing System." ***International Journal of Engineering - Transactions C: Aspects***, Vol. 30, No. 3, (2017), 448–455. https://doi.org/10.5829/idosi.ije.2017.30.03c.15
17. Refaat, S. S., Abu-Rub, H., Saad, M. S., Aboul-Zahab, E. M., and Iqbal, A. "Discrimination of stator winding turn fault and unbalanced supply voltage in permanent magnet synchronous motor using ANN." In International Conference on Power Engineering, Energy and Electrical Drives, (2013), 858–863. https://doi.org/10.1109/PowerEng.2013.6635722
18. Aberkane, M., Benouzza, N., Bendiabdellah, A., and Boudinar, A. H. "Discrimination between supply unbalance and stator short-circuit of an induction motor using neural network." ***International Review of Automatic Control***, Vol. 10, No. 5, (2017), 451–460. https://doi.org/10.15866/ireaco.v10i5.11912
19. Harir, M., Bendiabdellah, A., and Boudinar, A. H. "A proposed technique for discrimination between saturation phenomenon and short-circuit faults in induction motor." ***International Review on Modelling and Simulations***, Vol. 11, No. 5, (2018), 333–342. https://doi.org/10.15866/iremos.v11i5.15465
20. Zhang, C., Luo, L., He, J., and Liu, N. "Analysis of the short-circuit fault characteristics of permanent magnet synchronous machines." In Proceedings - 2015 Chinese Automation Congress, CAC 2015, (2015) 1913–1917. https://doi.org/10.1109/CAC.2015.7382816
21. Gherabi, Z., Toumi, D., Benouzza, N., and Henini, N. "Modeling and Diagnosis of Stator Winding Faults in PMSM using Motor Current Signature Analysis." In Proceedings 2019 International Aegean Conference on Electrical Machines and Power Electronics, ACEMP 2019 and 2019 International Conference on Optimization of Electrical and Electronic Equipment, OPTIM 2019, (2019), 227–232. https://doi.org/10.1109/ACEMP-OPTIM44294.2019.9007162
22. Lai, C., Aiswarya, B., Vicki, B., Lakshmi Varaha Iyer, K., and Kar, N. C. "Analysis of stator winding inter-turn short-circuit fault in interior and surface mounted permanent magnet traction machines." In 2014 IEEE Transportation Electrification Conference and Expo: Components, Systems, and Power Electronics - From Technology to Business and Public Policy, ITEC 2014, (2014), 1-6. https://doi.org/10.1109/itec.2014.6861775
23. Liang, W., Fei, W., and Luk, P. C. K. "An Improved Sideband Current Harmonic Model of Interior PMSM Drive by Considering Magnetic Saturation and Cross-Coupling Effects." ***IEEE Transactions on Industrial Electronics***, Vol. 63, No. 7, (2016), 4097–4104. https://doi.org/10.1109/TIE.2016.2540585

24. Nandi, S. “An Extended Model of Induction Machines with Saturation Suitable for Fault Analysis.” In Conference Record - IAS Annual Meeting (IEEE Industry Applications Society- Vol. 3), (2003), 1861–1868. https://doi.org/10.1109/ias.2003.1257822
25. Gherabi, Z., Djilali, T., Benouzza, N., and Denai, M. “Stator Inter-Turn Short-Circuit and Eccentricity Faults Detection in Permanent Magnet Synchronous Motors Using Line Current Spectrum Analysis.” ***International Review of Electrical Engineering***, Vol. 15, No. 1, (2020), 54–68. https://doi.org/10.15866/iree.v15i1.17638
26. Refaat, S. S., Abu-Rub, H., Mohamed, A., and Trabelsi, M. “Investigation into the effect of unbalanced supply voltage on detection of stator winding turn fault in PMSM.” In Proceedings of the IEEE International Conference on Industrial Technology, (2017), 312–317. https://doi.org/10.1109/ICIT.2017.7913102
27. Lee, C. Y. “Effects of unbalanced voltage on the operation performance of a three-phase induction motor.” ***IEEE Transactions on Energy Conversion***, Vol. 14, No. 2, (1999), 202–208. https://doi.org/10.1109/60.766984
28. Sahu, S., Dash, R. N., Panigrahi, C. K., and Subudhi, B. “Unbalanced voltage effects and its analysis on an induction motor.” In IEEE International Conference on Innovative Mechanisms for Industry Applications, ICIMIA 2017 - Proceedings, (2017), 263–268. https://doi.org/10.1109/ICIMIA.2017.7975616
29. Nandi, S., Toliyat, H. A., and Parlos, A. G. “Performance analysis of a single phase induction motor under eccentric conditions.” In Conference Record - IAS Annual Meeting (IEEE Industry Applications Society) (Vol. 1), (1997), 174–181. https://doi.org/10.1109/ias.1997.643024
30. Joksimović, G. M., Durović, M. D., Penman, J., and Arthur, N. “Dynamic simulation of dynamic eccentricity in induction machines - winding function approach.” ***IEEE Transactions on Energy Conversion***, Vol. 15, No. 2, (2000), 143–148. https://doi.org/10.1109/60.866991
31. Liang, Z., Liang, D., and Jia, S. “Inductance Calculation for the Symmetrical Non-Salient Dual Three-Phase PMSM Based on Winding Function Approach.” In ICEMS 2018 - 2018 21st International Conference on Electrical Machines and Systems, (2018), 269–274. https://doi.org/10.23919/ICEMS.2018.8549109
32. Gherabi, Z., Benouzza, N., Toumi, D., and Bendiabdellah, A. “Eccentricity Fault diagnosis in PMSM using Motor Current Signature Analysis.” In Proceedings 2019 International Aegean Conference on Electrical Machines and Power Electronics, ACEMP 2019 and 2019 International Conference on Optimization of Electrical and Electronic Equipment, OPTIM 2019, (2019), 205–210. https://doi.org/10.1109/ACEMP-OPTIM44294.2019.9007164

11. APPENDIX

TABLE A. PMSM parameters

Symbol	Description	Values	Units
V_n	Rated voltage	150	*V*
f_s	Rated frequency	66.7	*Hz*
I_n	Rated current	15.1	*A*
C_n	Rated torque	17.5	*Nm*
$\square_n$	Rated speed	2000	*rpm*
R_s	Stator resistance	0.295	Ω
L_s	Synchronous inductance	3.5	*mH*
J	Moment of inertia	3.10^{-4}	$Kg.m^2$
F	Viscous rubbing	0.017	*Nm/rad/s*
P	Number of pole pairs	2	-----
g_o	Nominal air gap	12	*mm*
r	Stator radius	64	*mm*
rr	Rotor radius	52	*mm*
l	Length of the machine	250	*mm*
N_s	Number of turn/coils	6	-----
h	Thickness of magnets	10	*mm*

Persian Abstract

چکیده

این مقاله یک رویکرد جدید از تبعیض بین گسل اتصال کوتاه، پدیده اشباع مغناطیسی (MSP) و عدم تعادل ولتاژ تأمین (SVU) در موتورهای همزمان آهن‌ربا (PMSMs) ارائه شده است. این رویکرد در پیگیری موقعیت همزمان در مختصات قطبی دامنه و زاویه فاز ولتاژ و سیگنال‌های FFT نشانگر جریان از همسازهای توصیف شده از سه پدیده است. نشانگر ولتاژ با استفاده از سه ولتاژ منبع تغذیه برای بررسی وضعیت منبع تغذیه تنظیم می‌شود. به همین روش، نشانگر جریان با استفاده از سه جریان خط برای تفکیک بین گسل ITSC و MSP تعریف می‌شود. برای برجسته کردن اثربخشی این رویکرد؛ یک سری شبیه‌سازی بر روی سیگنال‌های به دست آمده از یک مدل ریاضی از PMSM انجام می‌شود. این مدل در یک پسوند 2D از رویکرد عملکرد سیم پیچ اصلاح شده است.

IJE TRANSACTIONS A: Basics Vol. 33, No. 10, (October 2020) 1978-1985

International Journal of Engineering

Journal Homepage: www.ije.ir

Control of a Single Stage Boost Inverter Based on Dynamic Sliding Mode Control with Power Decoupling

F. Mohammadhassani, H. Gholizade Narm*

Faculty of Electrical Engineering and Robotics, Shahrood University of Technology, Shahrood, Iran

PAPER INFO

Paper history:
Received 03 May 2020
Received in revised form 18 June 2020
Accepted 04 August 2020

Keywords:
Boost Inverter
Harmonic Rejection
Power Decoupling
Dynamical Sliding Mode

ABSTRACT

In this paper, the problem of control a single-stage boost inverter is studied. The goal is to achieve a system with robustness against variations in parameters, fast response, high-quality AC voltage, and smooth DC current. To this end, a new type of dynamic sliding mode control is proposed to apply to various scenarios such as parameter uncertainties and DC input voltages. In comparison with the conventional double-loop controllers, the proposed sliding mode controller utilizes only a single loop in its design, while having attractive features such as robustness against parametric uncertainties. In addition, a methodology is proposed for the decoupling of double-frequency power ripples based on proportional-resonant (PR) control to remove the low-frequency current ripples without using additional power components. Compared to conventional controllers, the proposed controller provides several features such as fast and chattering-free response, robustness against uncertainty in the parameters, smooth control, proper steady-state error, decoupled power and good total harmonic distortion (THD) over the output voltage and input currents, and simple implementation. In a fair comparison with classical sliding mode control, simulation results demonstrate more satisfactory performance and effectiveness of the proposed control method.

***doi**: 10.5829/ije.2020.33.10a.16*

1. INTRODUCTION

As a critical component in energy transfer, single-phase Voltage Source Inverters (VSIs) are widely employed in energy storage systems, distributed generation systems, and renewable energy applications such as photovoltaic (PV) systems [1]. Due to inherent variability in renewable energy resources such as solar irradiation, VSIs usually require to provide both boost operation and DC-AC conversion. The main advantage of boost DC-AC inverters is achieving higher output voltage compared to input in a single stage [2]. This converter like other systems has to track a reference signal. Therefore, requires fast response along with robustness under load and variations in input voltage. These conditions increase the control complexity of the boost inverter. Since the boost inverter is composed from two boost DC/DC converters, controlling an AC boost inverter is even more complex. This is motivated an intense increase in the research in the area of optimal control strategies and resulted in a variety of solutions. To control of the single stage boost inverter, several methods are used such as: Combined fuzzy and adaptive control proposed in literature [3] and A Rule-Based two loop controller analyzed in literature [4] to reduce the second order harmonic of current. Two-loop sliding mode control was suggested [5] and a classic sliding mode controller was proposed [6] to control the boost inverter. To overcome the challenges with the sliding-mode controllers, a double-loop control scheme was presented by Özdemir and Erdem [7]. A single loop current control method was used [8] to reduce the harmonic content in the current. A voltage mode control method has been proposed [9].

On the other hand, on the AC side of the single-phase converter, the time-varying instantaneous power flows with the second-order harmonic. If this second-harmonic ripple power is not filtered correctly, it will propagate to

*Corresponding Author Institutional Email: *gholizade@shahroodut.ac.ir* (H. Gholizade Narm)

Please cite this article as: F. Mohammadhassani, H. Gholizade Narm, Control of a Single Stage Boost Inverter Based on Dynamic Sliding Mode Control with Power Decoupling, International Journal of Engineering (IJE), IJE TRANSACTIONS A: Basics Vol. 33, No. 10, (October 2020)... 1978-1985

DC side, which further lowers the efficiency and possibly imposes unintentional stress on the DC source. The undesirable ripples degrade system performance. For instance, they may reduce the maximum power point tracking (MPPT) for the PV panels, leading to light flicker in LED lighting applications that cause overheating of the batteries and decreasing the lifetime of the fuel cell. Second-order power mismatch between DC and AC sides must be handled through a mechanism generally known as "power decoupling" [10]. In this regard, the filtering methods are divided into two main categories: passive methods and active methods. Both methods are based on additional components, which in turn, increase the system complexity and cost while adding losses to the system that reduce the overall inverter efficiency [10-12]. Due to nonlinearities in the converter, harmonic generation is unavoidable. These harmonics are the major output quality issues. In other words, it is crucial to control the harmonics generated by these inverters to limit their adverse effects on the quality of the output voltage [10]. Therefore, to avoid creating harmonics, the controller must provide a high-quality sinusoidal output with minimal distortions [13, 14].

In this paper, instead of the traditional approach of controlling boost inverter, a novel control method is proposed to achieve the mentioned objectives. In this regard, a new dynamical sliding mode with delay compensation is initially presented to track the appropriate reference. Then, an innovative solution with no additional power electronics components is proposed to ensure the decoupling of the double frequency pulsating power. Finally, selected voltage harmonics are compensated using additional PR controllers to perform at particular harmonic frequencies to either reduce or eliminate them. The paper is organized as follows. Section II describes the boost inverter model. The proposed decoupling and harmonic rejection solutions and control are discussed in Section III, while simulation validation is presented in Section IV. Finally, Section V highlights the main paper contributions and concludes the study.

2. MODEL DESCRIPTION

The boost DC–AC inverter, also known as the boost inverter, is specifically interesting due to its capability in generating AC output voltages higher than the input DC voltage in just a single stage. The circuit implementation of the proposed boost inverter is illustrated in Figure 1 [15].

In Figure 1, S_1, S_2, S_3, and S_4 are power switches, L_1, L_2, C_1, C_2, and R_{out} are individual inductors and capacitors in boost converters, and the equivalent load in the output terminal, respectively. Moreover, $v_1, v_2, v_{in}, and\ V_{out}$ are individual output voltages

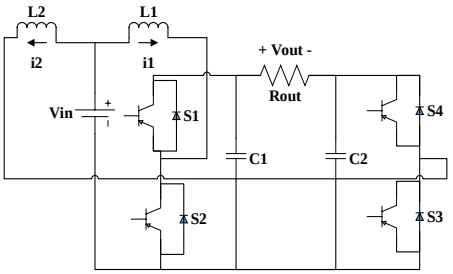

Figure 1. Circuit framework of single-stage boost inverter

for the two boost converters, and the input and output voltages for the boost inverter, respectively. As shown in Figure 1, the proposed inverter is composed of two conventional DC-DC converters, along with a connected load. In this topology, converters are driven by two 180° phase-shifted DC-biased sinusoidal references, while each generates a DC-biased Sine wave on the output, namely v_1 and v_2, respectively. In other words, each source generates a unipolar voltage to maximize the voltage excursion across the load.

The converter output voltages (v_1 and v_2), and the inverter output voltage (V_{out}) can be represented by

$$\begin{aligned} v_1 &= V_{dc} + V_m \sin\theta \\ v_2 &= V_{dc} + V_m \sin(\theta + \pi) \\ V_{out} &= v_1 - v_2 = (V_m + V_m)\sin\theta = 2V_m \sin\theta \end{aligned} \quad (1)$$

where V_{dc} is the DC offset voltage of each boost converter. To model the system dynamics, it is assumed that all the circuit components are ideal and that the boost inverter operates in a continuous conduction mode (CCM). The duty cycle D is defined as the time scale when switch S_2 is ON, while the duty cycle D' is the time scale when the switch S_4 is ON. According to this definition, the switch S_1 is ON during the time-scale $1 - D$ and the switch S_3 in $1 - D'$. When S_2 and S_4 are ON and S_1 and S_3 are OFF, the input power source v_{in} charges the inductors L_1 and L_2, and the capacitors C_1 and C_2 discharge to the output terminals v_1 and v_2, respectively. On the contrary, when S_1 and S_3 are ON and S_2 and S_4 are OFF, inductors L_1 and L_2 discharge to the capacitors and the output terminals. Consequently, by employing the averaging concept and the Kirchhoff's laws, the nonlinear state-space model for the boost inverter circuit with the stated variables can be obtained [15].

$$\begin{aligned} &L_1 \frac{di_1}{dt} = V_{in} - Dv_1 \; C_1 \frac{dv_1}{dt} = Di_1 - \frac{v_1 - v_2}{R_{out}} \; L_2 \frac{di_2}{dt} = \\ &V_{in} - D'v_2 \; C_2 \frac{dv_2}{dt} = D'i_2 + \frac{v_1 - v_2}{R_{out}} \; V_{out} = v_1 - v_2 \end{aligned} \quad (2)$$

where i_1 and i_2 are the currents for the inductors L_1 and L_2, while v_1 and v_2 are capacitor voltages. As stated earlier, v_{in}, V_{out}, D, and D' are the input DC voltage, output AC voltage, and the switching duty cycles,

respectively. The objective is to design switching pattern for D and D', such that:

$$\begin{matrix} V_{out} \to v_{ref} = Vsin(\omega t) \\ i_1 + i_2 \to I_{DC} \end{matrix} \quad (3)$$

with proper convergence speed and robustness under load, along with input-voltage variation and no power coupling and harmonics problems. Parameters V and ω are the amplitude and the frequency of the desired AC voltage, respectively.

3. PROPOSED CONTROL

In this study, two types of compensators are implemented, namely dynamic sliding-mode control for the voltage tracking and PR compensators for power decoupling and harmonic rejection. In the proposed strategy, control inputs (D and D') are generated according to the converter currents and voltages. The closed-loop system (based on the proposed controller) is comprised of two parts: the differential inverter and the control blocks. The control blocks contain a sliding-mode controller and two PR compensators. The control system is employed to track the following control objectives for the differential converter: 1) output voltage control, 2) power decoupling and 3) harmonic rejection.

3. 1. Reference Tracking The initial objective for the control problem is to design suitable control inputs (D and D′) to enforce the system output to track a sinusoidal reference v_{oref}, with the possible occurrence of uncertainties in the system. In other words, the proposed controller for the single-stage boost inverter aims to force the system states v_1 and v_2 to track reference output voltage for their respective converter (v_{1ref} and v_{2ref}). The two reference voltages are determined from the v_{oref}, DC input voltage, and nominal value of the states. Therefore, to control the single-stage boost inverter more effectively, a new dynamic sliding-mode control is proposed to minimize the error and adjust the duty cycle for the switches to ensure the system's stability. Moreover, it provides attractive features such as fast dynamic response, insensitivity to variations in plant parameters and external disturbance, and elimination of the chattering problem in practical senses. The performance of the proposed system is compared with the conventional sliding mode controller under different operating conditions. Therefore, in the following subsections, first, the Classical Sliding Mode Control (CSMC) and then the proposed Dynamic Sliding Mode Control (DSMC) is introduced.

Consider a continuous-time nonlinear model for the boost inverter described by the state-space representation as Equation (2). By defining $x = [x_1\ x_2\ x_3\ x_4\ ]^T = [i_1\ v_1\ i_2\ v_2\ ]^T$ is the state vector while $y = [v_1\ , v_2]$ and $u = [u_1\ ;\ u_2] = [D\ ; D']^T$ are the output and input vectors, respectively. In CSMC, the control objective is to drive the output voltages to the desired values. In CSMC, the sliding surface can be chosen as [8]:

$$s_i = \sum_{k=0}^{r_i-1} \lambda_k^{(i)} \left(y_i - y_i^d\right)^k, for\ i = 1, \dots, r_i - 1 \quad (4)$$

where y_i^d is the desired output, r_i is the relative error e_i, and $e_i^{(k)}$ is the k^{th} order derivative of the error. The control objective can be achieved by pushing the sliding surfaces (4) to zero.

In this paper, to control of boost inverter, a dynamic sliding mode control (DSMC) is proposed to perform the current-mode control. In this scheme, the controller focuses on the generating of AC voltage on the load rather than on the capacitors. The sliding surfaces are defined by:

$$\begin{matrix} s_1 = i_1 + k_{p1}(v_1 - v_{ref1}) + k_{i1} \int_0^t (v_1 - v_{ref1}) d\tau \\ s_2 = i_2 + k_{p2}(v_2 - v_{ref2}) + k_{i2} \int_0^t (v_2 - v_{ref2}) d\tau \end{matrix} \quad (5)$$

Theorem 1: The control law (6) pushes the sliding surfaces (5) to zero:

$$\begin{matrix} D = h_1^{-1}\ (x)\ (D_{eq} + K_1\ sign(s_1)) \\ D' = h_2^{-1}(x)\ (D'_{eq} + K_2\ sign(s_2)) \end{matrix} \quad (6)$$

where

$$\begin{matrix} D_{eq1} = \frac{v_{in}}{L_1} + k_{p1}\left(-\frac{x_2 - x_4}{RC_1} - \dot{x}_{2ref}\right) + k_{i1}(x_2 - \\ x_{2ref})\ \ D'_{eq1} = \frac{v_{in}}{L_2} + k_{p2}\left(\frac{x_2 - x_4}{RC_2} - \dot{x}_{4ref}\right) + k_{i2}(x_4 - \\ x_{4ref})\ h_1\ (x) = \left(\frac{x_2}{L_1} - \frac{x_1 k_{p1}}{C_1}\right)\ h_2\ (x) = \left(\frac{x_4}{L_2} - \frac{x_3 k_{p2}}{C_2}\right) \end{matrix} \quad (7)$$

and k_{pi}, k_{ii} and $K_i, i = 1, 2$ are positive constants and $\frac{x_2}{L_1} \neq \frac{x_1 k_{p1}}{C_1}$, $\frac{x_4}{L_2} \neq \frac{x_3 k_{p2}}{C_2}$.

Proof

Consider the following Lyapunov function:

$$\mathrm{V} = \frac{1}{2}\mathrm{ss}^{\mathrm{T}} = \frac{1}{2}(\mathrm{s}_1^2 + \mathrm{s}_2^2) \quad (8)$$

the derivative of V is:

$$\dot{V} = \mathrm{s}_1\dot{\mathrm{s}_1} + \mathrm{s}_2\dot{\mathrm{s}_2} \quad (9)$$

by substituting Equation (7) into Equation (6), we have

$$\begin{matrix} \dot{s} = \begin{pmatrix} K_1 sign(s_1) \\ K_2 sign(s_2) \end{pmatrix} \\ \dot{\mathrm{V}} = -\mathrm{s}^{\mathrm{T}} \begin{pmatrix} \mathrm{K}_1 \mathrm{sign}(\mathrm{s}_1) \\ \mathrm{K}_2 \mathrm{sign}(\mathrm{s}_2) \end{pmatrix} = -\mathrm{K}_1 \mathrm{s}_1 \mathrm{s\ ign}(\mathrm{s}_1) - \\ \mathrm{K}_2 \mathrm{s}_2 \mathrm{sign}(\mathrm{s}_2) = -\mathrm{K}_1 |\mathrm{s}_1| - \mathrm{K}_2 |\mathrm{s}_2| < 0 \end{matrix} \quad (10)$$

Since K_1 and K_2 are positive, $\dot{V} < 0$. As a result, the Lyapunov function V approaches zero and thus, s_1 and s_2 (as the sliding surfaces) approach zero as well.

Remark

If $h_1(x)$ and $h_2(x)$ are zero, D and D' are given by

Equation (11)

$$D = \frac{k_{p1}\, V_{in} + \frac{v_1 - v_2}{R}}{i_1 + k_{p1}\, v_1}$$
$$D' = \frac{k_{p2}\, V_{in} - \frac{v_1 - v_2}{R}}{i_2 + k_{p2}\, v_2} \quad (11)$$

3. 2. Power Decoupling In recent years, many of the proposed methods have aimed to eliminate low-frequency current ripples. According to literature [7,8] large electrolytic capacitors are utilized to suppress the current ripples. However, the electrolytic capacitor is likely to increase both the system's size and cost. Moreover, since electrolytic capacitors are devices with limited operating lifetime, they will also shorten the lifetime of the system. Various power decoupling techniques are discussed that require additional power components and energy storage elements to perform as power decoupling circuits and thus, are not preferred [12]. To overcome such shortcomings, a Proportional Resonant (PR) control method is proposed in this paper to eliminate the low-frequency current ripple of the boost inverter systems without using additional power components or electrolytic capacitor. The PR controller provides an infinity gain at a particular frequency (resonant frequency), while almost unity gain in other frequencies. A PR controller comprises of two parts, namely proportional and resonant, as expressed in Equation (12).

$$G_{PR}(s) = K_P + \frac{K_I}{s^2+\omega_0^2} \quad (12)$$

where ω_0 is the resonant frequency, K_P is the proportional gain and K_I is the integral gain. Since there exists high gain at a narrow band surrounding resonant frequency, the PR controller is capable of eliminating steady-state error. Note that K_I is related to bandwidth, and K_P determines the phase of bandwidth and gain margin. Since the objective in power decoupling is eliminating the second-order ripple current, a second-order PR controller G_{PR2} is employed to realize the zero-error tracking, defined as:

$$\mathrm{G_{PR2}(s)} = \mathrm{K_{P1}} + \frac{\mathrm{K_{I1}}}{\mathrm{s^2+(2\omega_0)^2}} \quad (13)$$

3. 3. Harmonic Rejection The distributed power generation systems generate harmonics due to the non-linearities in their converters. Moreover, such systems have major output quality issues, mainly due to the fact that the number of systems connected to the inverter is always increasing, indicating the significance of controlling the harmonics generated by these inverters to limit their adverse effects on the output voltage quality [13-14]. Therefore, to reject harmonics, the controller must be capable of providing high-quality sinusoidal output with minimal distortion. Selected harmonics in the voltage, including the 3rd, 5th, 7th, etc., can be compensated by additional PR controllers at particular harmonic frequencies. This compensation reduces the THD; therefore, the inverter is compliant with the IEEE and IEC standards [16]. In this paper, a selective harmonic compensator is designed to eliminate the 3rd harmonic. Then, a 3rd-order PR controller is employed defined by the transfer function as:

$$\mathrm{G_{PR3}(s)} = \mathrm{K_{P2}} + \frac{\mathrm{K_{I2}}}{\mathrm{s^2+(3\omega_0)^2}} \quad (14)$$

The closed loop system block diagram is illustrated in Figure 2.

As shown in Figure 2, the proposed control scheme is divided into three stages: the first stage consists of dynamic sliding control method in which transient behavior improvement and closed loop stability. Then the PR control concept is employed to eliminating the second-order ripple current in second stage and to reject harmonics in last stage.

4. SIMULATION RESULTS

The proposed controller is investigated through numerical simulation based on the nominal values provided in Table 1. Simulation results provided in this section are performed using Matlab/Simulink software. Delays are generally created by different factors. In boost inverters, calculation time and the PWM section are responsible for a delay time as large as approximately 1.5 times the sampling time. Therefore, simulations in this section are performed with consideration of delays, which makes it more difficult to obtain satisfactory performance and stability. For the sake of a fair comparison, the performance of the classical sliding mode control is simulated with similar values.

To verify the effectiveness of the proposed controller in decreasing the steady-state error, the reference and the rated performances of the boost-inverter is demonstrated

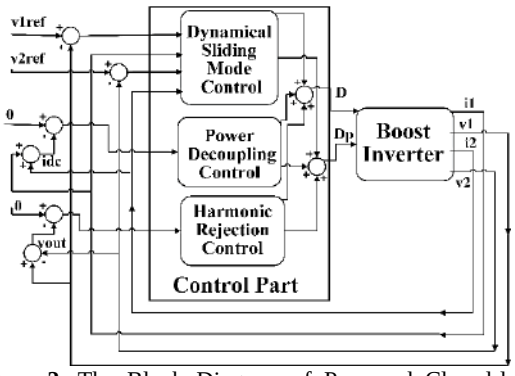

Figure 2. The Block Diagram of Proposed Closed-loop system

in Figure 3. The boost inverter is modeled in Equation (2), and is controlled by the dynamical SMC (DSMC) proposed in Euations (6) and (7).

To examine the performance of the controller against uncertainty, the system is initially simulated under load variations.

To this end, the load utilized in the simulation is changed according to a step function at the 0.06th second. The results are illustrated in Figure 4. It can be seen that the controller is robust under large load variations, since the output voltage remains stationary and the system recovered very fast.

In order to evaluate the robustness of the proposed strategy, concerning parameter uncertainties, simulation is performed under variation of c_1 from 100μF to 70μF at the 0.1th second as shown in Figure 9. In this case, the circuit is asymmetric. It is observed in Figure 5 that the considered variations do not impose significant effects on the output voltage for both DCSM and CSMC; however the error for CSMC is significantly more than DSMC technique.

To evaluate the performance of the controller under variation of the input voltage, where it drops from 48 to 38 at the 0.1th second. The simulation results are presented in Figure 6. Note that the DC component of the voltage on the capacitors is automatically adjusted when the input voltage changes. It should be pointed out that this perturbation rejection is achieved without input voltage measurement.

Figure 6 shows that however the error of DSMC does not change visibly, but the error of CSMC goes up sharply and does not come down.

TABLE 1. System parameters

Symbol	Value
L_1, L_2	$1mH$
C_1, C_2	$100\mu F$
V_{in}	$48volt$
V_{oref}	$120\sqrt{2}\,sin(120\pi t)$
R	100Ω

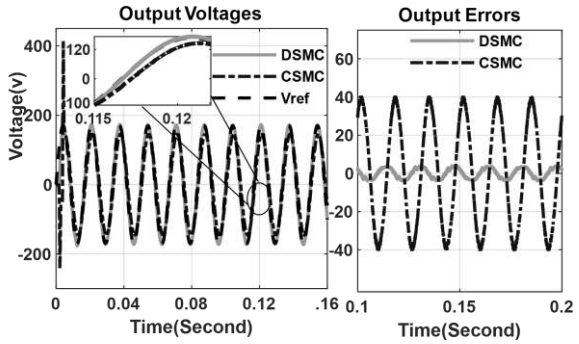

Figure 3. Nominal performance (left), Steady state error (right) of the proposed DSMC and CSMC

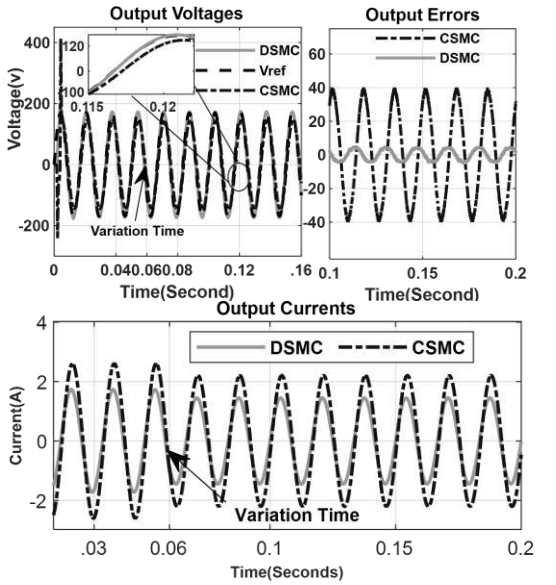

Figure 4. Performance of the proposed DSMC and CSMC under 50% load variation at second 0.06th Output Voltage (top-left), Steady state error (top-right) , Output Current (bottom)

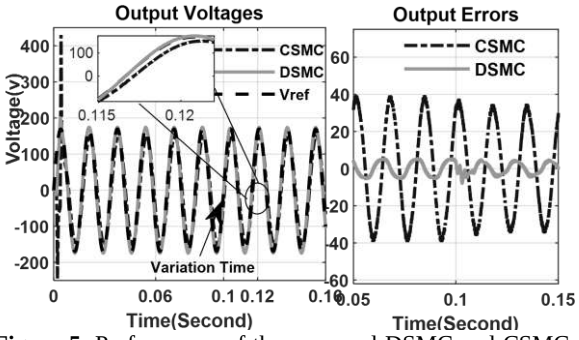

Figure 5. Performance of the proposed DSMC and CSMC under asymmetric parameter uncertainties (30% capacitance variation at second 0.1th)

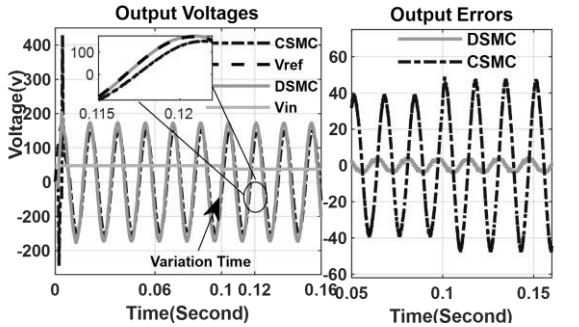

Figure 6. Performance (left), Steady state error (right) of the proposed DSMC and CSMC under 20% input voltage variation at 0.1th second

In the second part of the simulations, the power decoupling was evaluated for the boost inverter, according to the parameters listed in Table 1. In Figure 7,

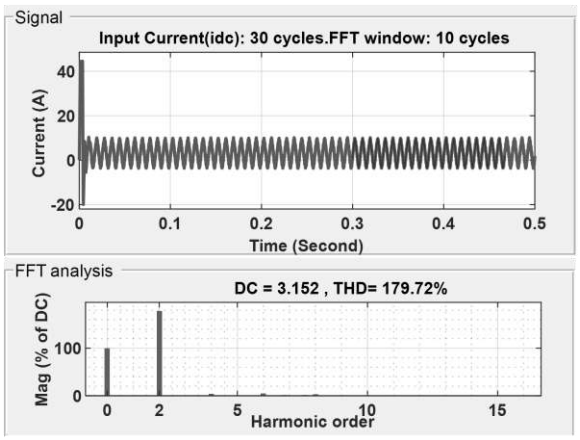

Figure 7. Simulation Result and FFT analysis of the input current i_{dc} applying DSMC without power decoupling

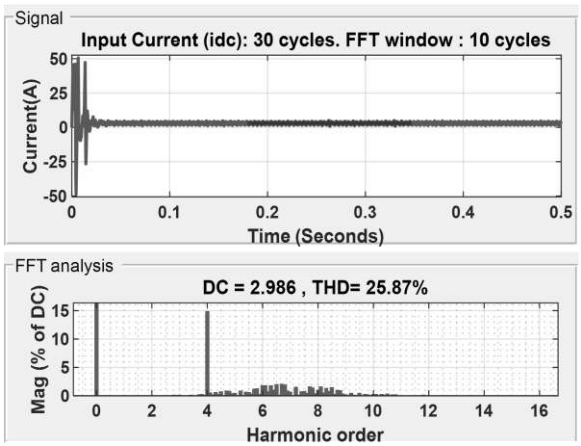

Figure 8. Simulation result and FFT analysis of the input current i_{dc} applying proposed DSMC with power decoupling

the result without power decoupling is demonstrated, while Figure 8 illustrates the condition in which power decoupling is considered.

As anticipated, without decoupling, the capacitors c_1 and c_2 in Figure 7 contain only a DC offset and an AC component at the fundamental frequency. Therefore, the DC offset cancels each other differentially, while the AC component is doubled at ω. Thus, the AC voltage is appropriate, while the DC input current i_{dc} is not constant. Consequently, power decoupling is necessary and as expected, using the proposed power decoupling technique, the second order component in the DC side is dramatically reduced to almost zero.

As can be seen in Figures 8 and 9, when the power decoupling is enabled, i_{dc} becomes constant and creates 3rd order harmonics on the output AC voltage. Therefore, the harmonic rejection is necessary at 3ω to produce the desired AC voltage and current waveforms. As expected, in Figure 10, using aforementioned harmonic compensator is lead to desired ac voltage withot 3th order harmonic. However The 3rd order harmonic compensator creates 4th order harmonic on i_{dc}. Therefore, the power decoupling technique must be capable of reducing this harmonic. The extended power decoupling is hence necessary and as expected, employing the proposed power.

Figure 11 shows that 4th order harmonic on i_{dc} is disappeared when the extended power decoupling is enabled. To get an overview of the performance of the closed loop system, the value of THD in the output voltage in different simulation scenarios are presented in Table 2.

As can be seen in last scenario of Table 2, when the 4th order power decoupling is enabled, the value of THD in the output voltage has increased because 4th order power decoupling creates 5th order harmonics on the output AC voltage.

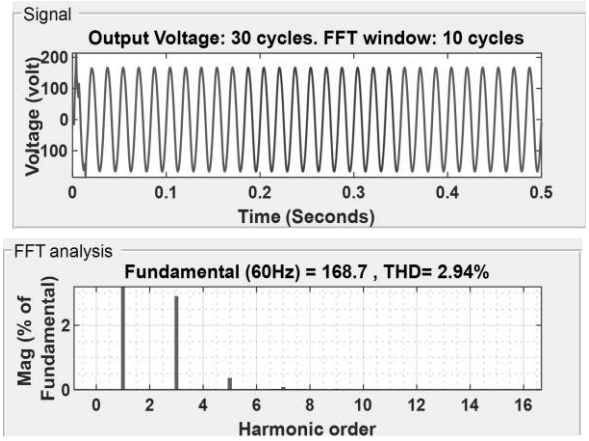

Figure 9. Simulation result and FFT analysis of the output voltage v_{ac} applying proposed DSMC and power decoupling

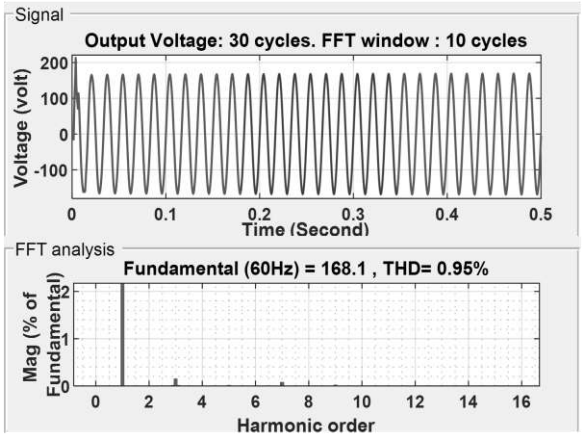

Figure 10. Simulation result and FFT analysis of the output voltage v_{ac} applying proposed DSMC, power decoupling, and 3rd order harmonic compensator

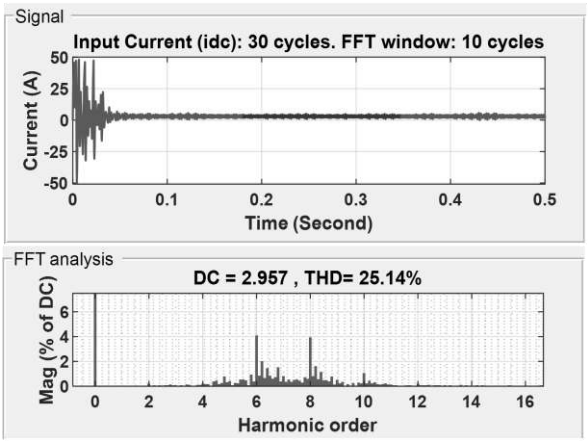

Figure 11. Simulation result and FFT analysis of the input current i_{dc} applying proposed DSMC, extended power decoupling and 3rd order harmonic compensator

TABLE 2. THD of output voltage in different simulation scenarios

Scenarios	THD%	
	i_{dc}	v_{out}
Without Power Decoupling and Harmonic Rejection	178.72	1.2
With Power Decoupling and Without Harmonic Rejection	25.87	2.94
With Power Decoupling and Harmonic Rejection	46.82	.95
With Extended Power Decoupling and Harmonic Rejection	25.14	1.51

5. CONCLUSION

This paper aimed to develop a dynamic sliding-mode control scheme for a single-stage boost inverter with power decoupling and harmonic rejection capabilities. This controller consists a dynamic sliding-mode controller proposed with a single loop to overcome uncertainties, time-delay and two Proportional Resonant (PR) current controllers with additional selective harmonic compensators which employed to achieve selected harmonic rejection of the output voltage and compensate the 2nd and 4th order ripples. Simulations on the inverter confirmed the effectiveness of the DSMC in providing several features such as fast and chattering-free response, robustness against uncertainty in the parameters, smooth control, proper steady-state error, decoupled power and good total harmonic distortion (THD) around 1.5% over the output voltage, and simple implementation. Plus, the effectiveness of the PR controllers in reducing selected harmonics in the input current and output voltage are demonstrated. Using this power decoupling scheme, smooth DC current and high-quality AC voltage can be obtained Moreover, to provide a fair comparison, the performance of the classical sliding mode control was simulated. As can be seen, using CSMC leads to high steady state error, which confirms that the error in CSMC was higher than DSMC.

5. REFERENCES

1. Tran, T.-T., Nguyen, M.-K., Oh, S.-H., Ko, P.-J. and Cho, G.-B., "A single-phase type-boost integrated inverter for photovoltaic applications", ***Journal of Clean Energy Technologies***, Vol. 6, No. 1, (2018).
2. Zhao, B., Abramovitz, A., Liu, C., Yang, Y. and Huangfu, Y., "A family of single-stage, buck-boost inverters for photovoltaic applications", ***Energies***, Vol. 13, No. 7, (2020), 1675. https://doi.org/10.3390/en13071675
3. Wai, R.-J., Chen, M.-W. and Liu, Y.-K., "Design of adaptive control and fuzzy neural network control for single-stage boost inverter", ***IEEE Transactions on Industrial Electronics***, Vol. 62, No. 9, (2015), 5434-5445. DOI: 10.1109/TIE.2015.2408571
4. Abeywardana, D.B.W., Hredzak, B. and Agelidis, V.G., "A rule-based controller to mitigate dc-side second-order harmonic current in a single-phase boost inverter", ***IEEE Transactions on Power Electronics***, Vol. 31, No. 2, (2015), 1665-1679. DOI: 10.1109/TPEL.2015.2421494
5. Lopez-Caiza, D., Flores-Bahamonde, F., Kouro, S., Santana, V., Müller, N. and Chub, A., "Sliding mode based control of dual boost inverter for grid connection", ***Energies***, Vol. 12, No. 22, (2019), 4241. https://doi.org/10.3390/en12224241
6. Flores-Bahamonde, F., Valderrama-Blavi, H., Bosque-Moncusi, J.M., Garcia, G. and Martinez-Salamero, L., "Using the sliding-mode control approach for analysis and design of the boost inverter", ***IET Power Electronics***, Vol. 9, No. 8, (2016), 1625-1634. DOI: 10.1049/iet-pel.2015.0608
7. Özdemir, A. and Erdem, Z., "Double-loop pi controller design of the dc-dc boost converter with a proposed approach for calculation of the controller parameters", ***Proceedings of the Institution of Mechanical Engineers, Part I: Journal of Systems and Control Engineering***, Vol. 232, No. 2, (2018), 137-148. https://doi.org/10.1177/0959651817740006
8. Chen, Y. and Zhang, B., Analysis of current-mode controlled pwm dc/dc converters based on espm, in Equivalent-small-parameter analysis of dc/dc switched-mode converter. 2019, Springer.131-158. http://dx.doi.org/10.1007/978-981-13-2574-8_7
9. Kumar, S.S. and Kumar, V., "Voltage mode control of integrated boost series parallel fly-back converter for energy storage applications", ***Energy Procedia***, Vol. 117, (2017), 62-70. https://doi.org/10.1016/j.egypro.2017.05.107
10. Xu, S., Cao, B., Chang, L., Shao, R. and Mao, M., "Single-phase voltage source inverter with voltage boosting and power decoupling capabilities", ***IEEE Journal of Emerging and Selected Topics in Power Electronics***, Vol. 8, No. 3, (2019). DOI: 10.1109/JESTPE.2019.2936136
11. Watanabe, H., Sakuraba, T., Furukawa, K., Kusaka, K. and Itoh, J.-i., "Development of dc to single-phase ac voltage source inverter with active power decoupling based on flying capacitor dc/dc converter", ***IEEE Transactions on Power Electronics***, Vol. 33, No. 6, (2017), 4992-5004. DOI: 10.1109/TPEL.2017.2727063
12. Xu, S., Chang, L., Shao, R. and Mohomad, A.H., "Power decoupling method for single-phase buck-boost inverter with energy-based control", in 2017 IEEE Applied Power Electronics Conference and Exposition (APEC), IEEE. (2017), 3426-3431. DOI: 10.1109/APEC.2017.7931188

13. Shawky, A., Sayed, M.A. and Takeshita, T., "Selective harmonic compensation of three phase grid tied sepic based differential inverter", in 2019 IEEE Applied Power Electronics Conference and Exposition (APEC), IEEE. (2019), 396-403. DOI: 10.1109/APEC.2019.8721854
14. Jiao, J., Hung, J.Y. and Nelms, R., "Improved selective harmonic compensation for single-phase inverters", in 2018 IEEE Applied Power Electronics Conference and Exposition (APEC), IEEE. (2018), 1329-1335. DOI: 10.1109/APEC.2018.8341189
15. Yu, Z., Hu, X., Yao, Z., Chen, L., Zhang, M. and Jiang, S., "Analysis and design of a transformerless boost inverter for stand-alone photovoltaic generation systems", ***CPSS Transactions on Power Electronics and Applications***, Vol. 4, No. 4, (2019), 310-319. DOI: 10.24295/CPSSTPEA.2019.00029
16. Std.-519, I., "Ieee recommended practices and requirements for harmonic control in electric power systems", New York, IEEE (1992).

Persian Abstract

چکیده

در این مقاله مسئله کنترل اینورتر افزاینده تک مرحله ای مورد بررسی می‌گیرد. هدف از کنترل در این مقاله، داشتن یک سیستم با پاسخ سریع، ولتاژ AC خروجی با کیفیت بالا، جریان DC صاف و مقاوم در برابر تغییر پارامترها است. برای این منظور نوع جدیدی از کنترل مود لغزشی دینامیکی ارائه می‌شود تا بر عدم قطعیت های پارامتری و تغییرات ولتاژ ورودی DC به خوبی غلبه کند. در مقایسه با کنترل کننده‌های دو حلقه ای مرسوم، کنترل کننده مود لغزشی پیشنهادی در این مقاله در حالیکه ویژگیهایی از قبیل مقاوم بودن در برابر عدم قطعیتهای پارامتری را ارائه می دهد، تنها از یک حلقه در طراحی خود استفاده می کند. به علاوه در این مقاله از یک روش مبتنی بر کنترل تناسبی- رزونانسی نیز برای دکوپله سازی توان در فرکانس های مرتبه زوج استفاده می‌شود تا ریپل جریان فرکانس پایین را بدون استفاده از المانهای قدرت یا خازنهای الکترولیت اضافی محدود کند. در مقایسه با کنترل کننده های مرسوم، کنترل کننده پیشنهادی در این مقاله ویژگیهای مطلوبی از جمله پاسخ بدون وزوز ، کنترل نرم، خطای حالت ماندکار مناسب، توان دکوپله و اعوجاج هارمونیکی کل مناسب در جریان ورودی و ولتاژ خروجی را در کنار پیاده سازی ساده ارائه می دهد. در یک مقایسه عادلانه با کنترل مود لغزشی کلاسیک، نتایج شبیه سازی، عملکرد و اثربخشی روش پیشنهادی را نشان میدهند.

International Journal of Engineering

Journal Homepage: www.ije.ir

A Multi-objective Sustainable Medicine Supply Chain Network Design Using a Novel Hybrid Multi-objective Metaheuristic Algorithm

F. Goodarzian, H. Hosseini-Nasab*, M. B. Fakhrzad

Department of Industrial Engineering, Yazd University, Yazd, Iran

PAPER INFO

Paper history:
Received 10 February 2020
Received in revised form 14 May 2020
Accepted 11 June 2020

Keywords:
Medicine Supply Chain Network
Sustainability
Mixed Integer Linear Programming Model
Multi-objective Problems
Hybrid Metaheuristic Algorithm
Taguchi Method

ABSTRACT

End-of-life products have a severe impact on the ecological system. Potential production policies and distribution strategies for the newly manufactured product have attracted significant attention to sustainable development. Sustainability in supply chain management has much importance to achieve eco-friendly goals. In this study, we have developed sustainable objectives in the supply chain optimization framework with different constraints. The trade-off between economic, environmental and social effects objectives have identified by ensuring the optimal allocation of different products among various levels. In this regard, a new sustainability multi-objective mixed-integer linear programming mathematical model in the medicine supply chain network is developed. Although the proposed model is an NP-hard problem, we develop a novel hybrid Particle Swarm Optimization and Genetic Algorithm to achieve Pareto solutions. Then, to adjust the important parameters of the algorithms and chose the optimum levels of the significant factors for more efficiency is employed the Taguchi method. The results show that the economic and environmental effects tend to be decreased and the social impacts tend to be increased in the medicine supply chain network which can exhibit the best sustainability performance. The various outcomes of numerical experiments indicate that the proposed solution algorithm is more reliable than other algorithms. The solution methods are complemented with several sensitivity analyses on the input parameters of the model.

***doi**: 10.5829/ije.2020.33.10a.17*

1. INTRODUCTION

Over the past few decades, significant attention has put on sustainability in supply chain design. To fulfill the market need on time, the maximum coverage distance of the customer's zone is much needed and falls under social issues. As the production and consumption processes of products involve various phases in which environmental impacts are very severe and harmful. Especially, end-of-use (EOU) and end-of-life (EOL) phases of products have significant impacts on the environment [1-3]. Therefore, a sustainable supply chain management (SSCM) network is designed and implemented efficiently by many researchers to overcome the social issue and environmental impacts. The SSCM contemplates over three objectives such as economic cost, social issues and environmental impacts, known as Tripple Bottom Line (TBL) objectives for sustainable development [4-6].

The concept of sustainability in the medicine supply chain management (MSCM) network has much importance and adaptability due to the significant involvement of social and environmental aspects [6, 7]. The demand for pharmaceutical products is very high due to continuous degradation in human health standards and life expectancy. Various fatal diseases require regular vaccination doses to cure the patient. For vaccination purposes, injections are one of the most extensively used medicated products. Presently, the one-time-use (OTU) needle and syringes are prevailing in the market. The usage of injections for different diseases such as Hepatitis, HIV, and AIDS annually yield in 16 billion

*Corresponding Author Institutional Email: *hhn@yazd.ac.ir* (H. Hosseini-Nasab)

Please cite this article as: F. Goodarzian, H. Hosseini-Nasab, M. B. Fakhrzad, A Multi-objective Sustainable Medicine Supply Chain Network Design using a Novel Hybrid Multi-objective Metaheuristic Algorithm, International Journal of Engineering (IJE), IJE TRANSACTIONS A: Basics Vol. 33, No. 10, (October 2020) 1986-1995

used needle and syringes which are toxic and severe [8-10]. Consequently, the environment and ecosystem have a significant adverse impact. Literature reveals that various research domain of medicine supply chain network MSCM has been covered in the last few years [11].

Some extensive literature survey papers in the field of SSCM have been presented by Cum et al. [12], Seuring [13], Brandenburg et al. [14]. Zhang et al. [15] discussed the multiple distribution channels in supply chain management (SCM) under stochastic uncertainty. They also developed the sustainable objectives comprising economic cost, improvement of customer services and reduction in environmental influences. The propounded Multi objective decision making supply chain management (MDCSCM) has been solved using the ant-bee colony method (MOABC) and made a comparative study with conventional SCM. Tsao et al. [16] also developed a computational study for sustainability in SCM. The multi-objective mathematical programming problem has formulated under uncertainty. The uncertain interactive method based on stochastic and fuzzy theory has been used to solve the model.

Pishvaee and Razmi [17] discussed the environmental effects of EOL products in supply chain management under uncertainty. The assessment of environmental impact has been done using the Eco-indicator 99 (LCA-based method) based on proposed supply chain design. A case study based on Iranian pharmaceutical companies has been presented under uncertainty. Lin et al. [18] presented the combination of sustainability and supply chain in terms of theoretical and managerial gaps. To identify the deficiencies of financing patterns, fuzzy TOPSIS has been adopted. After analyzing the results, significant aspects of the product delivery management policies have been highlighted or evacuated. Ahmadi et al. [19] incorporated the optimization mechanism in pharmaceutical supply chain management. The integrated component of PSCM has emerged into a good practice scheme for managerial points of view. Hulea et al. [20] recently suggested the optimal distribution of pharmaceutical products and presented a solution for pharmaceutical cold chain management using distributed ledger technology. The modeling of data and communication of system entities have well performed in the proposed study. Nasrollahi and Razmi [21] also discussed the integrated framework for PSCM design with a maximum expected coverage of demand. The proposed mathematical model has captured the sustainable objectives along with a set of constraints. The multi-objective Particle Swarm Optimization (PSO) and NSGA-II have been suggested to solve the propounded model. A computational study based on the private medical sector in the remote provinces of Iran has been presented to validate the model and solution algorithm.

The concept of sustainability has not been still incorporated in mathematical modeling of the MSCN problem. Therefore, all the above studies are confined to either economic objectives or environmental objectives related to their case study and lagging behind the sustainable objectives.

The first aim of this paper was to propose a new sustainable multi-objective MSCN which considers TBL objectives include minimization of total cost represents the economic cost, maximization of customer service coverage distance depicts the social issues and reduction in the environmental impacts reflects the environmental objective under a set of dynamic constraints which consequently results in the TBL approach.

Hence, an MSCN along with sustainable objectives is quite worth important to reveal the actual real-life scenario and could assist the decision-makers or managers to design the fruitful policies and strategies for the firm or company. Moreover, we have designed the model according to the input information of the parameter.

In addition, the second aim of this paper is to develop a novel multi-objective metaheuristic algorithm, namely, Hybrid Particle Swarm Optimization and Genetic Algorithm (HPSOGA) to find Pareto solutions and to solve the model. To summarize, the proposed paper illustrates some concerns that cover the literature gaps and can be categorized as follows:

- Designing a new sustainability MSCN considering,
- The aims of this MSCN include minimizing economic and environmental impacts and maximizing social effects,
- Developing a new hybrid metaheuristic algorithm for the first time to solve the sustainability MSCN,
- Providing several sensitivity analyses on the main parameters.

The suggested formulation and metaheuristic algorithms can be used for solving other similar multi-objective problems related to pharmaceutical and blood supply chain, perishable products supply chain networks, home health care problems, vehicle routing problems, green supply chain network, and other optimization problems. In any case, each algorithm or approach has its own advantages and limitations depending on the specific problem, so the comparison of performances could also be a significant and interesting issue for future research works.

The rest of this paper is organized as follows: section 2 is a mathematical model, problem description. The solution methodology to solve the presented model is stated in section 3. Section 4 is concerned with the Taguchi method and a numerical example, computational results. Section 5 explain the sensitivity analysis of parameters. Eventually, conclusions and future works are in section 6.

2. MATHEMATICAL MODELLING

2. 1. Problem Description The proposed MSCN paper is concerned with the one-time-use (OUT) medicated needle and syringe, multi-level and for a single period. The propounded MSCN has been depicted in Figure 1. The whole supply chain design comprises a forward and reverses chain. The flow of newly medicated products initiates from the manufacturing plants to different levels. Customer zones receive the products either directly from manufacturing plants or via distribution centers. The EOL phase of products starts from customer zones where the possible use of the products takes place. The reverse chain includes collection centers that are responsible for the accumulation of EOU products from different customer zones. Then EOL needle and syringes are shipped for incineration and underground disposal purposes. Thus, the continuous repetition of this procedure ensures the management of medicated infectious wastes.

The proposed sustainable MSCN model has integrated the versatile aspects of sustainability. The sustainable goals inherently capture the commercial purpose, i.e., minimization of the total cost incurred over each product; social target, i.e., maximize customers' service facility by covering the maximal distance of markets and environmental goals i.e., reduction in the ecological impacts, respectively.

2. 2. Notation

Indices

s	Index for supplier $s \in S$
m	Index for manufacturer $m \in M$
d	Index for distribution center $d \in D$
c	Index for customer $c \in C$
k	Index for collection center $k \in K$
n	Index for incineration center $n \in N$

Parameters

φ_s	Supplier capacity s
φ_m	Manufacturer capacity m
φ_d	Distribution center capacity d
φ_c	Customer demand c
φ_k	Collection center capacity k
φ_n	Incineration center capacity n
β_m	Fixed cost of manufacturer m
β_d	Fixed cost of distribution center d
β_k	Fixed cost of collection center k
β_n	Fixed cost of incineration center n
γ_m	Environmental impact of manufacturer m
γ_d	Environmental impact of distribution center d
γ_k	Environmental impact of collection center k
γ_n	Environmental impact of incineration center n
D_{ij}	Distance between two levels $[i,j \in S \cup^M \cup^D \cup^C \cup^K \cup^N, i \neq j]$
T_{ij}	Transportation cost between two levels $[i,j \in S \cup^M \cup^D \cup^C \cup^K \cup^N, i \neq j]$
E_{ij}	Environmental impacts between two levels $[i,j \in S \cup^M \cup^D \cup^C \cup^K \cup^N, i \neq j]$

Decision Variables

X_m	If manufacturers m is opened and closed1; otherwise 0
X_d	If distribution centers d is opened and closed1; otherwise 0
X_k	If collection centers k is opened and closed1; otherwise 0
X_n	If incineration centers n is opened and closed1; otherwise 0
Y_{sm}	If the products shipped from suppliers s to manufacturers m1; otherwise 0
Y_{md}	If the products shipped from manufacturers m to distribution centers d1; otherwise 0
Y_{dc}	If the products shipped from distribution centers d to customer c 1; otherwise 0
Y_{mc}	If the products shipped from manufacturers m to customer c 1; otherwise 0
Y_{ck}	If the products shipped from customer c to collection center k 1; otherwise 0
Y_{kn}	If the products shipped from collection center $k$to incineration center n1; otherwise 0
A_{sm}	The amount of products transported from different suppliers s to manufacturers m
A_{md}	The amount of products transported from manufacturers m to distribution centers d
A_{dc}	The amount of products transported from distribution centers d to customer c
A_{mc}	The amount of products transported from manufacturers m to customer c
A_{ck}	The amount of products transported from customer c to collection center k
A_{kn}	The amount of products transported from collection center $k$to incineration center n

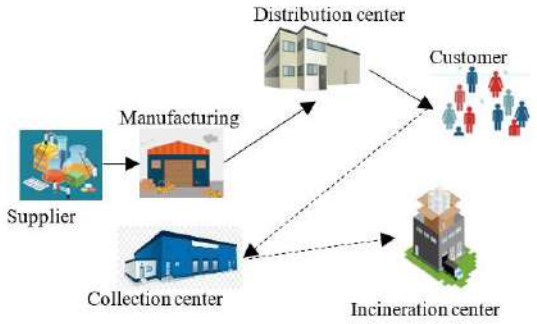

Figure 1. The structure of sustainability MSCN

2. 3. Mathematical Modeling

$$Min\ F_1 = \sum_{m\in M}\beta_m X_m + \sum_{d\in D}\beta_d X_d + \sum_{k\in K}\beta_k X_k + \sum_{n\in N}\beta_n X_n + \sum_{s\in S}\sum_{m\in M} T_{sm} A_{sm} + \sum_{m\in M}\sum_{d\in D} T_{md} A_{md} + \sum_{d\in D}\sum_{c\in C} T_{dc} A_{dc} + \sum_{m\in M}\sum_{c\in C} T_{mc} A_{mc} + \sum_{c\in C}\sum_{k\in K} T_{ck} A_{ck} + \sum_{k\in K}\sum_{n\in N} T_{kn} A_{kn} \quad (1)$$

$$Min\ F_2 = \sum_{m\in M}\gamma_m X_m + \sum_{d\in D}\gamma_d X_d + \sum_{k\in K}\gamma_k X_k + \sum_{n\in N}\gamma_n X_n + \sum_{s\in S}\sum_{m\in M} E_{sm}\,A_{sm} + \sum_{m\in M}\sum_{d\in D} E_{md}\,A_{md} + \sum_{d\in D}\sum_{c\in C} E_{dc}\,A_{dc} + \sum_{m\in M}\sum_{c\in C} E_{mc}\,A_{mc} + \sum_{c\in C}\sum_{k\in K} E_{ck}\,A_{ck} + \sum_{k\in K}\sum_{n\in N} E_{kn}\,A_{kn} \quad (2)$$

$$Max\ F_3 = \sum_{c\in C}\varphi_c\left(\sum_{m\in H_m} A_{mc} + \sum_{d\in H_d} A_{dc}\right) \quad (3)$$

$$s.t.$$

$$\sum_{m\in M} Y_{mc} + \sum_{d\in D} Y_{dc} \geq 1;\ \ \forall c \in C \quad (4)$$

$$\sum_{m\in M} A_{mc} + \sum_{d\in D} A_{dc} \cong \varphi_c;\ \ \forall c \in C \quad (5)$$

$$\sum_{m\in M} A_{mc} + \sum_{d\in D} A_{dc} \leq \varphi_m;\ \ \forall c \in C \quad (6)$$

$$\sum_{m\in M} A_{mc} \leq \varphi_d;\ \ \forall c \in C \quad (7)$$

$$\sum_{k\in K} A_{ck} \leq \varphi_k;\ \ \forall c \in C \quad (8)$$

$$\sum_{n\in N} A_{kn} \leq \varphi_n;\ \ \forall k \in K \quad (9)$$

$$A_{mc} = \{Y_{mc} = 1;\ \ \varphi_p; 0\};\ \forall\, m \in M, c \in C \quad (10)$$

$$A_{dc} = \{Y_{dc} = 1;\ \ \varphi_p; 0\};\ \forall\, d \in D, c \in C \quad (11)$$

$$Y_{mc} \leq X_m;\ \ \forall m \in M, c \in C \quad (12)$$

$$Y_{dc} \leq X_d;\ \ \forall\, d \in D, c \in C \quad (13)$$

$$X_m, X_d, X_k, X_n, Y_{sm}, Y_{md}, Y_{dc}, Y_{mc}, Y_{ck}, Y_{kn} \in \{0,1\}$$
$$A_{sm}, A_{md}, A_{dc}, A_{mc}, A_{ck}, A_{kn} \geq 0 \quad (14)$$

The first objective (1) represents the economic cost function which includes fixed price and transportation costs among different echelons.

In terms of the second objective (2), in this proposed sustainable MSCN, the computational study background is presented in Figure 1 and the OTU needle and syringes are the functional units which effectively ensures the fulfillment of timely demand from the customer by manufacturing and distributing the products in the forward chain and safely collection of EOL products in reverse chain. The essence and purpose of the implementation of the Eco-indicator method are to estimate and predict the environmental impacts throughout the life cycle of the process and products in the propounded sustainable MSCN configurations. The second step concerned with the description of the life cycle system. In this proposed sustainable MSCN paper, the different stages of new and EOL products include (I) production of OTU needles and syringes at manufacturing plant, (II) transportation of the products from production facility to customers and distribution centers, (III) transportation from production centers to customers, (IV) shipments of used products from customers to collection centers, (V) operating of EOL products at collection centers, e.g., disassembling, (XI) transportation from collection centers to incineration facility, and (XII) further handling and processing at incineration centers and under-ground disposal pits. In the third step, the quantification of life cycle stages of products and processes has performed by considering the most common characteristic features. Finally, at the fourth step, the final accurate value is determined by (I) predicting the relevant Eo-indicator, (II) performing the multiplication between amounts and corresponding indicator score and (III) summing up the auxiliary outcomes. Consequently, the modeling approach much requires the environmental impact values in terms of per one unit of products and materials.

The third objective function (3) addresses social benefit by maximizing customer services in terms of customer demand coverage. To ensure the maximal coverage of customer demand, few additional parameters are needed to express in the form of mathematical expression. Assumed that the maximum coverage distance is represented by R_{max}. Customers who fall within this distance range with an open facility are supposed to be well-served. The different echelons of manufacturing plant and distribution centers are responsible for the fulfillment of demand. The manufacturing plant and distribution centers would serve different customer c who fall within the coverage spectrum of maximum distance and are depicted as $H_m = \{m \in M: D_{mc} \leq R_{max}\}$ and $H_d = \{d \in D: D_{dc} \leq R_{max}\}$, respectively.

The following are the relevant constraints or restrictions under which the objective functions are to be optimized by yielding the most promising and systematic strategies for the distribution of syringe and needles among different customers in the proposed MSCN designed model. After the use of the syringe, the maximum collection of waste syringes has been developed for further disposal or incineration. For the sake of convenience, we have formulated the dynamic constraints that reveal each restriction efficiently. Since demand is allowed to fulfill by mainly two-echelon, i.e., manufacturing plant and distribution centers. Therefore, it has been assured that the demand would be met at least by one echelon and represented in Equation (4). The demand from customers is not always stable, but some estimation of the demand pattern is used to determine the actual consumption of the products. Flexibility among demand constraint has been postulated to reveal reality more clearly. Hence we have developed an equality constraint (≅) meaning ”essentially equal to” which signifies that more or less the constraints should be satisfied and are more flexible than inequality constraint.

To ensure that the demand must be satisfied by the shipping of the products from different sources point to customers, Equation (5) has been formulated. Different echelons have a certain capacity of the products to which the flow of products towards its destination is possible. Therefore, to ensure the capacity constraints over different echelons, Equations (6), (7), (8) and (9) have been effectively designed. The significance of to and for movement of products have also been depicted in Equations (10) and (11) by establishing the relationship between flow connectivity and the flow amount of the products between two echelons. The constraints are given in Equations (12) and (13) represents the flow of products that are associated with only open facilities in the proposed MSCN design network. Finally, constraint (14) states the type of decision variables.

3. SOLUTION METHODOLOGY

It has been proven that the sustainable MSCN problem is NP-hard [22-27]. Hence, the literature has seen several metaheuristics that were ordered to solve these NP-hard problems [28-30]. Among them, GA and PSO as a well-known population-based metaheuristic algorithm outperform most of the similar ones [31]. This advantage motivates us to use it again in our research. Besides, No Free Lunch theory says that there is no metaheuristic to show a good performance for all optimization problems [30]. Accordingly, the recent decade has seen a rapid development of metaheuristic methods [30, 31]. In this study, two nature-inspired algorithms, namely, GA and PSO as a population-based metaheuristic is used. A new hybrid method through integrating GA and PSO have been validated. The experimental results indicate that hybrid methods are always better than only using only one algorithm. Another main novelty of this study is to consider and to introduce a hybridization of these two algorithms for the first time. This study, a new hybrid algorithm (HPSO-GA) introduced due to the strength of search phrases, high convergence, and less computational time for the main two individual ones.

The reason for using these algorithms is that the real numbers are executed directly in the continuous space, and unlike other algorithms, it does not guarantee the existence of a definite solution. These algorithms require less number of parameters for adjusting that have an easy implement than other algorithms, have certain memory characteristics, high convergence rate, and highly flexible against optimal problems.

Therefore, the aim of this section is to present three effective meta-heuristic algorithms to solve the proposed model in real sizes. The MSCN model seeks to minimize the economic cost and environmental impacts and to maximize the social impacts. Although software programs make utilization of the branch and bound algorithm, it is not possible to overtake optimum or a near-optimum solution for large-size problems in a reasonable time. Then, the meta-heuristic algorithms to solve real size problems are used. Hence, we utilize two multi-objective meta-heuristic algorithms (PSO and GA). For more information about these algorithms refer to literature [25-30], respectively. Besides, our contribution in this paper, we developed a novel HPSOGA algorithm to solve the presented model.

In the present paper, the general framework of the solution representation performed for three products, two suppliers and two manufacturers are displayed in Figure 2. The numerical outcomes were obtained utilizing MATLAB (R2016b) on a computer with 6 GB RAM and a 2.50 GHz processor.

3. 1. HPSOGA Algorithm In this section, we will develop a novel hybrid algorithm for solving the sustainability MSCN problem by integrating GA and PSO. This hybrid algorithm will be described as follows.

1. Set up parameters involving:

(i) w: inertial weight,

(j) N: particle numbers,

(k) c_1 and c_2: learning factors,

(l) W_{max}:the maximum of velocity,

(m) $rand_1, rand_2$ and $rand_3$: random numbers in interval [0, 1],

(n) m_{rate}: mutation rate, and

(o) c_{rate}: crossover rate.

2. Adjust the range of searching for x. The domain will affect the searching velocity. Starts each particle randomly with an initial position, X_{id}, in the pre-determined domain and velocity, V_{id}, within the domain of maximum speed, V_{max}. Utilize the float coding procedure to create random numbers for the upper-level variables. Hence, variable y solves at a lower level. The position of each particle X_{id}, is as follows:

$$X_{id} = (x_{i1}, \dots, x_{in}, y_{i1}, \dots, y_{im}) \quad (15)$$

3. Calculate the value of fitness for each particle utilizing the following equation:

$$F = c^t X_{id} \quad (16)$$

4. All the particles into two clusters divide based on the efficiency of fitness value. The first group is particles with better the value of fitness:

$$X_{id}^{new} = \left(x_{11}, \dots, x_{(i/2)n}, y_{11}, \dots, y_{(i/2)m}\right) \quad (17)$$

Y_{sm}	s_1						s_2					
$m=1$	1	0	0	1	1	0	0	1	1	0	0	1
$m=2$	1	0	0	1	1	0	0	1	1	0	0	1

Figure 2. Solution representation

The second group is the particles with worse the value of fitness:

$$X_{id}^{n\acute{e}w} = \left(x_{(\frac{i}{2}+1)1}, \dots, x_{in}, y_{(\frac{i}{2}+1)1}, \dots, y_{im}\right) \quad (18)$$

5. Performance of the mutation and crossover for the first group to update the particles and calculate the corresponding the value of fitness. The equation of crossover is:

$$X_{id}^{new1} = Uniform(0,1)X_{id}^{n\acute{e}w} + (1 - Uniform(0,1)X_{id+1}^{n\acute{e}w}), id = 1,2, \dots, \frac{i}{2} - 1 \quad (19)$$

$$X_{id}^{new1} = Uniform(0,1)X_{id}^{n\acute{e}w} + (1 - Uniform(0,1)X_{id1}), id = i/2 \quad (20)$$

while the equation of mutation is:

$$X_{id}^{new2} = X_{id}^{new1} + rand_3 \times N(0,1) \quad (21)$$

Moreover, calculate the value of fitness for each new particle utilizing the following equation:

$$F = c^t X_{id}^{new2} \quad (22)$$

6. Update the current local best position, P_{id}, and global best position, P_{gd}.

7. Update all the particles, $X_{id} = (x_{i1}, \dots, x_{in}, y_{i1}, \dots, y_{im})$, attain from 5 utilizing the following equations:

$$v_{id}^{new} = v_{id}^{old} + c_1 \times rand_1 \times (P_{best\ id} - X_{id}) + c_2 \times rand_2 \times (G_{best\ id} - X_{id}), \quad (23)$$

$$X_{id}^{new} = X_{id}^{old} + v_{id}^{new} \quad (24)$$

Each particle's speed is limited by the pre-specified the maximum of speed, V_{max} , and each the position of particle, X_{id} which should be in the determined domain:

$$l \le x_i \le u \quad (25)$$

8. Stop condition if the determined number of generation is satisfied; otherwise, go back to 3.

3. COMPUTATIONAL RESULTS

In this section, the Taguchi procedure is utilized to tune the parameters of the PSO, GA, and HPSOGA algorithms, due to the algorithms parameter values on the quality of the solution is affected. Table 1 indicates various levels of the factors for PSO, GA, and HPSOGA. In the present paper based on the number of the factors and the levels, Taguchi procedure L27 for multi-objective PSO, GA, and HPSOGA algorithms are employed for the adjustment of the parameters for metaheuristics, respectively. Figures 3-5 display the S/N ratios.

Moreover, several numerical experiments are presented to validate the sustainable MSCN model and also to evaluate the efficiency and performance of the suggested four multi-objective meta-heuristic algorithms (PSO, GA, and HPSOGA) algorithm in terms of needed CPU time and the objective function value. To the best of our knowledge and according to the novelty of developed sustainable MSCN model, no existing study has treated a similar model in the literature. Therefore,

TABLE 1. Factors and levels of algorithms

Factor	Algorithm	Level	Value
Max-iteration	PSO	3	50,100,150
C_1 , C_2		3	0.5,0.75,1
W		3	0.5,0.75,1
W_{damp}		3	0.2,0.25,0.3
N_{pop}		3	50,75,100
Max-iteration	GA	3	50,100,150
P_c		3	0.25,0.5,0.75
P_m		3	1,3,5
N_{pop}		3	50,75,100
Max-iteration	HPSOGA	3	50,100,150
Max-sub iteration GA		3	1,2,3
Max-sub iteration PSO		3	2,3,4
N_{pop}		3	50,75,100

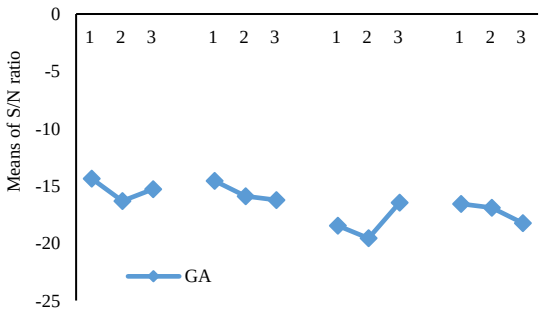

Figure 3. S/N ratio for the GA

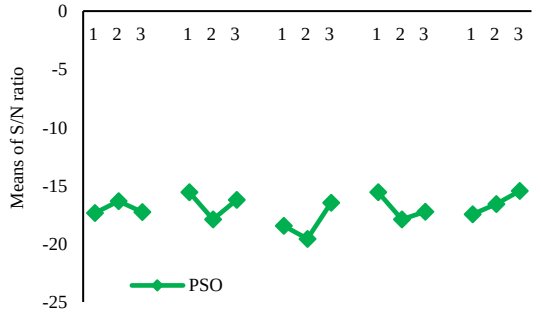

Figure 4. S/N ratio for the PSO

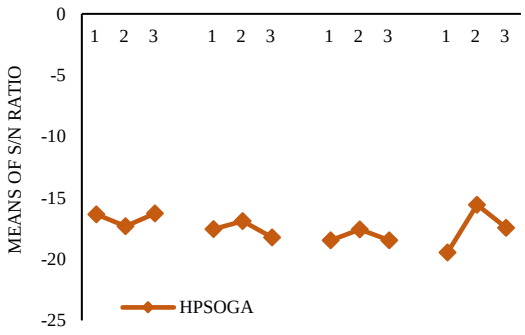

Figure 5. S/N ratio for the HPSOGA

the benchmarks existing in the literature are not available for the model, and an approach is needed to design the test problems. To show the complexity of the model, we need to design problems in different sizes. Then, six test problems are presented with ten runs including random data based on a uniform distribution. The problem sizes and parameter values are proposed in Tables 2 and 3, respectively.

Each instance was repeated 10 times for each run utilizing multi-objective PSO, GA, and HPSOGA algorithms for more accurate calculations. Furthermore, the average outcomes of the objective function of ten runs were chosen as the conclusion basis for the VNS algorithm. The objective function outputs for each problem size employing the multi-objective PSO, GA, and HPSOGA algorithms are presented in Table 4. Table 5 depicts the CPU time of meta-heuristic algorithms in each example. Computational times of the meta-heuristic algorithms in Figure 6 are displayed.

TABLE 2. The sample problem sizes

Example no.	Levels (#*s*#*m*#*d*#*c*#*k*#*n*#*p*#*t*)
1	(#2#2#3#3#4#5#5#1)
2	(#4#4#5#5#5#7#6#1)
3	(#6#6#7#7#6#8#7#1)
4	(#8#7#8#8#7#9#8#1)
5	(#10#8#9#9#8#10#9#1)
6	(#12#9#10#10#9#12#10#1)

TABLE 3. The generated parameters according to the uniform distribution

Parameters	Value	Parameters	Value
φ_s, φ_m,φ_d, φ_c, φ_k, φ_n	$\sim U(50000,60000)$	β_m, β_d, β_k, β_n	$\sim U(70000,80000)$
γ_m, γ_d, γ_k, γ_n	$\sim U(40000,50000)$	D_{ij}	$\sim U(25000,35000)$
T_{ij}	$\sim U(40000,80000)$	E_{ij}	$\sim U(35000,65000)$

4. SENSITIVITY ANALYSIS

To recognize the behavior of the MSCN model, two sensitivity analyses have been carried out on the significant parameters of the suggested model. Furthermore, an experiment problem such as 4 considering eight suppliers, seven manufacturers, eight DCs, eight customers, seven collection centers, nine

TABLE 4. The average outcomes for algorithms

Example no.		GA	HPSOGA	PSO
1	F1	3156	2677	3788
	F2	2788.1	1933.2	3208.1
	F3	3467	2921	3954
2	F1	4322.1	3126.2	4801.3
	F2	3780.2	2799.1	4102.4
	F3	4713	3741	5003
3	F1	4977.3	3702.4	5963.1
	F2	4105.4	2967.4	5288.1
	F3	5174	3944	6134
4	F1	5477.9	4012.5	6512.4
	F2	4901.3	3661.2	5880.2
	F3	5677	4231	6788
5	F1	6034.7	4566.2	7212.4
	F2	5632.7	4012.3	6770.3
	F3	6134	4677	7421
6	F1	7323.5	5334.8	7966.3
	F2	6944.3	4908.2	7239.1
	F3	7532	5466	8134

TABLE 5. The CPU time of algorithms

Example no.	GA	HPSOGA	PSO
1	4.61	3.02	6.73
2	15.21	10.23	19.27
3	21.43	15.45	38.31
4	87.91	63.52	143.48
5	94.78	75.33	178.54
6	123.45	81.21	212.27

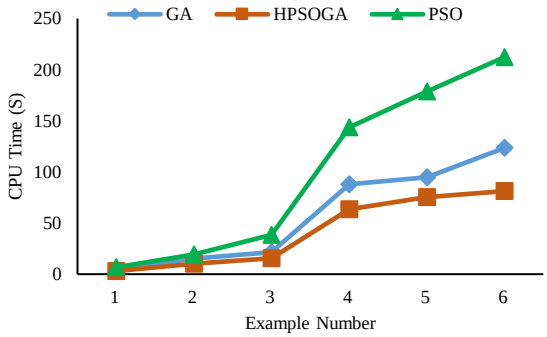

Figure 6. The average CPU time of algorithms

incineration centers, eight products, and one time periods are chosen. Then, the VNS algorithm the most reliable in this paper is considered to handle the presented model. A set of changes containing the environmental impacts $(\gamma_m, \gamma_d, \gamma_k, \gamma_n)$ and the transportation costs (T_{ij}) for the proposed MSCN model is analyzed. Each analysis is divided into five instances numbered as I1 to I5. Eventually, all outcomes are depicted in Tables 6 and 7 as well as Figures 7 and 8.

According to the transportation cost value, sensitivity analyses by increasing the amount of this parameter have been carried out. Details are presented in Table 6. To recognize the three objective functions behavior i.e. economic cost $(F1)$, environmental impact $(F2)$ and social impact $(F3)$, meanwhile, the average values are considered in this comparison as indicated in Figure 8. The outcomes illustrate that although by increasing the amount of this parameter the environmental impact is increased while the economic cost and social impact remains no change.

TABLE 6. Sensitivity analysis on transportation cost

Instances no.	$\gamma_m, \gamma_d, \gamma_k, \gamma_n$	$F1$	$F2$	$F3$
1	400	4012.5	3661.2	4231
2	600	4012.5	3788.2	4231
3	800	4012.5	3912.9	4231
4	1000	4012.5	4122.5	4231
5	1200	4012.5	4456.2	4231

TABLE 7. Sensitivity analysis on transportation time

Instances no.	T_{ij}	$F1$	$F2$	$F3$
1	2000	4012.5	3661.2	4231
2	6000	4341.2	3661.2	4231
3	8000	4813.6	3661.2	4231
4	10000	5431.1	3661.2	4231
5	12000	5812.1	3661.2	4231

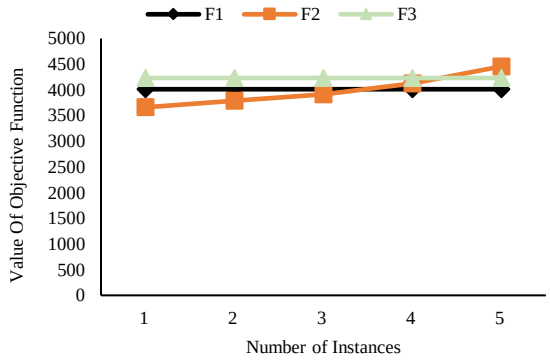

Figure 7. The sensitivity analysis based on transportation cost

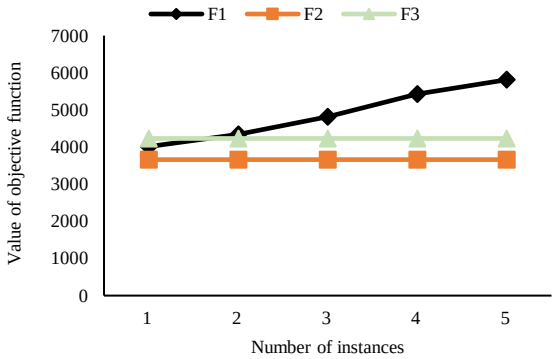

Figure 8. The sensitivity analysis based on transportation time

The transportation times to do some analyses are considered. The outcomes are indicated in Table 7. Moreover, the behavior of both objective functions is shown in Figure 9. By increasing the transportation costs, first of all, the behavior of the economic cost is increased. Hence, the environmental and social impacts are remained fixed and no change.

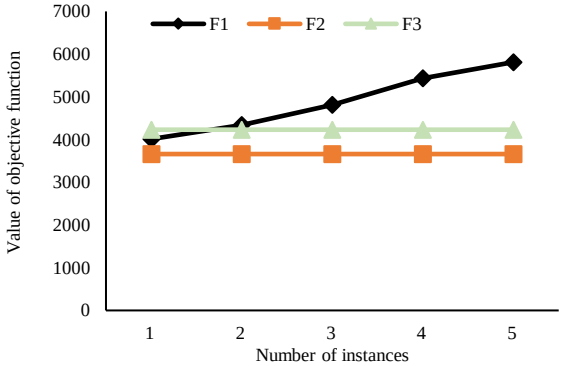

Figure 9. The sensitivity analysis based on transportation time

5. CONCLUSION AND FUTURE WORKS

The short communication taps into the collective experience and wisdom of global health supply chain professionals to identify and prioritize the top several global health medicine supply chain challenges: (1) lack of coordination, (2) inventory management, (3), absent demand information, (4) sustainability, (5) order management, (6) shortage avoidance. (7) expiration, (8) warehouse management, and (10) shipment visibility. These challenges must be addressed by researchers, policymakers, and practitioners alike if global medicine supply chains are to be developed and improved in emerging regions of the world.

Moreover, in the present paper, a new mathematical model for multi-objective sustainability MSCN was developed to address the fourth of challenge. The specific benefits of the presented model were as follows: a new MSCN with multi-suppliers, multi-manufacturers, multi-DCs, multi-customers, multi-collection centers, and multi- incineration centers. In this paper, we formulated the problem as a new mixed-integer linear programming model (MILP) to minimize the economic costs and environmental impacts and to maximize social impacts. To solve the presented model, we developed a novel hybrid particle swarm optimization and genetic algorithm (HPSOGA) and this algorithm is compared to original GA and PSO algorithms. Moreover, a parameter setting with carrying out the Taguchi procedure was proposed for choosing the optimal levels of the factors that affect the algorithm's efficiency. Besides, our sensitivity analysis over the environmental impacts and transportation cost displayed that an insensitive objective value to these parameters is selected enough large and the algorithm carries out correctly. The outcomes of the meta-heuristic algorithms indicated that the HPSOGA algorithm had better efficiency than the other algorithms in terms of CPU time and the objective function on 6 created random problems.

Furthermore, future studies can be used the hybrid meta-heuristic algorithms, heuristic method, and exact method *e.g.* Lagrangian relaxation or Benders algorithms as well as considering the model with stochastic and fuzzy parameters. Then, the interested scholars can add an objective function such as the maximization of the patient's satisfaction or quality level of service.

6. REFERENCES

1. Singh, S.K. and Goh, M., "Multi-objective mixed integer programming and an application in a pharmaceutical supply chain", ***International Journal of Production Research***, Vol. 57, No. 4, (2019), 1214-1237. Doi: 10.1080/00207543.2018.1504172
2. Weraikat, D., Zanjani, M.K. and Lehoux, N., "Improving sustainability in a two-level pharmaceutical supply chain through vendor-managed inventory system", ***Operations Research for Health Care***, Vol. 21, (2019), 44-55. Doi: pii/S2211692318300572
3. Chung, S.H. and Kwon, C., "Integrated supply chain management for perishable products: Dynamics and oligopolistic competition perspectives with application to pharmaceuticals", ***International Journal of Production Economics***, Vol. 179, (2016), 117-129. Doi: pii/S0925527316300913
4. Settanni, E., Harrington, T.S. and Srai, J.S., "Pharmaceutical supply chain models: A synthesis from a systems view of operations research", ***Operations Research Perspectives***, Vol. 4, (2017), 74-95. Doi: pii/S2214716016301105
5. Weraikat, D., Zanjani, M.K. and Lehoux, N., "Two-echelon pharmaceutical reverse supply chain coordination with customers incentives", ***International Journal of Production Economics***, Vol. 176, (2016), 41-52. Doi: pii/S0925527316000670
6. Tavakkoli-Moghaddam, R., Amiri, M. and Azizmohammadi, R., "Solving a redundancy allocation problem by a hybrid multi-objective imperialist competitive algorithm", ***International Journal of Engineering***, Vol. 26, No. 9, (2013), 1031-1042. Doi: article_72175.html
7. Mousazadeh, M., Torabi, S.A. and Zahiri, B., "A robust possibilistic programming approach for pharmaceutical supply chain network design", ***Computers & Chemical Engineering***, Vol. 82, (2015), 115-128. Doi: pii/S0098135415002203
8. Niaki, S., Najafi, A.A., Zoraghi, N. and Abbasi, B., "Resource constrained project scheduling with material ordering: Two hybridized meta-heuristic approaches", ***International Journal of Engineering***, Vol. 28, No. 6, (2015), 896-902. Doi: article_72530.html
9. Zahiri, B., Zhuang, J. and Mohammadi, M., "Toward an integrated sustainable-resilient supply chain: A pharmaceutical case study", ***Transportation Research Part E: Logistics and Transportation Review***, Vol. 103, (2017), 109-142. Doi: pii/S1366554517300509
10. Fathollahi-Fard, A.M., Ahmadi, A., Goodarzian, F. and Cheikhrouhou, N., "A bi-objective home healthcare routing and scheduling problem considering patients' satisfaction in a fuzzy environment", ***Applied Soft Computing***, Vol. 93, (2020), 106385. Doi: pii/S1568494620303252
11. Fakhrzad, M., Talebzadeh, P. and Goodarzian, F., "Mathematical formulation and solving of green closed-loop supply chain planning problem with production, distribution and transportation reliability", ***International Journal of Engineering***, ***Transactions C: Aspects,*** Vol. 31, No. 12, (2018), 2059-2067. Doi: article_82271.html
12. Crum, M., Poist, R., Carter, C.R. and Easton, P.L., "Sustainable supply chain management: Evolution and future directions", ***International Journal of Physical Distribution & Logistics Management***, (2011), Doi: 10.1108/09600031111101420/full/html
13. Seuring, S., "A review of modeling approaches for sustainable supply chain management", ***Decision Support Systems***, Vol. 54, No. 4, (2013), 1513-1520. Doi: pii/S0167923612001741
14. Brandenburg, M., Govindan, K., Sarkis, J. and Seuring, S., "Quantitative models for sustainable supply chain management: Developments and directions", ***European Journal of Operational Research***, Vol. 233, No. 2, (2014), 299-312. Doi: pii/S037722171300787X
15. Zhang, S., Lee, C.K.M., Wu, K. and Choy, K.L., "Multi-objective optimization for sustainable supply chain network design considering multiple distribution channels", ***Expert Systems with Applications***, Vol. 65, (2016), 87-99. Doi: pii/S0957417416304365
16. Tsao, Y.-C., Thanh, V.-V., Lu, J.-C. and Yu, V., "Designing sustainable supply chain networks under uncertain environments: Fuzzy multi-objective programming", ***Journal of Cleaner***

Production, Vol. 174, (2018), 1550-1565. Doi: pii/S0959652617325763

17. Pishvaee, M.S. and Razmi, J., "Environmental supply chain network design using multi-objective fuzzy mathematical programming", ***Applied Mathematical Modelling***, Vol. 36, No. 8, (2012), 3433-3446. Doi: S0307904X11006615
18. Lin, K.-P., Tseng, M.-L. and Pai, P.-F., "Sustainable supply chain management using approximate fuzzy dematel method", ***Resources, Conservation and Recycling***, Vol. 128, (2018), 134-142. Doi: pii/S0921344916303421
19. Ahmadi, A., Mousazadeh, M., Torabi, S.A. and Pishvaee, M.S., Or applications in pharmaceutical supply chain management, in Operations research applications in health care management. 2018, Springer.461-491. Doi: 10.1007/978-3-319-65455-3_18
20. Hulea, M., Rosu, O., Miron, R. and Aştilean, A., "Pharmaceutical cold chain management: Platform based on a distributed ledger", in 2018 IEEE International Conference on Automation, Quality and Testing, Robotics (AQTR), IEEE. 1-6. Doi: https://ieeexplore.ieee.org/abstract/document/8402709
21. Nasrollahi, M. and Razmi, J., "A mathematical model for designing an integrated pharmaceutical supply chain with maximum expected coverage under uncertainty", ***Operational Research***, (2019), 1-28. Doi: 10.1007/s12351-019-00459-3
22. Li, Y., Wei, Z., Zhao, J., Zhang, C. and Liu, Y., "Ambidextrous organizational learning, environmental munificence and new product performance: Moderating effect of managerial ties in china", ***International Journal of Production Economics***, Vol. 146, No. 1, (2013), 95-105. Doi: pii/S0925527312004744
23. Yadegari, E., Alem-Tabriz, A. and Zandieh, M., "A memetic algorithm with a novel neighborhood search and modified solution representation for closed-loop supply chain network design", ***Computers & Industrial Engineering***, Vol. 128, (2019), 418-436. Doi: pii/S0360835218306570
24. Akbarzadeh, Z., Safaei Ghadikolaei, A., Madhoushi, M. and Aghajani, H., "A hybrid fuzzy multi-criteria decision making model based on fuzzy dematel with fuzzy analytical network process and interpretative structural model for prioritizing larg supply chain practices", ***International Journal of Engineering***, Vol. 32, No. 3, (2019), 413-423. Doi: article_85659.html
25. Sadri Esfahani, A. and Fakhrzad, M., "Modeling the time windows vehicle routing problem in cross-docking strategy using two meta-heuristic algorithms", ***International Journal of Engineering***, Vol. 27, No. 7, (2014), 1113-1126. Doi: article_72345.html
26. Fakhrzad, M.B. and Goodarzian, F., "A fuzzy multi-objective programming approach to develop a green closed-loop supply chain network design problem under uncertainty: Modifications of imperialist competitive algorithm", ***RAIRO-Operations Research***, Vol. 53, No. 3, (2019), 963-990. Doi: 2019/03/ro180357/ro180357.html
27. Goodarzian, F. and Hosseini-Nasab, H., "Applying a fuzzy multi-objective model for a production–distribution network design problem by using a novel self-adoptive evolutionary algorithm", ***International Journal of Systems Science: Operations & Logistics***, (2019), 1-22. Doi: 10.1080/23302674.2019.1607621
28. Fakhrzad, M.B., Goodarzian, F. and Golmohammadi, A., "Addressing a fixed charge transportation problem with multi-route and different capacities by novel hybrid meta-heuristics", ***Journal of Industrial and Systems Engineering***, Vol. 12, No. 1, (2019), 167-184. Doi: article_78694.html
29. Sahebjamnia, N., Goodarzian, F. and Hajiaghaei-Keshteli, M., "Optimization of multi-period three-echelon citrus supply chain problem", ***Journal of Optimization in Industrial Engineering***, Vol. 13, No. 1, (2020), 39-53. Doi: article_538019.html
30. Tavakkoli-Moghaddam, R., "Solving a new multi-objective inventory-routing problem by a non-dominated sorting genetic algorithm", ***International Journal of Engineering***, Vol. 31, No. 4, (2018), 588-596. Doi: article_73156.html
31. Goodarzian, F., Hosseini-Nasab, H., Muñuzuri, J. and Fakhrzad, M.-B., "A multi-objective pharmaceutical supply chain network based on a robust fuzzy model: A comparison of meta-heuristics", ***Applied soft computing***, Vol. 92, (2020), 106331. Doi: pii/S1568494620302714

Persian Abstract

چکیده

پایان عمر محصولات تاثیر شدیدی بر سیستم محیط زیست دارد. سیاست‌های تولید بالقوه و استراتژی‌های توزیع برای محصول تولیدشده جدید به‌طور قابل توجهی توسعه پایداری را جذب کرده است. پایداری در مدیریت زنجیره‌تامین برای دستیابی به اهداف سازگار با محیط زیست از اهمیت بسیاری برخوردار است. در این مقاله، اهداف پایداری در چارچوب بهینه‌سازی زنجیره‌تامین با محدودیت‌های مختلف توسعه داده شده است. تعادل بین اهداف اقتصادی، محیط‌زیست و اجتماعی توسط تخصیص بهینه محصولات مختلف در بین سطوح مختلف مشخص شده است. ابتدا مسئله را به صورت یک مدل ریاضی برنامه‌ریزی مختلط عددصحیح خطی فرموله شده است، اگرچه مسئله زنجیره‌تامین پایدار در دسته مسائل NP-hard قرار دارد ما یک الگوریتم ترکیبی بهینه‌سازی انبوه ذرات و ژنتیک (HPSOGA) برای حل مدل پیشنهادی توسعه داده شده است و این الگوریتم با الگوریتم‌های ژنتیک و بهینه‌سازی انبوه ذرات مقایسه خواهد شد. در همین راستا، برای تنظیم پارامترهای مهم از الگوریتم‌ها و انتخاب سطوح بهینه از فاکتورهای مهم برای کارائی و عملکرد بیشتر از رویکرد تاگوچی استفاده شده است. در نتیجه خروجی‌های متفاوتی از مثال عددی نشان می‌دهد که الگوریتم ترکیبی HPSOGA از سایر الگوریتم‌ها کاراتر می‌باشد.

International Journal of Engineering

Journal Homepage: www.ije.ir

A Closed-loop Supply Chain Network Design Problem in Copper Industry

M. Akbari-Kasgari[a], H. Khademi-Zare*[a], M.B. Fakhrzad[a], M. Hajiaghaei-Keshteli[b], M. Honarvar[a]

[a] *Department of Industrial Engineering, Yazd University, Yazd, Iran*
[b] *Department of Industrial Engineering, University of Science and Technology of Mazandaran, Behshahr, Iran*

PAPER INFO

Paper history:
Received 05 June 2020
Received in revised form 02 September 2020
Accepted 03 September 2020

Keywords:
Mathematical Programming
Closed-loop Supply Chain
Copper Industry
Network Design

ABSTRACT

Undoubtedly, metals are the basis of the sustainable development of all human societies. In the last century, the role of copper, as the third most widely used metal, after steel and aluminum, has been crucial. Copper is a recyclable metal. It has many applications such as industrial electricity, plumping, wiring, electronic equipment, transportation, and infrastructure. Today, with the growth of the industry in societies, the demand for copper has increased. This motivated us to study its supply chain network design firstly. To the best of our knowledge, there is no research reported about copper supply chain network design. This paper aims to maximize the profit of the copper closed-loop supply chain. We formulate this network design problem as a Mixed Integer Programming model. The model is considered as single-objective and multi-product. The exact solution of the model is found by using GAMS software. Sensitivity analysis results provide useful results that managers can use them in decisions.

***doi**: 10.5829/ije.2020.33.10a.19*

1. INTRODUCTION

Industrial development has increased demands for basic metals such as steel, aluminium, copper, zinc, etc. [1]. Special features of copper make it a vital material for various sectors such as transportation, industrial electricity, plumping, wiring, electronic equipment, and infrastructure [2]. Today, copper demand growth is more than its supply growth. The reason for this matter is economic growth and population increase [2]. Therefore, the supply and demand management of copper and its products is an important issue that can be used as the concept of supply chain management.

Supply chain management is an approach that coordinates suppliers, manufactures, distributers, and retailers in order to satisfy the needs of customers as much as possible. In the meantime, the goal is to satisfy the proper service level [3]. Decisions in the supply chain are divided into three phases: strategic, tactical, and operational. In recent years, network design, which is one of the strategic level decisions, has become the most important issue due to competition in the world market.

Traditional network design in the supply chain determines the structure, number, and capacity of facilities. It also specifies the mode of transportation and the type of communication [4]. Reverse Logistics (RL) is a noticeable topic in developed countries. RL is concerned with returned product flow; while the Closed-Loop Supply Chain (CLSC) considers forward and backward flows [5]. Utilizing CLSC can be a way to achieve sustainable development goals in the industrial area. Many studies on the CLSC area have been done in various cases such as citrus [5], faucet [6], gold [7], tire [8], and oil [9] industries.

In mining industries, the use of metals such as copper and its products is increased with the development of industrial infrastructure in countries. Copper can be recycled again and again without losing its original properties.

Figure 1 shows copper mine production by region, 1960 versus 2018. In this figure, the production of different regions has changed over time. For example, the share of Latin American production in this period increased from 19 to 42%. The reason for the increase is

*Corresponding Author Institutional Email: *hkhademiz@yazd.ac.ir* (H. Khademi-Zare)

Please cite this article as: M. Akbari-Kasgari, H. Khademi-Zare, M.B. Fakhrzad, M. Hajiaghaei-Keshteli, M. Honarvar. A Closed-loop Supply Chain Network Design Problem in Copper Industry, International Journal of Engineering (IJE), IJE TRANSACTIONS A: Basics Vol. 33, No. 10, (October 2020) 2008-2015

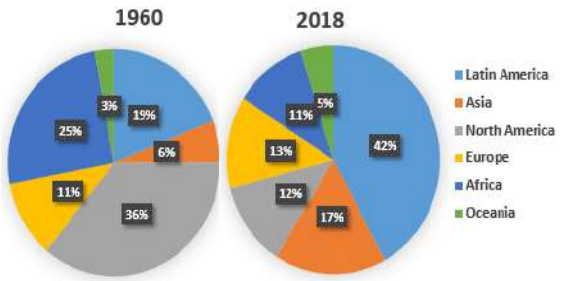

Figure 1. Copper mine production by Region, 1960 versus 2018 (ICSG)

the discovery of copper mines in Chile and Peru. These two countries are the largest copper producers in the world, located in Latin America. Production in Latin America in 1960 was less than 750,000 tones, but in 2018 it reached 8.7 million tones (The World Copper Factbook 2019). It can be concluded that the discovery or non-discovery of copper mines, as well as the use of reserves, affects the production trend in an area over time.

Researchers conducted studies on various areas of copper such as processing slags of copper production [10], renewable energy in copper production [11], copper mining productivity [12], improved copper smelter, and converter productivity [13]. There is no paper on copper Supply Chain Network Design (SCND), to the best of our knowledge, although network design is a configuration which can help the supply chain to perform well [14].

In this paper, we design an SCND model for the copper supply chain. Besides, the proposed model is designed as a closed-loop to put the aforementioned real-world suppositions into practice.

The Copper supply chain includes mining, refining, fabrication, manufacturing, use, waste management, and recycling stages. Minerals are extracted from mines, copper ores are crushed, concentrates and tailings are produced during processes, and the concentrates are converted to copper with higher purity in the smelter stage. In the fabrication stage, some semi-finished products are produced [1].

The rest of the paper is organized as follows: Section 2 reviews the literature briefly. The proposed problem is precisely defined and formulated in section 3. Section 4 explains the solution method and also presents computational experiments and sensitivity analysis. Finally, conclusion and future opportunities are brought in section 5.

2. LITERATURE REVIEW

The lack of rich literature in the SCND of the mining industry forced us to review the SCND models in other industries. In the following, we review the literature briefly. Pishvaee et al. [15] designed a multi-stage RL network. They proposed a Mixed Integer Linear Programming (MILP) model and solved it by a metaheuristic algorithm. Then, Kannan et al. [16] developed the pishvaee et al. [15] model by adding a term related to carbon to the objective function. They solved the MILP model by using an exact method and implemented it in plastic industry. Zadeh et al. [17] designed a steel supply chain network. Their model included iron ore mines, raw steel producers, steel companies, and also customers. They formulated the proposed network by using Mixed Integer Non-Linear Programming (MINLP) and MILP models by considering uncertainty and solved them by an exact method. The results showed that the MILP approach is better than MINLP for their model. Fallah-Tafti et al. [18] designed a CLSC network. They combined strategic and tactical decisions in order to make optimal decisions. The problem was formulated as a multi-objective MILP and solved by possibilistic-STEM. Ahmadi Yazdi and Honarvar [19] designed a logistic network and considered pricing policy in the dual-channel. They proposed a deterministic and a stochastic MILP model for the network. The scenario-tree method was used to solve the problem. Zohal and Soleimani [7] proposed a green forward/ reverse logistic network. In their integer linear programming model costs and emissions were minimized. They solved the model by metaheuristic and exact methods and implemented it in gold industry. Talaei et al. [20] proposed a green CLSC network. They formulated the problem as an MILP model. Costs and carbon dioxide emission rates were minimized in the model. An exact method was implemented to solve the uncertain model. Their case study was Copiers industry. Cheraghalipour et al. [5] proposed a citrus CLSC network. They formulated the problem as a Mixed Integer Programming (MIP) model and solved it by using metaheuristics algorithms. Jalali et al. [21] developed an SCND problem with disruption supposition. In their paper, a new two-stage stochastic MIP model was developed under uncertainty to minimize the costs. They solved the problem by using an exact method. Seifbarghi et al. [22] designed a CLSC network for paper industry. They formulated the problem as an MIP model. The model was solved by using fuzzy goal programming and applied in Iran. Zegordi et al. [23] designed a CLSC network. They also decided to supplier selection based on discount factor. The problem was formulated as an MIP model and costs were minimized on it. Then the model was solved by using an exact method. Leins et al. [24] investigated copper supply and value chain across Zambia, Switzerland and China. Valueworks have shown that mining infrastructures such as insurance, transportation, finance, trade, etc. affect the decisions of the copper supply chain. Among them, the financial issue was more important. Sherafati et al. [25] proposed an SCND problem. They maximized the profit and

prioritized the less developed regions in order to social community development in the uncertain model. The problem was formulated as an MINLP model and was solved by an exact method. They implemented the model in cable industry. Mardan et al. [26] designed a green CLSC network. The problem was formulated as an MILP model. They minimized the total costs and the environmental topic of the supply chain. The model was solved by using an exact approach. They implemented the model in wire-and-cable industry. Gholipoor et al. [6] presented a faucet CLSC network design problem. The objective function of the model was maximizing the profit. Also, they paid attention to environmental issue. The proposed model was as MILP by considering uncertainty. It was solved by an exact method and was implemented in a real case study. Valderrama et al. [14] designed a supply chain network in iron ore industry. Environmental and social aspects of sustainable development were considered in their research. They formulated the problem as an MILP model. The model was solved by an exact method.

A review of literature and Table 1 reveal gaps in previous researcher's studies, which we list here: 1- Despite the fact that mining industries are the basis of economic development in countries [27], a few studies have been done on their network design. 2- Despite the fact that copper mineral metal has high recyclability and factors such as population growth and increasing urbanization rates etc. increased its demand more than double between 1990 and 2015 [28], to the best of our knowledge, no studies have been performed on copper supply chain network design so far. 3- Network design provides the best structure for the supply chain so that it can have high economic performance in the long term [14], but to the best of our knowledge, there has not been a paper with a formal mathematical model for designing a copper supply chain network.

In this paper, we will cover deficit of research in the mining industry network design area. SCND models need to be applied in a specific industry because there is not the same solution for network design problems [14]. The copper industry is very important and it is necessary to pay attention to it because this useful metal has high recyclability and the development of human societies has increased its demand in recent years. Therefore, our contribution is to provide a network design model for the copper supply chain. In our proposed model copper scrap management is considered. This is very important and worthy for the following reasons: Copper is a non-renewable metal and has high recyclability. Also, the environmental aspect of sustainable development is considered by recycling it.

Regarding managerial insights, it should be said that our model can help managers to have proper strategic planning in the copper industry and similar industries. In addition, the recycling of scrap saves costs, energy, and consumption of this non-renewable metal and it does not endanger the rights of future generations.

3. PROBLEM FORMULATION

In this section, we propose and formulate a model for the aforementioned problem. As shown in Figure 2, factories manufacture products. Then, customers receive them through distribution centers. Distribution centers deliver them to customers. When customers used products, they return them to the scrap product warehouses as scrap. Then, scrap products are transported from scrap product warehouses to production factories.

Factories melt scrap and reuse them in production cycle. Figure 2 shows the proposed copper supply chain network.

This supply chain has some features that distinguish it from other supply chains, which we describe below: 1- In this chain, scrap does not turn into iron ore, which is a raw material. Rather, it is converted into usable products

TABLE 1. Literature review of SCND

Authors	Network			Model			Solution Method			Industry
	OL	CL	RL	MILP	MINLP	MIP	E	M	MCDM	
[15]			*	*				*		
[16]			*	*			*			Plastic
[17]	*			*	*		*			Steel
[18]		*		*					*	
[19]		*		*			*			
[7]		*		*			*	*		Gold
[20]		*		*			*			Copier
[5]		*				*		*		Citrus
[21]		*				*	*			
[22]		*				*			*	Paper
[23]		*				*	*			
[25]	*				*		*			Cable
[26]		*		*			*			Wire and Cable
[6]		*		*			*			Faucet
[14]		*		*			*			Iron Ore
This paper		*				*	*			Copper

OL: Open Loop CL: Closed Loop RL: Reverse Logistic MILP: Mixed Integer Linear Programming MINLP: Mixed Integer Non-Linear Programming MIP: Mixed Integer Programming E: Exact M: Metaheuristic MCDM: Multiple Criteria Decision Making

in the factory after some processes. These conditions save a lot of energy and costs. In copper production factories, there are two production technology (pyrometallurgy and hydrometallurgy). Extracted raw materials from the mine, can be produced in two technologies, but scrap can only be produced by one technology (pyrometallurgy). This feature forces us to use two different decision variables to show the amount of production in the factory (the details are described in the model). In fact, this feature differentiates the model structure (decision variables and constraints) of the copper supply chain network design problem from other existing models. 2- The location of the mines (as suppliers) are always fixed. It means that they are not potential and it cannot be decided to build them. Therefore, equipment and facilities in the chain should be set according to their locations. 3- Copper can be recycled again and again and its value does not decrease due to recycling. Also, recycled copper can be used in the same copper supply chain.

Model assumptions:

- The location of customers and mines are fixed and other locations are potential.
- Capacity of mines, factories, and warehouses are finite.
- There is no flow between the same facilities.
- It is assumed that scrap warehouses deliver scrap to the production factory based on their weight, and the scrap of all products is considered the same.
- Raw materials extracted from the mine can be produced by two production technology: Pyrometallurgy and Hydrometallurgy, but scrap can only be produced by Pyrometallurgy.

The indices, parameters, and decision variables are shown in Table 2, 3, and 4, respectively.

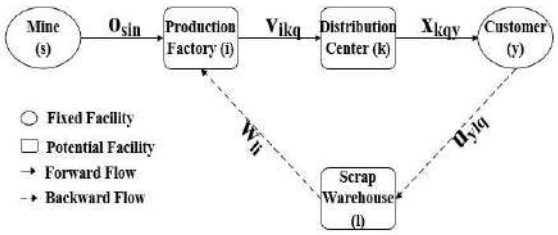

Figure 2. Proposed copper CLSC

TABLE 2. List of Indices

Indexes	Description
s	Fixed Suppliers (Mines) $s \in \{1,2,...,S\}$
i	Potential production factory $i \in \{1,2,...,I\}$
k	Potential distribution center $k \in \{1,2,...,K\}$
l	Potential scrap warehouse $l \in \{1,2,...,L\}$
y	Fixed customer zones $y \in \{1,2,...,Y\}$
q	Product type $q \in \{1,2,...,Q\}$
n	Raw Material $n \in \{1,2,...,N\}$
e	Production technology $e \in \{1,2,...,E\}$

TABLE 3. List of Parameters

Parameters	Description
sp_q	Unit selling price of product q
fc_i	Opening cost of production factory i
fk_k	Opening cost of distribution center k
fn_l	Opening cost of scrap warehouse l
$p1_{sn}$	Unit mining cost of raw material n from mine s
cc	Unit transportation cost between scrap warehouse and production factory
tc_n	Unit transportation cost of raw material n between mine and production factory
mc_q	Unit transportation cost of product q between production factory and distribution center
sc_q	Unit transportation cost of product q between distribution center and customer
bc_q	Unit transportation cost of scrap product q between customer and scrap warehouse
$e1_{si}$	Distance between mine s and production factory i
$e2_{ik}$	Distance between production factory i and distribution center k
$e3_{ky}$	Distance between distribution center k and customer y
$e4_{yl}$	Distance between customer y and scrap warehouse l
$e5_{li}$	Distance between scrap warehouse l and production factory i
pc_{qe}	Unit production cost of product q from production technology e (from raw material)
ts_q	Unit production cost of product q from scrap
$a2_q$	Unit cost-saving in production of product q due to recycling
$d1_{yq}$	Demand of customer y from product q
ε_{yq}	Amount of scrap product q returned from the customer y

cs_{sn}	Maximum capacity of mine s from raw material n
ci_{iq}	Maximum production capacity of production factory i from product q
ck_{kq}	Maximum capacity of distribution center k from product q
cn_{lq}	Maximum capacity of scrap warehouse l from product q
$a3_i$	Percentage of total production in production factory i that related to production from scrap
$a4_i$	Conversion rate of raw material to product in production factory i
$a5_i$	Conversion rate of scrap to product in production factory i

TABLE 4. List of Decision Variables

Decision Variables	Description
ift_i	1 if production factory i is opened and 0 otherwise
fk_k	1 if distribution center k is opened and 0 otherwise
fn_l	1 if scrap product warehouse l is opened and 0 otherwise
$o_{\sin}$	Flow of raw material n from mine s to production factory i
$v1_{iqe}$	Quantity of product q that produced in production factory i by production technology e (from raw material)
$v2_{iq}$	Quantity of product q that produced in production factory i from scrap
v_{ikq}	Quantity of product q that is transported from production factory i to distribution center k
x_{kqy}	Quantity of product q that is transported from distribution center k to customer y
u_{ylq}	Quantity of scrap product q that is transported from customer y to scrap warehouse l
w_{li}	Quantity of scrap that is transported from scrap warehouse l to production factory i

Equation (1) shows the objective function. It maximizes supply chain profit. The Profit equals revenues minus costs. In our model, the products are produced either from raw material or from scrap. The sum of these products is sold in the market and the revenue of the chain is equal to the value of their sales. Costs in our model include the following: opening costs, mining, transportation, and production.

$$\begin{aligned} MaxZ = & \sum_k \sum_y \sum_q (sp_q - (sc_q \times e3_{ky})) \times x_{kqy} - \\ & (\sum_s \sum_i \sum_n p1_{sn} + (tc_n \times e1_{si}) \times o_{\sin} + \\ & \sum_i \sum_q \sum_e pc_{qe} \times v1_{iqe} + \sum_i \sum_q (ts_q - a2_q) \times v2_{iq} \\ & + \sum_i \sum_k \sum_q mc_q \times e2_{iq} \times v_{ikq} + \\ & \sum_y \sum_l \sum_q bc_q \times e4_{yl} \times u_{ylq} + \\ & \sum_l \sum_i cc \times e5_{li} \times w_{li} + \\ & \sum_i fc_i \times ift_i + \sum_k fk_k \times ifk_k + \\ & \sum_l fn_l \times ifn_l) \end{aligned} \quad (1)$$

Equations (2)-(3) show production balance constraints.

$$\sum_e v1_{iqe} + v2_{iq} = \sum_k v_{ikq} \qquad \forall i, q \quad (2)$$

$$a3_i \times \sum_k \sum_q v_{ikq} = \sum_q v2_{iq} \qquad \forall i \quad (3)$$

Equations (4)-(6) show input and output balance constraints.

$$a4_i \times \sum_s \sum_n o_{\sin} = \sum_q \sum_e v1_{iqe} \qquad \forall i \quad (4)$$

$$a5_i \times \sum_l w_{li} = \sum_q v2_{iq} \qquad \forall i \quad (5)$$

$$\sum_i v_{ikq} = \sum_y x_{kqy} \qquad \forall k, q \quad (6)$$

Equation (7) shows demand balance constraint.

$$\sum_k x_{kqy} \le d1_{yq} \qquad \forall y, q \quad (7)$$

Equations (8)-(10) show scrap flow balance constraints in backward.

$$\sum_k x_{kqy} \ge \sum_l u_{ylq} \qquad \forall y, q \quad (8)$$

$$\sum_l u_{ylq} \le \varepsilon_{yq} \qquad \forall y, q \quad (9)$$

$$\sum_y \sum_q u_{ylq} = \sum_i w_{li} \qquad \forall l \quad (10)$$

Equations (11)-(14) show capacity constraints.

$$\sum_k \sum_q v_{ikq} \le \sum_q ift_i \times ci_{iq} \qquad \forall i \quad (11)$$

$$\sum_i \sum_n o_{\sin} \le \sum_n cs_{sn} \qquad \forall s \quad (12)$$

$$\sum_i \sum_q v_{ikq} \le \sum_q ifk_k \times ck_{kq} \qquad \forall k \quad (13)$$

$$\sum_{y}\sum_{q} u_{ylq} \le \sum_{q} ifn_{l} \times cn_{lq} \qquad \forall l \qquad (14)$$

Equation (15) shows the decision variables domain constraint.

$$ft_i, ifk_k, ifn_l \in \begin{cases}1\\0\end{cases}, \quad o_{\sin}, v1_{iqe}, v2_{iq}, v_{ikq}, x_{kqy}, u_{ylq}, w_{li} \ge 0 \qquad (15)$$

Constraint (2) shows that products are produced by raw materials and scrap in production factories. Constraint (3) shows that production from scrap is only a part of the total production in each production factory. Constraints (4-5) show that production factory inputs, which are raw materials and scrap, are converted into products after the production process. In mathematical equations, we used conversion coefficients to show the production process. Constraint (6) shows input and output balance for each distribution center. Constraint (7) shows demand constraint for each customer. Constraints (8-10) show scrap flow balance in backward. Equations (11-14) show capacity constraints for different facilities. Equation (15) shows the decision variables domain constraint.

4. SOLUTION APPROACH AND COMPUTATIONAL EXPERIMENTS

We solved all test problems by using the CPLEX solver of GAMS commercial software version 24.8.2. All calculations were done on a personal computer with Intel (R) Core (TM) i7-2670QM CPU @ 2.20 GHz, 8.00 GB RAM memory.

4. 1. Instances In this section, twelve test problems are examined in different sizes (small, medium, and large). There are four test problems in each size. They are shown in Table 5.

Table 5 shows that computational time and objective function value increase by increasing the size of the problem.

4. 2. Sensitivity Analysis In this section, the model parameters are changed to determine their effect on the objective function. Sensitivity analysis is performed on the first example from Table 5. The results are shown in Figure 3 and Table 6.

In sensitivity analysis, all parameters were changed by 70 and 130% of their original value. Among them, sp_q, fc_i, fk_k, $p1_{sn}$, tc_n, $e1_{si}$, $e3_{ky}$, pc_{qe}, ts_q, $a2_q$, $d1_{yq}$ parameters had the greatest impact on the objective function. According to Figure 3 and Table 6, a change in the amount of the mentioned parameters leads to changes in the objective function, but as can be seen, sp_q, pc_{qe}, and $d1_{yq}$ parameters have the greatest impact on the objective function compared to others.

The results of sensitivity analysis show that the demand, selling price and production cost are important factors in the proposed model and have a greater impact on the supply chain profit than other parameters. Supply chain managers can use these results to design

TABLE 5. Test problems

Size	Problem Number	Size of Problems (s, q, i, k, y, l, n, e)	Objective Function (Monetary Unit)	Computational Time (Second)
small	1	2,2,2,2,3,2,2,2	36634240	0.450
	2	2,2,2,2,4,2,2,2	52456140	0.567
	3	2,3,3,3,5,3,2,2	103578300	0.471
	4	2,3,3,3,6,3,2,2	119613100	0.494
medium	5	3,4,4,4,8,4,2,2	220126500	0.567
	6	3,4,4,4,9,4, 2,2	251435600	0.716
	7	3,5,5,5,10,5,2,2	364928900	0.625
	8	3,5,5,5,11,5,2,2	391258800	0.667
large	9	4,6,6,6,13,6,2,2	539564200	1.433
	10	4,6,6,6,14,6, 2,2	590285400	1.424
	11	4,7,7,7,15,7,2,2	731415700	1.698
	12	4,7,7,7,16,7, 2,2	780989400	1.765

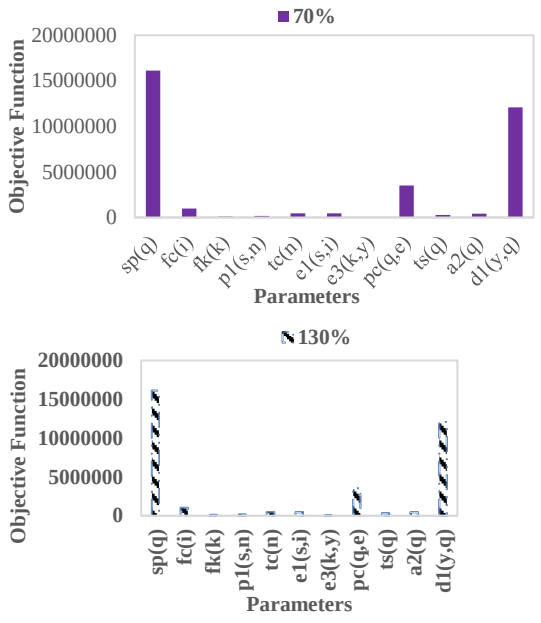

Figure 3. The parameters' impact on the objective function

network, market and customer issues, as well as production processes.

TABLE 6. Sensitivity analysis

parameter	Sensitivity analysis	Objective function	Difference of objective value	
			70%	130%
sp_q	70	20524640	16109600	16109610
	100	36634240		
	130	52743850		
fc_i	70	37624590	990350	990340
	100	36634240		
	130	35643900		
fk_k	70	36733010	98770	98760
	100	36634240		
	130	36535480		
$p1_{sn}$	70	36796160	161920	161910
	100	36634240		
	130	36472330		
tc_n	70	37083880	449640	449630
	100	36634240		
	130	36184610		
$e1_{si}$	70	37083880	449640	449630
	100	36634240		
	130	36184610		
$e3_{ky}$	70	36652050	17810	17800
	100	36634240		
	130	36616440		
pc_{qe}	70	40148700	3514460	3514450
	100	36634240		
	130	33119790		
ts_q	70	36928570	294330	294320
	100	36634240		
	130	36339920		
$a2_q$	70	36214110	420130	420130
	100	36634240		
	130	37054370		
$d1_{yq}$	70	24553710	12080530	12080540
	100	36634240		
	130	48714780		

5. CONCLUSION AND FUTURE STUDIES

The Demand for copper has increased by development of technology and communication infrastructure. Copper can be extracted from mines. Its mines are not distributed throughout the world uniformly. Therefore, it is necessary to optimize copper supply chain so that everyone can use it fairly. In addition, copper can be recycled again and again. But to the best of our knowledge, there is no paper about copper SCND.

In this paper, an MIP model for a copper CLSC is proposed. Section 3 of this paper, describes the assumptions and formulation of the problem. The problem is solved by an exact approach in GAMS 24.8.2 software with CPLEX solver. Sensitivity analysis is implemented for parameters of the model in section 4. In the future, the present model can be developed by considering the uncertainty of the parameters and vehicle routing operations.

6. REFERENCES

1. Zhang, L., Cai, Z., Yang, J., Yuan, Z. and Chen, Y., "The future of copper in China—A perspective based on analysis of copper flows and stocks", ***Science of the Total Environment***, Vol. 536, (2015), 142-149, https://doi.org/10.1016/j.scitotenv.2015.07.021.
2. Elshkaki, A., Graedel, T. E., Ciacci, L. and Reck, B. K., "Copper demand, supply, and associated energy use to 2050", ***Global Environmental Change***, Vol. 39, (2016), 305-315, https://doi.org/10.1016/j.gloenvcha.2016.06.006.
3. Simchi-Levi, D., Kaminsky, P., Simchi-Levi, E., and Shankar, R., "Designing and managing the supply chain: concepts, strategies and case studies. Tata McGraw-Hill Education", (2008).
4. Fleischmann, M., Bloemhof-Ruwaard, J. M., Dekker, R., Van der Laan, E., Van Nunen, J. A. and Van Wassenhove, L. N., "Quantitative models for reverse logistics: A review", ***European Journal of Operational Research***, Vol. 103, No. 1, (1997), 1-17, https://doi.org/10.1016/S0377-2217(97)00230-0.
5. Cheraghalipour, A., Paydar, M. M. and Hajiaghaei-Keshteli, M., "A bi-objective optimization for citrus closed-loop supply chain using Pareto-based algorithms", ***Applied Soft Computing***, Vol. 69, (2018), 33-59, https://doi.org/10.1016/j.asoc.2018.04.022.
6. Gholipoor, A., Paydar, M. M. and Safaei, A. S., "A faucet closed-loop supply chain network design considering used faucet exchange plan", ***Journal of Cleaner Production***, Vol. 235, (2019), 503-518, https://doi.org/10.1016/j.jclepro.2019.06.346 .
7. Zohal, M. and Soleimani, H., "Developing an ant colony approach for green closed-loop supply chain network design: a case study in gold industry", ***Journal of Cleaner Production***, Vol. 133, (2016), 314-337, https://doi.org/10.1016/j.jclepro.2016.05.091.
8. Sahebjamnia, N., Fathollahi-Fard, A. M. and Hajiaghaei-Keshteli, M., "Sustainable tire closed-loop supply chain network design: Hybrid metaheuristic algorithms for large-scale networks", ***Journal of Cleaner Production***, Vol. 196, (2018), 273-296, https://doi.org/10.1016/j.jclepro.2018.05.245.
9. Paydar, M. M., Babaveisi, V. and Safaei, A. S., "An engine oil closed-loop supply chain design considering collection risk", ***Computers & Chemical Engineering***, Vol. 104, (2017), 38-55, https://doi.org/10.1016/j.compchemeng.2017.04.005.

10. Yusupkhodjaev, A. A., Khojiev, S. T., Valiev, X. R., Saidova, M. S. and Omonkhonov, O. X., "Application of Physical and Chemical Methods for Processing Slags of Copper Production," ***International Journal of Advanced Research in Science, Engineering and Technology***, Vol. 6, No. 1, (2019), 7957.
11. Moreno-Leiva, S., Haas, J., Junne, T., Valencia, F., Godin, H., Kracht, W., Nowak, W. and Eltrop, L, "Renewable energy in copper production: A review on systems design and methodological approaches"**,** ***Journal of Cleaner Production***, Vol. 246, (2020), 118978, https://doi.org/10.1016/j.jclepro.2019.118978.
12. de Solminihac, H., Gonzales, L. E. and Cerda, R., "Copper mining productivity: lessons from Chile", ***Journal of Policy Modeling***, Vol. 40, No. 1, (2018), 182-193, https://doi.org/10.1016/j.jpolmod.2017.09.001.
13. Jak, E., Shishin, D., Hawker, W., Vaughan, J. and Hayes, P. C., "Improved copper smelter and converter productivity through the use of a novel high-grade feed", In Extraction 2018, 265-271, Springer, Cham, (2018), https://doi.org/10.1007/978-3-319-95022-8_21.
14. Valderrama, C. V., Santibanez-González, E., Pimentel, B., Candia-Véjar, A. and Canales-Bustos, L., "Designing an environmental supply chain network in the mining industry to reduce carbon emissions", ***Journal of Cleaner Production***, Vol. 254, (2020), 119688, https://doi.org/10.1016/j.jclepro.2019.119688.
15. Pishvaee, M. S., Kianfar, K. and Karimi, B., "Reverse logistics network design using simulated annealing", ***The International Journal of Advanced Manufacturing Technology***, Vol. 47, No. (1-4), (2010), 269-281, https://doi.org/10.1007/s00170-009-2194-5.
16. Kannan, D., Diabat, A., Alrefaei, M., Govindan, K. and Yong, G., "A carbon footprint based reverse logistics network design model", ***Resources, Conservation and Recycling***, Vol. 67, (2012), 75-79, https://doi.org/10.1016/j.resconrec.2012.03.005.
17. Zadeh, A. S., Sahraeian, R. and Homayouni, S. M., "A dynamic multi-commodity inventory and facility location problem in steel supply chain network design", ***The International Journal of Advanced Manufacturing Technology***, Vol. 70, No. (5-8), (2014), 1267-1282, https://doi.org/10.1007/s00170-013-5358-2.
18. Fallah-Tafti, A. L., Sahraeian, R., Tavakkoli-Moghaddam, R. and Moeinipour, M., "An interactive possibilistic programming approach for a multi-objective closed-loop supply chain network under uncertainty", ***International Journal of Systems Science***, Vol. 45, No. 3, (2014), 283-299, https://doi.org/10.1080/00207721.2012.720296.
19. Ahmadi Yazdi, A., "A two stage stochastic programming model of the price decision problem in the dual-channel closed-loop supply chain", ***International Journal of Engineering***, ***Transactions B: Applications,*** Vol. 28, No. 5, (2015), 738-745, doi: 10.5829/idosi.ije.2015.28.05b.12.
20. Talaei, M., Moghaddam, B. F., Pishvaee, M. S., Bozorgi-Amiri, A. and Gholamnejad, S., "A robust fuzzy optimization model for carbon-efficient closed-loop supply chain network design problem: a numerical illustration in electronics industry", ***Journal of Cleaner Production***, Vol. 113, (2016), 662-673, https://doi.org/10.1016/j.jclepro.2015.10.074.
21. Jalali, G., Tavakkoli-Moghaddam, R., Ghomi-Avili, M. and Jabbarzadeh, A., "A network design model for a resilient closed-loop supply chain with lateral transhipment", ***International Journal of Engineering***, Vol. 30, No. 3, (2017), 374-383, doi: 10.5829/idosi.ije.2017.30.03c.07.
22. Seifbarghi, M., Bozorgi-Amiri, A., Rahmani-Ahranjani, A. and Najafi, E., "Managing environmentally conscious in designing closed-loop supply chain for the paper industry", ***International Journal of Engineering***, Vol. 30, No. 7, (2017), 1038-1047, doi: 10.5829/ije.2017.30.07a.13.
23. Zegordi, S. H., Hosseinzadeh, A., Nahavandi, N. and Sadeghi Rad, R., "An integrated closed-loop supply chain configuration model and supplier selection based on offered discount policies", ***International Journal of Engineering***, Vol. 31, No. 3, (2018), 440-449, doi: 10.5829/ije.2018.31.03c.06.
24. Leins, S., Kesselring, R. and Schulz, Y., "Valueworks: effects of financialization along the copper value chain "*SNIS Working Papers*, (2019).
25. Sherafati, M., Bashiri, M., Tavakkoli-Moghaddam, R. and Pishvaee, M. S., "Supply chain network design considering sustainable development paradigm: A case study in cable industry", ***Journal of Cleaner Production***, Vol. 234, (2019), 366-380, https://doi.org/10.1016/j.jclepro.2019.06.095.
26. Mardan, E., Govindan, K., Mina, H. and Gholami-Zanjani, S. M., "An accelerated benders decomposition algorithm for a bi-objective green closed loop supply chain network design problem", ***Journal of Cleaner Production***, Vol. 235, (2019), 1499-1514, https://doi.org/10.1016/j.jclepro.2019.06.187.
27. Umar, Z., Shahzad, S. J. H. and Kenourgios, D., "Hedging US metals & mining Industry's credit risk with industrial and precious metals", ***Resources Policy***, Vol. 63, (2019), 101472, https://doi.org/10.1016/j.resourpol.2019.101472.
28. Kuipers, K. J., van Oers, L. F., Verboon, M. and van der Voet, E., "Assessing environmental implications associated with global copper demand and supply scenarios from 2010 to 2050", ***Global Environmental Change***, Vol. 49, (2018), 106-115, https://doi.org/10.1016/j.gloenvcha.2018.02.008.

Persian Abstract

چکیده

بی‌شک فلزات اساس توسعه پایدار همه جوامع بشری هستند. در قرن گذشته، نقش مس به عنوان سومین فلز پرکاربرد پس از فولاد و آلومینیوم، حیاتی بوده است. مس یک فلز قابل بازیافت است. آن کاربردهای زیادی مانند برق صنعتی، لوله‌کشی، سیم‌کشی، تجهیزات الکترونیکی، حمل‌ونقل و زیرساخت‌ها دارد. امروزه با رشد صنعت در جوامع، تقاضا برای مس افزایش یافته است. این به ما انگیزه داد تا برای اولین بار طراحی شبکه زنجیره تامین آن را مطالعه کنیم. بر مبنای بهترین دانش ما، تاکنون هیچ تحقیقی درباره طراحی شبکه زنجیره تامین مس انجام نشده است. هدف این مقاله، حداکثر کردن سود در زنجیره تامین حلقه بسته مس است. ما این مسئله طراحی شبکه را به صورت یک مدل برنامه‌ریزی عدد صحیح مختلط فرموله می‌کنیم. مدل به صورت یک هدفه و چند محصولی در نظر گرفته می‌شود. جواب دقیق مدل با استفاده از از نرم‌افزار گمز پیدا شده است. آنالیز حساسیت نتایج مفیدی ارائه می‌دهد که مدیران می‌توانند در تصمیم‌گیری‌ها از آنها بهره ببرند.

International Journal of Engineering

Journal Homepage: www.ije.ir

A Novel Excellence Model of the Information and Communications Technology Industry: Case Study on Telecommunications Backbone Network of Iran

M. R. Zare, A. Aghaie*, Y. Samimi, A. Asl Hadad

Faculty of Industrial Engineering, K. N. Toosi University of Technology, Tehran, Iran

P A P E R I N F O

Paper history:
Received 26 April 2020
Received in revised form 19 July 2020
Accepted 25 August 2020

Keywords:
Causal Relationships
Criterion Weights
Customized Excellence Model
European Foundation
Information and Communications Technology
Telecommunications Backbone Network

A B S T R A C T

Todays, Information and Communications Technology (ICT), as one of the most effective factors of the advancement in all the aspects such as governance, security and risk, economics and technology, which is among the industries rapidly growing and developing. This paper examines the specific criteria and standards of ICT area for improving the quality of the services of the Telecommunications Backbone Network of Iran (TBNI). The research was done through the two methods of data collection, library and the field study. European Foundation for Quality Management Excellence Model (EFQM) was selected as the base model and with full attention to the specific requirements of ICT industry and due to adapt this model from the viewpoints of the security and risk, governance and economic, a novel integrated excellence model of TBNI was developed and customized. To achieve the highest level of reliability and internal coherence of each criterion, based on expert opinion polls, sub-criteria was categorized and analyzed in several stages using the factor analysis approach. The causal relationships and the influence of the criteria of this model on each other were investigated and the weights of each criterion and sub-criteria, using the structural analysis and shannon entropy methods, were determined. The self-evaluation of TBNI was systematically carried out and major opportunities for the improvement had been identified. Results showed that the establishment of this model had led to an improvement in a quality of services provided by this network and the products of all organizations that use any services of TBNI.

***doi**: 10.5829/ije.2020.33.10a.20*

1. INTRODUCTION AND LITERATURE REVIEW

The ICT industry as a very important driver of the international economy, is the backbone of the modern business era, the pillar of the development of the countries and a benchmark for other leading industries and organizations. Government sector as an upstream authority plays a critical infrastructural role in ensuring an efficient, agile and sustainable ICT industry. All the communication tools used in human daily life benefit from a communication platform regarded as the backbone of the telecommunication network. In Iran, the Telecommunications Infrastructure Company (TIC) is solely in charge of the backbone of the telecommunication network of Iran (TBNI) and the only governing authority of the Ministry of ICT. Therefore, due to the role of this network in sustainable development and in order to meet the regulatory requirements and ever-growing beneficiaries' expectations, continual improvement of the service quality is of vital importance. One of the main purpose of this research is to provide a novel integrated excellence model for TBNI to achieve this ultimate goal.

TBNI provides the long-distance and the international remote traffic, supports and manages any type of voice, image and data traffic required by Iran for the operators, the government and non-governmental applicants, the natural and the legal entities and so on in the inter-provinces areas [1]. TBNI consist of three layers, i.e. the media layer, the transmission layer and the service layer [2].

The quality management and the excellence management approaches both have begun to develop and progress scientifically and practically in the 1960s [3].

*Corresponding Author Email: *aaghaie@kntu.ac.ir* (A. Aghaie)

Please cite this article as: M. R. Zare, A. Aghaie, Y. Samimi, A. Asl Hadad A Novel Excellence Model of the Information and Communications Technology Industry: Case Study on Telecommunications Backbone Network of Iran, International Journal of Engineering (IJE), IJE TRANSACTIONS A: Basics Vol. 33, No. 10, (October 2020) 2016-2029

The performance appraisal is an essential part of the measurement and learning process which engages the employees in the self-assessment and enables the organizations to systematically monitor and identify the strengths, the opportunities for improvement as well as the progress of the excellence programs [4–6]. The organizations of the private and the public sectors have adopted the use of the self-assessment methodology as an independent strategy [7]. There is a general agreement that a systematic framework or approach is needed to operate comprehensive quality management. However, there is no single universally accepted frame work [8]. National Quality Awards and Business Excellence Awards are a framework for recognizing the efforts of organizations that make significant progress and achieve world-class performance based on a set of quality and excellence management principles and criteria [9, 10]. There are several other national awards, formed based on their programs to improve the quality in various industries [11, 12]. Many companies have also encountered problems due to various weaknesses of these models such as the sophisticated evaluation criteria, the excessively administrative formalities, the rigid procedures, and the lack of concentration, limiting their use in practice [13]. Researchers have concluded that quality of products and customers satisfaction are the most important criteria in project planning and supply chain network [14–16]. The Customer satisfaction depends on product quality, price and customers' preferences and demand [17–19].

To develop the framework of the excellence models based on the specific requirements of each organization and industry is critical to achieve the organizational perfection [20, 21]. Metaxas and Koulouriotis [13], in a study conducted to bridge the gap in the researches ran between the years 1990 to 2016, found out today, the organizations, moving towards the excellence, perfection and improvement of their service quality, more than before get involved with the leaders of the respective fields. The highlight of this study was that the ability to adapt to a turbulent environment only existing in a limited number of the frameworks, thus the development of the models of the existing business excellence to allow the flexibility in the industries and the key sectors such as telecommunications, transportation and so on through the case studies and the empirical studies are essential [13]. By applying the ISO 9001 standard, the organizations have been on the path to success, so top organizations in the world must be able to identify the quality engineering tools correctly and focus their approaches on the active approaches instead of reactive ones, achieve the sustainable success and the equal satisfaction of the beneficiaries, using the Excellence Model framework [22]. The specific standard designed for the ICT industry is the Telecom Quality Management System (TL 9000), which provides the ICT suppliers and service providers with Information Navigation and enables them to have a global standard specific to this industry. In addition, according to the recommendations of International Telecommunication Union (ITU) [23], the enhanced Telecom operations map (eTOM) model is a framework for conducting the business processes in the ICT industry and is commonly used for the telecommunications business management. eTOM usually brings up along with IT Infrastructure Library (ITIL) and the frameworks of both eTOM & ITIL as a part of the comprehensive quality management in ICT industry and follow a customer-oriented pattern. One of the eTOM's strengths as a business process framework, belongs to Next Generation Operations Support System (NGOSS) program in the telecommunication's management society and its relationship with the other activities in process [24]. Pereira et al. [25] Using the pragmatic perspective and the value management professional frameworks, namely Control Objectives for Information and Related Technologies (COBIT 5) and Value from IT (Val IT 2.0) introduced a capability model for the value management of ICT [25]. Eskildsen et al. [26], in a study of Danish companies using the EFQM model for self-evaluation, found no relationship between the weights of the model criteria and the score of those criteria. Eskildsen et al. [27], examined the weights of the criteria of excellence in private and public organizations, and observed the differences between Danish public and private organizations, with greater emphasis on employees in the public organizations and on the systems in the private organizations. The results indicated that the private organizations placed more weights on the leadership, policy, and strategy criteria than the government organizations [27]. In an applied research, Zare et al. [2] also investigated the control and the promotion of the service quality management and excellence of ICT in TBNI through an experimental and case study. The results indicated that using a customized excellence model in this network would lead to the improvement of the control, service quality and the excellence of ICT industry in Iran [2].

In this research, after taking the principles of total quality management into consideration, the various business excellence models, as well as exclusive standards of ICT industry, as listed in Table 1, have been scrutinized. This paper first summarizes the criteria in different models of excellence and, by focusing on developing a scoring model, makes it possible to identify areas for improvement and evaluate the expected results in an integrated and structural manner. Our exploratory studies showed that to improve the quality of the service and flexibility in national ICT industry, the criteria of security and risk, governance and economy must be taken into account to achieve a comprehensive and customized domestic evaluation model. Therefore, one of the objectives of this research is to present a novel TBNI

excellence model, which requires a careful study based on a scientific methodology validated by the viewpoints of university as well as industry experts.

2. METHODOLOGY

This research had two stages, i.e. the structure of the TBNI excellence model, the causal relationships and the influence of the criteria of this model on each other. Accordingly, to evaluate the TBNI, three hypotheses (hypotheses 1-3) were presented in the model structural stage and 18 hypotheses (hypotheses 4-21) in the causal relationships section of the TBNI excellence model:

To evaluate the TBNI:

1. The governance factor should be added as an effective criterion to the benchmarks of the basic excellence model.
2. It is necessary to add the Security and Risk factors as the effective criteria to the benchmarks of the basic excellence model.
3. It is necessary to add the economic factor as an effective criterion to the benchmarks of the basic excellence model.

For the causal relationships and the influence of the criteria of TBNI excellence model on each other:

4. Governance criterion influences the leadership criterion.
5. Leadership criterion influences the strategy criterion.
6. Leadership criterion influences the partnerships and resources criterion.
7. Leadership criterion influences the economic criterion.
8. Strategy criterion influences the people criterion.
9. Strategy criterion influences the partnerships and resources criterion.
10. Leadership criterion influences the security and risk criterion.
11. People criterion influences the processes, products and services criterion.
12. Partnerships and resources criterion influences the processes, products and services criterion.
13. Economic criterion influences the processes, products and services criterion.
14. Processes, products and services criterion influences the society results criterion.
15. Processes, products and services criterion influence the customer results criterion.
16. Security and risk criterion affects the society results criterion.
17. People criterion influence the people results criterion.
18. Economic criterion influences the criterion of the business results.
19. Criterion of the society results influences the criterion of the business results.
20. Criterion of the customer results influences the criterion of the business results.
21. Criteria of processes, products and services influences the criterion of the people results.

TABLE 1. Criteria of Excellence Models and Standards

Model/ Standard	Leadership	Strategy	People	Partnership & Resource	Process, Product & Service	Customer Results	People Results	Society Results	Business Results	Security & Risk	Governance	Economic
FQM (2013)	✓	✓	✓	✓	✓	✓	✓	✓				
MBNQA	✓	✓	✓	✓	✓	✓	✓					
Deming	✓	✓	✓	✓	✓	✓	✓		✓			
eTOM	✓	✓	✓	✓	✓	✓	✓	✓	✓	✓	✓	✓
PRINCE 2	✓	✓	✓		✓							
IMS	✓	✓	✓	✓	✓	✓	✓	✓	✓	✓	✓	✓
NTQAC* surveyed	✓	✓	✓	✓	✓	✓	✓	✓	✓			✓
TL 9000	✓	✓	✓	✓	✓	✓	✓	✓				✓
ISMS	✓	✓	✓	✓	✓	✓		✓		✓		✓
COBIT 5	✓	✓	✓						✓		✓	✓
ITIL	✓	✓	✓		✓		✓			✓		✓
Val IT	✓	✓			✓						✓	✓
Xerox	✓	✓		✓	✓	✓	✓		✓			✓
The proposed model	✓	✓	✓	✓	✓	✓	✓	✓	✓	✓	✓	✓

***** National Telecommunications Quality Awards Countries

To test the first and the second hypotheses, the experts' opinions about the need to add or not to add the governance, security and risk criteria to the basic excellence model were asked, and to test the third hypothesis, the experts' opinion about the overlap or non-overlap of the economic sub-criteria and the sub-criteria of the basic excellence model were questioned.

To test hypotheses 4-21, the experts were asked to find out the amount of the impact of the customized excellence model of the TBNI on each other for extract the causal relationships of excellence model.

Two methods of data collection were used in this study. A library method was used to collect the information on the subject literature, the research backgrounds, and the related theories from the libraries and the specialized articles and the field method along with the questionnaire distribution among the experts was used to collect the information to test the research hypotheses. Also, the structural equation modeling and Shannon entropy were used which are the main new approaches for solve the complex models and enabling the researchers to show the simultaneous effects of the variables on each other with an emphasis on the measurement errors [28–30].

3. THE POPULATION AND STATISTICAL SAMPLE

This research is based on the data collection of the telecommunication backbone network of all 31 provinces of Iran. Using the previous studies for the first stage of the research, an analytical model was developed to prepare two questionnaires; the questionnaire was distributed amongst 110 experts and 97 questionnaires were collected. The components of the questionnaires related to this stage of the research are presented in Tables 2 and 3. The validity of the research questionnaires is the content validity type prepared based on the theoretical principles and approved by the academic and organizational experts familiar with the models of excellence. The statistical population of the study consisting of the experts and managers of TIC, the academic professors and the experts of the governance sector related to the ICT industry, were selected for the compiling and reporting the models of excellence.

TABLE 2. Components of the first questionnaire related to stage one

Criterion Model\Framework	Security & Risk	Governance
eTOM, IMS, ISMS, ITIL, COBIT 5& Val IT	Items 1~ 20	Items 21~ 25

TABLE 3. Components of the second questionnaire related to stage one

Model\ Standard	Criterion
EFQM 2013, eTOM, IMS, ISMS, ITIL, COBIT 5, Val IT, TL 9000, Xerox & National Telecommunications Quality Awards of the countries surveyed	Items 1~ 62

For the second stage of the research, two questionnaires were distributed among 168 ICT experts, and all the questionnaires were collected. A part of the questionnaires prepared was shown (see Appendix Table 11). The questionnaires were systematically distributed via the paperless system available at the TIC for the experts of the TBNI, working in 31 provinces of Iran as shown in Table 4 and their responses were received by the same way.

4. DATA ANALYSIS

Based on the results of the test for first questionnaire related to stage one (see Appendix Table 12), the P-value for all 25 items is less than 0.05 and is equal to zero, so, the non parametric test value was significant for all the items. The value of the test statistics is significantly large for all the items. Therefore, it can be concluded that in all the cases, the experts agreed to add the relevant items under the security, risk and governance criteria.

The results of the evaluation and the reliability analysis of the questionnaire showed that items (sub-criteria) which their deletions increased the Cronbach's alpha, were excluded from the questionnaire. Among the 1st to the 20th item which were related to the security and risk criterion, Cronbachs' alpha of 4 items, i.e. the first, second, fourth and eighth items were greater than 0.8857. As a result, deleting them increased the Cronbach's alpha. Therefore, the said four items were excluded from the security and risk criterion, and the other items remain. Cronbach's alpha in all the twenty-one to twenty-five items of the governance criterion was less than 0.777, so, deleting them made no change in Cronbach's alpha [31]. Therefore, they were acceptable and were not be eliminated.

The second questionnaire examined the experts' opinions on the items identified by the models of the organizational excellence and the performance management in the field of ICT as well as the manner of the items classifications in the formats of the different criteria. To this end, the latest edition of the EFQM was selected as the basic model and the economic criterion was added to its nine criteria. To define and consider the manner of the items classification of each criterion, the data of the survey were analyzed, and the addresses were asked to comment on the appropriate dimension for each item. Then, it was assessed whether at least 50% of the survey respondents agreed to add the relevant items. The

results indicated that the P-value was less than 0.05, and it was equaled to zero for all the items. Therefore, the non parametric test was significant for all the items.The result was presented (see Appendix Table 13). Based on the above analysis, the reliability of the questionnaire criteria was shown (see Appendix Table 14).

Given that in a number of the criteria, the high number of the items could be problematic for the applicability of the model in practice, the next step was using the factor analysis to summarize the number of the sub-criteria (items). Accordingly, on the security and risk, governance and economic criteria as described in Table 5, the sub-criteria having the coefficients greater than 0.7 were selected.

To test the hypotheses related to second stage of this research (hypotheses 4–21) and to prepare the information to derive a model to find out the impact of the indigenous model of the TBNI as well as to extract the causal relationships and the influence of the criteria of this model on each other by the academic professors in the field of the quality management, the technical experts of this field, and the consultants of implementing the models of excellence. They offered their suggestions on the type of the relationship between the organizational excellence criteria based on their technical knowledge and experience at the numerous meetings; the sessions were run in a brainstorming manner. Finally, after discussing and exchanging their opinions, they proposed

TABLE 4. Questionnaire distribution

Respondents						Number of questionnaires sent	Location of the province	Network location
A set of responses to the received questionnaires	Experts & University Professors	Responsible experts	Heads of Departments	Deputy General Manager	General Managers			
168	168	33	35	31	31	168	31 provinces of Iran	TBNI (All over the provinces of Iran)

TABLE 5. Items on security and risk, governance and economic criteria

Criterion	sub-criteria
Security & Risk	Ensure senior management and board that processes and controls are in compliance with accepted standards.
	Emergency Preparedness and Response.
	Risk assessment to determine appropriate controls to achieve acceptable levels of risk.
	Avoidance and dynamic identification of information security incidents.
	Continuous assessment of information security and appropriate corrections.
	Planning for security management in line with required services and policies.
	Perform security control activity.
	Assessment and Audit of Infrastructure Security Support.
Governance	Ensure the organization complies with all existing governments regulations.
	Ensures the firm complies with all relevant legal requirements.
	Legal Requirements and Other Requirements.
	Compliance of IT services with external laws and regulations.
	Establish an effective governance review.
Economic	Ensuring that the company earns money through billing and receivables.
	Manage customer billing query.
	Receiving and evaluating a bill.
	Customer Assets.
	Create value for the customer and the organization.
	Optimizing the cost of business processes.
	Determine the way to access financial resources.

a model in accordance with Figure 1. The mentioned model used the acronyms was shown (see Appendix Table 15).

According to the experts and using the specific questions related to the self-evaluation, an analytical model was developed to prepare two questionnaires. The questionnaire contained 48 questions concerning the enabler criteria and 25 questions related to the results criteria. The variables of this research were the criteria of the excellence model of the TBNI. These variables were included in a causal model.

The confirmatory factor analysis was used in this study; as the name implied, the factors and the relationship of them with each other as well as the other variables were determined, and the purpose of the test was to validate it with the real data.

In the confirmatory factor analysis model, the calculations were the first step in providing a factor model in relation to the structural relationship of the variables. The model was generally expressed by Equation (1):

$$X = \Lambda_X \xi + \delta \quad (1)$$

In this research, X vector was 12×1 criteria of excellence, ξ was the variable of excellence, Λ_X was the coefficient matrix, and δ was the error vector.

The present study used the maximum accuracy approach which was one of the most common estimations methods [34] as shown in Equation (2)

$$F_{ML} = \log|\Sigma| + tr(S\Sigma^{-1}) - \log|S| - q \quad (2)$$

In this function, Σ was the parametric covariance matrix, S was the covariance matrix of the sample, and q was the number of the explicit variables which its value in this model was 12.

The function used for estimating the factor score regression was achieved using Equation (3):

$$\hat{\xi} = \hat{\Phi}\hat{\Lambda}' \hat{\sum}^{-1} x \quad (3)$$

The coefficient X in the above equation was indeed, the regression coefficient between the latents and the explicit variables resulted from the least squares ordinary method.

First, the normality of the data should be checked. Ignoring this case can lead to the skewed results in the study. There were several ways for examining the normality of a variable. One of these methods was to draw the histogram of that variable, using spss software. This method might not work correctly in the small samples. Another way for examining the normality was to use the skewness and the kurtosis indices. Usually, the (-2,2) value for the skewness and the kurtosis indices indicated that the distribution was normal.

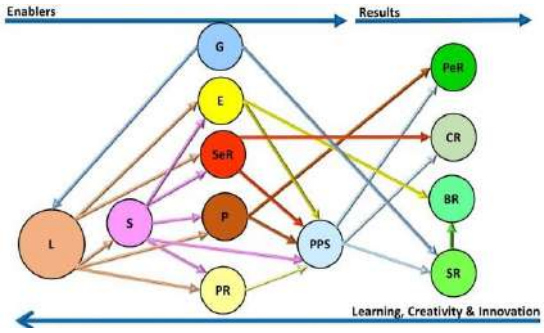

Figure 1. Initial Proposed Model

The proposed model was analyzed through the structural equations by Amos software. According to Table 6 obtained from the structural equation analysis, the proposed model was modified and validated as shown in Figure 2.

According to Table 7, the amount of the skewness and the kurtosis of the most observations was in the range (i.e. -2,2). Therefore, it could be deduced that the research data followed the normal distribution. In accordance with Table 6, p-value for the model relationships were all reported at 95% confidence level.

One of the main goals in using the structural equation modeling was to identify the degree of the compatibility between the experimental data with the conceptual and theoretical models. To identify the consistency of the experimental data and the conceptual model, the indicators and criteria were used, which were called "the goodness of fit of the model". In the structural equation modeling, the different indices were used to ensure the goodness of fit of the model. With regard to Table 7, the P-value obtained for chi-squared Index (CMIN) was equaled to zero which was less than 0.05, therefore, it could have deduced that the research model based on this indicator was properly desirable. According to Table 7, the value of Normed Chi-Square (CMIN/DF) index was 2.511. Therefore, the model proposed in this study had a suitable desirability from the viewpoint of this index. The value of RMR index was equaled to 0.118 and the value of RMSEA index was 0.0951. Therefore, the model proposed in the study was acceptable.

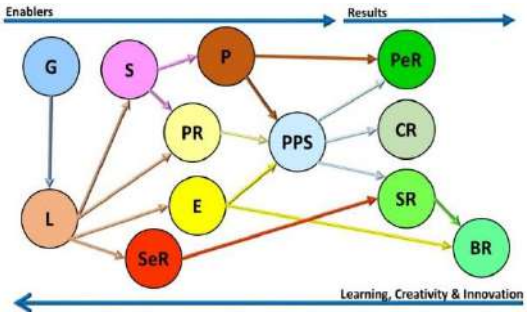

Figure 2. Modified Proposed Model

TABLE 6. Structural equation analysis

Relationship			Estimate	S.E	C.R	P-VALUE	Label
L	<-	G	0.908	0.139	6.51	000	Par-4
S	<-	L	0.899	0.098	9.19	000	0.902
PR	<-	L	0.445	0.231	1.93	0.054	Par-5
E	<-	L	0.710	0.104	6.80	000	Par-6
P	<-	S	0.928	0.135	6.89	000	Par-7
PR	<-	S	0.394	0.249	1.58	0.113	Par-8
SeR	<-	L	0.984	0.114	8.63	000	0.194
PPS	<-	P	0.178	0.096	1.86	0.063	Par-9
PPS	<-	PR	0.282	0.158	1.78	0.075	Par-11
PPS	<-	E	0.718	0.215	3.33	000	Par-12
SR	<-	PPS	1.592	0.329	4.83	000	0.799
CR	<-	PPS	0.619	0.111	5.57	000	Par-14
SR	<-	SeR	-0.888	0.277	-3.20	0.001	Par-78
PeR	<-	P	0.302	0.167	1.81	0.070	Par-10
BR	<-	E	0.222	0.103	2.15	0.032	Par-13
BR	<-	SR	0.353	0.072	4.89	000	Par-15
BR	<-	CR	0.735	0.158	4.64	000	Par-77
PER	<-	PPS	0.550	0.175	3.14	0.002	Par-79

4. 1. Weights of The TBNI Excellence Model Criteria To obtain the relative weights of each criterion and sub-criteria related to the developed and customized excellence model of the TBNI, we divided its coefficient by the total coefficients, and then, we multiplied the result by 1000; the results obtained from the structural analysis method as described in Table 8.

The Shannon entropy was another method to obtain the weights of each criterion and sub-criteria of the excellence model. The results obtained based on this method was presented (see Appendix Table 16). The results obtained from the paired T indicated there were no significant difference in the confidence level of 95% weights obtained by two methods of structural analysis and Shannon entropy (see Appendix Table 17).

5. THE TBNI EXCELLENCE MODEL

The TBNI excellence model, was designed as per Figure 3. The model's facade was a wheel as a symbol of the movement. The model had twelve criteria, eight of which were enablers, and the other four was the results. First criterion of the enablers placed in the middle of the model, was the leadership criterion. The other seven criteria from the enablers group were respectively the criteria of the governance, economy, people, strategy, processes, products & services, partnerships & resources and security & risk. The four results criteria were the Customer Result as the most important beneficiaries of the company, the Society Result and Business Result including the financial, non-financial and People Result as the most important part of the company's investments.

TABLE 7. chi-squared Index (CMIN)

Model	NPAR	CMIN	DF	P	CMIN/DF
Default model	164	6369.184	2537	0	2.511
Saturated model	2701	0	0		
Independence model	73	11599.557	2628	0	4.414

TABLE 8. Weights of the Enablers & Results criteria of TBNI Excellence Model Obtained from the structural analysis Method

Criteria (Enablers)	Weights	Criteria (Enablers)	Weights	Criterion (Results)	Weights
G	59	S	58	CR	95
L	67	PPS	63	BR	100
E	104	PR	69	SR	105
P	67	SeR	108	PeR	105

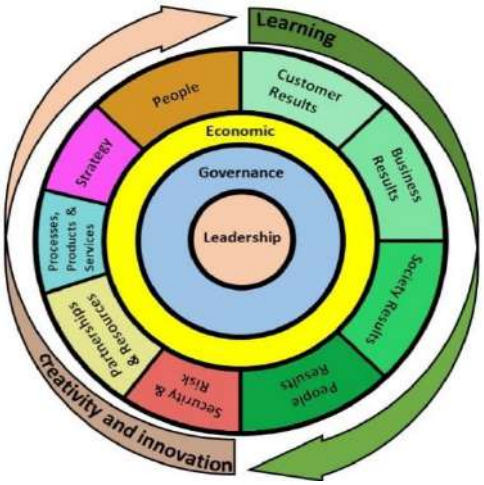

Figure 3. The TBNI Excellence model

The rotational force of the model began with learning from the results, continued with the creativity and innovation of the enablers towards the expected results. This movement along with the appropriate leadership role would never stop.

The analysis of each of the levels or steps of the maturity of the TBNI was as per Figure 4.

6. SELF ASSESSMENT OF THE TBNI

The self-assessment of the TBNI at the company level and 31 provinces of Iran were accomplished by the approach of stimulating the model based on RADAR Logic in 2019, by a team of experts including the university professors in the quality management fields, the ICT technical experts, the consultants specializing in the systematic implementation of the excellence models separating each of the twelve criteria of the model. With regard to the results and the consensus of the evaluation team, the TBNI achieved a score of 667 out of a total of 1000 points as per Table 9.

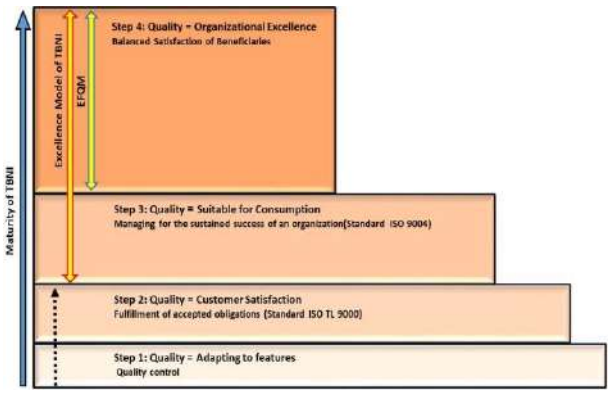

Figure 4. Steps of the maturity of the TBNI

6. 1. Improvement Opportunities According to the results of the evaluation, the major areas and projects to address improvement opportunities are identified and described in Table 10.

7. RESEARCH ACHIEVEMENTS

Some of the most important achievements of this research in the industry of ICT in Iran were as follows:

- To improve the quality of service of the TBNI.
- To improve the quality of service in the field of ICT industry of Iran.
- To operate and evaluate the communication networks based on the standard logic and techniques.
- To analyze the reports and to perform the field supervision in applying the priorities of the new technologies in conformity with the current requirements of the country through identifying the customer's needs and outsourcing the services.
- To explain and formulate big goals and strategies based on the national and international standards.
- To reconsider the approaches using the results of the content analysis based on the information sources to optimize the performance of the indicators.
- To increase the productivity.
- To identify the factors of creating the process values to the continual improvement of the service quality.
- To enhance the satisfaction of all the beneficiaries.
- To enhance the level of the quality of the services and products of all the organizations using in some ways the ICT services such as improvement of information security, enhancement of the national security, improvement of national health, enhancement of educational services, banking etc, across the country.

TABLE 9. Self-evaluation score of the TBNI

Criterion		Weights of model criteria Based on SEM method	Earned points
Enablers	L	67	41
	G	59	42
	SeR	108	75
	E	104	74
	P	67	41
	PPS	63	44
	S	58	40
	PR	69	47
Results	SR	105	64
	CR	95	67
	BR	100	64
	PeR	105	64
Total points		1000	667

TABLE 10. List of improvement opportunities

Item No.	Opportunities for Improvement
1	Revision of strategic document in line with governance tasks.
2	Development of communication infrastructure and fiber network in line with the role of governance in smart cities.
3	Futurology of cyber environment with preventive passive defense cyber approach.
4	Investigating the Role of Passive Economic Defense in Resistance, Economics.
5	Revision of the "Economic Justification of Projects" Executive Procedure.
6	Reviewing the performance of the supplier evaluation methodology in line with the organization's strategies.
7	Reviewing the Executive Process Management using the e-TOM Framework.
8	Development of process capability tools in network operations and management.
9	Development of information security management system on the backbone network.
10	Enterprise Risk Management (ERM) system deployment.
11	Developing Task Strategies in the Field of "Technology Management".
12	Reviewing the BSC-based strategic planning.
13	Developing a systematic approach to persuade partners and suppliers to develop company service processes.
14	Establishing a Customer Experience Management system (CEM) and revising the customer survey system.
15	Revise the "Staff Survey" method and analyze its results with the possibility of segmenting the results.
16	Development of comprehensive system of employee participation by modeling successful companies.
17	Develop a workflow approach and re-employ staff.
18	Reviewing the Method of Measuring Effectiveness of Informing Organizational Goals.
19	Revise the "Comprehensive Employee Information Program" based on the strategic needs of the organization.

8. CONCLUSION

In this research, the principles and criteria of promoting the quality management and excellence of the TBNI were investigated through the library and the field study. After reviewing various types of excellence models, standards and specific requirements of ICT field and different articles, we found out that the models submitted were generic and general. So, with full attention to the specific requirements and standards of ICT industry and due to adapt this model from the viewpoints of the security and risk, governance and economic, the excellence model of TBNI was developed and customized. The criteria of this model consist of the enablers and results. To achieve the highest level of reliability and internal coherence of each criterion, based on expert opinion polls, sub-criteria was categorized and analyzed in several stages using the factor analysis approach. The causal relationships and the influence of the criteria of this model on each other were investigated, and the weights of each criterion and sub-criteria, using the structural analysis and shannon entropy methods, were determined. The self-evaluation of the TBNI was systematically carried out and with regard to the results and the consensus of the evaluation team, the TBNI achieved a score of 667 out of a total of 1000 points. The major opportunities for the improvement had been identified as priorities and defined regarding the improvement measures and projects.

The present study sets a new and systematic procedure for achieving the goals which ICT managers are facing nowadays. In order to verify the new proposed excellence model by the research, after implementation at the pilot level in 31 provinces of the country, its results have been confirmed by ICT managers. According to the researchers' experience, one of the problems of ICT industry has been the lack of sufficient attention to economic issues and the complex issues of security and network risk. Therefore, in this regard, this model resolves and reduces career and management problems which managers are facing. Although economic issues, security and risk and even governance issues have been emphasized by the country's ICT executives, they have not been systematically integrated into a model of excellence. The results of this study include vital and important cases in a model of customized ICT excellence for the country and presented in the form of a new integrated model. The results showed that the establishment of this customized excellence model had led to an improvement in the quality of services provided by this network and the products of all organizations that use any services of TBNI.

According to the research achievements, the specific practical suggestion for further research is to localize, verify and apply this novel integrated excellence model to other related industries.

9. REFERENCES

1. Approved Statute of Telecommunications Infrastructure Company of Iran, (2012), https://www.tic.ir/fa/introduce/asasname.
2. Zare, M. R., Aghaei, A., Asl Hadad, A., and Samimi, Y. “Service Quality Management Modeling, Controlling and Upgrading as well as Communications and Information Technology Enhancement through Conducting a Case Study in the Parent Telecommunications Network of Iran.” ***Journal of Control***, Vol. 13, No. 1, (2019), 9–20. https://doi.org/10.29252/joc.13.1.9
3. Ghicajanu, M., Irimie, S., Marica, L., and Munteanu, R. “Criteria for Excellence in Business.” ***Procedia Economics and Finance***,

Vol. 23, (2015), 445–452. https://doi.org/10.1016/s2212-5671(15)00388-3

4. Taghizadehalvandi, M., and Kamisli Ozturk, Z. "Multi-objective Solution Approaches for Employee Shift Scheduling Problems in Service Sectors (RESEARCH NOTE)." ***International Journal of Engineering - Transactions C: Aspects***, Vol. 32, No. 9, (2019), 1312–1319. https://doi.org/10.5829/ije.2019.32.09c.12
5. Aydin, S., Kahraman, C., and Kaya, I. "A new fuzzy multicriteria decision making approach: An application for European Quality Award assessment." ***Knowledge-Based Systems***, Vol. 32, (2012), 37–46. https://doi.org/10.1016/j.knosys.2011.08.022
6. Porter, L., and Tanner, S. Assessing business excellence. Elsevier. (2012).
7. Claver, E., and Tarí, J. J. "The individual effects of total quality management on customers, people and society results and quality performance in SMEs." ***Quality and Reliability Engineering International***, Vol. 24, No. 2, (2008), 199–211. https://doi.org/10.1002/qre.885
8. Yusof, S. M., and Aspinwall, E. "Total quality management implementation frameworks: Comparison and review." ***Total Quality Management***. Vol. 11, No. 3, (2000), 281-294. https://doi.org/10.1080/0954412006801
9. Nagyova, A., and Pacaiova, H. "Maintenance evaluation based on the EFQM model excellence." In IOP Conference Series: Materials Science and Engineering (Vol. 393), (2018), https://doi.org/10.1088/1757-899X/393/1/012005
10. Lasrado, F. "Organizations Achieve Excellence Through Quality Awards." In Achieving Organizational Excellence. Management for Professional***s*** (pp. 27–36). Springer, Cham, (2018). https://doi.org/10.1007/978-3-319-70075-5_2
11. Mohammad, M., and Mann, R. National quality/business excellence awards in different countries. Centre for Organisational Excellence Research, (2010). Retrieved from www.coer.org.nz.
12. Lee, D. H., and Lee, D. H. "A comparative study of quality awards: Evolving criteria and research." ***Service Business***, Vol. 7, No. 3, (2013), 347–362. https://doi.org/10.1007/s11628-012-0172-8
13. Metaxas, I. N., and Koulouriotis, D. E. "Business excellence measurement: a literature analysis (1990–2016)." ***Total Quality Management and Business Excellence***, Vol. 30, No. 11–12, (2019), 1189–1218. https://doi.org/10.1080/14783363.2017.1356201
14. Mollaei, H. R., Tavakkoli-Moghaddam, R., and Toloie-Eshlaghy, A. "New Multi-objective Model for Multi-mode Project Planning with Risk A New Multi-objective Model for Multi-mode Project Planning with Risk." ***International Journal of Engineering - Transactions B: Applications***, Vol. 31, No. 5, (2018), 770–779. https://doi.org/10.5829/ije.2018.31.05b.12
15. Lasrado, F. "Introduction to Business Excellence." In Achieving Organizational Excellence. Management for Professionals (pp. 1–25). Springer, Cham, (2018). https://doi.org/10.1007/978-3-319-70075-5_1
16. Gandomi, A. H., Emrouznejad, A., Jamshidi, M. M., Deb, K., and Rahimi, I., Evolutionary Computation in Scheduling. Evolutionary Computation in Scheduling. Wiley, (2020). https://doi.org/10.1002/9781119574293
17. Ebrahimi, M., Tavakkoli-Moghaddam, R., and Jolai, F. "Bi-objective Build-to-order Supply Chain Problem with Customer Utility." ***International Journal of Engineering - Transactions A: Basics***, Vol. 31, No. 7, (2018), 1066–1073. https://doi.org/10.5829/ije.2018.31.07a.09
18. Safaeian, M., Fathollahi-Fard, A. M., Tian, G., Li, Z., and Ke, H. "A multi-objective supplier selection and order allocation through incremental discount in a fuzzy environment." ***Journal of Intelligent and Fuzzy Systems***, Vol. 37, No. 1, (2019), 1435–1455. https://doi.org/10.3233/JIFS-182843
19. Abdi, A., Abdi, A., Fathollahi-Fard, A. M., and Hajiaghaei-Keshteli, M. "A set of calibrated metaheuristics to address a closed-loop supply chain network design problem under uncertainty." ***International Journal of Systems Science: Operations and Logistics***, (2019), 1–18. https://doi.org/10.1080/23302674.2019.1610197
20. Lasrado, F. "Towards Developing a Framework for Achieving Organizational Excellence: Theoretical Foundations." In Achieving Organizational Excellence. Management for Professionals (pp. 173–193). Springer, Cham, (2018). https://doi.org/10.1007/978-3-319-70075-5_10
21. Metaxas, I. N., Koulouriotis, D. E., and Spartalis, S. H. "A multicriteria model on calculating the Sustainable Business Excellence Index of a firm with fuzzy AHP and TOPSIS." ***Benchmarking***, Vol. 23, No. 6, (2016), 1522–1557. https://doi.org/10.1108/BIJ-07-2015-0072
22. Murmura, F., Casolani, N., Liberatore, L., and Vicentini, A. "An empirical analysis of ISO 9001:2008 application in Italian services and manufacturing companies." ***Total Quality Management and Business Excellence***, Vol. 29, No. 7–8, (2018), 786–797. https://doi.org/10.1080/14783363.2016.1237286
23. Enhanced Telecom Operations Map (eTOM) - Process Decompositions and Descriptions', ITU-T Recommendation M.3050.2, (2007). https://www.itu.int/rec/T-REC-M.3050.2-200703-I/en.
24. Lu, H., Wang, Y., Min, L., and Huang, Z. "OSS/BSS framework based on NGOSS." In IFCSTA 2009 Proceedings - 2009 International Forum on Computer Science-Technology and Applications (Vol. 1), (2009), 466–471. https://doi.org/10.1109/IFCSTA.2009.120
25. Pereira, C., Ferreira, C., and Amaral, L. "It value management capability enabled with COBIT 5 framework." In Lecture Notes in Business Information Processing (Vol. 299), (2017), 431–446. https://doi.org/10.1007/978-3-319-65930-5_35
26. Eskildsen, J. K., Kristensen, K., and Jørn Juhl, H. "The criterion weights of the EFQM excellence model." ***International Journal of Quality & Reliability Management***, Vol. 18, No. 8, (2001), 783–795. https://doi.org/10.1108/EUM0000000006033
27. Eskildsen, J. K., Kristensen, K., and Jørn Juhl, H. "Trends in EFQM criterion weights; the case of Denmark 1998-2001." ***Measuring Business Excellence***, Vol. 6, No. 2, (2002), 22–28. https://doi.org/10.1108/13683040210431437
28. Liu, X., Tian, G., Fathollahi-Fard, A. M., and Mojtahedi, M. "Evaluation of ship's green degree using a novel hybrid approach combining group fuzzy entropy and cloud technique for the order of preference by similarity to the ideal solution theory." ***Clean Technologies and Environmental Policy***, Vol. 22, No. 2, (2020), 493–512. https://doi.org/10.1007/s10098-019-01798-7
29. Jöreskog, K. G., Olsson, U. H., and Wallentin, F. Y. Multivariate Analysis with LISREL. Springer, (2016). https://doi.org/10.1007/978-3-319-33153-9
30. Kline, R. Principles and practice of structural equation modeling. Guilford publications, Guilford publications, (2015).
31. Mansourfar, K. Advanced statistical methods: Using applied software. Tehran University Press, (2006).

10. APPENDIX A. SUPPLEMENTARY DATA

TABLE 11. A part of the questionnaire related to second stage

Criterion	Sample
Governance	The organization's ICT services comply with external laws and regulations.
Security & Risk	Activities related to controlling network security are aligned effectively with the organization's overall goals.
Economic	The cost of business processes are optimized.
Leadership	Leaders define, review, control, and extract improvements to the organization's management and performance system.
Strategy	The strategy of the organization is based on understanding the needs and expectations of the stakeholders and the external environment of the organization.
People	People throughout the organization communicate efficiently and effectively.
Partnerships & Resources	Manage technology to support achieving organizational strategies.
Processes, Products & Services	Processes are designed and managed to optimize to value for stakeholders.
Customer Results	Changes in customer perceptions and performance indices are due to its effective planning and implementation in the empowerment sector.
People Results	Human resource performance and perception indicators are based on clear logic and to achieve overall goals of the organization.
Society Results	The organization assessed community perceptions through surveys or other forms of feedback, measured the organization's internal performance indicators, and had a positive and consistent trend.
Business Results	Key performance indicators of financial, non-financial perceptions and performance of a business are aligned with and identified with service quality strategies as well as the expectations and expectations of the relevant community and institutions.

TABLE 12. Assumption test results for 25 items from the set of security & risk criteria and governance criteria

Model / Framework	Item (Sub-Criteria)	Median	Q1	Q3	Min	Max	IQR	Wilcoxon Test Stat	P-Value
eTOM	1	3	2	3	2	3	1	903	0
	2	3	3	3	-3	3	0	877	0
	3	3	2	3	0	3	1	861	0
	4	3	2	3	-3	3	1	873	0
IMS	5	3	2	3	0	3	1	861	0
	6	3	3	3	2	3	0	903	0
	7	3	3	3	1	3	0	903	0
	8	3	3	3	1	3	0	903	0
	9	3	2	3	1	3	1	903	0
ISMS	10	3	2	3	-2	3	1	896	0
	11	3	2	3	1	3	1	903	0
	12	3	2	3	1	3	1	903	0
	13	3	2	3	1	3	1	903	0
	14	3	2	3	1	3	1	903	0
	15	3	2	3	1	3	1	903	0
ITIL	16	3	2	3	1	3	1	903	0
	17	3	2	3	-2	3	1	891	0
	18	3	2	3	-2	3	1	895.5	0
	19	3	3	3	1	3	0	903	0

	20	3	2	3	1	3	1	903	0
eTOM	21	2	2	3	-3	3	1	817	0
	22	3	2	3	1	3	1	903	0
IMS	23	2	2	3	-3	3	1	829	0
COBIT 5	24	3	2	3	1	3	1	903	0
VAL IT	25	3	2	3	0	3	1	861	0

TABLE 13. The binomial test results

Item (Sub-Criteria)	Mod (Criteria)	Num-mod (No. of +ve Comments)	P-Value
2	1	55	0
8	1	55	0
15	1	55	0
22	1	55	0
24	1	55	0
57	1 & 10	30	0.59
1	2	55	0
9	2	55	0
12	2	55	0
21	2	55	0
50	2 & 10	34	0.105
4	3	52	0
7	3	55	0
14	3	55	0
17	3	55	0
20	3	53	0
6	4	53	0
10	4	55	0
11	4	55	0
18	4	55	0
19	4	55	0
3	5	53	0
5	5	55	0
13	5	54	0
16	5	55	0
23	5	55	0
28	5	37	0.014
33	5	40	0.001
39	5	51	0
49	5	42	0
59	9 & 10	33	0.177
60	9	36	0.03
61	9	37	0.014

62	9	36	0.03
25	10	43	0
26	10	36	0.03
27	5 & 10	30	0.59
29	4 & 10	32	0.281
30	10	39	0.003
31	10	53	0
32	10	45	0
34	10	42	0
35	10	48	0
36	10	41	0
37	10	44	0
38	5 & 10	34	0.105
41	10	48	0
42	10	51	0
43	10	35	0.058
44	10	42	0
45	10	41	0
46	10	48	0
47	10	39	0.003
48	10	37	0.014
51	4 & 10	28	1
52	10	41	0
53	10	52	0
54	10	42	0
55	10	46	0
56	10	50	0
58	10	50	0
40	4 &10	24	0.419

TABLE 14. Cronbach's alpha dimensions

Criterion	**Cronbach's Alpha**
Leadership	0.9023
Strategy	0.8943
People	0.7423
Partnerships & Resources	0.8894
Processes, Products & Services	0.8533
Security & Risk	0.9177
Governance	0.7770
Economic	0.9521
Business Results	0.8166

TABLE 15. Criteria abbreviations

Criterion	Initials	Criterion	Initials
Leadership	L	Partnerships & Resources	PR
Governance	G	Processes, products & Services	PPS
Economic	E	People Results	PeR
Security & Risk	SeR	Customer Results	CR
People	P	Society Results	SR
Strategy	S	Business Results	BR

TABLE 16. Weights of the enablers & results criteria of TBNI excellence model obtained by the Shannon entropy method

Criteria (Enablers)	Weights	Criteria (Enablers)	Weights	Criterion (Results)	Weights
	69	S	42	CR	87
L	63	PPS	58	BR	87
E	149	PR	52	SR	75
P	79	SeR	111	PeR	128

TABLE 17. T-test: Paired two samples for means

Title	Variable 1	Variable 2
Mean	83.33333333	83.33333
Variance	434.0606061	1012.606
Observations	12	12
Pearson Correlation	0.780735461	
Hypothesized Mean Difference	0	
Df	11	
t Stat	0	
P(T<=t) one-tail	0.5	
t Critical one-tail	1.795884819	
P(T<=t) two-tail	1	
t Critical two-tail	2.20098516	

Persian Abstract

چکیده

امروزه فناوری اطلاعات و ارتباطات (فاوا) به عنوان یکی از تاثیرگذارترین عوامل پیشرفت در تمامی ابعاد مانند حاکمیت، امنیت و ریسک، اقتصاد و تکنولوژی، از جمله صنایعی به شمار می‌رود که به سرعت در حال رشد و توسعه است. این مقاله معیارها و استانداردهای خاص حوزه فاوا برای ارتقاء کیفیت سرویس‌های شبکه مادر مخابراتی ایران را مورد بررسی قرار داده است. پژوهش حاضر از طریق دو روش گردآوری اطلاعات کتابخانه‌ای و مطالعات میدانی انجام پذیرفته است. مدل تعالی بنیاد کیفیت اروپا به عنوان مدل پایه انتخاب و با توجه کامل به الزامات خاص صنعت فاوا و تطبیق این مدل از دیدگاه امنیت و ریسک، حاکمیتی و اقتصادی، مدل نوین تعالی شبکه مادر مخابراتی ایران طراحی و بومی‌سازی گردید. جهت دستیابی به بالاترین سطح قابلیت اطمینان و انسجام درونی هر معیار، با استفاده از نظرسنجی خبرگان زیر معیارها در چندین مرحله و با رویکرد تحلیل عاملی دسته‌بندی و مورد تجزیه و تحلیل قرار گرفته است. روابط علّی و تأثیر معیارهای این مدل بر یکدیگر بررسی و وزن هر یک از معیارها و زیرمعیارها با استفاده از روش‌های معادلات ساختاری و آنتروپی شانون تعیین گردیده است. خود ارزیابی از شبکه مادر مخابراتی ایران بصورت سیستماتیک انجام و اهم فرصت‌های بهبود شناسایی شده است. نتایج نشان داد که استقرار این مدل بومی منجر به ارتقاء کیفیت سرویس‌های ارائه شده توسط این شبکه و محصولات کلیه سازمان‌هایی است که به نوعی از سرویس‌های شبکه مادر مخابراتی ایران استفاده می‌نمایند.

International Journal of Engineering

Journal Homepage: www.ije.ir

Co-TiO_2 Nanoparticles as the Reinforcement for Fe Soft Magnetic Composites with Enhanced Mechanical and Magnetic Properties via Pulse Electrodeposition

M. Vosough, S. Sharafi, G. R. Khayati*

Department of Materials Science and Engineering, Faculty of Engineering, Shahid Bahonar University of Kerman, Kerman, Iran

P A P E R I N F O

Paper history:
Received 24 May 2020
Received in revised form 23 July 2020
Accepted 2 August 2020

Keywords:
Fe based Composite
Pulse Electrodeposition
Soft Magnetic Properties
Vickers Microhardness

A B S T R A C T

This study is an attempt to produce surface nanocrystalline composite of Fe-Co-TiO_2 at various current densities in the range of 20 to 50 mA/cm^2 via pulse electrodeposition method. The prepared composites were characterized by field emission scanning microscope (FESEM), electron dispersive spectrum (EDS), Vickers microhardness, vibrating sample magnetometer (VSM), and x- ray diffraction techniques (XRD). The results showed that the formation of cauliflower morphology was preferred at lower current densities. Moreover, the higher current densities enhanced the Fe content and at the same time diminished the Co and TiO_2 contents of prepared surface composites. XRD patterns and Rietveld analysis confirmed the formation of combinations of BCC (as dominant) and FCC phases. Higher current density enhanced the saturation magnetization and decreased lower coercivity due to the higher Fe content and the reduction of TiO_2 nanoparticles in coatings. In addition, the lowest coercivity and highest saturation magnetization were gained at 50 mA/cm^2, while, the maximum microhardness obtained at 30 mA/cm^2.

***doi**: 10.5829/ije.2020.33.10a.21*

1. INTRODUCTION

Fe-Co alloys are one of the most important structural components due to their amazing magnetism properties [1, 2]. All materials that are magnetized by the application of a magnetic field are called magnetic materials. Depending on how they respond to the magnetic field, magnetic materials are classified as follows:

Ferromagnetic: Some metallic materials have a permanent magnetic moment in the absence of an external field and exhibit very large magnetism and are permanent magnets. Intermediate metals such as iron (in the form of BCC or α-Fe), cobalt and nickel show this property.

Antiferromagnetic: In these materials, the adjacent magnetic moment vectors are equal in the size but in opposite in direction. Therefore, they neutralize each other. If such a material is placed in a magnetic field, the torques are amplified in the same direction as the field, and the material exhibits a weak magnetic property.

Ferrimagnetic: In these materials, the directions of the magnetic moment vectors are adjacent to each other, but their size is not equal. The behavior of these materials is similar to that of ferromagnetic materials.

There is a group of permanent magnets known as ferrites [3]. Films have special properties that are substantially different from their material in bulk. This difference is due to their physical dimensions, geometric shape and microstructure. In addition, these features can be greatly modified to achieve the desired properties [3]. Thin films with thick of submicron and properties caused by their two main features including low thickness and high ratio of surface area with many applications in modern technologies. Some of these features included the increase in resistivity, light interference, tunneling, surface magnetization and critical temperature change of superconductors [4]. According to the performance and properties of the films, they can also be used to improve

*Corresponding Author Institutional Email: *khayatireza@gmail.com* (G. R. Khayati)

Please cite this article as: M. Vosough, S. Sharafi, G. R. Khayati , Co-TiO_2 Nanoparticles as the Reinforcement for Fe Soft Magnetic Composites with Enhanced Mechanical and Magnetic Properties via Pulse Electrodeposition , International Journal of Engineering (IJE), IJE TRANSACTIONS A: Basics Vol. 33, No. 10, (October 2020) 2030-2038

technologies such as solar cells, sensors, optical applications, electronics, and ferroelectrics [4-5].

There are various techniques for the preparation of these alloys including sputtering, sol-gel, molecular beam epitaxy, electrodeposition, and vacuum evaporation [6]. In this regard, low cost, simplicity of electrodeposition, and determination of sediment rate and coating thickness in a wide range caused by the introduction of this process as a hot issue for various areas of research. Significant magnetization (M_s) and negligible coercivity (H_c) are the remarkable characteristics of Fe-Co film produced by electrodeposition. However, these coatings suffer from low mechanical properties, especially hardness; and such disadvantages restricted their usages, significantly [7-8]. In many cases, a ceramic or composite such as metal nanoparticles are utilized to promote the hardness of Fe-Co coatings.

Nevertheless, in the usual mode of direct current electrodeposition, as the procedure continues, one layer of negatively charged type coats the cathode in which is a barrier layer among the deposit-electrolyte interface and charged particles. Pulse electroplating can effectively modify this process [9]. According to the literature, various attempts were carried out to compensate and enhanced the hardness of these coatings by adding oxide nanoparticles or usages of pulse current with respect to the direct current through the preparation of composite coatings [10]. In pulse electrodeposition, the current includes two modes that the layer charges through on-time and discharges somewhat through off-time. This makes swifter transmission of the charged particles via the layer and raises the amount of micro and nano-sized augmentation. In pulse electroplating the duty cycle has been expressed according to Equation (1) [11]:

$$\text{Duty cycle} = \frac{T_{ON}}{T_{ON}+T_{OFF}} = T_{ON}f \quad (1)$$

where T_{ON}, T_{OFF} and f are on-time, off-time and pulse frequency, respectively; frequency has been calculated in the Equation (2):

$$Frequency = \frac{1}{T_{ON}+T_{OFF}} = \frac{1}{T} \quad (2)$$

This research was done to obtain the optimal pulse plating conditions for a cobalt iron coating with titanium dioxide nanoparticles as dopant. The current density has been selected and investigated as the most important factor in current study.

Table 1 summarized the works that have tried to enhance the hardness of these coatings via electrodeposition technique. As abbreviated in Table 1, the main contributions of the current study are:

(i) Usage of pulse current for preparation of Fe-Co-TiO_2 composite by electroplating;
(ii) The acceptable saturation magnetization of coatings compared to similar coatings prepared by direct current electrodeposition;
(iii) Usage of relatively negligible reinforcement compared to other researches (about 0.1 vol.%) and as a consequence, its lower relating cost;
(iv) Determination of residual strength in the prepared coating.

2. EXPERIMENTAL

The chemical materials used in current study were purchased from Merck Company including, iron (III) sulfate (99.99 wt.%), cobalt (II) sulfate (99.99 wt.%), boric acid (99.99 wt.%), L-Ascorbic acid (99.98 wt.%), saccharin and sodium dodecyl sulfate (99.98 wt.%). TiO_2 (99.99 wt.%, 20-30 nm) was provided from US Research Nanomaterials, Inc, USA.

Copper plate (10×10×1 mm) and nickel sheet (20×20×1 mm) were used as cathode and anode,

TABLE 1. Side by side comparison of literatures that compared the mechanical properties of prepared coatings

Ref/year	Coating	Electroplating method		Magnetic parameters		Micro-hardness (HV)	Thickness (μm)	Reinforcement percent (vol.% in bath)	Residual stress (MPa)
		Direct	Pulse	M_s (emu/g)	H_c (Oe)				
Shao/ 2001	Fe-Co-TiO_2	√	-	25.24	150	214.14	20-25	1-2	-
Ghaferi/ 2016	Fe-Co-W	√	-	60-860	76-21	300	18	0.32	-
Iryna Yu/2017	Fe-Co-Mo	-	√	-	-	-	8-10	1.46	-
Yousefi/ 2016	Fe-Ni-TiO_2	-	√	5-16.40	-	536 to 638	-	2.50	-
Takuya Nakanishi/2001	Co-Ni-Fe	-	√	391.79	30<	-	-	-	-
Torabinejad/2017	Fe-Ni-Co	-	√	-	-	519 to 570	120	-	-
Current study	Fe-Co-TiO_2	-	√	13.33-27.83	196.63-122.91	74.3 to 173	20	**0.10**	85 to 253

respectively. The vertical distance of anode to the cathode was adjusted to be about 3 cm. First, the surfaces of cathode copper samples were electro polished at the current density of 1.5 A/m^2 for 60 sec in equi-volume of HNO_3 and de-ionized solution to obtain the mirror surface. Afterward, the substrates were washed in acetone and distilled water to eliminate the pollution and then immersed instantly in the electrodeposition cell.

The electrodeposition bath contains, 50 g/L iron (III) sulfate ($Fe_2(SO_4)_3$), 62.5 g/L cobalt (II) sulfate ($CoSO_4.7H_2O$), 30 g/L Boric acid (H_3BO_3), 3.5 g/L L-Ascorbic acid ($C_6H_8O_6$), 0.8 g/L saccharin ($C_7H_5NO_3S$), 0.3 g/L Sodium dodecyl sulfate-SDS ($C_{12}H_{25}NaO_4S$) and 1 g/L TiO_2 nanoparticles. Also, the pulse electroplating parameters for construction of Fe-Co-TiO_2 coatings were: current density (20, 30, 40 and 50 mA/cm^2), duty cycle (50 %), pulse frequency (100 Hz), pulse on-off time (5-5 ms), stirring speed (300 rpm), pH (=2) and temperature (25 °C).

The experiments were carried out in plating cell with the volume of 100 mL. Double-distilled water was used as solvent to provide the electrolytes from precursors. pH was controlled by the addition of NaOH and H_2SO_4. To decrease the possibility of anodic reaction of Fe (ferric to ferrous reaction), use of ascorbic acid as antioxidant was necessary. In addition, sodium dodecyl sulfate as surfactant in the bath was employed to inhibit the agglomeration of TiO_2 nanoparticles. All experiments were performed at 25 °C with aggressive stirring rate (300 rpm). To plate each sample and having the films with similar thickness, the electric charge has been kept at 50 coulombs. Rectifier model BHP 2056 used to provide direct current through the electrodeposition. Various current densities in the range of 20-50 mA/cm^2 were applied at constant deposition time equal to 20 min. In addition, the pulse frequency and duty cycle were fixed at permanent fluctuation of 100 Hz and 50 %, respectively. The time of "On" and "Off" were set to 5 msec.

To investigate the surface characteristics, including chemical composition and morphology field emission scanning electron microscopy (FESEM, Hitachi S4160 model) equipped with the EDX point chemical Analyzer were used [8-10]. The phase analyses of Fe-Co-TiO_2 films were done by XRD technique (Philips, X'pert-MPD system by Cu-K_α). Scherrer equation [12] was used to estimate the average particle size of Fe-Co-TiO_2 after the removal of the peak broadening of X-ray due to the instrumental error by Warren's method [12]. Rietveld refinement was performed using materials analysis by diffraction (MAUD) program.

To measure the magnetic properties of the samples VSM (Meghnatis Daghigh Kavir Co. Iran) as magnetic hysteresis loops was used. The samples by dimension of 0.5 mm × 0.5 mm × 1 μm were prepared. Then, the magnetic measurement of samples was performed at 25 °C under the aligned magnetic field to be about ±10000 Oe. Vickers microhardness was used to determine the hardness of the sample by applying the load of 50 g for 15 sec on the sample.

For each sample, evaluation is done on 5 points of the surface and their average was reported as the final valuably. The copper sheet does not have any influence on the microhardness due to the insignificant permeation depth (to be about 1-2 μm) [13].

3. RESULTS AND DISCUSSION

3. 1. Compositio and Morphology Analysis of Prepared Coatings As shown in Figure 1, there is a close relationship between the current density and morphology. Accordingly, it was possible to prepare a dense and smooth Fe-Co-TiO_2 coating in the wide range of current densities by adjusting the pulse electrodeposition parameters. During electroplating, the discontinuity of current at certain intervals led to an immense increase in nucleation rate. Hence, the deposited coatings by pulse electroplating have higher density and smaller grain sizes, so that a smoother surface is expected. In addition, it has been observed that TiO_2 nanoparticles were distributed at the surface of depositions. Figs. 1 (a-d) illustrate a mixed morphology containing fine nodular and small needles, which confirm the dispersion of phases containing cobalt and iron through the coatings. Similar observations have been reported for morphological investigation of other investigations [14-16]. The analogous and condensed surface may be due to the utilization of pulse electroplating and the distribution of TiO_2 nanoparticles through the sample surface [11]. As shown in the Figure 1(a)-(d), by enhancing of current density, the coatings have become coarser with a great nodule and cauliflower morphologies. It seems that higher current density decreased the amount of TiO_2 nanoparticles and Co in the coating.

According to the results, by increasing the current density, micro-cracks are appearing on the surface of samples and have been perceived that the surface of depositions becomes coarser with non-uniformity in morphologies.

There are diverse mechanisms to explain this phenomenon, including that the preferred absorption of intermediary species prevents normal co-deposition performance. By increasing the current density, the conditions have been more appropriate for the formation of hydrogen and by consumption of H^+ around the cathode, the pH increased locally. This condition significantly promoted the formation of metallic hydroxide [13, 17-18].

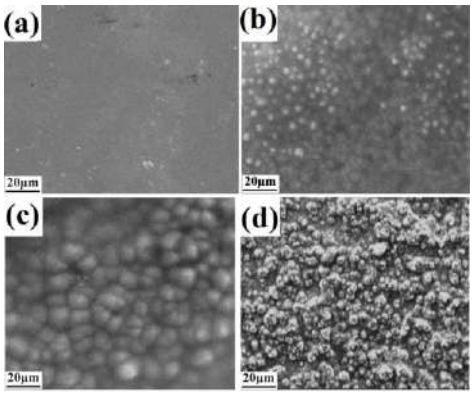

Figure 1. FESEM images of Fe-Co-TiO_2 coatings at different current densities prepared at (a) 20, (b) 30, (c) 40 and (d) 50 mA/cm^2

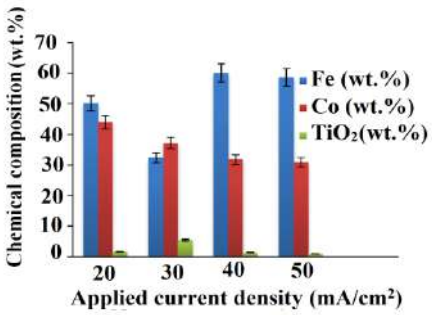

Figure 2. Chemical composition of the coatings at various current densities based on EDX analysis.

Since the desirability to absorb iron hydroxide is higher than that of cobalt hydroxide [19, 20], an increase in the amount of iron deposition is predictable. The white dots in Figure 1 confirm the distribution of TiO_2 nanoparticles on the coating which is more clearly seen in Figures 1a and 1b.

Based on the results, it can be concluded that the optimal conditions is satisfied at the current density of 40 mA/cm^2. At this current density, the amount of iron and TiO_2 are balanced and a smooth coating with suitable magnetic and mechanical properties is obtained. In addition, the amount of iron on the coating is higher than the prepared coating at 50 mA/cm^2. This is due to anomalous codeposition and less tendency of the noble metal to deposit.

In Figure 1 (current density 30 mA/cm^2), the amount of iron has dropped sharply due to the increase in TiO_2 content, so we see larger granules in this current density. The effect of increasing current density on increasing the iron content and reducing the gross amount of coating is confirmed [11, 13, 16]. The mass ratio of the components is determined according to the previous works with different dopants [11, 13]. As illustrated in Figure 2, the weight percent of Co and Fe in the coating for the sample prepared at 20 mA/cm^2 were 43.9 wt. % and 50.1 wt. %, respectively. However, in the case of 50 mA/cm^2, the weight percent of Co and Fe contents were 30.8 and 58.6 wt. %, respectively. On the other hand, due to the reduction of cathodic over potential, the possibility of a reaction at the electrode surface was decreased. In this condition, the amount of Fe increased in the deposit. According to the literature [21-23], higher current densities enhanced the diffusion of Fe to the coating and as a consequence enhanced the magnetic properties.

As shown in Figure 2, the dependency of current density and TiO_2 content in deposition results from two various behaviors. In the range of 20 to 30 mA/cm^2, enhancing the current density increased the TiO_2 contents of coatings, while in the range of 40 to 50 mA/cm^2, this behavior was reversed. As shown, the TiO_2 content of coating dropped from 5.4 wt. % (in 30 mA/cm^2) to 1.2 wt. % (in 40 mA/cm^2) and 0.8 wt. % (in 50 mA/cm^2). In this regard, by changing the current density from 20 to 30 mA/cm^2, decreasing the rate of iron and cobalt ions has been enhanced due to increasing of metal ions absorbed by TiO_2 nanoparticles [24, 25]. By addition of current density (until 50 mA/cm^2) that promotes the deposition speed of metal ions respect to TiO_2 particles. This consequence can be related to a greater decrement of metallic ions in electrolyte due to the decreasing rate of metallic ions around the TiO_2 is less than the value of it for free metal ions by increasing in current density [11, 26-27].

There are various theories for this phenomenon. According to Lu et al. [4] the preferential absorption of intermediate species prevents normal deposition. As the current density increases, the conditions for hydrogen regeneration become more suitable. In this condition, by consuming H^+ around the cathode, the pH in this area will increase and will be the dominant species as hydroxide. Because of the tendency to absorb the iron hydroxide is far greater than that of cobalt hydroxide, the increase in the amount of deposited iron occurs [15, 25].

The prior studies have shown that any increase in the current density up to the critical value extremely enhanced the deposition rate of particles to a maximum value. While, in the current densities than higher than that of this threshold, the possibility of co-deposition of TiO_2 nanoparticles was decreased [11]. The behavior of TiO_2 nanoparticles explained by Guglielmi's model as a function of current density [11, 13]. Accordingly, the absorption of metallic ions at the surface of nanoparticles had been occurred in the first step. After traveling from the diffusion layer, the surrounded TiO_2 nanoparticles with the ionic cover distributed at the cathode. Then, the deposition of TiO_2 nanoparticles on the cathode surface takes place weakly. At the same time as the evacuation of metallic ions at the cathode surface occurs, TiO_2 nanoparticles accumulated and penetrated inside the Fe-Co coating. Hence, at high current densities including

and over 40 mA/cm^2, the metal deposition process is overcome to the co-deposition of nanoparticles, so it can be seen that in these current densities, significant reduction of nanoparticles inside the coating is visible.
In confirmation of the EDX results, the XRD analysis of samples was also performed. Moreover, in spite of EDX limitations, the usage of this analysis is very common in phase analysis [8-10].

3. 2. Samples Characterization The structural changes of coatings prepared at various current densities were investigated by XRD patterns (Figure 3). XRD pattern of TiO_2 (JCPDS No. 4-0477) confirmed the high purity and crystalline nature of TiO_2 nanoparticles as reinforcement. TiO_2 peaks with significant intensity were not detected in the XRD patterns of Fe-Co-TiO_2 composite coatings. This is due to the very low content (lower than 5 wt.%) of the co-deposited TiO_2 nanoparticles in the Fe-Co matrix. Since, in this study TiO_2 nanoparticles with anatase phase was used due to its better magnetic properties compared to the other two phases. It was necessary to note that phases less than 5 % by weight cannot be observed in XRD. As shown, there is remarkable dependency between the XRD spectra and relating current density in a way that by an increase in current density, the intensity of cobalt peaks was dramatically diminished. Albeit, there is more Fe, at higher current densities. Similar consequences have been presented by other studies. According to the results, cobalt structures contain two phases , FCC and/or HCP. During electrodeposition, atomic hydrogen may react with cobalt and produce metastable cobalt hydride with FCC structure. Atomic hydrogen is then removed from the sediment due to the decomposition and formation of stable cobalt with HCP structure. It has been reported that the co-deposition of atomic hydrogen with Co in electroplating can create cobalt hydride with low stability and an FCC structure [11]. Dissociation of this phase leads to the removal of hydrogen through the deposition and as a result, Co changes to a more stable HCP phase. Besides this, TiO_2 nanoparticles can enhance the performance of preparedness of the structural coating in structural usages. TiO_2 peaks with low intensity were observed in XRD spectra of Fe-Co-TiO_2 deposited coatings which confirm that very low amount of TiO_2 nanoparticles in the Fe-Co coating (maximum of TiO_2 was about 5.4 wt. %).

The average grain size of coatings determined by Scherrer equation [12] and the results are summarized in Table 2. Measurements were repeated three times at each angle and the mean values were reported. It can be concluded that the average grain size has been less than 21 nm.

It should be noted that the load transfer process happens in several steps. Transfer ions from electric binary layer to the free positions and their attractions, shallow penetration of adsorbed ions toward the steps, and finally transfer ions from steps to the edges. Any increase in the current density (or higher over potential), enhanced the superficial penetration of ions and the atoms are transmitted faster toward the growing active centers (steps and edges) and consequently facilitated the growth of grains. On the other hand, the germination energy barrier changed by an inverse relationship with the square of over potential. Any increment in the current density increased the over potential. In this condition, the germination rate has enhanced and the grain size will become smaller. It can be concluded that these two parameters compete for the control of the coating grain size. In this research, both factors have similar influences and annihilate their effects. Therefore, the grain size does not show remarkable variations through investigating the region.

Increasing the current density increases the surface penetration of the ions and causes the atoms to move more rapidly to the active growth centers (stairs and edges), thus facilitating the growth of grains. On the other hand, the germination energy barrier is inversely related to the super-potential square. As the current density increases, the germination rate enhances and the grain size becomes smaller. Here, at higher densities, the two factors have the same effect and destroy each other's effects. Therefore, no significant changes in grain size are observed.

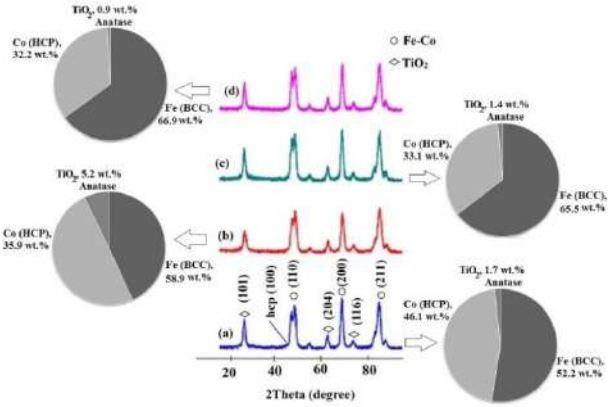

Figure 3. XRD patterns of Fe-Co-TiO_2 coatings at different current densities obtained from (a) 20, (b) 30, (c) 40 and (d) 50 mA/cm^2

TABLE 2. Results of Scherrer equation by consideration of various peaks for determination of the average grain size

Current density (mA/cm^2)	2 theta (Degree)	FWHM	Crystallite size (nm)
20	45.25	0.54	15
30	45.70	0.50	19
40	44.68	0.46	21
50	45.10	0.45	21

As shown in Figure 3, the results of Rietveld analysis also confirmed the XRD results and the grain size of the Scherrer equation.

3. 2. Magnetic Properties Saturation magnetization (M_s) is an inherent characteristic and can be considered as material property. While, coercivity (H_c) is an external characteristics and is a function of several factors such as crystalline nature, chemical composition, particle size, microstructure, thickness, and residual stresses of the prepared coatings by electrodeposition. The hysteresis loops of depositions at various current densities are presented in Figure 4. Moreover, Table 3 shows the magnetic data, i.e., saturation magnetization, for various samples. According to the results, it can be seen that all of the coatings have soft magnetic property (coercivity less than 200 Oe) and any enhancement in the current density, changed the saturation magnetization. Hereon, there is a same opinion, which decrement in non-magnetic element causes for the increase in saturation magnetization. Furthermore, the Fe content of the deposition has an important effect on the saturation magnetization due to the superior magnetic property of iron compared to the other constituents. The most important ferromagnetic elements are cobalt, nickel, and iron, in this sample the higher content of Co can compensate the lower content of Fe in prepared coating [19].

Conforming to the consequences of EDX, the amount of iron in electroplating deposition had increased. However, the TiO_2 content decreased by enhancing the current densities higher than 30 mA/cm^2. Hence, higher current density induced higher saturation magnetization and decreased the coercivity, simultaneously. On the other hand, by an increment in the current density, the amount of TiO_2 nanoparticles decreases, and hence saturation magnetization declines. As mentioned, the coercivity is an extrinsic feature and the grain size is one of the most substantial factors that alter the coercive fields. Decrement in the grain size according to Equation (3) lead to a reduction in magnetic coercivity.

$$H_C = P_C \frac{k_1^4}{J_s A^2} D^6 \quad (3)$$

in which, H_c, A, K_1, J_s, P_c and D, are coercivity, exchange stiffness constant, magneto-crystalline anisotropy, the magnetic moment, a constant of the order of unity and the crystallite size, respectively. By increasing the grain size to the values less than the exchange length, the effect of exchange interactions dominates on the adverse effect of the grain size. Thus, magnetic moments are getting on the same direction, and the coercivity decreases.

For each magnetic material, there is an exchange length, which is explained with Equation (4):

$$L_{ex} = \sqrt{\frac{A}{K_1}} \quad (4)$$

As shown in Equation (5), in the case that the grain size is greater than the exchange length, the coercivity increases due to the reduction in the grain size:

$$H_c \sim \sqrt[3]{\frac{KT_cK_1}{aM_s}} \frac{1}{D} \quad (5)$$

where, M_s, T_c, a, and K are the saturation magnetization, Curie temperature, lattice constant and Boltzmann constant, respectively. It is obvious that the coercivity measurement of iron-based alloys is conforming to the random anisotropy model (RAM). The previous studies demonstrate that the exchange length (L_{ex}) for ferromagnetic material depends on the amount iron in the deposition, so that reduction of iron content leads to the increase in L_{ex}. Consequently, the exchange length was smaller than the grain size for all electroplating coatings (D). Thus, decrementing the grain size led to the increases in coercivity. The results obtained from experimental have a high concordance with RAM theory for all electrodeposition composition. As shown in Figure 5, by enhancing the current density, the coercivity was decreased due to the increase in the grain size. Furthermore, the VSM results revealing the coatings have the soft magnetic property due to the amount of coercivity between 100-200 Oe and thin hysteresis curve. Maximum M_s and minimum of H_c reported in prepared coatings at 50 mA/cm^2 and can be proposed as good candidates for magnetic usages. Also, the amount of reinforcement (TiO_2 nanoparticles) in this sample is at its least, and promotes the magnetic properties due to the presence of higher constituents, i.e., Co and Fe as magnetic elements.

3. 3. Microhardness The dependency of microhardness and current density are shown in Figure 6. In general, by creating a solid solution, microhardness increases due to the reduction in dislocation mobility. On the other hand, according to Hall-Petch Equation (6), the decrement in the grain size leads to an increase in microhardness:

$$H = H_0 + kD^{-0.5} \quad (6)$$

where H_0 and k are constants related to hardness and D is the grain size obtained by Scherrer equation. Moreover, the consequences display that by increasing the iron content, the microhardness was decreased; so, lower hardness values are related to the greater iron content. In summary, an increase in current density in the range 20-30 mA/cm^2, enhanced the microhardness of coatings. However, in the higher current densities (40 and 50 mA/cm^2), a significant decrement in microhardness has been observed due to the lower content of TiO_2 as reinforcement.

One way to increase the mechanical properties of the coating is to dope ceramic nanoparticles to the composition. The growth of the grains is limited by the

TABLE 3. The saturation magnetization values of Fe-Co-TiO_2 coatings as a function of variation of current density (M_s (emu/g))

Current density (mA/cm^2)	Saturation magnetization (emu/g)	Coercivity (Oe)
20	13.33	196.63
30	17.61	191.87
40	24.17	146.00
50	27.83	122.91

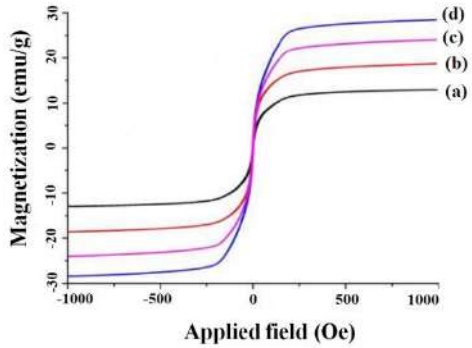

Figure 4. The hysteresis loops of Fe-Co-TiO_2 coatings at different current densities (a) 20, (b) 30, (c) 40 and (d) 50 mA/cm^2

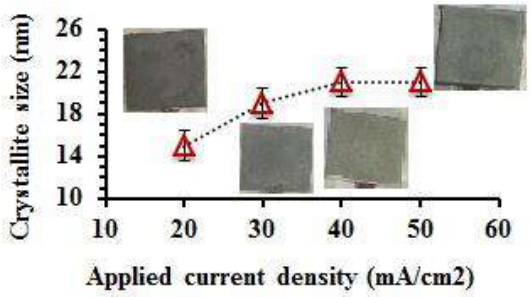

Figure 5. The alterations of grain size of coatings at diverse current densities

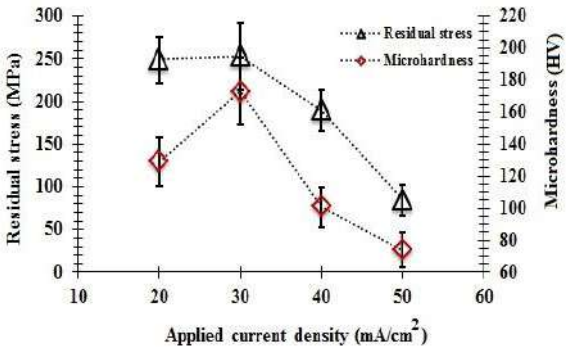

Figure 6. Effect of current density on the microhardness and residual stress of coatings.

distribution of TiO_2 nanoparticles in Fe-Co precipitate. In addition, the plastic deformation process reduces the composition of Fe-Co due to the combined effects of grain refinement and dispersive strengthening mechanisms. The maximum value of microhardness is to be about 173 HV, which is related to 30 mA/cm^2 current density. It means that the amount of TiO_2 played an administrated effect on the microhardness.

Residual stress defined as the stresses that remain in a body after the removal of all external forces. This stress can exist as tensile (positive) or compressive (negative). As a general trend, most metal and ceramic coatings have internal stresses. In addition, the compressive stresses in coatings are generally preferred due to the significant improvement of hardness and fatigue life of prepared composites. According to Figure 6, the values obtained from the residual stress and the hardness of the coating is well proportioned. On the other hand, the coatings with higher residual stress have consequently maximum hardness.

As can be seen in Figures 5 and 6, the magnitude of error bars in investigating parameters, i.e., crystalline size, microstructure and residual stress, are proportional to the current densities. In this regard, by increasing the current density to 40 and 50 mA/cm^2, more uniform coverage is obtained and the magnitude of error bars is reduced. In other words, the distribution of data in the range of 40 to 50 mA/cm^2 of current density is more balanced and uniform. This behavior can be related to the higher reproducibility of prepared composites at higher current densities than 40 mA/cm^2.

4. CONCLUSIONS

Preparation of Fe-Co-TiO_2 composite using pulse electrodeposition at various current densities is the subject of this study. The structural changes, mechanical and magnetic properties of samples were thoroughly investigated. XRD patterns demonstrated that the dominant structure is BCC. Albeit, increment in the current density led to be added a mixed-phase including BCC and FCC and the saturation magnetization has a direct relationship and coercivity value has a reverse relationship with Fe content of coatings. In addition, by increasing TiO_2 nanoparticles, the coercivity value increases. Through the investigated ranges of parameters, the maximum M_s, as well as the minimum H_c belonged to the sample at 50 mA/cm^2. Therefore, Fe-Co alloys prepared by pulse electroplating at a current density of 40 mA/cm^2 can be introduced as the optimal coating due to the optimization of magnetic and mechanical properties together. While the maximum amount of residual stress and microhardness belonged to the coatings prepared at 30 mA/cm^2. The other conclusion was the positive effect

of Co in enhanced magnetization saturation at a relatively similar level to the Fe content.

5. REFERENCES

1. Liu, W., Ou, S., Chang, Y., Chen, Y., Liang, Y., Chang, C., Chu, C., Wu, T., "Magnetic properties, adhesive characteristics, and optical properties of $Co_{40}Fe_{40}W_{20}$ films ", ***Surface Engineering***, Vol. 36, (2020), 1-8, DOI: 10.1080/02670844.2020.1753398.
2. Maliar, T., Cesiulis, H., Podlaha, EJ., "Coupled Electrodeposition of Fe–Co–W Alloys: Thin Films and Nanowires", ***Frontiers in Chemistry***, Vol. 7, (2019), 542, DOI: 10.3389/fchem.2019.00542.
3. Kołodziej, M., Śniadecki, Z., Musiał, A., Pierunek, N., Ivanisenko, Y., Muszyński, A., Idzikowski, B., "Structural transformations and magnetic properties of plastically deformed FeNi-based alloys synthesized from meteoritic matter", ***Journal of Magnetism and Magnetic Materials***, Vol. 502, (2020), 166577, DOI: 10.1016/j.jmmm.2020.166577.
4. Lu, W., Jia, M., Ling, M., Xu, Y., Shi, J., Fang, X., Song, Y., Li, X., "Phase evolution and magnetic properties of FeCo films electrodeposited at different temperatures", ***Journal of Alloys and Compounds***, Vol. 637, (2015), 552-556, DOI: 10.1016/j.jallcom.2015.03.036.
5. Toghraei, M., Siadati, H., "Electrodeposited Co-Pi Catalyst on α-Fe_2O_3 Photoanode for Water-Splitting Applications", ***International Journal of Engineering, Transactions C: Aspects***, Vol. 31, No. 12, (2018), 2085-2091, DOI: 10.5829/ije.2018.31.12c.13.
6. Sajjadnejad, M., Omidvar, H., Javanbakht, M., "Influence of pulse operational parameters on electrodeposition, morphology and microstructure of Ni/nanodiamond composite coatings", ***International Journal of Electrochemical Science***, Vol. 12, (2017), 3635-3651, DOI: 10.20964/2017.05.52.
7. Pashai, E., Najafpour, G. D., Jahanshahi, M., Rahimnejad, M., "Highly Sensitive Amperometric Sensor Based on Gold Nanoparticles Polyaniline Electrochemically Reduced Graphene Oxide Nanocomposite for Detection of Nitric Oxide", ***International Journal of Engineering, Transaction B: Applications***, Vol. 31, No. 2, (2018), 188-195, DOI: 10.5829/ije.2018.31.02b.01.
8. Arjmand, S., Khayati, G., Akbari, G., "Al/Ti_5Si_3-Al_3Ti composite prepared via in-situ surface coating of Ti using tungsten inert gas welding", ***Journal of Alloys and Compounds***, Vol. 808, (2019), 151739, DOI: 10.1016/j.jallcom.2019.151739.
9. Sistaninia, M., Doostmohammadi, H., Raiszadeh, R., "Formation Mechanisms and Microstructure Characterization of Al/Al_3Ni In-situ Composite by Compound Casting", ***Metallurgical and Materials Transactions B***, Vol. 50, (2019), 3020–3026, DOI: 10.1007/s11663-019-01682-1.
10. Adineh, M., Doostmohammadi, H., "Microstructure, mechanical properties and machinability of Cu–Zn–Mg and Cu–Zn–Sb brass alloys", ***Materials Science and Technology***, Vol. 35, No. 12, (2019), 1504-1514, DOI: 10.1080/02670836.2019.1630089.
11. Yousefi, E., Sharafi, S., Irannejad, A., "The structural, magnetic, and tribological properties of nanocrystalline Fe-Ni permalloy and Fe-Ni-TiO_2 composite coatings produced by pulse electro co-deposition", ***Journal of Alloys and Compounds***, Vol. 753, (2018), 308-319, DOI: 10.1016/j.jallcom.2018.04.232.
12. Khayati, G.R., Janghorban, K., "Preparation of nanostructure silver powders by mechanical decomposing and mechanochemical reduction of silver oxide", ***Transactions of Nonferrous Metals Society of China***,Vol. 23, (2013), 1520-1524, DOI: 10.1016/S1003-6326(13)62625-4.
13. Ghaferi, Z., Sharafi, S., Bahrololoom, M., "The role of electrolyte pH on phase evolution and magnetic properties of CoFeW codeposited films", ***Applied Surface Science***, Vol. 375, (2016), 35-41, DOI: 10.1016/j.apsusc.2016.03.063.
14. Yoosefan, F., Ashrafi, A., Monir vaghefi, S., Constantin, I., "Synthesis of CoCrFeMnNi High Entropy Alloy Thin Films by Pulse Electrodeposition: Part 1: Effect of Pulse Electrodeposition Parameters", ***Metals and Materials International***, Vol. 26, (2019), 1262-1269, DOI: 10.1007/s12540-019-00404-1.
15. Barati Darband, Gh., Aliofkhazraei, M., Sabour Rouhaghdam, A., "Facile electrodeposition of ternary Ni-Fe-Co alloy nanostructure as a binder free, cost-effective and durable electrocatalyst for high-performance overall water splitting", ***Journal of Colloid and Interface Science***, Vol. 547, (2019), 407-420, DOI: 10.1016/j.jcis.2019.03.098.
16. Saebnoori, E., Vali, I., Yousefpour, M., "Surface Activation of Ni-Ti Alloy by Using Electrochemical Process for Biomimetic Deposition of Hydroxyapatite Coating", ***International Journal of Engineering, Transactions A: Basics***, Vol. 27, No. 10, (2014), 1627-1634, DOI: 10.5829/idosi.ije.2014.27.10a.17.
17. Chen, M., Lan, L., Shi, X., Yang, H., Zhang, M., Qiao, J., "The tribological properties of Al0.6CoCrFeNi high-entropy alloy with the σ phase precipitation at elevated temperature ", ***Journal of Alloys and Compounds***, Vol. 777, (2019), 180-189, DOI: 10.1016/j.jallcom.2018.10.393.
18. Torabinejad, V., Aliofkhazraei, M., Assareh, S., Allahyarzadeh, M., Rouhaghdam, A.S., "Electrodeposition of Ni-Fe alloys, composites, and nano coatings–A review", ***Journal of Alloys and Compounds***, Vol. 691, (2017), 841-859, DOI: 10.1016/j.jallcom.2016.08.329.
19. Khazaei, M., Sarvestani, E., and Khayati, G., "Modeling and optimization of chemical composition of nano/amorphous Fea.Nib.Nbc.Zrd alloy prepared via high-energy ball milling with enhanced soft magnetic properties; A mixture design approach", ***Journal of Alloys and Compounds***, Vol. 841, (2020), 155646, DOI: 10.1016/j.jallcom.2020.155646.
20. Lim, D., Ku, B., Seo, D., Lim, C., Oh, E., Shim, S., Baeck, S., "Pulse-reverse electroplating of chromium from Sargent baths: Influence of anodic time on physical and electrochemical properties of electroplated Cr ", ***International Journal of Refractory Metals and Hard Materials,*** Vol. 89, , (2020), 105213, DOI: 10.1016/j.ijrmhm.2020.105213.
21. Saad, S., Boumerzoug, Z., Helbert, A.L., Brisset, F., Baudin, T., "Effect of TiO_2-Nanoparticles on Ni Electrodeposition on Copper Wire", ***Metals,*** Vol. 10, (2020), 406, DOI: 10.3390/met10030406.
22. Wang, Y., Gao, W., He, Z., Zhang, S., Yin, L., "Improved mechanical properties of Cu–Sn–Zn–TiO_2 coatings", ***International Journal of Modern Physics B***, Vol. 34, No. 01, (2020), 2040039, DOI: 10.1142/S0217979220400391.
23. Yar-Mukhamedova, G., Ved', M., Yermolenko, I., Sakhnenko, N., Karakurkchi, A., Kemelzhanova, A., "Effect of Electrodeposition Parameters on the Composition and Surface Topography of Nanostructured Coatings by Tungsten with Iron and Cobalt", ***Eurasian Chemico-Technological Journal***, Vol. 22, No. 1, (2020), 19-25, DOI: 10.18321/ectj926.
24. Ved', M., Sakhnenko, N., Yermolenko, I., Yar-Mukhamedova, G., Atchibayev, R., "Composition and Corrosion Behavior of Iron-Cobalt-Tungsten", ***Eurasian Chemico-Technological Journal***, Vol. 20, No. 2, (2018), 145-152, DOI: 10.18321/ectj697.
25. Seyedraoufi, Z., Mirdamadi, Sh., Rastegari, S., "Electrodeposition of Nano Hydroxyapatite Coating on Biodegradable Mg-Zn Scaffold", ***International Journal of Engineering***, Vol. 27, No. 6, (2014), 939-944, DOI: 10.5829/idosi.ije.2014.27.06c.12.
26. Chunyang, M., Danqiong, Z., Zhipeng, M., "Effects of duty cycle and pulse frequency on microstructures and properties of

electrodeposited Ni–Co–SiC nanocoatings", ***Ceramics International***, Vol. 46, (2020), 12128-12137, DOI: 10.1016/j.ceramint.2020.01.258.

27. Yousefi, E., Irannejad, A., Sharafi, S., "Electrodeposition and characterization of nanocrystalline Fe−Ni−Cr alloy coatings synthesized via pulse current method", ***Transactions of Nonferrous Metals Society of China***, Vol. 29, (2019), 2591-2603, DOI: 10.1016/S1003-6326(19)65166-6.

Persian Abstract

چکیده

در این مطالعه سعی شده تا کامپوزیت نانوبلور Fe-Co-TiO_2 در چگالی جریان‌های مختلف در بازه (۲۰–۵۰ mA/cm^2) از طریق آب‌کاری پالسی تهیه شود. کامپوزیت‌های آماده شده با روش های FESEM، EDS، ریزسختی‌سنجی ویکرز، VSM و XRD مشخصه‌یابی شدند. نتایج نشان داد که شکل گیری مورفولوژی گل کلم در چگالی جریان پایین‌تر ارجحیت داشته است. علاوه بر این، چگالی جریان بالاتر باعث افزایش مقدار آهن در ترکیب شده و هم زمان از مقدار Co و TiO_2 پوشش ها کاسته می‌شود. الگوهای XRD و آنالیز ریتولد تشکیل ترکیب BCC (به عنوان فاز غالب) و FCC را تایید کرد. چگالی جریان بالاتر به دلیل وجود آهن بیشتر و نانوذرات TiO_2 کمتر، باعث ایجاد مغناطش اشباع بالاتر و همچنین وادارندگی کمتر شده است. همچنین، کمترین وادارندگی و بیشترین مغناطش اشباع در چگالی جریان ۵۰ mA/cm^2 به دست آمد. این در حالی بود که حداکثر میکروسختی در چگالی جریان ۳۰ mA/cm^2 ایجاد شده بود.

International Journal of Engineering

Journal Homepage: www.ije.ir

The Effect of Rapid Deformation Process to Improve Creep and Tensile Resistance of AZ91 Magnesium Alloy Plates

H. Agha Amini Fashami[a], N. Bani Mostafa Arab*[a], M. Hosseinpour Gollo[a], B. Nami[b]

[a] *Mechanical Engineering, Shahid Rajaee Teacher Training University, Tehran, Iran*
[b] *Materials Engineering, Shahid Rajaee Teacher Training University, Tehran, Iran*

P A P E R I N F O

Paper history:
Received 28 December 2019
Received in revised form 25 June 2020
Accepted 13 August 2020

Keywords:
Rapid Deformation Process
Multi-Pass Friction Stir Processing
Tensile Strength
Creep
AZ91 Alloy

A B S T R A C T

Demand for increasing strength to weight ratio, elimination of electromagnetic waves, and vibration damping has led to the wide application of magnesium-base alloys such as AZ91 in various industries like aerospace, military, vehicle, and shipbuilding. However, because of the unstable secondary particles and casting defects located on the rough grain boundaries and in the dendritic regions, due to sliding of the grain boundary, the creep resistance and tensile strength of Mg alloys at high temperatures reduce. To improve the high-temperature properties, rapid deformation processes such as friction stir processing can be employed. In this study, the influence of multi-pass friction stir processing on microhardness, tensile, and creep behavior of AZ91 at several temperatures from 25 to 210 °C has been studied. Optical microscopy and scanning electron micrograph were used to study the microstructure of the cast and processed samples and Clemex commercial software was used for grain size measurement. The experimental results indicated that at room temperature, the microhardness, tensile, and creep strength of the processed samples as compared to the unprocessed ones increased by 23, 29 and 38%, respectively. In addition, after multi-pass friction stir processing, the tensile and creep strength of the samples at 210 °C increased by 31 and 47%, respectively. Also, the average grain size of the multi-passed friction stir processed AZ91 alloy decreased by 88%. The maximum ultimate tensile strength of 276 MPa was obtained at the tool rotational speed of 1200 r/min, the traverse speed of 60 mm/min, and the tool tilt angle of 3°. The empirical results indicated that this rapid deformation process can be useful in enhancing the mechanical properties of AZ91 alloy at high temperatures.

***doi**: 10.5829/ije.2020.33.10a.22*

1. INTRODUCTION

Among the magnesium alloys, the AZ family has excellent properties such as castability at room temperature. However, $Mg_{17}Al_{12}$ particles with the low melting point (120 °C) on the rough grain boundaries and in the dendritic regions reduce the mechanical properties of these alloys at high temperatures. Friction stir processing (FSP) is a process to improve the tribological and microstructural properties of metallic materials. During FSP, sufficient heat is created to soften the material without melting which causes dynamic recrystallization of rough grains. In fact, due to the mechanical turbulence and stirring action using a rotating tool, the high strain rate deformation occurs. Therefore, FSP should cause a homogeneous microstructure, breakdown of the grains, decrease the size of $Mg_{17}Al_{12}$ eutectic particles, distribute the particles on the grain boundaries, reduce the casting defects and hence improve the mechanical properties [1]. However, the improvement of properties after FSP is highly dependent on the process parameters such as tool rotational speed, traverse speed, axial force, tool dimension and tool tilt angle. Recently, several works attempted to develop the performance of this process and increase the mechanical properties via FSP.

In recent years, many researchers [2-7] have demonstrated the effect of single-pass FSP on the mechanical properties of different alloys, especially cast

*Corresponding Author Institutional Email: *n.arab@sru.ac.ir* (N. Bani Mostafa Arab)

Please cite this article as: H. Agha Amini Fashami, N. Bani Mostafa Arab, M. Hosseinpour Gollo, B. Nami, The Effect of Rapid Deformation Process to Improve Creep and Tensile Resistance of AZ91 Magnesium Alloy Plates, International Journal of Engineering (IJE), IJE TRANSACTIONS A: Basics Vol. 33, No. 10, (October 2020) 2039-2046

alloys. Buffa et al. [8] reported the effect of water-cooling FSP on microstructure and tensile properties of 304L stainless steel. Their empirical and numerical reports indicate that water cooling increased the strength and reduced the ductility of the material; especially in the thermomechanically-affected zone (TMAZ). Cavaliere and Marco [9] stated that after single-pass FSP on AZ91, the superplasticity behavior improved. Feng [10] reported that single-pass FSP increased the tensile stress of AZ91 alloy at room temperature.

According to Sun and Apelian's research [11], after performing FSP on aluminum alloy, the size of secondary particles reduced, but the microstructure was not homogenous. Raja and Pancholi [12] reported after single-pass FSP on AZ91 alloy, the coarse structure of the α-Mg field refined slightly, the network of secondary particles dissolved, and the mechanical properties (such as tensile and impact) at room temperature improved. Lua and Zhangb. [13] reported that after FSP, the β-$Mg_{17}Al_{12}$ networks broke into smaller particles, but the microstructure of AZ91 alloys was not finely equiaxed.

Heidarpour et al. [14] investigated the microstructure and tensile properties of AZ91 after water-submerged FSP and non-cooled FSP. Their results show that after FSP, the rough casting structure converted into coaxial grains, and the lattice $Mg_{17}Al_{12}$ eutectic phases converted into pin-like particles on the grain boundaries. The structure of water-submerged FSP samples was more homogenous than that of the non-cooled processed samples; however, the ductility of the specimens after submerged FSP dramatically reduced. Edwin and Shamsudeen [15] studied the effect of tool pin length on microstructure and tensile strength during single-pass FSP. Their report shows that with increasing the pin length, tensile strength improved. However, increasing the length of the pin causes the tool to break quickly. Govindaraju et al. [16] studied the microstructure and mechanical properties of friction stir processed AZ91D with different heat treatment conditions. Wang et al. [2] conducted FSP on as-cast AZ31 to refine grains, homogenize the microstructure, and dissolve the secondary phases. Wang et al. [17] found that after FSP on Mg alloy, with dissolving the rough phases, the tensile and ductility properties were increased.

Mamaghani et al. [18] studied the effect of types of nanoparticles and process parameters on morphological and hardness properties of acrylonitrile butadiene styrene (ABS) plates. For this purpose, a slot with given dimensions (the depth and width) was created on the ABS sheets, and then three types of nanoparticles "nano clay, nano Fe_2O_3, and multi-walled carbon nanotube" were added to the slot. The workpieces were friction stir processed under different rotational and traverse speeds.

In addition, some researchers investigated the effective strain [19], temperature field [20, 21], microstructural modification [22] and material flow [23, 24] during single-pass FSP and friction stir welding (FSW) using 2-dimensional and 3-dimensional numerical modeling. Nie et al. [25] investigated the residual stresses and temperature field during FSW. Richards developed their model using two separate heat sources defined with Fortran77 DEFLUX subroutines. The modified model has been used to predict the thermal field around the tool [26]. Tutunchilar et al. [23] modeled the flow of material when a cylindrical pin was used for performing this process. They investigated the material behavior with the point tracking method. Rahul et al. [24] showed that during FSP on Mg alloys, the material flow around the pin is asymmetric. Assidi et al. [27] used 3D Forge3 finite element software based on Arbitrary Lagrangian-Eulerian formulation and automatic remeshing for modeling FSP.

Also, in recent years, FSP has been introduced as a relatively new way to create a homogeneous and fine-grained coating with improved resistance to wear and corrosion. Mostafapour et al. [28] studied the deposition of Al7075-T6 coating on Al2024-T351 substrates and investigated the effects of the rotational speed, axial force, and feed rate on the mechanical properties and microstructure of the specimens. Vahdati et al. [29] investigated the production of Al7075 surface composites using reinforcing particles (Al_2O_3) and FSP process.

Previous studies show that during single-pass FSP, thermal accumulation and asymmetric material flow applied to the samples may result in the growth of the grains adjacent to the process regions, non-homogenous structure, and imperceptible increase or reduction of mechanical properties. It is possible to prepare finer-grain specimens with improved strength and produce modified wide plates through multi-pass friction stir processing (MPFSP). In this section, some studies on performing MPFSP were reviewed. Chai et al. [30] subjected AZ91 plates with a thickness of 6 mm to two-pass FSP. Their results show that some coarse β-$Mg_{17}Al_{12}$ phases that existed after the first pass of FSP break and dissolve into the matrix under the action of the second pass of FSP. Lu et al. [31] conducted two-pass FSP (with water cooling) on cast AZ91 plates. Their results show that the microhardness, tensile strength, and elongation of the processed specimens were 94.7 HV, 155.5 MPa, and 31.5%, respectively, which were more than that of the base plates. Allavikutty et al. [32] developed a layered microstructure with three different configurations by MPFSP on AZ91 using three various tools with probe lengths of 4, 5, and 7 mm. The configurations were half thickness processed, surface modified, and full

thickness processed. They concluded that the fatigue properties improved with increasing the fraction of the friction stirred processed regions in AZ91 alloy.

Alavi et al. [33], studied the influence of overlapping ratio on graining, ductility, and tensile strength at room temperature after performing water-cooling FSP on AZ91. Mansoor and Ghosh [3], carried out the MPFSP on extruded ZK60 Mg plates to improve the mechanical properties. Nakata et al. [34] reported after MPFSP on A383 plate, the casting defects eliminated, microstructure refined, and ductility improved.

Sato and Park [4], mentioned that MPFSP is a process for the modification of AZ91 casting. Venkateswarlu et al. [35] investigated the effect of overlapping ratio(OR) and processing direction on the improvement of the tensile and ductility of AZ31 alloy.

Xicai et al. [5], conducted the two-pass FSP (with water cooling) on AZ61 magnesium alloy to improve the microstructure and dissolution of the β-phases. However, due to the adverse effect of texture evolution, the tensile strength of the two-pass processed workpiece compared to friction stir processed samples decreased.

A review of previous studies shows that the effect of consecutive passes (more than two passes) on mechanical properties and microstructure modification of AZ91 at high temperatures has not yet been investigated. As explained, in recent years, FSP has been the subject of many research studies. However, few studies have been conducted on MPFSP as a process to modify wide surfaces. In this research, the effect of MPFSP with 50% OR on microstructure, microhardness, tensile, and creep strength of AZ91 alloy at several temperatures from 25 to 210 °C were investigated. In the next sections, the description of materials, equipment, and tests are presented. In section 3, the results and discussion are presented and at the end, in section 4, conclusions are given.

2. MATERIALS AND METHODS

The workpiece material selected for this study was magnesium alloy AZ91 in the form of casting plates with the dimensions of 600×300×10 mm. The chemical composition of this alloy is listed in Table 1. The physical and mechanical properties of AZ91 are given in Table 2 [5, 36]. The tool was prepared from H13 tool steel with a pin size of 4mm diameter, 4mm length, and a flat shoulder with the diameter equal to 18mm. The tool properties are shown in Table 3 [37].

The tool was rotated clockwise and tilted 3 degrees opposite to the processing direction with 1mm of penetration depth. The process was performed using a universal milling machine DECKEL FP4M with

TABLE 1. The Chemical Composition of the AZ91 alloy

Al	Zn	Mn	Si	Fe	Ni	Mg
8.8	0.7	0.2	0.03	0.002	0.0002	Bal.

TABLE 2. The material properties of AZ91 at 25 ˚C

The important properties of AZ91	Value
"Young`s modulus of elasticity (GPa)"	46
"Poisson`s ratio"	0.33
"Thermal conductivity ($Wm^{-1}K^{-1}$)"	72
Coefficient of thermal expansion ($^0C^{-1}$)"	2.4×10^{-5}
Density (kg m^{-3})	1810
Specific heat capacity (J Kg^{-1} $^0C^{-1}$)	1050
Solidus temperature(^0C)	470
Liquids temperature (^0C)	595

TABLE 3. The material properties of H13

The essential properties of AZ91	Value
"Emissivity"	0.7
Coefficient of thermal expansion ($^0C^{-1}$)	1.17×10^{-5}
"Poisson`s ratio"	0.3

different rotational and traverse speeds. The traverse speeds were 40, 60, and 80mm/min. Also, the tool rotational speeds of 1000 and 1200 rpm were selected. To find suitable values for process parameters, the processed specimens were inspected for process defects. Small defects on the surface could be detected using the liquid penetrate test method according to the ASME-Section V standard (article 6). In addition, for the detection of internal defects, the radiography test according to EN1435 standard using panoramic XXG300s equipment was employed. Process defects were observed as shown in Figures 1 and 2. Finally, the rotational speed of 1200 rpm and the traverse speed of 60 mm/min were selected for producing defect-free samples. The friction stir processed workpiece, with the selected parameters is shown in Figure 3.

The OR is used to determine the overlapping area between two consecutive passes and is defined by Equation (1) [35].

$$OR = 1 - \left(\frac{l}{d_{probe}} \right) \quad (1)$$

where l and d_{probe} are "the distance between the centers of two consecutive passes" and "the pin diameter", respectively. After performing MPFSP on AZ91 plates with the selected parameters, the optical microscopy (OM, OLYMPUS CKX53 model) and scanning electron

microscopy (SEM, VEGA TESCAN-XMU model) were used to study the microstructure of the processed samples. In addition, the Vickers microhardness of the samples was measured on the cross section perpendicular to the processing path under 100 g loading for 15 s.

Standard tensile test specimens with 20mm length and the width of 6mm were cut using wire cut electro-discharge machining according to the ASTM standard E8/E8M [38]. These samples were parallel and perpendicular to the processing path (as shown in Figure 4). After preparing sub-size samples, the tensile tests were performed using the Zwick Roell testing device with the strain rate of 10^{-3} s^{-1}, at several temperatures of 25, 140, 170, and 210°C.

For conducting the impression creep test, the test samples with dimensions of 8×8×8 mm were prepared. The details of the impression creep test were explained by Mahmudi et al. [39]. The creep-testing device equipped with a controllable temperature furnace was used to carry out the constant-temperature, and constant-load impression creep tests with a simple cylindrical indenter having 2mm diameter. Also, the impression tests were performed at several temperatures (25, 140, 170, and 210°C).

Figure 1. Radiographic images with different rotational and progressive speeds

Figure 2. Defects detected by the penetrant test

Figure 3. The friction stir processed workpiece with selected parameters

3. RESULTS AND DISCUSSION

3. 1. The Microhardness Test The hardness profiles in the stirred zone-up and stirred zone-down are shown in Figure 5. The profiles show that after MPFSP, generally, the hardness of processed workpieces increased to 87 VHN (Vickers hardness number), which was 23% more than the hardness of the base workpiece (71 VHN). As shown in Figure 5, the hardness of the stirred zone-up is more than the hardness of the stirred zone-down.

3. 2. The Microstructures The metallographic samples were prepared through the standard polishing method and then etched. The microstructure of the casting plates and multi-pass processed samples were studied using OM and SEM. The casting defects such as tunnels, grooves, cavities, and nonadhesion between the field and secondary particles are observed in Figure 6a. In addition, Figure 6b shows the microstructure of the cast workpiece that consists of non-homogenous grains and the network of eutectic phases in the α-Mg field.

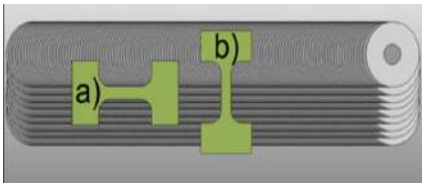

Figure 4. Cutting direction of the tensile test samples (a) Parallel and (b) perpendicular to the process path

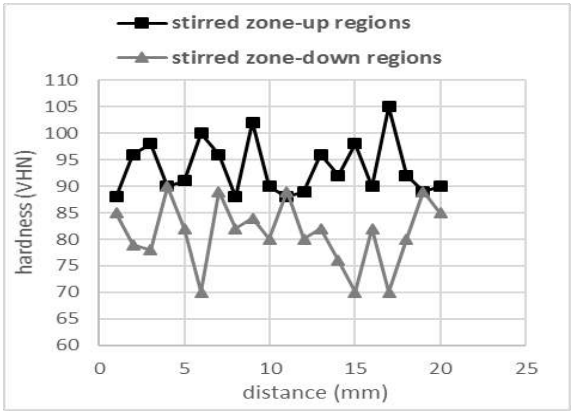

Figure 5. The hardness profiles in the stirred zone-up and stirred zone-down

After MPFSP, the microstructure refined, the grain size decreased, the eutectic lattice phases converted into the spherical shape particles, and the casting defects reduced as shown in Figure 7. After MPFSP, as shown in Figures 7b and 7c, the microstructure was non uniform. Because of intense deformation at the tool shoulder-workpiece interface, grains in the stirred zone-up can be coarser than those in the stirred zone-down, and the dislocations density in stirred zone-up is more than that in the stirred zone-down [40]. Since the microhardness of the processed samples is affected by the microstructural properties, dynamic recrystallization, texture changes, and especially the dislocations density [40]; therefore, the hardness in the zone-up is more than that in the stirred zone-down.

The average grain size of cast samples is about 98 µm. During FSP, the grains are refined. The average grain size of the MPFS Processed AZ91 alloy is about 11 µm and homogenous grains with reduced casing defects were observed. The CLEMEX commercial software was used for grain size measurement.

In a similar paper, El-Danaf et al. [41] investigated the effect of FSP on the grain size of cold-rolled sheets of AA5083. They reported that decreasing the grain size causes increase in hardness from 80 to 95HV on the nugget center. Nascimento et al. [42] studied the effect of FSP on the aluminum alloy (AA5083) for obtaining a uniform hardness using one-pass and multi-pass processes.

3. 3. Tensile Test The tensile test results for the base metal and the processed samples are given in Figure 8. As shown, the yield and ultimate stresses of the single-pass and MP processed samples at room temperature (parallel to the processing paths) increased by about 21 and 29% compared to the base workpiece. Improving the mechanical properties of the processed samples can be attributed to the refinement of the grains size in the processed zone and modifying the microstructure after MPFSP. In a similar research on AZ31, Feng and Ma [10] concluded that reducing the grain size increases strength. On the other hand, the recrystallization process reduces the density of dislocations. The competition between reducing the strength caused by decreasing the dislocations density and increasing the strength caused by reducing the grain size affects the hardness and tensile properties. In this research, the effect of reducing grain size is more effective, and the strength increased. Besides, after performing FSP, because of the elimination of defects and crushing of the unstable lattice intermetallic phases into the matrix, the microstructure and mechanical properties, especially at high temperatures improved. As shown in Figure 8, the yield and ultimate stresses of multi-pass processed samples at 140, 170, and 210°C increased by about 23 and 31% compared to the base workpieces. Reducing the tensile strength at a perpendicular direction to the processing path can be due to the development of firm basal texture in several non-perpendicular directions [43].

3. 4. Creep Test The creep behavior of base workpiece and the processed samples was investigated by impression testing in which the indenter is a circular cylinder with a flat end. After loading, the penetration depth of the indenter was measured automatically depending on time up to 4000s. The power-law equation defines the creep rate in the steady-state stage. When the impression test is used to determine creep resistance, the strain creep rate is calculated using the "impression depth of indenter"/time slope (V_{imp}=dh/dt) and equivalent stress is defined using the relation between the force applied to the punch and diameter of indenter

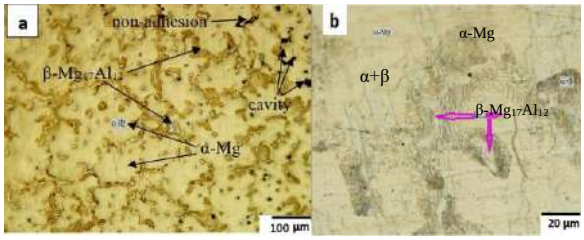

Figure 6. Unprocessed specimen of AZ91 alloy

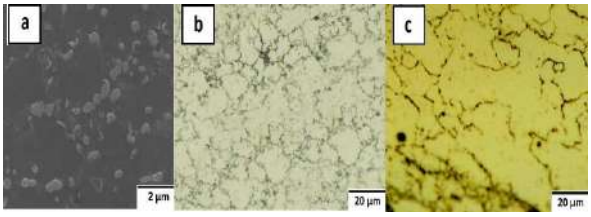

Figure 7. The microstructure of a) processed specimen of AZ91 alloy using SEM, b) stir zone-down region, c) stir zone-up region

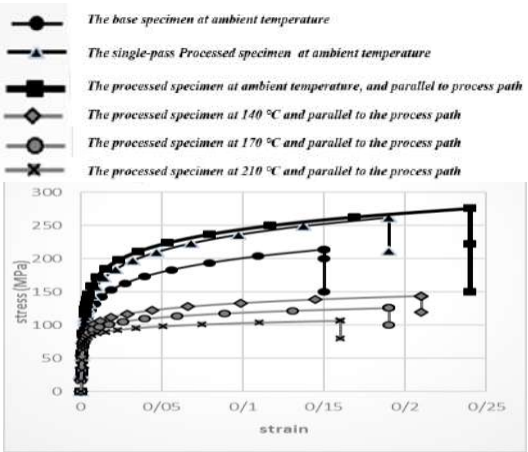

Figure 8. The Stress-strain diagrams for all sample

($\sigma_{imp} = 4F/\pi\varphi^2$). Here, F is the load and φ is the indenter diameter. Using the above equations and rearranging the power-law equation, the impression creep can be characterized by Equation (2).

$$\frac{V_{imp}T}{G} = A\left(\frac{\varphi c_2}{c_1^n}\right)\left(\frac{b}{d}\right)^p\left(\frac{bD_0}{k}\right)^n\left(\frac{\sigma_{imp}}{G}\right)^n \exp\left(\frac{Q_C}{RT}\right) \quad (2)$$

A: The constant,
b: The burgers vector,
d: The grain diameter,
D_0: The frequency index,
K: The Boltzmann's constant,
n: The stress exponent,
Qc: The creep-activation energy,
R: The universal gas constant.

Using this equation, to calculate the stress exponent n, the curve of $\ln(V_{imp}T/G)$ against $\ln(\sigma_{imp}/G)$ at constant T is plotted. Also, the activation energy Qc can be evaluated from a curve of $\ln(V_{imp}T/G)$ against (1/T) at constant (σ_{imp}/G). The shear modulus in this equation depends on the testing temperature. In this study, the creep of the base and processed samples is investigated at several temperatures when the $\sigma_{imp}/G \sim 0.034$ is constant.

The "G (MPa) =18,460–8.2T (K)" is the relation to calculate the shear modulus (G) of the AZ91 magnesium alloy at different temperatures (T). Here, by calculating the impression depth/time slope in the steady-state stage, the effect of FSP and temperature on the creep rate can be investigated. Figure 9 shows the penetration depth of indenter at different times when the tests were performed at three temperatures of 140, 170, and 210°C on cast and friction stir processed specimens.

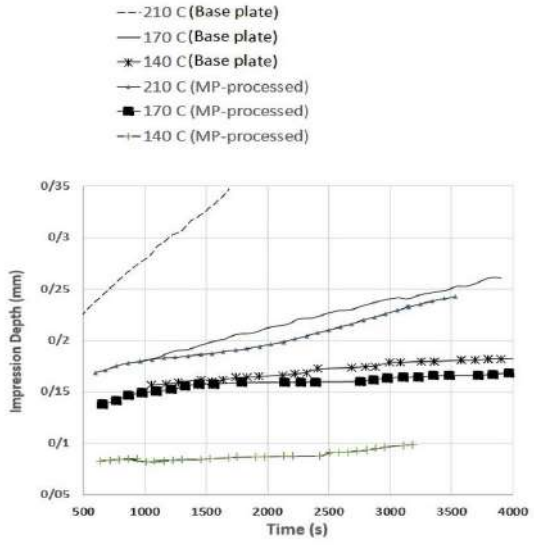

Figure 9. The plot of impression depth against time at temperatures of 140, 170, and 210 °C for casting and MPFS Processed specimens

As shown in Figure 9, based on the penetration rate of the indenter, creep strength of the processed specimens at 210, 170, and 140 °C are more than that of the unprocessed specimens by about 47, 36, and 33%, respectively. As shown in Figure 6, the microstructure of the cast specimen was found to be unstable due to the network of eutectic particles on the grain boundary during cooling. As shown in Figure 7, the size of grains decreased and β-particles dissolved in the matrix. Therefore, the negative effects of reducing the strength due to the softening of eutectic phases, especially at high temperatures is decreased.

4. CONCLUSIONS

According to the experimental results, the following conclusions could be given:

1. The microhardness of the processed samples is more than that of the base material by about 23%.
2. The microhardness in the stirred zone-up is more than that in the stirred zone-down by about 14%.
3. The yield and tensile strength of specimens after processing increased by about 21 and 29% compared to the base workpiece (at room temperature).
4. The main factors for increasing the tensile strength of the MPFSP samples are considered to be the casting and processing defects, homogenous microstructure, and dissolution of the β-phases.
5. Improvement of tensile and creep properties at high temperatures is far more significant than that at room temperature. The yield and ultimate stresses of multi-pass processed samples at 140, 170, and 210°C increased by about 23% and 31% compared to the base workpiece.
6. The creep resistance of friction stir processed samples was more than that of the unprocessed ones by about 38%.
7. The microstructure investigation shows that after FSP with the selected parameters, defects such as cracks, cavity, interconnection, non-adhesion between the field, secondary phase particles, and rough network phases, which cause stress concentration and lead to accidental and bad time failure are removed, and the microstructure is modified.

5. REFERENCES

1. Mordike, B. and Ebert, T., "Magnesium: Properties—applications—potential", ***Materials Science and Engineering: A***, Vol. 302, No. 1, (2001), 37-45. DOI: 10.1016/S0921-5093(00)01351-4
2. Wang, Y., Huang, Y., Meng, X., Wan, L. and Feng, J., "Microstructural evolution and mechanical properties of mgznyzr alloy during friction stir processing", ***Journal of Alloys***

and Compounds, Vol. 696, No., (2017), 875-883. DOI: 10.1016/j.jallcom.2016.12.068

3. Mansoor, B. and Ghosh, A., "Microstructure and tensile behavior of a friction stir processed magnesium alloy", ***Acta materialia***, Vol. 60, No. 13-14, (2012), 5079-5088. DOI: 10.1016/j.actamat.2012.06.029
4. Sato, Y., Park, S., Matsunaga, A., Honda, A. and Kokawa, H., "Novel production for highly formable mg alloy plate", ***Journal of Materials Science***, Vol. 40, No. 3, (2005), 637-642. DOI: 10.1007/s10853-005-6301-1
5. Luo, X., Cao, G., Zhang, W., Qiu, C. and Zhang, D., "Ductility improvement of an az61 magnesium alloy through two-pass submerged friction stir processing", ***Materials***, Vol. 10, No. 3, (2017), 253. DOI: 10.3390/ma10030253
6. Gangil, N., Maheshwari, S. and Siddiquee, A.N., "Influence of tool pin and shoulder geometries on microstructure of friction stir processed aa6063/sic composites", ***Mechanics & Industry***, Vol. 19, No. 2, (2018), 211. DOI: 10.1051/meca/2018010
7. Kordestani, F., Ghasemi, F.A. and Arab, N.M., "An investigation of fsw process parameters effects on mechanical properties of pp composites", ***Mechanics & Industry***, Vol. 17, No. 6, (2016), 611. DOI: 10.1051/meca/2016012
8. Buffa, G., Hua, J., Shivpuri, R. and Fratini, L., "A continuum based fem model for friction stir welding—model development", ***Materials Science and Engineering: A***, Vol. 419, No. 1-2, (2006), 389-396. DOI: 10.1016/j.msea.2005.09.040
9. Cavaliere, P. and De Marco, P., "Fatigue behaviour of friction stir processed az91 magnesium alloy produced by high pressure die casting", ***Materials Characterization***, Vol. 58, No. 3, (2007), 226-232. DOI: 10.1016/j.matchar.2006.04.025
10. Feng, A. and Ma, Z., "Enhanced mechanical properties of mg–al–zn cast alloy via friction stir processing", ***Scripta materialia***, Vol. 56, No. 5, (2007), 397-400. DOI: 10.1016/j.scriptamat.2006.10.035.
11. Sun, N. and Apelian, D., "Friction stir processing of aluminum cast alloys for high performance applications", ***Jom***, Vol. 63, No. 11, (2011), 44-50. DOI: 10.1007/s11837-011-0190-3
12. Raja, A. and Pancholi, V., "Effect of friction stir processing on tensile and fracture behaviour of az91 alloy", ***Journal of Materials Processing Technology***, Vol. 248, No., (2017), 8-17. DOI: 10.1016/j.jmatprotec.2017.05.001
13. Lu, Z.L. and Zhang, D.T., "Microstructure and mechanical properties of a fine-grained az91 magnesium alloy prepared by multi-pass friction stir processing", in Materials Science Forum, Trans Tech Publ. Vol. 850, 778-783. DOI: 10.4028/www.scientific.net/MSF.850.778
14. Heidarpour, A., Ahmadifard, S. and Rohania, N., "Fsp pass number and cooling effects on the microstructure and properties of az31", ***Journal of Advanced Materials and Processing***, Vol. 6, No. 2, (2018), 47-58. DOI: http://jmatpro.iaun.ac.ir/article_623137.html
15. Shamsudeen, S. and Dhas, J.E.R., "Optimization of multiple performance characteristics of friction stir welded joint with grey relational analysis", ***Materials Research***, Vol. 21, No. 6, (2018). DOI: 10.1590/1980-5373-mr-2017-1050
16. Govindaraju, M., Vignesh, R.V. and Padmanaban, R., "Effect of heat treatment on the microstructure and mechanical properties of the friction stir processed az91d magnesium alloy", ***Metal Science and Heat Treatment***, Vol. 61, No. 5-6, (2019), 311-317. DOI: 10.1007/s11041-019-00422-1
17. Wang, Q., Xiao, L., Liu, W., Zhang, H., Cui, W., Li, Z. and Wu, G., "Effect of heat treatment on tensile properties, impact toughness and plane-strain fracture toughness of sand-cast mg-6gd-3y-0.5 zr magnesium alloy", ***Materials Science and Engineering: A***, Vol. 705, (2017), 402-410. DOI: 10.1016/j.msea.2017.08.100
18. Mamaghani Shishavan, S., Azdast, T., Mohammadi Aghdam, K., Hasanzadeh, R., Moradian, M. and Daryadel, M., "Effect of different nanoparticles and friction stir process parameters on surface hardness and morphology of acrylonitrile butadiene styrene", ***International Journal of Engineering, Transactions A: Basics***, Vol. 31, No. 7, (2018), 1117-1122. DOI: 10.5829/ije.2018.31.07a.16
19. Asadi, P., Mahdavinejad, R. and Tutunchilar, S., "Simulation and experimental investigation of fsp of az91 magnesium alloy", ***Materials Science and Engineering: A***, Vol. 528, No. 21, (2011), 6469-6477. DOI: 10.1016/j.msea.2011.05.035
20. Swaminathan, S., Oh-Ishi, K., Zhilyaev, A.P., Fuller, C.B., London, B., Mahoney, M.W. and McNelley, T.R., "Peak stir zone temperatures during friction stir processing", ***Metallurgical and Materials Transactions A***, Vol. 41, No. 3, (2010), 631-640. Doi: 10.1007/s11661-009-0140-7
21. Yu, Z., Zhang, W., Choo, H. and Feng, Z., "Transient heat and material flow modeling of friction stir processing of magnesium alloy using threaded tool", ***Metallurgical and Materials Transactions A***, Vol. 43, No. 2, (2012), 724-737. DOI: 10.1007/s11661-011-0862-1
22. Shercliff, H.R., Russell, M.J., Taylor, A. and Dickerson, T.L., "Microstructural modelling in friction stir welding of 2000 series aluminium alloys", ***Mechanics & Industry***, Vol. 6, No. 1, (2005), 25-35. DOI: 10.1051/meca:2005004
23. Tutunchilar, S., Haghpanahi, M., Givi, M.B., Asadi, P. and Bahemmat, P., "Simulation of material flow in friction stir processing of a cast al–si alloy", ***Materials & Design***, Vol. 40, (2012), 415-426. DOI: 10.1016/j.matdes.2012.04.001
24. Jain, R., Pal, S.K. and Singh, S.B., "Finite element simulation of pin shape influence on material flow, forces in friction stir welding", ***The International Journal of Advanced Manufacturing Technology***, Vol. 94, No. 5-8, (2018), 1781-1797. DOI: 10.1007/s00170-017-0215-3
25. Nie, L., Wu, Y. and Gong, H., "Prediction of temperature and residual stress distributions in friction stir welding of aluminum alloy", ***The International Journal of Advanced Manufacturing Technology***, Vol. 106, No. 7-8, (2020), 3301-3310. DOI: 10.1007/s00170-019-04826-4
26. De Dear, R.J. and Brager, G.S., "Thermal comfort in naturally ventilated buildings: Revisions to ashrae standard 55", ***Energy and Buildings***, Vol. 34, No. 6, (2002), 549-561. DOI: 10.1016/S0378-7788(02)00005-1
27. Assidi, M., Fourment, L., Guerdoux, S. and Nelson, T., "Friction model for friction stir welding process simulation: Calibrations from welding experiments", ***International Journal of Machine Tools and Manufacture***, Vol. 50, No. 2, (2010), 143-155. DOI: 10.1016/j.ijmachtools.2009.11.008
28. Mostafapour, A., Moradi, M., Kamali, H. and Saleh Meiabadi, M., "Multi-response optimization of the mechanical and metallurgical properties of al7075-t6 deposition process on al2024-t351 by friction surfacing using rsm and the desirability approach", ***Iranian Journal of Materials Forming***, Vol. 7, No. 1, (2020), 100-115. DOI: 10.22099/IJMF.2020.35736.114
29. Vahdati, M. and Moradi, M., "Statistical analysis and optimization of the yield strength and hardness of surface composite al7075/Al_2O_3 produced by fsp via rsm and desirability approach", ***Iranian Journal of Materials Forming***, Vol. 7, No. 1, (2020), 32-45. DOI: 10.22099/IJMF.2020.35554.1143
30. Chai, F., Yan, F., Lu, Q. and Fang, X., "Microstructures and mechanical properties of az91 alloys prepared by multi-pass friction stir processing", ***Journal of Materials Research***, Vol. 33, No. 12, (2018), 1789-1796. DOI: 10.1557/jmr.2018.98

31. Lu, Z., Zhang, D., Zhang, W. and Qiu, C., "Microstructure and properties of az91 magnesium alloy prepared by multi-pass friction stir processing under different cooling conditions", ***Journal of Aeronautical Materials***, Vol. 36, (2016), 33-38. DOI: 10.11868/j.issn.1005-5053.2016.1.006
32. Allavikutty, R., Pancholi, V. and Mishra, B.K., Layered microstructure generated by multipass friction stir processing in az91 alloy and its effect on fatigue characteristics, in Proceedings of fatigue, durability and fracture mechanics. 2018, Springer.213-222. DOI: 10.1007/978-981-10-6002-1_17
33. Nia, A.A., Omidvar, H. and Nourbakhsh, S., "Effects of an overlapping multi-pass friction stir process and rapid cooling on the mechanical properties and microstructure of az31 magnesium alloy", ***Materials & Design***, Vol. 58, (2014), 298-304. DOI: http://jmatpro.iaun.ac.ir/article_623137.html
34. Nakata, K., Kim, Y., Fujii, H., Tsumura, T. and Komazaki, T., "Improvement of mechanical properties of aluminum die casting alloy by multi-pass friction stir processing", ***Materials Science and Engineering: A***, Vol. 437, No. 2, (2006), 274-280. DOI: 10.1016/j.msea.2006.07.150
35. Venkateswarlu, G., Devaraju, D., Davidson, M., Kotiveerachari, B. and Tagore, G., "Effect of overlapping ratio on mechanical properties and formability of friction stir processed mg az31b alloy", ***Materials & Design***, Vol. 45, (2013), 480-486. DOI: 10.1016/j.matdes.2012.08.031
36. Hasan, M. and Begum, L., "Semi-continuous casting of magnesium alloy az91 using a filtered melt delivery system", ***Journal of Magnesium and Alloys***, Vol. 3, No. 4, (2015), 283-301. DOI: 10.1016/j.jma.2015.11.005
37. Yuan, Y., Guo, Q., Sun, J., Liu, H., Xu, Q., Wu, Y., Song, D., Jiang, J. and Ma, A., "High mechanical properties of az91 mg alloy processed by equal channel angular pressing and rolling", ***Metals***, Vol. 9, No. 4, (2019), 386. DOI: 10.3390/met9040386
38. Standard, A., "E8/e8m-13a.(2013).“Standard test methods for tension testing of metallic materials.”", ***ASTM International***, Vol. 1, No. 1-27.
39. Mahmudi, R., Geranmayeh, A. and Rezaee-Bazzaz, A., "Impression creep behavior of lead-free sn–5sb solder alloy", ***Materials Science and Engineering: A***, Vol. 448, No. 1-2, (2007), 287-293. DOI: 10.1016/j.msea.2006.10.092
40. Miranda, R.M., Gandra, J.P., Vilaca, P., Quintino, L. and Santos, T.G., "Surface modification by solid state processing, Woodhead Publishing, (2013). ISBN: 9780857094698
41. El-Danaf, E.A., El-Rayes, M.M. and Soliman, M.S., "Friction stir processing: An effective technique to refine grain structure and enhance ductility", ***Materials & Design***, Vol. 31, No. 3, (2010), 1231-1236. DOI: 10.1016/j.matdes.2009.09.025
42. Nascimento, F., Santos, T., Vilaça, P., Miranda, R. and Quintino, L., "Microstructural modification and ductility enhancement of surfaces modified by fsp in aluminium alloys", ***Materials Science and Engineering: A***, Vol. 506, No. 1-2, (2009), 16-22. DOI: 10.1016/j.msea.2009.01.008
43. Cipoletti, D.E., Bower, A.F. and Krajewski, P.E., "Anisotropy in plastic deformation of extruded magnesium alloy sheet during tensile straining at high temperature", ***Integrating Materials and Manufacturing Innovation***, Vol. 2, No. 1, (2013), 81-100. DOI: 10.1186/2193-9772-2-4

Persian Abstract

چکیده

تقاضا برای افزایش نسبت استحکام به وزن، حذف امواج الکترومغناطیسی و میرایی ارتعاشات، باعث افزایش کاربردآلیاژ های منیزیم از جمله AZ91 در صنایع مختلف مانند هوافضا، نظامی، خودروسازی و کشتی سازی گردیده است. البته به دلیل حضور ذرات ناپایدار ثانویه در مرز دانه ها و مناطق دندریتی، استحکام کششی و مقاومت خزشی آلیاژهای منیزیم در دماهای بالا کاهش می یابد. برای بهبود این خواص در دمای بالا، از فرآیندهای تغییر شکل سریع مانند فرایند اصطکاکی اغتشاشی استفاده می شود. در این تحقیق، تأثیر فرایند اصطکاکی اغتشاشی چند پاسه بر میکروسختی، رفتار کششی و خزشی آلیاژ منیزیم AZ91 مورد بررسی قرار گرفته است. همچنین از تصاویر میکروسکوپهای نوری و الکترونی برای مطالعه ریز ساختار نمونه ها استفاده شده است. نتایج نشان می دهد که در دمای اتاق، میکرو سختی، استحکام کششی و مقاومت خزشی به ترتیب حدود ۲۳، ۲۹ و ۳۸ درصد بهبود یافته اند. همچنین پس از فرایند اصطکاکی اغتشاشی چند پاسه، استحکام کششی و خزشی در دمای ۲۱۰ درجه سانتیگراد به ترتیب ۳۱ و ٤٧ درصد افزایش یافت. بیشترین استحکام نهایی کششی برابر با ۲۷٦ مگا پاسکال در سرعت چرخشی ۱۲۰۰ دور در دقیقه، سرعت خطی ٦۰ میلیمتر بر دقیقه و زاویه ابزار ۳ درجه بدست آمد. نتایج تجربی نشان می دهد که فرایند چندپاسه می تواند دربهبود خواص مکانیکی آلیاژ در دماهای بالا مفید باشد.

International Journal of Engineering

Journal Homepage: www.ije.ir

An Adaptively-damped Compressible-liquid Model for Non-cavitating Hydraulic Surges

R. J. Chandran*, R. Raju, A. Salih

Department of Aerospace Engineering, Indian Institute of Space Science and Technology, Thiruvananthapuram, Kerala, India

PAPER INFO

Paper history:
Received 09 May 2020
Received in revised form 22 June 2020
Accepted 03 August 2020

Keywords:
Two-equation Model
Hydraulic Surge
Compressible Liquid
Variable Friction Coefficient
Non-cavitating Flow
Adaptive Damping

ABSTRACT

This research presents a compact and computationally-efficient two-equation compressible-liquid model. The model is specifically developed for the numerical computation of hydraulic surges in pipes under high fluid pressure where cavitation is absent. The proposed model aims to simplify the three-equation model of Neuhaus et al. for two-phase cavitational hammers. Compressible effects in liquid during the transients are considered by including a suitable equation of state into the model. A tunable function of the relative local pressure fluctuation called 'Variable Friction Coefficient' (VFC) for the flow transients is also incorporated into the model. For the accurate modeling of wave propagation, the split-coefficient matrix (SCM) method for characteristic-direction based splitting of eigenvalues is used in the study. The results show that the proposed two-equation model can reproduce the results from the three-equation model at a substantially reduced computational cost. The integration of the variable friction coefficient into the two-equation compressible-liquid model further improved the solver capability. The results computed using this aggregate solver are superior to the original three-equation model and the two-equation model without VFC. The results also suggest that the variable friction coefficient imparts adaptive damping capability to the solver model. This feature of the model is visible in the improved accuracy in the modeling of decaying pressure waves. The aggregate solver model, i.e., `the variable friction coefficient integrated two-equation compressible-liquid model,' offers a greatly simplified mathematical model and an inexpensive computational solver for the simulation of hydraulic surges in non -cavitating flow transients.

***doi**: 10.5829/ije.2020.33.10a.23*

1. INTRODUCTION

The hydraulic surge in pipes is a widely studied flow phenomenon in fluid dynamics due to its high practical relevance in the safety of water-supply for industrial and irrigation applications. Theory and experiments on fluid transients in systems and the studies on the various parameters affecting water hammer is available in [1]. The non-linear oscillations in visco-elastic pipelines conveying fluid is mathematically simulated in [2]. Modelling and optimizing hydraulic transients in water distribution systems, using the classical gradient and heuristic optimization techniques is reported in [3]. The study [4] analyses and designs surge tank, a device used to mitigate the effects of valve closure induced water hammer. Measurement systems like the optical-based device presented in [5], shall soon lead to precisely recorded hydraulic surge data. Numerical modeling plays a significant role in the detection of destruction under the influence of cavitation. The pressure fluctuations on the bed of the compound flip buckets of a dam spillway are experimentally and numerically investigated in [6] and [7]. Numerical detection of cavitation damage level and location on dam spillways is presented in [8]. Corrosion is another factor that determines the safety of pipelines, and the protection systems are essential against corrosion, especially for oil and gas pipelines [9].

In most of the two-phase cavitation models like those studied in [10] and [11], the gaseous components are modeled as compressible fluids, whereas, the liquid component, which is usually water, is invariably treated to be incompressible. There are many practical situations where considering the liquid compressibility, though

*Corresponding Author Email: *jishnuchnadranr@gmail.com* (R. J. Chandran)

Please cite this article as: R. J. Chandran, R. Raju, A. Salih, An Adaptively-damped Compressible-liquid Model for Non-cavitating Hydraulic Surges, International Journal of Engineering (IJE), IJE TRANSACTIONS A: Basics Vol. 33, No. 10, (October 2020) 2047-2056

mild, may contribute to the completeness of the model. Simulation of transient flows in visco-elastic pipes with vapor cavitation reported in [12] employs a compressible model for both the liquid and gaseous phases. For hydraulic surges arising from sudden valve closures at high operating pressures, the cavitation effects are generally absent. For such cases, a comparatively simple mathematical model is preferred, which drastically reduces the computational cost to simulate the flow transient.

In this work, a simplified mathematical model is presented, which is computationally inexpensive to model non-cavitating hydraulic surges. The prescribed model addresses the compressibility effects in the liquid handled in addition to the savings offered in computation. Another innovation in this work is the incorporation of a variable friction coefficient to the model to improve the prediction of transient surge pressure variation. This new friction coefficient is introduced as a function of local pressure fluctuation with the aim to adapt to the local requirements of wave damping.

The following section outlines the research methodology employed. The subsequent section presents the two-equation model, which includes the details of the liquid's compressible treatment and the defining of the variable friction coefficient. The mathematical formulation and the corresponding computational strategy used to develop the solver are detailed in Section 4. Section 5 describes the problem setup and selection of the computational domain. The numerical results for the transient cases from the simulation are thoroughly analyzed and are compared against their corresponding experimental values in the results and discussion section.

2. RESEARCH METHODOLOGY

A three-equation model is presented by Neuhaus et al. in [13] for calculations of thermo-hydraulic pressure surges in pipes. A modification to this model, a two-equation single-phase model, is presented in this study for hydraulic surge estimation for high-pressure flow cases where cavitation effects are negligible. The proposed single-phase model incorporates an equation of state (EOS) to take into account the compressibility effects of the liquid. The EOS relates the fluid density and signal wave speed to its pressure. The specific EOS we have used is the Modified Noble-Abel Stiffened Gas equation of state (Modified NASG EOS) [14], which is a highly accurate non-isothermal EOS for liquid water. The work also presents a variable friction coefficient, defined in the form of a tunable function of local pressure, to improve the accuracy of the numerical solver.

The computational model presented in the study is used to simulate the hydraulic surge and related flow transients associated with sudden valve closure experiments conducted at the Pilot Plant Pipework (PPP) test rig of Fraunhofer, UMSICHT, Germany [15]. The Split-Coefficient Matrix (SCM) method [16], which uses characteristic direction based splitting, is used for modeling the wave propagation during the fluid transient. This powerful solution technique for wave propagation related fluid flow problems, is used for the numerical solution of two-phase flow equations in [17], and for the study of axially coupled vibration response of a fluid-conveying pipeline excited by water hammer in [18].

The proposed computational model is validated against the experimentally measured values reported in [15]. The two-equation model is compared to the original three-equation model to showcase the model simplification and improvements in saving the cost of computation. The flow chart below shows the research methodology used.

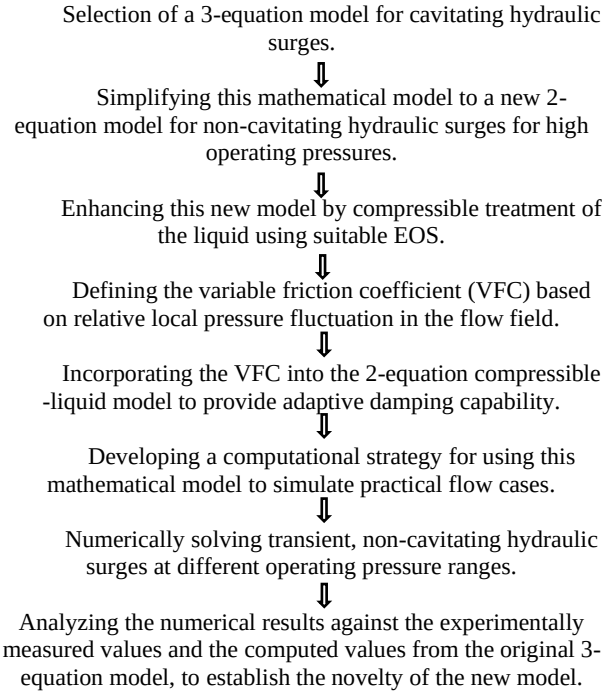

3. THE TWO-EQUATION COMPRESSIBLE-LIQUID MODEL

A three-equation two-phase model is proposed in [13] for numerical simulation of the cavitational hammer and related thermo-hydraulic pressure surges. The three equations used in this mathematical model are: the conservation equations for mass for the liquid phase, the gas phase (air-vapour mixture), and a combined momentum equation for both the phases.

The flow model also incorporates steady and unsteady friction models, as well as the effects of degassing. The results from this mathematical model are validated

against a series of experiments at the Pilot Plant Pipework (PPP), Fraunhofer UMSICHT. The report [15] shows the results from the three-equation mathematical model performing well with two-phase flow cases at low operating pressures. For high operating pressures reported in [15], this model performs satisfactorily only with the incorporation of FSI into the model.

Here we propose a two-equation single-phase model as a modification to the three-equation model described in [13], for flow situations where no cavitation effects are present. The proposed model tries to simulate the flow physics without using the FSI algorithm in the model, which considerably reduces the computational complexity. For single-phase flow in a horizontal pipe, in the absence of cavitation effects, the three-equation model [13] discussed above reduces to a two-equation system as follows.

$$\frac{1}{a^2}\frac{\partial p}{\partial t}+\frac{u}{a^2}\frac{\partial p}{\partial x}+\rho\frac{\partial u}{\partial x}=0 \quad (1a)$$

$$\frac{\partial u}{\partial t}+u\frac{\partial u}{\partial x}+\frac{1}{\rho}\frac{\partial p}{\partial x}=-\frac{4\tau}{\rho d} \quad (1b)$$

where p, u, and ρ, and are respectively the pressure, axial velocity and density of the flow. The symbol a represents the speed of propagation of wave in the medium and τ is the shear force due to skin friction and d is the pipe diameter. The variables x and t denotes the spatial and temporal coordinates.

Equation (1a) represents the mass balance for the liquid, and the Equation (1b) represents the momentum balance for the liquid phase. The mass balance for gas phases identically satisfies due to the single-phase consideration. Equations (1a) and (1b) form a system of PDEs with the dependent variables u, p, and ρ. The temperature is assumed to be constant during the flow process, and the energy balances are thus automatically satisfied. The density ρ of the liquid is treated as a variable using an appropriate compressible model, as discussed in section 3.1, and the shear stress τ is estimated using an unsteady friction model, as explained in section 3.2.

3. 1. The Compressible Model for Water In the present study, water is modeled as a compressible liquid as it is subject to high pressures both at operating and surge conditions. The density of liquid water is estimated using the modified NASG equation of state (EOS) proposed in [14]. This EOS relates the pressure p, the specific volume v, and the specific internal energy ε of the liquid as follows:

$$p=(\gamma-1)\frac{(\varepsilon-q)}{(v-b)}-\gamma p_\infty \quad (2)$$

In Equation (2) γ is the ratio of specific heats, p_∞ is the stiffening parameter, q is the heat bond of liquid water and b represents the covolume of the fluid. The relation for speed of sound in unconfined liquid compatible with the EOS is given by Equation (3) as follows

$$c=\sqrt{\frac{\gamma v^2(p+p_\infty)}{v-b}} \quad (3)$$

Radial expansion of the pipe is considered while estimating the speed of propagation of wave (a) in water, using the following relation

$$a=\frac{1}{\sqrt{\frac{1}{c^2}+(1-\nu^2)\frac{\rho d}{Es}}} \quad (4)$$

In Equation (4), ν and E are respectively the Poisson's ratio and the Youngs modulus of pipe material, and s is the pipe wall thickness.

3. 2. The Variable Friction Coefficient It is a common observation that in the modeling of fluid hammer problems, discrepancies arise in the numerically computed data over the experimental or field data measured while using a steady shear stress model [19, 20]. Daily et al. [21] conducted laboratory experiments and found that these discrepancies are positive for accelerating flows and are negative for decelerating flows. A detailed review of the wall shear stress models used in the modeling of hydraulic transients is available in [22]. The relation of energy loss coefficient with transition geometry of a pipe, flow Reynolds number, and the relative roughness of the wall are outlined in [23]. The unsteady shear stress model used with the three-equation model in [13] takes the following form for single-phase liquid flow case as given by Equation (5).

$$\tau=\left(k\,\frac{\rho d}{4}a\right)sign(u)\frac{\partial u}{\partial x} \quad (5)$$

where k is the unsteady friction coefficient accounting for damping of pressure waves.

Daily et al. further showed that, for an unsteady shear stress model of the form of Equation (5), the coefficient k is a measure of the deviations due to unsteadiness of the wall shear and momentum flux. The extended thermodynamics approach by Axworthy et al. [24] supports this claim and reports the poor agreement between model and data while using a constant k value.

This study is further extended by replacing the pressure wave damping coefficient, k, by a variable friction coefficient, k_v. Unlike the constant coefficient, k, the new coefficient, k_v, is a function, which uses the ratio of the magnitude of local pressure fluctuations to the maximum possible pressure fluctuation for the cases considered. For the initial operating conditions of pressure p_0, density ρ_0, velocity u_0, and signal speed a_0, the magnitude of maximum possible pressure fluctuation $\triangle p_{max}$ is computed using the well established Joukowsky equation as follows:

$$\triangle p_{max}=\rho_0 a_0 \triangle u=\rho_0 a_0|u_0-0|=\rho_0 a_0|u_0| \quad (6)$$

The importance of Joukowsky relation given by Equation (6) in the theory of water hammer is outlined in [25]. A similar non-dimensional parameter is defined in [26], using the Joukowsky pressure rise, to study the wave attenuation in fluid transients.

The magnitude of fluctuation in pressure at any local point `*i*' is calculated as the absolute value of the difference between the local pressure p_i and the operating pressure p_0. The variable friction coefficient, k_v is thus defined as:

$$k_v = m_1\left[1 - \left(\frac{|p_i - p_0|}{\triangle p_{max}}\right)^{m_2}\right] \tag{7}$$

In Equation (7), m_1 and m_2 are tunable parameters. With this definition of the variable friction coefficient, k_v, the equation for shear stress can be written as:

$$\tau = \left(k_v \frac{\rho d}{4} a\right) sign(u) \frac{\partial u}{\partial x} \tag{8}$$

The shear stress computed from Equation (8) is used to estimate the source term in Equation (1b). The newly introduced variable friction coefficient, which uses the ratio of the local pressure fluctuations, which is transiently varying quantity, is expected to take care of the deviations due to unsteadiness, of the wall shear, and momentum flux to some extent.

4. MATHEMATICAL MODEL AND COMPUTATIONAL STRATEGY

The two-equation model is initially converted to the corresponding matrix form, and the resulting matrix system is then solved in a two-step process. The process involves converting the governing equations into characteristic form and solving them using the split coefficient matrix technique. The details are as given below.

4. 1. Mathematical Model in Matrix Form The governing relations of the two-equation model given by Equations (1a) and (1b) can be written in the compact matrix from as:

$$\begin{bmatrix} \frac{1}{a^2} & 0 \\ 0 & 1 \end{bmatrix}\begin{bmatrix} \frac{\partial p}{\partial t} \\ \frac{\partial u}{\partial t} \end{bmatrix} + \begin{bmatrix} \frac{u}{a^2} & \rho \\ \frac{1}{\rho} & u \end{bmatrix}\begin{bmatrix} \frac{\partial p}{\partial x} \\ \frac{\partial u}{\partial x} \end{bmatrix} = \begin{bmatrix} 0 \\ \frac{-4\tau}{\rho d} \end{bmatrix} \tag{9}$$

Equation (9) is of the form:

$$A\frac{\partial U}{\partial t} + B\frac{\partial U}{\partial x} = S \tag{10}$$

In Equation (10), the matrices and vectors are as in Equation (11)

$$A = \begin{bmatrix} \frac{1}{a^2} & 0 \\ 0 & 1 \end{bmatrix}, B = \begin{bmatrix} \frac{u}{a^2} & \rho \\ \frac{1}{\rho} & u \end{bmatrix}, S = \begin{bmatrix} 0 \\ \frac{-4\tau}{\rho d} \end{bmatrix}, U = \begin{bmatrix} p \\ u \end{bmatrix} \tag{11}$$

Premultiplying Equation (10) by A^{-1}, we obtain the following standard form in Equation (12)

$$\frac{\partial U}{\partial t} + C\frac{\partial U}{\partial x} = A^{-1}S \tag{12}$$

From the coefficient matrices A and B, the corresponding Jacobian matrix C and the eigenvalue matrix $\wedge$ are obtained as follows:

$$C = A^{-1}B = \begin{bmatrix} u & \rho a^2 \\ \frac{1}{\rho} & u \end{bmatrix} \text{ and } \wedge = \begin{bmatrix} u-a & 0 \\ 0 & u+a \end{bmatrix} \tag{13}$$

Splitting the Jacobian matrix C in Equation (13) into left and right eigenvectors (Z and Z^{-1}), we obtain

$$C = Z \wedge Z^{-1} = \begin{bmatrix} -\rho a & \rho a \\ 1 & 1 \end{bmatrix}\begin{bmatrix} u-a & 0 \\ 0 & u+a \end{bmatrix}\begin{bmatrix} -\frac{1}{2\rho a} & \frac{1}{2} \\ \frac{1}{2\rho a} & \frac{1}{2} \end{bmatrix} \tag{14}$$

In the first step of computation, the source term is excluded from Equation (12) and the resulting equation takes the form

$$\frac{\partial U}{\partial t} + C\frac{\partial U}{\partial x} = 0 \tag{15}$$

The split form of the Jacobian matrix C from Equation (14) is substituted into Equation (15). The resulting equation is premultiplied by Z^{-1} to obtain the following equation

$$Z^{-1}\frac{\partial U}{\partial t} + \wedge\, Z^{-1}\frac{\partial U}{\partial x} = 0 \tag{16}$$

Defining the characteristic vector W as given in [27], such that

$$\partial W = Z^{-1}\partial U \tag{17}$$

Equation (16) changes to the following relation

$$\frac{\partial W}{\partial t} + \wedge\frac{\partial W}{\partial x} = 0 \tag{18}$$

Linearizing Equation (17) similar to [28] we can compute the characteristic variable vector W using Equation (19)

$$W = Z^{-1}U = \begin{bmatrix} -\frac{p}{2\rho a} + \frac{u}{2} \\ \frac{p}{2\rho a} + \frac{u}{2} \end{bmatrix} \tag{19}$$

Equation (15) is thus transformed to the corresponding characteristic form in Equation (18).

4. 2. The Two-step Computational Algorithm The solution of the two-equation model given by Equation (10) is obtained in a two-step process. In the first step, the system of equations in the characteristic form excluding the source terms given by Equation (18), is solved for an intermediate time step denoted by`⋆' starting from the n^{th} time step. The semi-discretized form of this equation for the i^{th} spatial grid is as follows:

$$W_i^\star = W_i^n - \triangle t \left[\Lambda \frac{\partial W}{\partial x}\right]_i^n \quad (20)$$

The split coefficient matrix (SCM) method is used for solving the above system in Equation (20). The SCM method is used to split the eigenvalue matrix Λ into characteristic speed matrices with the positive and negative eigenvalues separated into the respective matrices Λ^+ and Λ^- as follows

$$\Lambda^+ = \frac{\Lambda + |\Lambda|}{2} \quad \text{and} \quad \Lambda^- = \frac{\Lambda - |\Lambda|}{2} \quad (21)$$

Using Λ^+ and Λ^- from Equation (21), the properties are updated to the intermediate time step as follows

$$W_i^\star = W_i^n - \frac{\triangle t}{\triangle x}\left[\Lambda^+ \left(\frac{\partial W}{\partial x}\right)^- + \Lambda^- \left(\frac{\partial W}{\partial x}\right)^+\right]_i^n \quad (22)$$

An explicit third-order upwind method is used for spatial discretization of the convective terms in Equation (22).

On completion of the first step of computation, the primitive variable vector is recovered from the characteristic variable vector as $U_i^\star = ZW_i^\star$. In the second step, the effect of the source term is integrated into the solution by retaining only the transient and source terms in Equation (10) as follows

$$\frac{\partial U}{\partial t} = A^{-1}S \quad (23)$$

and the semi-discretized form of Equation (23) is given below in Equation (24)

$$U_i^{n+1} = U_i^\star + \triangle t[A^{-1}(U_i^n)S(U_i^n)] \quad (24)$$

Since there is no source term in the mass balance equation for liquid, only the momentum equation needs to be solved in the source term integration step. From the momentum equation, the velocity of flow is updated as

$$u_i^{n+1} = u_i^\star - \triangle t \left(\frac{4\tau}{\rho d}\right) \quad (25)$$

In Equation (25), $u^\star$ is the component of the primitive variable vector $U^\star$.

5. PROBLEM SET-UP AND COMPUTATIONAL DOMAIN

The experimental data used for validation of the mathematical model are from two high-pressure experiments conducted by Neuhaus et. al [15] at the Pilot Plant Pipework (PPP) test rig at Fraunhofer UMSICHT. The schematic of the PPP experimental setup with measurement points is shown in Figure 1.

Demineralized tap water from the reservoir B1 is pumped into a 110 mm inner diameter and 170 m long steel pipeline. This pumping initially pressurizes the entire pipeline to the high pressure maintained inside the reservoir. The valve located between the pressure transducers P02 and P03 closes almost instantaneously at $t = 0$ while the pump remains running. Due to the sudden closure of the valve, a strong rarefaction wave is generated towards the downstream of it. This wave traverses further downstream towards the reservoir B1. Vapor bubbles can form at locations where the fluid pressure goes below its vapor pressure. The rarefaction waves generated oscillate in the pipe system and undergo multiple reflections at the boundaries until they get completely dissipated.

The two high pressure experiments chosen for validation of the method are the Experiment No. 415 and Experiment No. 347 mentioned in [15]. The details of the experiments are provided in Table 1.

The valve closure Experiments No. 415 and No. 347 correspond to the operating pressure ranges of 19.65 bar and 12.50 bar, respectively, with the temperature close to 20◦C. For these two high-pressure experiments, the lowest values of transient pressure measured are well above the saturation pressure of the liquid, due to which the effects due to cavitation are absent. The pressure transducer P03 shown in Figure 1, located at a distance of 0.2 m downstream of the valve, records the transient pressure data. Numerically computed results using the proposed model are validated against these experimentally measured data. The single-phase two-equation model can be used to simulate the

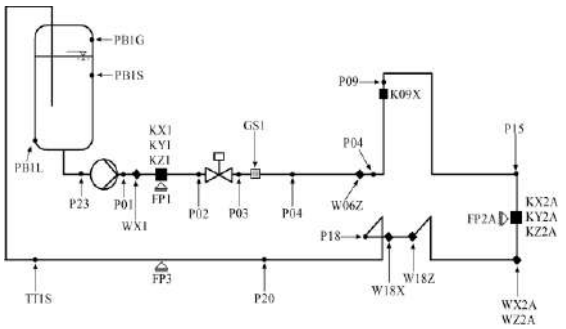

Figure 1. Schematic of the Fraunhofer UMSICHT PPP experimental setup with measurement points

TABLE 1. Details of the experimental conditions

Exp. No	Fluid Velocity, V [m/s]	Flow Rate, Q [m ^{3}/hr]	Temperature, T[◦C]	Pressure, P_R [bar]
415	1.00	33.2	21.9	19.65
347	1.01	33.4	20.3	12.50

hydraulic surges in these two valve closure experiments, as both do not report cavitation effects.

The entire downstream side of the valve up to the reservoir B1, which is 149.4 m long, is the chosen computational domain. In our model, we have not considered the fluid-structure interactions in the pipe flow. A simplified one-dimensional straight pipe section of length 149.4 m is chosen for computation, as shown in Figure 2.

For the purpose of computation, the one-dimensional domain is divided into 747 uniformly sized control volumes, each of size $\triangle x = 0.2$ m. From the stability considerations, a CFL number of 0.03 is found to be optimal and the corresponding time step size $\triangle t$ is calculated to be close to 5×10^{-6} s.

6. RESULTS AND DISCUSSION

A two-level performance analysis of the proposed two-equation model is presented in the study. In the first level, the two-equation model with compressible formulation for the liquid is evaluated against the experimentally measured data and the three-equation model of Neuhaus, which treats the liquid part as incompressible. In the second level of analysis, the variable friction coefficient is integrated into the two-equation compressible-liquid model, which is then compared for performance against the experimental results as well as the numerical results from the three-equation model. The detailed analyses of the results are provided below.

6. 1. The Two-equation Compressible-liquid Model with Constant Friction Coefficient The transient flow problem of sudden valve closure in a steel pipe and the associated pressure surge are mathematically formulated using the proposed two-equation compressible-liquid model. This one-dimensional system of equations is solved numerically, and the results are compared against the numerical results computed using the existing three-equation model and with the transient pressure data measured experimentally. The experiment data were those measured using the pressure transducer P03 for Experiment Nos 415 and 347 reported in [15]. In the case of Experiment No. 415, the transient data measured for the first 3 s from the closure of the valve is used, while for Experiment No. 347, the measured data for the first 5 s is considered. The unsteady friction formulation reported in [13] is used with both the computational models. An optimized value of 0.18 is used for the constant friction coefficient k in the simulation of these experiments.

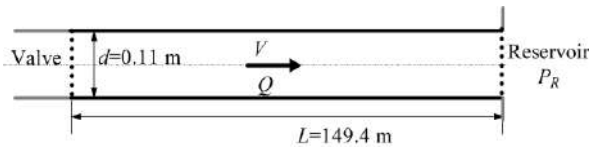

Figure 2. Schematic of the flow domain geometry and boundary conditions for computation

In Figure 3, the continuous black color curve shows the experimentally measured transient pressure profile for Experiment No. 415. A strong rarefaction wave is generated just downstream of the valve immediately after its closure as the inertia of moving fluid creates a low-pressure area in the downstream region of the valve. The crests (peaks) and troughs (anti-peaks) seen from the experimental pressure profile indicate the rarefaction waves propagating back and forth along the length of the pipe, undergoing multiple reflections at the boundaries.

Due to frictional forces in the pipe flow system, these waves lose their energy and dissipate into a steady-state, which is evident from the decreasing amplitude of the pressure with time. The continuous blue colored curve in Figure 3 represents the transient pressure profile computed using the three-equation model [15]. Numerical results obtained from the present two-equation compressible-liquid model are displayed using the magenta colored curve in Figure 3.

For Experiment.No.347, the measured values of the transient pressure variation at the location P03 are shown using the continuous black curve in Figure 4.

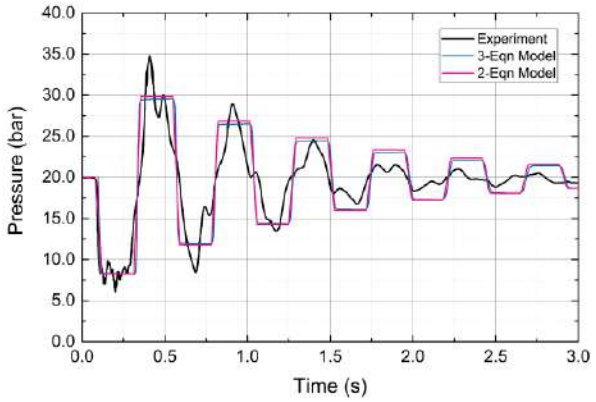

Figure 3. Comparison of measured and calculated pressure at P03 for experiment 415

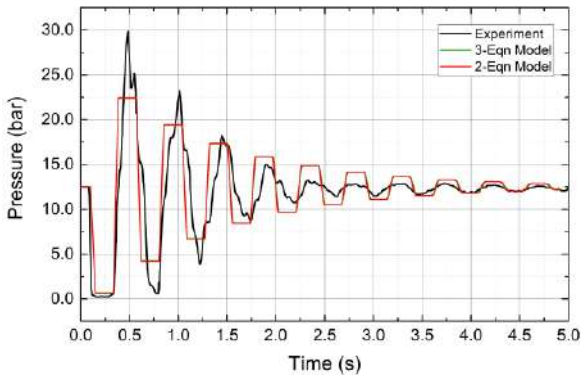

Figure 4. Comparison of measured and calculated pressure at P03 for experiment 347

The numerically computed transient pressure profiles using the three-equation and the two-equation models are shown in Figure 4 using the green colored and the red colored curves, respectively. As observed from Figures 3 and 4, the transient pressure profile predicted by the two-equation model proposed is in close agreement to that obtained from the existing three-equation model. However, one could notice that the two-equation model reproduced this numerical solution using a much simplified mathematical formulation, which requires considerably reduced computational effort.

On closer observation, one may find that the two-equation model predicts the peak pressures marginally higher than that of the three-equation model throughout the transient. This is visible in a better manner with Experiment No.415, as seen from Figure 3, which involves a comparatively high operating pressure. This increase in the pressure magnitude could be attributed to the compressible treatment of the liquid, which accounts for the increase in the density of the liquid at high pressures. The compressible treatment also leads to the accurate estimation of wave speeds within the fluid, which adds to the magnitude of the calculated surge pressure.

The computed frequency of the wave propagation is observed to be in close agreement with the experimental results. However, the amplitude of pressure peaks from the numerical results is not in good agreement with the measured values. The structural interactions with the fluid flow, which are not accounted for in the present model, is a possible reason for this disparity in the results. From the experimental and numerical pressure profiles displayed in Figures 3 and 4, an important observation is made as follows. During the initial phase of the transient, the magnitude of the pressure peaks and anti-peaks are highly under-predicted, and at the later phase, they are over-predicted in the numerical results. This observation is due to the over-damping induced by the constant friction coefficient for the initial transient phase and vice-versa. This improper damping technique using a constant friction coefficient, adds to the variation of the numerical results from the measured values.

6. 2. The Two-equation Compressible-liquid Model with Variable Friction Coefficient A variable friction coefficient is proposed in this study to address the deficiencies of the constant friction coefficient model. The constant value of the friction coefficient, which is applied throughout the computation, makes it inflexible to the varying flow situations. This fixed amount of damping may prove to be excessive for a particular part of the transient while it may be insufficient for the rest. The definition of the varying friction coefficient k_v, which is a function of the relative local pressure fluctuation, has been outlined in section 3.2.

The magenta curve in Figure 5 and the red curve in Figure 6 displays the numerical results obtained with the two-equation compressible-liquid model using the variable friction coefficient k_v for the Experiments 415 and 347, respectively.

In these figures, the numerical results from the two-equation model are compared against those computed using the three-equation model, and with the measured values from the corresponding experiments. The comparison reveals that the proposed two-equation model with the variable friction coefficient improves the result considerably from the three-equation model with a constant friction coefficient. This improvement is not only in terms of better estimation of peak pressures but also in closely reproducing the transient trend observed with experimental pressure measurements. The maximum pressure estimated by the new computational model using k_v is 1.18 bar (or 4%) higher for Experiment No.415 and by 1.22 bar (or 5.5%) higher for Experiment.No.347 when compared to the results from the three-equation model, which is reasonable improvement in quantitative terms. The proposed two-equation model can also reproduce the shape of the pressure profile much closer to the shape of the experimental profile by producing sharper peaks and anti-peaks. Values of the parameters m_1 and m_2 in Equation (9) are observed to be optimal in the range 0.3-0.5 for such experiments.

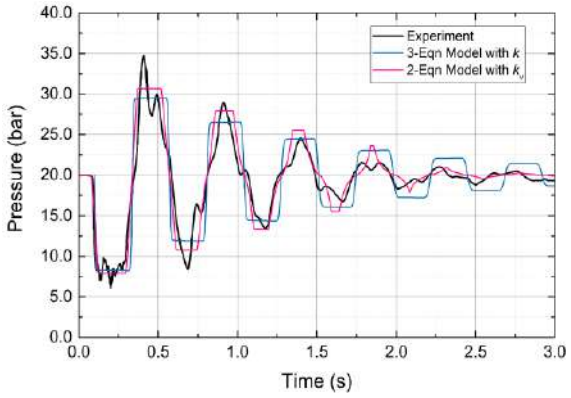

Figure 5. Numerical results from the 2-equation compressible model with k_v for Experiment No. 415

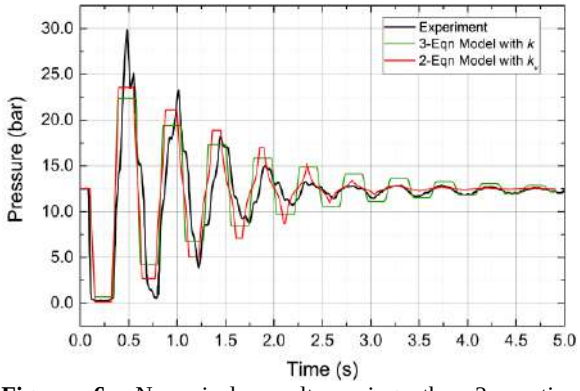

Figure 6. Numerical results using the 2-equation compressible model with k_v for Experiment No. 347

The damping provided by the variable friction coefficient is adaptive to the magnitude of pressure fluctuation at any local point. This capability is imparted through the unique function definition for k_v . It is visible from the numerical pressure profiles in Figures 5 and 6 that the variable friction coefficient provides low damping at the initial stage of the transient where larger pressure peaks are existent. Similarly, towards the later phase of the transient, the variable friction coefficient adapts to the pressure's diminishing magnitude. This adaptive damping capability improves the accuracy of the computed transient surge data, which is crucial to the pipe structure's safety. The flexibility added to the mathematical model by the variable friction coefficient to predict the numerical results close to measured data is notable, specifically towards the end of the transient in Figures 5 and 6.

The compressible model used for the liquid not only helps in the accurate prediction of the fluid density but also provides an excellent estimate of the wave speeds, both of which are crucial flow parameters varying with pressure. The proposed two-equation model, with the variable friction coefficient, is a highly simplified mathematical model capable of estimating the transient pressure variation accurately. This model's ability to follow the transient variations in the experimentally measured pressure profile, even without the inclusion of any fluid-structure interaction (FSI) algorithm, is a substantial improvement over the three-equation model.

There are visible variations in the numerical results during the initial stage of the transients. The main reason for these is that the effects of pipe mountings and support structures are neglected in the computational model. The lack of complete information regarding the exact nature of valve closure is another cause for any mismatches between the simulation results and the measured values. As observed from the experimental results, the maximum surge in pressure due to the sudden closure of the valve reaches much higher magnitudes than the operating pressure. The compressible model presented in the study, to a particular extent, could take this into account by relating these pressures to the corresponding liquid density and signal propagation speed. The variable friction coefficient also adds novelty to the model through the adaptive feature. Based on the above discussions, the proposed model is an efficient computational tool for modeling and prediction of pressure surges in flow systems where cavitational effects are absent.

7. CONCLUSIONS

A two-equation compressible-liquid model is developed for the simulation of non-cavitating hydraulic surges. The proposed model is limited to single-phase non-cavitating flow simulations. This model uses a suitable equation of state to consider the compressibility effects in the liquid at high-pressure ranges. The model has the capability to accurately compute the fluctuations in density and wave speed in the liquid. The work also presents a uniquely defined variable friction coefficient, which is a function of the local pressure fluctuation. This new variable friction coefficient is superior to the constant friction coefficient that it adaptively damps the numerically computed transient pressure fluctuations. This adaptive damping capability helps the model to predict the transient pressure in a similar trend as observed with the experimentally measured data. The analysis reveals that the proposed model is computationally inexpensive and provides better accuracy in comparison to the three-equation model. The flexibility offered by a variable friction coefficient to the mathematical model in selectively treating transient pressure gradients is a significant contribution of this study. The two-equation compressible-liquid model with the variable friction coefficient is thus quantitatively and qualitatively superior to the existing model for computational applications for high-pressure pipelines for non-cavitating hydraulic surges. A possible future extension of this work is the incorporation of advanced numerical techniques for this model to provide high stability for transient two-phase flow modeling. The three-equation model as well can then be used with compressible-liquid and variable friction capabilities to model even cavitating hydraulic surges. Extending the use of the variable friction coefficient defined in this study to a wide variety of transient flow applications is another possible area of research.

8. REFERENCES

1. Bergant, A., Tijsseling, A.S., Vítkovský, J.P., Covas, D.I.C., Simpson, A.R. and Lambert, M.F., "Parameters affecting water-hammer wave attenuation, shape and timing-part 1: Mathematical tools", ***Journal of Hydraulic Research***, Vol. 46, No. 3, (2008), 373-381. doi: 10.3826/jhr.2008.2848
2. Khudayarov, B., Turaev, F. “Mathematical simulation of nonlinear oscillations of viscoelastic pipelines conveying fluid”. ***Applied Mathematical Modelling,*** Vol. 66, (2019), 662-679. doi: https://doi.org/10.1016/j.apm.2018.10.008
3. Skulovich, O., Perelman, L., Ostfeld, A. “Modeling and optimizing hydraulic transients in water distribution systems”. ***Procedia Engineering,*** Vol. 70, (2014), 1558-1565. doi: https://doi.org/10.1016/j.proeng.2014.02.172
4. Moghaddam, M. A. "Analysis and design of a simple surge tank." ***International Journal of Engineering Transactions A,*** Vol. 17, No. 4, (2004), 339. doi: http://www.ije.ir/article_71544.html
5. Zamani, J., M. A. Samimi, F. Sardarzadeh, and M. H. Ghezelayagh. "An Optical Measurement System to Measure Velocity and Provide Shock Wave Pressure Diagrams.", ***International Journal of Engineering***, Vol. 33, No. 3, (2020), 505-512. doi: 10.5829/ije.2020.33.03c.15
6. Yamini, O. A., Kavianpour, M. R., Mousavi, S. H., Movahedi, A., and Bavandpour, M. "Experimental investigation of pressure

fluctuation on the bed of compound flip buckets." ***ISH Journal of Hydraulic Engineering,*** Vol. 24, No. 1, (2018), 45-52. doi: https://doi.org/10.1080/09715010.2017.1344572

7. Yamini, O. A., Kavianpour, M. R., and Movahedi, A. "Pressure Distribution on the Bed of the Compound Flip Buckets." ***The Journal of Computational Multiphase Flows,*** Vol. 7, No. 3, (2015), 181–94. doi:10.1260/1757-482X.7.3.181.
8. Fadaei-Kermani, E., Barani, G. A., and Ghaeini-Hessaroeyeh, M. "Numerical Detection of Cavitation Damage on Dam Spillway." ***Civil Engineering Journal,*** Vol. 2, No. 9, (2016), 484-490. doi: 10.28991/cej-2016-00000051
9. Nikitin, E., Shumatbaev, G., Terenzhev, D., Sinyashin, K., and Rastergaev, E. "New Sintanyl Phosphonates for Protection of Oil and Gas Pipelines from Steel Corrosion." ***Civil Engineering Journal*** Vol. 5, No. 4 (2019), 789-795. doi: 10.28991/cej-2019-03091288
10. Sadafi, M., Riasi, A., Nourbakhsh, S.A. "Cavitating flow during water hammer using a generalized interface vaporous cavitation model". ***Journal of Fluids and Structures,*** Vol. 34, (2012), 190-201. doi: https://doi.org/10.1016/j.jfluidstructs.2012.05.014
11. Pinho, J., Lema, M., Rambaud, P., Steelant, J. "Multiphase investigation of water hammer phenomenon using the full cavitation model". ***Journal of Propulsion and Power,*** Vol. 30, No. 1, (2014), 105-113. doi: https://doi.org/10.2514/1.B34833
12. Hadj-Taieb, L., Hadj-Taieb, E. "Numerical simulation of transient flows in viscoelastic pipes with vapour cavitation". ***International Journal of Modelling and Simulation,*** Vol. 29, No. 2, (2009), 206-213. doi: https://doi.org/10.1080/02286203.2009.11442526
13. Neuhaus, T., Dudlik, A. "Experiments and comparing calculations on thermohydraulic pressure surges in pipes". ***Kerntechnik,*** Vol. 71, No. 3, (2006), 87-94. doi: 10.3139/124.100280
14. Chandran, R. J., Salih, A. "A modified equation of state for water for a wide range of pressure and the concept of water shock tube". ***Fluid Phase Equilibria,*** Vol. 483, (2019), 182-188. doi: https://doi.org/10.1016/j.fluid.201811.032
15. Neuhaus, T., Dudlik, A., Tijsseling, A.S. "Experiments and corresponding calculations on thermohydraulic pressure surges in pipes". CASA-report 545. (2005). url: https://research.tue.nl/files/2312420/602216.pdf
16. Chakravarthy, S., Anderson, D., Salas, M. "The split coefficient matrix method for hyperbolic systems of gasdynamic equations". In: 18th Aerospace Sciences Meeting. (1980), 268. doi: https://doi.org/10.2514/6.1980-268
17. Wang, Z., Su, G., Qiu, S., Tian, W. "Preliminary study on split coefficient matrix method for two-phase flow equation solving". ***Atomic Energy Science and Technology,*** Vol. 49, No. 6, (2015), 1045-1050. Retrieved from: http://inis.iaea.org/search/search.aspx?orig_q=RN:48072547
18. Zhang, T., Tan, Z., Zhang, H., Fan, J., Yang, Z. "Axial coupled response characteristics of a fluid-conveying pipeline based on split-coefficient matrix finite difference method". ***Zhendong yu Chongji/Journal of Vibration and Shock,*** Vol. 37, (2018), 148-154. doi: 10.13465/j.cnki.jvs.2018.05.022.
19. Pezzinga, G., Ghidaoui, M.S., Axworthy, D.H., Zhao, M., McInnis, D.A. "Extended thermodynamics derivation of energy dissipation in unsteady pipe flow". ***Journal of Hydraulic Engineering,*** Vol. 127, No. 10, (2001), 888-890. doi: https://doi.org/10.1061/(ASCE)0733-9429(2001)127:10(888)
20. Ghidaoui, M.S., Mansour, S. "Efficient treatment of the vardy-brown unsteady shear in pipe transients". ***Journal of Hydraulic Engineering,*** Vol. 128, No. 1, (2002), 102-112. doi: https://doi.org/10.1061/(ASCE)0733-9429(2002)128:1(102)
21. Daily, J., Hankey Jr, W., Olive, R., Jordaan Jr, J. "Resistance coefficients for accelerated and decelerated flows through smooth tubes and orifices". ***Tech. Rep.; Massachusetts Inst of Tech Cambridge***. (1955). url: https://apps.dtic.mil/dtic/tr/fulltext/u2/a280851.pdf
22. Ghidaoui, M.S., Zhao, M., McInnis, D.A., Axworthy, D.H. "A Review of Water Hammer Theory and Practice". ***Applied Mechanics Reviews,*** Vol. 58, No. 1, (2005), 49-76. doi: https://doi.org/10.1115/1.1828050
23. Nosrati, K., Tahershamsi, A., and Taheri, S. H. S. "Numerical Analysis of Energy Loss Coefficient in Pipe Contraction Using ANSYS CFX Software." ***Civil Engineering Journal*** Vol. 3, No. 4 (2017): 288-300. doi: 10.28991/cej-2017-00000091
24. Axworthy, D.H., Ghidaoui, M.S., McInnis, D.A. "Extended thermodynamics derivation of energy dissipation in unsteady pipe flow." ***Journal of Hydraulic Engineering,*** Vol. 126, No. 4, (2000): 276-287. doi: https://doi.org/10.1061/(ASCE)0733-9429(2000)126:4(276)
25. Ghidaoui, M. S. "On the fundamental equations of water hammer". ***Urban Water Journal,*** Vol. 1, No. 2, (2004), 71-83. doi: https://doi.org/10.1080/15730620412331290001
26. Wahba, E. "Modelling the attenuation of laminar fluid transients in piping systems". ***Applied Mathematical Modelling,*** Vol. 32, No. 12, (2008), 2863-2871. doi: https://doi.org/10.1016/j.apm.2007.10.004
27. Toro, E. "Riemann Solvers and Numerical Methods for Fluid Dynamics: A Practical Introduction". ***Springer Berlin Heidelberg***; (2013). ISBN 9783662039151. doi: 10.1007/b79761
28. Peng, J., Zhai, C., Ni, G., Yong, H., Shen, Y. "An adaptive characteristic-wise reconstruction weno-z scheme for gas dynamic euler equations". ***Computers & Fluids,*** Vol. 179, (2019), 34-51. doi: https://doi.org/10.1016/j.compfluid.2018.08.008.19

Persian Abstract

چکیده

هدف این تحقیق ارائه یک مدل دومعادله‌ای و محاسباتی کاراً برای یک سیال تراکم‌پذیر است. این مدل به‌طور خاص برای محاسبه‌ی عددی موج‌های هیدرولیکی در لوله‌های سیال تحت فشار بالا که در آن کاویتاسیون وجود ندارد، ایجاد شده است. هدف از ارائه‌ی این مدل ساده‌تر کردن مدل سه‌معادله‌ای نیوهاوس (Neuhaus) و همکاران برای ضربه‌ی قوچ (چکش کاویتاسیون) سیال دوفازی است. اثرات تراکم‌پذیری در مایع در طول گذار با بهره‌گیری از معادله‌ی حالت مناسب در مدل در نظر گرفته می‌شود. یک تابع تنظیم‌پذیر از نوسانات فشار نسبی موضعی به نام "ضریب اصطکاک متغیر" (VFC) برای جریان‌های گذرا نیز در مدل گنجانیده شده است. برای مدل‌سازی دقیق انتشار موج از روش ماتریس ضریب تقسیم (SCM) برای تقسیم بر اساس مقادیر ویژه در این مطالعه استفاده شده است. نتایج نشان می‌دهد که مدل دومعادله‌ای پیشنهادی می‌تواند نتایج حاصل از مدل سه‌معادله‌ای را با کاهش چشم‌گیری در هزینه‌های محاسباتی به دست آورد. ادغام ضریب اصطکاک متغیر در مدل مایع تراکم‌پذیر دومعادله‌ای قابلیت حل را بیشتر بهبود می‌بخشد. نتایج محاسبه شده با استفاده از این حل‌کننده‌ی کل نسبت به مدل اصلی سه‌معادله‌ای و مدل دومعادله‌ای بدون VFC برتری دارد. نتایج همچنین حاکی از آن است که ضریب اصطکاک متغیر قابلیت میرایی سازگاری را با مدل حل‌کننده ارائه می‌دهد. این ویژگی مدل در بهبود دقت در مدل‌سازی امواج فشار میرا قابل مشاهده است. مدل حل کل به عنوان مثال: "ضریب اصطکاک متغیر یک‌پارچه مدل دو معادله‌ای مایع فشارپذیر یک مدل ریاضی بسیار ساده و یک حل‌کننده‌ی محاسباتی ارزان‌قیمت برای شبیه‌سازی موج‌های هیدرولیک در جریان‌های گذار بدون کاویتاسیون ارائه می‌دهد.

International Journal of Engineering

Journal Homepage: www.ije.ir

Effect of Porous Medium Positioning on Heat Transfer of Micro-channel with Jet

M. Alibeigi, S. D. Farahani*

Department of Mechanical Engineering, Arak University of Technology, Arak, Iran

P A P E R I N F O

Paper history:
Received 26 May 2020
Received in revised form 16 June 2020
Accepted 03 August 2020

Keywords:
Micro-channel
Porous Media
Heat Transfer
Nano-Fluid

A B S T R A C T

In this paper, the influence of the locating additive or placing porous-medium film on the heat transfer of a micro-channel by injecting fluid from its lower wall is investigated. The boundary condition slip-walls for the lower and higher walls of the micro-channel and orderly, as insulation and constant temperature is considered, respectively results show that the heat transfer increased with increasing Darcy number and the porous-medium film thickness. The consequences disclosed that the place of the porous-film has a substantial effect on heat transfer. The percentage changes observed for cases such the porous layer in the middle of the micro-channel, near the two upper and lower walls, near the upper wall, near the upper wall and in the form of a rib, along the length of the micro-channel with L /3 and L/5 is -14%, 2.25%, 5.46%, 55.53%, 70.5% and 86.27% for nusselt number compared to the porous layer-less state.

***doi**: 10.5829/ije.2020.33.10a.24*

1. INTRODUCTION

In recent decades, with the development of electronic devices in very small dimensions, it is necessary to improve the conditions for the transfer of heat by using devices in the dimensions of the smallest increase. Microchannel heat exchangers can be used for this purpose. In addition, the use of new technologies such as nanotechnology has recently received a great deal of attention [1].

Numerous research sources have examined the effect of the cross-sectional shape of the channels, the location of the channels, the number of channels and the size and structure of the microchannel. Yang et al. [2] examined the performance of a microchannel heat transfer with needle-shaped blades in a laboratory and standard manner. Five different cross-sectional areas for needle-shaped blades were examined. They also used ionized water as a working fluid for cooling. Their results showed that the shape of the needle blades plays an important role in conveying heat transfer and fluid pressure drop. One of the results of their simulation, which is in good agreement with the laboratory results, is that the lowest thermal resistance is related to geometries with hexagonal cross section and the lowest pressure point is related to circular geometry. Wang et al. [3] studied the effect of rectangular, trapezoidal and triangular geometries on the flow characteristics and heat transfer characteristics. After conducting experiments, they found that the microchannel with a rectangular cross-section had the lowest thermal resistance and best thermal performance. But it does increase the pressure drop. Chen et al. [4] simulated numerical and three-dimensional heat transfer and fluid flow within a microchannel with different cross sections. The results showed that the triangular microchannel had the best thermal performance and the rectangular section with the best performance. While the results of the work of Gonasgaren et al. [5], who also studied the effect of different geometries on the transfer properties of heat and current flow, showed that the microchannel performs the function with the cross section and the rectangular section had the highest transfer coefficient.

Many studies have been done to increase heat transfer from microchannels. One way is to use nanofluids, which can significantly increase heat transfer [6, 7]. Research

*Corresponding Author Institutional Email: *sdfarahani@arakut.ac.ir* (S. D. Farahani)

Please cite this article as: M. Alibeigi, S. D. Farahani, Effect of Porous Medium Positioning on Heat Transfer of Micro-channel with Jet, International Journal of Engineering (IJE), IJE TRANSACTIONS A: Basics Vol. 33, No. 10, (October 2020) 2057-2064

on fluid flow and heat transfer in porous media has attracted the attention of many researchers in recent decades. Porous environment is a material consisting of a solid network connected by empty spaces or gaps between them. The empty spaces between the solid network allow fluid to flow into the network. In a natural porous environment, the distribution of pores is irregular in shape and size. Coastal sand, limestone and human lungs are examples of natural porous materials. Mathematical discovery in MCHS with the least square methods and numerical methods for chosen the best nano-fluid based on saturated porous medium was reported [8]. Usage of ZnO–water nano-fluids in corrugated channels with designing of the plate-fin heat exchangers with configuration of changing geometry such kinds of a) house-shaped channel, b) semicircular channel, c) trapezoidal channel, and d) straight channel were numerically studied [9].

The effects of solid phase generative heat on the generative entropy with an analytical model conferring to first law and second law of thermodynamics in micro-channel with porous water-Al_2O_3 nano-fluid flow in asymmetrically heated was developed. That exposed the minimization of generative entropy generative was the intensification of solid-phase generative heat supplementary reduces the discrepancy between the two models to less than 1% [10]. Represented nano-fluid through a horizontal porous micro-channel was studied for effects of magneto-fluid dynamics (MHD) arena and heat generation in the solid on the generated entropy by the heat transfer practices with an extensive variability of Re and Bejan number [11]. Mass transfer and forced heat transfer convection of Cu-water nano-fluid through a horizontal porous micro-channel considered which sound effects of numerous factors such as slip parameter, nanoparticle volume fraction, asymmetric heat flux and some dimensionless numbers such as Darcy number, Hartmann number, Brinkman number on total heat transfer and fluid flow profiles studied in details [12]. Shiriny et al. [13] examined the effect number of injection and number of volume fraction for maximum Nusselt number. Jalali et al. [14] observed that higher heat transfer coefficient was achieved by using 2.5 wt % Al_2O_3 nano-fluids compared to 1.0 wt % Al_2O_3 nano-fluids. There is also research on the production of hybrid nanoparticles and its effect on increasing heat transfer [15-18]. Shokouhmand et al. [19] investigated convective heat transfer and laminar flow by using lattice boltzmann method (LBM) in two channel configurations in a canal full of an inserting porous. Miroshnichenko et al. [20] studied effect of heat source and nanoparticle/water on free convection heat transfer within an inclined cavity. Nojoomizadeh et al. [21] examined the numerical forced convection heat transfer with Darcy number by blend of water and Fe_3O_4 nanoparticles in a two-dimensional micro-channel. Their conclusion was observing rise of the slip velocity in the semi-upper and a decrease in the slip velocity in the semi-lower of the micro-channel [21]. The principal of liquid and solid phases on the heat transfer progression, investigators had assumed a two-phases model for the nano-fluid flow for assessment of temperature and velocity differences in two phases of the liquid and solid phases. In fact, the relative velocity and temperature of each phase was negligible [22-24]. A three-dimension porous-heat sink model identified the ideal geometric parameters of the micro-channel as a heat sink fulled with porous medium by using a combination including an optimization approach of simplification of the conjugate-gradient method [25].

According to the previous literature, little research has been done on the position of the porous material on the heat transfer in the microchannels. In this study, the influence of using porous medium in three cases, which porous-medium the position of locating of porous such close to the upper and lower walls, placing porous medium middle of the micro-channel and placing porous medium selectively on dividable section on the amount of heat transfer is investigated. A two-dimensional micro-channel on the lower wall with several openings for fluid injection is considered. The lower wall of micro-channel resumed the insulation wall and the upper wall have a constant temperature and slip boundary condition on the walls is deliberated. The combination of nanoparticle with water is also considered as working fluids. The porous-film thickness on the heat transfer from the channel is examined. Numerical simulation is performed by using Comsol software where solution of its is finite element method (FEM).

2. MATERIALS AND METHODS.

In this study, a two-dimensional micro-channel with porous medium and injection with inlet velocity u_c and three different jet inlet velocities $u_d = 0.5u_c$ considered. A schematic of the physical models of the problem under study is shown in Figure 1. For the micro-porous channel, three cases have been given. Firstly, the porous medium with two separated walls has two states: 1. near the upper and lower walls with two equal separated τ thickness layer (Figure 1(a)); 2. in the middle of the micro-channel with putting two side nearly in the middle with 2τ thickness (Figure 1(b)). Secondly, the porous medium with one wall has two states 1. near the upper wall with τ thickness (Figure 1(c)); 2. near the upper wall with τ thickness and adding a ribbed τ thickness with N=100 teeth to the one-sided porous (Figure 1(d)). Thirdly, the porous medium with two separated walls with distinguishing rather than the first case with $\tau = H$ thickness the has two states: 1. divided the channel by 3 equal sections and put the porous layer in the middle

section(Figure 1(e)); 2. divided the channel by 5 equal sections and the porous layer one in between puts in the periodically distance in two L/5 section (Figure 1(f)). The material is porous medium of aluminium foam. In Figure 1, orderly H_0, τ, H, L and D are the thickness of non-porous media, the thickness of porous media, micro-channel width, micro-channel length and $D = 0.007L$ is the diameter of each injection. From the lower wall of the micro-channel there are three openings for injections τ is chosen $\tau = H \times (0.05, 0.1, 0.2, 0.3, 0.4)$ in this case.

Momentum, continuity and energy equations that are major equations following as:

$$u\frac{\partial u}{\partial x} + v\frac{\partial u}{\partial y} = -\frac{\partial p}{\partial x} + \frac{1}{\mathrm{Re}}\left(\frac{\partial^2 u}{\partial x^2} + \frac{\partial^2 v}{\partial y^2}\right) \quad (1)$$

$$\frac{\partial u}{\partial x} + \frac{\partial v}{\partial y} = 0 \quad (2)$$

$$u\frac{\partial T}{\partial x} + v\frac{\partial T}{\partial x} = -\frac{\partial p}{\partial x} + \frac{1}{\mathrm{Re}\,\mathrm{Pr}}\left(\frac{\partial^2 T}{\partial x^2} + \frac{\partial^2 T}{\partial y^2}\right) \quad (3)$$

The dimensionless parameters mostly used in this numerical study are:

$$X = \frac{x}{H},, L^* = \frac{L}{H}, \beta^* = \frac{\beta}{H} \quad (4)$$

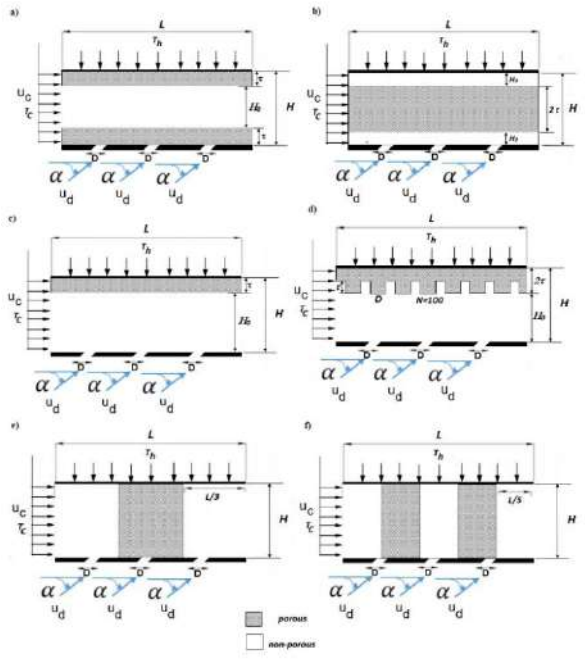

Figure 1. 2-D shemataic of micro-channel with different position of porous layer

$$Y = \frac{y}{H}, H^* = \frac{H_0}{H}, \tau^* = \frac{\tau}{H} \quad (5)$$

$$U = \frac{u}{u_c}, V = \frac{v}{v_c}, U_d = \frac{u_d}{u_c}, V_d = \frac{v_d}{v_c}, P = \frac{\Delta p}{\rho_{nf} u_c{}^2} \quad (6)$$

$$\theta = \frac{T - T_C}{T_h - T_C}, \mathrm{Re} = \frac{u_c H}{\nu_f} \quad \mathrm{Pr} = \frac{\nu_f}{\alpha_f} \quad (7)$$

In heat transfer the most significant dimensionless number is local Nusselt number which defined as follows: [9]

$$Nu(x) = \frac{hD_h}{k} \quad (8)$$

where D, h and k are the hydraulic diameter, heat transfer convection coefficient and thermal conductivity. In this case, the dimensionless boundary conditions are:

$$U_C = 1, \quad V = 0, \quad \theta = 0 \quad For \quad X = 0, 0 \le Y \le 1 \quad (9)$$

$$\frac{\partial U}{\partial X} = 0, \quad V = 0, \quad \frac{\partial \theta}{\partial Y} = 0 \quad For \quad X = L^*, 0 \le Y \le 1 \quad (10)$$

$$U_S = \beta^* \left(\frac{\partial U}{\partial Y}\right)_{Y=0}, \quad V = 0, \quad \frac{\partial \theta}{\partial Y} = 0 \quad For \quad Y = 0, 0 \le X \le L^* \quad (11)$$

$$U_S = \beta^* \left(\frac{\partial U}{\partial Y}\right)_{Y=1}, \quad V = 0, \quad \theta = 1 \quad For \quad Y = 1, 0 \le X \le L^* \quad (12)$$

the boundary conditions of the injection jets bounded by,

$$U_d = 0.5\cos(\alpha), \quad V_d = 0.5\cos(\alpha), \quad \theta = 0 \quad (13)$$

When the working fluid is the nanofluid, nanofluid properties are given in Table 1 in terms of nanofluid volume fraction, φ.

Representively, adding porous material to the micro-channel the dimensionless momentum equation is [26]:

TABLE 1. Thermophysical properties of nano-fluid Zno/Water [9]

Volume fraction	$\phi = 0$	$\phi = 1\%$	$\phi = 3\%$	$\phi = 5\%$
Density $(\frac{kg}{m^3})$	998.2	1043.1	1135.2	1037.6
Viscosity $(Pa.s)$	$8.9E^{-4}$	$9.1265E^{-4}$	$9.6042E^{-4}$	0.001
Specific Heat $(J/kg.k)$	4182	3981.2	3633.8	3338.5
Conductivity $(w/m.k)$	0.6	0.7360	0.9846	1.23

TABLE 2. Thermophysical properties of porous material [27, 28]

$\rho_p (kg/m^3)$	$c_{p,p} (J/kg.K)$	$k_p (W/m.k)$	$\kappa (m^2)$	ε_p
400s	400	5.8	10^{-5}	0.8

$$-\frac{\partial P}{\partial X}+\mu_{eff}\frac{\partial^2 U}{\partial Y^2}+\frac{\mu_f}{\kappa}U=0 \quad (19)$$

The conservation energy is:

$$\nabla.\left(\left(\rho c_p\right)_{eff} uT\right)=\nabla.\left(k_{eff}\nabla T\right) \quad (20)$$

Where μ_{eff} is the dynamic viscosity of the porous medium, phase which has been chosen and κ is the permeability the equilibrium of heat transfer between the porous medium and the nanofluid, the thermal effectiveness conductivity k_{eff} can be determined using the following equation [26]:

$$k_{eff}=\left(1-\varepsilon_p\right)k_p+\varepsilon_p k_{nf} \quad (21)$$

Where ε_p is the porosity of porous media part along the micro-channel and, the dimensionless Nusselt number for adding porous to the nanofluid defined as:

$$Nu=-\frac{k_{eff}}{k_f}\frac{\partial\theta}{\partial Y}\Big|_{Y=Y_0} \quad (22)$$

Representively, the Brownian motion calculated the slip velocity U_s by following equation [29].

$$U_s=\frac{2k_bT}{\pi\mu_f d_S^2} \quad (23)$$

where the Boltzmann constant k_b =1.3807×10^{-23} J/K and d_S = 40 nm, the Darcy number for this case defined as:

$$Da=\frac{\kappa}{D_h^2} \quad (24)$$

where D_h is the hydraulic diameter.

Finite element method with PARDISO algorithm used. Discretization P1+P1 method with maximum residual of 10^{-3} was used. Also, near the slip walls the mesh determined finer than the others additionally, the effect of changing nanoparticle with volume fraction various. Changing of base fluid in the end, adding of Aluminum porous foam on the nanoparticles for enhancing heat transfer were investigated, temperature, and streamlines contours and Nusselt number curves are presented.

3. GRID INDEPENDENCY

In numerical solution, the triangle meshes with boundary layer meshes near to the walls was chosen, the size of the mesh affects the accuracy and time of the solution. The smaller the mesh, the more accurate the solution becomes, but the time required to solve it also increases. To ensure accuracy, the grid study for averaged Nusselt number is presented in Table 3. A 50×500 grid has been used to continue the study.

4. RESULTS

In this study, the effect of porous medium layer on heat transfer from a two-dimensional micro-channel is explored. To make sure the accuracy of the numerical solution presented in this numerical study, the results of the present numerical solution were compared with shiriny et al. [13]. This comparison was made for the case where the Reynolds number is 100 and illustrated in Figure 2. At this point is a moral match between the results of the present study and the reference and there is less than 7% difference.

Figures 3. displays for the slip velocity and Nusselt number changes with the change of the nano-fluid volume fraction. Volume fractions of 1, 3, and 5 percent are taken. It can be realized that with increasing volume fraction, Nusselt number has been reduced 2.017% cause of the increasing k in the equation (24). The slip velocity has any changing with alternative of volume fraction. Volume fraction changes do not have a substantial effect on slip velocity. Figures 4 shows changes in slip velocity and Nusselt number by τ^* nearby the micro-channel walls. The working fluid is water. As τ^* increases, the gradient of temperature changes on the surface increases, which leads to an increase in heat transfer coefficient. The gradient of the velocity modifications on the surface decreases, which directs to a reduction in the slip velocity. It can be observed increasing the thickness of the porous medium layer, the Nusselt number increased for each τ^* about13.4% and the slip velocity for each τ^* decreased 9.99%. The transfer coefficient of heat transfer is higher in systems be made of porous media. One of the vital reasons for this is the increase in the porous media for thermal conductivity factor.

TABLE 3. The nusselt average for different position of porous H for $\varphi=5\%, \mathrm{Re}=100, \beta^*=0.1$

Grid	10×100	50×500	75×1000
Middle	5.2566	5.2351	5.236
Two-sided	4.9642	4.9492	4.948

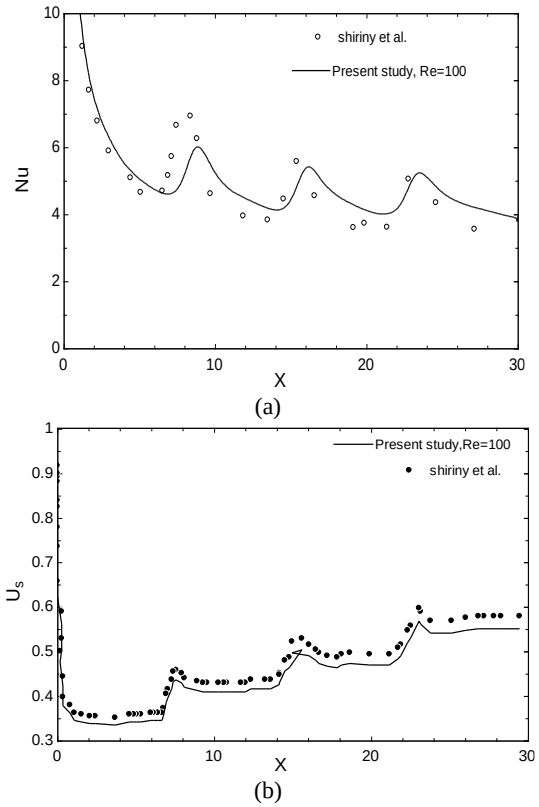

Figure 2. Validation of numerical solution results a)Nu and b)slip velocity for Re=100

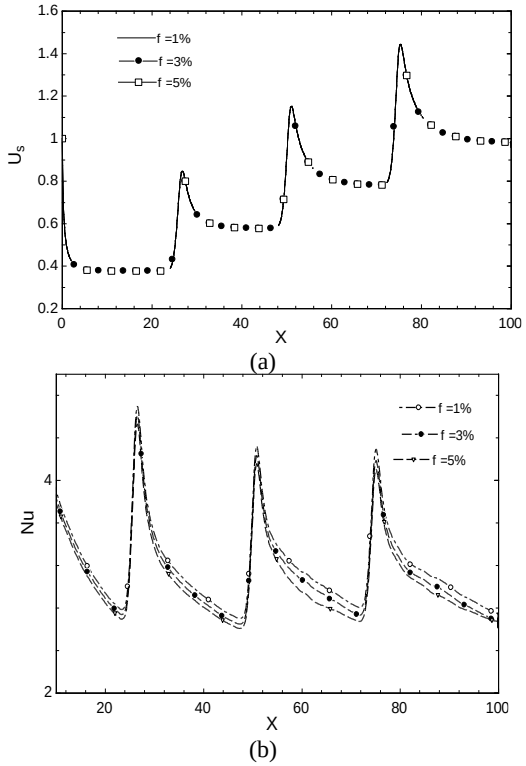

Figure 3. Variations of Nusselt number and slip velocity with nano fluid volume fraction

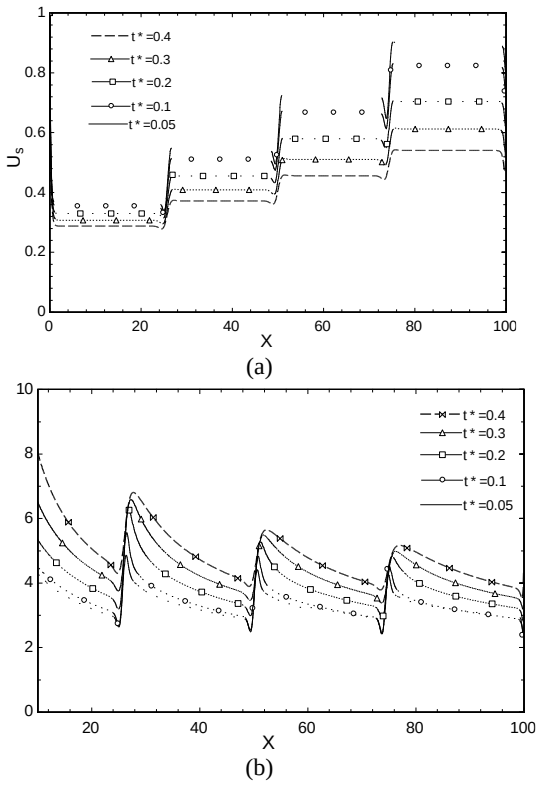

Figure 4. Variations of Nusselt number and slip velocity with porous layer thickness for two-sided porous

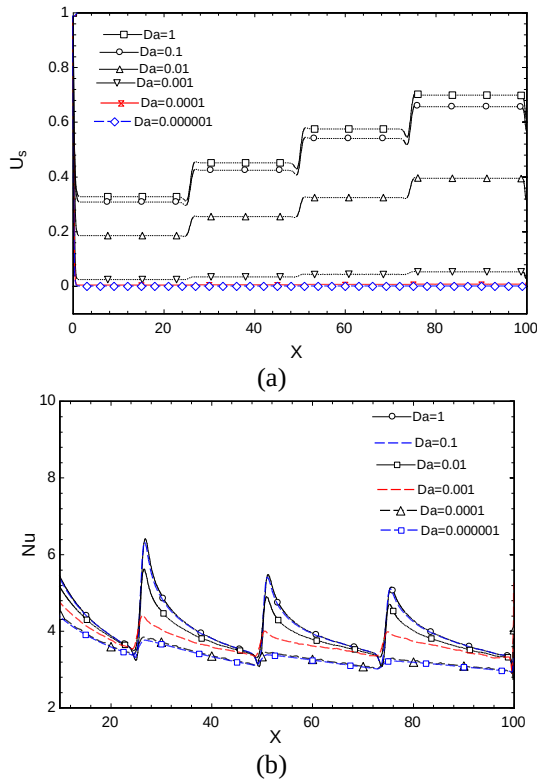

Figure 5. Variations of Nusselt number and slip velocity with Darcy number for two-sided porous with $\tau^* = 0.2$

Figure 5. indicates the effect of permeability on the Nusslet number and slip velocity. The Darcy number has been utilized to variation of the permeability. With cumulative Da number as shown, the fluid flows more simply and the boundary layer becomes thinner. By accumulative the permeability of the porous solid-wall temperature furthermore, the overall heat transfer increases from the mini-channel. An increase in Darcy's number leads to an increase in U_s and Nu . Figure 6 shows that the changes in heat transfer coefficient and slip velocity are similar for both porous layer placement states; close to the horizontal wall and the central wall of the micro-channel.

As the porous-film thickness of the porous medium on the rise, the slip velocity reduces and the heat transfer coefficient increases. As revealed in Figure 1., for more comparison divided the channel two cases, divided by 3 equal sections and putting the porous medium in the middle section and divided the channel by 5 equal sections and putting two porous medium in the section 2, 4. It has been compared two case with non-porous medium and shown the nusslet number and slip velocity in figure and made known as the enhancing supremely the Nusslet number against the non-porous micro-channel cause of the interface of fluid with the impact of porous medium intensification of heat transfer shown in Figure 7. The average nusslet number for three sections is about 7.1784 and for five sections is 7.8422 against the non-porous has been 4.2138 shown that increasing 70.35% Nusselt number for three sections and increasing 86.10% versus non- porous. For slip velocity increased for more impact of fluid and porous media shown in Figure 7. In addition, almost in X=80 the flow has been fully developed and the slip velocity shall be constant till the end of micro-channel.

Slip velocity variations and Nusselt number have been studied for the case where the porous medium layer is just near the top wall and is ribbed, and the results were compared in Figure 8. When the porous layer is close to the wall, amount of the heat transfer factor is greater than when the porous-film layer is in the medium of the channel. The presence of a rib causes a pattern of flow change and turbulence in the flow, which direct to a change in the field of velocity and temperature. The percentage change in the number of nussult is observed for cases where the porous layer in the central of the micro-channel, near the two longitudinal-walls and inferior-walls, near the upper wall, and near the upper wall and in the form of a rib is -14%, 2.25%, 5.46% and 55.53%, respectively, compared to the porous layer-less state. The highest heat transfers and slip velocity in Figure 7. are associated to the instance of the porous layer is in the form of a rib.

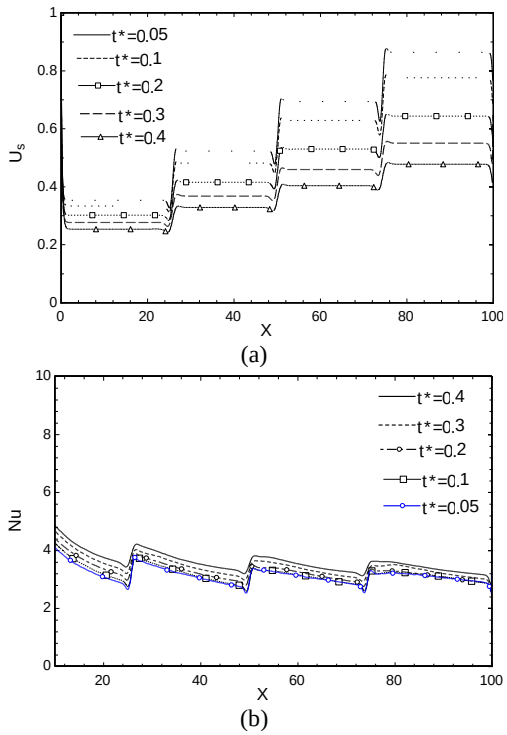

Figure 6. Variations of Nusselt number and slip velocity with thickness of porous layer for middle porous

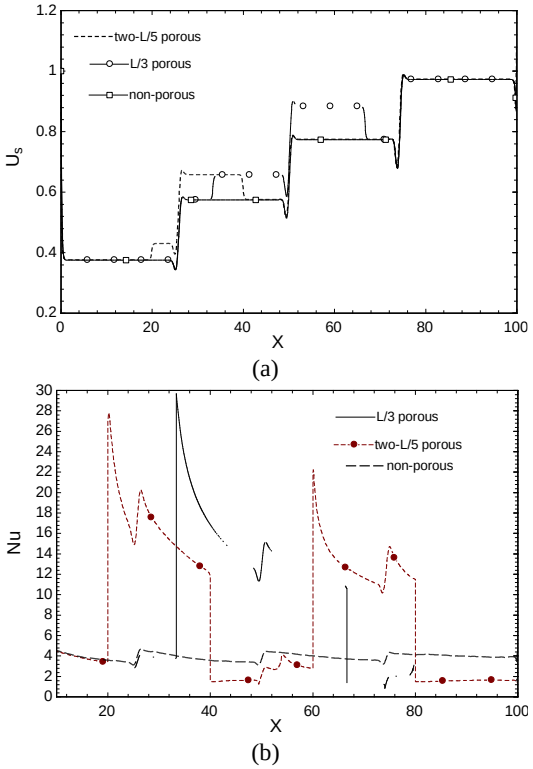

Figure 7. Variations of Nusselt number and slip velocity with porous medium intensification of heat transfer

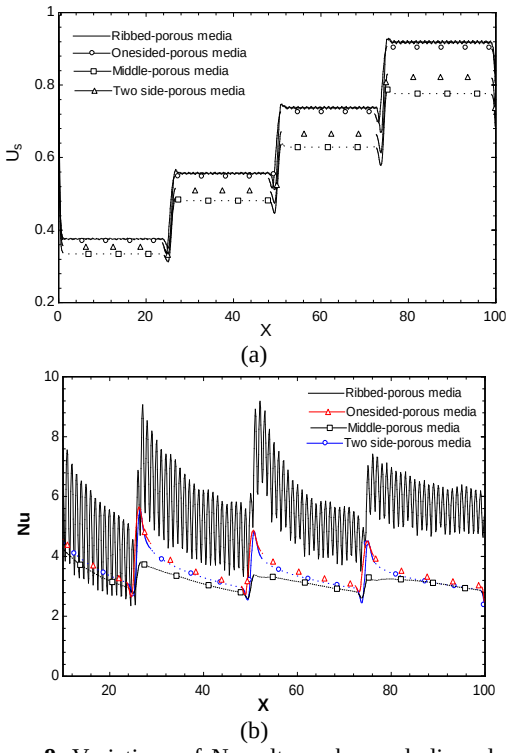

Figure 8. Variations of Nusselt number and slip velocity with the changing placing of porous layer thickness

5 .CONCLUSIONS

In this study, the efficacy of the position of the porous material within a microchannel on heat transfer characteristics was analyzed. A number of several placing of the porous layer were tested. Modeling has been operated in the Comsol software with finite element method. The demonstration results with enlarging the amount of φ, dimensionless Nu number decreased. As the porous-film medium thickness rises, the heat transfer factor growths and the slip velocity decreases. Changes in heat transfer and slip velocity are proportional to the change in Da. Heat transfer is greater by placing a porous layer near the wall than in the center of the channel. The highest heat transfer is in the case where the porous layer is located along the length of the micro-channel with $L/5$ and heat transfer enhancement is 86.27%. It is specified that the amount of heat transfer from the micro-channel is a strong function of how the porous medium is located. Eventually, in near future of micro-channel with porous-medium the position of locating of porous cause of enhancement heat transfer will be important.it will be settled instead of the heat sinks, steam methane reforming reactor, nanoelectromechanical systems (NEMS)-based, microelectromechanical systems (MEMS), MHD properties and heat exchangers such as plate-pin heat exchanger.

6. REFERENCES

1. Tuckerman, D.B. and Pease, R.F.W., "High-performance heat sinking for vlsi", ***IEEE Electron Device Letters***, Vol. 2, No. 5, (1981), 126-129. http://dx.doi.org/10.1108/HFF-04-2018-0149
2. Yang, D., Wang, Y., Ding, G., Jin, Z., Zhao, J. and Wang, G., "Numerical and experimental analysis of cooling performance of single-phase array microchannel heat sinks with different pin-fin configurations", ***Applied Thermal Engineering***, Vol. 112, (2017), 1547-1556. http://dx.doi.org/10.1016/j.applthermaleng.2016.08.211
3. Wang, H., Chen, Z. and Gao, J., "Influence of geometric parameters on flow and heat transfer performance of micro-channel heat sinks", ***Applied Thermal Engineering***, Vol. 107, (2016), 870-879. https://doi.org/10.1016/j.applthermaleng.2016.07.039
4. Chen, Y., Zhang, C., Shi, M. and Wu, J., "Three-dimensional numerical simulation of heat and fluid flow in noncircular microchannel heat sinks", ***International Communications in Heat and Mass Transfer***, Vol. 36, No. 9, (2009), 917-920. https://doi.org/10.1016/j.icheatmasstransfer.2009.06.004
5. Gunnasegaran, P., Mohammed, H., Shuaib, N. and Saidur, R., "The effect of geometrical parameters on heat transfer characteristics of microchannels heat sink with different shapes", ***International Communications in Heat and Mass Transfer***, Vol. 37, No. 8, (2010), 1078-1086. http://dx.doi.org/10.1016%2Fj.icheatmasstransfer.2010.06.014
6. Masuda, H., Ebata, A., Teramae, K., Hishinuma, N. and Ebata, Y., "Alteration of thermal conductivity and viscosity of liquid by dispersing ultra-fine particles (dispersion of γ- Al_2O_3, SiO_2 and TiO_2 ultra-fine particles)", ***Netsu Bussei*** 1993 Vol. 7, No. 4, (1993). https://doi.org/10.2963/jjtp.7.227
7. Khanafer, K., Vafai, K. and Lightstone, M., "Buoyancy-driven heat transfer enhancement in a two-dimensional enclosure utilizing nanofluids", ***International Journal of Heat and Mass Transfer***, Vol. 46, No. 19, (2003), 3639-3653. https://doi.org/10.1016/S0017-9310(03)00156-X
8. Pourmehran, O., Rahimi-Gorji, M., Hatami, M., Sahebi, S. and Domairry, G., "Numerical optimization of microchannel heat sink (mchs) performance cooled by kkl based nanofluids in saturated porous medium", ***Journal of the Taiwan Institute of Chemical Engineers***, Vol. 55, (2015), 49-68. https://doi.org/10.1016/j.jtice.2015.04.016
9. Ajeel, R.K., Salim, W.-I. and Hasnan, K., "Comparative study of the thermal performance of corrugated channels using ZnO–water nanofluid", ***Journal of Thermophysics and Heat Transfer***, Vol. 33, No. 2, (2019), 508-516. https://doi.org/10.2514/1.T5497
10. Ting, T.W., Hung, Y.M. and Guo, N., "Entropy generation of viscous dissipative nanofluid convection in asymmetrically heated porous microchannels with solid-phase heat generation", ***Energy Conversion and Management***, Vol. 105, (2015), 731-745. https://doi.org/10.1016/j.enconman.2015.08.022
11. Hosseini, S., Ghasemian, M., Sheikholeslami, M., Shafee, A. and Li, Z., "Entropy analysis of nanofluid convection in a heated porous microchannel under mhd field considering solid heat generation", ***Powder Technology***, Vol. 344, (2019), 914-925. https://dx.doi.org/10.1016/j.powtec.2018.12.078
12. Moshizi, S., "Forced convection heat and mass transfer of mhd nanofluid flow inside a porous microchannel with chemical reaction on the walls", ***Engineering Computations***, (2015). https://doi.org/10.1108/02644401211246283
13. Shiriny, A., Bayareh, M. and Nadooshan, A.A., "Nanofluid flow in a microchannel with inclined cross-flow injection", ***SN Applied Sciences***, Vol. 1, No. 9, (2019), 1015. .https://doi.org/10.1007/s42452-019-1050-y

14. Jalali, E. and Karimipour, A., "Simulation the effects of cross-flow injection on the slip velocity and temperature domain of a nanofluid flow inside a microchannel", ***International Journal of Numerical Methods for Heat & Fluid Flow***, (2019). http://dx.doi.org/10.1108/HFF-04-2018-0149
15. Barzegar, M.H. and Fallahiyekta, M., "Increasing the thermal efficiency of double tube heat exchangers by using nano hybrid", ***Emerging Science Journal***, Vol. 2, No. 1, (2018), 11-19. https://doi.org/10.28991/esj-2018-01122
16. Manikandan, G., Yuvashree, M., Sangeetha, A., Bhuvana, K. and Nayak, S.K., "Liver tissue regeneration using nano silver impregnated sodium alginate/pva composite nanofibres", ***SciMedicine Journal***, Vol. 2, No. 1, (2020), 16-21. https://doi.org/10.28991/SciMedJ-2020-0201-3
17. Kostikov, Y.A. and Romanenkov, A.M., "The technology of calculating the optimal modes of the disk heating (ball)", ***Civil Engineering Journal***, Vol. 5, No. 6, (2019), 1395-1406. https://doi.org/10.28991/cej-2019-03091340
18. Su, C. and Cheng, Y.-h., "Numerical and experimental research on convergence angle of wet sprayer nozzle", ***Civil Engineering Journal***, Vol. 4, No. 9, (2018), 1985-1995. https://doi.org/10.28991/cej-03091132
19. Shokouhmand, H., Jam, F. and Salimpour, M., "The effect of porous insert position on the enhanced heat transfer in partially filled channels", ***International Communications in Heat and Mass Transfer***, Vol. 38, No. 8, (2011), 1162-1167.http://dx.doi.org/10.1016%2Fj.icheatmasstransfer.2011.04.027
20. Miroshnichenko, I.V., Sheremet, M.A., Oztop, H.F. and Abu-Hamdeh, N., "Natural convection of Al_2O_3/H_2O nanofluid in an open inclined cavity with a heat-generating element", ***International Journal of Heat and Mass Transfer***, Vol. 126, No., (2018), 184-191. https://doi.org/10.1016/j.ijheatmasstransfer.2018.05.146
21. Nojoomizadeh, M., Karimipour, A., Firouzi, M. and Afrand, M., "Investigation of permeability and porosity effects on the slip velocity and convection heat transfer rate of fe3o4/water nanofluid flow in a microchannel while its lower half filled by a porous medium", ***International Journal of Heat and Mass Transfer***, Vol. 119, (2018), 891-906. https://doi.org/10.1016/j.ijheatmasstransfer.2017.11.125
22. Kalteh, M., Abbassi, A., Saffar-Avval, M. and Harting, J., "Eulerian–eulerian two-phase numerical simulation of nanofluid laminar forced convection in a microchannel", ***International Journal of Heat and Fluid Flow***, Vol. 32, No. 1, (2011), 107-116. https://doi.org/10.1016/j.ijheatfluidflow.2010.08.001
23. Moshizi, S., Malvandi, A., Ganji, D. and Pop, I., "A two-phase theoretical study of al2o3–water nanofluid flow inside a concentric pipe with heat generation/absorption", ***International journal of thermal sciences***, Vol. 84, (2014), 347-357. https://doi.org/10.1016/j.ijthermalsci.2014.06.012
24. Rashidi, M., Hosseini, A., Pop, I., Kumar, S. and Freidoonimehr, N., "Comparative numerical study of single and two-phase models of nanofluid heat transfer in wavy channel", ***Applied Mathematics and Mechanics***, Vol. 35, No. 7, (2014), 831-848. https://doi.org/10.1007/s10483-014-1839-9
25. Hung, T.-C., Huang, Y.-X., Sheu, T.-S. and Yan, W.-M., "Numerical optimization of the thermal performance of a porous-microchannel heat sink", ***Numerical Heat Transfer, Part A: Applications***, Vol. 65, No. 5, (2014), 419-434. https://doi.org/10.1080/10407782.2013.836005
26. Guo, Z., Saunders, N., Miodownik, A. and Schillé, J., *Aluminium alloys, their physical and mechanical properties, j. Hirsch, b. Skrotzki, and g. Gottstein, ed*. 2008, Wiley-VCH.
27. Mohammed, R.H., Mesalhy, O., Elsayed, M.L., Huo, R., Su, M. and Chow, L.C., "Performance of desiccant heat exchangers with aluminum foam coated or packed with silica gel", ***Applied Thermal Engineering***, Vol. 166, (2020), 114626. https://doi.org/10.1016/j.applthermaleng.2019.114626
28. Nield, D.A. and Bejan, A., "Convection in porous media, Springer, Vol. 3, (2006). https://doi.org/10.1007/978-1-4614-5541-7
29. Brinkman, H., "The viscosity of concentrated suspensions and solutions", ***The Journal of Chemical Physics***, Vol. 20, No. 4, (1952), 571-571. https://doi.org/10.1063/1.1700493

Persian Abstract

چکیده

در این مقاله اثر لایه متخلخل بر روی انتقال حرارت یک میکروکانال با تزریق مایع از دیواره پایینی آن بررسی شده‌است .شرایط عدم لغزش در دیواره میکروکانال در نظر گرفته شده‌است و شرط مرزی برای دیواره‌های بالایی و پایین مجرای سرریز به عنوان عایق و دمای ثابت در نظر گرفته می‌شود .نتایج نشان داده شده است در که موقعیت لایه متخلخل تاثیر قابل‌توجهی بر انتقال گرما دارد .درصد تغییر در عدد ناسلت برای مواردی مشاهده می‌شود که در آن لایه متخلخل در دیواره فوقانی و نزدیک دیواره فوقانی و در شکل یک دنده و در بخش بخش تقسیم شده شده بر L/3 و L/5 ترتیب ، ٪۲.۲۵ ،٪ ۵.٤٦ ،٪ ۷۰.۵ و٪ ۸٦.۲۷ در مقایسه با حالت بدون لایه متخلخل بوده‌است.

International Journal of Engineering

Journal Homepage: www.ije.ir

Micro-structural Deformation Field Analysis of Aluminum Foam using Finite Element Method and Digital Image Correlation

B. Akhavan[a], A. Pourkamali Anaraki*[b], A. Malian[c], Y. Taraz Jamshidi[b]

[a] *Department of Industrial Engineering, IAU Tehran North Branch, Tehran, Iran*
[b] *Department of Mechanical Engineering, Shahid Rajaee Teacher Training University, Tehran, Iran*
[c] *Department of Civil Engineering, Surveying Group, Shahid Rajaee Teacher Training University, Tehran, Iran*

PAPER INFO

Paper history:
Received 23 February 2020
Received in revised form 19 June 2020
Accepted 26 August 2020

Keywords:
Digital Image Correlation
Response Surface Methodology
Aluminum Foam
Computed Tomography Imaging
Finite Element Method

ABSTRACT

Porous materials especially closed-cell metallic foams play important roles among novel materials because of their good characteristics e.g. high strength to weight ratio and crashworthiness. On the other hand, mechanical behavior determination and detailed characterization are essential in efficient manipulation and material tailoring. In the present research especial hybrid experimental-numerical approach is used for aluminum foam behavior determination as to the main goal, i.e. continuous deformation field measurement using digital image correlation (DIC) and finite element analysis (FEA) on porous specimen's surface. To overcome the 3D modelling problem of closed-cell foams structure, we present the method based on CT-scan and digital optic microscope imaging combination. In the experimental part of the study, aluminum foams and proper specimens are manufactured, and then high-resolution digital imaging and illumination setup are employed. Finally, the deformation field is obtained using DIC. On the other hand, measurement verification and DIC parameters optimization processes are conducted using ABAQUS 2019 with comprehensive mesh independency study and response surface methodology (RSM) respectively as major research achievement. Finally, correlation equations based on high regression models are obtained. Using detailed geometrical micro-model and optimal DIC parameters yields to good numerical-experimental accordance. The novel approach of combined CT and digital microscope imaging instead of industrial micro-CT lowered imaging costs while yielded to accurate numerical results.

***doi**: 10.5829/ije.2020.33.10a.25*

NOMENCLATURE

u, v	Displacement concerning x and y axes	H	Shannon entropy (bit/pixels)
$\vec{P}$	Displacement vector	DLP	Dose length product (mGy.cm)
LS	Least squares correlation	$CTDI$	CT-scan dose index (mGy)
f, g	Gray level function in reference and current configurations	L_s	Scan length (cm)
n	Subset size (pixels)	HU	Hounsfield unit
$H(\vec{P})$	Hessian operator	SNR	Signal to noise ratio
E	Small strain tensor	S_{subset}	Subset size (pixels)
ε	Strain tensor	R_{subset}	Subset radius (pixels)
$ZNCC$	The zero-mean normalized sum of squared differences	$SFOV$	Scan field of view

1. INTRODUCTION

Novel methods of experimental stress and strain analysis play an important role in material behavior characterization. For instance, using rosettes were the most reliable approach in mechanical parameters extraction. Although they had several problems such as adhesive effect, discrete strain filed determination, high

*Corresponding Author Institutional Email: *ali_pourkamali@sru.ac.ir*
(A. Pourkamali Anaraki)

Please cite this article as: B. Akhavan, A. Pourkamali Anaraki, A. Malian, Y. Taraz Jamshidi, Micro-structural Deformation Field Analysis of Aluminum Foam using Finite Element Method and Digital Image Correlation, International Journal of Engineering (IJE), IJE TRANSACTIONS A: Basics Vol. 33, No. 10, (October 2020) 2065-2078

operational cost, impossible to use on porous surfaces, etc. Digital image correlation (DIC) is one of the most efficient approaches that overcome many of the mentioned disadvantages. Digital image correlation is a technique that attempts to find correlations and similarities between the reference image segment and deformed configuration. Skozrit et al. [1] investigated elastic-plastic and failure of various aluminum alloys both numerically and experimentally. They conducted static and dynamic tensile tests and also three-point bending experiment with different strain rates. They manipulated the two-dimensional plane stress finite element analysis. For validation purposes in the displacement and strain field, they performed several DIC measurements. Also, they used infrared thermography as an efficient tool for damage propagation survey. The digital correlation technique also used for material parameter identification as well [1]. Begonia et al. [2] studied strain and displacement field in mouse forearm bone using a non-contact DIC method under uniaxial compression loading. The digital image correlation method is employed on mechanical characterization and deformation measurement of two dimensional SiC/SiC composite pipes [3]. Mehdikhani et al. [4]studied the deformation field and whole strain tensor of the composite cross-section and its fibers in the micro-scale. Their investigations are focused on using the DIC technique with the SEM images for three-point bending tests of fiber-reinforced laminates.

Due to the brilliant high-temperature behavior of ceramic matrix composites, Whitlow et al. [5] conducted comprehensive in-situ health monitoring of SiC/SiC and their service life using the DIC method. They studied the ultimate strength and effects of fiber properties on it. Gerbig et al. [6] coupled the conventional finite element method with the DIC technique. The estimated material parameters corresponded to the non-uniform displacement distribution in the tensile test specimen. They also used an optimization approach for validation purposes. Engqvist et al. [7] studied strain filed and deformation mode of loaded glass polycarbonate using DIC. They loaded novel specimen bi-axially for localized strain investigations. Opera et al. [8] used infra-red thermography and image processing in metal dynamic yield behavior determination. For comparison purposes, they used 3D digital image correlation. Ceramic blocks and composite resins are widely used in dentistry. Jiang et al. [9] studied the stress intensity factor in these materials using the DIC method. In such small parts, it is impossible to use conventional stress analysis and standard specimens. Nguyen et al. [10] investigated the mechanical behavior of cortical bone using a multi-scale micro-macro method and DIC technique. They captured images in both scales during the loading condition. The main goal is to determine material properties on several scales. A wide range of composite applications and complex nature of fatigue and crack growth using classical methods are the main research idea. Aparna et al. [11] studied cracking and stress intensity measurement using DIC in the fatigue test of GFRP. Feng et al. [12] studied the effects of fiber reinforced polymer confinement technique to overcome the drawbacks of rubberized concrete. Statistical models were also developed based on experimental using response surface methodology (RSM). Finally, the regression analysis was performed to develop response equations based on quadratic models. Obianyo et al. [13] investigated the efficiencies of sedimentation tanks with horizontal and vertical baffle mixers, and also determined the optimal values of factors of clarification in the sedimentation tanks. Response surface methodology was further used for the present analysis of data in this study for more reliable study because it optimized the responses of variables. Sharif et al. [14] studied the use of cellulose dust produced in the drying section of paper mills as a potential adsorbent to remove methylene blue dye. They manipulated the RSM or simply the response surface methodology with CCD which stands for central composite design. Yang et al. [15]investigated the effect of using aluminum foam in sound absorption application for mining industry. They showed that using this kind of porous material yielded to the noise reduction in mining chute. In addition to, the aluminum foam has major positive effect on vibration reduction. Hosseini Ravandi et al. [16] manipulated the image processing technique for lightness change of fabric appearance. He also used ANOVA technique for correlation measurment purposes. Fattahzade et al. [17] presented the new approach of monitoring using sequential images. They used statistical methods and measured correlation between images for defect detection process.

In the present paper, digital images captured during the uniaxial compression test of aluminum foams are analyzed using the DIC technique. So continuous displacement and strain fields are measured on the external surface of the specimen. These results could be used in the stress field, energy absorption capacity, and also material parameters identification. The procedure is categorized into several steps such as specimen manufacturing and preparation for a compression test, imaging system and illumination setup, DIC-based measurement using initial setting, DIC parameters optimization using RSM, and validation process using FE simulations. Also, an analysis of variance is used for response regression and significant factors determinations. For high accuracy FE analysis, micro-structural foam modeling is performed using CT-scan and digital optic microscope. Because micro CT is an expensive procedure, we used a conventional CT-scan device. To enhance the modeling resolution, mesh refinement technique is employed using the optical microscope imaging. Using CT-scan instead of micro-CT

for geometric modeling with acceptable accuracy is considered as a novelty. Furthermore, using RSM-based optimization enhances the deformation field estimation with high desirability value. Finally, FE results and DIC measurement calculations are in good agreement. The whole research process and methodology is illustrated in the following flowchart (see Figure 1). After the introduction section which consists of literature review and process flowchart, the materials and methods section is appeared. This section consists of sample preparation process and uniaxial test method, DIC method theoretical aspects and modeling techniques using CT-scan. The next section consists of results interpretation and discussion, verification methodology, and parametric study and optimization using DOE and RSM techniques. The last section consists of conclusions and major research findings.

2. MATERIALS AND METHODS

2. 1. Specimen Preparation and Uniaxial Compression Test Aluminum foams are employed as the main material used in the present research. The mentioned Alporas foams are manufactured using liquid state method with 2% TiH_2 and 1.5% Calcium. Additives are used as the blowing agent and viscosity enhancer respectively, at 680 deg. Manufactured blocks have 100×50×10 cm dimensions. Precision sizing of specimens is performed by CNC milling. Finally, several aluminum foam specimens are prepared and sized for compression tests. Present foam specimen densities are generally 300 and 500 kg/m^3 depending on the location in the manufactured block. Because of the melt hydrostatic pressure and bubble growth, the bottom half of the block has 500 and the top half has 300 kg/m^3 densities respectively. Standard uniaxial tension test is conducted to determine the mechanical properties of aluminum foam, according to ASTM B557. Mechanical behavior analysis of cubic closed-cell aluminum foam specimens is performed using quasi-static compression testing using ZWICK 100 apparatus with a five mm/min loading rate. Prepared specimens and loading device are shown in Figure . Prepared specimens have approximately 40×40×40 mm dimensions to ensure at least six complete cells in each direction. This guarantees rather a uniform deformation without localized failure and collapses. Furthermore, specimens are prepared large enough for better imaging and illumination during compressive loading. Specimen density in the present research is 500 kg/m^3.

2. 2. Digital Image Correlation Technique Implementation Digital image correlation is a technique of finding correlation and similarities between the reference image and deformed configuration in loading conditions. So, images are discretized initially to several subsets. Comparing reference and possible current subsets lead to displacement vector calculation. Using small deformation assumption in any increments, we have equations for displacement vector components in every pixel as below (Equations (1)-(3)) [18].

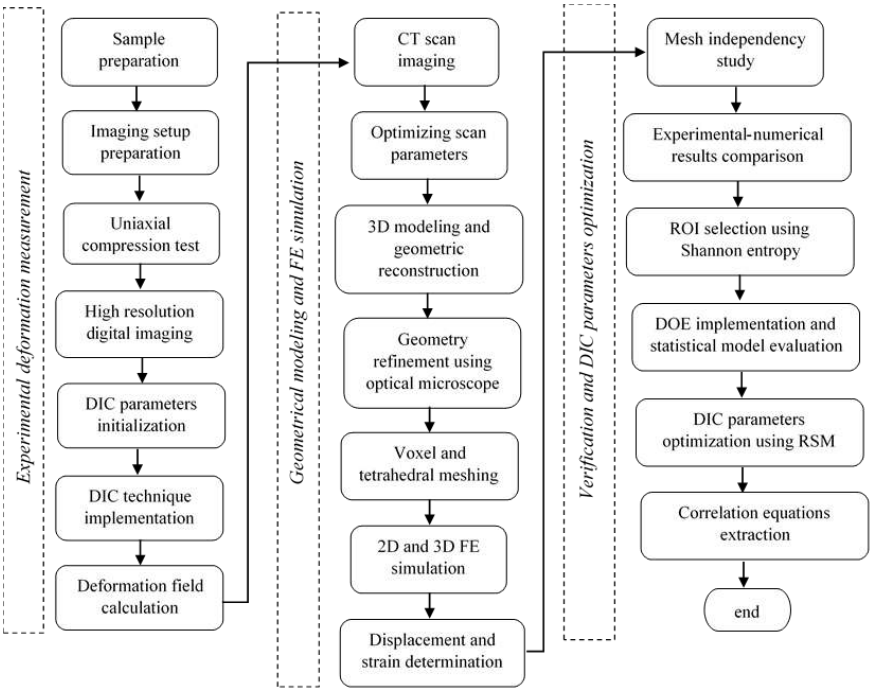

Figure 1. Research process and methodology flowchart

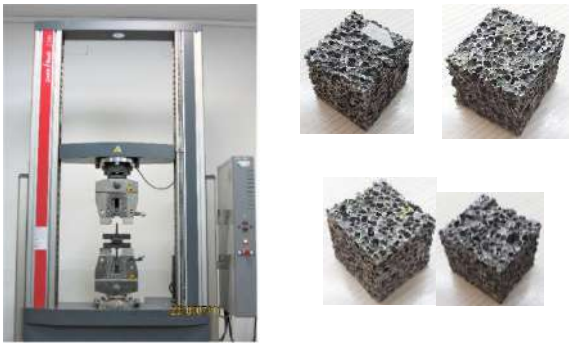

(a) (b)

Figure 2. Zwick100 loading device (a), and prepared specimens for uniaxial compression test (b)

$$u_s = u + \frac{\partial u}{\partial x}\Delta x + \frac{\partial u}{\partial y}\Delta y \quad (1)$$

$$v_s = v + \frac{\partial v}{\partial x}\Delta x + \frac{\partial v}{\partial y}\Delta y \quad (2)$$

Furthermore, the main DIC objective is focused on displacement vector determination $\vec{P}$ (Equation (3)).

$$\vec{P} = \left\{u, \frac{\partial u}{\partial x}, \frac{\partial u}{\partial y}, v, \frac{\partial v}{\partial x}, \frac{\partial v}{\partial y}\right\}^T = \{P_i\}^T, i = 0, \dots, 5 \quad (3)$$

There are several correlation definitions such as cross-correlation, CC and least squares, LS (Equation (4)). In the present paper, the least square method is used to obtain accurate results. Furthermore, we manipulate ZNCC correlation formulation to lower the noise sensitivity problem. Hence:

$$LS = \frac{\sum_{i,j=-(n-1)/2}^{+(n-1)/2}\{f(x,y) - g(x^*,y^*)\}^2}{\sum_{i,j=-(n-1)/2}^{+(n-1)/2} f(x,y)^2} \quad (4)$$

In which n is subset size, and i and j are pixel counters. Functions f and g are gray levels in reference and current configuration. Deformed subset finding is equivalent to the minimum LS value. Newton-Raphson approach is employed for the minimization procedure, as formulated in Equation (5). So

$$\nabla LS = \frac{\partial LS}{\partial P_k} = \frac{2}{\sum_{i,j=-(n-1)/2}^{+(n-1)/2} f(x,y)^2} \cdot \sum_{i,j=-(n-1)/2}^{+(n-1)/2}\{f(x,y) - g(x^*,y^*)\}\frac{\partial g}{\partial P_k} \quad (5)$$

Using the $\vec{P}_0$ as an initial displacement vector components estimates, the general Newton-Raphson form appears as below (Equation (6)).

$$\vec{P}_{n+1} - \vec{P}_n = -H(\vec{P}_n)^{-1} \cdot \nabla LS(\vec{P}_n) \quad (6)$$

In which H is the Hessian operator. Using the iterative procedure, the displacement vector $\vec{P}$ is calculated within the desired tolerance [19]. Also, using high-resolution images and proper filtering may help increase measurement accuracy [20]. After displacement field calculation, strain tensor components could be determined using kinematic equations as below. Using small displacement assumption, these equations reduced to (Equations (7)-(9))

$$E_{xx} = \frac{\partial u}{\partial x} \quad (7)$$

$$E_{yy} = \frac{\partial v}{\partial y} \quad (8)$$

$$E_{xy} = \frac{1}{2}\left\{\frac{\partial u}{\partial y} + \frac{\partial v}{\partial x}\right\} \quad (9)$$

2. 3. Noise and Illumination Sensitivity During the experiments and imaging process, noise and light illumination variations are inevitable. Hence, using correlation criteria with minimum sensitivity to these alternations in the DIC method is essential. Main noise sources are summarized as light variation during specimen deformation, low image resolution, inaccurate focus, or even lens distortion effects. There are many criteria such as cross-correlation, normalized cross-correlation, the sum of squared differences, and the zero-mean normalized sum of squared differences, ZNCC (Equations (10), (11). The latter criterion is one of the most efficient definitions in noisy conditions. In the present paper, ZNCC and LS are used as correlation criteria [21]. So,

$$C_{ZNCC} = \sum_{i=-M}^{M}\sum_{j=-M}^{M}\left\{\frac{[f(x_i,y_j)-f_m]\times[g(x_i^*,y_j^*)-g_m]}{\Delta f \Delta g}\right\} \quad (10)$$

In which $M = (n-1)/2$. Also, we have

$$f_m = \frac{1}{(2M+1)^2}\sum_{i=-M}^{M}\sum_{j=-M}^{M} f(x_i,y_j)$$
$$\Delta f = \sqrt{\sum_{i=-M}^{M}\sum_{j=-M}^{M}\left[f(x_i,y_j) - f_m\right]^2}$$
$$g_m = \frac{1}{(2M+1)^2}\sum_{i=-M}^{M}\sum_{j=-M}^{M} g(x_j^*,y_j^*) \quad (11)$$
$$\Delta g = \sqrt{\sum_{i=-M}^{M}\sum_{j=-M}^{M}\left[g(x_j^*,y_j^*) - g_m\right]^2}$$

Subset size plays an important role in DIC calculations. Subset size selection is a trade-off between several factors such as deformed subset discovery probability and results accuracy. In other words, using too small subset leads to improper subset finding. On the other hand, a large subset size increases the computational error. During deformation, it is possible to occur subset infinitesimal deformation in the sub-pixel scale. Due to the discrete nature of image gray values, sub-pixel calculations are meaningless [21]. To overcome the mentioned limitation, the bi-cubic interpolation technique is employed as shown in Figure . In this figure, horizontal x and y plane are pixel coordinates and the

vertical axis is gray values related to each pixel. Proper bi-cubic interpolation shows good agreement with actual gray values.

2. 4. Speckle Pattern Evaluation and Entropy Determination One of the most important factors affecting displacement field calculations is speckle pattern or simply gray index distribution and randomness. Shannon entropy is used to evaluate the quality of random patterns. This criterion is actually information contents expected value in a gray-scale image (Equation (12)). So,

$$H = \sum_{k=0}^{M} p_k \log\left(\frac{1}{p_k}\right) \quad (12)$$

In which H is Shannon entropy in bit per pixels, p_k is the normalized probability of each gray values, and $M = 255$ is the number of gray value in each pixel, i.e. $2^{\beta} - 1$ for β -bit images. Parameter p_k could be obtained using the image histogram. To enhance the DIC calculation accuracy and proper region-of-interest (ROI) selection, entropy values are determined for different sections of reference images. Maximum entropy leads to more accurate results. In Figures 4 and 5 four different regions with high entropy values and their corresponding histogram are shown. These regions are chosen to be manipulated as optimum ROIs. As shown, entropy values are within 7.28 to 7.53. Despite the fact, there are approximately random speckle patterns on specimens due to the manufacturing process, cutting, machining, and grinding, we used several other methods such as paint spraying and abrasive papers in order to enhance entropy values [22].

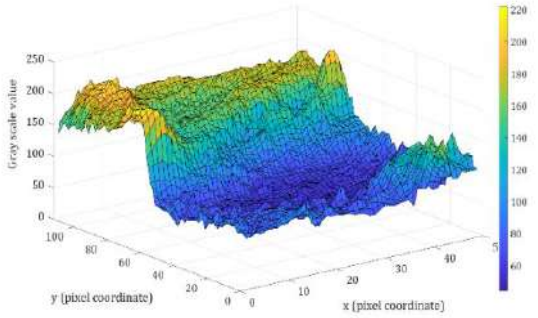

Figure 3. Bi-cubic interpolation of gray levels used in sub-pixel displacement determination

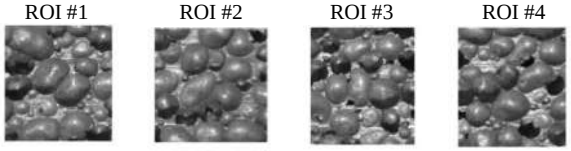

Figure 4. Four reference image segments with high entropy

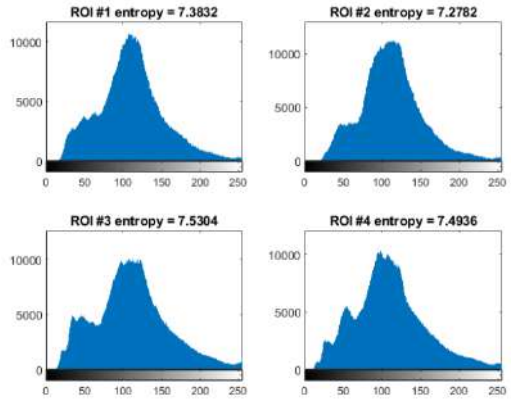

Figure 5. Four reference image segments histograms and Shannon entropy

2. 5. Micro-Structure Modeling Using Digital Images and Computed Tomography Using computed tomography is a newly emerged technique in geometric modeling of cellular microstructure. So we use the CT-scan device on prepared specimens for modeling purposes. As mentioned, using low-cost CT instead of micro-CT for 3D modeling is considered as an advantage. Furthermore, we choose for several CT imaging settings and protocols to enhance the modeling quality. Finally, the optimum values for CT imaging parameters are obtained. In the present research, the CT-scan device is *GE 16 slices* with 0.1 to 0.2 mm slice thickness, small scan field of view (SFOV) of 154, 120 kV voltage, 100 mA current, and 1-s full helical scan setting. The mentioned settings are chosen after the iterative process of optimization and qualitative evaluation of captured images. Significant parameters are voltage, current, slice increment, and scan field of view. Voltage variation levels are 100, 120, and 140 kV. It is seen that decreasing current leads to an increase in image noise and artifact. Although the image contrast may increase slightly. On the other hand, the increasing voltage to 140 kV does not control image noise considerably. So the optimum voltage is chosen to be 120 kV. For the present CT-scan device, there are three current options in the aforementioned voltage. The proper values are 80, 100, and 120 mA [23]. Corresponding to the present scan condition, volumetric CT-scan dose index, $CTDI_{vol}$ is 37.17 mGy, dose length product, DLP (formulated in Equation (13)) is 297.6 mGy.cm, dose efficiency is 85.7%, radiation exposure time is 14.2 s, and the phantom length is 16 cm [24]. So we have:

$$DLP(mGy \cdot cm) = CTDI_{vol}(mGy) \cdot L_s(cm) \quad (13)$$

In which L_s is scan length. The specimen's scan dimension is about 8 cm. After scanning with optimum settings, the diVision Lite commercial software is used for quality evaluation. In Figure 6 one CT-scan slice of

two different foam specimens is shown. Artifact occurrence is severe in metal CT images especially metallic foams. Using optimum settings and proper protocol minimizes the undesired effects [25]. Image enhancement and noise reduction are achieved using a non-linear median filter [20]. Foam specimens used in CT-scan imaging have the approximate dimension of 58×40×41 and 46×43×42 mm. We crop desired specimens corresponding to the uniaxial compression experiments for simulation purposes after 3D modeling. The 3D models used in FE simulations are cubes with at least approximately 40 mm dimension. Another significant parameter affecting 3D geometric reconstruction is the CT-scan threshold measured with the Hounsfield unit (HU). This index corresponds to the distinction capability of metal from voids [26]. Altering the HU lead to different model densities. Knowing the 300 to 500 kg/m^3 density range of aluminum foam is equivalent to -500 to 500 HU [27].

The current increase is similar to the voltage parameter. So the optimum current value is chosen to be 100 mA. Goal functions in CT-scan parameters are signal to noise ratio, SNR and contrast to noise ratio SNR. The scan field of view is chosen corresponding to the specimen dimensions. In contrast to mA and kV, an increase in SFOV leads to noise increases. The Mimics Research 21.0 commercial software is used for modeling purposes [28]. In Figure 7 the whole process of 3D geometric reconstruction is shown.

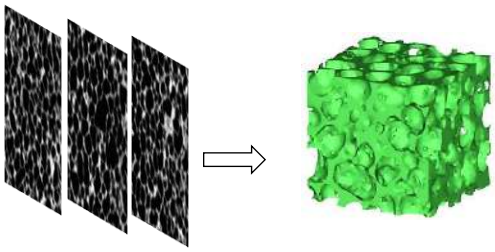

Figure 7. Process of 3D model reconstruction in Mimics using CT-scan slices

2. 6. Mesh Generation Using Voxel and Tetrahedral Elements Mesh generation is the most important step in FE simulations. In the present research, we used two types of elements for comparison purposes, i.e. 8-noded voxel brick and 4-noded tetrahedral element with linear interpolation shape function. Each approach has its unique merits and disadvantages. Voxel elements have a minimum computational cost because they have the minimum number of nodes and elements. Because they have jagged geometry, they did not fit geometry completely. Using tetrahedral elements may help overcome this problem especially in the curved regions. Although using a 4-noded element leads to the dramatic increase in computational cost. Another disadvantage is related to the higher error in deformation field calculations. Refining tetrahedral mesh could help to enhance the calculations [29]. In Figure two types of finite element models with tetrahedral and brick elements are shown.

To obtain the optimum mesh density with acceptable accuracy and relatively low computational cost, four FE models are generated and simulations are performed. In Table 1 mesh independency analysis results are shown. In this table, computation cost and results agreement index are given in normalized form concerning optimum

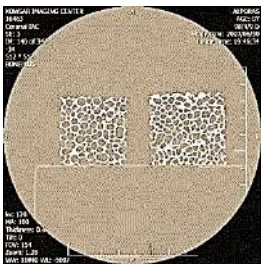

Figure 6. CT-scan slice image quality evaluation for two different metallic foams in diVision Lite

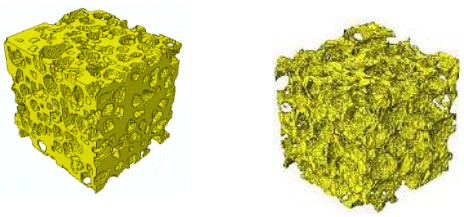

Figure 8. Finite element model of cellular solid using CT-scan images, (a) Voxel brick element and (b) tetrahedral element

TABLE 1. Mesh independency study for different mesh size

Agreement with Ref. solution	Normalized computation time	App. Node no. (×1000)	App. Element no. (×1000)	Voxel size	Mesh density	Mesh geometry
1.02	5.3	1817	1169	1	fine	Hexahedral brick (Voxel)
1.0	1.0	348	206	2	Relatively fine	
1.56	0.45	122	72	3	Average	
0.25	0.12	42	25	4	Coarse	

mesh density, i.e. relatively fine. As observed, using fine mesh leads only 2% results variations but 5 times increase in computational cost. On the other hand, using average and coarse mesh increase calculation error to 56 and 75%.

2. 7. Finite Element Simulation Implementation

Finite element simulation with explicit dynamic step and reduced loading rate is performed for quasi-static results using ABAQUS commercial software. Optimized mesh contained hexahedral brick C3D8 and tetrahedral C3D4 elements. The universal loading device plateau is modeled using R3D4 rigid elements. To obtain smooth results with minimum noise, anti-aliasing and Butterworth filters with 2kHz cutoff frequency are employed [30]. Simulation inputs and material properties are obtained using tensile tests with ASTM B577 standard [31] as shown in Table 2.

3. RESULTS AND DISCUSSIONS

3. 1. Displacement And Strain Field Measurement Using DIC

In this section, digital images captured during the compression test of aluminum foam specimens are used to obtain displacement and strain field using the DIC technique. Digital image correlation outputs are displacement vector (u, v) and strain tensor $(\varepsilon_{xx}, \varepsilon_{yy}, \varepsilon_{xy})$. The process of field variable determination has many parameters affecting output accuracy. These parameters are summarized as current and reference configuration, ROI, subset size, subset spacing, solution tolerance, calibration factor, lens distortion factor, strain radius, etc. Generally, predefined settings are proper and DIC outputs have a relatively low computational error. But DIC implementation for the porous surface of foams requires iteration for proper settings selection to avoid solution divergence. In Table 3 initial settings are illustrated. In the later section, we employ RSM based optimization to find optimum parameters of DIC to achieve minimum error. Altering various settings lead to significant parameter identification. In brief, the most significant factors in displacement field calculation are subset radius and subset spacing both in pixels. For strain measurement, there is one more factor, i.e. strain radius. For validation purposes, displacement vector and the strain tensor components are compared with corresponding FEA results in a particular point as shown in Figure 9.

After DIC implementation, horizontal displacement u, and vertical displacement v are obtained in continuous contour form. It is worth noting that v displacement contour is smoother than u contour. It is because of the mechanical behavior of porous solids. In other words,

TABLE 2. Material mechanical and physical properties used in FE simulation

Poisson's ratio	Yield strength (MPa)	Tangent modulus (GPa)	Young's modulus (GPa)	Mass density (kg/m^3)	Material
0.35	76	0.47	69	2700	Aluminum

TABLE 1. Initial DIC parameters

Max. allowable iterations	Solution tolerance	Strain radius (pixel)	Subset spacing (pixel)	Subset radius (pixel)	ROI size (mm)
60	1.0e-7	15	1.0	34	20-40
Solution	**Loading disp.**	**Frame No.**	**Seed position**	**Thread No.**	**ROI shape**
direct	0.576 mm	20	Quarter ROI	4-8	Rectangular

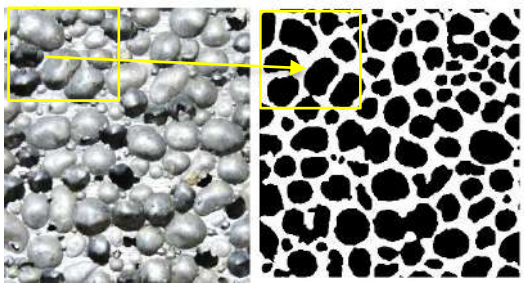

(a) (b)

Figure 9. The particular point used for validation purpose and field measurement, (a) digital image and (b) filtered binary image for FE modeling

the displacement field in direction of loading is quite smooth but because of the low Poisson's ratio and localized cell buckling, there is a non-smooth contour and a high amount of computational error in the transverse direction. Vertical and horizontal displacements are measured using DIC after averaging field values in the neighboring region. These values are 0.35 and 0.07 mm. To ensure the validity of the results, three distinct compression experiments are performed and their results are reported as an average value. In addition, the DIC procedure is done for strain measurement calculation. The strain field calculation is ε_{xx}, ε_{yy} and ε_{xy} measurement. Due to the small values,

normal strains are reported as percent and shear strain is reported as a degree. A higher computational error in strains is due to the derivation of the displacement field. Although there is a smooth contour in the strain field, because of the averaging and interpolation process. The contour smoothness in strain calculation is related to the strain radius parameter. Normal vertical and horizontal strains are -0.7 and 1.2% and shear strain is 1.6°. Strain field is a combination of both tensile and compressive normal strain because of the localized nature cell walls and faces deformation.

3. 2. Results Verification Using FEA and DIC

Because of the porous nature of the metallic foam, it is impossible to use contact methods of strain measurement such as strain rosettes. Furthermore, many experimental methods cannot determine the field variable in continuous form. So for verification purposes, FE analysis is chosen. In this way, the major requirement is accurate geometric modeling and meshing for simulation. As mentioned before, CT-scan images and digital microscopy techniques are employed in geometric reconstruction and modeling. Digital microscopy images with 800X zoom are used in micro-structural details refinement e.g. cell edge, that rather low-resolution CT-scan failed to model. In Figure 10 it is shown that cell edge thickness varies from 0.2 to 0.4 mm. using this method, the FE model updated with actual values of micro-structural feature dimensions and hence true foam relative densities are obtained in modeling.

FE simulation results compared to DIC outputs of aluminum foam are shown in Figure 11. In these contours, v-displacement and u-displacement are shown.

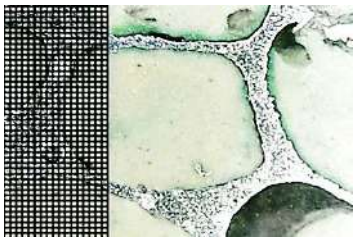

Figure 10. Digital microscope image used in micro-structural detail measurements with a scale of 0.1 mm

These values are approximately 0.4 and 0.083 mm. Hence, relate errors corresponded to the DIC measurements are 15 and 19% respectively. The error values show good agreement between DIC and FEA outputs. Furthermore, strain tensor components are obtained within the FE analysis. So ε_{yy}, ε_{xx}, and ε_{xy} are -1.08, 0.161, and 2.6°. DIC relative errors in strain field measurements are 55, 34, and 65%. A higher amount of error is related to the derivation operator in strain calculation from the displacement field.

As it is mentioned, strain components contour plots are FEA and DIC main results. So in Figure 12 the normal and shear strain contours are shown. Furthermore, the FEA outputs are compared to the DIC results. As it is obvious, there are more discontinuity rather than displacement contours. It is because of the inherent error of derivation operator. It is worth noting that normal and shear components of strain tensor are measured higher than FEA values. It guarantees that we can rely on the DIC values and in this way we are on the safe side.

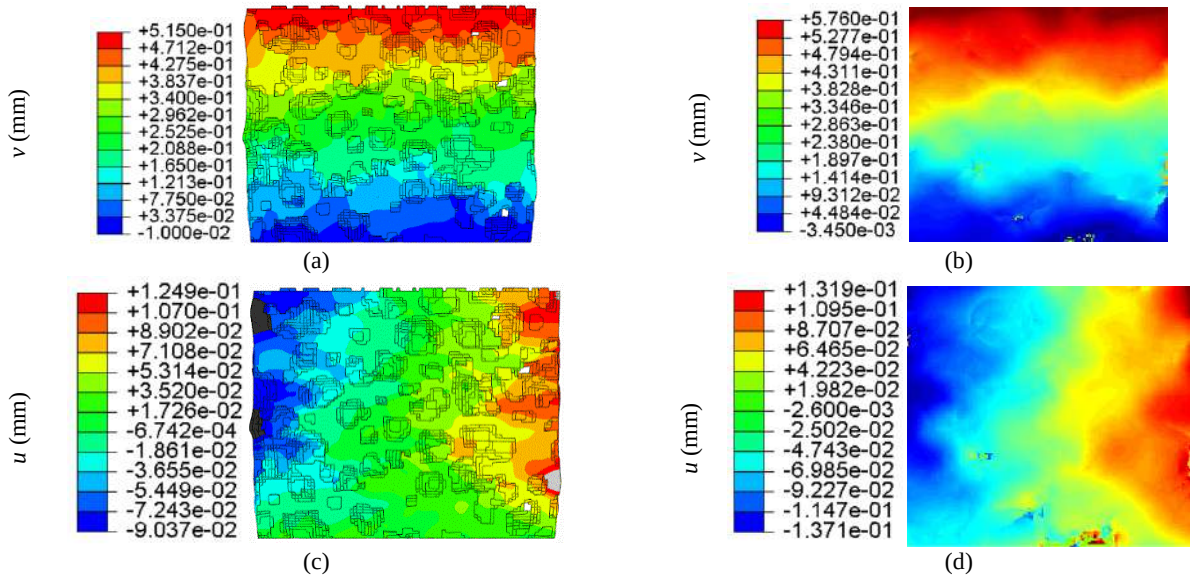

Figure 11. Displacement field determined by FEA on the porous surface of foam specimen, (a) FEM v-disp., (b) DIC v-disp., (c) FEM u-disp., and (d) DIC u-disp

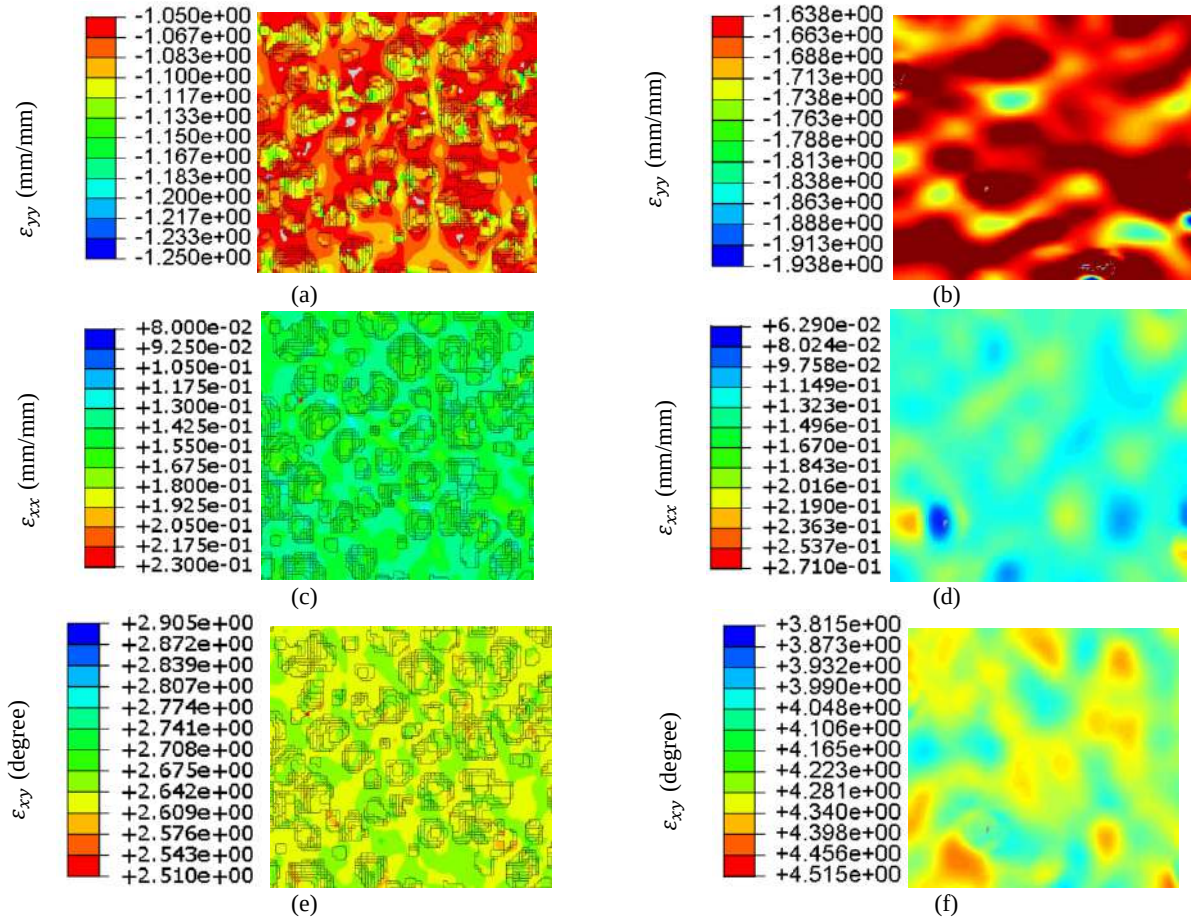

Figure 12. Strain field determined by FEA on the porous surface of foam specimen, (a) FEM $\boldsymbol{\varepsilon_{yy}}$, (b) DIC $\boldsymbol{\varepsilon_{yy}}$, (c) FEM $\boldsymbol{\varepsilon_{xx}}$, (d) DIC $\boldsymbol{\varepsilon_{xx}}$, (e) FEM $\boldsymbol{\varepsilon_{xy}}$, (f) DIC $\boldsymbol{\varepsilon_{xy}}$

Mehdikhani et al. [4] are also compare the FEA and DIC results. But they used 2D cross-sectional model of micro fibers. We modeled the porous media with detailed micro-structure in 3D space. Also they used free meshing technique with the triangular element in contrast to the structured voxel mesh in the present research. As a comparison to the previous research, it is worth noting that Begonia et al. [2] studied porous media also. They investigated the mechanical behavior of mouse forearm in micro-scale. Also, they studied the method of finding proper ROI for DIC implementation. They used the iterative approach, while we manipulated the Shannon entropy methodology.

3. 3. Experimental Design and DIC Output Effective Factors Identification In the previous section, displacement and strain field variables are illustrated in the form of contour plots. Variables are determined using initial settings. The main goals of the design of experiments (DOE) and response surface methodology (RSM) implementation are the identification of important factors in DIC response and also optimizing these factors to obtain measurements with minimum error. Using five levels RSM with the central composite design approach instead of the conventional factorial method helps to decrease the number of experiments and also increases the accuracy. There are two factors and two responses in DIC measurement of displacement, i.e. subset radius and spacing as factors and u-disp. and v-disp. as responses. For strain measurement, there are three factors and responses namely, subset radius, subset spacing, and strain radius as factors and ε_{yy}, ε_{xx}, and ε_{xy} as responses. These parameters and their corresponding levels are summarized in Table 4.

Finally, several DOE runs are performed with displacement and strain measurements for various factor levels. These factors and corresponding responses for displacement prediction using DIC are summarized in Table 5. Note that the average value of the leverage parameter for the whole experimental design is 0.4615. It guarantees that no need to repeat any experiment. Due to the R^2 and adjusted R^2 with 0.906 and0.8388 values for u-disp. and 0.7911 and 0.6418 for v-disp., the quadratic

TABLE 2. Factors and levels used in DOE with RSM

Analysis	$-\alpha$, $+\alpha$ (-2,+2)	Low (-1)	Mean (0)	High (+1)	Brief symbol	Symbol	factor
Disp. and strain	26, 42	30	34	38	A	R_{subset}	Subset radius
Disp. and strain	0, 4	1	2	3	B	S_{subset}	Subset spacing
strain	5, 25	10	15	20	C	R_{strain}	Strain radius

TABLE 3. Experimental design and displacement vector responses from DIC

Std. order	Run No.	R_{subset} ($pixel$)	S_{subset} ($pixel$)	u (mm)	v (mm)
4	1	38	3	0.0768	0.3595
3	2	30	3	0.0663	0.3465
12	3	34	2	0.0718	0.3545
11	4	34	2	0.0725	0.3495
6	5	42	2	0.0886	0.392
2	6	38	1	0.0793	0.371
13	7	34	2	0.0742	0.356
10	8	34	2	0.0686	0.3465
9	9	34	2	0.0707	0.364
5	10	26	2	0.0847	0.3745
7	*11*	*34*	*0*	*0.0863*	*0.399*
1	12	30	1	0.0895	0.4025
8	*13*	*34*	*4*	*0.0779*	*0.392*

model is selected. Considering Box-Cox graphs for u-disp. and v-disp. shows that the optimum λ values are 1.7 and -2.5.

Analysis of variance is used for displacement and strain regression. Results show that in v-disp. regression subset radius squared and subset spacing squared terms are significant because they have the lowest p-values. In other words, p-values less than 0.05 and more than 0.1 have corresponded to the significant and insignificant terms respectively. Furthermore, the degree of freedom related to both responses is five. So u-disp. and v-disp. regression equations (Equations (14), (15)) are as below. Note that the brief symbol of each factor is used.

$$(u)^{1.5}=0.0192+0.0003A-0.0015B+0.0022AB+0.0016A^2+0.0011B^2 \quad (14)$$

$$(v)^{-2.5}=13.47-0.1300A+0.5247B-0.8608AB-0.5962A^2-0.8096B^2 \quad (15)$$

To guarantee model validity, there are several criteria. Four major criteria are the Box-Cox graph, the normal plot of residuals, plot of predicted values vs. actual, and also residuals vs. predicted values. In Figure 13 four important plots are shown for u-disp. response. Firstly the Box-Cox offers $\lambda = 1.7$. Non-curved plot of residuals also is required as an index of validation. Also predicted vs. actual values show good agreement. Finally, the random distribution of externally studentized residuals with -3 to +3 values is good enough. In Figure 14 contour plot and the spatial surface of u-disp. the response is shown.

Considering the results shows that there is a negligible perturbation in mid-point neighbor. Although, the effect of subset spacing is generally descending and the effect of subset radius is descending and ascending for values less than mid-point and more than mid-point respectively. In a small subset radius, the negative slope of subset spacing has significant growth. On the other hand, in large subset spacing, the ascending effect of the subset radius is significant. Analyzing strain responses also lead to quadratic model regression. In strain regression, minimum R^2 and adjusted R^2 values are 0.82 and 0.65. Strain equations with quadratic form have nine degrees of freedom. Also, the four aforementioned criteria are controlled to ensure the model validity. Perturbation plots of strain regressions show that horizontal strain sensitivity in mid-point has concave upward variation behavior. In vertical strain, there is similar behavior for subset radius with horizontal strain. In shear strain, subset radius and strain radius have ascending and descending variations respectively. Subset spacing also has downward convex variation. Strain radius has the most significant effect in vertical and shear strains. Considering the analysis of variance results shows that the most important term in vertical and horizontal strains is subset radius squared. In shear strain regression, the most important terms are strain radius and subset spacing squared.

3. 4. Effective Factors Optimization of Field Variables Determination After modeling desired responses using quadratic regression, the optimization process is performed to find optimum DIC setting parameters to obtain results with minimum error. Based on validated and verified FE outputs, these values are considered as the goal values. Goal responses are 0.083 and 0.4 mm for u-disp. and v-disp. Furthermore, the optimization constraints are the actual factor ranges in DOE. In Table 6 optimization results for displacement measurement using DIC are summarized. According to

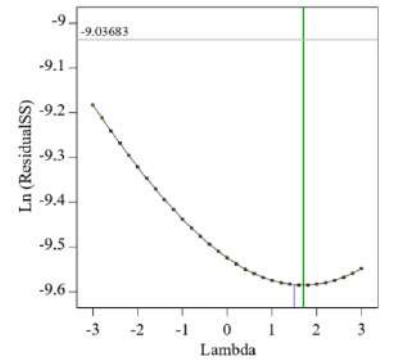

(a)

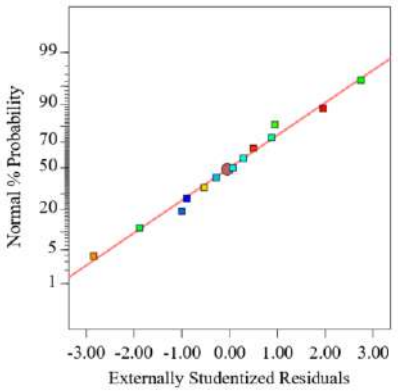

(b)

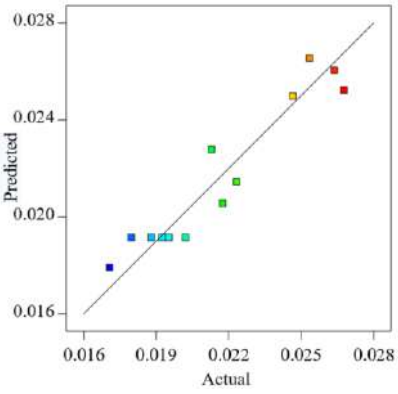

(c)

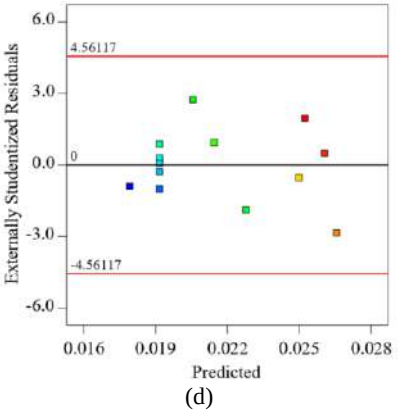

(d)

Figure 13. Statistical criteria for model evaluation, (a) Box-Cox plot, (b) normal residuals, (c) actual vs. predicted values, and (d) residuals vs. predicted values

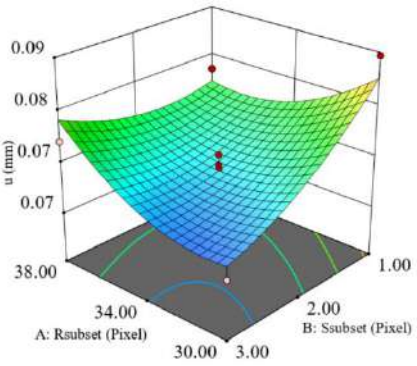

(a)

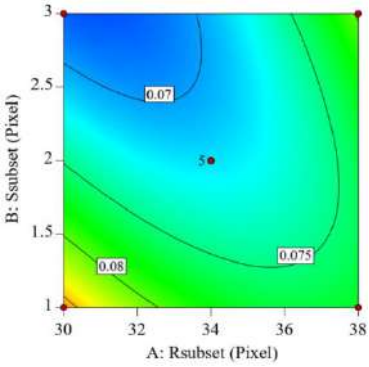

(b)

Figure 14. Regression of u-disp. response, (a) spatial surface representation, and (b) contour plot

the optimization results, there are eight solutions with desirability from 71 to 41%. Selecting a proper solution has corresponded to two aspects, i.e. higher desirability and integer number in factors. Another point is that we should analyze desirability values according to each response separately in addition to combined desirability. Considering the whole solutions lead to $R_{subset} = 30$ and $S_{subset} = 1$ for displacement measurement using DIC. It is worth noting that the mentioned solution is not unique for strain components too. So the optimization process is performed for strain measurement.

Strain factor optimization leads to 53 solutions with 82 to 31% desirability. The first solution has 82%

TABLE 4. Optimization results for displacement measurement using DIC

desirability	v	u	S_{subset}	R_{subset}	No.
0.712	0.387	0.086	1.000	30.000	1
0.707	0.386	0.086	1.024	30.000	2
0.689	0.383	0.085	1.091	30.000	3
0.591	0.376	0.080	3.000	38.000	4
0.574	0.375	0.080	2.963	38.000	5
0.572	0.375	0.080	3.000	37.864	6
0.427	0.368	0.077	1.000	38.000	7
0.413	0.367	0.077	1.000	37.400	8

combined desirability. Its corresponding factors are 38, 1, and 11 pixels for subset radius, spacing, and strain radius respectively. To reduce computational costs, we can opt for solutions with lower desirability values, e.g. solution No. 38 with 68% desirability. Using this technique leads to an increase in computational speed with the factor of 2. In this way, strain measurement desirability has only 3% lowered in contrast to displacement optimization. The corresponding strain radius is 20 pixels.

4. CONCLUSIONS

Novel structures employment requires a good knowledge of their behavior and accurate deformation measurement under the loading conditions. In the present paper, micro-structural deformation and field variable measurements are performed using digital image correlation during uniaxial compression tests. Finite element simulation of the actual lattice structure is also implemented for verification purposes. Also, CT-scan images and digital optical microscope images are used in modeling procedure by image processing. RSM and DOE techniques are also employed for optimization purposes. The most important applications of the present results are utilizing the labs with simple portable system to measure the deformation, strain, and stress fields, eliminating the measurement error of the contact experimental stress analysis methods, using DIC as a tool for health monitoring, tailoring the cellular solids by accurate determination of their mechanical properties, and using the present system for failure mode and localization determination in microstructures. Furthermore, we present the method of mesh and geometry refinement using the hybrid approach of CT-scan imaging and optical digital microscope image processing.

It is worth noting that we bridge between experiment-based measurement method (DIC) and numerical simulation (FEA). The main contribution is to present the hybrid methodology and strategy of verified measurement and field variables determination with minimized cost. Also, we present several correlation equations with experimental design and statistical methods for the main field variables, as well as DIC parameters optimization using response surface methodology. In addition, we optimize the computed tomography settings using the iterative approach. It yields to high-quality CT images with minimum artifacts to reach enhanced 3D model.

The main limitations and suggestions for future works are summarized below.

- We should use the controlled environment and dark boxes to minimize the illumination noise.
- The present method could be applied only on specimens with high porosity because of their two-dimensional strain field.
- Due to a large number of incremental images during axial loading, the image processing and DIC implementation are time-consuming.
- We need the accurate micro-structural model in FE simulations for verification purposes.
- Using two or more cameras for 3D strain tensor determination could be done in future.
- Infra-red thermography is also could be added to the present system for failure mode and location determination.

The most important results are summarized below:

- During the compression test, comprehensive DIC system implementation and analysis are done and major effective factors, e.g. illumination, rate of the capturing are identified.
- 3D dynamic FE simulation is performed as a verification tool with detailed mesh sensitivity analysis for the continuous field calculation.
- CT-scan images are obtained and processed and detailed 3D cellular models with accurate density values are modelled as FEM input.
- Using CT-scan imaging with optimized settings instead of the expensive micro-CT for 3D modelling with acceptable accuracy is considered a novelty.
- Digital microscope imaging is employed for foam model fine-tuning especially in cell edges and faces to reach the highest accuracy.
- The relative error of DIC measurement and FEA results for vertical and horizontal displacements are 15 and 19%. The corresponding values for normal vertical and horizontal strain are 55 and 34%. This error for the shear strain is 65%.
- Higher error for strain tensor is related to the numerical problems using derivation operator.
- Normal vertical and horizontal strain component values are -1.08 and 1.6% and the shear strain is about 2.6 degrees in FEA.
- Horizontal displacement is modelled using a quadratic correlation with ANOVA approach. To obtain higher accuracy results, the corresponding transformation power is 1.5.
- vertical displacement is modelled using a quadratic correlation. The corresponding transformation power is -2.5.
- To reduce the number of experiments, the central composite design approach of RSM is implemented and quadratic regression of displacement and strain field is obtained.

- Response surface methodology is employed to optimize DIC parameters such as subset reduce, subset spacing, and strain deduce.
- The most important factor in normal strain is the subset radius squared. Also, the most effective terms in shear strain prediction are strain radius and subset spacing squared.
- Displacement measurement optimization leads to 71% desirability with subset radius and spacing of 30 and 1 pixels respectively.
- Strain optimization with the highest desirability leads to subset radius, spacing, and strain radius of 38, 1, and 11.
- Considering computational cost and desirability of 68% together lead to similar factors with displacement measurement.

5. REFERENCES

1. Skozrit, I., Frančeski, J., Tonković, Z., Surjak, M., Krstulović-Opara, L., Vesenjak, M., Kodvanj, J., Gunjević, B. and Lončarić, D., "Validation of numerical model by means of digital image correlation and thermography", ***Procedia Engineering***, Vol. 101, (2015), 450-458. DOI: 10.1016/j.proeng.2015.02.054
2. Begonia, M.T., Dallas, M., Vizcarra, B., Liu, Y., Johnson, M.L. and Thiagarajan, G., "Non-contact strain measurement in the mouse forearm loading model using digital image correlation (dic)", ***Bone***, Vol. 81, (2015), 593-601. DOI: 10.1016/j.bone.2015.09.007
3. Bernachy-Barbe, F., Gélébart, L., Bornert, M., Crépin, J. and Sauder, C., "Characterization of sic/sic composites damage mechanisms using digital image correlation at the tow scale", ***Composites Part A: Applied Science and Manufacturing***, Vol. 68, (2015), 101-109. DOI: 10.1016/j.compositesa.2014.09.021
4. Mehdikhani, M., Aravand, M., Sabuncuoglu, B., Callens, M.G., Lomov, S.V. and Gorbatikh, L., "Full-field strain measurements at the micro-scale in fiber-reinforced composites using digital image correlation", ***Composite Structures***, Vol. 140, (2016), 192-201. DOI: 10.1016/j.compstruct.2015.12.020
5. Whitlow, T., Jones, E. and Przybyla, C., "In-situ damage monitoring of a sic/sic ceramic matrix composite using acoustic emission and digital image correlation", ***Composite Structures***, Vol. 158, (2016), 245-251. DOI: 10.1016/j.compstruct.2016.09.040
6. Gerbig, D., Bower, A., Savic, V. and Hector Jr, L.G., "Coupling digital image correlation and finite element analysis to determine constitutive parameters in necking tensile specimens", ***International Journal of Solids and Structures***, Vol. 97, (2016), 496-509. DOI: 10.1016/j.ijsolstr.2016.06.038
7. Engqvist, J., Wallin, M., Ristinmaa, M. and Hall, S.A., "Modelling and experiments of glassy polymers using biaxial loading and digital image correlation", ***International Journal of Solids and Structures***, Vol. 102, (2016), 100-111. DOI: 10.1016/j.ijsolstr.2016.10.013
8. Krstulović-Opara, L., Surjak, M., Vesenjak, M., Tonković, Z., Kodvanj, J. and Domazet, Ž., "Comparison of infrared and 3d digital image correlation techniques applied for mechanical testing of materials", ***Infrared physics & technology***, Vol. 73, (2015), 166-174. DOI: 10.1016/j.infrared.2015.09.014
9. Jiang, Y., Akkus, A., Roperto, R., Akkus, O., Li, B., Lang, L. and Teich, S., "Measurement of j-integral in cad/cam dental ceramics and composite resin by digital image correlation", ***Journal of the Mechanical Behavior of Biomedical Materials***, Vol. 62, (2016), 240-246. DOI: 10.1016/j.jmbbm.2016.05.012
10. Nguyen, M.-T., Allain, J.-M., Gharbi, H., Desceliers, C. and Soize, C., "Experimental multiscale measurements for the mechanical identification of a cortical bone by digital image correlation", ***Journal of the Mechanical Behavior of Biomedical Materials***, Vol. 63, (2016), 125-133. . DOI: 10.1016/j.jmbbm.2016.06.011
11. Aparna, M.L., Chaitanya, G., Srinivas, K. and Rao, J.A., "Fatigue testing of continuous gfrp composites using digital image correlation (DIC) technique a review", ***Materials Today: Proceedings***, Vol. 2, No. 4-5, (2015), 3125-3131. DOI: 10.1016/j.matpr.2015.07.275
12. Feng, X., Tufail, R.F. and Zahid, M., "Experimental investigation and statistical modeling of frp confined ruc using response surface methodology", ***Civil Engineering Journal***, Vol. 5, No. 2, (2019), 268-283. DOI: 10.28991/cej-2019-03091243
13. Obianyo, J.I. and Agunwamba, J., "Efficiencies of horizontal and vertical baffle mixers", ***Emerging Science Journal***, Vol. 3, No. 3, (2019), 130-145. DOI: 10.28991/esj-2019-01176
14. Sharif, S.H., Archin, S. and Asadpour, G., "Optimization of process parameters by response surface methodology for methylene blue removal using cellulose dusts", ***Civil Engineering Journal***, Vol. 4, No. 3, (2018), 620-634. DOI: 10.28991/cej-0309121
15. Yang, K., Zou, J. and Shen, J., "Vibration and noise reduction optimization design of mine chute with foam aluminum laminated structure", ***International Journal of Engineering***, ***Transactions B: Applications,*** Vol. 33, No. 8, (2020), 1668-1676. DOI: 10.5829/ije.2020.33.08b.26
16. Hosseini Ravandi, S., "Assessing of fabric appearance changes using image processing techniques", ***International Journal of Engineering***, Vol. 12, No. 2, (1999), 99-106.
17. Fattahzadeh, M. and Saghaei, A., "A statistical method for sequential images–based process monitoring", ***International Journal of Engineering***, Vol. 33, No. 7, (2020), 1285-1292. DOI: 10.5829/ije.2020.33.07a.15
18. Poissant, J. and Barthelat, F., "A novel "subset splitting" procedure for digital image correlation on discontinuous displacement fields", ***Experimental Mechanics***, Vol. 50, No. 3, (2010), 353-364.
19. Li, X., Fang, G., Zhao, J., Zhang, Z. and Wu, X., "Local hermite (lh) method: An accurate and robust smooth technique for high-gradient strain reconstruction in digital image correlation", ***Optics and Lasers in Engineering***, Vol. 112, No., (2019), 26-38. DOI: 10.1016/j.optlaseng.2018.08.022
20. Gonzalez, R.C., Woods, R.E. and Eddins, S.L., "Digital image processing using matlab, Pearson Education India, (2004).
21. Pan, B., Dafang, W. and Yong, X., "Incremental calculation for large deformation measurement using reliability-guided digital image correlation", ***Optics and Lasers in Engineering***, Vol. 50, No. 4, (2012), 586-592. DOI: 10.1016/j.optlaseng.2011.05.005
22. Peretzki, E., Stockmann, M., Lehmann, T. and Ihlemann, J., "A new surface preparation method for microscopic digital image correlation applications", ***Materials Today: Proceedings***, Vol. 12, (2019), 377-382. DOI: 10.1016/j.matpr.2019.03.138
23. Romans, L., "Computed tomography for technologists: A comprehensive text, Lippincott Williams & Wilkins, (2018).
24. Hsieh, J., "Computed tomography: Principles, design, artifacts, and recent advances, SPIE press, Vol. 114, (2003).
25. Kak, A.C. and Slaney, M., *Principles of computerized tomographic imaging. New york: The institute of electrical and electronics engineers*. 1988, Inc.
26. Wendt, R., *The mathematics of medical imaging: A beginner's guide*. 2010, Soc Nuclear Med.

27. Akar, A., Baltaş, H., Çevik, U., Korkmaz, F. and Okumuşoğlu, N., "Measurement of attenuation coefficients for bone, muscle, fat and water at 140, 364 and 662 kev γ-ray energies", ***Journal of Quantitative Spectroscopy and Radiative Transfer***, Vol. 102, No. 2, (2006), 203-211. DOI: 10.1016/j.jqsrt.2006.02.007

28. Talebi, S., Sadighi, M. and Aghdam, M., "The effect of impact energy parameters on the closed-cell aluminum foam crushing behavior using x-ray tomography method", ***AUT Journal of Mechanical Engineering***, Vol. 2, No. 1, (2018), 107-116. DOI: 10.22060/mej.2017.13385.5613

29. Talebi, S., Sadighi, M., Aghdam, M. and Mirbagheri, S., "Micro–macro analysis of closed-cell aluminum foam with crushing behavior subjected to dynamic loadings", ***Materials Today Communications***, Vol. 13, (2017), 170-177. DOI: 10.1016/j.mtcomm.2017.10. 004

30. Systemes, D., *Abaqus 6.9 documentation, dassault systemes simulia corp, providence, ri, USA*. 2009.

31. Jamshidi, Y.T., Anaraki, A.P., Sadighi, M., Kadkhodapour, J., Mirbagheri, S.M.H. and Akhavan, B., "Micro-structure analysis of quasi-static crushing and low-velocity impact behavior of graded composite metallic foam filled tube", ***Metals and Materials International***, (2019), 1-14. DOI: 10.1007/s12540-019-00502-0

Persian Abstract

چکیده

مواد متخلخل به ویژه فوم‌های فلزی با توجه به ویژگی‌هایی مانند نسبت استحکام به وزن و ارزش تصادف بالا، دارای جایگاه ویژه‌ای در میان مواد نوین هستند. از طرف دیگر سفارشی سازی این مواد مستلزم مشخصه‌یابی دقیق می‌باشد. در پژوهش حاضر، متدولوژی ترکیبی خاصی جهت شناسایی رفتار فوم‌های آلومینیومی ارائه شده است. از جمله دستاوردهای پژوهشی می‌توان به ادغام دو روش همبستگی تصاویر و اجزای محدود در اندازه‌گیری پیوسته میدان جابجایی و کرنش اشاره نمود. یکی از چالش‌های اساسی در شبیه‌سازی جامدات سلولی، مدلسازی ریزساختار آن و سپس تولید مش می‌باشد. برای حل این مشکل نیز از روش استفاده همزمان از تصاویر توموگرافی و میکروسکوپ نوری در فرآیند بازسازی هندسی استفاده شده است. پس از تولید نمونه‌های فوم فلزی و چیدمان سیستم تصویربرداری، نمونه‌ها تحت فشار محوری قرار گرفته و تصویربرداری با کیفیت انجام می‌شود. نهایتاً با استفاده از تکنیک همبستگی، میدان جابجایی و کرنش محاسبه می‌شود. از طرف دیگر به منظور صحه‌گذاری نتایج اندازه‌گیری و با هدف بهینه‌یابی تنظیمات روش همبستگی، به ترتیب از شبیه‌سازی عددی اجزای محدود با نرم‌افزار آباکوس همراه با مطالعه استقلال مش‌بندی و متدولوژی سطح پاسخ استفاده شده است. در نهایت معادلات همبستگی براساس مدل‌های رگرسیون مراتب بالا استخراج شده است. استفاده از مدل ریزساختاری و نیز پارامترهای بهینه روش همبستگی به تطابق مناسب میان نتایج شبیه‌سازی و تجربی منجر شده است. استفاده از تصویربرداری توموگرافی به همراه اصلاح جزییات به کمک تصاویر میکروسکوپ نوری به جای میکرو سی تی، در عین حصول دقت مناسب، هزینه‌های تصویربرداری را به نحو چشمگیری کاهش می‌دهد.

International Journal of Engineering

Journal Homepage: www.ije.ir

Experimental Investigation of Spur Gear Tooth Crack Location and Depth Detection using Short-time Averaging Method and Statistical Indicators

E. Rezaei, M. Poursina*, M. Rezaei

Department of Mechanical Engineering, Faculty of Engineering, University of Isfahan, Isfahan, Iran

PAPER INFO

Paper history:
Received 29 March 2020
Received in revised form 27 April 2020
Accepted 12 June 2020

Keywords:
Spur Gear
Tooth Root Crack
Short-Time Averaging
Transmission Error
Test Rig

ABSTRACT

Gear systems are one of the most functional power transmission systems in the industry. Crack is one of the common defects in gears which is caused by excessive loading, sudden impact and shortcomings in the gears construction. Initially, the crack will not result in structure collapse, but its growth can lead to irreparable damage. Therefore, detecting the crack and determining its location and depth are very important in this respect. In this paper, two encoders are used to obtain the spur gear pair transmission error speed. Moreover, the short-time averaging method (STAM) has been proposed thereby detecting the crack location and some statistical indicators have been used to estimate the crack depth in the spur gear tooth. For this purpose, a dynamical model in which mesh stiffness varying with time has been deployed to achieve the transmission error speed of the gear system. Additionally, a gear test rig including a single-stage gearbox, two encoders, and also an electronic board has been used. Encoders were installed on input and output shafts and the angular position of each shaft in time was saved in the computer using the electronic board. In addition, the transmission error speed was obtained by analyzing the received signals. Then, short-time averaging method was used to identify the crack location. Ultimately, some indicators such as ABS-max, FM0, Energy Ratio (ER) and Residual Signal Average were applied to the simulated results and experimental signals to fine the crack depth ratio. According to the results of this study, it seems safe to conclude that the STAM is a useful method in cracked tooth detection and the indicators have acceptable accuracy to find the crack depth ratio.

***doi**: 10.5829/ije.2020.33.10a.26*

1. INTRODUCTION

Gear transmissions are widely utilized in various types of machines and also ranked as one of the significant mechanical components. The crack existing in the gear tooth causes an increase of vibration and generation of additional noise in the gear system. Initially, this defect does not result in the inefficiency of the system, but it can lead to irreparable damage as it grows. Therefore, the remaining life can be calculated and also the suitable program can be provided for the maintenance by detecting the faults in the early stages. The fault detection requires skill in defect detection using signals. The vibrations generated by gearboxes have a complex structure. In addition, these vibrations can be a sign of gear state, so theyprovide us with valuable information.

According to An et al. [1], machinery fault diagnosis systems, which focus on the detection of health conditions after the occurrence of certain faults, have attracted considerable attention from practitioners and scholars. Gearbox vibration signals received from different situations have been used to detect gearbox fault. Then, the signals are processed and analyzed using certain math operations. Finally, a specific method is provided to find gearbox defects. Any tendency to deviate from healthy values indicates a system failure or defect. Currently, there are some methods such as statistical indicators, time synchronous averaging (TSA), amplitude and phase demodulation, residual signal method, autoregressive models (AR) utilized to detect some of the defects using gearbox signals [2]. Effective methods, like empirical mode decomposition [3], spectral kurtosis [4, 5], stochastic

*Corresponding Author Institutional Email: *poursina@eng.ui.ac.ir* (M. Poursina)

Please cite this article as: E. Rezaei, M. Poursina, M. Rezaei, Experimental Investigation of Spur Gear Tooth Crack Location and Depth Detection using Short-time Averaging Method and Statistical Indicators, International Journal of Engineering (IJE), IJE TRANSACTIONS A: Basics Vol. 33, No. 10, (October 2020) 2079-2086

resonance [6], time–frequency analysis [7], [8] wavelet transform [9], sparse representation [10], and deep learning [11], have been applied and proposed for gearbox fault diagnosis. For monitoring vibration-based gearbox condition, Sait et al. [12] presented a review of several methods and indicators such as crest factor, Root Mean Square (RMS), kurtosis, wavelet transform, residual signal, difference signal, band-pass mesh signal, and Winger-Ville distribution. Braun et al. [13] simultaneously used the averaging method to identify gear defects. This method has a significant impact on the effecient extraction of various signal indicators and can be used to detect gear-related defects. Wan et al. [14] determined the dynamic response of a single-stage gearbox in which the driver's gear had a total crack in the tooth root. They utilized the Fourier transform and probed the effect of the crack on the dynamic response in the time and frequency domains. Qi et al. [15] proposed a method, which combines Fractional Fourier Transform (FrFT) and the Hilbert Transform (HT) to identify the sidebands of signal measured under the run-up process. The HT is utilized to construct the analytic representation of the measured signal, which has a better energy concentration in comparison with the measured signal in the fractional domain. Accordingly, the ability of extracting weak sidebands of FrFT is enhanced. Simulation case study and experimental case study are carried out to verify the effectiveness of the proposed method.

Mohammed and Rantatalo [16] calculated the mesh stiffness of spur gear pair and simulated the dynamics of a pair of the spur gear. They used the residual signal to signalize the crack effect on the simulated vibration signal and compared three different residual techniques. Rezaei et al. [17] proposed a new analytical approach for crack modeling in spur gears. This approach can model more than one crack in one tooth and in various locations of the gear. Rezaei et al. [18] investigated the detection possibility of two cracks in helical gear teeth in divergent situations of cracks placement using transmission error ratio method. They used the residual signal to signalize the crack effect in the simulated vibration signal.

As stated earlier, many methods have been used to detect the crack. These methods do not have an optimal result in some cases. In the present study, short space time averaging of the main signal is proposed to extract the location and size of the local defects such as the tooth root crack. Based on this method, a rectangular movable window function with a width of a signal pulse (equivalent to a cyclic gear cycle) is used for processing.

2. EXPRIMENTAL TEST RIG

To identify the crack, a gear test device, including a motor, generator, inverter, single stage gearbox, encoders and electronic board, as shown in Figure 1, is used. The motor speed is controlled by the inverter and its power is converted through one-stage reduction gearbox with a ratio of 2. Moreover, the gearbox output is connected to the generator with a belt and a pulley. Power is transferred to the generator and eventually consumed in the thermal elements. Using a wire cutting machine, a crack with the dimensions, as illustrated in Figure 2, is created on the tooth 21 from the zero point of the encoder. The crack depth is 3.5 mm and its angle from the midline of the tooth is 70 degrees. The cracked gear and the utilized system characteristics are shown in Figure 2 and Table 1, respectively.

3. SHORT-TIME AVERAGING

In the process of fault diagnosis, the measured vibration signals of weak fault damage are often interfered by strong background noise, so that it is difficult to detect the localized damage at the early stage. According to the short-time averaging method, a window function with a constant width moves from the start point of the signal to the endpoint and in each point of its motion,

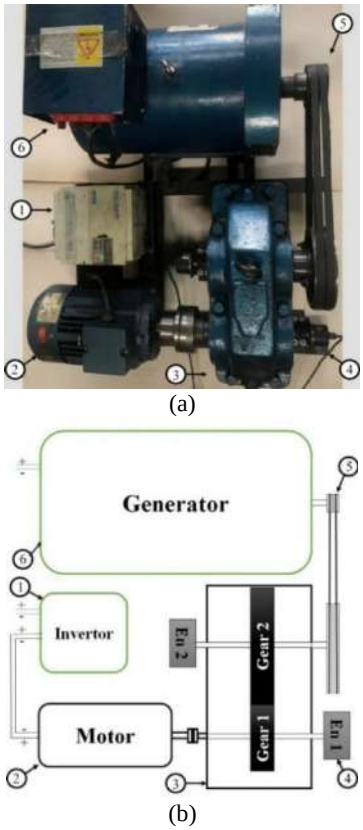

(a)

(b)

Figure 1. Spur gear pair experimental test rig (a) Real photo and (b) Schematic structure plan 1- Inverter 2- Electric motor 3- One stage gearbox 4- Encoder 5- Double-row pulley 6- Generator

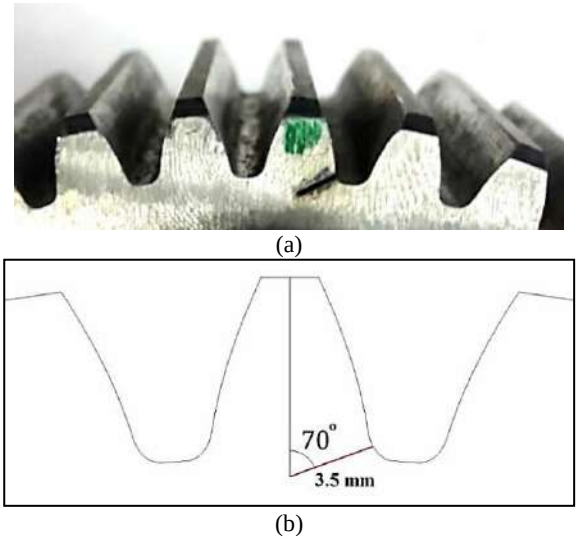

(a)

(b)

Figure 2. Cracked gear (a) using wire cut (b) dimensions of the crack

the average of the data available in the window is defined as the short-time average of the point. This method can be used to diagnose and find the location of the local faults in periodic signals. As shown in Figure 3, in a periodic signal such as transmission error with no local faults, in various regions in which widths are equal to signal period, such as (1), (2) and (3), the average of the data in each window is equal. The mean is normally taken from an equal number of the data on either side of a central value. This ensures that variations in the mean are aligned with the variations in the data rather than being shifted in time.

In the present study, the short-time averaging of the original signal is proposed to extract the local defects location and size such as the tooth gear crack. The equation of the rectangular window function is defined as Equation (1):

$$f_w(x) = \begin{cases} 1 & -\frac{w}{2} < x < \frac{w}{2} \\ 0 & x \le -\frac{w}{2} \ ; x \ge \frac{w}{2} \end{cases} \quad (1)$$

where w is the window width calculated as follows:

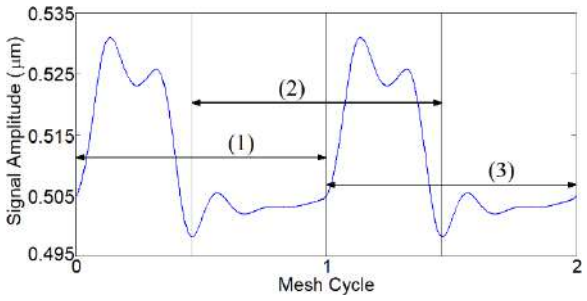

Figure 3. Comparison of three regions signal average with equal widths

$$w = \frac{360}{N_1} \quad (2)$$

where N_1 is the number of pinion teeth.

Since the dynamic response of the gear system is intermittent, if it is not defective, the mean values of the stated short time will be constant. In the presence of local defects such as tooth crack, the average value is changed and the defect area is well represented. The only problem of this method is its low precision in displaying the desired defect range due to the window width. If the average value of each window is assigned to its midpoint, the defect area calculated by this method is $w/2$ times faster and $w/2$ later than the actual value of the defect area. In this regard, two different methods of averaging are simultaneously used to accurately calculate the exact area of the defect area: i.e. forward averaging and backward averaging. The average value of the data in each window in the forward and upward averaging is allocated to the first and last points in the window, respectively.

These two methods have been applied to a transmission error signal having a crack of 270 degrees, and the results are presented in Figure 4. In the backward averaging, the first point of the climb is the correct result, and its end point is the false result. Conversely, in the forward averaging, the first point of the climb is the wrong result and the final result is correct. Therefore, the initial point of the backward averaging and the endpoint of the forward averaging can be considered the start and end points of the real flaw area, respectively. The area between the two vertical lines is magnified in Figure 5. Besides,

TABLE 1. Spur gear pair parameters

Parameter	Pinion	Gear
Normal Module (mm)	2.5	2.5
Teeth Number	43	85
Normal Pressure Angle (deg.)	20	20
Face Width (mm)	40	40
Internal Radios (mm)	25	30
Young's Modulus (GPa)	200	200
Poison's Ratio	0.3	0.3
Mass (Kg)	0.677	1.259
Mass Moment of Inertia ($gr.m^2$)	1.774	5.808
Rotation Speed (rpm)	1000	506
Bearings Radial Stiffness (KN/mm)	23.87	46.922
Bearings Axial Stiffness (KN/mm)	0.951	2.079
Motor Power (KW)	2.7	
Damping Ratio	1	

according to the theory and diagram of Figure 4, it can be easily observed that the only subtle difference between the two methods is concerned with a horizontal displacement of the window width. Therefore, as shown in Figure 5, only one of the two methods (here backward averaging) can be exerted to calculate the crack region.

In this case, the starting point of leaving α_1 is correct and its ending point α_2 must be corrected according to Equation (3) by decreasing the width of the window:

$$\alpha_{2_c} = \alpha_2 - w \tag{3}$$

Additionally, using the value of α_1, the number of the cracked teeth can be simply calculated as shown in Equation(4):

$$N_{Crack} = \left[\frac{N_1 \alpha_1}{360}\right] \tag{4}$$

where $[\frac{N_1 \alpha_1}{360}]$ represents the function of the nearest integer value.

4. STIMATION OF THE DEPTH OF THE CRACK

Statistical indicators are one of the tools used to detect defects in gears. Thus, the statistical indices and different diagnostic indicators are applied to the system dynamics response and finally the effects of crack length and depth can be closely observed and considered. Accordingly, the crack size in a gear is estimated based on its dynamic response. Here, the maximum statistical index and the FM-zero diagnosis indicator have been used.

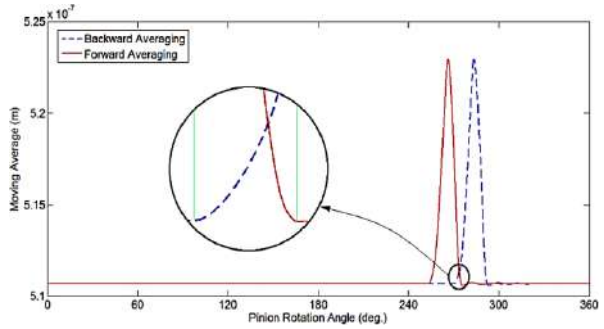

Figure 4. Forward averaging and backward averaging

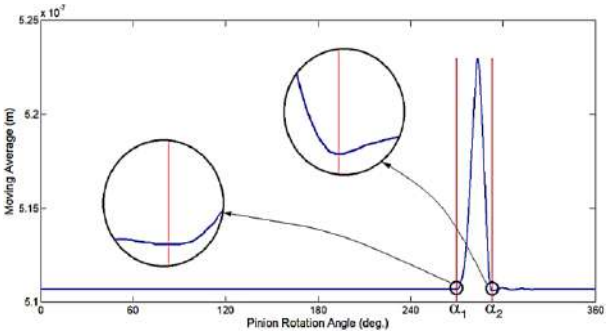

Figure 5. Detecting the points at the beginning and the end of the crack in the backward averaging

4. 1. ABS Max The maximum amount of dynamic response data can be an important indicator in determining an increase in dynamic response and decrease of the stiffness of the conflict due to the presence of the crack. This is due to the fact that an increase in the dynamic response at the moment of a faulty dentine contact directly affects the maximum value. The impact of this indicator is, of course, higher than the average. The ABS max is defined as the maximum value of the absolute values of the dynamic response data [19].

4. 2. FM0 This parameter has been developed as a strong display for large defects in gear cogs, although it is not very useful for small defects. By comparing the maximum distance between the peaks of the signal and the total frequency range of the gear 2 and its harmonics, large changes are detected in the conflict pattern. The FM0 index is calculated as follows [20]:

$$FM0 = \frac{PP_x}{\sum_{n=0}^{H} P_n} \tag{5}$$

where PP_x is the maximum distance between the peaks, P_n is the harmonic amplitude of the $^{n\text{-th}}$ signal and H is the total number of harmonic signals in the frequency spectrum.

4. 3. Energy Ratio (ER) The energy ratio is defined as the ratio of the square root mean squared of the difference signal to the root mean squared of the normal signal:

$$ER = \frac{RMS_d}{RMS_r} \tag{6}$$

In the event of a fault, the energy is transferred from the normal signal to the differential signal.

4. 4. Residual Signal Average If the residual signal values in a full period are present as a vector over time, the mean value would be calculated as follows:

$$mean_r = \frac{1}{N}\sum_{i=1}^{N} x_i \tag{7}$$

where, x_i, N and $mean_r$ are the residual signal data, the number of data and the mean of data, respectively. Due to the presence of cracks in a tooth, the mesh stiffness is reduced and the dynamic response of the system increases, as a result of which the average residual signal data will also increase.

5. RESULTS AND DISCUSSION

Due to the time interval availability of each pulse by an encoder, in calculating the transmission error, there is a

possibility of accumulated error. To prevent the accumulation of errors, the elimination of the integration and the derivation of the data, the transmission error speed of the system is measured. Initially, the output signals from the encoders are obtained and then, the transmission error speed is obtained for 10 rounds of pinion. The output signal from the encoder is so that the time difference between the pre-pulse and the current pulse is recorded as a number. As known, the transmission error can be calculated as follows [21]:

$$TE = R_p\theta_p - R_g\theta_g \quad (8)$$

By differentiating the equation concerning the time:

$$\frac{dTE}{dt} = R_p\frac{d\theta_p}{dt} - R_g\frac{d\theta_g}{dt} \quad (9)$$

The encoders have 3600 pulses, so the angular distances between every two consecutive pulses are equal to 0.1 degrees as below:

$$d\theta_p = d\theta_g = \Delta\theta = 0.1° \quad (10)$$

So, the transmission error speed can be obtained by:

$$\frac{dTE}{dt} = \dot{TE} = \Delta\theta\left(\frac{R_p}{\Delta t_1} - \frac{R_g}{\Delta t_2}\right) \quad (11)$$

To have a more precise and clear signal and reduce the noise, measured and computed errors and other unwanted components from the signal, it is crucial to get the signal for several rotations of the pinion and then use the time-synchronous averaging method (TSA). TSA can be calculated by dividing the raw signal of several rotations of the pinion into equal parts related to the number of rotations and averaged as follows [2]:

$$y_i = \frac{1}{R}\sum_{j=0}^{R-1} x_{nj+i} \quad (12)$$

where R is the number of rotations and n is the number of data points in each rotation.

The number of these data is 36,000 in the first encoder and 18,211 in the second encoder. The difference between these numbers is due to the gear ratio.The transmission error speed of the experimental gear pair system in 10 rotations of the pinion is presented in Figure 6. After using TSA, the transmission error speed of the system in one rotation of the pinion is obtained as shown in Figure 7. According to this diagram, the signal changes from the values of 0.026 to 0.028 second of the pinion rotation that will be 114 and 133 degrees of the pinion rotation with respect to the teeth number and rotatioanal speed. To achieve exact results, the short-time averaging method is used to extract the crack effect in the signal and determine its location. In Figure 8, the results of this method are presented.

Compared to other intelligent fault diagnosis methods, this method has advantages such as simplicity

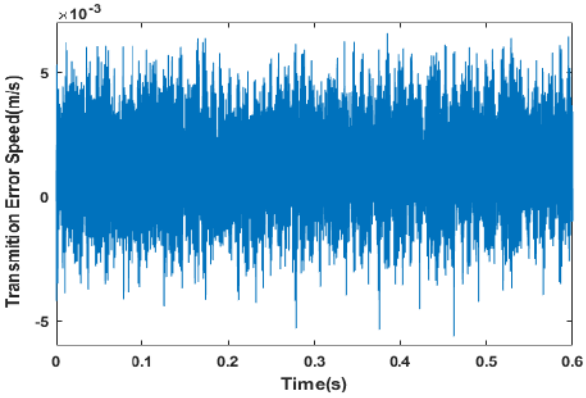

Figure 6. Transmission error speed of the experimental gear pair system in 10 rotations of the pinion

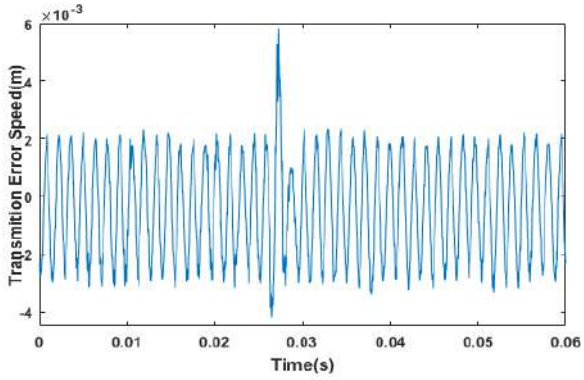

Figure 7. The system transmission error speed in one rotation of the pinion obtained by TSA

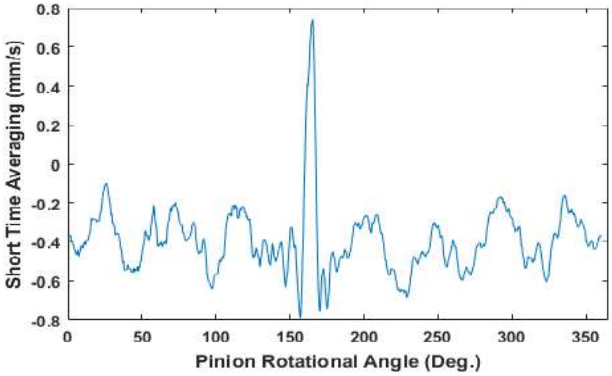

Figure 8. The Short-Time Averaging result of the signal shown in "Figure 7"

of learning for the researchers, no need for additional knowledge in the field of intelligent methods, much easier coding and execution, and much less computing volume due to a much lower number of simulation runs.

In the short-time averaging results, half of the window width should be used, that is, half denture involvement cycle (about four degrees). The angular values obtained for the beginning and the end of the change closed are considered as a result; the values

obtained in this method will be 155 and 177 degrees, respectively. According to this figure, the 21st tooth of the pinion enters into contact at 155 degrees and exits at 177 degrees of the pinion rotation angle, so the crack is certainly in the 21st tooth. It should be noted that the 20th and 22nd teeth cannot cover the whole region of the crack effect. Moreover, according to the angles that obtained for the crack zone and the contact zone of the 21st tooth, it can be figured out that the crack is a full face-width crack. Completely monotonic effects (completely ascending or descending) of the depth of the crack on the applied indicators on the transmission error speed make it possible to find the fault by such a simple method instead of complex and intelligent methods of fault diagnosis or optimization. In the following, it is assumed that the cracks on the total pinion tooth and its depth vary linearly, the stiffness of the gear mesh for the different crack depths is calculated and the dynamic response is obtained. Then, the values obtained from some indicators applied to the dynamic response are achieved for different crack depths. On the other hand, the values of these indices applied to the experimental test signal are also available. The graph of the variations of each indicator and the method of estimating the crack depth using its experimental values are shown in Figure 9. Also, the experimental values of the indices and the depth of the crack ratio estimated by each indicator and their response error percentage are presented in Table 2. Respecting the results of this Table, crack depth has been estimated by the indicators

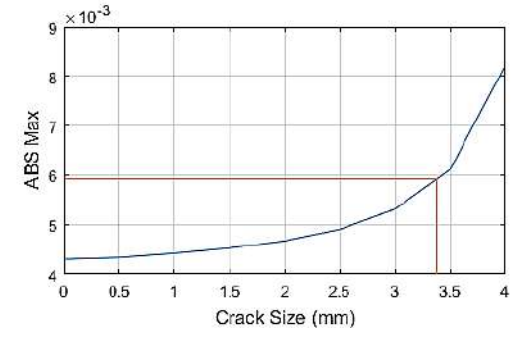

(a)

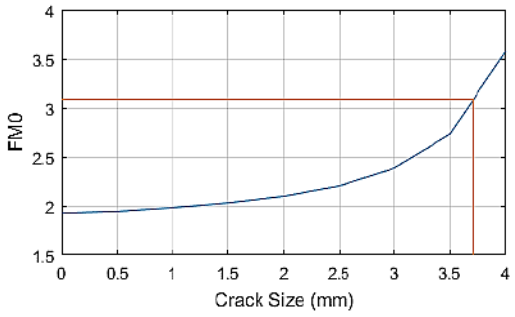

(b)

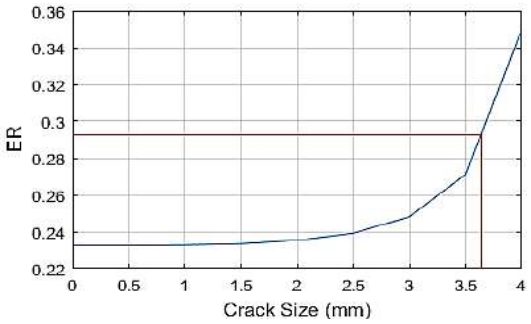

(c)

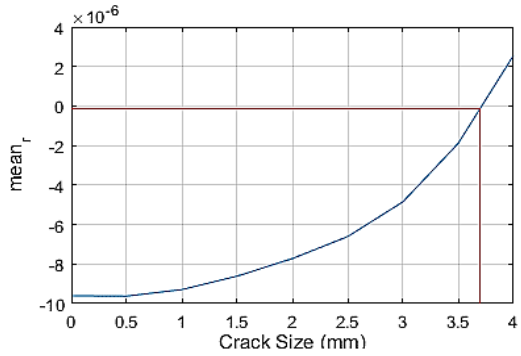

(d)

Figure 9. The results of the indicators obtained by dynamic simulation with various crack depths (a) *ABS Max* (b) *FM0* (c) *ER* (d) *mean _r*

TABLE 2. The estimated crack depth ratio by applying the indicators to experimental signal

Index	Experimental value	Crack depth	Error (%)
ABS Max	5.9e-3	3.38 mm	3.4
FM0	3.1104	3.67 mm	4.8
ER	0.2922	3.63 mm	3.7
Mean_r	-2.1414e-5	3.66mm	4.6

with plausible accuracy. As can be seen, the FM0, ER and mean _r estimate the crack depth size with good agreement (fewer than 5 % error) and positive error; the indicator ABSmax also estimates it with the negative error about 3.4 percent with respect to the previous factors. The average of the estimated values of the crack depth ratio is calculated as 3.585 mm, which has a 2.42% error to its real value of 3.5 mm.

6. CONCLUSION

The tooth root cracks can increase the generated vibration and noise in the gear systems. The crack does not initially result in the collapse of the structure. However, its growth can lead to irreparable damage. Therefore, detecting crack and determining its location and depth are very important for this purpose. Fault

detection increases efficiency and eliminates unnecessary inspections. By the fault detection in the early stages, the remaining life can be calculated and also a suitable program can be provided for maintenance. Many methods have been used to detect the crack. In some cases, these methods do not have an acceptable result. In the present study, the transmission error speed has been calculated via two encoders and ARM board; the short-time averaging of this signal is proposed to extract the location and size of the local defects, such as the tooth root crack. In this method, a rectangular movable window function with a width of a signal pulse (equivalent to a cyclic gear cycle) is used for processing. According to the results, the only tooth corresponding to the obtained values was the 21st with the start and end angles of the 155 and 177 degrees of pinion rotation, respectively. Beyond, the ABSmax, FM0, ER and mean _r estimate the crack depth size with good agreement (fewer than 5 % error). Regarding the results achieved in this study, it seems safe to conclude that the STAM was a useful method concerning cracked tooth detection.

7. REFERENCES

1. An, Z., Li, S., Wang, J., Qian, W. and Wu, Q., "An intelligent fault diagnosis approach considering the elimination of the weight matrix multi-correlation", ***Applied Sciences***, Vol. 8, No. 6, (2018), 906. doi: 10.3390/app8060906
2. Mohammed, O.D., "Dynamic modelling and vibration analysis for gear tooth crack detection", Luleå tekniska universitet, (2015),
3. Singh, J., Darpe, A. and Singh, S., "Bearing damage assessment using jensen-rényi divergence based on eemd", ***Mechanical Systems and Signal Processing***, Vol. 87, (2017), 307-339. doi: 10.1016/j.ymssp.2016.10.028
4. Wang, Z., Du, W., Wang, J., Zhou, J., Han, X., Zhang, Z. and Huang, L., "Research and application of improved adaptive momeda fault diagnosis method", ***Measurement***, Vol. 140, (2019), 63-75. doi: 10.1016/j.measurement.2019.03.033
5. Wang, T., Chu, F., Han, Q. and Kong, Y., "Compound faults detection in gearbox via meshing resonance and spectral kurtosis methods", ***Journal of Sound and Vibration***, Vol. 392, (2017), 367-381. doi: 10.1016/j.jsv.2016.12.041
6. Lei, Y., Han, D., Lin, J. and He, Z., "Planetary gearbox fault diagnosis using an adaptive stochastic resonance method", ***Mechanical Systems and Signal Processing***, Vol. 38, No. 1, (2013), 113-124. doi: 10.1016/j.ymssp.2012.06.021
7. Wang, S., Chen, X., Cai, G., Chen, B., Li, X. and He, Z., "Matching demodulation transform and synchrosqueezing in time-frequency analysis", ***IEEE Transactions on Signal Processing***, Vol. 62, No. 1, (2013), 69-84. doi: 10.1109/TSP.2013.2276393
8. Yang, Y., Dong, X., Peng, Z., Zhang, W. and Meng, G., "Vibration signal analysis using parameterized time–frequency method for features extraction of varying-speed rotary machinery", ***Journal of Sound and Vibration***, Vol. 335, No., (2015), 350-366. doi: 10.1016/j.jsv.2014.09.025
9. Wang, D., Tsui, K.-L. and Qin, Y., "Optimization of segmentation fragments in empirical wavelet transform and its applications to extracting industrial bearing fault features", ***Measurement***, Vol. 133, (2019), 328-340. doi: 10.1016/j.measurement.2018.10.018
10. Han, T., Jiang, D., Sun, Y., Wang, N. and Yang, Y., "Intelligent fault diagnosis method for rotating machinery via dictionary learning and sparse representation-based classification", ***Measurement***, Vol. 118, (2018), 181-193. doi: 10.1016/j.measurement.2018.01.036
11. Ding, X. and He, Q., "Energy-fluctuated multiscale feature learning with deep convnet for intelligent spindle bearing fault diagnosis", ***IEEE Transactions on Instrumentation and Measurement***, Vol. 66, No. 8, (2017), 1926-1935. doi: 10.1109/TIM.2017.2674738
12. Sait, A.S. and Sharaf-Eldeen, Y.I., A review of gearbox condition monitoring based on vibration analysis techniques diagnostics and prognostics, in Rotating machinery, structural health monitoring, shock and vibration, volume 5. 2011, Springer.307-324.
13. Braun, S., "The synchronous (time domain) average revisited", ***Mechanical Systems and Signal Processing***, Vol. 25, No. 4, (2011), 1087-1102. doi: 10.1016/j.ymssp.2010.07.016
14. Wan, Z., Cao, H., Zi, Y., He, W. and He, Z., "An improved time-varying mesh stiffness algorithm and dynamic modeling of gear-rotor system with tooth root crack", ***Engineering Failure Analysis***, Vol. 42, (2014), 157-177. doi: 10.1016/j.engfailanal.2014.04.005
15. Zhou, Q., Wu, C. and Fan, Q., "Gear fault diagnosis under the run-up condition using fractional fourier transform and hilbert transform", in International Conference on Mechanical Design, Springer., (2019), 918-943. doi: 10.1007/978-981-32-9941-2_77
16. Mohammed, O.D. and Rantatalo, M., Residual signal techniques used for gear fault detection, in Current trends in reliability, availability, maintainability and safety. 2016, Springer.157-163. doi: 10.1007/978-3-319-23597-4_12
17. Rezaei, E., Poursina, M., Rezaei, M. and Ariaei, A., "A new analytical approach for crack modeling in spur gears", ***Jordan Journal of Mechanical and Industrial Engineering***, Vol. 13, No. 2, (2019) 69-74.
18. Rezaei, M., Poursina, M., Jazi, S.H. and Aboutalebi, F.H., "Multi crack detection in helical gear teeth using transmission error ratio", ***Journal of Mechanical Science and Technology***, Vol. 33, No. 3, (2019), 1115-1121. doi: 10.1007/s12206-019-0111-x
19. Alkhadafe, H., Al-Habaibeh, A. and Lotfi, A., "Condition monitoring of helical gears using automated selection of features and sensors", ***Measurement***, Vol. 93, (2016), 164-177. doi:10.1016/j.measurement.2016.07.011
20. Sharma, V. and Parey, A., "A review of gear fault diagnosis using various condition indicators", ***Procedia Engineering***, Vol. 144, (2016), 253-263. doi: 10.1016/j.proeng.2016.05.131
21. Radu, M., Andrei, L. and Andrei, G., "A perspective on gear meshing quality based on transmission error analysis", in 8TH International Conference on Advanced Concepts in Mechanical Engineering, IOP Publishing. Vol. 444, (2018).

Persian Abstract

چکیده

چرخدنده ها یکی از کارآمدترین سیستم های انتقال نیرو در صنعت هستند. ترک یکی از نقایص رایج در چرخ دنده‌ها بوده که در اثر بارگذاری بیش از حد ، ضربه ناگهانی و کاستی در ساخت دنده ها ایجاد می‌شود. در ابتدا ، ترک منجر به شکست دنده نمی‌شود اما رشد آن می‌تواند به آسیب های جبران ناپذیری منجر شود. بنابراین ، تشخیص ترک و تعیین محل و عمق آن بسیار کارآمد است. در این تحقیق ، از دو انکودر برای محاسبه سرعت خطای انتقال استفاده شده است. همچنین، روش میانگین گیری زمان کوتاه برای شناسایی محل ترک و برخی از شاخص های آماری مورد استفاده برای تخمین عمق ترک در دندانه پیشنهاد شده است. برای این منظور ، از یک مدل دینامیکی با سفتی درگیری متغیر با زمان برای دستیابی به سرعت خطای انتقال سیستم دنده استفاده شده و همچنین از یک سیستم تست چرخدنده شامل موتور ، ژنراتور ، اینورتر ، گیربکس تک مرحله ای ، دو انکودر و یک برد الکترونیکی جهت آزمایش عملی استفاده گردیده است. انکودرها روی شفتهای ورودی و خروجی نصب می شوند و موقعیت زاویه ای بر حسب زمان هر شافت با استفاده از برد الکترونیکی در رایانه ذخیره می‌شود. علاوه بر این ، سرعت خطای انتقال با تجزیه و تحلیل سیگنال های دریافت شده بدست می‌آید. پس از آن ، از روش میانگین زمان کوتاه برای شناسایی محل ترک استفاده شده است. سپس برخی از شاخص ها مانند ABS-max ، FM0 ، نسبت انرژی (ER) و میانگین سیگنال باقی مانده برای نتایج شبیه سازی شده و از سیگنال های تجربی استفاده می شوند تا نسبت عمق ترک را پیدا کند. با توجه به نتایج به دست آمده در این مطالعه ، می توان نتیجه گرفت که میانگین گیزی زمان کوتاه یک روش مفید در تشخیص دندانه ترک خورده است و شاخص ها از دقت قابل قبولی برای پیدا کردن نسبت عمق ترک برخوردار هستند.

International Journal of Engineering

Journal Homepage: www.ije.ir

Numerical Investigation of Hazardous Gas Dispersion Over Obstacles and Residential Areas

E. Fatahian, H. Salarian, H. Fatahian*

Department of Mechanical Engineering, Nour Branch, Islamic Azad University, Nour, Iran

P A P E R I N F O

Paper history:
Received 10 May 2020
Received in revised form 30 June 2020
Accepted 21 July 2020

Keywords:
Gas Dispersion
Computational Fluid Dynamics
Mass Fraction
Obstacles
Turbulence

A B S T R A C T

In the present study, an attempt has been made to use Computational Fluid Dynamics (CFD) in the assessment of hazardous gas dispersion over obstacles. For this aim, the accidental dispersion of hazardous gas from the hole and the effect of different parameters such as changes in inlet wind velocity, the direction of the pollutant cloud and its movement, mass fraction of gas dispersion, and the pressure distribution were numerically analyzed. The flow was assumed as three-dimensional, unsteady, turbulent, and compressible. Different turbulent models were used in modeling the gas release and the most accurate one was suggested. The numerical simulation demonstrated that the gas mass fraction increased significantly due to the sudden dispersion of the gas. The amount of gas concentration gradually decreased after the formation of pollutant clouds by moving in the horizontal direction. Moreover, gas mass fraction had decreased by increasing the height. Comparing the results revealed that the pollutant cloud did not cover the surrounding area in the wind velocity of 1 m/s. Therefore, the pollutant clouds generated in this case could not impose a threat. In higher wind velocities (3 m/s and 5 m/s), the pollutant cloud approximately covered the surrounding areas, which caused a severe threat. The maximum overpressure at the hole is 5.7 Pa for a wind velocity of 5 m/s, while the maximum negative pressure was about -7.1 Pa. The influencing radius was obtained about 9.3 m. The overpressure did not cause obvious damage to buildings but led to a slight hurt to humans.

***doi**: 10.5829/ije.2020.33.10a.27*

1. INTRODUCTION

The hazardous gas dispersion in the environment indicates a dangerous risk for people living close to chemical plants. Because heavy gas tends to stay at a lower level and disperse at a slower pace in the atmosphere, potentially they are dangerous [1-3]. The possible release and dispersion of hazardous gas to the atmosphere are occurred due to terrorist attacks, human error, and mechanical failure, etc. [1]. Nowadays, many countries have been troubled by air pollution and haze. Natural gas gain popularity with the characteristics of high environmental benefit and social benefit. The laying of gas pipeline mileage also increases rapidly to meet the increasing demand for natural gas. At the same time, concerns about the potential towards that natural gas spill could pose have been raised [4]. Accidental dispersion of hazardous gas has been investigated by many researchers and numerical models adapted for loss prevention targets in process and chemical industries [5,6]. Urban areas are easily involved in the gas dispersion. They are classified with complex geometry from numerous buildings. These obstacles significantly affect wind velocity because wakes, recirculation, and preferential paths can strongly complicate the scenario in simulations [7]. Mainly, numerical models for gas dispersion are characterized into three types [8], phenomenological models [9,10], integral models, and CFD models [11-13]. CFD-based tools can be used for simulation of the diverse problems in engineering [14-17] and the complex urban geometries involved to investigate the impact of multiple large obstacles on hazardous gas dispersion. Recently, implementing the CFD method to model the dispersion of gas has been more common as computers are becoming more capable and faster. Beside, CFD methods give more accurate results compared to traditional

*Corresponding Author Email: *fatahianhossein@gmail.com* (H. Fatahian)

Please cite this article as: E. Fatahian, H. Salarian, H. Fatahian, Numerical Investigation of Hazardous Gas Dispersion Over Obstacles and Residential Areas, International Journal of Engineering (IJE), IJE TRANSACTIONS A: Basics Vol. 33, No. 10, (October 2020) 2087-2094

models of gas dispersion [18-20].

Pontiggia et al. [21] applied a CFD technique to analyze hazardous gas releases. They validated their CFD results with experimental data and good agreement was achieved. In their study, More precisely, a new methodology including the effects of atmospheric stratification on gas dispersion was developed. Li et al. [22] experimentally and numerically studied the release and dispersion of gas. A multi-phase model is developed and validated against available experimental data. Their model could support risk assessment. Moen et al. [23] investigated and validated different turbulence models in hazardous gas dispersion. For all cases, they concluded that standard k-ε and RNG k-ε models showed reasonable results. Han et al. [24] experimentally and numerically investigated the sulfur hexafluoride gas dispersion properties for an industrial building. The removal of sulfur hexafluoride was more effective as the air outlets and inlets were arranged on the same side of the wall. In the study of Eberwein et al. [25], for risk research with new energy carrier LNG in land transport, CFD simulations for LNG-vapor dispersion was considered. They concluded that the most effective parameter for modeling the dispersion was turbulence boundary conditions at the domain boundary. Issakhov and Omarova [26] numerically considered the dispersion and movement of pollutant emission between several houses. They found that using solid grass barriers caused to increase in the concentration of pollutants on the road. On the other hand, they significantly protected nearby houses. Michioka et al. [27] used the large eddy simulation method to analyze the impact of wind-direction fluctuation on the dispersion of gas. It was concluded that the instantaneous turbulent flow with a low-frequency was produced both with and without wind-direction fluctuation.

The present study aimed to evaluate the sudden gas dispersion around buildings from a hole intended at the ground. The novelty of the present work was an integration of gas dispersion with the subsequent formation of pollutant gas cloud consequence. For this aim, a three-dimensional CFD model was conducted. Actually, the flow characteristics, the surrounding area of obstacles, and distance between them can significantly affect the concentration distribution. Furthermore, changes in inlet wind velocity, the concentration of gas, pollutant cloud, and flow characteristics were studied in detail. In addition, the turbulence models in CFD simulations were assessed based on experimental data to select the most appropriate model for further studies.

2. MODEL DESCRIPTION and BOUNDARY CONDITIONS

In the present study, ANSYS design modeler was used to design and model the geometry. Figure 1 illustrates the computational domain including obstacles and residential areas. A 100 m × 75 m × 30 m domain was set for the computational domain and a hole for gas dispersion with a diameter of 20 mm was assumed. The dimensions of the obstacles considered in the simulation are presented in Table 1. Defining the boundary condition is an important step in the implementation of simulations. For the inlet side, the boundary condition was considered as velocity inlet. For the up and side planes, zero flux planes were used. For the outlet, the boundary condition was assumed to pressure outlet. Furthermore, the no-slip boundary condition was considered for the lower side, buildings, and reservoirs. The mass flow inlet condition was imposed for gas dispersion.

A three-dimensional mesh was used for the computational domain (Figure 2a). Also, fine meshes were used to generate the grid for the areas which are more sensitive to have higher accuracy in computations. Also, Figure 2b demonstrates the entire and closer view of the grid, respectively.

3. NUMERICAL PROCEDURE and GOVERNING EQUATIONS

In the present work, simulations were implemented using ANSYS CFX along with the finite volume method

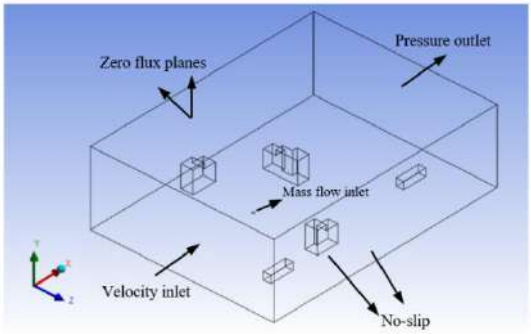

Figure 1. Computational domain

TABLE 1. The dimensions of the obstacles

Obstacles	Dimensions (m)
Reservoir 1	10×3×3
Reservoir 2	10×3×3
Building 1	5×5×9
Building 2	5×4×9
Building 3	5×5×9
Building 4	5×5×7
Building 5	5×4×9
Building 6	4×5×7
Building 7	5×5×7

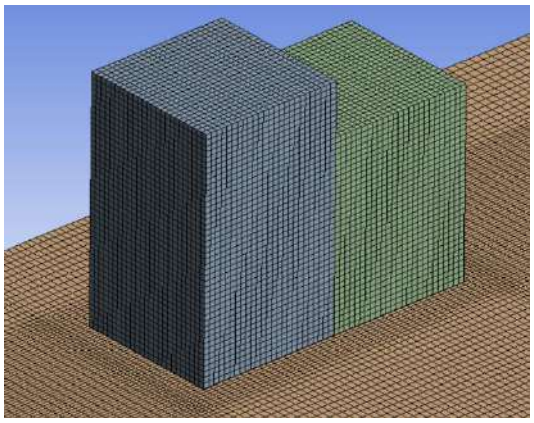

Figure 2. Computational grid for the building and ground

(FVM) to discretize the equations. Moreover, the unsteady Reynolds-Averaged Navier-Stokes (URANS) equations were adapted. Navier-Stokes Equations are solved using CFD code with specific model equations, such as energy balance, species diffusion, and turbulence which can be defined as follows:

$$\frac{\partial \rho}{\partial t} + \nabla.\left(\rho \vec{v}\right) = 0 \quad (1)$$

$$\frac{\partial}{\partial t}\left(\rho \vec{v}\right) + \nabla.\left(\rho \vec{v}\vec{v}\right) = -\nabla p + \nabla.\left(\bar{\bar{\tau}}\right) + \rho \vec{g} \quad (2)$$

$$\frac{\partial (\rho C_v T)}{\partial t} + \nabla.\left(\rho \vec{v} C_p T\right) = \nabla.(K_T \nabla T) \quad (3)$$

where ρ represents the density, t shows the time, v denotes the velocity, p indicates the pressure, τ denotes the shear stress, g is the gravity acceleration, C_v and C_p denote the specific heats, T indicates the temperature, and k_T is the thermal conductivity.

The gas dispersion process behaves as an unsteady turbulent flow. An appropriate turbulence model is required for describing the turbulence in the gas dispersion process and make the governing equations close [28]. In this study, different turbulent models were used to select the most suitable one for further studies.

Moreover, the Upwind second-order method is used to discretize the continuity, momentum, energy, k, and ω. Also, The SIMPLE algorithm is applied for pressure-velocity coupling. The convergence criteria are considered to be less than 10^{-5} for all equations. In this study, the wind velocity at the inlet (velocity inlet boundary condition) is equal to 1, 3, and 5 m/s. For the accidental release of hazardous gas for 20 seconds, CO_2 is released at a constant mass inflow rate (m_i) of 3.65 kg/s. The variable mass inflow rate equal to m_i during the release phase (kg/s) (Q_i) is defined by a step function to enter the boundary conditions of the inlet gas (Figure 3) [29, 30]:

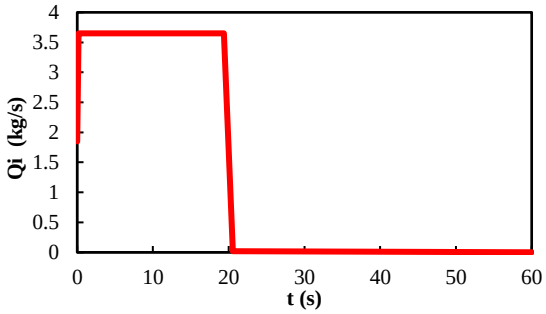

Figure 3. Q_i in terms of time (s) for the accidental release of hazardous gas

$$Q_i = m_i \times step\left[-\frac{(t-t_0)(t-t_1)}{t_c^2}\right] \quad (4)$$

where Q_i is variable mass inflow rate equal to m_i during the release phase, m_i represents the constant mass inflow rate, t denotes the time (s), t_c represents the time constant equal to 1 s, t_0 indicates the time of release initiation (s), t_1 is the release phase duration (s).

4. CODE VALIDATION

In the present study, four different grids with cell numbers of 430000, 690000, 920000, and 1050000 were generated to investigate the grid independence study using the ANSYS Meshing. The grid independence study was carried out for calculating the mass fraction of the gas dispersion along the longitudinal axis of the computational domain. Consequently, there was a negligible difference between the results of the finest grid and the grid with 920000 cells. Therefore, the grid with 920000 cells was used for selecting a favorable grid size for saving the computation time and providing better accuracy. Figure 4 indicates the detail of the grid independence study.

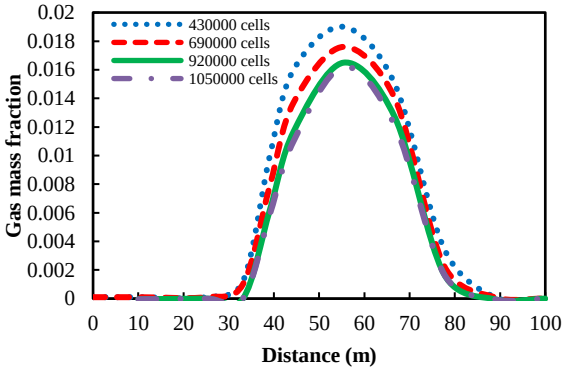

Figure 4. Grid independence study

In order to consider and choose the most appropriate turbulent model, the predicted numerical results were compared with the experimental data [29], which is shown in Figure 5. Comparing the gas concentration for different turbulent models revealed that the RNG k-ε turbulent model demonstrated better agreement with the experimental data [29]. Thus, further simulations were conducted using the RNG k-ε turbulent model.

5. RESULTS AND DISCUSSION

Figure 6 demonstrates the changes of pressure along the longitudinal axis of the computational domain for the three wind velocities of 1, 3, and 5 m/s in the x-axis direction. As it can be seen, sudden changes in pressure occurred at the gas dispersion location which has lower values at low wind velocity (1 m/s). The more changes in pressure were observed by increasing the wind velocity so that it caused a sharp increase in pressure and then significantly decreased. Finally, the pressure tends to zero at the end of the computational range for all three cases.

The maximum overpressure distributed in the center of the hole, and the overpressure gradually reduced in a radial direction. The maximum overpressure at the hole is 5.7 Pa for a wind velocity of 5 m/s, while the maximum negative pressure was about -7.1 Pa. The areas with positive and negative pressure were in dynamic change during the gas dispersion process. The influencing radius was obtained about 9.3 m. The overpressure did not cause obvious damage to buildings but led to a slight hurt to humans.

Figure 7 depicts the changes in the mass fraction of gas dispersion along the longitudinal axis of the computational domain for the three wind velocities of 1, 3, and 5 m/s. From these figures, due to the sudden dispersion of the gas, its mass fraction increased with a sharp slope. Furthermore, the amount of gas concentration gradually decreased after the formation of pollutant clouds by moving in the x-axis. It is obvious

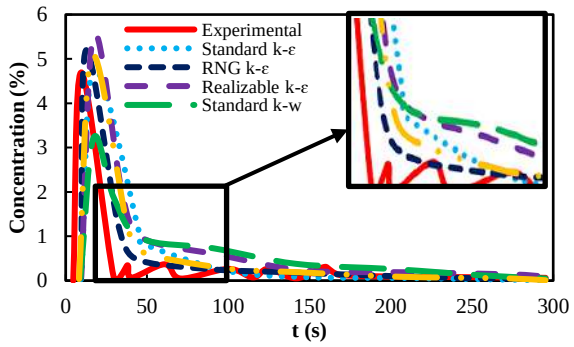

Figure 5. Comparison between gas concentrations of the present study and experimental data [29]

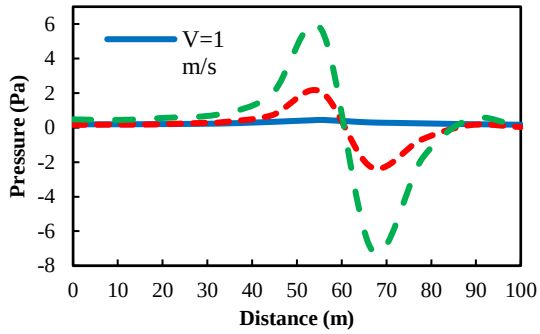

Figure 6. The changes in pressure in terms of different wind velocities

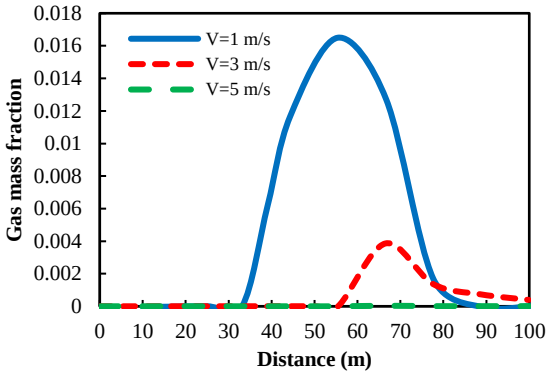

Figure 7. The changes in the gas mass fraction in terms of different wind velocities

that there is a maximum value for three cases which decreased dramatically as the wind velocity increased.

Comparing the results demonstrated that changes in wind velocity significantly affected the distribution of gas clouds. The wind is the main driving force for gas dispersion under great wind velocity [28].

The gas mainly dispersed along the vertical direction, in which the surrounding area is not covered by the gas cloud in the wind velocity of 1 m/s. Therefore, the pollutant cloud generated in this case could not impose a threat. In higher wind velocities (3 and 5 m/s), the pollutant cloud approximately covered the surrounding areas, which caused a severe threat.

The size of the coverage area depended on the pollutant cloud length. The greater pollutant cloud length was generated under the higher wind velocity. Hence, the size of the coverage area also raised with increasing wind velocity. The pollutant cloud at lower wind velocity (1 m/s) had greater gas mass fraction since the lower wind velocity cannot dissipate gas timely [28].

Figures 8 to 10 illustrate the changes in the mass fraction of dispersion gas along the longitudinal axis of the computational domain for the three wind velocities of 1, 3, and 5 m/s, and three different heights of 0, 3 and 6 m, respectively. For this purpose, three lines along the x-

axis are used, which the height of 0 m (Y = 0 m) means the ground surface. By considering these figures, the formation of the pollutant cloud, its concentration, and the direction of movement can be well determined. It is clear that the mass fraction of gas had decreased by increasing the height from the ground surface. It should be mentioned that with the increase of wind velocity and height, the maximum range of gas mass fraction had moved forward in the x-axis direction.

Figure 11 shows the gas concentration profile with the velocity profile at different wind velocities. From the figures, it can be seen that a high-velocity gradient develops a turbulent flow. The sharper velocity gradient is observed with higher wind velocity. Furthermore, the gas concentration is decreased as the wind velocity increased. Whereas increasing the wind velocity from 1 m/s to 5 m/s caused the gas concentration to decrease approximately 59%.

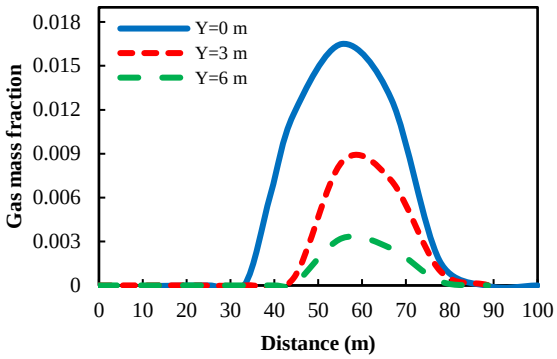

Figure 8. The changes in the gas mass fraction at V = 1 m/s

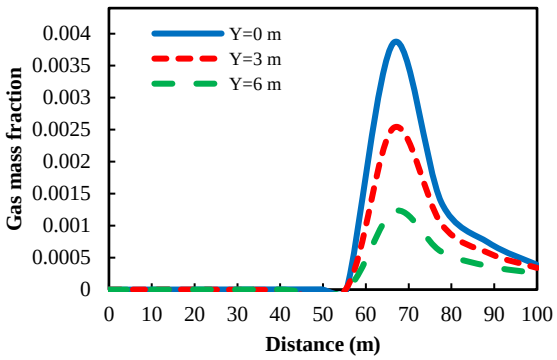

Figure 9. The changes in the gas mass fraction at V = 3 m/s

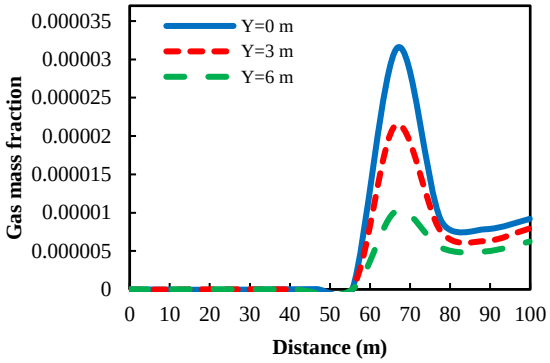

Figure 10. The changes in the gas mass fraction at V = 5 m/s

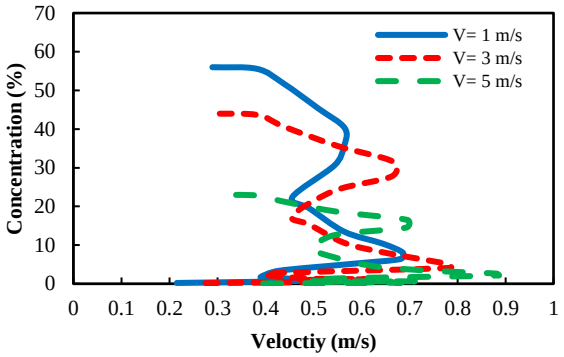

Figure 11. Gas concentration profile with the velocity profile

Figure 12 illustrates the concentration fields of the x-z cross profile at the hole location and the obstacles, respectively. The instantaneous gas concentration distribution and development process of the pollutant cloud due to the incoming wind flow is clearly shown in this figure. During the initial stage of gas dispersion, the pollutant cloud with greater concentration moved along downwind in 5 s, and gradually impinged on the buildings in 15 s. After that, the majority of pollutant clouds moved upwards which caused to increase in the height of the pollutant cloud with dispersion time. Finally, the pollutant cloud completely spread and covered the surrounding areas in 35 s. It is noteworthy that the concentration of gas pollutants decreased with dispersion time whereas it tended to zero. However, the buildings should be located far enough from the threat coverage area. The influencing radius was predicted by about 11.6 m in wind velocity of 1 m/s. The high concentration of gas in this area can obviously damage humans such as pulse rate increase, nausea, headaches, and unconscious.

As mentioned earlier in Figure 7, the gas concentration decreased as wind velocity increased. This phenomenon is due to the fact that the higher wind velocity can carry more fresh air and cause faster dispersion and stronger dilution, resulting in a smaller threat area.

Figures 13 to 15 demonstrate the pressure distribution over the obstacles and residential area. It is evident that the maximum value of pressure increased as the wind velocity raised. Also, there is a high-pressure field in the locations near the buildings. There is a maximum value of pressure at the front of the buildings and a negative pressure area at the back of the buildings.

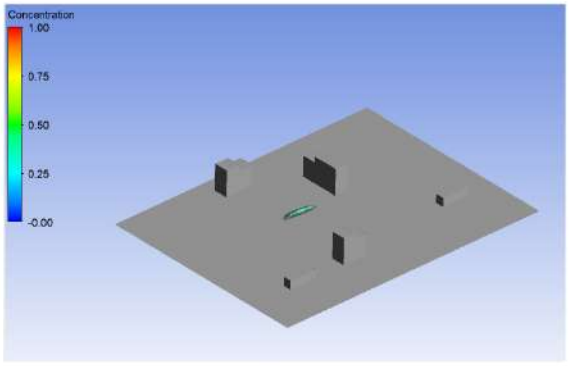

5 s

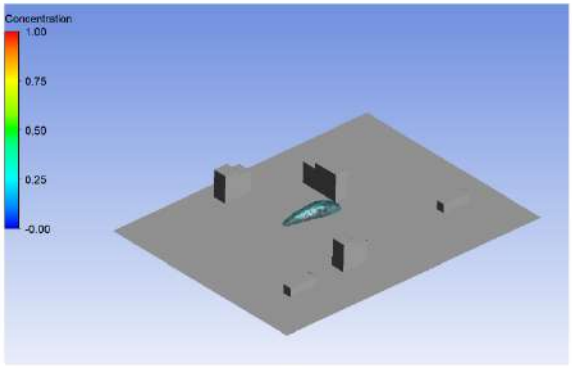

15 s

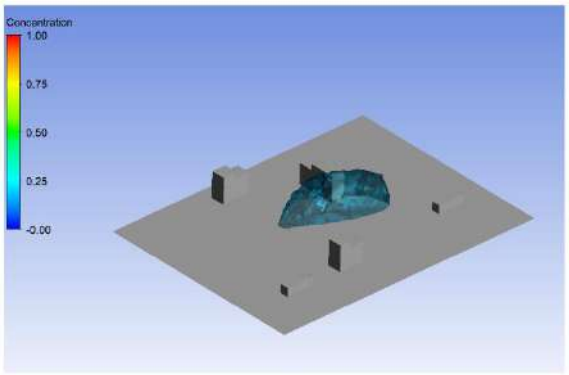

25 s

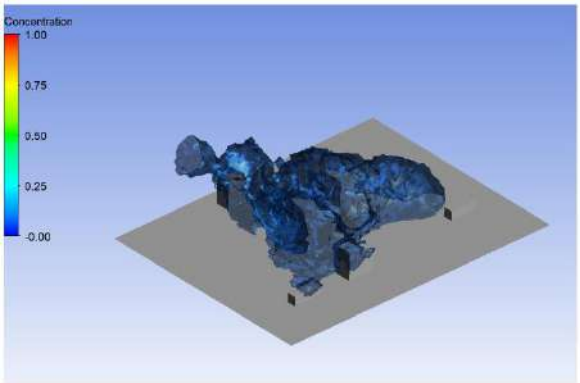

35 s

Figure 12. The development process of pollutant cloud

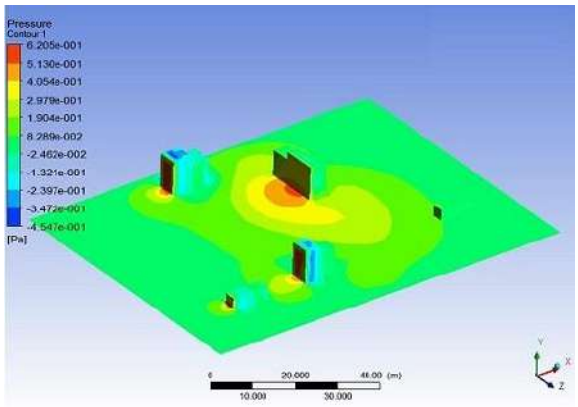

Figure 13. Pressure distribution at V = 1 m/s

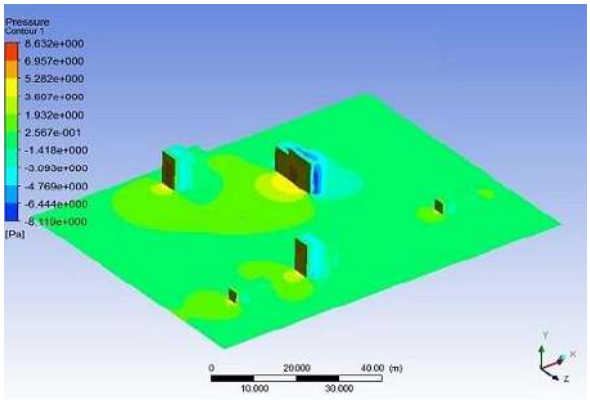

Figure 14. Pressure distribution at V = 3 m/s

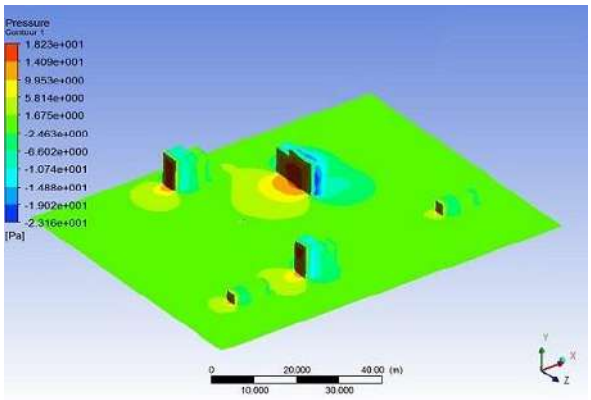

Figure 15. Pressure distribution at V = 5 m/s

6. CONCLUSION

In the present study, the sudden dispersion of gas from a hole intended at the ground was numerically analyzed using the CFD method. The numerical simulation was implemented using ANSYS CFX. For this purpose, a hole with a 20 mm diameter was considered and the

effects of changes inlet wind velocity, the direction of the pollutant cloud and its movement, mass fraction of gas dispersion, and the pressure distribution were studied. The flow was considered as three-dimensional, unsteady, turbulence, and compressible. The choice of turbulence model is a key in dispersion simulation using CFD codes. The results showed that the RNG k-ε turbulence model was suitable for simulating the gas dispersion.

The incoming wind flow carried the pollutant with high concentrations in 5 s of release and continued gradually with impingement on the buildings in 15 s. The height of the pollutant cloud increased with lower concentration which covered the surrounding areas in 35 s. Furthermore, the gas concentration decreased as wind velocity increased. This can be explained by the fact that more fresh air was carried with higher wind velocity. This resulted in faster dispersion and stronger dilution, and a smaller threat area.

7. REFERENCES

1. Mirzaei, F., Mirzaei, F., and Kashi, E., "Turbulence Model Selection for Heavy Gases Dispersion Modeling in Topographically Complex Area", ***Journal of Applied Fluid Mechanics,*** Vol. 12, No. 6, (2019), 1745-1755. doi: 10.29252/jafm.12.06.29685
2. Jiang, Y., Xu, Z., Wei, J., and Teng, G., "Fused CFD-interpolation model for real-time prediction of hazardous gas dispersion in emergency rescue", ***Journal of Loss Prevention in the Process Industries,*** Vol. 63, (2020), 103988. doi: 10.1016/j.jlp.2019.103988
3. Liu, X., Peng, Z., Liu, X., and Zhou, R., "Dispersion characteristics of hazardous gas and exposure risk assessment in a multiroom building environment", ***International Journal of Environmental Research and Public Health,*** Vol. 17, No. 1, (2020), 199-210. doi: 10.3390/ijerph17010199
4. Zhang, Q. X., Mo, S. J., and Liang, D., "Numerical simulation of natural gas release and risk zone forecast in urban areas", ***Procedia Engineering,*** Vol. 71, (2014), 470-475. doi: 10.1016/j.proeng.2014.04.067
5. Zhang, Y., Wang, L., Li, A., and Tao, P., "Performance evaluation by computational fluid dynamics modelling of the heavy gas dispersion with a low Froude number in a built environment", ***Indoor and Built Environment,*** Vol. 29, No. 5, (2020), 656-670. doi: 10.1177/1420326X19856041
6. Hanna, S. R., and Britter, R. E., Wind flow and vapor cloud dispersion at industrial and urban sites. John Wiley & Sons, 2010.
7. Pontiggia, M., Derudi, M., Alba, M., Scaioni, M., and Rota, R., "Hazardous gas releases in urban areas: assessment of consequences through CFD modelling", ***Journal of Hazardous Materials,*** Vol. 1-3, (2010), 589-59. doi: 10.1016/j.jhazmat.2009.11.070
8. Duijm, N. J., Carissimo, B., Mercer, A., Bartholome, C., and Giesbrecht, H., "Development and test of an evaluation protocol for heavy gas dispersion models", ***Journal of Hazardous Materials,*** Vol. 56, No. 3, (1997), 273-285. doi: 10.1016/S0304-3894(97)00069-1
9. Britter, R. E., and McQuaid, J., HSE Contract Research Report No. 17. Workbook on the Dispersion of Dense Gases, 1988.
10. Britter, R. E., "Atmospheric dispersion of dense gases", ***Annual Review of Fluid Mechanics,*** Vol. 21, No. 1, (1989), 317-344. doi: 10.1146/annurev.fl.21.010189.001533
11. Cai, J., Chen, J., Ahmad, S., Zhao, J., Cheng, H., Zi, S., and Xiao, J., "Investigation into the effect of upstream obstacles and hazardous sources on dispersion in the urban environment with LES model", ***Journal of Hazardous Materials,*** Vol. 390, (2020), 121953. doi: 10.1016/j.jhazmat.2019.121953
12. Hsieh, K. J., Lien, F. S., and Yee, E., "Dense gas dispersion modeling of CO2 released from carbon capture and storage infrastructure into a complex environment", ***International Journal of Greenhouse Gas Control,*** Vol. 17, (2013), 127-139. doi: 10.1016/j.ijggc.2013.05.003
13. Li, X., Abbassi, R., Chen, G., and Wang, Q., "Modeling and analysis of flammable gas dispersion and deflagration from offshore platform blowout", ***Ocean Engineering,*** Vol. 201, (2020), 107146. doi: 10.1016/j.oceaneng.2020.107146
14. Eslami Afrooz, I., and Chuan Ching, D. L., "Effect of Novel Swirl Distributor Plate on Hydrodynamics of Fluidized Bed Gasifier", ***International Journal of Engineering, Transactions A: Basics,*** Vol. 32, No, 10, (2019), 1358-1365. doi: 10.5829/ije.2019.32.10a.04
15. Rayenia, A. D., and Nassab, S. G., "Effects of Gas Radiation on Thermal Performances of Single and Double Flow Plane Solar Heaters", ***International Journal of Engineering, Transactions C: Aspects,*** Vol. 33, No. 6, (2020), 1156-1166. doi: 10.5829/ije.2020.33.06c.14
16. Fatahian, H., Hosseini, E., and Fatahian, E., "CFD simulation of a novel design of square cyclone with dual-inverse cone", ***Advanced Powder Technology,*** Vol. 31, No. 4, (2020), 1748-1758. doi: 10.1016/j.apt.2020.02.007
17. Fatahian, E., Salarian, H., and Fatahian, H., "A parametric study of the heat exchanger copper coils used in an indirect evaporative cooling system", ***SN Applied Sciences,*** Vol. 2, No, 1, (2020), 112-120. doi: 10.1007/s42452-019-1915-0
18. Kashi, E., Mirzaei, F., and Mirzaei, F., "Analysis of gas dispersion and ventilation within a comprehensive CAD model of an offshore platform via computational fluid dynamics", ***Journal of Loss Prevention in the Process Industries,*** Vol. 36, (2015), 125-133. doi: 10.1016/j.jlp.2015.05.019
19. Sun, B., Wong, J., Wadnerkar, D., Utikar, R. P., Pareek, V. K., and Guo, K., "Multiphase simulation of LNG vapour dispersion with effect of fog formation", ***Applied Thermal Engineering,*** Vol. 166, (2020), 114671. doi: 10.1016/j.applthermaleng.2019.114671
20. Dasgotra, A., Teja, G. V., Sharma, A., and Mishra, K. B., "CFD modeling of large-scale flammable cloud dispersion using FLACS", ***Journal of Loss Prevention in the Process Industries,*** Vol. 56, (2018), 531-536. doi: 10.1016/j.jlp.2018.01.001
21. Pontiggia, M., Derudi, M., Busini, V., and Rota, R., "Hazardous gas dispersion: a CFD model accounting for atmospheric stability classes", ***Journal of Hazardous Materials,*** Vol. 171, No. 3, (2009), 739-747. doi: 10.1016/j.jhazmat.2009.06.064
22. Li, X., Chen, G., and Khan, F., "Analysis of underwater gas release and dispersion behavior to assess subsea safety risk", ***Journal of Hazardous Materials,*** Vol. 367, (2019), 676-685. doi: 10.1016/j.jhazmat.2019.01.015
23. Moen, A., Mauri, L., & Narasimhamurthy, V. D., "Comparison of k-ε models in gaseous release and dispersion simulations using the CFD code FLACS", ***Process Safety and Environmental Protection,*** Vol. 130, (2019), 306-316. doi: 10.1016/j.psep.2019.08.016
24. Han, O., Zhang, Y., Li, A., Li, J., Li, Y., and Liu, H., "Experimental and numerical study on heavy gas contaminant dispersion and ventilation design for industrial buildings",

Sustainable Cities and Society, Vol. 55, (2020), 102016. doi: 10.1016/j.scs.2020.102016

25. Eberwein, R., Rogge, A., Behrendt, F., and Knaust, C., "Dispersion modeling of LNG-Vapor on land–A CFD-Model evaluation study", ***Journal of Loss Prevention in the Process Industries,*** Vol. 65, (2020), 104116. doi: 10.1016/j.jlp.2020.104116
26. Issakhov, A., and Omarova, P., "Numerical simulation of pollutant dispersion in the residential areas with continuous grass barriers", ***International Journal of Environmental Science and Technology,*** Vol. 17, No. 1, (2020), 525-540. 10.1007/s13762-019-02517-x
27. Michioka, T., Takimoto, H., Ono, H., and Sato, A., "Large-eddy simulation of the effects of wind-direction fluctuations on turbulent flow and gas dispersion within a cubical canopy", ***Boundary-Layer Meteorology,*** Vol. 173, No. 2, 243-262, (2019). doi: 10.1007/s10546-019-00467-y
28. Li, X., Chen, G., Zhang, R., Zhu, H., and Xu, C., "Simulation and assessment of gas dispersion above sea from a subsea release: A CFD-based approach", ***International Journal of Naval Architecture and Ocean Engineering,*** Vol. 11, No. 1, (2019), 353-363. doi: 10.1016/j.ijnaoe.2018.07.002
29. Sklavounos, S., and Rigas, F., "Validation of turbulence models in heavy gas dispersion over obstacles", ***Journal of Hazardous Materials,*** Vol. 108, No. 1, (2004), 9-20. doi: 10.1016/j.jhazmat.2004.01.005
30. Rice, R. G., and Do, D. D., Applied mathematics and modelling for chemical engineers. John Wiley & Sons, 2012.

Persian Abstract

چکیده

در مطالعه حاضر، تلاش شده است تا از روش دینامیک سیالات محاسباتی جهت ارزیابی پراکندگی گازهای خطرناک همراه با موانع استفاده شود. برای این منظور، پراکندگی تصادفی گازهای خطرناک از سطح و تأثیر پارامترهای مختلف از جمله تغییر سرعت باد ورودی، جهت ابر آلاینده و حرکت آن، کسر جرمی پراکندگی گاز و توزیع فشار به صورت عددی مورد بررسی قرار گرفته است. جریان به صورت سه بعدی، ناپایا، آشفته و تراکم پذیر فرض شده است. از مدل های توربولانسی مختلف در مدل سازی انتشار گاز استفاده شده است و دقیق ترین مدل پیشنهاد شده است. نتایج عددی نشان داده است که کسر جرمی گاز به دلیل پراکندگی ناگهانی گاز به طور قابل توجهی افزایش یافته است. با حرکت در محور افقی میزان غلظت گاز به تدریج کاهش می یابد. علاوه بر این، کسر جرمی گاز با افزایش ارتفاع کاهش یافته است. با مقایسه نتایج، مشخص شده است که ابر آلاینده در سرعت باد ۱ متر بر ثانیه محیط اطراف را پوشش نمی دهد. بنابراین، ابر آلاینده تولید شده در این حالت، نمی تواند تهدیدی را ایجاد کند. در سرعت های بالاتر باد (۳ متر بر ثانیه و ۵ متر بر ثانیه)، ابر آلاینده تقریباً مناطق اطراف را پوشانده است، که این امر تهدید قابل توجهی را ایجاد کرده است. حداکثر فشار در سوراخ ۵/۷ پاسکال برای سرعت باد ۵ متر بر ثانیه بوده است، در حالی که حداکثر فشار منفی در حدود ۷.۱- پاسکال بوده است. شعاع تأثیرگذار در حدود ۹.۳ متر بدست آمده است. فشار بیش از حد باعث ایجاد صدمات آشکار در ساختمان ها نشده است اما منجر به صدمه اندکی به انسان ها شده است.

International Journal of Engineering

Journal Homepage: www.ije.ir

Numerical Investigation of Nonlinear Oscillations and Compression-Only Behavior of a Coated Microbubble Near an Elastic Wall

S. B. Hosseini, M. Mahdi*

Mechanical Engineering Department, Shahid Rajaei Teacher Training University, Tehran, Iran

P A P E R I N F O

Paper history:
Received 15 June 2020
Received in revised form 09 July 2020
Accepted 17 August 2020

Keywords:
Compression-Only Behavior
Elastic Wall
Nonlinear Oscillations
Subharmonic Component
Ultrasound Contrast Agents

A B S T R A C T

During the ultrasound imaging process, the ultrasound contrast agents (UCAs) are beating near the blood vessel wall. Therefore, the purpose of the present simulation study is to investigate the effect of the presence of an elastic wall on the radial and frequency acoustic response of a UCA microbubble oscillating in a nonlinear regime. For this reason, the numerical simulation of the dynamic behavior of a coated microbubble was performed using coding in MATLAB and a Rayleigh-Plesset equation modified by Doinikov. To study the nonlinear bubble oscillations, its compression-only behavior and the sub-harmonic nonlinear component are taken from a nonlinear shell model presented by Marmottant et al. Initially, coated bubble oscillations in two linear and nonlinear regimes were investigated for two types of shell models, and it was observed that presence of the elastic wall affects the bubble's compression-only behavior. Finally, due to the importance of the subharmonic component in the nonlinear oscillation of the coated bubble, the threshold of the appearance of subharmonic components for a coated bubble near an elastic wall was investigated using the Fast Fourier Transform (FFT) and compared with the oscillation in the infinite fluid.

***doi**: 10.5829/ije.2020.33.10a.28*

1. INTRODUCTION

The mechanism of diagnostic imaging in medicine by ultrasound is based on the scattering and reflection of the ultrasound waves sent from the target tissue. Unlike body tissues, the scattering properties of blood are very poor and ultrasound transmitted waves attenuate after reflection and reduce imaging quality due to the low reflection of blood and some tissues against ultrasound waves which either absorb or transmit the ultrasound waves. To increase the reflectance of ultrasound beams, micrometer coated bubbles (ultrasound contrast agents) that are covered by a stabilizing shell (a variety of proteins such as lipid or albumin) are intravenously injected. These contrast agent microbubbles due to their oscillations prevent the wave attenuation, and increase the acoustic differentiation between blood and tissue during an ultrasound examination and improve image quality. The UCA microbubbles usually have a small size of about microns (1 to 10 micrometers) that enables them to pass through the smallest capillaries in the body. Bubble coating has been done to increase the stability of the free bubbles, prevent its rapid dissolution, and prevent their agglomeration which has led to the production of different generations of UCA bubbles. Adding a special coating with a certain viscosity and elasticity to the free bubbles alters the surface tension of the bubbles and consequently changes their acoustic behavior dramatically. In medical applications, UCA microbubbles move near boundary surfaces such as the wall of a laboratory container or the wall of a blood vessel. Therefore, the theoretical models that predict the effect of a wall on the dynamics of a UCA microbubble are interesting. Studying this information is important for determining the imaging methods and the microbubble parameters owing to their ability to optimize imaging clarity, improve imaging quality, and assist the development of new imaging strategies.

*Corresponding Author Institutional Email: *M.mahdi@sru.ac.ir* (M. Mahdi)

Please cite this article as: S. B. Hosseini, M. Mahdi, Numerical Investigation of Nonlinear Oscillations and Compression-Only Behavior of a Coated Microbubble Near an Elastic Wall, International Journal of Engineering (IJE), IJE TRANSACTIONS A: Basics Vol. 33, No. 10, (October 2020) 2095-2104

The dynamics of the bubble in an ultrasonic field is described by the Rayleigh-Plesset (RP) equation, but the addition of a shell to the bubble and the presence of a wall near the bubble will change the above equation. To study the dynamics of the coated bubble, De Jong et al. [1] presented the first models and parameters (shell friction and shell elasticity) to determine the coating effects. Church et al. [2] developed the first accurate model of coating theory by a layer of incompressible rubber material using a Modified Rayleigh-Plesset equation. Hoff et al. [3] used a thin-shell model of polymer and observed that this coating increases the bubble shell resistance by up to 20 times compared to the free gas bubble. Later, De Jong et al. [4] investigated the response of the UCA in nonlinear regimes appearing at high pressures and observed that nonlinear bubble oscillations produce harmonics and sub-harmonics in the bubble behavior.

Several researchers like Brennen [5], Leighton [6], and Blake and Gibson [7] investigated the dynamics of a free gas bubble near a solid boundary. In medical imaging, bubbles may be in the proximity of the vessel or capillary that will therefore affect the pressure propagated from the bubble. It has provided a motivation for studying the effect of a boundary on a coated bubble. For the first time, Herring [8] made numerical study of the free bubble near the wall. Then, Strasberg [9] and Blue [10] examined the effect of a rigid wall on the resonant frequency of a free bubble. In their assumptions, the interaction of a bubble with a rigid boundary is mathematically equivalent to the interaction between two pulsating, in-phase, and adjacent bubbles. Since then, this equivalence has been utilized in many studies, such as the study reported by Doinikov et al. [11], to investigate the dynamical behavior of bubbles. Tomita and Shima [12] also presented a modified Rayleigh-Plesset equation for a free bubble that incorporated the rigid wall effects and the compressibility of the fluid around the bubble. This equation, developed by the Image Source Method, was used by Doinikov et al. [13] to derive a modified Rayleigh-Plesset equation for a bubble near a fluid layer of finite thickness. Experimental data show that the proximity of a boundary to the bubble and the mechanical properties of the material of the shell can cause significant changes in the amplitude of the micro bubble's oscillation and its propagated pressure [14]. Many theoretical studies predicted that the resonance frequency of a UCA near a boundary can be reduced or increased depending on the mechanical properties of the boundary [15]. In an experimental work, Garbin et al. [14] observed that the oscillation amplitude of a BR-14 microbubble near the wall of an OptiCell chamber is suppressed by more than 50%.

These findings prompted scientists to focus on the interaction of the UCA microbubbles and the ultrasound waves, and the effect of vessel wall proximity to have a better understanding of its behavior in an ultrasound field. Various modeling studies have been conducted to understand the bubble response when it passes along the vessel wall. Primary studies such as that reported by Leighton [6] investigated the response of the bubble near the rigid wall of the vessel. However, the recent studies indicate the need for a comprehensive understanding of the more flexible boundaries effect because these boundaries are biologically more important. Doinikov et al. [11] modeled the UCA microbubbles responses using the modified Rayleigh-Plesset equation near the rigid wall and analyzed it. Overvelde et al. [16] investigated the presence of a rigid wall and its effect on the behavior of the UCA microbubbles. They found that, in particular, the resonance frequency of the microbubbles and the intensity of the scattered pressure field varied, so that the maximum resonance frequency of the bubble attached to the wall was 50% lower than the bubble in the infinite fluid. Doinikov et al. [13] investigated the oscillating UCA responses near a thin layer of finite density. They attempted to develop a new theoretical model to investigate the effects of the layer thickness and density on the pressure field scattered from the bubble. In 2013, Aired et al. [17] investigated the dynamics of the coated bubble near three different types of the wall, two different distances from the wall, and three different initial radii. They studied the changes of fundamental and second harmonic frequencies. Garashchuk et al. [18] also considered different models of coated bubbles and investigated their multi-dynamic stability and the occurrence of complex three-dimensional nonlinear dynamics. Dvinikov et al. [15] investigated the interaction of bubbles and walls at arbitrary distances to complete their earlier theory. Their simulation results showed that the bubble resonance frequency near the wall is dependent on the distance from the wall and the elastic properties of the wall.

In the present study, a Rayleigh-Plesset equation modified by Doinikov is used to simulate the UCA microbubble behavior near an elastic wall of finite thickness to investigate how the elastic wall proximity affects the microbubble behavior and the acoustic response of the microbubble. Therefore, for the first time, for a coated bubble near an elastic wall with finite thickness, the occurrence of the nonlinear oscillations and its resulting components (such as harmonic components and compression-only behavior) have been simulated. Due to the importance of nonlinear bubble oscillations in medical applications, the focus of this paper is on the nonlinear behavior of the UCA microbubble near an elastic wall. The bubble oscillation behavior is simulated using the fourth-order Runge-Kutta method and the Doinikov equation and is compared with the experimental results.

2. THEORY

Up to now, several types of Rayleigh-Plesset equations have been derived for coated bubbles, but for a coated bubble several factors influence its dynamic behavior (including the presence of a wall near the bubble). Today, there are varieties of ultrasound medical technologies that use UCAs, in which, the microbubble interactions occur with different boundaries. In clinical applications, such as ultrasound imaging, these boundaries could be the blood vessel wall, while in the laboratory applications could be the wall of laboratory containers made of various materials.

2. 1. Coated Bubble in Infinite Fluid and Near an Elastic Wall Almost all the mathematical models of microbubble dynamics are based on modifications of the Rayleigh-Plesset equation, which is for the growth and collapse of a gas bubble and can be expressed in a new context. Assuming a polytropic law for bubble gas and regardless of the vapor pressure inside the bubble, the following form of the modified Rayleigh-Plesset equation can be used to model the dynamics of coated microbubbles in an infinite fluid [19]:

$$\rho_l\left[R\ddot{R}+\frac{3}{2}\dot{R}^2\right]=\left(P_0+\frac{2\sigma(R_0)}{R_0}\right)\left(\frac{R_0}{R}\right)^{3k}\left(1-\frac{3k\dot{R}}{c}\right)-\frac{2\sigma(R)}{R}-\frac{4\mu\dot{R}}{R}-\frac{4\dot{R}}{R^2}K_s\left(R,\dot{R}\right)-P_0-P_{ac}(t) \quad (1)$$

where R is the bubble radius, R_0 the initial bubble radius, k the ratio of specific heats of the gas, P_0 the hydrostatic ambient pressure, μ the fluid viscosity, σ(R) the effective surface tension of the bubble, c the speed of sound at ambient, ρ the density of the surrounding liquid, K_s the shell viscosity and $P_{ac}(t)$ the external excitation pressure applied to the bubble. To model the pressure field scattered from the bubble in an infinite fluid, one obtains [19]:

$$P_{scater}(r,t)=\frac{\rho_l R}{r}\left(R\ddot{R}+2\dot{R}^2\right) \quad (2)$$

where P_{scater} is the scattered pressure from the bubble and r the measured distance from the center of the bubble [20]. Nevertheless, the theoretical models that predict the effect of a wall on the dynamics of a coated microbubble receive much attention, because, in medical applications (laboratory, therapeutic, and imaging), the UCA microbubbles move near different boundary surfaces.

Figure 1 shows a schematic of a coated bubble near an elastic wall of finite thickness. The bubble is at a distance d from the wall (environment 2) and h is the thickness of the wall. The wall material is assumed to be an elastic solid with a density of ρ_2, a bulk modulus K_{wall}, and a shear modulus μ_{wall}. The back wall environment is also assumed to be an ideal and incompressible fluid with a density of ρ_3.

Because the presence of a wall affects the behavior of the UCA microbubbles, Doinikov et al. [13] developed a

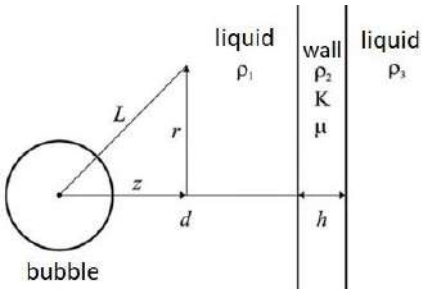

Figure 1. Schematic of a bubble near an elastic wall with finite thickness

modified Rayleigh-Plesset family of equation for a coated microbubble near an elastic wall of finite thickness to investigate the effect of the presence of a wall on the UCA microbubble acoustic response. These equations are as follows [13]:

$$\ddot{R}R(1-\alpha)+\frac{3}{2}\dot{R}^2\left(1-\frac{4\alpha}{3}\right)=\frac{1}{\rho_l}\left[\left(P_0+\frac{2\sigma}{R_0}\right)\left(\frac{R_0^3-a^3}{R^3-a^3}\right)^{\gamma}-\frac{2\sigma(R)}{R}-4\mu\frac{\dot{R}}{R}-P_0-P_{ac}(t)-S\right] \quad (3)$$

The variable α is as follows [13]:

$$\alpha=\left(\frac{\rho_1-\beta}{\rho_1+\beta}\right)\frac{R}{2h}-\left(\frac{\beta-\rho_2}{\beta+\rho_2}\right)\frac{R}{2(h+t)}+\frac{(\rho_1-\beta)(\beta-\rho_2)}{(\rho_1+\beta)(\beta+\rho_2)}\frac{R}{2t} \quad (4)$$

Equation (3) neglects the radiation damping due to the liquid compressibility. This effect can be taken into account by one of the most common modified Rayleigh-Plesset equations for compressible fluids such as Keller-Miksis equation. These equations are as follows [13]:

$$\ddot{R}R\left(1-\alpha-\frac{\dot{R}}{c}\right)+\frac{3}{2}\dot{R}^2\left(1-\frac{4\alpha}{3}-\frac{\dot{R}}{3c}\right)=\frac{1}{\rho_l}\left(1+\frac{\dot{R}}{c}+\frac{R}{c}\frac{d}{dt}\right)\left[\left(P_0+\frac{2\sigma}{R_0}\right)\left(\frac{R_0^3-a^3}{R^3-a^3}\right)^{\gamma}-\frac{2\sigma(R)}{R}-4\mu\frac{\dot{R}}{R}-P_0-P_{ac}(t)-S\right] \quad (5)$$

where S is the term describing shell effect and a is the radius of the bubble's van der Waals hard core. The acoustic pressure wave scattered from the coated bubble near an elastic wall at L distance from the center of the bubble is as follows [13]:

$$P_{scater}=\frac{\rho_l(R^2\ddot{R}+2R\dot{R}^2)}{L}\left[1-\left(\frac{\rho_1-\beta}{\rho_1+\beta}\right)\frac{L}{\sqrt{L^2+4d^2-4dz_l}}-\left(\frac{\beta-\rho_3}{\beta+\rho_3}\right)\frac{L}{\sqrt{L^2+4(d+h)^2-4(d+h)z_l}}+\frac{(\rho_1-\beta)(\beta-\rho_3)}{(\rho_1+\beta)(\beta+\rho_3)}\frac{L}{\sqrt{L^2+4h^2-4hz_l}}\right] \quad (6)$$

If L is large compared to d and h, Equation (6) can be rewritten as follows [13]:

$$P_{scater}=\frac{\rho_l(R^2\ddot{R}+2R\dot{R}^2)}{L}\frac{4\beta\rho_3}{(\rho_1+\beta)(\beta+\rho_3)} \quad (7)$$

After that, in 2013, Aired et al. [17] considered some modifications to improve an equation for the coated bubble dynamics near an elastic wall using the De Jong shell as follows [13]:

$$\ddot{R}R(1-\alpha)+\frac{3}{2}\dot{R}^2\left(1-\frac{4\alpha}{3}\right)=\left[\left(P_0+\frac{2\sigma}{R_0}\right)\left(\frac{R_0}{R}\right)^{3\gamma}\left(1-\frac{3\gamma}{c}\dot{R}\right)-\frac{2\sigma(R)}{R}-4\mu\frac{\dot{R}}{R}-P_0-P_{ac}(t)-4\chi\left(\frac{1}{R_0}-\frac{1}{R}\right)-\frac{4K_s\dot{R}}{R^2}\right] \quad (8)$$

where K_s and χ are shell viscosity and shell elasticity, respectively. Marmottant et al [21] also introduced a shell model that is suitable for high amplitude oscillations. This model assumes an elastic shell with buckling and rupture states. Three important factors are involved in the performance of this shell model.

1-the buckling radius which plays a major role in predicting the compression-only behavior, 2-the compressibility of the shell material and 3-the rupture radius which plays the major role in predicting the disappearance of compression-only behavior [19–22].

$$\sigma(R)=\begin{cases}0 & R\le R_{buckling}\\ \chi\left(\frac{R^2}{R_{buckling}^2}-1\right) & R_{buckling}\le R \ \&\ R\le R_{rupture}\\ \sigma_{water} & R\ge R_{rupture}\end{cases} \quad (9)$$

$$K_s(R)=K_s$$

$$f_0=\frac{1}{2\pi R_0}\sqrt{\frac{1}{\rho}\left(3\gamma P_0+\frac{4\sigma(R_0)}{R_0}(3\gamma-1)+\frac{4\chi}{R_0}\right)} \quad (10)$$

And the critical radius of this model is as follows [21]:

$$R_{rupture}=R_{buckling}(1+\sigma_{water}/\chi)^{1/2} \quad (11)$$

$$R_{buckling}=R_0(1+\sigma(R_0)/\chi)^{-1/2} \quad (12)$$

In the Marmottant model, the effective surface tension operates within a certain range; for the values more than $R_{rupture}$ the bubble behaves like a free gas bubble, and for the values less than $R_{buckling}$ the bubble shell folds. For the latter, the effective surface tension is considered to be zero.

2. 2. Validation of Numerical Model In section 2.2, the numerical outputs are validated with experimental results to ensure the accuracy of the simulation results. First, by using the Rayleigh-Plesset model, the dynamics of a free bubble is simulated, and then by using the modified Rayleigh-Plesset improved by Doinikov for the coated bubbles, the dynamics of a coated bubble is simulated. Figure 2 is obtained using the experimental results by Lofstedt et al. [22], and Figure 3 is established using the experimental results by Garbin et al. [14]. The latter authors had recorded the dynamic behavior of a coated bubble by high-speed cameras near an elastic wall. In the validation section, the excitation pulse is applied as a Gaussian pulse with the frequency and amplitude according to the experimental conditions.

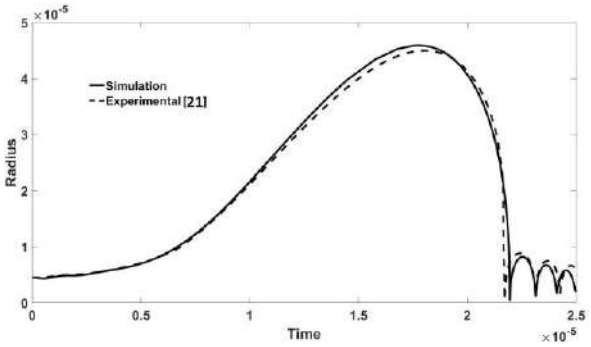

Figure 2. Validation of numerical solution and the experimental data for radial oscillation of a free bubble (Rayleigh–Plesset equation), (R_0 = 1.6μm, P_a = 0.2 MPa, f = 2 MHz)

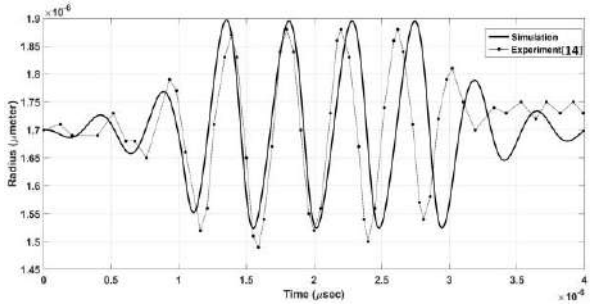

Figure 3. Validation of numerical solution and the experimental data for radial oscillation of an encapsulated bubble near an elastic wall (modified Rayleigh–Plesset equation by Doinikov), (R_0 = 1.7 μm, P_a = 58 KPa, f = 2.5 MHz, $\chi = 0.32$ N/m, K_s = 2.10^{-9} kg/s, d = 100 μm)

It can be seen from Figure 3 that both numerical and experimental results oscillate around the equilibrium radius of 1.7μm with the same trend and at the top of the graph, there is an average difference of 0.6% in amplitude. It is also observed that the numerical results predict the process of changing the oscillatory, compression, and expansion behavior of the bubble are well in accordance with the experimental results. The fourth-order Runge-Kutta method has been used for simulation. This method has been used due to resistance to divergence and stiff problems. Validations were performed under the following physical conditions (for Figure 3) [14]:

$R_0 = 1.7$ (μm) $\quad \gamma = 1.07 \quad \sigma_L = 0.072$ (N/m)

$K_s = 0.72e^{-8}$ (Kg/s) $\quad d = 50$ (μm) $\quad \chi = 0.51$ (N/m)

$\mu_L = 0.001$ (Pa. s) $\quad P_a = 200$ (KPa) $\quad P_a = 200$ (KPa)

$P_0 = 101325$ (Pa) $\quad h = 75$(μm) $\quad c = 1500$ (m/s)

$\rho_L = 1000$ (kg/m^{-3}) $\quad \rho_{wall} = 1060$ (kg/m^{-3})

$P_{ac}(t) = P_a \sin(2\pi ft)\exp[-(\frac{2ft}{N})^4]$

Besides, the numerical outputs in the field of frequency response are validated by comparing with the experimental results. Figures 4 and 5 are presented by

applying a Marmottant nonlinear shell model to the coated bubble dynamic equation and then by employing Equation (7). By applying Fast Fourier Transform (FFT) on the pressure wave propagated from the bubble, the frequency responses of the fundamental and subharmonic components are obtained and compared with the experimental results by Paul et al. [19]. Validations were performed under the following physical conditions (for Figures 4 and 5) [19]:

$R_0 = 1.6\ (\mu m)$ $P_0 = 101325\ (Pa)$ $\gamma = 1.07$

$K_s = 1.2e^{-8}\ (Kg/s)$ $\chi = 0.51\ (N/m)$ $c = 1500\ (m/s)$

$\mu_L = 0.001\ (Pa.s)$ $P_a = 1.6\ (MPa)$ $f = 3\ (MHz)$

$\rho_L = 1000(kg/m^{-3})$ $\sigma_L = 0.072\ (N/m)$

$P_{ac}(t) = P_a \sin(2\pi ft)$

Figure 6 shows the frequency response spectrum emitted from a coated bubble using a Marmottant nonlinear shell model.

3. DISCUSSION

When the bubble is excited by an acoustic pulse, the pressure waves are propagated by the bubble oscillation. The wave propagated by the bubble may have different frequency components depending on the intensity of the excitation. In this scattered pressure wave from the bubble, there is always a fundamental component which is the frequency of excitation of the bubble. As the excitation intensity increases, the higher harmonic components, which are integer coefficients of the fundamental component (such as nf_i), can also appear in the Fourier spectrum of the bubble frequency responses. As the excitation pulse intensities increase, nonlinear components, such as sub-harmonic and ultra-harmonic components, also appear in the pressure spectrum scattered from the bubble, where the sub-harmonic components are as the coefficient of $1/2f_i$, and the ultra-harmonic components are as the coefficient of $2.3f_i$. As the excitation pulse intensities increase, the bubble oscillation frequency response spectrum enters the saturation phase with severe noises. The nonlinear components are integrated into these noises and are no longer detectable. Since the wave propagated from the bubble contains a set of mentioned above frequencies, it is therefore necessary to extract and analyze each of these waves by applying the Fourier series to the time domain transfer. The current simulation study aims to show how the presence of an elastic boundary affects the radial and frequency response of a UCA bubble in a nonlinear oscillatory regime. The bubble and shell properties used in the numerical simulation are listed in Table 1. Simulations were performed under the following physical conditions [13]:

$\mu_L = 0.001\ (Pa.s)$ $\sigma_L = 0.072\ (N/m)$ $\gamma = 1.07$

$\mu_{wall} = 1.34\ (GPa)$ $P_0 = 101325\ (Pa)$ $d = 2R_0$

$\rho_L = 1000\ (kg/m^{-3})$ $K = 3.75\ (GPa)$ $R_0 = 1.6\ (\mu m)$

$\rho_{wall} = 1060\ (kg/m^{-3})$ $c = 1500\ (m/s)$ $h = 75\ (\mu m)$

In the simulation steps, the excitation pulse is applied as a burst sinusoidal pulse with a specified frequency and amplitude.

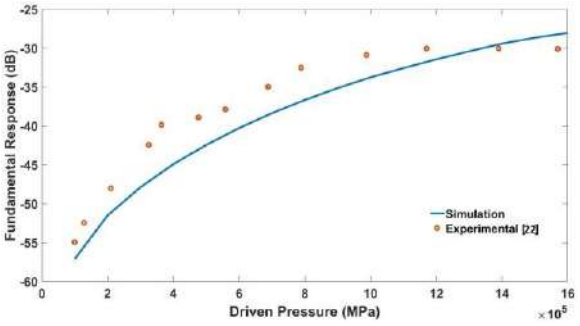

Figure 4. Validation of numerical solution and the experimental data for fundamental response of Sonazoid bubble (f = 3 MHz)

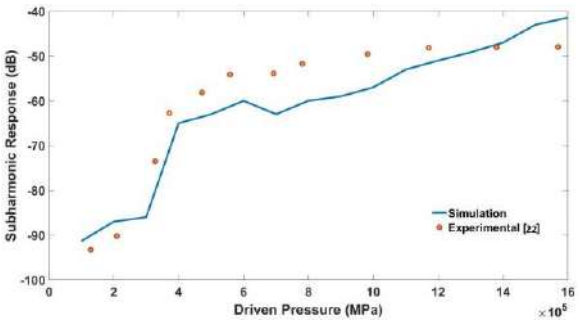

Figure 5. Validation of numerical solution and the experimental data for subharmonic response of Sonazoid bubble (f = 3 MHz)

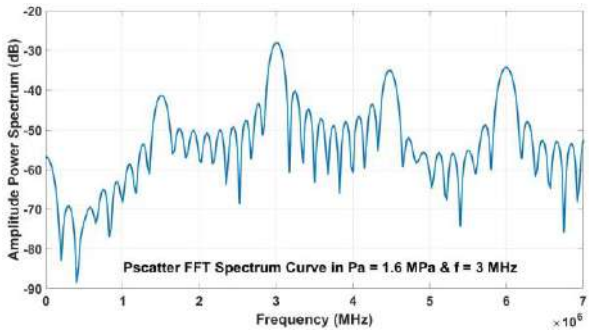

Figure 6. Frequency spectrum of a Sonazoid bubble (P_a = 1.6 MPa, f = 3 MHz)

TABLE 1. Marmottant Model Parameters [21]

$K_s(Kg/s)$	$\chi(N/m)$
1.2×10^{-8}	0.53

3. 1. Investigation of the Nonlinear Bubble Oscillation and Compression-only Behavior Near an Elastic Wall The coated bubble oscillations are linear or nonlinear depending on the magnitude of their excitation pressure. In the low excitation amplitudes, the behavior of the coated bubble is quite linear and does not affect the nonlinear factors in the radius-time graph and its frequency response spectrum. Most of the linear shell models presented for the linear oscillations assume a bubble surface tension as a constant number, but, at higher excitation pressure amplitudes, the coated microbubble behavior tends to become nonlinear. Therefore, the nonlinear factors will appear in the radius-time graph and its frequency response spectrum (such as ultra-harmonic and sub-harmonic components). Under these conditions, the bubble in the compression phase will experience the buckling state of the bubble shell due to the zero value of the surface tension. On the other hand, in the expansion phase of the bubble, the surface tension of the shell has increased rapidly, and this sudden change causes asymmetry in the bubble radial behavior in the radius-time graph. This phenomenon is called the compression-only behavior and was discovered by De Jong during the high-speed imaging of phospholipid-coated microbubbles. In the compression-only behavior, the changes of the bubble radial in the compression phase ($\Delta R^- = R_0 - R_{min}$) are greater than that in the expansion phase ($\Delta R^+ = R_{max} - R_0$). Only the nonlinear shell models can detect the compression-only behavior and the nonlinear bubble oscillation because they assume that the bubble shell behavior is physically different in the expansion and compression phase. In fact, the main disadvantage of the early models for the bubble dynamics is the linearity of their shell descriptors. Therefore, they are not capable to describe the nonlinear effects such as the compression-only behavior and the dependence of the shell material properties on the initial bubble radius. For this reason, a Marmottant nonlinear shell model is used here to investigate the nonlinear oscillation regime of the bubble.

According to Figures 7 and 8, and regarding the amplitude of excitation pressure and excitation frequency, the bubble experiences linear oscillations. Both the linear and nonlinear shell models used in this simulation have clearly shown the differences in the magnitude of bubble oscillation amplitude. The compression-only behavior is observed in the Marmottant nonlinear shell model, while the De Jong linear shell model does not predict it because the bubble buckling state is not considered in the compression phase. It can be seen that in the nonlinear shell model, the bubble oscillation amplitude is 0.45 μm and the dimensionless parameter E/C (the ratio of expansion to the bubble compression) is 0.5; but in the linear shell model, these values are 0.26 μm and 1.15, respectively. In this case, except for the fundamental component (f_0)

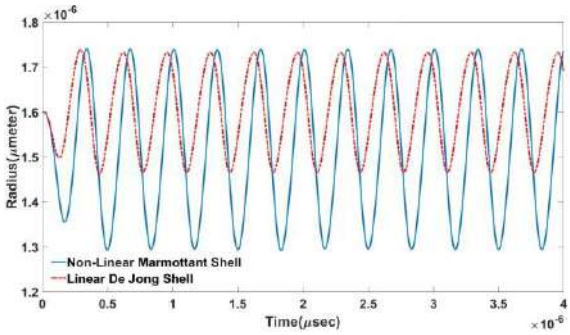

Figure 7. Radius-time curve for a 1.6 μm Sonazoid bubble in the linear oscillation regime for the linear De Jong shell and the nonlinear Marmottant shell (P_a = 0.1 MPa, f = 3 MHz)

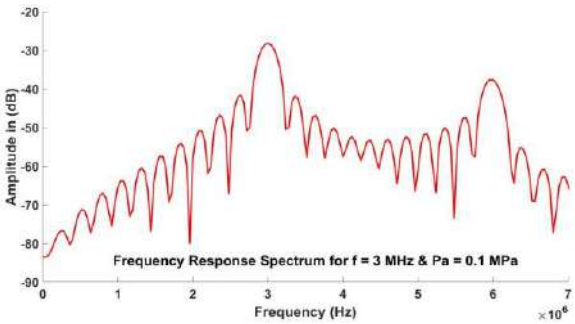

Figure 8. Frequency spectrum curve for a 1.6 μm Sonazoid bubble in the linear oscillation regime (P_a = 0.1 MPa, f = 3 MHz)

and the higher harmonics ($2f_0$), no nonlinear component is seen in the bubble frequency response spectrum.

But, regarding Figures 9 and 10 and the nonlinear oscillation conditions for the bubble, it is observed that in addition to the asymmetry and nonlinearity of the bubble radial behavior in the frequency response spectrum, nonlinear components such as sub-harmonic ($1/2\ f_0$) and ultra-harmonic components ($3/2\ f_0$) have also appeared. It is also observed that the compression-only behavior disappears after a certain excitation pressure amplitude due to the rupturing of the bubble shell and the coated bubble becomes a free bubble. The shell rupture occurs due to violent bubble oscillations and high bubble expansions. Consequently, when the bubble surface tension is fixed ($\sigma = \sigma_{water}$), the bubble no longer exhibits the compression-only behavior (since the variable surface tension in the Marmottant model plays a major role in the prediction of the compression-only behavior). Then, with increasing the excitation pressure amplitude, the bubble radius in the expansion phase becomes larger than the compression phase ($\Delta R^+ > \Delta R^-$), in contrast to the compression-only behavior. When the excitation frequency increases, this behavior will be delayed by decreasing the mechanical index of the bubble ($MI = P_a/\sqrt{f}$ where P_a is the amplitude of the excitation pressure

and f is the excitation frequency). Therefore, at higher excitation frequencies the compression-only behavior disappears at higher excitation pressure amplitudes.

Figures 11 shows the radius-time graphs for a coated bubble at two excitation frequencies of 3 MHz and 6 MHz and at different excitation pressure amplitudes. The linear and nonlinear changes in bubble oscillations can be studied using these figures. It is observed that the bubble oscillations near the elastic wall are more restricted than those in the infinite fluid, although for the lower excitation frequencies this radial oscillation suppression is more significant. It is also observed that as the excitation frequency increases, nonlinear bubble oscillation is suppressed and the bubble needs higher excitation pressure amplitude for nonlinear oscillations.

On the other hand, in the low excitation pressure amplitude the bubble oscillations are linear and at the same time the bubble experiences compression-only behavior. While, with increasing amplitude of excitation pressure, the bubble has nonlinear oscillations and the compression-only behavior is also disappeared. Also, as previously stated, by increasing the excitation frequency and consequently decreasing the mechanical index, the compression-only behavior of the bubble is delayed. For more explanation, in Figures 11a to c with an excitation frequency of 3 MHz, the compression-only behavior gradually disappears with increasing the amplitude of excitation pressure; whereas, in Figures 11d to f with an excitation frequency of 6 MHz, with increasing excitation pressure amplitude the compression-only behavior is still observed.

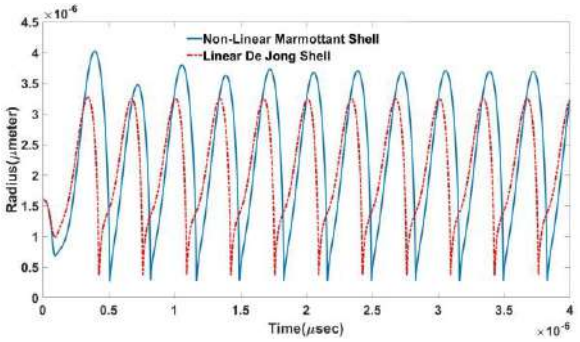

Figure 9. Radius-time curve for a 1.6 µm Sonazoid bubble in the nonlinear oscillation regime for the linear De Jong shell and the nonlinear Marmottant shell (P_a = 1 MPa, f = 3 MHz)

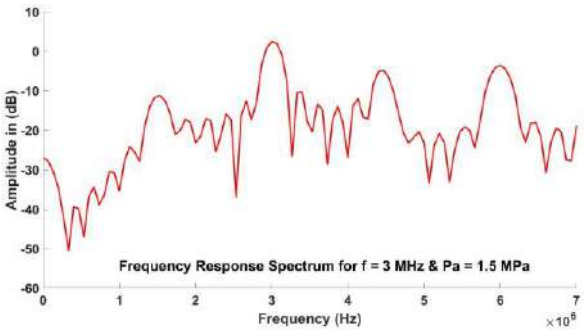

Figure 10. Frequency spectrum curve for a 1.6 µm Sonazoid bubble in the nonlinear oscillation regime (P_a = 1 MPa, f = 3 MHz)

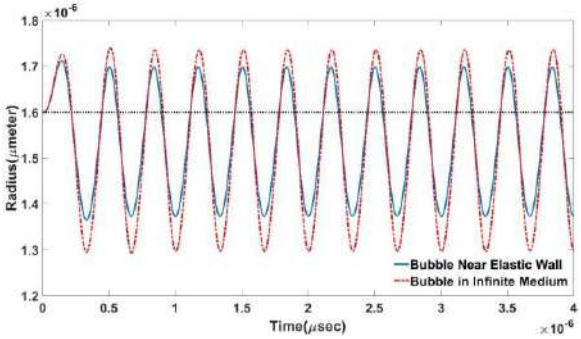

(a) P_a = 0.1 MPa, f = 3 MHz

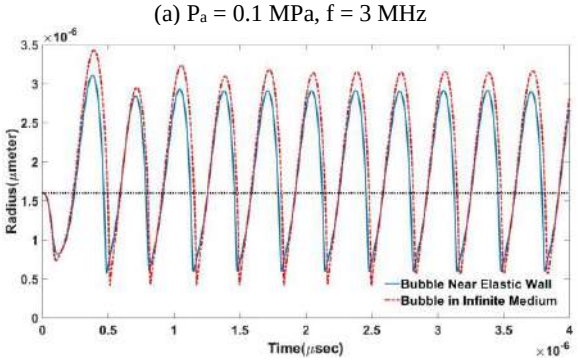

(b) P_a = 0.8 MPa, f = 3 MHz

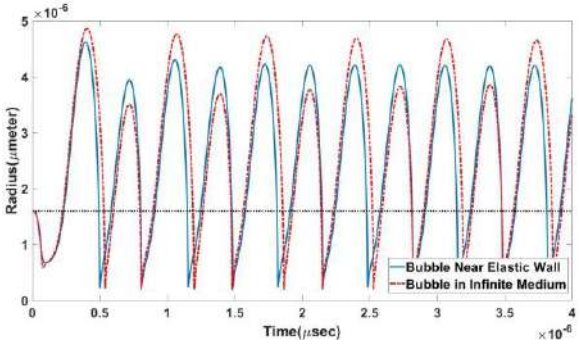

(c) P_a = 1.5 MPa, f = 3 MHz

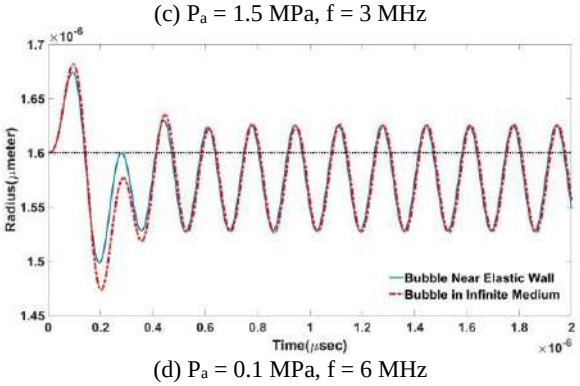

(d) P_a = 0.1 MPa, f = 6 MHz

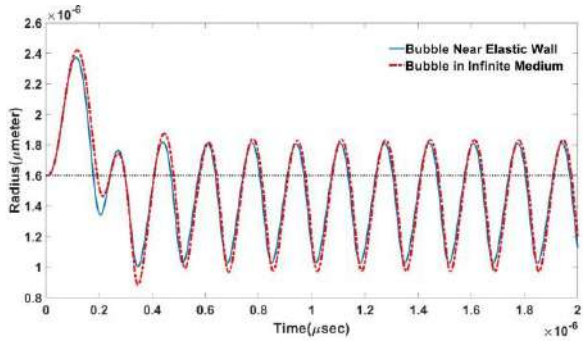

(e) P_a = 0.8 MPa, f = 6 MHz

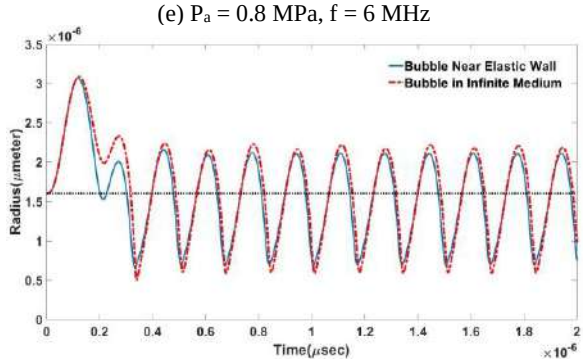

(f) P_a = 1.5 MPa, f = 6 MHz

Figure 11. Radius-time curves for a 1.6 µm Sonazoid bubble according to the presence of the wall

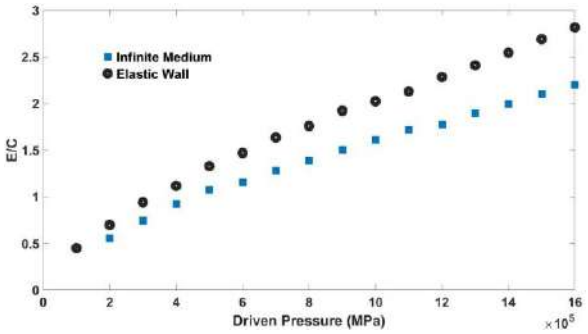

Figure 12. E/C values for a 1.6 µm Sonazoid bubble as a function of excitation pressure in both cases, the bubble oscillates near an elastic wall and an infinite liquid (f = 3 MHz)

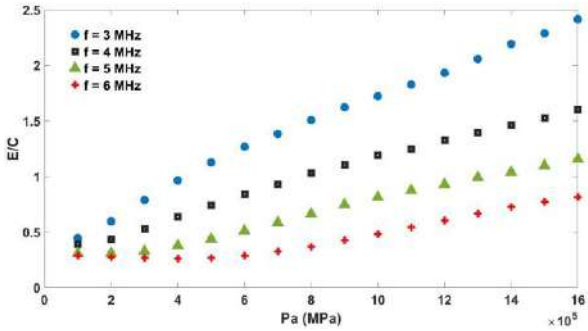

Figure 13. E/C values for a 1.6 µm Sonazoid bubble as a function of excitation pressure at different frequency (in the case of the bubble oscillates near an elastic wall)

In the following, the compression-only behavior of the coated microbubble is investigated by the E/C dimensionless parameter in terms of different excitation pressure amplitudes. As shown in Figure 12, at a constant excitation frequency (3 MHz) and a constant excitation pressure amplitude, the bubble near the elastic wall has a less tendency to maintain the compression-only behavior. Hence, by increasing the amplitude of the excitation pressure from 0.1 to 1.6 MPa, the difference of the dimensionless E/C parameter between the two diagrams of the cases with and without wall increases from 0 to 0.619. In other words, the bubble shell when the bubble is oscillating near an elastic wall will rupture at lower pressure amplitude compared to oscillation in an infinite fluid. It may be due to the suppression of the bubble oscillations near the elastic wall. Oscillation of the bubble near a wall causes a reflected wave from the wall. This reflected wave suppresses bubble Oscillations and the bubble is less likely to retain the compression-only behavior. It is also seen in Figure 13 that for a coated bubble oscillating near an elastic wall, increasing the excitation pressure amplitude, as previously mentioned, attenuates the compression-only behavior, and whatever the excitation frequency will be higher, the disappearance of the compression-only behavior would be delayed. It can be seen that at the excitation frequency of 3 MHz, the compression-only behavior disappears at the excitation pressure of 0.5 MPa. While, at the excitation frequency of 6 MHz even at the excitation pressure amplitude of 1.6 MPa this phenomenon still exists, and at the excitation pressure of 1.6 MPa and for both the excitation frequencies of 3 and 6 MHz, the difference of E/C parameter value is 1.6. Since by increasing the excitation frequency the nonlinear bubble oscillations are limited. Hence, rupturing of the bubble shell requires more excitation pressure amplitude, therefore, the compression-only behavior disappears.

3. 2. Investigation of the Frequency Response of Coated Bubble Near an Elastic Wall In Section 3.2, the physical properties of both the bubble and wall and the nonlinear shell model are selected as before. The sub-harmonic components in modern medical imaging methods are so important, therefore their detection and prediction are imperative. On the other hand, the sub-harmonic components appear in the nonlinear bubble oscillation regime and accordingly at high excitation pressure amplitudes. These components will disappear after a critical excitation pressure amplitude and the bubble frequency-response spectrum will be saturated. Therefore, the nonlinear components cannot be distinguished from noise. Based on this, it is very important to determine the threshold of the excitation pressure amplitude.

In Figure 14, the sub-harmonic thresholds for a Sonazoid bubble with an initial radius of 3 μm and with similar physical properties to that of previously mentioned are given for two states of the nonlinear bubble oscillation near an elastic wall and an infinite fluid. In this graph, the sub-harmonic threshold value as a function of the excitation frequency divided by the bubble resonance frequency is investigated for the nonlinear Marmottant model. In the simulation process, the sub-harmonic components are not present at low excitation pressures, but with increasing the amplitude of the excitation pressure at a certain pressure value, the first sub-harmonics components will appear in the bubble frequency-response spectrum. In fact, the sub-harmonics thresholds occur at a certain value of excitation frequency within a particular excitation pressure range. The figure shows that at a given excitation frequency, the coated bubble near an elastic wall has a higher sub-harmonic threshold. It may be due to the effect of the reflected waves from the wall on the adjacent bubble that makes the bubble to be more resistant against nonlinearity than the bubbles in the infinite fluid. Therefore, the bubble requires more excitation pressure amplitude to produce sub-harmonic components. Thus, it can be concluded that the presence of a wall, in general, does not change the behavior of sub-harmonic components qualitatively, but in terms of quantitative measures, it will change (the sub-harmonic threshold level increases).

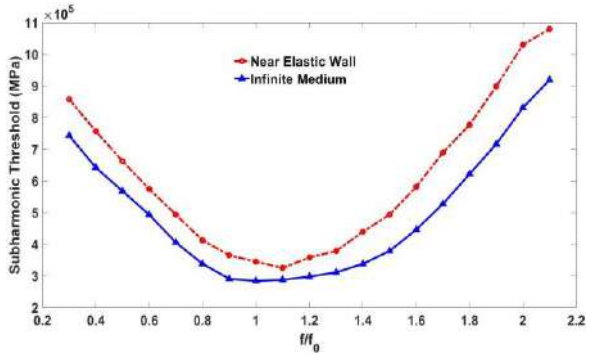

Figure 14. Subharmonic threshold curve for a 3 μm Sonazoid bubble in both cases, the bubble oscillates near an elastic wall and an infinite liquid

4. CONCLUSION

In this paper, the nonlinear behavior of a coated microbubble with a focus on the proximity of an elastic wall is investigated. Initially, as the ability of the selected shell model to predict the nonlinear components is crucial, the effect of the selective shell model on the simulation results for a coated bubble near the elastic wall was investigated using both the De Jong linear shell model and the Marmottant nonlinear shell model. It was found that both models well described the compression-only behavior and difference in the bubble oscillation amplitude. Then, due to the importance of nonlinear bubble oscillations in medical applications, the oscillations of a bubble near an elastic wall in several different excitations have been studied to investigate the nonlinear behavior of the bubble and its compression-only behavior. It was observed that the bubble near the elastic wall is less prone to maintain the compression-only behavior than the bubble in the infinite fluid, and change in the excitation frequency can delay the disappearance of the compression-only behavior. As the excitation pressure amplitude increased from 0.1 to 1.6 MPa, the difference between the two diagrams in the dimensionless E/C parameter in both with and without wall cases enlarged from 0 to 0.619. It was also found that for the bubble oscillation near the elastic wall, with increasing excitation pressure amplitude the intensity of compression-only behavior of the bubble weakened, and whenever the excitation frequency was higher, the disappearance of the compression-only behavior was delayed. Furthermore, because there is a great deal of focus on sub-harmonic components in modern medical imaging techniques, the sub-harmonic threshold has been investigated. Investigations showed that at a given excitation frequency, the coated bubble near an elastic wall has a higher sub-harmonic threshold than the bubble in the infinite fluid.

5. REFERENCES

1. De Jong, N., Hoff, L., Skotland, T., and Bom, N. "Absorption and scatter of encapsulated gas filled microspheres: Theoretical considerations and some measurements." ***Ultrasonics***, Vol. 30, No. 2, (1992), 95–103. https://doi.org/10.1016/0041-624X(92)90041-J
2. Church, C. C. "The effects of an elastic solid surface layer on the radial pulsations of gas bubbles." ***Journal of the Acoustical Society of America***, Vol. 97, No. 3, (1995), 1510–1521. https://doi.org/10.1121/1.412091
3. Hoff, L., Sontum, P. C., and Hovem, J. M. "Oscillations of polymeric microbubbles: Effect of the encapsulating shell." ***The Journal of the Acoustical Society of America***, Vol. 107, No. 4, (2000), 2272–2280. https://doi.org/10.1121/1.428557
4. De Jong, N., Bouakaz, A., and Frinking, P. "Basic acoustic properties of microbubbles." ***Echocardiography***. Vol. 19, No. 3, (2002), 229-240. https://doi.org/10.1046/j.1540-8175.2002.00229.x
5. Brennen, C. Cavitation and bubble dynamics. Oxford University Press, (1995).
6. Leighton, T. G. "The inertial terms in equations of motion for bubbles in tubular vessels or between plates." ***The Journal of the Acoustical Society of America***, Vol. 130, No. 5, (2011), 3333–3338. https://doi.org/10.1121/1.3638132
7. Blake, J. R., and Gibson, D. C. "Cavitation Bubbles Near Boundaries." ***Annual Review of Fluid Mechanics***, Vol. 19, No. 1, (1987), 99–123. https://doi.org/10.1146/annurev.fl.19.010187.000531
8. Herring, C. "Theory of the pulsations of the gas bubble produced

by an underwater explosion." In Technical Report 236, Columbia University, Division of National Defense Research, (1941).

9. Strasberg, M. "The Pulsation Frequency of Nonspherical Gas Bubbles in Liquids." ***Journal of the Acoustical Society of America***, Vol. 25, No. 3, (1953), 536–537. https://doi.org/10.1121/1.1907076
10. Blue, J. E. "Resonance of a Bubble on an Infinite Rigid Boundary." ***The Journal of the Acoustical Society of America***, Vol. 41, No. 2, (1967), 369–372. https://doi.org/10.1121/1.1910347
11. Doinikov, A. A., Zhao, S., and Dayton, P. A. "Modeling of the acoustic response from contrast agent microbubbles near a rigid wall." ***Ultrasonics***, Vol. 49, No. 2, (2009), 195–201. https://doi.org/10.1016/j.ultras.2008.07.017
12. Tomita, Y., and Shima, A. "Mechanisms of impulsive pressure generation and damage pit formation by bubble collapse." ***Journal of Fluid Mechanics***, Vol. 169, (1986), 535–564. https://doi.org/10.1017/S0022112086000745
13. Doinikov, A. A., Aired, L., and Bouakaz, A. "Acoustic response from a bubble pulsating near a fluid layer of finite density and thickness." ***The Journal of the Acoustical Society of America***, Vol. 129, No. 2, (2011), 616–621. https://doi.org/10.1121/1.3531839
14. Garbin, V., Cojoc, D., Ferrari, E., Di Fabrizio, E., Overvelde, M. L. J., Van Der Meer, S. M., De Jong, N., Lohse, D., and Versluis, M. "Changes in microbubble dynamics near a boundary revealed by combined optical micromanipulation and high-speed imaging." ***Applied Physics Letters***, Vol. 90, No. 11, (2007), 114103. https://doi.org/10.1063/1.2713164
15. Doinikov, A. A., and Bouakaz, A. "Interaction of an ultrasound-activated contrast microbubble with a wall at arbitrary separation distances." ***Physics in Medicine and Biology***, Vol. 60, No. 20, (2015), 7909–7925. https://doi.org/10.1088/0031-9155/60/20/7909
16. Overvelde, M., Garbin, V., Dollet, B., De Jong, N., Lohse, D., and Versluis, M. "Dynamics of Coated Microbubbles Adherent to a Wall." ***Ultrasound in Medicine and Biology***, Vol. 37, No. 9, (2011), 1500–1508. https://doi.org/10.1016/j.ultrasmedbio.2011.05.025
17. Aired, L., Doinikov, A. A., and Bouakaz, A. "Effect of an elastic wall on the dynamics of an encapsulated microbubble: A simulation study." ***Ultrasonics***, Vol. 53, No. 1, (2013), 23–28. https://doi.org/10.1016/j.ultras.2012.03.008
18. Garashchuk, I. R., Sinelshchikov, D. I., and Kudryashov, N. A. "Nonlinear Dynamics of a Bubble Contrast Agent Oscillating near an Elastic Wall." ***Regular and Chaotic Dynamics***, Vol. 23, No. 3, (2018), 257–272. https://doi.org/10.1134/S1560354718030036
19. Paul, S., Katiyar, A., Sarkar, K., Chatterjee, D., Shi, W. T., and Forsberg, F. "Material characterization of the encapsulation of an ultrasound contrast microbubble and its subharmonic response: Strain-softening interfacial elasticity model." ***The Journal of the Acoustical Society of America***, Vol. 127, No. 6, (2010), 3846–3857. https://doi.org/10.1121/1.3418685
20. Paul, S. "Acoustic characterization of ultrasound contrast microbubbles and echogenic liposomes: applications to imaging and drug-delivery", Doctoral Dissertations, University of Delaware, USA, (2013). Retrieved from https://udspace.udel.edu/handle/19716/20934
21. Marmottant, P., van der Meer, S., Emmer, M., Versluis, M., de Jong, N., Hilgenfeldt, S., and Lohse, D. "A model for large amplitude oscillations of coated bubbles accounting for buckling and rupture." ***The Journal of the Acoustical Society of America***, Vol. 118, No. 6, (2005), 3499–3505. https://doi.org/10.1121/1.2109427
22. Löfstedt, R., Barber, B. P., and Putterman, S. J. "Toward a hydrodynamic theory of sonoluminescence." ***Physics of Fluids A***, Vol. 5, No. 11, (1992), 2911–2928. https://doi.org/10.1063/1.858700

Persian Abstract

چکیده

از آن جا که در فرایند تصویربرداری فراصوتی عوامل تقابلی فراصوتی در حال ضربان در مجاورت دیواره‌ی رگ خونی هستند، هدف این پژوهش مطالعه‌ی شبیه‌سازی حاضر این است که بررسی کنیم چگونه حضور یک دیواره‌ی کش‌سان بر پاسخ آکوستیک شعاعی و فرکانسی یک میکروحباب عامل تقابلی فراصوتی که در حال نوسان در یک رژیم غیرخطی است، تاثیر می‌گذارد. به‌همین دلیل در این مقاله شبیه‌سازی عددی رفتار دینامیک یک میکروحباب پوشش‌دار با استفاده از کدنویسی در متلب و یک معادله رایلی–پلیست اصلاح شده توسط دوینیکف انجام شده است. به‌منظور بررسی نوسانات غیرخطی حباب، رفتار انقباض غالب آن و مولفه غیرخطی زیرهارمونیک از یک مدل پوسته‌ی غیرخطی که توسط مارموتنت و همکاران ارائه شده، بهره گرفته شده است. ابتدا نوسانات حباب پوشش‌دار در دو رژیم خطی و غیرخطی برای دو نوع مدل پوسته بررسی شده است. درنهایت، به دلیل اهمیت مولفه‌ی زیرهارمونیک در نوسان غیرخطی حباب پوشش‌دار با استفاده از تبدیل فوریه (FFT) آستانه‌ی ظهور مولفه‌های زیرهارمونیک برای یک حباب پوشش‌دار در نزدیکی یک دیواره‌ی کش‌سان بررسی گردیده و با حالت نوسان در مایع بی‌کران مقایسه شده است.

IJE TRANSACTIONS A: Basics Vol. 33, No. 10, (October 2020) 2105-2112

International Journal of Engineering

Journal Homepage: www.ije.ir

Heat Transfer Performance Analysis and Optimization of Exhaust Gas Recirculation Cooler with Different Structural Characteristics

C. H. Liu*[a], S. C. Li[a], C. Liu[b], J. Shi[a], D. M. Zhang[c]

[a] *College of Automobile and Transportation Engineering, Liaoning University of Technology, Jinzhou, China*
[b] *Jinzhou Liansheng Automobile Parts Co., Ltd., Jinzhou, China*
[c] *BMW Brilliance Automotive Ltd., Shenyang, China*

P A P E R I N F O

Paper history:
Received 09 June 2020
Received in revised form 03 July 2020
Accepted 03 August 2020

Keywords:
Exhaust Gas Recirculation Cooler
Heat Transfer
Fluid Simulation
Structural Optimization

A B S T R A C T

In order to improve the heat transfer performance of an exhaust gas recirculation (EGR) cooler, different structural characteristics are numerically and experimentally studied. In numerical analyses, the presented pitted tube model and inner fin model, are compared under two typical working conditions, heat transfer efficiency solutions of inner fin model were 3~5% higher than that of pitted tube model. The inner fin model also gives smaller gas side pressure drop, which is only 17% of the pitted tube model. Then, the structural optimization of the inner fin model by analysing the various amplitude A was investigated. It is shown that increasing A results in increment of heat transfer efficiency and gas side pressure drop, the temperature requirement is satisfied and pressure drop is minimized when A=0.9 mm. The optimized numerical heat transfer efficiency solutions were 86.4% and 84%, and experimental results were 88.5% and 86.3% corresponding to working conditions, respectively. A good agreement was obtained. The optimized inner fin structure can be used efficiently to improve the heat transfer performance for an EGR cooler, the study method has been proven to be feasible by the simulations and experiments.

***doi**: 10.5829/ije.2020.33.10a.29*

NOMENCLATURE

t_{gi}	Gas side inlet temperature (℃)	f	Darcy Friction Factor
t_{go}	Gas side outlet temperature (℃)	v_v	Volume average flow velocity (m/s)
t_{li}	Liquid side inlet temperature (℃)	v	Gas flow velocity (m/s)
t_{lo}	Liquid side outlet temperature (℃)	D	Hydraulic diameter of the pipe (m)
h	Heat transfer coefficient (W/m^2℃)	g	Gravitational constant (m/s^2)
S	Heat transfer area (m^2)	$S_{indirect}$	Indirect heat transfer area (mm^2)
S_s	Section area (m^2)	H	Distance between adjacent fins (mm)
q_m	Mass flow rate (kg/h)	L_w	Wavelength of the fins (mm)
q_{mg}	Gas mass fow rate (kg/h)	A	Amplitude of the fins (mm)
q_{ml}	Liquid mass fow rate (kg/h)	$V_{simulation}$	Value of corresponding simulation
Q	Heat exchanged between the gas and liquid (W)	$V_{experiment}$	Value of corresponding experiment
Q_g	Gas side heat loss (W)	**Greek Symbols**	
Q_l	Liquid side heat gain (W)	η	Heat transfer efficiency (%)
c_{pg}	Specific heat capacity of gas (J/kg℃)	ΔP	Gas side pressure drop (Pa)
c_{pl}	Specific heat capacity of liquid (J/kg℃)	ΔT_{lm}	Log-mean temperature difference (℃)
L	Length of the pipe (m)	ρ	Gas density (kg/m^3)

*Corresponding Author Institutional Email: *qcxy_lch@lnut.edu.cn* (C.H. Liu)

Please cite this article as: C. H. Liu, S. C. Li, C. Liu, J. Shi, D. M. Zhang, Heat Transfer Performance Analysis and Optimization of Exhaust Gas Recirculation Cooler with Different Structural Characteristics, International Journal of Engineering (IJE), IJE TRANSACTIONS A: Basics Vol. 33, No. 10, (October 2020) 2105-2112

1. INTRODUCTION

Because of the implementation of China VI emission standard, all manufacturers are developing diesel engines that satisfy the new emission regulations. EGR systems make the exhaust gas pass through a cooler and valve into the cylinder to burn again, as shown in Figure 1 [1-3], which is an important measure to reduce NOx, which is widely applied to diesel engines [4, 5].

In current products, the spiral tubes in Figure 2(a) are commonly used in an EGR cooler, the heat transfer performance of spiral structure was studied by number of researchers [2, 6-8]. The heat transfer efficiency was shown in the range of 60 to 80% [2, 6, 8, 9]. According to limited studies of pitted tubes (Figure 2b), it was found that more heat transfer area can enhance the heat transfer efficiency and increase the local turbulence of the fluid level significantly [10]. But few studies focussed on its application in an EGR cooler. Some studies considered an inner fin (Figure 2c) structure [2, 11-13] to increase heat radiating area, the efficiency was improved by about 20% compared with the spiral tubes. The fin pitch and wave pitch parameters of the inner fin was studied by number of authors [11, 13, 14] to determine their effects on transfer efficiency, but few studies focussed on the effect of the amplitude parameter in the fin structure.

Based on the above analysis, the widely used traditional spiral tube is not suitable for the strict emission standard. The application of the pitted tube in an EGR cooler has not been studied clearly yet. The inner fin structure has been proved to have good heat transfer performance due to the additional indirect heat transfer area, however the influence of the fin amplitude parameter has not been investigated yet. Hence, in this study the validation is extended and presented below.

The CFD simulation method is universally applied in numerical study [15]. An experiment is usually used to verify the simulation results [16]. Therefore, this study presents two new types of heat transfer structures, such as the pitted tube type and inner fin type, the results are investigated numerically and experimentally. Firstly, in section 2 two types of structures are simulated by widely used Fluent [17, 18], the heat transfer performance is analysed by comparing the gas temperature, velocity, heat transfer efficiency and pressure drop; the heat transfer efficiency of traditional spiral tube is also compared. Then, in section 3 the selected heat transfer structural parameter is optimized. Finally, in section 4 the heat transfer performance experiment is conducted to verify the numerical solutions. Figure 3 presents the flowchart of this study.

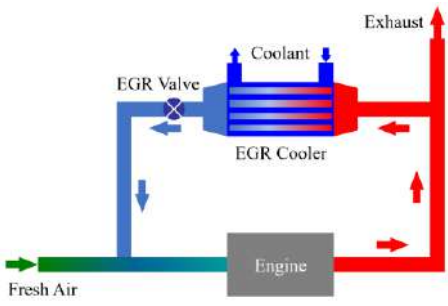

Figure 1. EGR cooler schematic diagram

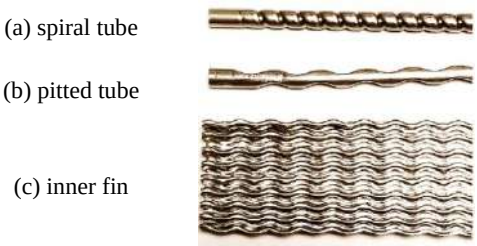

Figure 2. Heat exchange structures

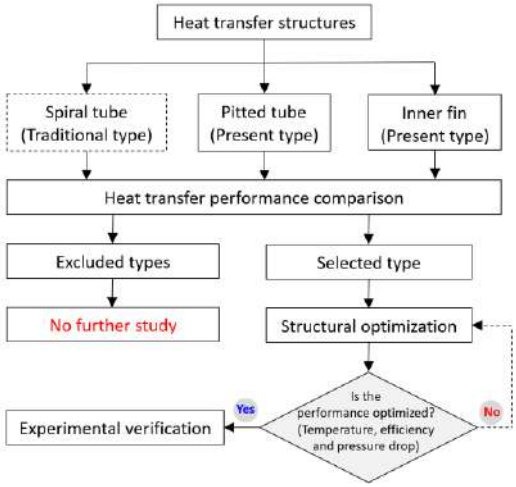

Figure 3. Flowchart of the study

2. COMPARISON OF HEAT TRANSFER SCHEMES

2. 1. Simulation Model Three-dimensional models were established in CATIA (Figure 4). Two coolers have the same external structure size. Table 1 lists the main heat transfer schemes parameters.

The CFD models were meshed by tetrahedral elements. The material of the exhaust gas, coolant and solid were set as dry air, liquid saturated water and 316L stainless steel. A realizable k-epsilon model was selected for calculation, and upwind second-order difference equations were used for the momentum equation and energy equation.

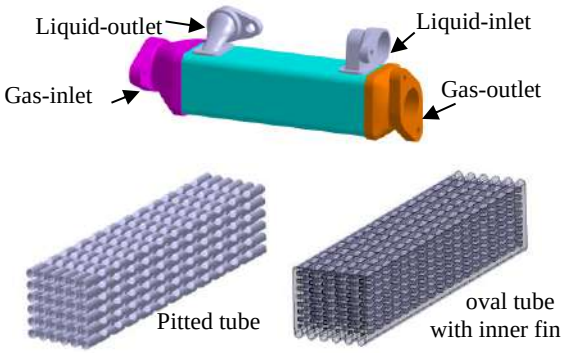

Figure 4. EGR cooler model

TABLE 1. Heat transfer schemes parameters comparison

Model	Number of tubes	Tube Length (mm)	Heat transfer area(mm^2)	
Pitted tube	36	185	Direct	117534
Inner fin	6	185	Direct	103296
			Indirect	289523

2. 2. Boundary Conditions For CFD simulation, the mass flow inlet and the pressure outlet boundary conditions are adopted. According to the real engine test, two representative working conditions (as shown in Table 2) were provided by the engine works to determine the boundary conditions.

2. 3. Simulation Results and Discussion One longitudinal and nine transverse (including inlet and outlet) sections were selected to show the results as defined in Figure 5. Figures 6 and 7 show the gas side temperature distribution and area average velocity under each working condition, respectively. For convenience of comparison, figures chose the same contour range. The area average temperature and velocity data of transverse sections are plotted in Figures 8 and 9. Tables 3 and 4 compare the simulation results of the two kinds of different heat transfer structures under two working conditions. Equation (1) calculates the heat transfer efficiency η [19]. Figure 10 compares heat transfer efficiency values of three types of EGR coolers.

$$\eta = \left(t_{gi} - t_{go}\right) / \left(t_{gi} - t_{li}\right) \quad (1)$$

TABLE 2. Boundary conditions

Working condition	Inlet flow (kg/h)		Inlet temperature(℃)		Target gas outlet(℃)
	Liquid	Gas	Liquid	Gas	
1	1500	78	84.5	495	140
2	1500	86.5	84.0	420	140

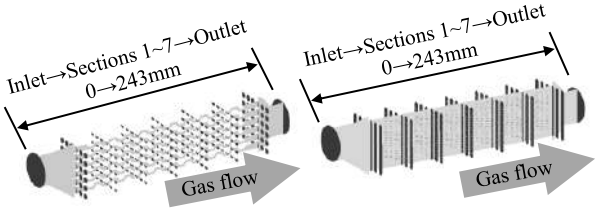

Figure 5. Sections definition

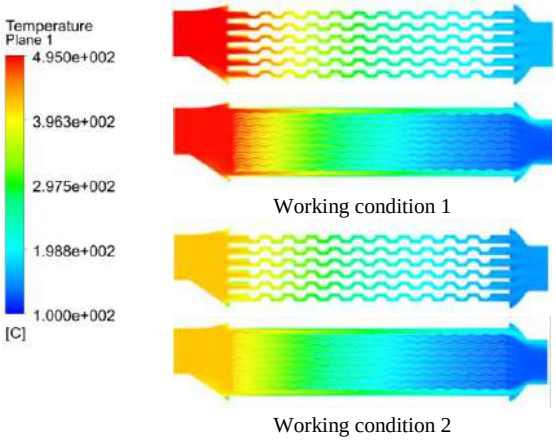

Figure 6. Temperature contours comparison

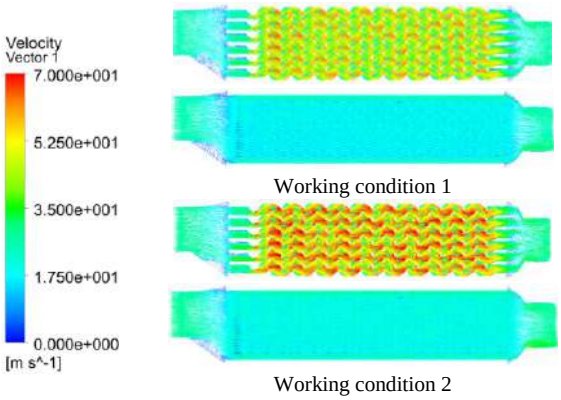

Figure 7. Velocity contours comparison

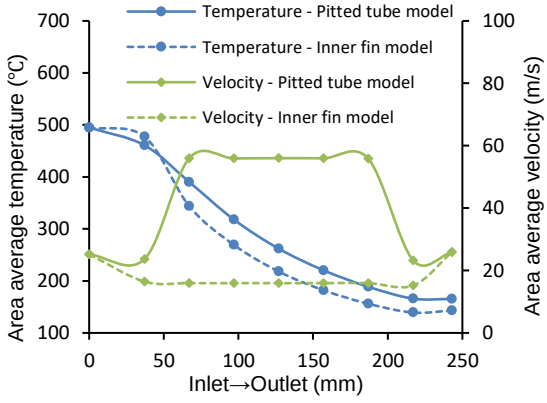

Figure 8. Transverse sections results of working condition 1

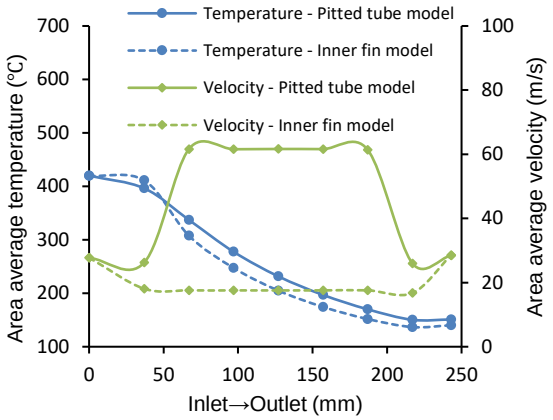

Figure 9. Transverse sections results of working condition 2

From the temperature results in Figures 6, Tables 3 and 4, it is observed that the gas outlet temperature of inner fin model is significantly lower than that in pitted tube model for each working condition. Figures 8 and 9 compare the temperatures from inlet to outlet, the inner fin model shows better cooling performance from section 2 until to outlet. Tables 3 and 4 show that the heat transfer efficiency of the pitted tube is lower than the inner fin schemes. To verify the advantage of the new types of coolers, the heat transfer efficiency results of traditional spiral tube reported in literature [6, 9] are also compared in Figure 10. The advantage of the new types are obvious, the efficiency is improved from 60 to 80% level. Furthermore, the efficiency of the inner fin structure is better than the pitted tube by more than 3~5%. This trend is caused by the indirect area generated by the inner fin model. According to Equations (2), (3) and (4) [20, 21], the heat exchanged between the gas and liquid is related to the heat transfer area, and the outlet temperature will be affected by the heat loss of gas side and heat gained by liquid side. Larger transfer area exchanged more heat and resulted low gas side outlet temperature as compared in Tables 3 and 4.

$$Q = hS\Delta T_{lm} \tag{2}$$

$$Q_g = q_{mg} c_{pg} \left(t_{gi} - t_{go}\right) \tag{3}$$

$$Q_l = q_{ml} c_{pl} \left(t_{li} - t_{lo}\right) \tag{4}$$

It can also be seen from the comparison of flow velocities in Figures 7, 8 and 9 that the highest gas velocity occurs at the pitted tube model under working condition 2. According to the relationship of velocity and cross-section area given by Equation (5) [22], this high flow velocity is caused by large gas inlet flow and relatively smaller cross-section area. Equation (6) [23] reveals the relationship of pressure drop and velocity, smaller cross-section area subsequently causes larger pressure drop, this is verified by the pressure drop results in Tables 3 and 4, the inner fin structure gas side pressure drop is only about 17% of the pitted tube structure, this also confirm the volume average velocity results.

$$v = \frac{q_m}{\rho S_s} \tag{5}$$

$$\Delta P = f \frac{L}{D} \frac{\rho v^2}{2g} \tag{6}$$

As discussed above, the present two types of heat transfer structures have obvious advantage in heat transfer efficiency. Because of the unstable diesel quality in China, the reduction of the pressure drop can effectively prevent the formation of carbon deposition, the inner fin type model with low pressure drop will be more suitable for the application. However, the outlet temperature to of the gas side is slightly higher than the design target in condition 1; the inner fin heat transfer structure needs to be optimized to meet the requirements better.

TABLE 3. Results of working condition 1

Model	Pitted tube	Inner fin
t_o (°C)	165.3	143.1
ΔP (Pa)	9890	1728
V_v (m/s)	29.2	16.3
η	80.3%	85.7%

TABLE 4. Results of working condition 2

Model	Pitted tube	Inner fin
t_o (°C)	150.0	140.2
ΔP (Pa)	11583	2031
V_v (m/s)	32.2	18.0
η	80.4%	83.3%

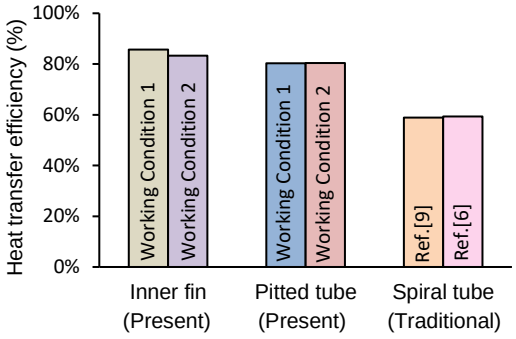

Figure 10. Heat transfer efficiency of different structures

3. INNER FIN STRUCTURE OPTIMIZATION

3. 1. Optimization Parameters Determination of Inner Fin Figure 11 shows the basic structure, the indirect area can be extended and heat transfer performance can be improved by reducing the wavelength Lw and the wave spacing H according to literature [11, 13, 14]. However, the effect of amplitude A has not been clearly studied for an EGR cooler. In theory, when A is reduced, the fin ripple structure tends to be smooth, the indirect transfer area will reduce, which will also reduce the heat transfer ability [24]. When A is increased, the gas turbulence area will extend and the cooling efficiency will be enhanced [25].

The parameters of the original fin model are L_w = 10 mm, H = 2 mm, and A = 0.6 mm. According to design experience and relevant research, the space used to continue to reduce the size of L and H for optimization is very small. Therefore, the main optimization parameter is the fin amplitude A. Based on the original fin structure scheme, different amplitudes A = 0.9 mm, A = 1.2 mm and A = 1.5 mm are built for comparative analysis. Table 5 summarizes the indirect areas of different A.

3. 2. Optimization Results and Discussion The boundary conditions were consistent with those of the earlier stage. Figure 12 is the comparison of the results of outlet temperature and heat transfer efficiency according to changing A. Figure 13 compares the results of gas pressure drop and volume average velocity according to changing in A. Figure 14 illustrates the velocity vector of different A under each working condition.

In Figure 12, it can be found that the outlet temperature and efficiency of condition 1 are higher than condition 2, this trend is related to the relatively high inlet temperature according to Equations (1) ~ (4). Figure 12 also shows that increasing amplitude A (increasing indirect transfer area) results in improvements of the gas outlet temperature and heat transfer performance. When A = 1.5 mm, the efficiency is the best, reaching 88.3% in condition 1.

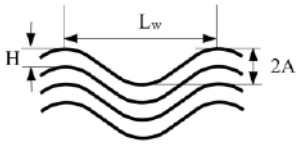

Figure 11. Geometric parameters of wavy inner fin

TABLE 5. Comparison of indirect heat transfer area

A(mm)	0.6	0.9	1.2	1.5
$S_{indirect}(mm^2)$	289523	296646	306711	319535

In Figures 13 and 14, it can be seen that the flow velocity and pressure drop of condition 1 are lower than condition 2 because of the smaller mass flow rate of condition 1, according to Equation (5). In Figures 13 and 14 it also can be seen that the velocity is increased with A, according to the relationship of velocity and pressure given by Equation (6). The pressure drop also increases rapidly, and the pressure drop on the gas side reaches its maximum when A = 1.5 mm. When A = 0.9 mm, the gas-outlet temperature of condition 1 is 140.2 ℃, condition 2 is 137.7 ℃, which are close to the design requirements, and the pressure drop of condition 1 is 2121 Pa, condition 2 is 2292 Pa, which are approximately 30% lower than that of A = 1.5 mm.

Considering that a larger pressure drop will accelerate the ageing of the cooler, the gas side pressure drop should be reduced as much as possible. According to design experience and similar research, the simulated outlet temperature is usually higher than the experimental value [26, 27], so A = 0.9 mm was chosen as the optimized value, it can meet the design requirements and minimize the pressure drop.

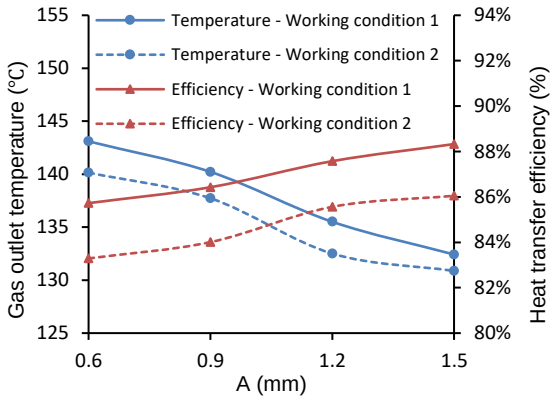

Figure 12. Temperatures and efficiencies of different A

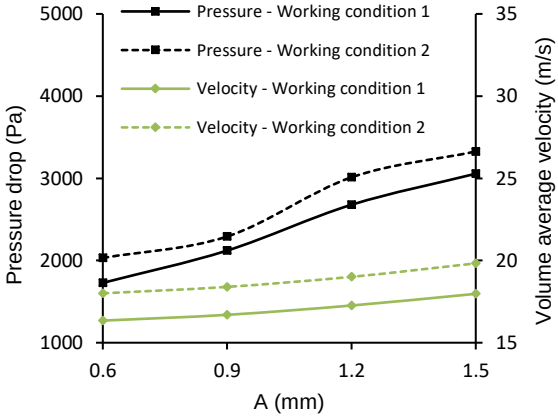

Figure 13. Pressure and velocities of different A

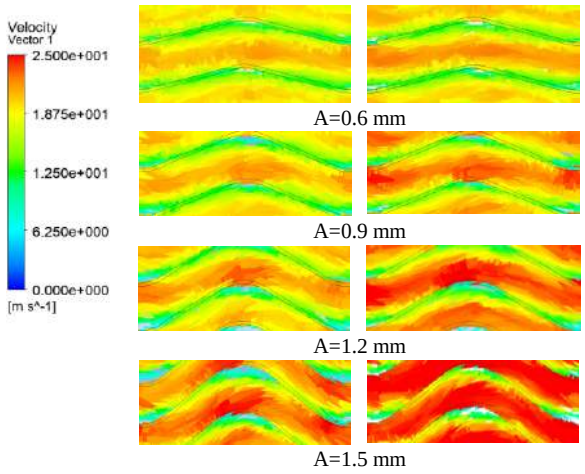

Figure 14. Velocity contours of different A

4. HEAT TRANSFER PERFORMANCE EXPERIMENT

A sample product was manufactured, and the adapter was matched with the heat exchange performance test bench (Figure 15).

Tables 6 and 7 are the experiment and simulation comparisons of the gas side outlet temperatures and heat transfer efficiency under two working conditions, respectively. The difference between the experimental and simulated results is calculated by Equation (7):

$$Difference = \left(V_{simulation} - V_{experiment}\right)/V_{experiment} \times 100\% \quad (7)$$

In Table 6, the simulation data of the gas side outlet temperature is approximately 6% higher than the actual experiment, the calculation accuracy is good, which conforms to the accuracy range of similar simulation [27].

By comparing data stated in Table 7, the actual experimental heat transfer efficiency is slightly higher than that of the simulation value, which also conforms to the trend that the temperature simulation value is higher

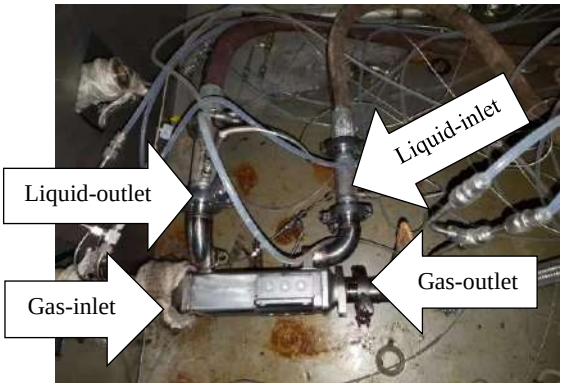

Figure 15. Product and test bench

TABLE 6. Gas outlet temperature comparison

Working condition	Simulation (℃)	Experiment (℃)	Present Difference	Ref. Difference
1	140.2	131.5	6.6%	8.6% [27]
2	137.7	130.0	6.0%	

TABLE 7. Heat transfer efficiency comparison

Working condition	Simulation	Experiment	Present Difference	Ref. Difference
1	86.4%	88.5%	-2.4%	-3.97% [6]
2	84.0%	86.3%	-2.7%	

than the experimental value. The heat transfer efficiency deviation value is less than 3%, compared with the difference of similar study [6], the present simulation accuracy is good.

From the above results, the simulation data and the experimental data are in good agreement. The optimized scheme has a certain design margin, which can effectively compensate for the degradation caused by the ageing during actual use.

5. CONCLUSION

To meet the development requirements, an EGR cooler was designed and manufactured. Two new types of coolers were numerically investigated by comparing the heat transfer area, temperature variation, heat transfer efficiency, flow velocity and gas pressure drop. The efficiency results were also compared by the traditional spiral tube. Then, due to the advantages in comparisons, the inner fin model was selected for subsequent structural optimization to meet the temperature and pressure drop requirements. Finally, the optimized model was verified by experiment, and the following conclusions are obtained:

(1) Heat transfer efficiencies of new types (pitted tube and inner fin) are above 80%, have approximate 20% advantage compared with the traditional spiral tube. The heat transfer efficiency of inner fin model is 3~5% higher than the pitted tube due to the indirect transfer area.

(2) The cross-section flow velocity of inner fin model is about 30% of pitted tube model, and the pressure drop of the inner fin cooler is about only 17% of the pitted tube type. The pressure drop advantage of the inner fin structure is obvious.

(3) Through the inner fin structure optimization, the gas outlet temperature decreases and efficiency increases with the increasing amplitude A. Larger A also leads to high velocity and pressure drop. In order to meet the temperature target and minimize the pressure drop, A is

optimized as 0.9 mm. Numerical t_{go}=140.2 ℃ and 137.7℃, ΔP=2121 Pa and 2292 Pa for working conditions 1 and 2, respectively.

(4) The experimental temperature results are about 6% lower than the numerical values, and the heat transfer efficiency results were slightly higher (less than 3%) than the numerical values. The results are in good agreement with numerical values.

Thus, the study has achieved the purpose of improving the heat transfer performance of an EGR cooler, it will be beneficial for similar developments. However, the optimization was processed by comparing the given geometric parameters, more accurate algorithm and multi parameters optimization will be considered in the future study.

6. REFERENCES

1. Shabgard, H., Kheradmand, S., Farzaneh, H. and Bae, C., "Numerical simulation of cooling performance of an exhaust gas recirculation (EGR) cooler using nano-fluids", ***Applied Thermal Engineering***, Vol. 110, (2017), 244-252. DOI: 10.1016/j.applthermaleng.2016.08.139
2. Hoseini, S.S., Najafi, G., Ghobadian, B., Yusaf, T. and Mamat, R., "Experimental and numerical analysis of flow and heat transfer characteristics of EGR cooler in diesel engine", ***Applied Thermal Engineering***, Vol. 140, (2018), 745-758. DOI: 10.1016/j.applthermaleng.2018.05.058
3. Kim, H.-M., Lee, D.-H., Park, S.-K., Choi, K.-S. and Wang, H.-M., "An experimental study on heat exchange effectiveness in the diesel engine EGR coolers", ***Journal of Mechanical Science and Technology***, Vol. 22, No. 2, (2008), 361-366. DOI: 10.1007/s12206-007-1102-x
4. Pourfallah, M., Ranjbar, A.A., Mirsalim, S.M. and Mirsalim, S.M., "Studying the Effect of Reformer Gas and Exhaust Gas Recirculation on Homogeneous Charge Compression Ignition Engine Operation", ***International Journal of Engineering, Transactions B: Applications***, Vol. 28, No. 8, (2015), 1199-1208. DOI: 10.5829/idosi.ije.2015.28.08b.13
5. Mohebbi, A., Jafarmadar, S., Pashae, J. and Shirnezhad, M., "Experimental Studying of the Effect of EGR Distribution on the Combustion, Emissions and Perforemance in a Turbocharged DI Diesel Engine", ***International Journal of Engineering, Transactions A: Basics***, Vol. 26, No. 1, (2013), 73-82. DOI: 10.5829/idosi.ije.2013.26.01a.10
6. Hoseini, S.S., Najafi, G. and Ghobadian, B., "Experimental and numerical investigation of heat transfer and turbulent characteristics of a novel EGR cooler in diesel engine", ***Applied Thermal Engineering***, Vol. 108, (2016), 1344-1356. DOI: 10.1016/j.applthermaleng.2016.08.018
7. Ghassembaglou, N. and Torkaman, L., "Efficient design of exhaust gas cooler in cold EGR equipped diesel engine", ***Alexandria Engineering Journal***, Vol. 55, No. 2, (2016), 769-778. DOI: 10.1016/j.aej.2016.01.023
8. Jang, S., Park, S., Choi, K. and Kim, H., "Experimental investigation of the influences of shape and surface area on the EGR cooler efficiency", ***Heat and Mass Transfer***, Vol. 47, No. 6, (2010), 621-628. DOI: 10.1007/s00231-010-0754-8
9. Seo, Y.-H., Lee, H.-M., Jeon, S.-K., Ku, T.-W., Kang, B.-S. and Kim, J., "Homogenization of dimpled tube and its application to structural integrity evaluation for a dimple-type EGR cooler using FEM", ***International Journal of Precision Engineering and Manufacturing***, Vol. 13, No. 2, (2012), 183-191. DOI: 10.1007/s12541-012-0023-5
10. Fu, Z., Research on Heat Transfer Performance of Pits Flat Tube. 2016, Hubei University of Technology: Wuhan.
11. Park, S., Choi, K., Kim, H. and Lee, K., "Influence of PM fouling on effectiveness of heat exchanges in a diesel engine with fin-type EGR coolers of different sizes", ***Heat and Mass Transfer***, Vol. 46, No. 11-12, (2010), 1221-1227. DOI: 10.1007/s00231-010-0652-0
12. Park, S.-K., Lee, J. and Kim, H.-M., "Experimental study on the spiral and oval spiral EGR cooler efficiencies in a diesel engine", ***Heat and Mass Transfer***, Vol. 50, No. 12, (2014), 1783-1789. DOI: 10.1007/s00231-014-1362-9
13. Lee, J. and Min, K., "A study of the fouling characteristics of EGR coolers in diesel engines", ***Journal of Mechanical Science and Technology***, Vol. 28, No. 8, (2014), 3395-3401. DOI: 10.1007/s12206-014-0752-8
14. Jang, S.-H., Hwang, S.-J., Park, S.-K., Choi, K.-S. and Kim, H.-M., "Effects of PM fouling on the heat exchange effectiveness of wave fin type EGR cooler for diesel engine use", ***Heat and Mass Transfer***, Vol. 48, No. 6, (2011), 1081-1087. DOI: 10.1007/s00231-011-0950-1
15. Kostikov, Y.A. and Romanenkov, A.M., "Approximation of the Multidimensional Optimal Control Problem for the Heat Equation (Applicable to Computational Fluid Dynamics (CFD))", ***Civil Engineering Journal***, Vol. 6, No. 4, (2020), 743-768. DOI: 10.28991/cej-2020-03091506
16. Topçuoğlu, K., "Trombe Wall Application with Heat Storage Tank", ***Civil Engineering Journal***, Vol. 5, No. 7, (2019), 1477-1489. DOI: 10.28991/cej-2019-03091346
17. Janani, M., Prakash, D., Harini, E. and Harish, T., "Enhancement of Heat Transfer over a Double Forward Facing Step with Square Obstacle through Taguchi's Optimization Technique", ***International Journal of Engineering, Transactions B: Applications***, Vol. 30, No. 8, (2017), 1253-159. DOI: 10.5829/ije.2017.30.08b.19
18. Sengupta, A.R., Gupta, R. and Biswas, A., "Computational Fluid Dynamics Analysis of Stove Systems for Cooking and Drying of Muga Silk", ***Emerging Science Journal***, Vol. 3, No. 5, (2019), 285-292. DOI: 10.28991/esj-2019-01191
19. Chen, Y.Y., Cai, Y.X., Li, X.H., Shi, Y.X. and Zheng, Y., "Experimental study on regenerating fouled EGR cooler by ntpi technology", ***International Journal of Automotive Technology***, Vol. 16, No. 2, (2015), 183-191. DOI: 10.1007/s12239-015-0020-7
20. Pradeep, G.V. and Narasimha, K.R., "Experimental Investigations on the Thermal Performance of a Vertical Closed Loop Pulsating Heat Pipe Using Binary Mixture of Fluids", ***International Journal of Engineering, Transactions B: Applications***, Vol. 31, No. 5, (2018). DOI: 10.5829/ije.2018.31.05b.16
21. Zhang, W., Yang, X., Wang, T., Peng, X. and Wang, X., "Experimental Study of a Gas Engine-driven Heat Pump System for Space Heating and Cooling", ***Civil Engineering Journal***, Vol. 5, No. 10, (2019), 2282-2295. DOI: 10.28991/cej-2019-03091411
22. F.Bailin, Pei, Z., H.Ganghan and W.YanJun, "Research on Properties of Fluid Pressure Drop for Electric Vehicle IGBT Pin Fin Heat Sink", ***International Journal of Engineering, Transactions A: Basics***, Vol. 28, No. 4(A), (2015). DOI: 10.5829/idosi.ije.2015.28.04a.18
23. Al-Obaidi, A.R., "Investigation of fluid field analysis, characteristics of pressure drop and improvement of heat transfer in three-dimensional circular corrugated pipes", ***Journal of Energy Storage***, Vol. 26, (2019), 101012. DOI: 10.1016/j.est.2019.101012

24. Li, X.N., Research on design and performance optimization of diesel engine waste heat recovery bottoming system and exhaust heat exchanger. 2014, Tianjin University: Tianjin.

25. Wang, Y., He, H., Xu, Z. and Liu, J., "Thermodynamic Performance Simulation of Diesel EGR Cooler with Finned Tube ", ***Advanced Materials Research***, Vol. 97-101, (2010), 3345-3348. DOI: 10.4028/www.scientific.net/AMR.97-101.3345

26. Ren, X.S., Simulation and experimental study on EGR cooler of automovile diesel engine. 2013, Zhejiang University: Hangzhou.

27. Lu, L., Zhang, Z.D. and Yin, C.B., "Performance simulation and structure improvement of EGR cooler", ***China Mechanical Engineering***, Vol. 26, No. 17, (2015), 2369-2373. DOI: 10.3969/j.issn.1004-132X.2015.17.016

Persian Abstract

چکیده

به منظور بهبود عملکرد انتقال حرارت کولر گشتاور اگزوز (EGR)، خصوصیات ساختاری مختلف به صورت عددی و تجربی مورد مطالعه قرار گرفته است. در آنالیزهای عددی ، مدل لوله سوراخ دار ارائه شده و مدل باله داخلی در دو شرایط کاری معمولی مقایسه می شوند ، راه حل های بازده انتقال حرارت مدل باله داخلی ۵ ۳ ۳ بیشتر از مدل لوله سوراخ دار است. مدل داخلی باله همچنین افت فشار جانبی گاز کمتری را نشان می دهد که تنها ۱۷٪ مدل لوله سوراخ دار است. سپس بهینه سازی ساختاری مدل باله داخلی با تجزیه و تحلیل دامنه های مختلف A مورد بررسی قرار گرفت. نشان داده شده است که افزایش A منجر به افزایش راندمان انتقال حرارت و افت فشار جانبی گاز می شود ، دمای مورد نیاز رضایت بخش است هنگامی که A = 0.9 میلی متر افت می کند افت فشار به حداقل می رسد. راه حل های بهینه سازی انتقال حرارت عددی بهینه شده ۸٦/٤ درصد و ۸٤ درصد و نتایج آزمایش به ترتیب با ۸۸/۵ درصد و ۸٦/۳ درصد مربوط به شرایط کار بودند. توافق خوبی حاصل شد. از ساختار باله داخلی بهینه شده می توان برای بهبود عملکرد انتقال حرارت برای یک کولر EGR استفاده کرد، روش مطالعه با استفاده از شبیه سازی ها و آزمایشات اثبات شده است.

International Journal of Engineering

Journal Homepage: www.ije.ir

Influence of Geological and Technological Parameters on Effectiveness of Hydrochloric Acid Treatment of Carbonate Reservoirs

S. N. Krivoshchekov*[a], K. A. Vyatkin[b], K. A. Ravelev[b], A. A. Kochnev[a,c]

[a] *Department of Petroleum Geology, Perm National Research Polytechnic University, Perm, Russia*
[b] *Department of Oil and Gas Technology, Perm National Research Polytechnical University, Perm, Russia*
[c] *Branch of LLC "LUKOIL-Engineering"-"PermNIPIneft", Perm, Russia*

PAPER INFO

Paper history:
Received 08 April 2020
Received in revised form 03 July 2020
Accepted 21 July 2020

Keywords:
Carbonate Deposits
Correlation Dependencies
Flow Studies
Hydrochloric Acid Treatment
Stimulation of Oil Production
Tomographic Research

ABSTRACT

Hydrochloric acid treatment is the most common oil production stimulation treatment to date. Yet, most of operations fail to deliver the targeted results. For a more competent design of acid treatment of carbonate reservoirs, flow studies on core samples are conducted preliminary to determine the most effective acid composition and the technology of its injection into formation. The authors believe that, at present, processing of flow research results is incorrect, as not all parameters are taken into account when making recommendations. This study examined the influence of geological and technological parameters on effectiveness of hydrochloric acid treatment. In the course of studies using the flow unit and X-ray tomography, a number of factors have been identified that affect the outcome of the treatment. The volume of acid composition required to create a highly conductive channel in a core sample is a parameter using which it is possible to conduct a comparative analysis of effectiveness of the acid compositions under test and the methods of their injection. Therefore, exactly this parameter is used as a core in this paper, based on which the authors have derived an integrated indicator that provides for the most reliable evaluation of the flow study results. Using this indicator, it is possible to provide more competent recommendations as to the choice of acid compositions and the technology of oilfield hydrochloric acid treatments, which will provide the greatest effect of the planned operations to enhance oil recovery.

***doi**: 10.5829/ije.2020.33.10a.30*

NOMENCLATURE

V_{AC}	Acid composition volume in pore volume, required to create a through channel	k_p	Coefficient of absolute gas permeability of a core sample before treatment (10^{-3} μm^2)
q	Rate of acid composition injection into a core sample (cm^3/min)	P_{inj}	Maximum excess pressure of acid composition injection into a core sample (MPa)
Karbon	Carbonate content of a rock sample (%)		

1. INTRODUCTION

More than 50% of oil in the Volga-Ural region (Russia) is recovered from carbonate rocks that feature complex geology, low porosity and permeability properties. This causes a wide range of issues in their development [1]. Various geotechnical procedures (GTP) applied to enhance reservoir properties, increase reservoir-to-well hydrodynamic connectivity and decrease flow resistance in the bottom hole zone (BHZ).

Hydrochloric acid treatment (HAT) is one of the most common methods of oil production stimulation for carbonate rocks, as of today [2–6]. The high effectiveness of acid treatment results from the growth of field

*Corresponding Author Email: *krivoshchekov@gmail.com* (S.N. Krivoshchekov)

Please cite this article as: S. N. Krivoshchekov, K. A. Vyatkin, K. A. Ravelev, A. A. Kochnev, Influence of Geological and Technological Parameters on the Effectiveness of Hydrochloric Acid Treatment of Carbonate Reservoirs, International Journal of Engineering (IJE), IJE TRANSACTIONS A: Basics Vol. 33, No. 10, (October 2020) 2113-2119

indicators following the geotechnical procedures. The relevance of scientific studies in the interaction of hydrochloric acid compositions with carbonate rocks is stipulated by a very extensive practice of application of this technology.

To enhance the effectiveness of the hydrochloric acid effect on reservoir, a large number of modifications of acid compositions (AC) are being currently developed, contributing to the individual nature of the process of the treatment of productive sediments near wellbore [7–9]. To exercise a competent approach to the design of hydrochloric acid treatment, physical and chemical properties of formation fluids, lithologic and mineralogical composition, type of rock paleolithic facies and pressure-temperature conditions will be taken into account [10]. Furthermore, the success of well stimulation measures is achieved by preliminary evaluation of oil production growth, carried out with the help of hydrodynamic simulators [11, 12] and using the results of laboratory studies [13–21].

Simulation of the AC injection into oil-bearing reservoir is performed under laboratory conditions with the help of core testing flow units. Up-to-date laboratory equipment enables to recreate realistic reservoir conditions when performing a HAT. The key objective of the flow unit application is to determine the effectiveness of a particular AC under set conditions of its injection into a rock. One of the principal evaluation parameters is the volume of acid composition in the pore volume required for 'breakthrough', i.e. the creation of a high-conductive channel. This parameter allows performing an integrated analysis of AC selection effectiveness and technological parameters of its injection.

As part of this research, works presenting core sample flow studies and evaluation of their results as per above indicator have been reviewed. The authors believe that currently the processing of flow test results is incorrect, due to the determination of AC efficiency based on a single parameter indicated in recommendations when conducting the hydrochloric acid treatment at the oilfield.

Thus, for example, works [22–24] present diagrams of the obtained dependency of the AC amount in pore volume at breakthrough on the rate of its injection into a rock sample. The above papers demonstrate a relationship between these parameters. The presented dependency is used to study and derive results of the AC application effectiveness determination based on the results of laboratory tests. The analysed materials have become the reason for doubts, which called for the assumption of the presence of a number of other additional parameters that comprehensively affect the acidizing effectiveness, enable reliable evaluation of the results of core sample flow studies and provision of recommendations on hydrochloric acid treatment to maximize well productivity. This study is relevant due to the small number of successful treatments at real sites, despite preliminary laboratory studies, extensive experience in the application and simplicity of this bottomhole zone treatment technology [25, 26].

2. MATERIALS AND METHODS

2. 1. Effectiveness Factors in Acid Treatment

To support the advanced hypothesis, the objective of the integrated research of factors that affect the effectiveness of acidification will allow to competently design hydrochloric acid treatment of wells to achieve the target values. To achieve this objective, authors carried out flow tests on standard core samples using AFS-300 modular computer-controlled system. The rock samples were collected from a carbonate reservoir of a field that is a part of the petroleum play of Perm Krai. Due to high heterogenic nature and stratification, the core samples were collected for research over the entire interval of oil-saturated formation thickness from the wells of the target facility

Mineralogical composition, as it is known, impacts the success of the HAT. To reduce errors in remove the further study, experiments were carried out to determine the carbonate content of samples from the formation under study. These samples were referenced by depth against the core samples tested on AFS-300 flow unit, which was implemented to minimize errors. The experiments were performed using a KM-04M carbonate metering device that allows determining the mass ratio of calcite, dolomite, and insoluble residue in the sample under study. According to obtained results, quite a wide range of variation in the carbonate content of the deposit understudy was established - from 82.6 to 97.9 %

In the next stage, the principal part of laboratory work was conducted on the above mentioned flow unit. For more extensive coverage of the results and to accurately establish the factors that affect the amount of AC when forming a 'wormhole', tests were conducted on 27 samples from the target facility. The acid composition was selected based on the analytical review of scientific works, FLUXOCORE-210 has been selected as the most effective acid composition that delivered proven application results [27]. According to obtained field data, it is assumed that the following factors influence the determination of the AC volume in the pore volume at breakthrough V_{AC}:

- Karbon – carbonate content of a rock sample (%);
- q – rate of acid composition injection into a core sample (cm^3/min);
- P_{inj} – maximum excess pressure of acid composition injection into a core sample (MPa);
- k_p – coefficient of absolute gas permeability of a core sample before treatment (10^{-3} μm^2).

Prior to AC injection into the core sample, the k_p value was determined using the flow unit for further

dependency study. It was determined in advance by the authors, the injection rate was constant during the process of AC injection due to stable operation of the injection pump. Using pressure sensors on two ends of the standard core sample, the flow unit was recording the values from the two ends continuously during the experiment. After the test, when processing the results, the authors determined P_{inj} from the graphs and deduced the dependencies presented hereinafter.

The authors have proposed an integrated indicator given in Equation (1). This study is mainly aimed to investigate the influence of the integrated indicator on the V_{AC} parameter.

$$k = \frac{P_{inj} \cdot q}{\frac{Karbon}{100} \cdot k_p} \quad (1)$$

The arrangement of parameters in the numerator and denominator relies on the V_{AC} increase/decrease through the increase/decrease of independent parameters. For example, it is known that a sample with high permeability from straight calcite requires a smaller amount of acid to create a high-conductive channel. Then the V_{AC} will be increasing with higher pressures and injection rates.

2. 2. Conducting of Flow and Tomography Studies

To check the advanced assumption given in Equation (1), the procedure of determination of correlation dependency between the presented parameters was carried out, by analogy with the work reported in literature [28].

For example, the authors hereof have presented processing of the results that describes the process of V_{AC} determination upon completion of testing of a rock samples under test in the flow unit. A simulation of acid treatment design at reservoir pressure of 13.2 MPa, P_{inj} was 1.668 MPa, where the 'wormholing' has commenced. The analysis of the diagram in Figure 1 allowed to determine that the injected volume of acid, which was equal to 1.162 in pore volume, created a valid through the channel, the beginning and the end of which can be seen at the ends of the core sample (Figure 2). To make the creation of a full end-to-end channel more convincing the authors carried out studies on the microfocus system of X-ray test with the function of computer tomography on the basis of X-ray of Nikon X-ray unit Metrology XT H22. This system allows visualizing the void space by creating a 3D model. The results of the study conducted before and after the AC injection into the rock sample allow to visually assess changes in the structure of the void space. Based on these results, it is possible to accurately determine the degree of void space growth, as well as the direction and nature of 'wormholing' in the rock sample when simulating the AC injection in the flow unit.

Figure 3 shows images of 3D models of the void space of the sample under study before and after AC injection in the flow unit. Comparative analysis of the

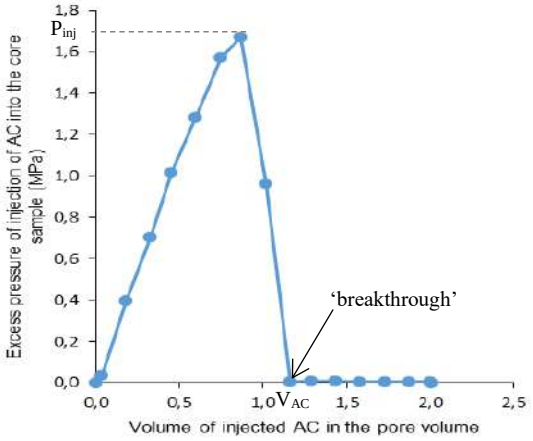

Figure 1. Dynamics of change in excess pressure of AC injection into the core sample with volume of injected AC in pore volume

(a)

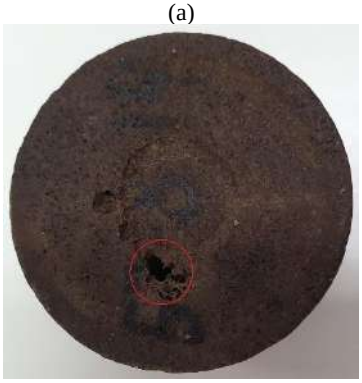

(b)

Figure 2. Photographs of core end faces after acid treatment: (a) inlet; (b) outlet

image of 3D-models of the void space structure allows to draw a conclusion about the growth of the total void and creation of a high-conductive channel in the sample under study from the reviewed productive formation. The figure above clearly shows the system of voids in the sample before AC treatment, which changes significantly after the flow test. Figure 3(b) visually illustrates the formed 'wormholing' that commenced at P_{inj} equal to

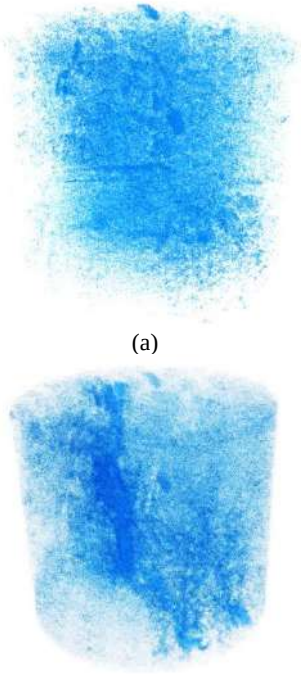

(a)

(b)

Figure 3. Images of 3D models of void space structure of the sample under study: a) before acid treatment; b) after acid treatment

1.668 MPa. During the injection of V_{AC} equal to 1.162, a valid through channel was formed under the influence of excessive injection pressure and AC solvent power.

The authors hereof tested all 27 samples following the same pattern to establish the characteristics of dependencies and confirm the proposed hypothesis. The significance of the proposed expression constitutes the larger proportion, because with its help, the evaluation of the choice of parameters at hydrochloric acid treatment will comprehensively cover a range of factors rather than a single one.

3. RESULTS OF CORRELATION DEPENDENCIES DETERMINATION

Upon the detailed description of the laboratory method of determining the V_{AC} value, and the 'wormhole' representation we can proceed to determination of characteristics of the strength of the relationship between independent parameters and V_{AC}. Expertise in the correlation analysis allows to estimate the significance of linear relationship between two sets of values. With the help of linear coefficient of pair correlation, it is possible to give a statistical estimation of the calculations made by the authors, i.e. to check the considered dependencies for adequacy. Figure 4 show diagrams of V_{AC} dependencies on P_{inj}, q, Karbon and k_p, respectively, based on the results of laboratory testing of 27 core samples. The pair correlation coefficients presented in Table 1 were derived from these graphs, as well.

By analysing the diagrams (Figure 4) and the values in Table 1, we can qualitatively characterize the strength of relationship of parameters on the Chaddock scale. The coefficient of pair correlation between the number sets of q and V_{AC} is very low, so there is no relationship between these parameters. This suggests the wrong approach to evaluating the results given in the above works. The presented results of the laboratory studies show that it is impossible to derive any dependencies on the two parameters under consideration, therefore, 'validated' conclusions on these indicators are incorrect. It is also noted that the relationship between the two pairs of sets $P_{inj} - V_{AC}$ and $k_p - V_{AC}$ are characterized by high strength. High negative value of the pair correlation coefficient corresponds to the second pair of number sets, which indicates the inverse relationship of the specified parameters, as assumed in Equation (1). Given that the pair correlation coefficients of $q - V_{AC}$ and Karbon $- V_{AC}$ sets are very small, it is impossible to confirm the position in the numerator or denominator for each independent parameter.

The results of the conducted analysis of dependencies of independent parameters and V_{AC} allow to state that the research of one parameter only makes it unsubstantiated to process flow studies with the subsequent provision of recommendations on HAT at problem facilities due to underestimation of other factors. In the absence of analysis of other parameters, oil production stimulation jobs may fail to achieve the targeted results.

Further, the relationship between the integrated indicator proposed by the authors hereof and the V_{AC} has been studied, the diagram of their dependency given in Figure 5. The linear coefficient of the pair correlation is 0.874, which is significant. On the Chaddock scale, the coefficient characterizes a very strong relationship. It means that the proposed idea of the integrated approach to the evaluation of the AC effectiveness and injection conditions, based on the V_{AC} parameter, has a statistical validity, since there is a high correlation relationship.

Visually, Figure 5 shows that the dependency trend (Equation (1)) tends to the power law. This is also confirmed by the highest value of approximation

TABLE 1. Obtained Coefficients of Pair Correlation of Parameters Influencing the AC Volume in the Pore Volume at Breakthrough

Parameter	Pair Correlation Coefficient
P_{inj}	0.82472
q	-0.13149
Karbon	-0.01289
k_p	-0.75491

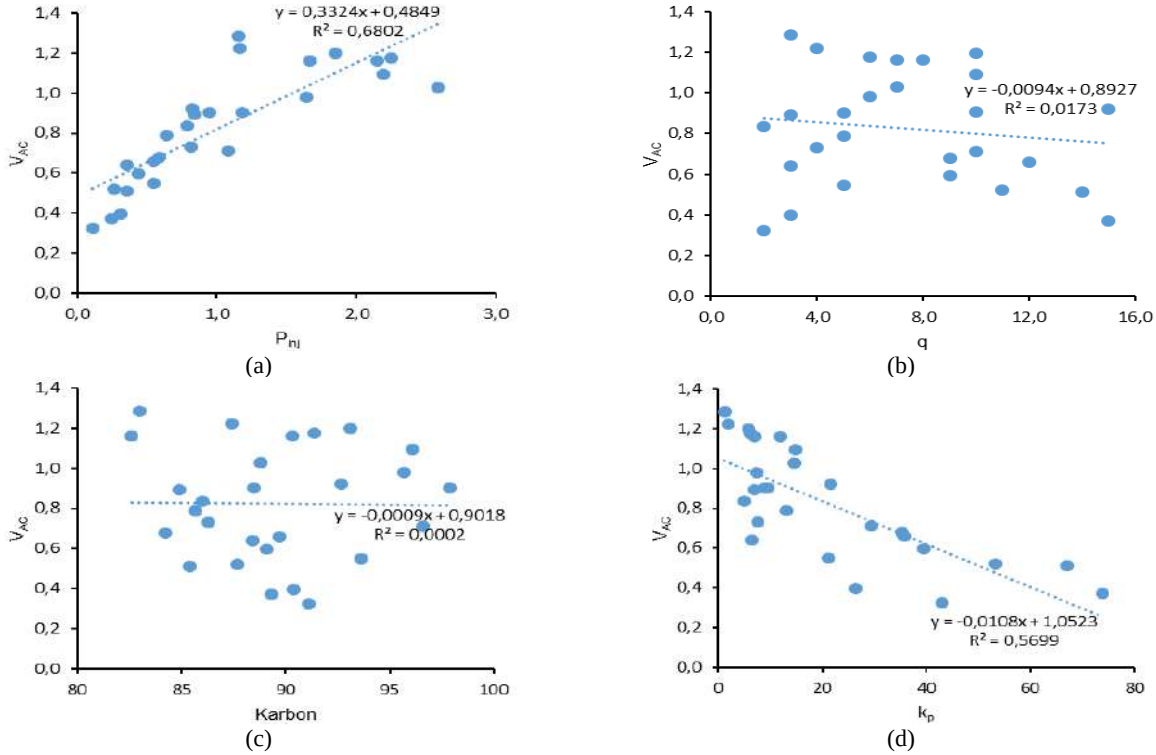

Figure 4. Diagrams of dependency of AC volume in pore volume at breakthrough on: a) maximum excess pressure of AC injection into core sample; b) AC injection rate into core sample; c) carbonate content of rock sample; d) absolute gas permeability coefficient of core sample before treatment

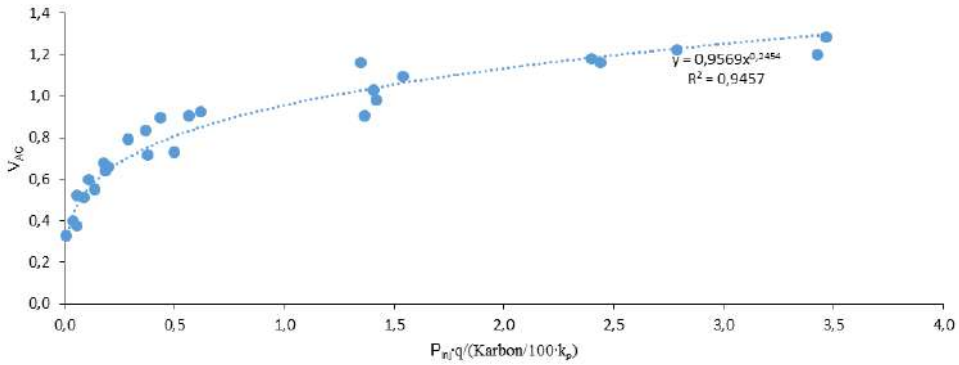

Figure 5. Diagram of dependency of AC volume in pore volume at breakthrough on the integrated indicator proposed by the authors herein

coefficient R^2 (Table 2). The reviewed dependency is best described by the power-law equation given below (Equation (2)):

$$V_{AC} = 0{,}9569 \cdot \left(\frac{P_{inj} \cdot q}{\frac{Karbon}{100} \cdot k_p} \right)^{0{,}2454} \quad (2)$$

This conclusion is based both on visual impressions and on rigorous quantitative calculation using approximation coefficient. Due to the high value of valid approximation between such two sets of numbers as an integrated

TABLE 2. Obtained Values of Approximation Coefficients for Various Regression Equations

Dependency	R-Squared Value
Exponential	0.6271
Polynomial	0.8791
Linear	0.7636
Power-Law	0.9457
Logarithmic	0.9176

indicator and V_{AC}, we can say that the proposed indicator has a valid proof of application in the comparative characteristics of the AC effectiveness and the technological conditions of its injection. The average inaccuracy of the calculated V_{AC} value is 7.1%. It is critical to use this parameter for more substantiated recommendations on acid treatment of carbonate reservoirs based on the results of flow and X-ray tomography studies. To make the most of the oil recovery enhancement, the integrated indicator including lithologic, mineralogical and flow properties of the reservoir, as well as technological parameters of AC injection, shall be taken into account. At present, the given dependency is unique and relevant, since a large number of hydrochloric acid treatment jobs do not deliver target figures, due to under-researched features of the acidification process

4. CONCLUSION

In the conclusion, it is noted that the dependency (1) advanced by the authors has been confirmed. This dependency is validated by statistical indicators calculated based on laboratory research on the core samples from the oilfield in Perm Krai. The authors emphasize the fact that the V_{AC} is affected by a number of factors. These parameters depend on the way acid is injected into the core sample, and flow, lithologic and mineralogical properties of the rock sample. An individual study of each independent parameter may cause invalid results. Following the study results, the integrated indicator has been proposed, which can be used as a reference coefficient to evaluate the AC effectiveness and to determine the most optimal injection technology. Further practical application of this set of parameters will result in an increased number of efficient geotechnical procedures and enhance the effectiveness of oil production stimulation methods.

5. ACKNOWLEDGEMENTS

This research was carried out with the financial support of the Ministry of Science and Higher Education of the Russian Federation as part of a government assignment. "Grant number FSNM-2020-0027"

6. REFERENCES

1. Avdeev, I. V., and Kochnev, A. A. "Analysis of geological-technical measures efficiency on the example of the tournaisian-famennian object of the Ozernoye deposit." ***Geology, Geophysics and Development of Oil and Gas Fields***, Vol. 337, No. 1, (2020), 48–52. https://doi.org/10.30713/2413-5011-2020-1(337)-48-52 [Russian]
2. Singh, R., Tong, S., Panthi, K., and Mohanty, K. K. "Stimulation of calcite-rich shales using nanoparticle-microencapsulated acids." ***SPE Journal***, Vol. 24, No. 6, (2019), 2671–2680. https://doi.org/10.2118/195695-PA
3. Ridner, D., Frick, T., Zhu, D., Hill, A. D., Angeles, R., Vishnumolakala, N., and Shuchart, C. "Influence of transport conditions on optimal injection rate for acid jetting in carbonate reservoirs." ***SPE Production and Operations***, Vol. 35, No. 1, (2019), 137–146. https://doi.org/10.2118/189546-PA
4. Sarmah, A., Farid Ibrahim, A., Nasr-El-Din, H., and Jackson, J. "A New Cationic Polymer System That Improves Acid Diversion in Heterogeneous Carbonate Reservoirs." ***SPE Journal***, (2020). https://doi.org/10.2118/194647-pa
5. Moid, F., Rodoplu, R., Nutaifi, A. M., and Kayumov, R. "Acid Stimulation Improvement with the use of New Particulate Base Diverter to Improve Zonal Coverage in HPHT Carbonate Reservoirs." In International Petroleum Technology Conference, Society of Petroleum Engineers (SPE), (2020). https://doi.org/10.2523/iptc-20154-abstract
6. Aidagulov, G., Gwaba, D., Kayumov, R., Sultan, A., Aly, M., Qiu, X., Almajed, H., and Abbad, M. "Effects of pre-existing fractures on carbonate matrix stimulation studied by large-scale radial acidizing experiments." In SPE Middle East Oil and Gas Show and Conference, MEOS, Society of Petroleum Engineers (SPE), (2019). https://doi.org/10.2118/195153-ms
7. Alkandari, D. K., AlTheferi, G. M., Almutawaa, H. M., Almutairi, M., Alhindi, N., Al-Rashid, S. M., and Al-Bazzaz, W. H. A. "Technical advancement of carbonate acid stimulation injection." In Kuwait Oil and Gas Show and Conference 2019, KOGS, Society of Petroleum Engineers (SPE), (2019). https://doi.org/10.2118/197982-ms
8. M. Kh. Musabirov, A. Yu. Dmitrieva, RF Khusainov, EM Abusalimov, BG Ganiev, and FZ Ismagilov. "Efficiency improvement of foam-acid treatments and selective large-volume acidizing at carbonate reservoirs of Tatneft PJSC." ***Oil Industry Journal***, Vol. 2019, No. 11, (2019), 116–119. Retrieved from https://www.onepetro.org/journal-paper/OIJ-2019-11-116-119-RU [Russian]
9. Shirley, R. M., and Hill, A. D. "Experimental investigation of particulate polylactic acid diversion in matrix acidizing." In SPE International Symposium on Oilfield Chemistry, Society of Petroleum Engineers (SPE), (2019). https://doi.org/10.2118/193565-ms
10. Kootiani, R. C. "Investigation of a Powerful Tool for the Development of Thinly Bedded Carbonate Reservoirs." ***International Journal of Engineering Journal - Transactions C: Aspects*** , Vol. 27, No. 12, (2014), 1945–1952. https://doi.org/10.5829/idosi.ije.2014.27.12c.18
11. Khuzin, R., Shevko, N., and Melnikov, S. "Improving Well Stimulation Technology Based on Acid Stimulation Modeling, Lab and Field Data Integration." In SPE Russian Petroleum Technology Conference, Society of Petroleum Engineers (SPE), (2019). https://doi.org/10.2118/196976-MS
12. Ali, M. T., Ezzat, A. A., and Nasr-El-Din, H. A. "A Model To Simulate Matrix-Acid Stimulation for Wells in Dolomite Reservoirs with Vugs and Natural Fractures." ***SPE Journal***, Vol. 25, No. 02, (2020), 0609–0631. https://doi.org/10.2118/199341-pa
13. Hall-Thompson, B., Ernesto, A. R., Abdulrahman, N., and Alsuhaimi, A. "Acid stimulation-best practices for design, selection and testing of acid recipes in low permeability carbonate reservoirs." In International Petroleum Technology Conference (IPTC), (2020). https://doi.org/10.2523/iptc-19690-ms
14. Abdrazakov, D., Ziauddin, M., Vernigora, D., Beletskaya, A., Yakimchuk, I., Olennikova, O., Usoltsev, D., Nikolaev, M., Panga, M., and Burlibayev, A. "Integration of latest laboratory,

software and retarded acid technologies to increase efficiency of acid treatments in carbonates: Case studies from central Asia." In International Petroleum Technology Conference (IPTC), (2019). https://doi.org/10.2523/iptc-19546-ms

15. Phan Thi, L. A., Do, H. T., and Lo, S. L. "Enhancing decomposition rate of perfluorooctanoic acid by carbonate radical assisted sonochemical treatment." ***Ultrasonics Sonochemistry***, Vol. 21, No. 5, (2014), 1875–1880. https://doi.org/10.1016/j.ultsonch.2014.03.027
16. S. N. Krivoshchekov, A. A. Melekhin, M. S. Turbakov, A. A. Shcherbakov, and N. I. Krysin. "Development of a telemetric system for monitoring downhole parameters in the course of wells construction." ***Oil Industry Journal***, Vol. 2017, No. 9, (2017), 86–88. Retrieved from https://www.onepetro.org/journal-paper/OIJ-2017-09-086-088-RU [Russian]
17. Kameda, T., Tochinai, M., and Yoshioka, T. "Treatment of hydrochloric acid using Mg–Al layered double hydroxide intercalated with carbonate." ***Journal of Industrial and Engineering Chemistry***, Vol. 39, (2016), 21–26. https://doi.org/10.1016/j.jiec.2016.04.018
18. Liu, N., and Liu, M. "Simulation and analysis of wormhole propagation by VES acid in carbonate acidizing." ***Journal of Petroleum Science and Engineering***, Vol. 138, (2016), 57–65. https://doi.org/10.1016/j.petrol.2015.12.011
19. Snoeck, C., and Pellegrini, M. "Comparing bioapatite carbonate pre-treatments for isotopic measurements: Part 1-Impact on structure and chemical composition." ***Chemical Geology***, Vol. 417, (2015), 394–403. https://doi.org/10.1016/j.chemgeo.2015.10.004
20. Burgos-Cara, A., Ruiz-Agudo, E., and Rodriguez-Navarro, C. "Effectiveness of oxalic acid treatments for the protection of marble surfaces." ***Materials and Design***, Vol. 115, (2017), 82–92. https://doi.org/10.1016/j.matdes.2016.11.037
21. Ghommem, M., Zhao, W., Dyer, S., Qiu, X., and Brady, D. "Carbonate acidizing: Modeling, analysis, and characterization of wormhole formation and propagation." ***Journal of Petroleum Science and Engineering***, Vol. 131, (2015), 18–33. https://doi.org/10.1016/j.petrol.2015.04.021
22. Glushchenko, V., and Ptashko, O. "Filtratrion research of novel acidic compounds for treatment of carbonate reservoirs (Russian)." ***Perm Journal of Petroleum and Mining Engineering***, Vol. 2014, No. 11, (2014), 45–56. https://doi.org/10.15593/2224-9923/2014.11.5 [Russian]
23. Trushin, Y., Aleshchenko, A., Danilin, K., Folomeev, A., Haydar, A., Gorin, A., and Sharifullin, A. "Complex approach to the design of acid treatment of carbonate reservoirs." In Society of Petroleum Engineers - SPE Russian Petroleum Technology Conference (RPTC), (2019). https://doi.org/10.2118/196977-ms
24. Plotnikov, V., Rekhachev, P., Barkovsky, N., Amirov, A., Mikhaylov, N., and Popov, S. "Study in efficiency of acid compositions application in the clastic reservoirs of perm region based on experimental studies of core sample." In Society of Petroleum Engineers - SPE Russian Petroleum Technology Conference (RPTC), (2018). https://doi.org/10.2118/191667-18rptc-ms
25. Liu, P., Yao, J., Couples, G. D., Ma, J., Huang, Z., and Sun, H. "Modeling and simulation of wormhole formation during acidization of fractured carbonate rocks." ***Journal of Petroleum Science and Engineering***, Vol. 154, (2017), 284–301. https://doi.org/10.1016/j.petrol.2017.04.040
26. Santos, R. M., Chiang, Y. W., Elsen, J., and Van Gerven, T. "Distinguishing between carbonate and non-carbonate precipitates from the carbonation of calcium-containing organic acid leachates." ***Hydrometallurgy***, Vol. 147–148, (2014), 90–94. https://doi.org/10.1016/j.hydromet.2014.05.001
27. Putilov, I., Krivoshchekov, S., Vyatkin, K., Kochnev, A., and Ravelev, K. "Methods of Predicting the Effectiveness of Hydrochloric Acid Treatment Using Hydrodynamic Simulation." ***Applied Sciences***, Vol. 10, No. 4828, (2020), 1–13. https://doi.org/10.3390/app10144828
28. Aggarwal, Y., Aggarwal, P., Sihag, P., Pal, M., and Kumar, A. "Estimation of punching shear capacity of concrete slabs using data mining techniques." ***International Journal of Engineering - Transactions A: Basics***, Vol. 32, No. 7, (2019), 908–914. https://doi.org/10.5829/ije.2019.32.07a.02

Persian Abstract

چکیده

تیمار چاه نفت با اسید هیدروکلریک رایج‌ترین روش تحریک تولید نفت تا به امروز است. با این حال، بسیاری از عملیات نتوانسته نتایج هدفمندی را ارائه دهد. به منظور طراحی صحیح‌تر برای تصفیه اسید مخازن کربنات، مطالعات جریان در نمونه‌های هسته اولیه برای تعیین مؤثرترین ترکیب اسید و فناوری تزریق آن در شکل‌گیری انجام می‌گیرد. نویسندگان معتقدند، در حال حاضر، پردازش نتایج تحقیقات جریان نادرست است، زیرا همه پارامترها هنگام تهیه در نظر گرفته نمی‌شوند. در این مطالعه تأثیر پارامترهای زمین‌شناسی و فناوری در اثربخشی تیمار اسید هیدروکلریک مورد بررسی قرار گرفت. در طی مطالعات با استفاده از واحد جریان و توموگرافی اشعه ایکس عوامل مختلفی شناسایی شده‌اند که بر نتیجه درمان تأثیر می‌گذارد. حجم ترکیب اسید مورد نیاز برای ایجاد یک کانال بسیار رسانا در یک نمونه اصلی یک پارامتر است که با استفاده از آن می‌توان تجزیه و تحلیل مقایسه‌ای از اثربخشی ترکیبات اسیدی مورد آزمایش و روش‌های تزریق آن‌ها را انجام داد. بنابراین، دقیقاً از این پارامتر به عنوان هسته در این مقاله استفاده می‌شود، بر اساس آن نویسندگان یک شاخص یکپارچه را تهیه کرده‌اند که قابل اطمینان‌ترین ارزیابی نتایج مطالعه جریان را فراهم می‌کند. با استفاده از این شاخص، می‌توان توصیه‌های صحیح‌تری در مورد انتخاب ترکیبات اسیدی و فناوری تیمارهای اسید هیدروکلریک اسید نفتی ارائه داد، که بیشترین تأثیر عملیات برنامه‌ریزی شده را برای تقویت بازیافت نفت ارائه می‌دهد.

AIMS AND SCOPE

The objective of the International Journal of Engineering is to provide a forum for communication of information among the world's scientific and technological community and Iranian scientists and engineers. This journal intends to be of interest and utility to researchers and practitioners in the academic, industrial and governmental sectors. All original research contributions of significant value focused on basics, applications and aspects areas of engineering discipline are welcome.

This journal is published in three quarterly transactions: Transactions A (Basics) deal with the engineering fundamentals, Transactions B (Applications) are concerned with the application of the engineering knowledge in the daily life of the human being and Transactions C (Aspects) - starting from January 2012 - emphasize on the main engineering aspects whose elaboration can yield knowledge and expertise that can equally serve all branches of engineering discipline.

This journal will publish authoritative papers on theoretical and experimental researches and advanced applications embodying the results of extensive field, plant, laboratory or theoretical investigation or new interpretations of existing problems. It may also feature - when appropriate - research notes, technical notes, state-of-the-art survey type papers, short communications, letters to the editor, meeting schedules and conference announcements. The language of publication is English. Each paper should contain an abstract both in English and in Persian. However, for the authors who are not familiar with Persian, the publisher will prepare the latter. The abstracts should not exceed 250 words.

All manuscripts will be peer-reviewed by qualified reviewers. The material should be presented clearly and concisely:

- *Full papers* must be based on completed original works of significant novelty. The papers are not strictly limited in length. However, lengthy contributions may be delayed due to limited space. It is advised to keep papers limited to 7500 words.
- *Research* notes are considered as short items that include theoretical or experimental results of immediate current interest.
- *Technical notes* are also considered as short items of enough technical acceptability with more rapid publication appeal. The length of a research or technical note is recommended not to exceed 2500 words or 4 journal pages (including figures and tables).

Review papers are only considered from highly qualified well-known authors generally assigned by the editorial board or editor in chief. Short communications and letters to the editor should contain a text of about 1000 words and whatever figures and tables that may be required to support the text. They include discussion of full papers and short items and should contribute to the original article by providing confirmation or additional interpretation. Discussion of papers will be referred to author(s) for reply and will concurrently be published with reply of author(s).

INSTRUCTIONS FOR AUTHORS

Submission of a manuscript represents that it has neither been published nor submitted for publication elsewhere and is result of research carried out by author(s). Presentation in a conference and appearance in a symposium proceeding is not considered prior publication.

Authors are required to include a list describing all the symbols and abbreviations in the paper. Use of the international system of measurement units is mandatory.

- On-line submission of manuscripts results in faster publication process and is recommended. Instructions are given in the IJE web sites: www.ije.ir-www.ijeir.info
- Hardcopy submissions must include MS Word and jpg files.
- Manuscripts should be typewritten on one side of A4 paper, double-spaced, with adequate margins.
- References should be numbered in brackets and appear in sequence through the text. List of references should be given at the end of the paper.
- Figure captions are to be indicated under the illustrations. They should sufficiently explain the figures.
- Illustrations should appear in their appropriate places in the text.
- Tables and diagrams should be submitted in a form suitable for reproduction.
- Photographs should be of high quality saved as jpg files.
- Tables, Illustrations, Figures and Diagrams will be normally printed in single column width (8cm). Exceptionally large ones may be printed across two columns (17cm).

PAGE CHARGES AND REPRINTS

The papers are strictly limited in length, maximum 6 journal pages (including figures and tables). For the additional to 6 journal pages, there will be page charges. It is advised to keep papers limited to 3500 words.

Page Charges for Papers More Than 6 Pages (Including Abstract)	
For International Author ***	**$55 / per page**
For Local Author	**100,000 Toman / per page**

AUTHOR CHECKLIST

- Author(s), bio-data including affiliation(s) and mail and e-mail addresses).
- Manuscript including abstracts, key words, illustrations, tables, figures with figure captions and list of references.
- MS Word files of the paper.

International **J**ournal of **E**ngineering, P.O. Box 13145-1659, Tehran, I.R. Iran
Materials and Energy Research Center, 5 Ahuramazda St., Alvand Ave., Argentina Sq., Tehran, Islamic Republic of Iran
www.merc.ac.ir - www.emerc.ac.ir

THOMSON REUTERS

WEB OF SCIENCE

Scopus®

CAS®
A DIVISION OF THE
AMERICAN CHEMICAL SOCIETY

Google
Scholar